JPL Publication 97-21, Vol. 1

Summaries of the Seventh JPL Airborne Earth Science Workshop January 12–16, 1998

Volume 1. AVIRIS Workshop

Robert O. Green
Editor

December 1998

National Aeronautics and
Space Administration

Jet Propulsion Laboratory
California Institute of Technology
Pasadena, California

This publication was prepared by the Jet Propulsion Laboratory, California Institute of Technology, under a contract with the National Aeronautics and Space Administration.

Abstract

This publication contains the summaries for the Seventh JPL Airborne Earth Science Workshop, held in Pasadena, California, on January 12-16, 1998. The main workshop is divided into three smaller workshops, and each workshop has a volume as follows:

1. Airborne Visible/Infrared Imaging Spectrometer (AVIRIS) Workshop

2. Airborne Synthetic Aperture Radar (AIRSAR) Workshop

3. Thermal Infrared Multispectral Scanner (TIMS) Workshop

Contents

Volume 1: AVIRIS Workshop

VOLUME 2: AIRSAR TABLE OF CONTENTS

VOLUME 3: TIMS TABLE OF CONTENTS

USING MIXTURE ANALYSIS FOR SOIL INFORMATION EXTRACTION FROM AN AVIRIS SCENE AT THE WALNUT GULCH EXPERIMENTAL WATERSHED - ARIZONA

L. Accioly, A.R. Huete, K. Batchily

The University of Arizona
Soil, Water and Environmental Science Dept.
429 Shantz Bldg. #38 Tucson-AZ 85721

Introduction

Due to its ubiquitous presence, soil is present in almost all applications of image-based spectral mixture analysis (SMA). In many studies, however, most of the interest is given to the fraction of the vegetation endmember and its relationship to plant biophysical parameters (Dereck et al., 1996; Leeuwen et al., 1997). One of the few examples of the application of mixture analysis directly to soil is given by Huete and Escadafal (1991). These authors used SMA for soil biophysical information extraction in the region from 400 to 900 nm . They found that the variability of 46 soils from different types of environments could be explained by four independent basis curves, which in linear combination were able to reconstitute the experimental data set. These authors, however, did not use spectral mixture analysis to produce soil spectral maps.

Mixture analysis can be applied on the basis of spectra extracted from the image (image endmembers) and/or on the basis of pure spectra from lab of field (reference endmembers). When the spatial variability within a pixel is high, as in a semiarid scrubland, mixture analysis on the basis of image endmembers has been shown more accurate than maximum likelihood supervised classification (Fernandes et al. 1996)

The general objective of this study was to derive soil spectral maps of an AVIRIS scene at the Walnut Gulch Experimental Watershed using mixture analysis. The specific objectives are to: (a) evaluate the dimensionality of AVIRIS data (i.e., how many endmembers); (b) find the physical meaning of the dimensions (i.e., what feature in the ground each endmember represents); and (c) determine the spatial abundances of the endmembers throughout the AVIRIS scene of the Walnut Gulch Experimental Watershed.

Methodology

The study site is located within the Walnut Gulch Experimental Watershed, Tombstone, Arizona. The area of the Watershed imaged by AVIRIS is dominated by six soil series: McAllister, Stronghold, Graham, Tombstone, Baboquivari and Epitaph (Fig. 1). When considering the parent material, some of the major soils in this Watershed such as Stronghold and Tombstone were largely influenced by the presence of limestone, while others, such as Baboquivari and McAllister have as their parent material mixed fan alluvium. Graham and Epitaph soil series are dark soils originating from slope alluvium and residuum from basaltic rocks.

AVIRIS data were collected over the study area on May 14, 1991(dry season). The original image was displayed and each band was examined for noise. A total of 167 "good" bands resulted from this visual inspection . The original AVIRIS image came as a scaled radiance image and was processed to continental surface reflectance imagery by using the Atmosphere Removal Program (ATREM) (Gao et al., 1996). The atmospheric model was midlatitude summer with derivation of water vapor using the default center channels for areas covered by soils (Gao et al., 1996).

Field Spectra Collection

Field spectra were collected for bare soils and other materials such as vegetation (grass, forbes, shrubs), rocks, and litter with an SE590 Spectron spectroradiometer for the range of 0.45 to 0.90 μm, with 10 nm sampling interval and 15° field of view. Each of the six soil series had one representative spectra except Stronghold which had three due to the differences in surface cover.

Spectral Mixture Analysis

The general form of the SMA equation for each band is:

$$P_c = \sum_{i=1}^{N} F_i R_{i,c} + E_c \qquad \text{with the constraint that}$$

$$\sum_{i=1}^{N} F_i = 1$$

where P_c is the relative reflectance value in channel c of an image pixel; F_i is the fraction of the endmember i; $R_{i,c}$ is the relative reflectance of the endmember i in channel c; N is the number of endmembers; and E_c is the error for channel c of the fit of N spectral endmembers.

For a better selection of reference and image endmembers, the soil field spectra were clustered and the spectral classes analyzed. Field spectra were collected for the interval from 0.45 to 0.90 μm. A 10 percent constant reflectance curve was tested as a shade image endmember.

To avoid use of extensive spectral libraries, target test analysis (Malinowski and Howery, 1980) was utilized to test for suspected reference endmembers in the AVIRIS scene:

$$[R]_{real} = [R]_A[T]$$

$$T_i = [\lambda]^{-1}[R]_A^I R_i$$

where $[R]_{real}$ is the real reference endmember spectra matrix, $[R]_A$ is the abstract reference endmember spectra matrix , [T] is the transformation matrix , T_i is a least squares column vector transformer for each of the n endmembers, and R_i is the associated target test column vector, containing the spectral signatures of the suspected reference endmembers. To determine if the spectral signature of the suspected reference endmembers is present in the data set, we compute the predicted spectral signature R_p:

$$R_p = [R]_A T_i .$$

If each element of the predicted spectral signature is equal to the corresponding element of the test signature, within experimental error, then the suspected reference endmember is present in the data set and the column vector transformer T_i is included in the transformation matrix.

Results and Discussion

Mixture Analysis Using Image Endmembers

The cluster analysis showed that four soil classes can be separated from the field spectra. One of the spectral classes encompasses Stronghold, Tombstone and Baboquivari soil series while the other soil series

(McAllister, Graham, and Epitaph) fall in three different classes. These results gave the starting point for the selection of image endmembers through the location of pixels where the soil field spectra were collected. In addition to the soil image endmember, a green vegetation image endmember was included in the model. The visual inspection of the error image was used as the criteria for selecting the best combination of image endmembers. The best combination of image endmembers was given by the spectra of pixels extracted from the following areas: McAllister soil, Stronghold soil, Graham soil and green vegetation. The fact that Graham and Epitaph are spectrally too dark made the modeled shade spectra useless. Thus, the visual inspection of the error images from the models that included modeled shade, Graham and Epitaph soils, presented no significant differences when mixed with the other selected image endmembers (McAllister, Stronghold, and green vegetation). The combined average rms error after applying mixture analysis to the 167 AVIRIS bands was 2.6 % reflectance.

The fraction images were rescaled to remove the contribution of green vegetation and soil spectral maps were produced for each of the soil image endmembers. Figures 2 and 3 present the spectral maps for Graham and McAllister soils. The map for McAllister fraction image shows that most of pixels containing more than 70% of this soil are located in the left portion of the AVIRIS image. These results agreed with field observations of the spatial distribution of McAllister soil. However, areas occupied by baboquivari and part of the area occupied by Stronghold were misclassified as containing a high proportion of McAllister. Pixels having less than 30 % of McAllister soil are located in the upper left corner, and in the middle bottom of the AVIRIS image. The map for Graham soil/shade image endmember shows that pixels with more than 70 % of the area covered by this endmember correspond to areas occupied by Graham and Graham Lampshire soils. Areas with more than 35 % of Graham soil/shade image endmember that are close to Graham soil were associated to Epitaph soil series (compare to Fig. 1). Since Graham, Graham Lampshire and Epitaph soils do not occur in the left side nor in the upper part of the AVIRIS image, the spectral map for these portions was highly influenced by topographic shade. Thus, shade occurrence was less in the gentler slope areas occupied by McAllister than in the Stronghold areas which are more affected by the slop

Mixture Analysis Using Reference Endmembers

Target testing was applied to the AVIRIS image to detect the presence of reference endmembers. Since most of the spectral library (including all spectra other than soils) was collected for the range 0.45 to 0.90 μm, we used a subset spectral range of the AVIRIS data for modeling the image on the basis of reference endmembers. Target testing successfully predicted the presence of at least seven reference endmembers: McAllister, Stronghold, and Graham soils, dry forbes, litter, dry grass, and green vegetation (given by the spectra of walnut leaf). Figure 4 presents two examples of the results of target testing. The error in the predicted spectra occurred mostly in the NIR and was attributed to the uneven correction of the atmospheric effect by ATREM

The seven reference endmember spectra were used for modelling 46 bands of AVIRIS data in the inteval from 0.45 to 0.90 μm. Spectral mixture analysis, however, could not be successfully applied to the combination of the seven reference endmembers. Smith et al. (1994) pointed out that the input of a high number of reference endmembers can result in an unstable solution for the fraction due to the loss of contrast between endmembers. Roberts et al. (1992) suggested the use of a subset of AVIRIS data in mixture analysis as one way to work with the high number of reference endmembers.

In this study, a subset of nine pixels extracted from each of the following soils; McAllister, Stronghold, and Graham were used for spectral recomposition on the basis of the reference endmembers detected by target testing. Six of the seven reference endmembers were found on those pixels. As an example, the spectra from pixels extracted from McAllister were mixed with the spectra from litter and dry forbes (Fig 5a). Figure 5b shows the contribution of each material for the mixed spectra of McAllister soil. The average rms error for the fit of the model for these pixels was 2.5 % reflectance. Fractions of green vegetation as low as 10 % were detected in pixels extracted from Stronghold and Graham soils.

Conclusions

The SMA produced soil spectral maps with good agreement with field results for the following image endmembers: McAllister, Stronghold, and Graham soils. Graham and shade fractions were spectrally similar but

could be separated in the spatial context of Graham soil/Shade spectral map.

Target testing showed that there were at least seven reference endmembers in the AVIRIS image: McAllister, Stronghold, and Graham soils, dry forbes, litter, dry grass and green vegetation (walnut). Spectral mixture analysis, however, could not be run simultaneously for the seven reference endmembers. Spectral mixture analysis, when applied to a subset of pixels, detected the presence and quantified the fractions of six of the seven reference endmembers identified using target testing.

References

Dereck, R.P., F.G. Hall, and E.F. LeDrew. 1996. A comparison of NDVI and spectral mixture analysis for estimating biophysical properties in boreal forest terrain. In Proceedings of IGARSS, 1996, 230-232.

FernadesR., J.R. Miller, and L.E. Band. 1996. Comparison of linear least squares unmixing methods and guassian maximum likelihood classification. In Proceeding of IGARSS 1996, 420-422.

Gao, B. C., K.B. Heidebrecht, and A.F.H. Goetz. 1996. Atmospheric Removal Program (ATREM) Users Guide, Centre for the Study of Earth from Space, Cooperative Institute for Research in Environmental Science, University of Colorado, Bouder.

Huete, A.R. and Escadafal, R. 1991. Assessment of biophysical soil properties through spectral decomposition techniques. Remote Sen. Environ. 35:149-159.

Leeuwen, W.J.D., A.R. Huete, C.L. Walthall, S.D. Prince, A. Begue, and J.L. Roujean. 1997. Deconvolution of remotely sensed spectral mixtures for retrieval of LAI, fAPAR, and soil brightness. Journal of Hydrology 188: 697-724

Malinowski, E.R., and D.G. Howery. 1980. Factor analysis in chemistry. John Wiley & Sons, New York, NY.

Roberts, D.A., M.O. Smith, D.E. Sabol, J.B. Adams, and S. Ustin. 1992. Mapping the spectral variability in photosynthetic and non-photosynthetic vegetation, soils and shade using AVIRIS. Summaries of the 3rd Annual JPL Airborne Geoscience Workshop. AVIRIS Workshop, R.O. Green ed. Pasadena, CA, June 1-5, 1992, Vol. 1. P.38-40.

Smith, M.O., J.B. Adams, and D.E. Sabol 1994. Mapping sparse vegetation canopies. In J. Hill and J. Megier ed. Imaging spectrometry - a tool for environmental observations. Kluwer Academic Publishers, Dordrecht, The Netherlands. p 221-235.

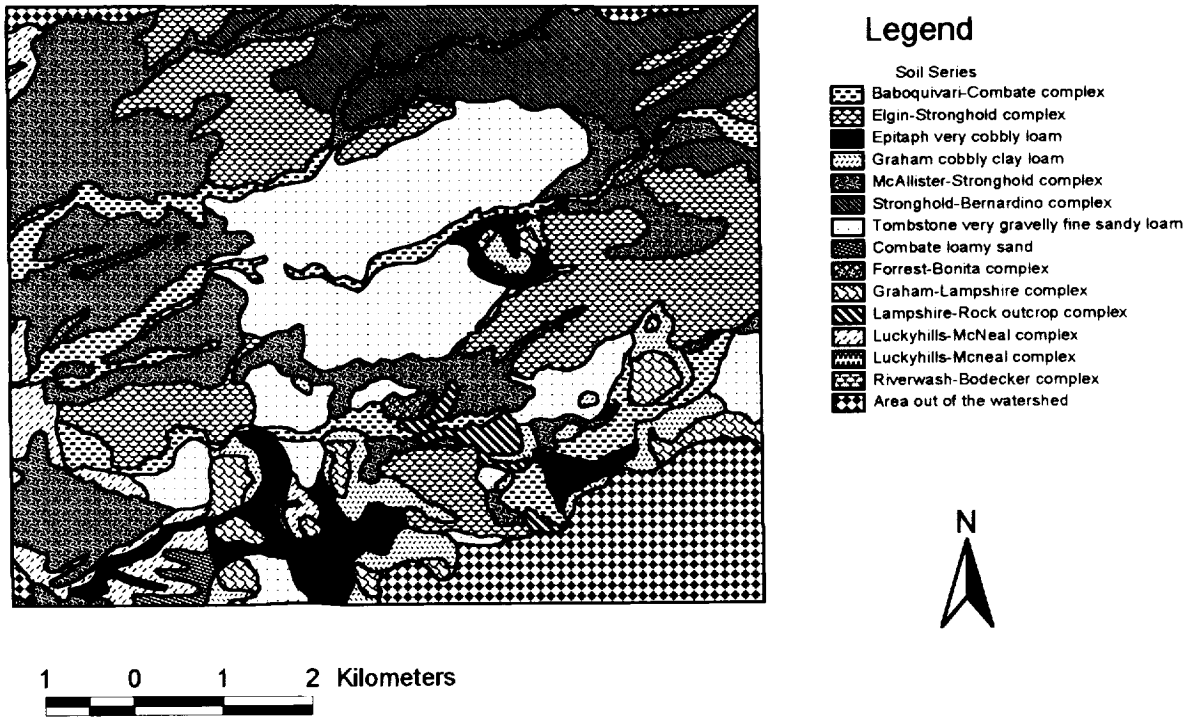

Figure 1. Soil map of the area of the Walnut Gulch Experimental Watershed imaged by AVIRIS

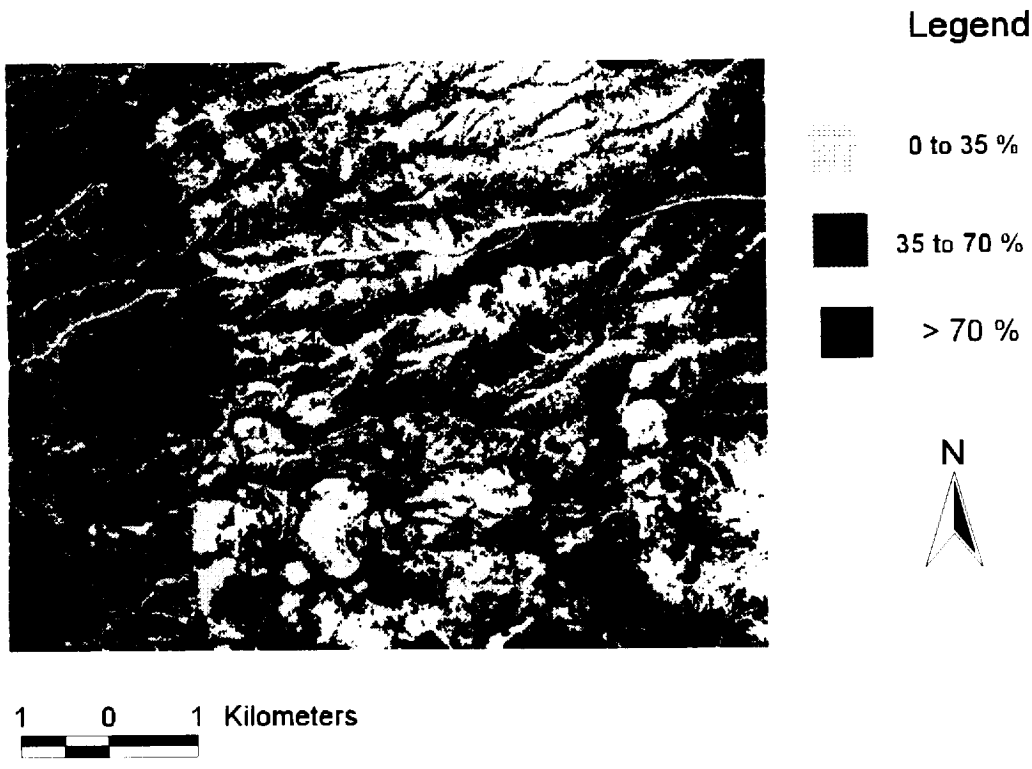

Figure 2. Soil spectral map for McAllister image endmember

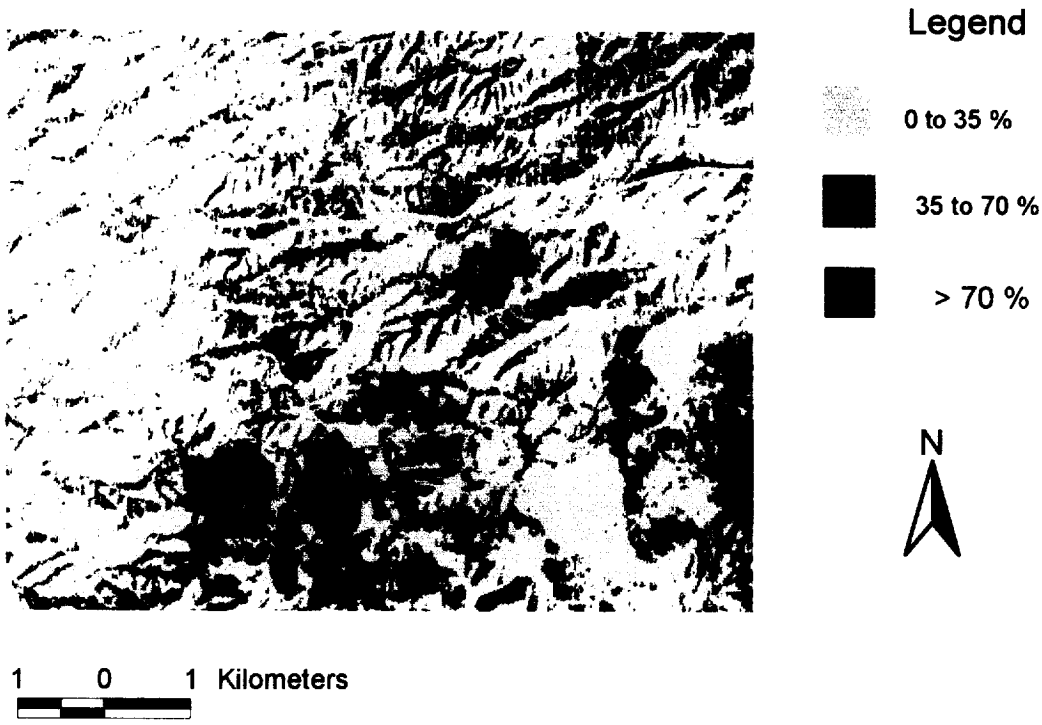

Figure 3. Spectral map for Graham soil/shade image endmember

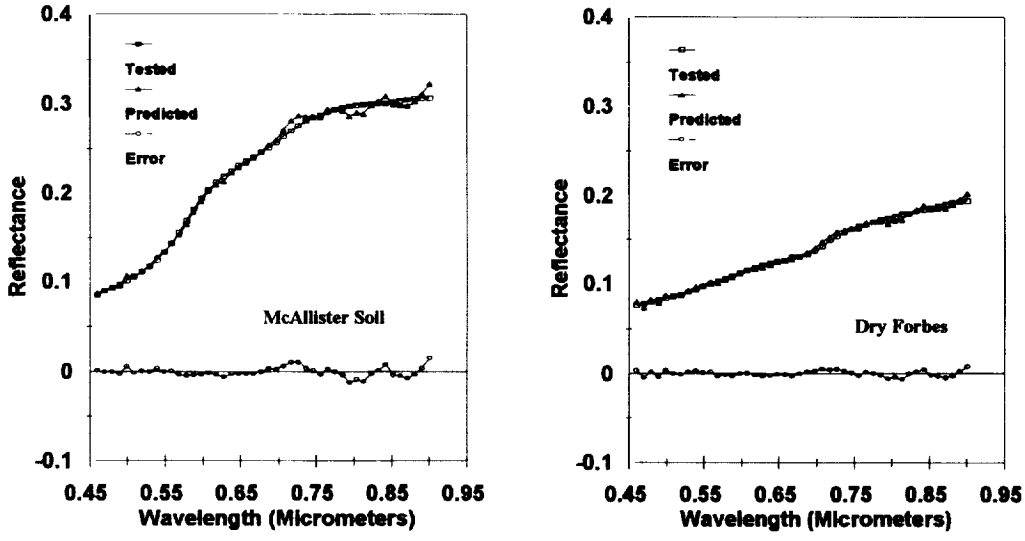

Figure 4. Target testing results for McAllister soil and dry forbes

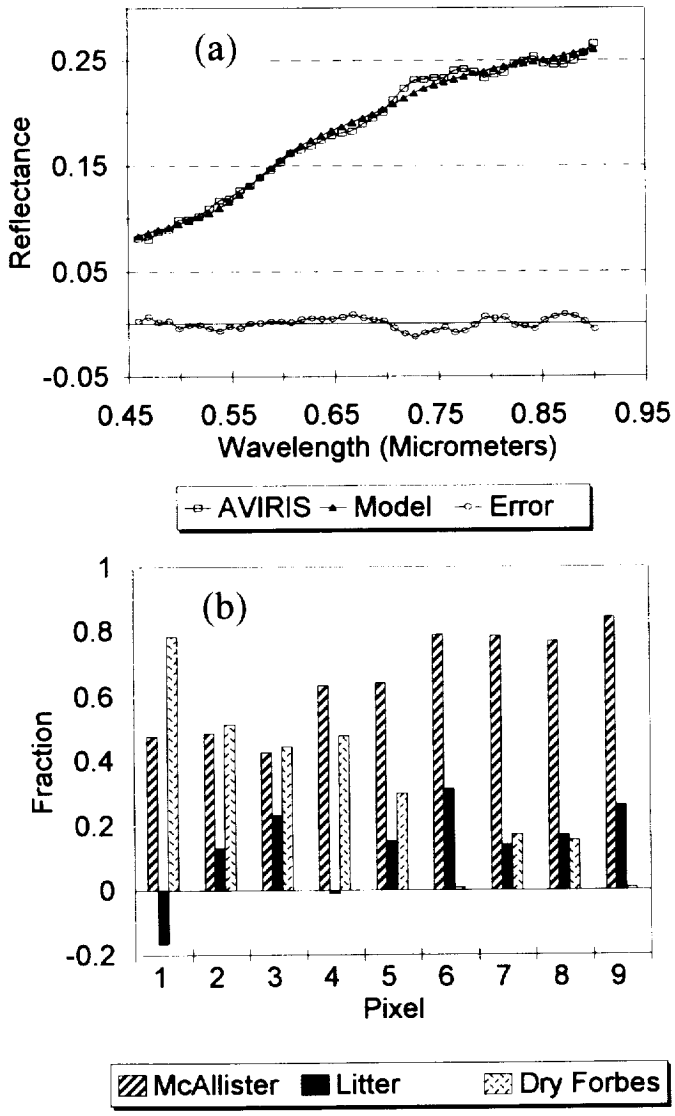

Figure 5. Spectral pixel recomposition (a) and reference endmember fractions (b) for the subset of pixels used as McAllister image endmember

FLAASH, A MODTRAN4 ATMOSPHERIC CORRECTION PACKAGE FOR HYPERSPECTRAL DATA RETRIEVALS AND SIMULATIONS

S. Adler-Golden[1], A. Berk[1], L.S. Bernstein[1], S. Richtsmeier[1], P.K. Acharya[1], and M.W. Matthew[1],
G.P. Anderson[2], C. L. Allred[2], L.S. Jeong[2], and J.H. Chetwynd[2]

[1]Spectral Sciences, Inc.,
99 South Bedford St., Burlington, MA 01803

[2]Phillips Laboratory, Geophysics Directorate,
Hanscom AFB, MA 01731

1. INTRODUCTION

FLAASH (Fast Line-of-sight Atmospheric Analysis of Spectral Hypercubes) is a MODTRAN-based "atmospheric correction" software package which is being developed by the Air Force Phillips Laboratory, Hanscom AFB and Spectral Sciences, Inc. to support current and planned IR-visible-UV hyperspectral and multispectral sensors. The main objectives are to provide (1) accurate, physics-based derivation of surface and atmospheric properties (such as surface albedo, surface altitude, water vapor column, aerosol and cloud optical depths, surface and atmospheric temperatures), (2) minimal computation time requirements, and (3) an interactive, user-friendly interface for running arbitrary MODTRAN calculations. FLAASH is written in the Interactive Data Language (IDL) (Research Systems, Inc., Boulder, CO) for compatibility with a wide variety of computer platforms and to facilitate its use with IDL-based display/analysis software such as ENVI.

FLAASH draws heavily on existing spectral analysis methods and codes that have been developed for both research and general use (e.g., Gao *et al.*, 1996; Green *et al.*, 1996; King *et al.*, 1992; Richter, 1996; Wan and Li, 1997). It is designed as a general-purpose code and is being developed in parallel with upgrades to MODTRAN in order to take advantage of the latest improvements in accuracy and speed. FLAASH is currently interfaced with a pre-release version of MODTRAN4 (Berk *et al.*, 1996). This paper briefly describes the progress achieved to date in the code development and presents some preliminary results. The initial version of FLAASH provides the following capabilities:

- Support for AVIRIS, HYDICE, and similar near-IR/visible/UV sensors;
- A graphical user interface for performing MODTRAN4 spectral calculations, including data simulations;
- Data-derived column water vapor and relative surface altitude (from column oxygen) image files and displays, and aerosol property retrieval capability based on known surface reflectances;
- Atmospherically corrected images (i.e., surface spectral reflectances) for non-thermal wavelengths (mid-IR through UV), including an image-sharpening adjacency effect correction.

The algorithm for deriving the surface and atmospheric properties utilizes the full MODTRAN4 accuracy and accounts for adjacency effects associated with atmospheric scattering. Compared to previous versions of MODTRAN, the new correlated-k radiation transport algorithm in MODTRAN4 (Berk *et al.*, 1994) provides improved accuracy in treating molecular absorption over scattering paths. In addition, an order of magnitude reduction in computation time is achieved by using MODTRAN4's lower resolution (15 cm^{-1}) option.

Brief descriptions of the computational approach and representative results of hyperspectral data analyses using FLAASH are presented below.

2. METHODOLOGY

As in other first-principles atmospheric correction codes, model simulations of the spectral radiance are performed for appropriate atmospheric and viewing conditions over a range of surface reflectances. The desired properties (reflectance, column water vapor, etc.) are derived from the spectral radiance at each image pixel using look-up tables that are generated from these simulations. To minimize the number of simulations (i.e., MODTRAN runs) required to generate the tables, a physics-based parameterization of the radiance-reflectance relationship is used. This relationship can vary across the scene due to variations in water vapor column density. Therefore, as in the ATREM code (Gao *et al.*, 1996) the water vapor column is first determined for each pixel, then the result is used as an input to the surface reflectance retrieval algorithm.

The initial version of FLAASH handles the mid-IR through UV wavelengths where thermal emission can be neglected. For this situation the spectral radiance L^* at a sensor pixel may be parameterized as (Staenz *et al.*, 1996; Vermote *et al.*, 1995; Williams *et al.*, 1992)

$$L^* = A\rho/(1-\rho_e S) + B\rho_e/(1-\rho_e S) + L^*_a \qquad (1)$$

where ρ is the pixel surface reflectance, ρ_e is an average surface reflectance for the surrounding region, S is the spherical albedo of the atmosphere, L^*_a is the radiance backscattered by the atmosphere, and A and B are coefficients that depend on atmospheric and geometric conditions. The first term in Equation (1) corresponds to the radiance from the surface that travels directly into the sensor, while the second term corresponds to the radiance from the surface that is scattered by the atmosphere into the sensor.

The values of A, B, S, and L^*_a may be determined empirically from MODTRAN spectral radiance calculations for three different spatially and spectrally uniform reflectances (such as $\rho=\rho_e=0$, 0.5, and 1.0). The backscattered radiance term L^*_a is simply the radiance for zero surface reflectance ($\rho=\rho_e=0$). The first (direct radiance) term is output by MODTRAN separately from the total radiance L^*; thus, the second (scattered radiance) term is isolated by subtracting the direct surface radiance and L^*_a from the total radiance. Equation (1) applies rigorously to monochromatic light. However, because S is small (of order 10^{-2} to 10^{-1} for clear sky) the radiance-reflectance relationship is sufficiently linear that Equation (1) accurately describes integrated in-band (i.e., sensor channel) radiances as well as true monochromatic radiance.

The spatially averaged reflectance ρ_e is used to account for "adjacency effects"--i.e., radiance contributions that, because of atmospheric scattering, originate from parts of the surface not in the direct line of sight. Strictly speaking, the ρ_e's in the numerator of the second term and in the denominators of the first and second terms are not identical. The former represents a weighted average over the surface region (typically around 1 km in width when viewed from a high-altitude sensor) that contributes to forward scattering from the ground into the sensor, while the latter represents an average over a larger region that contributes to the scattering back down to the ground. However, because S is small and the size of the averaging region is non-critical, the two averaged reflectances may be equated with little error.

The method for solving Equation (1) for the surface reflectance ρ in FLAASH parallels that in the ATCOR2 code (Richter, 1996) but differs in detail. The steps are as follows:

1. MODTRAN4 spectral radiance calculations for surface reflectances of 0, 0.5, and 1.0 are performed for a range of water vapor column densities to determine the Equation (1) parameters as a function of wavelength and water vapor column. The parameters for a spectral interval containing a selected water band are used to determine water vapor column densities for each pixel. The method, which is similar to the two-band method used in ATCOR2, involves comparisons of data and simulations for in-band and out-of-band radiance averages using a look-up table. The water column densities and the Equation (1) parameters for the entire wavelength region are stored for subsequent use.

2. A spatially averaged radiance image L^*_e is generated by convolving the radiance image L^* with a spatial weighting function appropriate for the sensor altitude, aerosol scale height, and aerosol scattering phase function.

3. From the resulting L^*_e an approximate ρ_e is generated from Equation (1) using ρ_e to represent all of the surface reflectances.

4. The resulting ρ_e is combined with the radiance L^* to solve Equation (1) for ρ.

To save computation time in processing the image, steps 3 and 4 are actually performed on a grid of trial L^*, L_e^*, wavelength, and water column values, and the resulting ρ values are entered into a 4-dimensional look-up table. The ρ calculation for each pixel is then carried out in a single step by interpolating between the table values.

The computation time consumed for a typical analysis of an 0.4-2.5 μm hyperspectral image on a 200-MHz personal computer is on the order of ten minutes for the MODTRAN4 calculations (depending on the number of water vapor column amounts and atmospheric layers and on the code options used) plus ten to fifteen minutes for the data inversion (water column determination, spatial averaging, and generation of surface reflectance) for an AVIRIS 224-channel, 512x614-pixel image. Since the MODTRAN4 outputs are stored, they can be re-used to analyze a series of images taken under similar atmospheric conditions.

In addition to determining the water vapor column density, FLAASH derives pressure altitudes by applying the same method to the oxygen 762 nm absorption band. Because MODTRAN4's correlated-k algorithm more accurately represents molecular absorption in the presence of scattering, the water vapor and oxygen densities derived from FLAASH are expected to be more accurate than those obtained using previous versions of MODTRAN as well as from more approximate radiation transfer algorithms.

3. RESULTS

Several AVIRIS and HYDICE images have been analyzed to test the initial FLAASH code. Some results from 1994 AVIRIS data are shown in Figures 1 through 4. The "US Standard" model atmosphere was assumed in the MODTRAN simulations.

Figures 1a and 1b show images of derived visible albedo and column water vapor for Cuprite, Nevada (image No. PG02104). Altitude maps based on US Geological survey data and derived from the O_2 band are shown in Figures 2a and 2b, respectively. The water vapor and derived altitude images were pixel-averaged somewhat to improve the signal-to-noise. As expected, the water vapor is strongly correlated with the altitude. The lowest column water vapor (dark regions in Figure 1b) occurs over two mountain ridges which lie on either side of the north-south highway discernable in Figure 1a and rise several hundred meters above a flat region to the southeast. The altitudes derived from the O_2 band show these same qualitative features.

A quantitative comparison between the O_2 band-derived and actual surface altitudes is shown in Figure 3. The derived relative and absolute altitudes are both accurate to around 200 m or better. Similar altitude precision from O_2 band data was reported in a study by Green *et al.* (1996) of a different AVIRIS scene. As the O_2 band actually measures air pressure, the absolute altitudes are sensitive to the local weather conditions. For relative altitudes the main source of error is spectral non-linearity of the reflectance in the O_2 band region, which varies with the type of terrain and is especially pronounced with vegetation. We expect that better accuracy will be obtained in the future by developing a background-subtraction or terrain-dependent correction procedure.

Figure 4 shows two greyscale images of visible reflectance derived from an image of Moffett Field, CA (No. PG02106). This scene, at the edge of San Francisco Bay, contains a wide variety of features such as buildings, pavement, surface vegetation, streams, and salt ponds. The left hand images shows the reflectance generated using the full method described in the previous section, while the right hand image shows the reflectance generated without accounting for adjacency effects. The difference in contrast is striking and illustrates the importance of

incorporating adjacency effects in atmospheric correction of variegated scenes.

We are currently analyzing HYDICE measurements of scenes containing spectrally calibrated targets. Comparisons of retrieved and known surface reflectances will be very useful for inferring aerosol properties, which are the major source of uncertainty in visible and UV surface reflectance retrievals for clear-sky conditions. Either calibrated targets or "dark" pixels (known to contain vegetation or water) can be compared with retrieved reflectances as an aerosol optical property is varied, the property being retrieved from the best fit. Aerosol properties which may be potentially retrieved (i.e., to which the comparisons are sensitive) include the optical depth, albedo, and scattering phase function (via the adjacency effect).

4. CONCLUSION

Development of FLAASH, a fast software package for atmospheric correction and modeling of hyperspectral images using MODTRAN4, has begun with a focus on sensors covering mid-IR through UV wavelengths. An initial version of the code has been developed for analysis of AVIRIS and HYDICE data. Future efforts will focus on accuracy evaluations, improvements to MODTRAN4, incorporation of a comprehensive library of reflectance spectra, incorporation of aerosol retrieval techniques, and extensions of FLAASH to additional sensors and to the thermal IR region.

5. ACKNOWLEDGEMENT

The work at Spectral Sciences was supported by the US Air Force Contract no. F19628-91-C-0145.

6. REFERENCES

Berk, A, L.S. Bernstein, D.C. Robertson, P.K. Acharya, G.P. Anderson, and J.H. Chetwynd, 1996, "MODTRAN Cloud and Multiple Scattering Upgrades with Application to AVIRIS," Summaries of the Sixth Annual JPL Airborne Earth Science Workshop, JPL Publication 96-4, Vol. 1, Pasadena, California, pp. 1-7.

Gao, B.-C., K.B. Heidebrecht, and A.F.H. Goetz, 1996, "Atmosphere Removal Program (ATREM) Version 2.0 Users Guide," Center for the Study of Earth from Space/CIRES, University of Colorado, Boulder, Colorado, 26 pages.

Green, R.O., D.A. Roberts, and J.E. Conel, 1996, "Characterization and Compensation of the Atmosphere for Inversion of AVIRIS Calibrated Radiance to Apparent Surface Reflectance," Summaries of the Sixth Annual JPL Airborne Earth Science Workshop, JPL Publication 96-4, Vol. 1, Pasadena, California, pp. 135-146.

King, M. D., Y. J. Kaufman, W. P. Menzel, and D. Tanre, 1992, "Remote Sensing of Cloud, Aerosol, and Water Vapor Properties from the Moderate Resolution Imaging Spectrometer (MODIS)," IEEE Transactions on Geoscience and Remote Sensing, Vol. 30, pp. 2-27.

Richter, R, "Atmospheric Correction of DAIS Hyperspectral Image Data," 1996, SPIE AEROSENSE '96 Conference, Orlando, FL, April 8-12, SPIE Proceedings, Vol. 2758.

Staenz, K., D.J. Williams, and B. Walker, 1996, "Surface Reflectance Retrieval from AVIRIS Data Using a Six-Dimensional Look-Up Table," Summaries of the Sixth Annual JPL Airborne Earth Science Workshop, March 4-8, 1996, JPL Publication 96-4, Vol. 1, Pasadena, California, pp. 223-229.

Vermote, E., D. Tanre, J.L. Deuze, M. Herman, and J.J. Morcrette, 1994, "Second Simulation of the Satellite Signal in the Solar Spectrum (6S)," 6S User Guide Version 6.0, NASA-GSFC, Greenbelt, Maryland, 134 pages.

Wan, Zhengming, and Z.-L. Li, 1997, "A Physics-Based Algorithm for Retrieving Land-Surface

Emissivity and Temperature from EOS/MODIS Data," IEEE Transactions on Geoscience and Remote Sensing, Vol. 35, pp. 980-996.

Williams, D.J., A. Royer, N.T. O'Neill, S. Achal, and G. Weale, 1992, "Reflectance Extraction from CASI Spectra Using Radiative Transfer Simulations and a Rooftop Radiance Collector," Can. Journal of Remote Sensing, Vol. 18, pp. 251-261.

Figures 1a and 1b. Derived ground albedo (left) and column water vapor (right) for an AVIRIS image of Cuprite, NE. Darker regions in Figure 1b (right) denote lower water content.

Figures 2a and 2b. Altitude maps for the same image. Left: USGS data. Right: derived from the O_2 absorption band. Darker regions denote higher altitude.

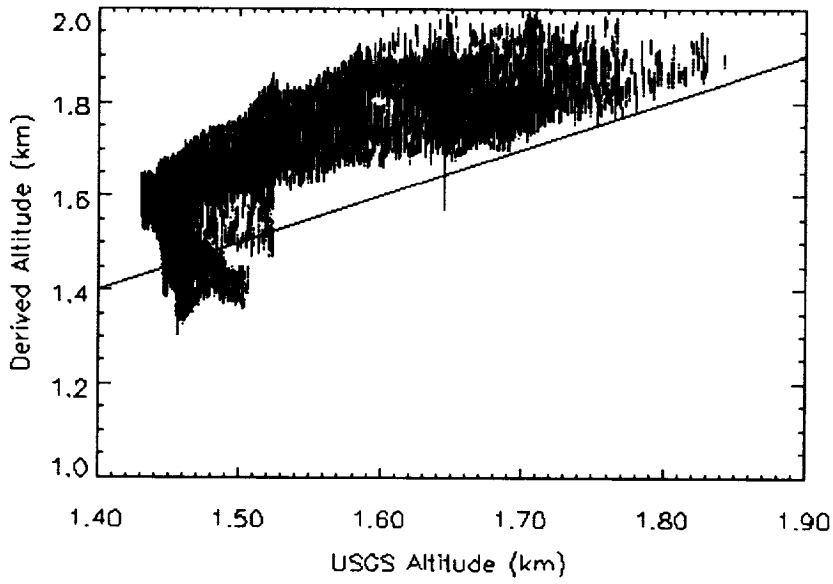

Figure 3. Comparison of actual (USGS) and derived surface altitudes for the Cuprite scene. Solid line denotes ideal agreement for the assumed US Standard model atmosphere.

Figure 4. Derived reflectance images for AVIRIS Moffett Field scene with (left) and without (right) adjacency correction.

A REVIEW OF THE NEW AVIRIS DATA PROCESSING SYSTEM

Mikael Aronsson

Jet Propulsion Laboratory, California Institute of Technology, 4800 Oak Grove Drive, Pasadena, CA 91109

1. INTRODUCTION

The processing of AVIRIS data - from VLDS[1] flight tape to delivered data products - has traditionally been performed in essentially the same way, from the beginning of the AVIRIS project up to and including the 1996 flight season. Starting with the 1997 flight season, a drastically different paradigm has been used for the processing of AVIRIS data. This change was made possible by the recent development of and related availability of affordable data storage devices.

2. DESCRIPTION OF THE PREVIOUS GENERATION DATA PROCESSING SYSTEM FOR AVIRIS

The first generation AVIRIS data processing system evolved, via incremental improvements from code originally developed for a VAX computer system, into a fairly complex set of software modules, executed on a network of Sun and Solbourne computers. The original code was written in FORTRAN and assembler, but by the time the migration to the UNIX-based systems took place, the code had been translated to C. The software modules were governed and driven by a Sybase relational database management system. The Sybase system was also used to store all the meta data (or, the data about the data) for all AVIRIS runs. The data from the runs themselves were stored in two magnetic tape-based forms. The first form used 10- or 12-bit data words[2] that were recorded in-flight on the VLDS flight tape. The second used 16-bit decommutated data words recorded on 4mm DAT tape, that was kept as a permanent archive of all AVIRIS runs.

Just like the AVIRIS instrument itself, the software modules were gradually improved over the years and had reached a significant level of complexity by the 1996 flight season, primarily caused by the desire to maintain backwards compatibility so that data from any flight season could be processed with the current version of the software modules. Here follows a brief description of the software modules' major functionalities as they appeared during the 1996 flight season (cf. figure 1). Before the first software module could be executed, information about the flight tape had to be entered in one of the Sybase tables. The first step of processing consisted of the VPS module, which operated on a complete flight tape, i.e., typically on a collection of 5 to 20 runs. VPS stands for VLDS PBN Scan, where PBN in turn stands for Principal Block Number. When data are recorded on the VLDS tape, they are laid down in consecutively numbered (and hence uniquely identified) swipes, each such swipe consisting of 64 kbytes of data. One 64 kbyte swipe is called a Principal Block. The major purpose of the VPS program module was to scan the VLDS tape in order to identify the Principal Block Number for the beginning and ending of each run, and also to estimate the size of each run in the process. This information was stored in a Sybase table.

Once the complete flight tape had been scanned by the VPS module, the remainder of the processing was performed on discrete runs or 6-scene parts of runs, should they be longer than 6 scenes. A scene is an artificial delimiter of each 512 lines (or major frames) of image data from a run. This delimiter had been

---

1 VLDS is the acronym for the Metrum Very Large Data Store storage system, which is the VHS-tape based recording system used to record data acquired by the AVIRIS instrument.

2 AVIRIS data were recorded on the VLDS tapes as 10-bit raw data words in 1994 and earlier years. The world length was increased to 12 bits in 1995.

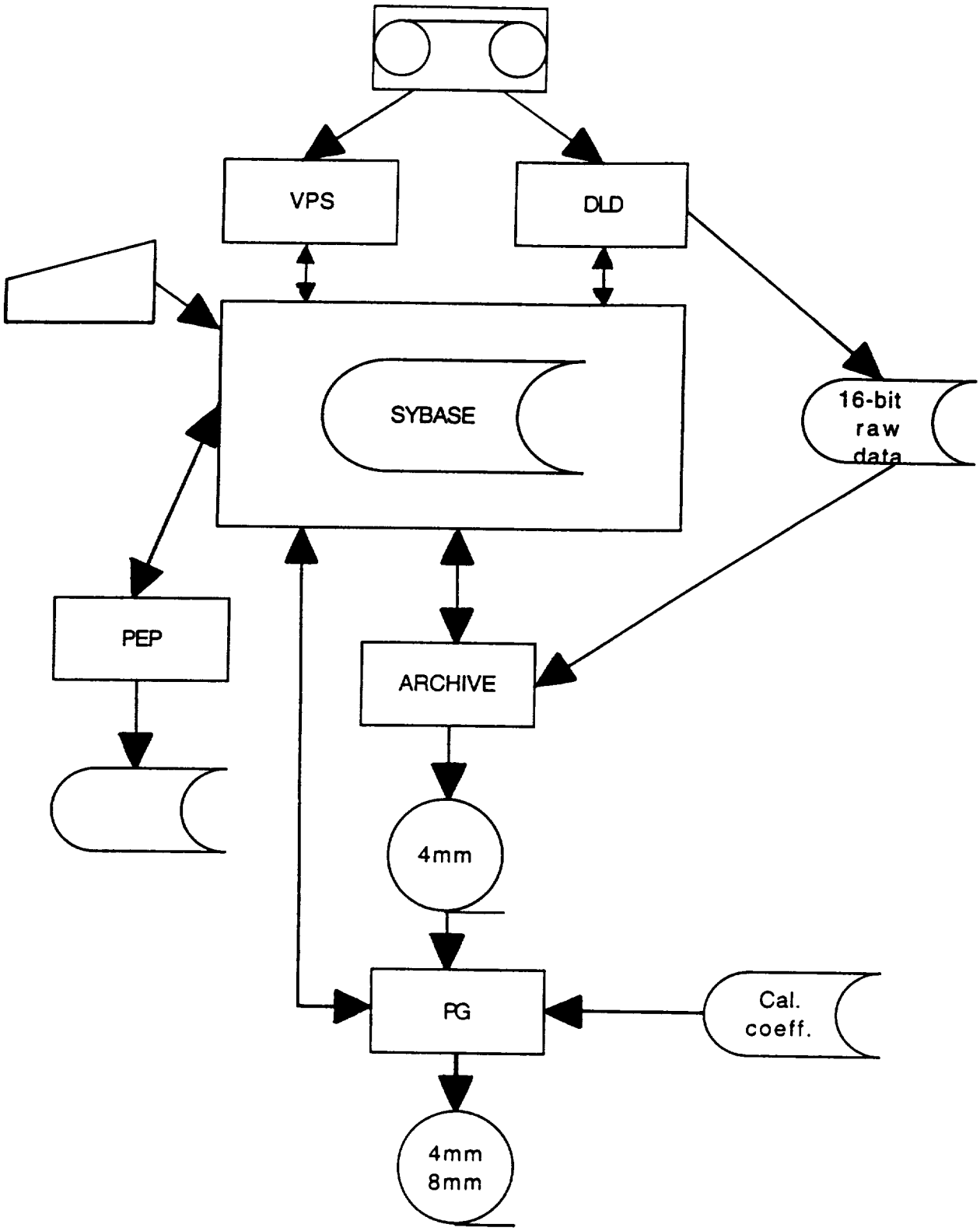

Figure 1. The first generation AVIRIS data processing system.

devised in the early days of AVIRIS, since this was the amount of data that would fit on one 9-track magnetic tape. The transition from 9-track tape to 4mm DAT tape allowed fitting larger amounts of data on each tape. The upper limit for what could fit on one tape was at this point not the delimiting factor any more. Instead, the delimiting factor was defined by the amount of AVIRIS data that could fit on any of the hard discs available in the AVIRIS Data Processing system (used for intermediate storage during processing of AVIRIS data), which was the origin of the 6-scene upper limit for AVIRIS datasets. The second step of processing, performed by the DLD module, would thus operate on datasets consisting of at most 6 scenes. DLD was an abbreviation of the word download, which describes the major action taken by this module, i.e., data was read from the VLDS tape and downloaded (or written) to a temporary disc file. Exactly which dataset would be downloaded was decided automatically by an algorithm that prodded one of the Sybase tables (even though a skilled operator could affect the order of downloading by manipulating the database). The raw 10- or 12-bit data words, as written on the VLDS tape, were converted to 16-bit integers as part of the process and more meta data was extracted and entered in Sybase tables. Since this was done in parallel with reading the data off of the VLDS tape and writing it to disc, the DLD module was rather slow and time consuming.

Once DLD had been completed, the data could be moved from the temporary disc file to a permanent archival storage device. This was done by the program module ARCHIVE and this program would write the AVIRIS data, on a scene-by-scene basis, to a 4mm DAT archive tape. Each archive tape would include a precal file, up to six scenes of science data, and a postcal file. In the early years there was only one copy of each archive tape made, but learning from experience, we eventually switched to making two copies of each tape. The ARCHIVE program module would also extract information to be used by the following program module and write this information to Sybase tables. ARCHIVE furthermore added information to yet another Sybase table in order to keep track of what dataset was archived on what tape.

The next step of processing was done by a program module called PEP, which was an acronym for Performance Evaluation Program. This program module would utilize the extracted information from the AVIRIS data in order to facilitate monitoring of the AVIRIS instrument's performance, as well as the performance of the VLDS recorder. The output from this module was automatically e-mailed to several individuals within the AVIRIS project and also stored in Sybase tables (for later perusal and trend analysis).

The final step of processing, called PG (for Product Generation), would be performed on request only. An investigator - or anyone else interested in a specific dataset (or run) - would submit a request, including information about what flight, run, and scene(s) were desired. This information, as well as a significant amount of additional information related to the request, would be entered into Sybase tables. The PG program module would then prod the tables, read the corresponding data off of the appropriate archive tape, calibrate the data, and write the resulting files to a PG tape. Depending on the investigator's request, the PG tape could be either a 4mm DAT tape or an 8mm EXABYTE tape and the data would be ordered and processed on a scene-by-scene basis, with a maximum of six scenes included per tape. In addition to the (one to six scenes of) science data, each PG tape would also include a number of ancillary files, e.g., pre- and postcalibration data, engineering and navigation data, calibration data, documentation, etc. The PG module would also produce a number of additional products, e.g., single-band images, spectral plots, etc., to be used in-house for quality control.

The processing of AVIRIS data was a slow and cumbersome process because all processing was governed by, and the software modules frequently interacted with, the Sybase relational database management system. Another reason for the slow processing speed was the multiple steps of tape input/output (tape i/o).

3. THE CURRENT GENERATION DATA PROCESSING SYSTEM

By the end of the 1996 flight season, large scale disc storage technology had become quite affordable, both as far as hard discs and virtual disc systems were concerned. The prospect of being able to access several years worth of AVIRIS data on-line, coupled with the desires to decrease the amount of tape i/o, to decrease or eliminate the reliance on the Sybase database system, to retire the old, increasingly complex software modules, and to speed up through-put, led to the decision to purchase several pieces of hardware and to design a new generation of software for processing of AVIRIS data. The hardware acquisitions included sixteen 9-GB and

eight 23-GB disc drives, first one and later a second 62-GB RAID-5[3] system, and an AMASS[4] system, originally designed to hold 2 TB of data, but recently upgraded to 3 TB. A set of new software modules was developed in tandem with these hardware acquisitions. We adopted something we refer to as the "KISS" principle for the development of the software, where "KISS" stands for "Keep It Simple, Stupid." This meant that, instead of designing large and complex program modules that would handle multiple tasks and be compatible no matter what year the data to be processed were from, smaller program modules, that were designed to handle only one year's data, were written (even though some modules do in reality not change from one year to another). Each module was designed to handle only a limited set of tasks, in order to keep the modules simple and easily maintainable. The new software does not interface with the Sybase database system and processing is hence not driven by the database. Instead, the new software system is governed by the operator running the software, i.e., he or she decides what program module to run and on what dataset. And, finally, the input to and output from the different program modules are kept on disc whenever possible, which significantly has speeded up the processing time. Here follows a brief description of the software modules of the new AVIRIS data processing system (cf. figure 2).

The first step of processing is performed by the VTOD program module, where VTOD stands for VLDS TO Disc. This program first scans the VLDS tape in order to find the filemarks identifying the end of each run. The data are then copied verbatim (i.e., as 12-bit raw data words) to disc, with each run making up a uniquely named file. The only exception from this rule occurs when a run is longer than approximately 7,400 major frames (or lines), which in accordance with the old way of thinking, equalled about 14.5 scenes. This, in turn, was approximately equal to a disc file size of 1.5 GB and the following paragraph will explain the rationale behind this limitation. VTOD normally operates on a complete flight tape.

The second software module is called EXP, which is short for EXPansion. The EXP module reads the raw 12-bit data, identifies the major frame sync words, and expands each 12-bit data word to a 16-bit data word. The result is written to disc and the resulting file is approximately 33% larger than the corresponding input file. This means that the maximum 12-bit raw data input file size of 1.5 GB is expanded to a 2 GB output file. Two GB is the largest file size the UNIX operating system can handle, hence the limitation of approximately 7,400 lines per file. The resulting output files are finally moved from regular hard disc to the AMASS system for permanent storage. This program module normally operates on all files from a flight tape as one batch job.

The third step of processing is done by the PE program module, where PE stands for Performance Evaluation. This module extracts information from the precal portion of the file output by EXP. The information extracted includes background noise and the difference between high (shutter open) and dark (shutter closed) signal for the four spectrometers, detector, spectrometer, scanner optics and on-board calibrator temperatures, and more. These values are written to a file and a number of key parameters are flagged if they do not meet predetermined threshold values, which could indicate a problem with the instrument. The file containing this information is saved for future trend analysis and it is also automatically e-mailed to certain key persons.

---

3 The RAID-5 is a hard disc system, consisting of eight 9-GB discs with accompanying proprietary VERITAS software. RAID is an acronym for Redundant Array of Inexpensive Disks, which means that the discs are set up so that part of the combined storage capacity is used for storing duplicate information about the data stored in the disc array. The duplicate data allows regeneration of the data in case of disc failure. The suffix 5 designates a specific type of RAID system, where the data is "striped" (or interleaved) across the discs in the array and the data redundancy is provided by the use of parity information. The complete set of discs appears to the user as one large disc.

4 The AMASS Storage Management System from EMASS is a virtual disc system consisting of a hard disc cache and four DLT (Digital Linear Tape) drives with automatic loading/unloading of tapes. It is governed by an on-line AMASS database. Even though the bulk of the 3 TB of data are stored on DLT tape, data is automatically swapped between tape and the disc cache, giving the user the impression that all the data are available on-line (i.e., as if all the data were residing on hard disc).

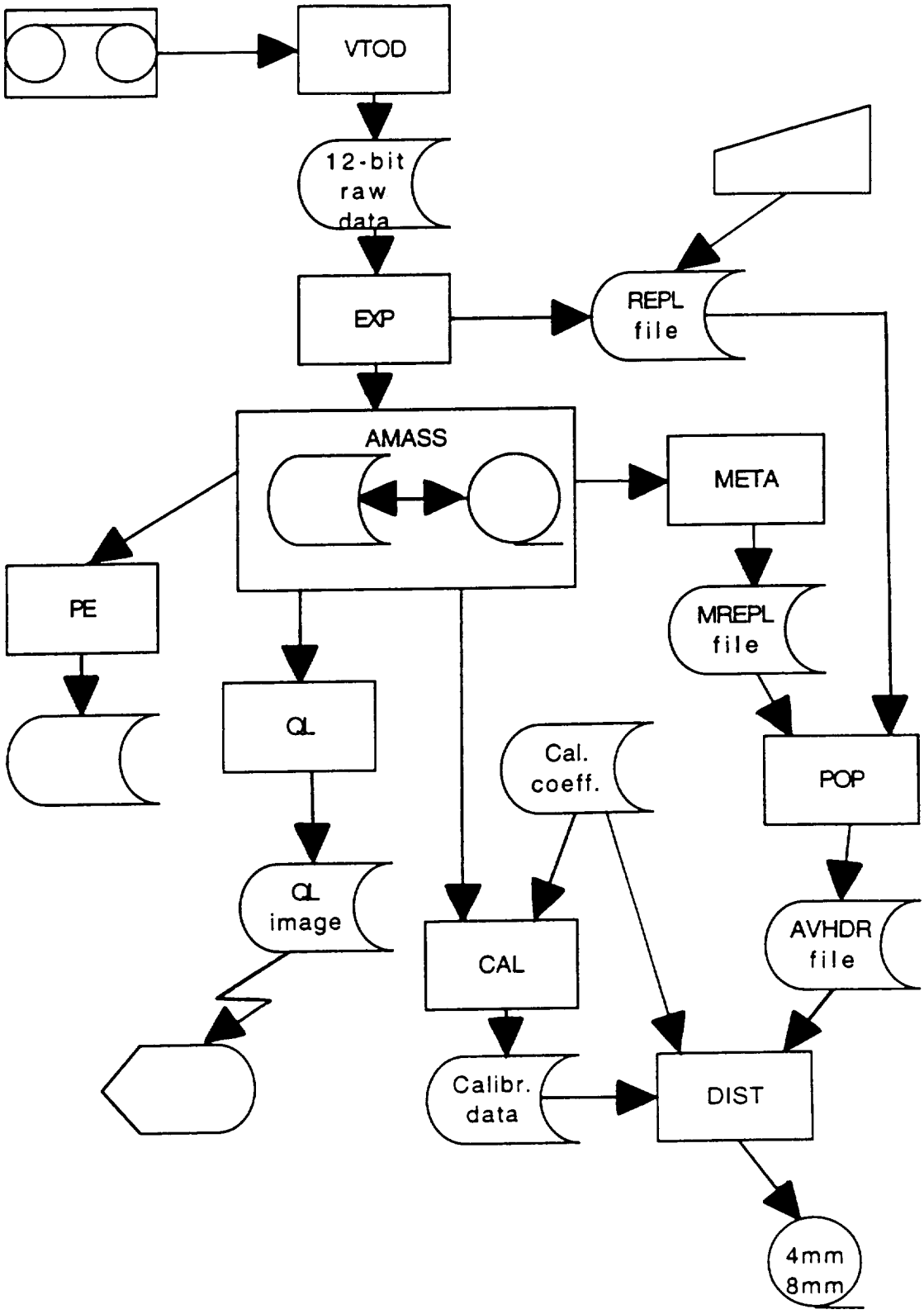

Figure 2. The second generation AVIRIS data processing system.

Next follows a manual step, where the operator enters information related to a particular run into an ASCII text file, referred to as the AVHDR (short for AVIRIS header) file. This is currently done via a text editor, such as emacs or vi, but will eventually be done via a GUI (= Graphical User's Interface). Among the information entered is Site name, Location, Investigator, Start and End Date, Time, Latitude and Longitude (nominal values, as given by the pilot), Comments about the run (from the pilot, the AVIRIS experiment coordinator and/or the operator), etc. Since this currently is a manual step, operation is limited to one file at a time.

The next software module is called META, and this module extracts meta data from each run. This meta data (or data about the data) includes Major Frame Counts (both total and by major frame type), Start and End Date, Time, Latitude, Longitude and Altitude (from the navigation and engineering data), as well as indications of missing lines, etc. META normally operates on all runs from a flight tape as one batch job.

The information manually entered by the operator and automatically extracted by the META software module is not entered directly into the actual AVHDR file. Instead, the information resides in intermediate files that are merged and copied to the AVHDR file by the next program module, called POP (which is short for POPulate, since this program populates the real AVHDR file with data). The POP module also extracts some of the information from the AVHDR file for generation of the Quicklook index file (see below).

Next follows the QL software module. This module generates a (subsampled) Quicklook (or QL) image of one band (normally band 34) of the science data in an AVIRIS run. The output is converted to JPEG format and the resulting file is moved to the AVIRIS FTP site, so that the QL image can be accessed by the investigators as well as any other interested party. The updated Quicklook index file (generated by POP, as described in the previous paragraph) is also moved to the FTP site.

At this point it is time to calibrate the data. This is done by a software module, appropriately named CAL, that reads the expanded raw data, extracts pre- and postcal data, as well as navigation, engineering, and dark signal data. CAL, furthermore, performs the calibration of the science data and also generates a browse image file and a number of quality control files (to be used in-house). All generated files are written to disc in preparation for the following step.

The final step of processing in the new software system is performed by a module named DIST (which is short for DISTribution). This module assembles the files produced by CAL (except for the in-house quality control files), the AVHDR file generated by the POP module, calibration constants files, and a documentation (or readme) file. All these files are placed in a special directory and the UNIX tar command, that creates a tape archive of the files, is issued. The resulting tar file is copied to a 4mm DAT or 8mm EXABYTE tape, which is sent to the investigator.

4. PERFORMANCE COMPARISON

It was estimated in the early days of AVIRIS' existence that the archiving of a completely full flight tape would take approximately 9 working days and that the retrieval processing (or product generation) would take an additional 60 working days (Reimer, et al., 1987). By 1992 the original processing system had been replaced by a Sun-based system and at that time the archiving of a full flight tape could be accomplished in 5 working days, while the product generation required approximately 5-10 working days (Hansen, et al., 1992). Through continued improvements over the years, the processing time had been further reduced by 1996, so that the archiving process could be accomplished in 3-4 working days and the product generation could be completed in another 5-7 working days, for a complete processing time of approximately 10 working days per flight (or VLDS) tape.

Once the new generation software and hardware system was completely in place (by the summer of 1997) we were able to process a completely full flight tape - all the way from VLDS tape to distributed data products - in the span of two working days, which represents a five-fold reduction in processing time.

5. FUTURE PLANS

Some of the software modules are currently used in their beta test versions. The process of replacing the beta modules with production versions has top priority in 1998. One of the beta modules is DIST, that currently can only produce tapes in tar format. It is anticipated that the conversion to the production version of this module will also include an upgrade that will allow us to produce distribution tapes that will have each discrete file written as a separate file on the tape (in a similar fashion to the PG tapes produced by the old software system) instead of bundling all files into one tar file.

As mentioned earlier, the manual step of entering the flight log information is scheduled for an upgrade to a GUI. In the long term we are even considering eliminating this step as part of the post-flight data processing done at JPL. We will instead have the Experiment Coordinator file this information electronically at the time of the flight.

At the present time, most of the software modules must be manually executed. In the long term this may get replaced with an automated system. We are looking into at least two different options, one being the usage of so-called cron jobs. A cron job is an automatic process that executes one (or several) software modules at a specific time each day. We could thus have a cron job that, e.g., at midnight each day identifies all new (and hence unprocessed) AVIRIS runs residing on the disc system and processes them. In fact, we are already experimenting with this option on a limited scale. Another option would utilize scripts that link the different software modules together, so that when one module, e.g., VTOD has successfully completed processing of a VLDS tape, the next module (which is EXP) would be automatically initiated, etc.

Besides processing all the data from the 1997 flight season, we have begun reprocessing the previous years' data with the new software. The plan is to continue this effort until all data back to 1992 have been reprocessed.

We are also planning a number of hardware upgrades. The computer used for processing of all the data will get upgraded CPUs, which should improve the processing throughput. Another upgrade that is planned for the coming year is the acquisition of a 0.5 TB hardware RAID-3[5] disc subsystem. This disc system will allow us to store a whole year's worth of AVIRIS runs simultaneously on hard disc, thus enabling rapid comparisons, trend analysis, and other processing on a complete flight season.

6. ACKNOWLEDGEMENT

The work described in this paper was performed at the Jet Propulsion Laboratory under a contract with National Aeronautics and Space Administration.

7. REFERENCES

Hansen, E.G., Larson, S., Novack, H.I., Bennett, R., "AVIRIS ground data processing system", Summ. Third Annual JPL Airborne Geoscience Workshop, JPL Publication 92-14, Jet Propulsion Laboratory, Pasadena, CA, Vol. 1, 1992, pp. 80-82.

Reimer, J.H., Heyada, J.R., Carpenter, S.C., Deich, W.T.S., Lee, M., "Airborne Visible/Infrared Imaging Spectrometer (AVIRIS) ground data-processing system", Imaging Spectroscopy II, Proceedings of SPIE, Volume 834, 1987, pp. 79-90.

---

5 The RAID-3 system is similar to the RAID-5 system, with the major difference being exactly how the data stripes and parity information is laid out across the discs.

SOURCES OF VARIABILITY IN PLANT CANOPY HYPERSPECTRAL DATA IN A SAVANNA ECOSYSTEM

Gregory P. Asner, Carol A. Wessman, C. Ann Bateson

Cooperative Institute for Research in Environmental Sciences
University of Colorado, Boulder, CO 80309-0216

1. INTRODUCTION

The relative importance of the plant structural, biophysical, and biochemical attributes of vegetation that determine a hyperspectral reflectance signal have not been well quantified. Vegetation reflectance is primarily a function of tissue optical properties (leaf, woody stem, standing litter), canopy structural attributes (e.g. leaf and stem area), soil reflectance, illumination conditions, and viewing geometry. Foliage and non-photosynthetic vegetation (NPV) affect the radiation field through their reflectance and transmittance characteristics (Ross 1981, Asner et al. 1998). Leaf optical properties are a function of leaf structure, water content, and the concentration of biochemicals (e.g. lignin, cellulose, nitrogen) (Gates et al. 1965, Wooley 1971, Fourty et al. 1996). However, several studies have demonstrated that leaf-level variability in carbon and nitrogen chemistry plays a small role in determining canopy reflectance characteristics in comparison to leaf water content and leaf area index (LAI) (Jacquemoud 1993, Baret et al. 1994, Jacquemoud et al. 1995).

In this paper, we use a combination of field and modeling techniques to quantify the relative contribution of leaf, stem, and litter optical properties, and canopy and landscape structural attributes, to the hyperspectral reflectance characteristics of a spatially complex savanna ecosystem. In contrast to recent studies focused on scaling within-leaf biochemical characteristics to leaf and canopy scales (Jacquemoud et al. 1995), this study approaches the scaling problem from the observed variability in tissue optical properties, then examines the importance of this tissue-level variability in comparison to canopy structural variability at landscape scales using a plant canopy radiative transfer model.

2. METHODS

2.1 Study Site

The Texas A&M La Copita Research Area is located on the Rio Grande Plains of southern Texas (27°40'N, 98°12'W), roughly 80km west of Corpus Christi. Like many regions of the western United States, the area has endured over a century of heavy grazing and fire suppression, leading to the encroachment of woody plant species into ecosystems once dominated by grasses. Woody plant canopies are dominated by the leguminous tree *Prosopis glandulosa* var. *glandulosa*, with many secondary shrubs, all imbedded in a relatively continuous herbaceous cover dominated by C_4 grasses. Among woody species at La Copita, leaf area index (LAI) ranges from roughly 2.0-5.0. Among grass species, LAI ranges from approximately 0.5-2.5 (Wessman et al. 1998).

2.2 Tissue Optical Properties

A comprehensive analysis of the characteristics and variability in leaf, woody stem, and standing litter optical properties across a 900 km Texas climate gradient was recently reported (Asner et al. 1998). A goal of the present study was to focus on the portion of the data set representing the variability in foliar, litter, and woody stem optical properties at the ecosystem level. At La Copita, we collected 400 samples (200 foliar, 200 litter+woody stem) representing the dominant woody plant and herbaceous species.

Leaves of woody plant species (trees, shrubs, sub-shrubs) were sampled by clipping five to ten branches from individual plants. Grass and standing litter samples were collected by placing whole grass clumps (including some roots and soil) into bags to maintain leaf moisture conditions. All measurements were subsequently conducted within 15 minutes of sample collection. Hemispherical reflectance and transmittance spectra (400-2500 nm) were obtained using a full-range spectroradiometer (Analytical Spectral Devices, Inc., Boulder, CO), a $BaSO_4$ integrating sphere (LI-1800, Licor Inc., Lincoln, NE), and a light source modified for full-range spectral measurements (Asner et al. 1998). The ASD spectrometer acquires measurements in 1.4 nm intervals in the visible/NIR (full-width at half-maximum = 3-4 nm) and 2.2 nm (FWHM = 10-12 nm) in the shortwave IR (SWIR) region. Each reflectance and transmittance measurement was comprised of a 200 spectrum average. A modified version of the Daughtry et al. (1989) method for spectral analyses of needle leaves was used for the leaflets of species not completely covering the sample port on the integrating sphere (e.g. *Acacia*, *Prosopis*, green and senescent grass leaves).

Woody stem material was collected from trees and shrubs by removing thin, opaque slices of the outer bark. Flat areas on the stems were chosen to ensure that the sample port of the integrating sphere would close properly. Reflectance spectra were collected from 5-10 individuals of each species, with each sample consisting of a 200 spectrum average.

2.3 Soil Reflectance

Full spectral range (400-2500 nm) soil reflectance measurements were collected at La Copita. A variety of soil types were sampled within one hour of solar noon. The fiber optic of the spectrometer was held 1m above ground level in a nadir position, and care was taken to ensure that only bare soil was sampled. Soil reflectance measurements were also collected after rainfall events to capture the variability caused by soil wetting.

2.4 Radiative Transfer Modeling

We used a discrete ordinates plant canopy radiative transfer model in which single scattering is solved exactly while multiple scattering is simplified to a single-angle problem (zenith). Iaquinta and Pinty (1994) first introduced this simplification in the multiple scattering component which sharply improved computation time while still producing top-of-canopy reflectance values with reasonable accuracy. We restructured the model to include both leaf and non-photosynthetic vegetation (NPV) in the radiative transfer equation formulation (Wenhan 1993, Asner and Wessman 1997), but maintained the Iaquinta and Pinty (1994) multiple scattering calculation. The revised model is designed explicitly for use with hyperspectral data, as wavelength-independent calculations (e.g. leaf angle distribution) are made only once per simulation, while those calculations requiring the leaf and stem optical properties (e.g. multiple scattering) are iterated by wavelength.

Leaf, woody stem, litter, and soil spectra were convolved to AVIRIS spectral response curves to produce 220 optical channels ranging from 400-2450 nm. All canopy and landscape reflectance analyses were subsequently based on the AVIRIS channels. The model produces top-of-canopy reflectance values from the following parameters: leaf and stem area index (LAI, SAI), leaf and stem angle distributions (LAD, SAD), leaf and stem hemispherical reflectance and transmittance properties and soil reflectance ($\rho_{leaf}(\lambda)$, $\tau_{leaf}(\lambda)$, $\rho_{stem}(\lambda)$, $\tau_{stem}(\lambda)$, $\rho_{soil}(\lambda)$), sun and view zenith and azimuth angles (θ_{sun}, ϕ_{sun}, θ_{view}, ϕ_{view}), and a hot-spot parameter for each vegetation component (H_{stem}, H_{leaf}):

$$\begin{aligned} R(\lambda) &= f\,(\text{GEOMETRY, STRUCTURE, TISSUES, } \rho_{soil}(\lambda)) \\ \text{where GEOMETRY} &= (\theta_{sun}, \phi_{sun}, \theta_{view}, \phi_{view}, H_{stem}, H_{leaf}) \\ \text{STRUCTURE} &= (\text{LAI, SAI, LAD, SAD}) \\ \text{TISSUES} &= (\rho_{leaf}(\lambda), \tau_{leaf}(\lambda), \rho_{stem}(\lambda), \tau_{stem}(\lambda)) \end{aligned} \quad (1)$$

Scattering characteristics at the tissue and soil level are modeled as isotropic. LAI and SAI are given on a m^2m^{-2} basis, and LAD and SAD can be modeled as erectophile, planophile, plagiophile, or uniform (deWit 1965). For

analyses here, tree and grass LAD were set to plagiophile and erectophile, respectively. Tree stem angle distribution and grass litter angle distribution were also set at erectophile. Viewing and solar geometry as well as a hot-spot parameterization are used in simulating the canopy-level anisotropy. For all analyses in this paper, solar zenith and azimuth angles (θ_{sun}, ϕ_{sun}) were set at 30° and 0°, respectively. View zenith and azimuth angles (θ_{view}, ϕ_{view}) were both set to 0°.

2.5 Leaf Optical Variability versus Canopy Structure

The importance of leaf optical variability was tested at the canopy level. Two standard deviations about the mean of measured leaf reflectance and transmittance spectra (total range = 4 s.d.) were used as the criteria to determine the role of leaf-level variation at canopy scales. Tree canopy simulations also used the mean woody stem reflectance spectrum from field measurements, and herbaceous canopies used the mean of the standing litter optical properties. The importance of LAI variation on canopy reflectance was tested using the LAI range from measurements made at La Copita. These changes were evaluated by calculating first derivatives along each canopy reflectance spectrum (Wessman et al. 1989).

3. RESULTS AND DISCUSSION

3.1 Tissue and Soil Optical Variability

Here, we will not discuss the similarities and differences in tissue optical characteristics by species, genera, growthforms, lifeforms, or functional groups, as much of this discussion took place in Asner et al. (*in press, in review*). Instead, we will simply define the total variance in the optical properties of leaves, woody stems, and standing litter material at La Copita to facilitate an analysis of their importance at canopy and landscape scales.

Mean (±1 s.d.) reflectance and transmittance properties of woody plant and grass leaves from La Copita are shown in Figure 1. Grasses had consistently higher reflectance values than woody plant species throughout the visible spectral range (t-tests at each wavelength, $p < 0.05$), whereas woody species had higher values throughout the NIR region (t-tests, $p < 0.05$). There were no significant reflectance differences between woody plant and grass vegetation types in the shortwave-IR (SWIR) spectral region. In comparing transmittance spectra, the grass group was consistently lower than the woody plant group in the NIR. No other differences were found in the visible or SWIR spectral regions. Standing litter and woody stem optical properties were generally more variable in comparison to fresh leaves (Figure 2).

Mean (±1 s.d.) soil reflectance is shown in Figure 3. Strong absorption features centered near 1400 and 1900 nm are due to atmospheric water, preventing measurements and subsequent modeling of these spectral regions.

3.2 Leaf Optical Variability at Canopy Scales

Figure 4 shows the effect of varying the leaf optical properties by ±2 s.d. from their mean in canopies with low and high LAI (1.5, 5.0). The former is a common LAI scenario for grass cover at La Copita, and the latter represents the highest values for the woody plant canopies found there. Leaf optical variability played a small role in driving canopy reflectance changes in the low LAI scenario. Under low LAI conditions, the total range in canopy reflectance induced by leaf optical variability ranged in magnitude from <1% in the visible region to a maximum of 4% in the NIR, then decreased again in the SWIR range (2-3%). At high canopy LAI, the effects of leaf optical variability were more pronounced, with maximum effects in the NIR (10-12%). In the visible spectral region and along the "red edge" (~ 700 nm), effects of leaf-level variation were still extremely small. Leaf effects at canopy scales were greater in the 1600-1800 nm spectral range than in the 2000-2500 nm range because the single scattering albedo (= reflectance+transmittance/2) of fresh green leaves is higher in the 1700 nm than in the 2200 nm region (Figure 1).

3.3 Canopy Reflectance Sensitivity to LAI

Changes in canopy LAI strongly influenced canopy reflectance signatures (Figure 5a), with the most pronounced effect in the NIR and the smallest effect on the visible spectral region. Large increases in NIR reflectance with increasing LAI result from multiple scattering of photons, while small decreases in visible reflectance (increased absorption) are due to the presence of more chlorophyll in the higher LAI canopies. In general, structure enhances canopy reflectance in spectral regions where the scatterers are "bright" (e.g. NIR for green leaves), and enhances canopy absorption in "dark" regions (e.g. 680 nm for green leaves). The effect of adding LAI diminished as total canopy LAI increased, thus a small leaf area increase in a low LAI canopy had a much greater impact than did a similar increase in a high LAI canopy. Deepening of the two water absorption features within the NIR (~ 1000 and 1200 nm) was also apparent. While the overall NIR trend was toward increased scattering with increased LAI, these NIR plateau water absorption features "lagged" behind the rest of the plateau due to enhanced water absorption as canopy biomass (e.g. LAI) increased. Analysis of first derivatives supports this conclusion, as the slope of the reflectance continuum in these regions increased as LAI increased (Figure 5b). Other derivative results indicate the following regions to be highly sensitive to changes in canopy LAI: (1) the 695-700 nm region (the red edge), (2) the 1275-1375 nm region of the NIR plateau, and (3) the SWIR region between 1500-1800 nm. When LAI > 0.5, first derivative spectra in the visible and SWIR (2000-2500 nm) regions contain little to no information on changing LAI.

3.4 Standing Litter Variability in Grass Canopies

The presence of standing litter has a significant impact on grass canopy reflectance. Figure 5c shows the result of increasing the relative proportion of standing litter (0-100%) in a grass canopy with total plant area index (PAI) = 1.4. As the relative abundance of litter increased, canopy reflectance increased significantly throughout the shortwave spectrum, with the largest changes in the NIR (18-25% absolute) and SWIR (12-21%) regions. The chlorophyll and pigment absorption features (~ 450 and 680 nm) and NIR plateau observed in green canopies deteriorated as litter increased. The visible-to-NIR transition (the red edge) flattened and became a nearly linear reflectance continuum characteristic. The features near 2075 and 2200 nm found in litter optical properties (Figure 2b) emerged at the canopy level as well.

There were several distinct changes in the reflectance continuum (as determined via first derivatives) that resulted from the presence of standing litter in a canopy (Figure 5d). First, the visible spectral region was highly sensitive to increases in canopy litter, particularly in the 550-700 nm range. This region was only mildly sensitive to changes in LAI (when LAI was low), thus the visible range is a good candidate for assessing canopy litter content via first derivative spectra. The far SWIR region from 2000-2100 nm and near 2250 nm was also sensitive to litter in comparison to LAI or leaf angle changes. First derivative spectra in these SWIR regions were more than three times as sensitive to litter content variation than to LAI or LAD variation.

3.5 Woody Stems in Tree and Shrub Canopies

Figure 6a depicts the radiative contribution of woody stems to a hypothetical tree canopy. We varied the proportion of stem area within the mean plant area index (PAI) value for tree canopies at La Copita (from Wessman et al. 1998). A range of stem area index (SAI) values were taken from a similar savanna tree canopy in North Texas (Asner et al. *in review*). The contribution of stem surfaces to canopy reflectance was significant. Increases in the percentage of stem material in a canopy had the following effects on canopy reflectance: (1) decreased the strength of the 680 nm absorption feature, (2) the strength of the entire NIR plateau decreased, (3) the entire SWIR region was elevated, and (4) the difference in magnitude of the NIR plateau and the local maxima centered at roughly 1680 and 2200 nm decreased.

The role of varying stem optical properties on canopy reflectance was much smaller than that of leaf optical variability (Figure 6b). For the hypothetical tree canopy (LAI = 3.5, SAI = 0.60), stem properties caused maximum canopy reflectance changes of 2-3% in the NIR. However, this result is largely dependent on the location of woody material within the canopy (van Leeuwen and Huete 1996). In this modeling scenario, the

woody stems and foliage were assumed to be equally distributed (vertically) throughout the canopy. Stem optical variability will thus have a greater or lesser effect on canopy reflectance depending on the level of interaction that woody material has with photons that ultimately exit the canopy.

3.6 Variation in Vegetation Cover

Changing vegetation cover had the largest effect in the SWIR (2000-2500 nm) and visible spectral regions (Figure 7). When the percentage vegetation cover decreased, spectral features associated with bare soil emerged at the pixel level (e.g. 2150 and 2350 nm). This analysis emphasizes the difficulty in estimating vegetation characteristics (e.g. LAI, foliar biochemistry) in non-continuous vegetation covers.

4. CONCLUSIONS

This study used an approach to combine field observations with mechanistic modeling to uncover which factors influence hyperspectral reflectance in a spatially complex savanna ecosystem. Evidence from the analyses presented in this paper indicates:

- Variation in canopy LAI is the dominant control on canopy reflectance data (with the exception of soil reflectance in sparse canopies such as shrublands).
- Variability in leaf optical properties plays a very small role in determining canopy reflectance variability in this savanna ecosystem. We predict that these results would apply to other canopies with LAI < 5.0, but the degree to which this is true also depends on variability in leaf angle distribution.
- Stem material plays a small but significant role in determining canopy reflectance in woody plant canopies with LAI < 5.0.
- Standing litter significantly affects the reflectance characteristics of grassland canopies. Small increases in the percentage of standing litter lead to disproportionately large changes in canopy reflectance.
- Vegetation cover variation has the potential to dominate the reflectance spectrum because soils tend to be much brighter in the visible and SWIR and darker in the NIR than vegetation canopies. Therefore, quantitative analyses of vegetation structure and biochemistry must account for horizontal discontinuities in the canopy which significantly affect AVIRIS data.

The results presented here are idealistic in that only canopy-level reflectance was simulated without the added complexity of the atmosphere. If the influence of the atmosphere can be adequately removed, then the trends found here remain pertinent to the interpretation of hyperspectral remote sensing data. One important advantage of imaging spectrometry is that the calibration to reflectance (e.g. atmospheric removal) is approached in a physically robust manner (Gao et al. 1993). Nonetheless, our ability to quantitatively employ remote sensing data relies on improving the ways in which radiometric and atmospheric errors can be minimized.

5. ACKNOWLEDGMENTS

This work was supported by NASA Innovative Research Grant NAGW-4689, NASA Interdisciplinary Science Grant NAGW-2662, and a NASA Earth System Science Fellowship to G.P.A.

6. REFERENCES

Asner, G.P. and C.A. Wessman, 1997, "Scaling PAR absorption from the leaf to landscape level in spatially heterogeneous ecosystems," Ecol. Mod. 101:145-163.

Asner, G.P., C.A. Wessman, D.S. Schimel, and S. Archer, 1998, "Variability in leaf and litter optical properties: implications for BRDF model inversions using AVHRR, MODIS, and MISR," Remote Sens. Environ. 63:100-118.

Baret, F., V.C. Vanderbilt, M.D. Steven, and S. Jacquemoud, 1994, "Use of spectral analogy to evaluate canopy reflectance sensitivity to leaf optical properties," Remote Sens. Environ. 48:253-260.

Daugherty, C.S.T., K.J. Ranson, and L.L. Biehl, 1989, "A new technique to measure the spectral properties of conifer needles," Remote Sens. Environ. 27:81-91.

deWit, C.T., 1965, "Photosynthesis of leaf canopies," Agricultural Research Report 663, Pudoc Publication, Wageningen, The Netherlands.

Fourty, Th., F. Baret, S. Jacquemoud, G. Schmuck, and J. Verdebout, 1996, "Leaf optical properties with explicit description of its biochemical composition: direct and inverse problems," Remote Sens. Environ. 56:104-117.

Gao, B.-C., K.B. Heidebrecht, and A.F.H. Goetz, 1993, "Derivation of scaled surface reflectance from AVIRIS data," Remote Sens. Environ. 44:165-178.

Gates, D.M., H.J. Keegan, J.C. Schleter, and V.R. Wiedner, 1965, "Spectral properties of plants," Appl. Opt. 4:11-20.

Iaquinta, J. and B. Pinty, 1994, "Adaptation of a bidirectional reflectance model including the hot-spot to an optically thin canopy," Proc. 6th Int'l Symp. Phys. Meas. Sign. Remote Sens., pp. 683-690.

Jacquemoud, S., 1993, "Inversion of the PROSPECT+SAIL canopy reflectance model from AVIRIS equivalent spectra: theoretical study," Remote Sens. Environ. 44:281-292.

Jacquemoud, S., F. Baret, B. Andrieu, F.M. Danson, and K. Jaggard, 1995, "Extraction of vegetation biophysical parameters by inversion of the PROSPECT+SAIL models on sugar beet canopy reflectance data. Application to TM and AVIRIS sensors," Remote Sens. Environ. 52:163-172.

Ross, J.K., 1981, The radiation regime and architecture of plant stands. Kluwer Boston, Inc., Hingham, MA.

van Leeuwen, W.J.D. and A.R. Huete, 1996, "Effects of standing litter on the biophysical interpretation of plant canopies with spectral indices," Remote Sens. Environ. 55:123-134.

Wenhan, Q., 1993, "Modeling bidirectional reflectance of multicomponent vegetation canopies," Remote Sens. Environ. 46:235-245.

Wessman, C.A., J.D. Aber, and D.L. Peterson, 1989, "An evaluation of imaging spectrometry for estimating forest canopy chemistry," Int'l J. Remote Sens. 10:1293-1316.

Wessman, C.A., E.M. Nel, C.A. Bateson, and G.P. Asner., 1998, "A method to access absolute fIPAR of vegetation in spatially complex ecosystems," Proc. 7th Annual JPL Airborne Earth Sci. Workshop.

Wooley, J.T., 1971, "Reflectance and transmittance of light by leaves," Plant Physiol. 47:656-662.

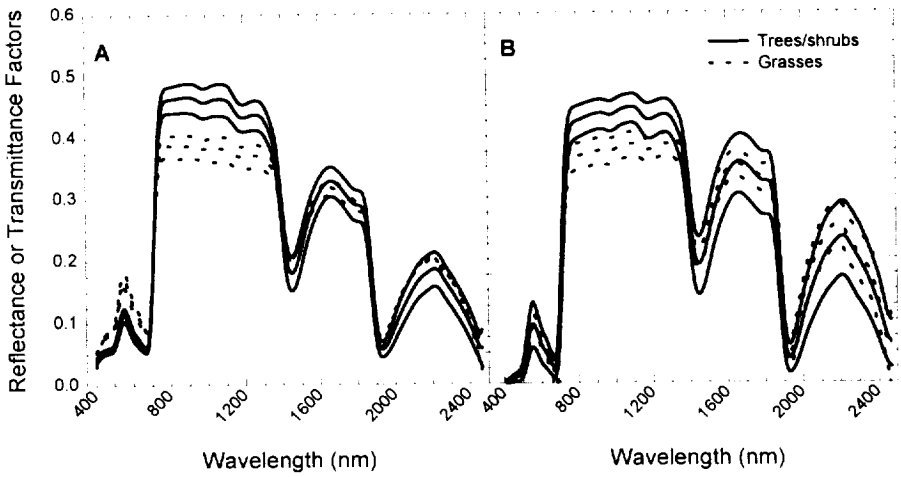

Figure 1. (A) Mean (+/-1 s.d.) hemispherical reflectance spectra for woody plant and grass leaves. (B) Mean (+/-1 s.d.) hemispherical transmittance spectra for woody plant and grass leaves.

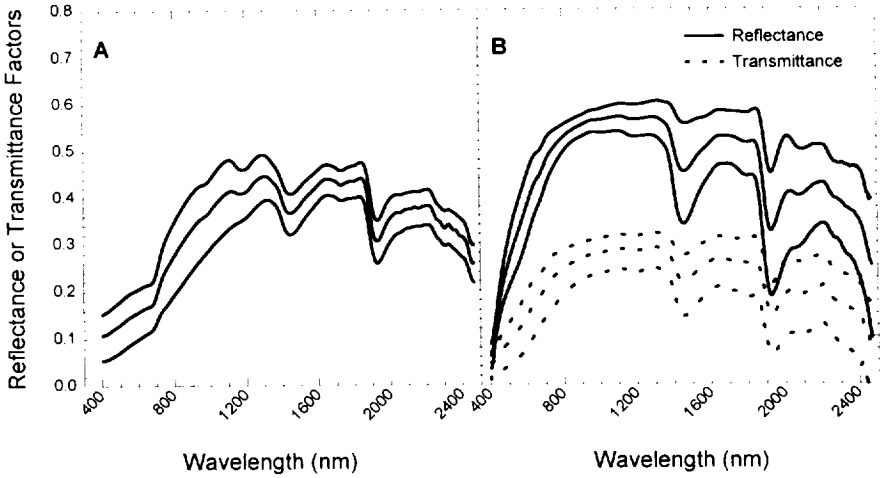

Figure 2. (A) Mean (+/-1 s.d.) hemispherical reflectance spectra for woody plants stems. (B) Mean (+/-1 s.d.) hemispherical reflectance and transmittance spectra for standing grass litter material.

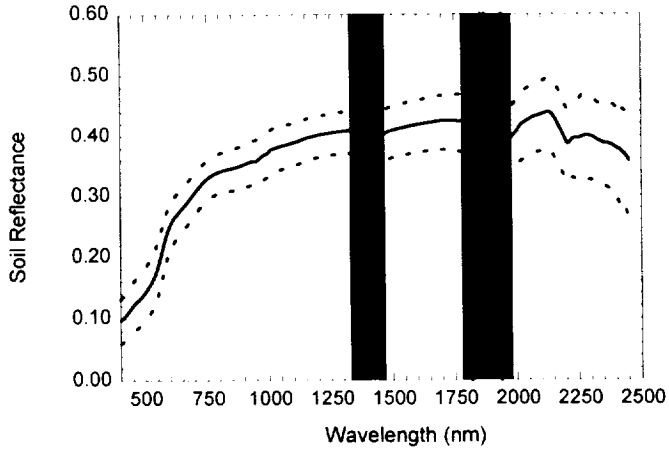

Figure 3. Mean (+/-1 s.d.) of nadir soil reflectance spectra

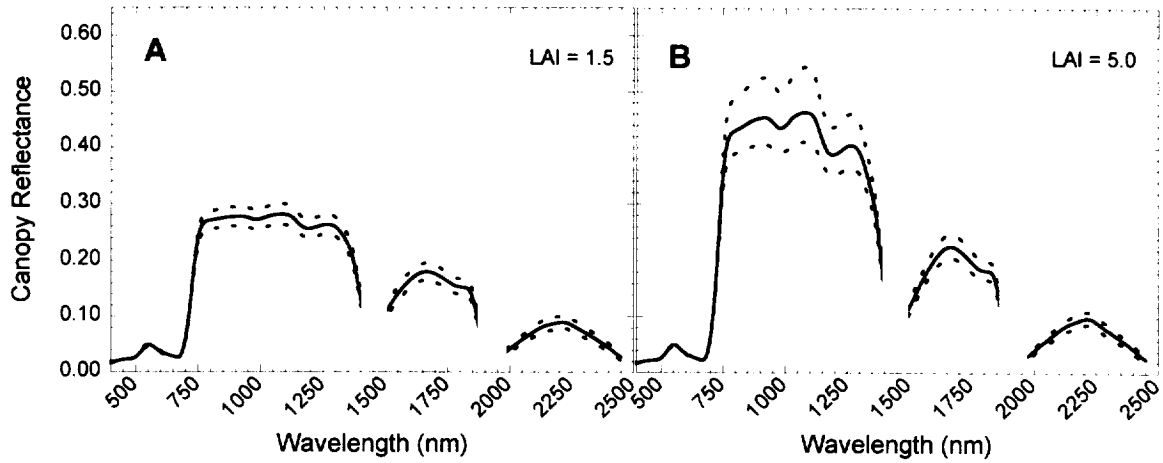

Figure 4. Range (dotted lines) in canopy reflectance resulting from measured variation in leaf optical properties (4 standard deviations). (A) Canopy LAI = 1.5 (B) Canopy LAI = 5.0

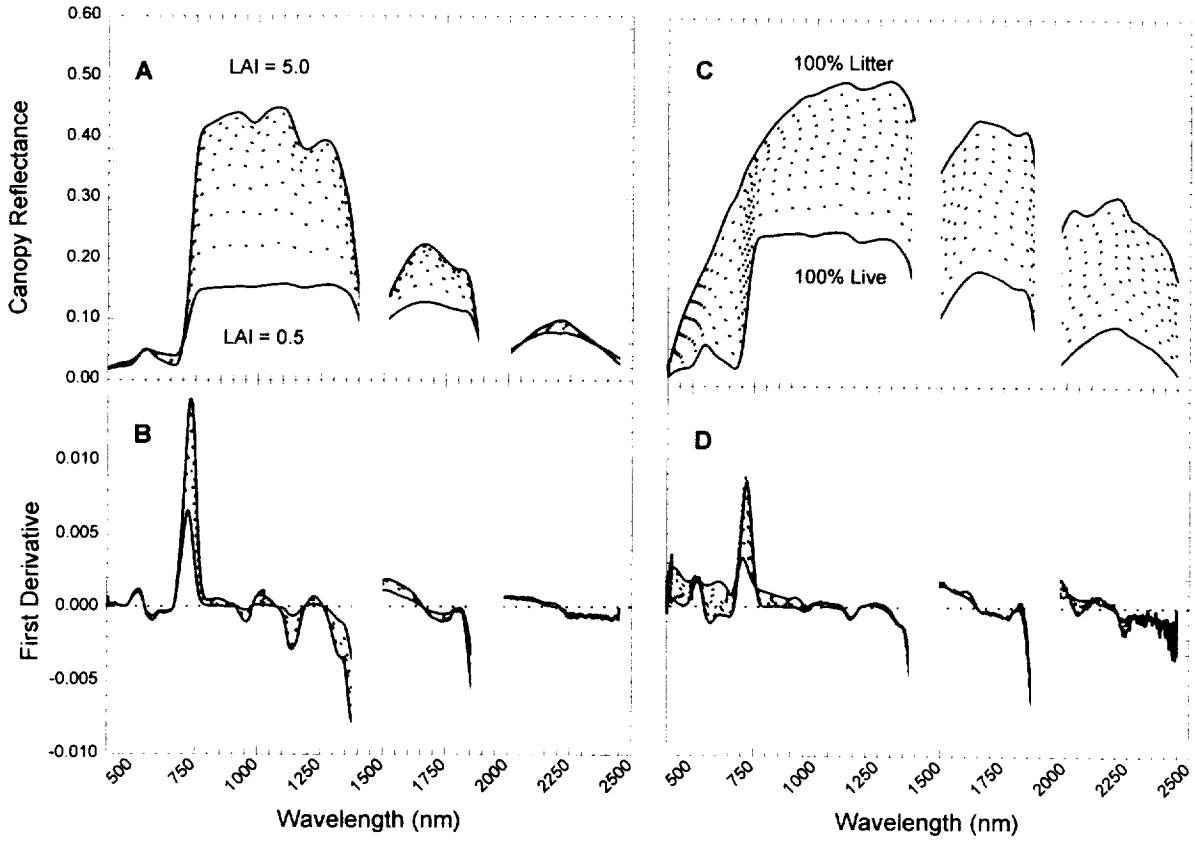

Figure 5. (A) Effect of increasing LAI on tree canopy reflectance. (B) Resulting first derivative spectra with increasing LAI. (C) Effect of increasing litter fraction on grass canopy reflectance. (D) Resulting first derivative spectra with increasing litter fraction.

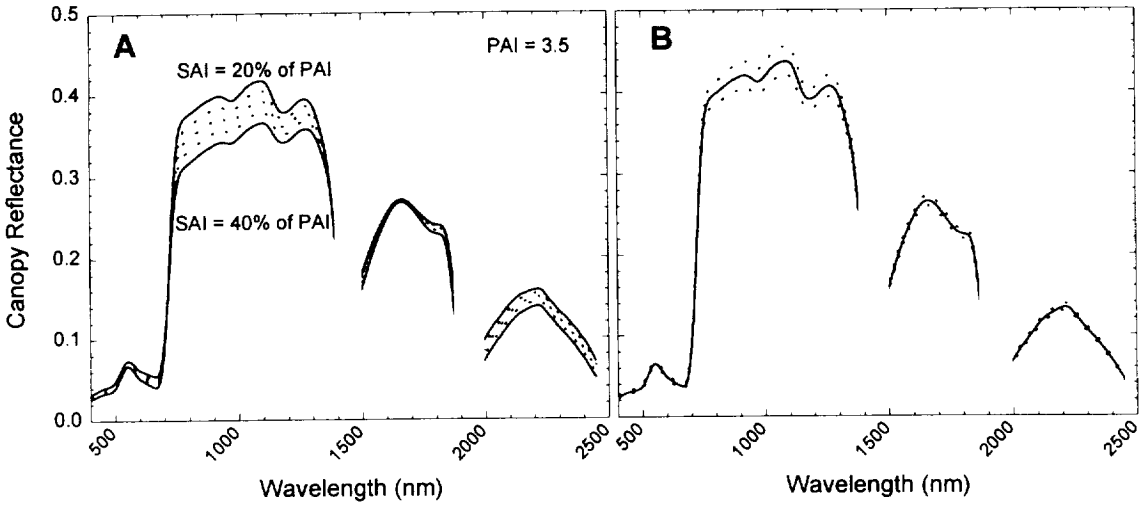

Figure 6. (A) Change in canopy reflectance with increasing percentage of woody stem material. Whole plant area index = 3.5, and stem fraction increased from 20-40%. (B) Variation in canopy reflectance due to measured stem optical variability. LAI = 3.5 and SAI = 0.65 (from Asner et al. in review).

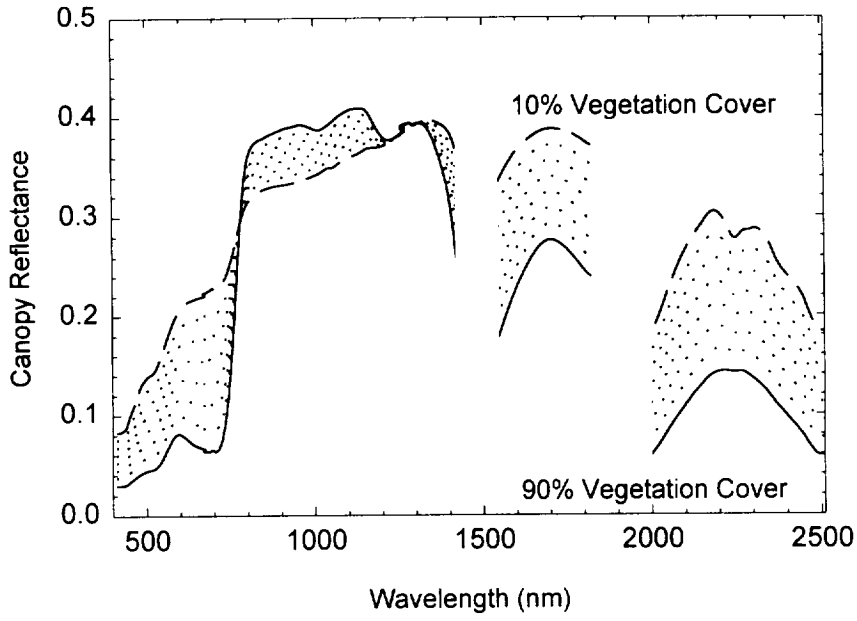

Figure 7. Changes in AVIRIS pixel reflectance due to changes in vegetation cover.

USE OF AVIRIS DATA FOR MINERALOGICAL MAPPING IN TROPICAL SOILS, IN THE DISTRICT OF SÃO JOÃO D'ALIANÇA, GOIÁS.

Gustavo Macedo de Mello Baptista[1], Éder de Souza Martins[1 & 2], José da Silva Madeira Netto[2], Osmar Abílio de Carvalho Jr.[1], and Paulo Roberto Meneses[1].

[1]Instituto de Geociências, Universidade de Brasília. E-mail: gustavom@cdsid.com.br

[2]Centro de Pesquisas Agropecuárias dos Cerrados (Embrapa / CPAC)

1. INTRODUCTION

Soil cartography in Central Brazil is available only in large scales. The increased agriculture pressure over these lands require basic soil knowledge obtainable in more detailed surveys. Data collected by hyperspectral sensors may represent a valuable source of information for soil scientists, mainly in the distinction of mineralogical classes.

Previous studies have shown the possibility of using indices developed from high-resolution diffuse reflectance spectra obtained in laboratory to estimate hematite content, and the Ki ratio (molecular ratio of SiO_2 and Al_2O_3). In this work we use AVIRIS data to verify the possibilities offered by hyperspectral data to differentiate tropical soils mineralogy.

AVIRIS data from São João D'Aliança district, Goiás state (950816L2 scene 3) after atmospheric correction and reflectance transformation were used. Field work was conducted to sample the main soil units. The location of the sampled points was obtained with a GPS, which allowed the precise plotting in the image. Samples were air-dried and sieved to 2 mm before being used for laboratory determination of 400 to 2500 nm spectral reflectance. X ray diffractions of these samples were also obtained.

Most of the scenes considered were covered by crop residues, pasture and native Cerrado vegetation with only a few hundred hectares of bare soils. The bare soil areas were considered in this work. Kaolinite, goethite and quartz were present in all samples. Gibbsite and hematite were also present in some sampled soils. Features attributable to kaolinite, gibbsite, hematite and goethite were clearly detected in the spectra obtained in the laboratory and in the AVIRIS data. The occurrence of these minerals was confirmed by the X-ray diffraction data.

2. SPECTRAL CHARACTERISTICS OF THE MAIN MINERALS OF TROPICAL SOILS

Tropical soils are usually highly weathered, due mainly to warm and wet climate. Their mineralogy is characterized by a reduced number of components with kaolinite, iron and aluminum oxides as the most frequent minerals in the clay fraction and quartz in the sand and silt fractions. The amounts and proportions of these components are important for soil classification and management. The knowledge of reflectance spectra of these components is important for utilization of image spectroscopy for soil studies applications.

2.1 Kaolinite ($Al_2SiO_5(OH)_4$)

Kaolinite is the most frequent clay mineral found in tropical soils. Its reflectance spectra have characteristic sharp features in the reflected infrared region. The kaolinite main spectral features are associated with the molecular vibrations of the OH^- of its crystalline net. In the near infrared the most perceptible features are associated with the overtones of fundamental OH- stretching mode (2s) in 1400 nm and to combinations involving OH-stretching and Al-OH bending modes (d + s), in 2200 nm (Hlavay et al., 1977). Figure 1 presents the diffuse reflectance spectra of a kaolinite sample from Mesa Alta (New Mexico).

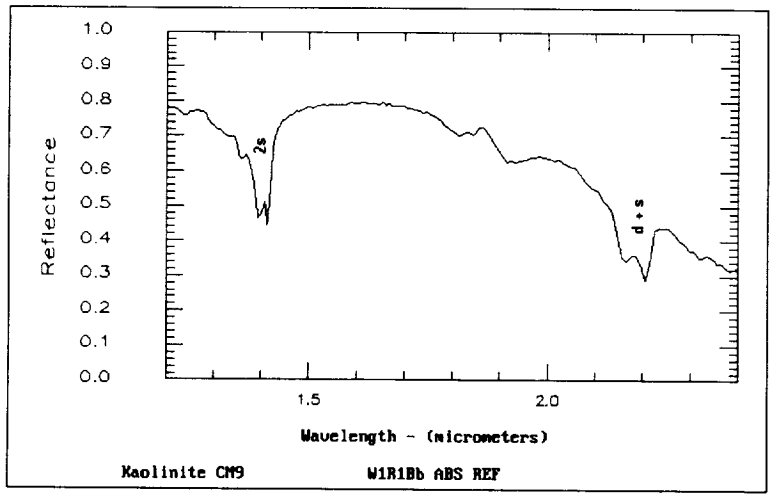

Figure 1. Diffuse reflectance spectra of a kaolinite sample, entitled CM9 of the USGS spectral library, from Mesa Alta (New Mexico), show absorption bands.

2.2 Gibbsite ($Al_2O_3 3H_20$)

Soils, which have been subject to pronounced alteration, like the oxisols located in the old erosion surfaces, may present a large amount of gibbsite on their composition. In some cases it may be the most important mineral in the clay fraction.

Gibbsite, as kaolinite, presents spectral features due to OH^- vibrations. In the near infrared gibbsite presents harmonic molecular vibrations (2s) close to 1550 nm and the combinations of the type d + s close to 2300 nm (Hunt et al., 1971). The bands of absorption of the water are shown to 1400 nm (2s) and to 1900 nm (d + s). The Figure 2 presents the characteristic features of a gibbsite sample (HS423 of the library of USGS), from Brazil.

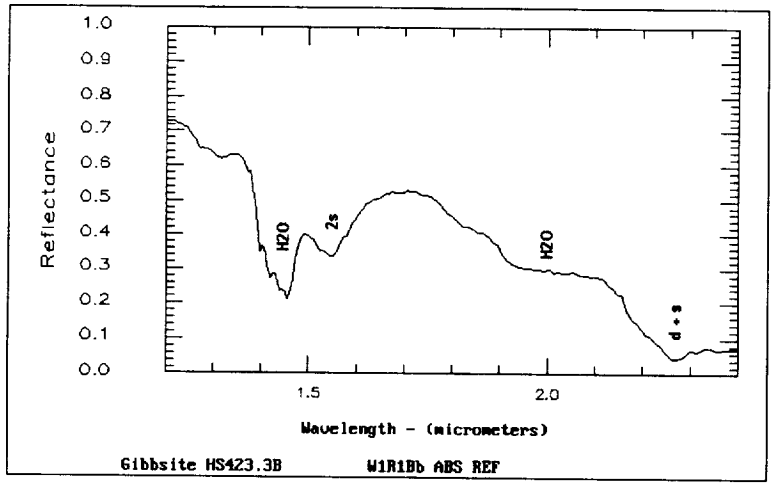

Figure 2. Characteristic features of a gibbsite sample (HS423 of the library of USGS), from Brazil.

2.3 Goethite (FeOOH) and Hematite (Fe_2O_3)

Goethite (FeOOH) and hematite (Fe_2O_3) are the most frequently occurring ferric iron (Fe^{3+}) minerals found in tropical soils. They result from the oxidation of iron present as Fe^{2+} in primary minerals in the soil forming process. The predominance of one or other of these minerals has been related to pedoclimatic factors and the understanding of their occurrence is important in the study of tropical soils.

These iron oxides have different reflectance features in the visible and near infrared spectra. Some of these features are responsible for their colors: red for hematite and brown-yellow for goethite. Sherman and Waite (1985) showed that the difference between the colors of those two minerals is determined by the transition 2(6A1) => 2(4T1), that happen in 480 nm for the goethite and 530 nm for the hematite.

The figure 3 shows the diffuse reflectance spectra of a goethite (a) and hematite (b). The goethite sample (WS222 - USGS spectral library) it is coming of Superior it Mines, Marquette, Michigan, while the one of hematite (GDS27 - USGS spectral library), is a synthetic sample (Baker Analyzed Reagent).

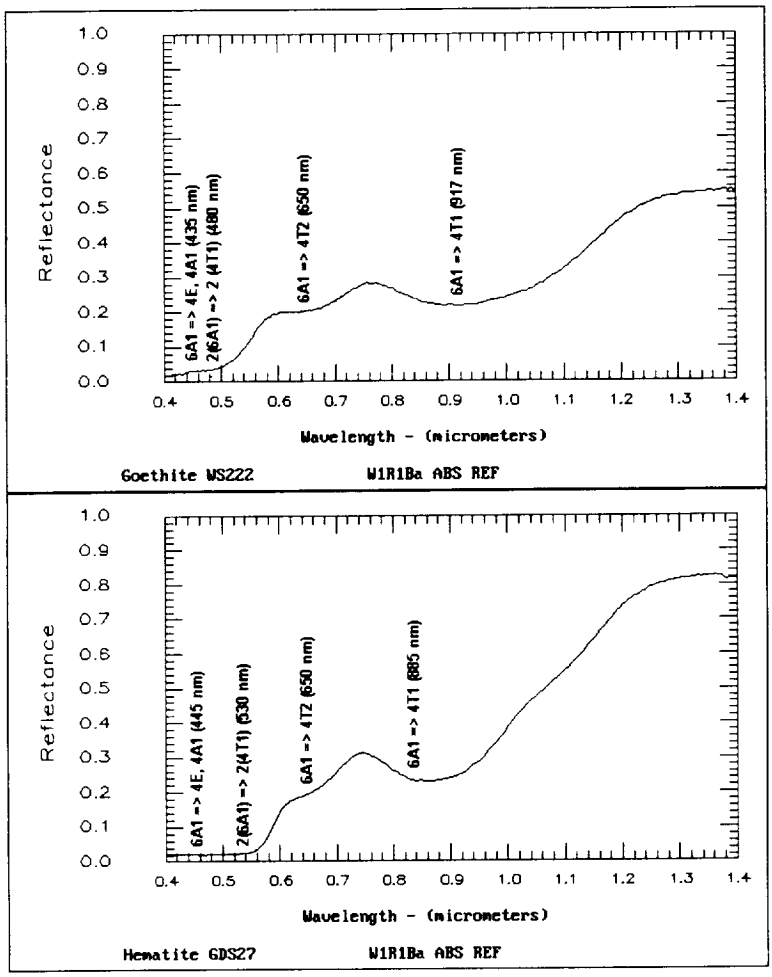

Figure 3. Diffuse reflectance spectra of a goethite (a) and hematite (b).

3. METHODOLOGY

The adopted methodological steps are subdivided in 3 stages: atmospheric correction and reduction of AVIRIS radiance to scaled surface reflectance; gathering of soil samples in the field; and spectro-radiometry and X-ray diffraction analysis of soil samples.

The image of São João D'Aliança district, Goiás state (950816L2 scene 3) was selected, due to the presence of bare soil areas associated to topographical variations.

3.1 Atmospheric Correction and Reduction of AVIRIS Radiance to Scaled Surface Reflectance

This was done at INPE (National Institute of Space Researches - São José of Campos, São Paulo) using Green's method (Green et al., 1991), counting with the participation of Dr. Robert O. Green in the determination of the correction parameters.

That method is based on the model of radioactive transfer MODTRAN. According to Clark et al. (1995) the correction is accomplished by adjusting the oxygen, carbon dioxide and water levels of each pixel. Although it spends 50 times more computer time than other models, this method is considered as one of the best procedures for atmospheric correction and derivation of scaled surface reflectance from AVIRIS data.

3.2 Soil Sampling

Field work was conducted to sample the main soil units. At the time of the AVIRIS flight most of the soil surface was covered by crop residues, which limited the bare soils to two fields: one represented by a uniform flat (slope < 3%) area with clayey Dark Red Latosol (points 1 and 2). The other by a gently sloping (<8%) area with clayey Dark Red Latosol (point 7), sandy loam Red Yellow Latosol (point 6), Cambisol (point 4) and Quartz sands (points 3).

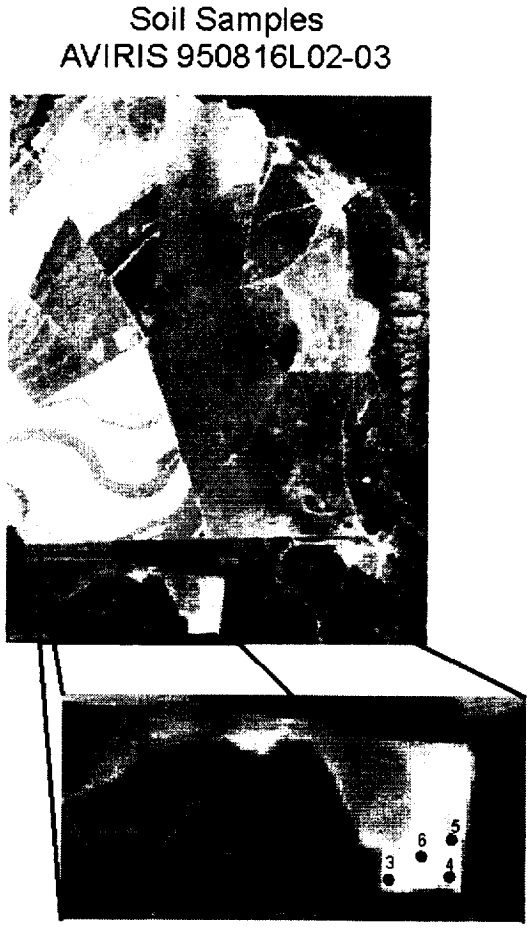

Figure 4. Soil samples sites.

3.3 Radiometry and X-ray Diffraction Experiments

The radiometry experiments were accomplished in Embrapa/CPAC, being used a radiometer GER (Geophysical & Environmental Research Corp.), model MARK V. That instrument has a spectral range of 300 to

2500 nm, with spectral bandwidth of 2 nm in the 300 nm to 1000 nm region and 4 nm in the 1000 to 2500 nm region.

X-ray diffraction data were obtained for the powder, between 2 and 80° 2θ, with step of sweeping of 0.02° 2θ using an apparatus with a Cu tube and a Ni filter. The quantification of the minerals was obtained with the aid of an analysis program - Jade for Windows®.

4. RESULTS

The spectral results will be presented considering two wavelength intervals: 450 nm to 1100 nm, visible and near infrared and to 2000 nm at 2400nm, short wave infrared.

The mineralogical composition of the A horizon of the sampled soils, is presented in table 1.

Table 1. Mineral composition of the A horizon of the sampled soils

Samples	Hematite (%)	Goethite (%)	Kaolinite (%)	Gibbsite (%)	Quartz (%)
1	7.8	2.9	47.7	26.1	15.5
2	8.5	3.4	37.9	30.0	20.3
3	0.5	0.8	3.3	0.0	95.4
4	1.5	1.3	17.4	4.5	75.3
5	2.0	0.4	11.9	2.3	83.4
6	1.3	1.2	10.2	2.5	84.8
7	4.0	0.6	29.3	10.8	55.4

Except for samples 3 and 6, all the samples presented more than 70% of hematite composing the free iron oxides. The sample 3 present more goethite than hematite and the sample 6, very seemed values.

Samples 1 and 2 present the highest values of gibbsite, showing a high degree of weathering. Sample 3, a Quartz Sand (Quartzpsament), presented no gibbsite. In samples 3 to 6 kaolinite clearly prevails over gibbsite. Sample 7 presented an intermediate value gibbsite. These variations in the kaolinite/gibbsite proportions are a good example of the variability of the weathering degree usually found in Central Plateau of Brazil.

Figures 5 to 10 present X-ray diffractograms and reflectance spectra (2000 to 2400 nm) obtained in the laboratory and with AVIRIS for selected samples. Sample 1 presented high kaolinite and gibbsite values as evidenced by the diffractogram (10° to 20° 2θ) of figure 5. The spectra of figure 6 show the features that can be attributed to kaolinite and gibbsite in the data obtained in laboratory as well as with AVIRIS. Similar results are observed for sample 2 (figures 7 and 8). It is important to note that variations in the intensities of the features attributable to kaolinite and gibbsite in samples 1 and 2 in the diffractogram are also found in the reflectance spectra. Results for the sample 3 (Quartzpsaments) with low contents of kaolinite and absence of gibbsite are presented in figures 9 and 10 showing agreement between X-ray and reflectance data. Madeira Netto (1993) has reported a good correlation between the intensity of absorption of kaolinite and gibbsite measured in diffuse reflectance spectra and contents of those minerals in latosols. This author has also derived an index from kaolinite and gibbsite intensities of absorption that correlates strongly with the ratio of kaolinite and gibbsite contents in the soil which is very useful for estimating the weathering degree of soils from reflectance data. Since a very limited amount of data is available, these relationships could not be tested for AVIRIS data. However the trends observed, indicates the potential of this hyperspectral images for quantification purposes of those important minerals.

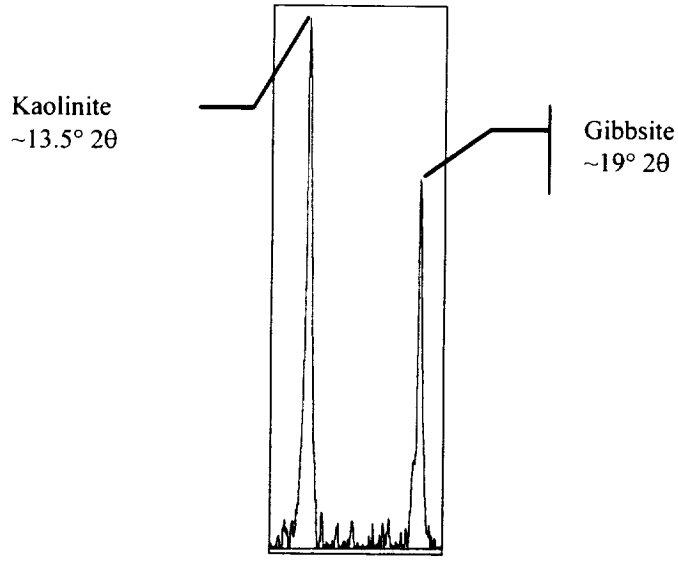

Figure 5. Diffractogram of soil sample 1.

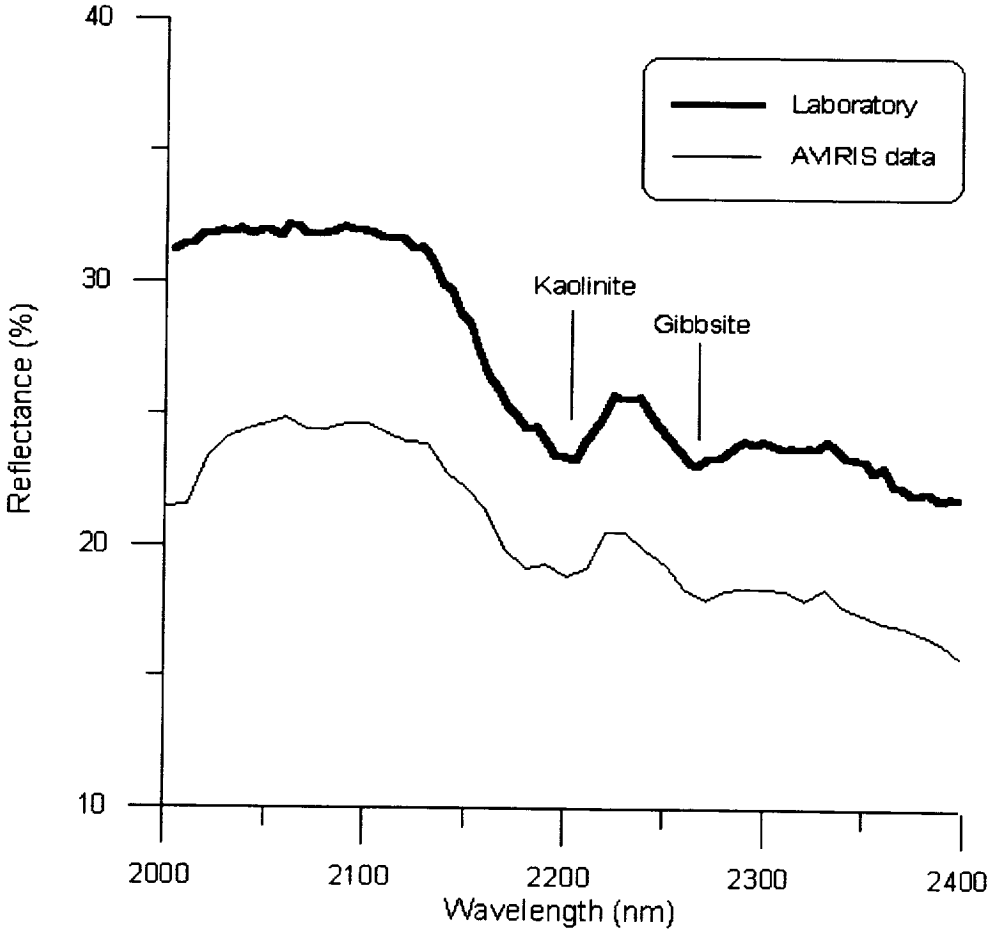

Figure 6. Spectral curves of soil sample 1 in short wave infrared region.

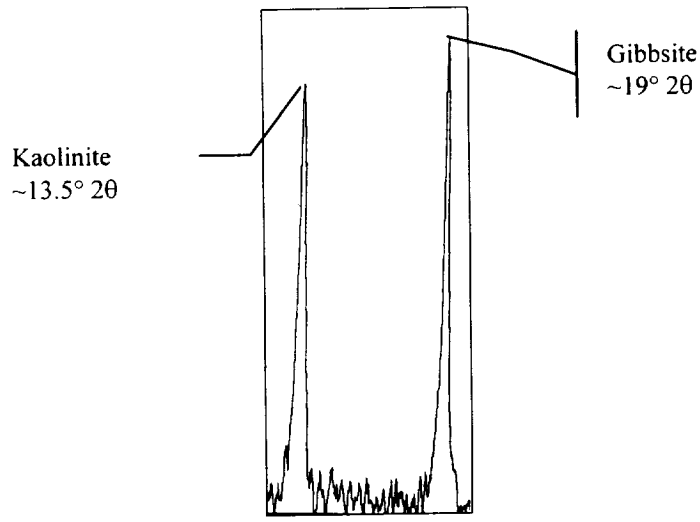

Figure 7. Diffractogram of soil sample 2.

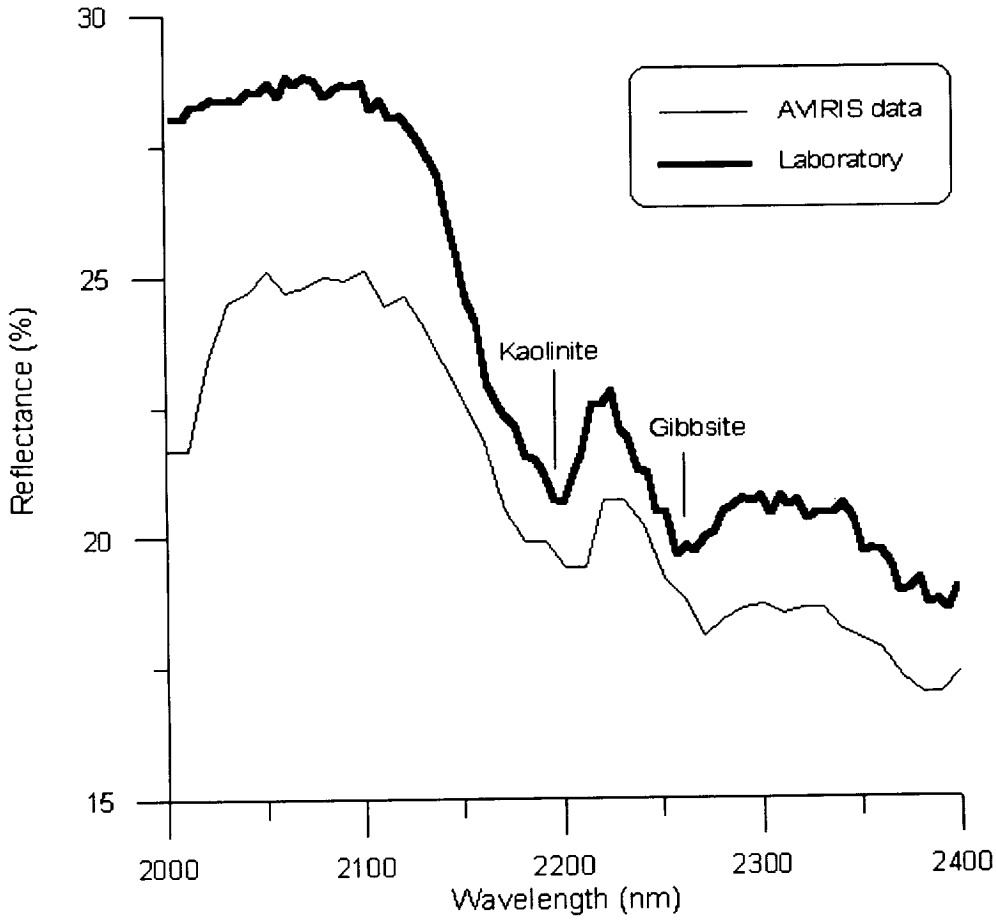

Figure 8. Spectral curves of soil sample 2 in short wave infrared region.

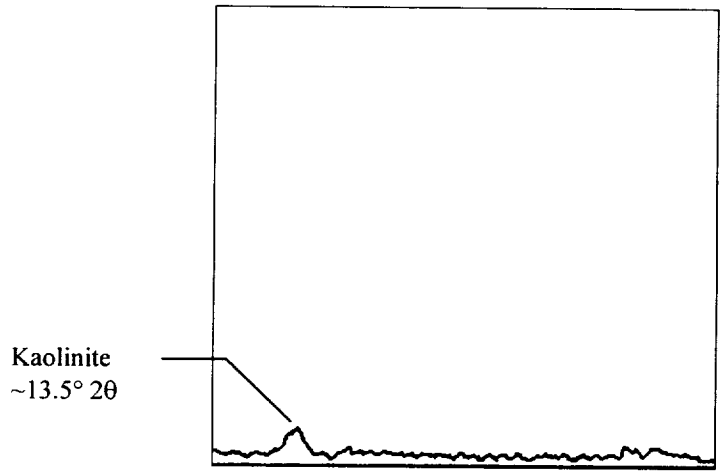

Figure 9. Diffractogram of soil sample 3.

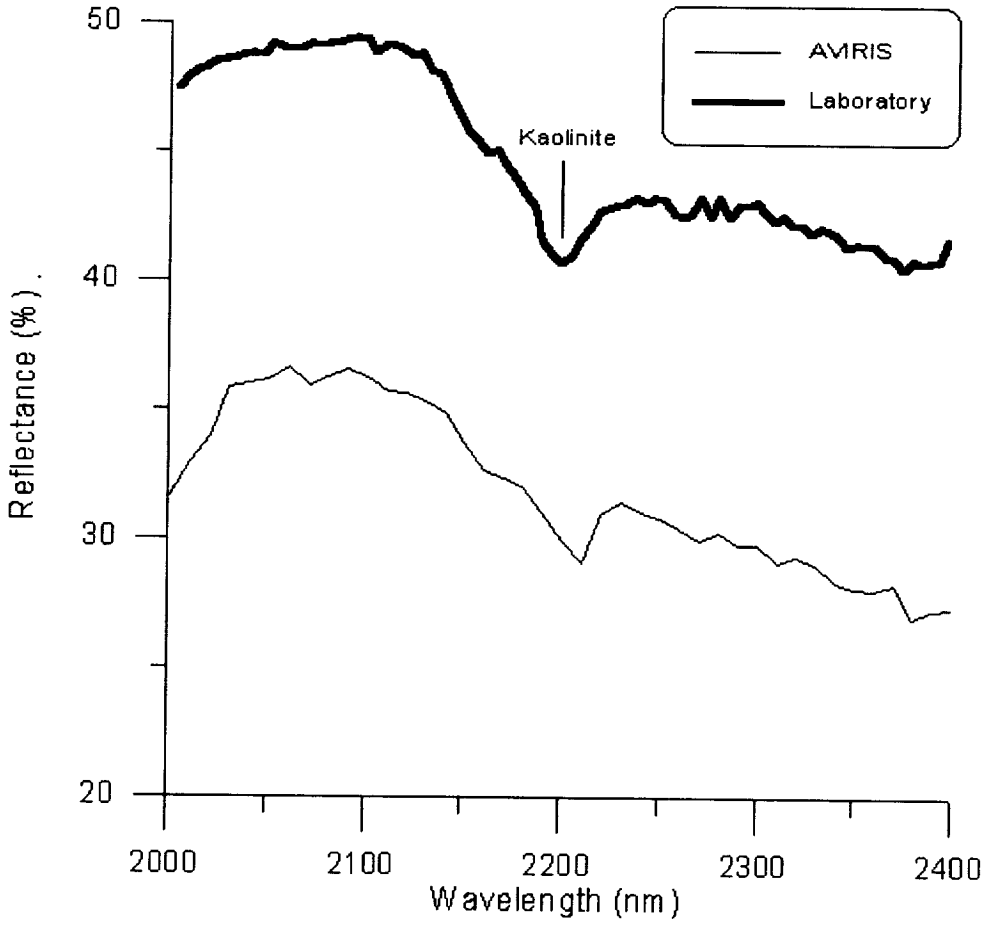

Figure 10. Spectral curves of soil sample 3 in short wave infrared region.

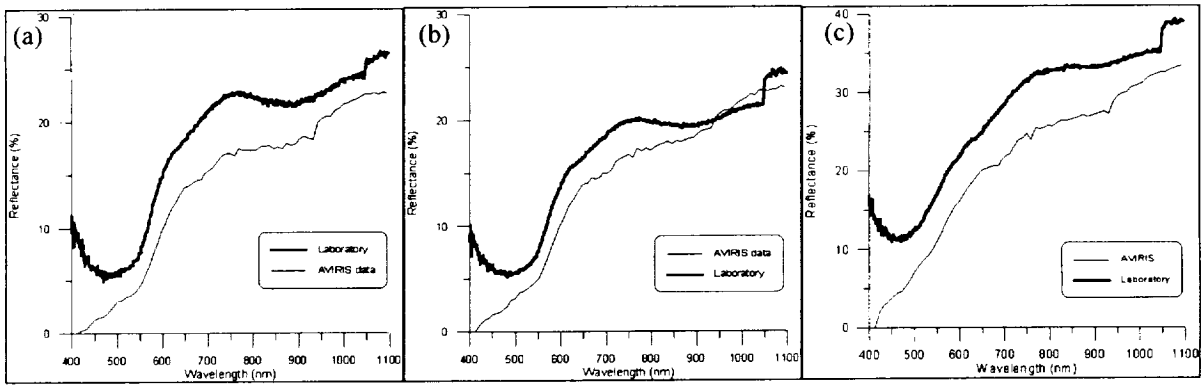

Figure 11. Spectral curves of soil samples 1 (a), 2 (b) and 3 (c) in visible and near infrared region.

Figure 11 shows the visible to near infrared spectra (400nm – 1100 nm) of points 1, 2 and 3 obtained with a GER – MARK V spectroradiometer and with AVIRIS. The general shapes of the curves obtained in the laboratory are similar to the ones reported by Valeriano et al. (1995) for the corresponding soil types. The strong feature observed at 1050 nm is due to detector change during data acquisition. The other features are due mainly to Fe^{3+} electronic transitions: close to 450 and 900 nm in a broad concave shape and an inflection close to 650 nm. The position of the minima close to 450 nm is the determining factor for the differences in soil color and are related to the goethite / hematite relative composition (Madeira Netto, 1997). The spectra obtained by AVIRIS present a clear difference from the ones obtained at laboratory mainly in the 400 nm to 500 nm range. Note that the reflectance values at 400 nm are set to 0 for all the spectra. This apparent abnormality seems to be the origin of the discrepancies observed in the blue-green wavelength. The features centered at ~650 nm and ~900 nm can also be observed in the AVIRIS spectra, although the intensities are not as strong as in the MARK V spectra.

5. CONCLUSIONS

AVIRIS spectral data may be a valuable aid in the study of tropical soil mineral components, mainly in the wavelength range where the characteristic features of kaolinite and gibbsite are present.

In relation to the iron oxides, a problem was detected in the blue/green region, where the data of AVIRIS don't correspond to the spectral data obtained in laboratory. Two hypotheses are considered: a problem with the sensor system, because the first 4 bands present reflectance values equal to zero, for all the pixels of the image; or a problem in the processing of atmospheric correction, that could have suppressed the information of the first 4 bands.

The next steps to be adopted in exploring the potentialities of AVIRIS will include increasing the number of the samples and of soil types covered, more precise chemical and mineralogical studies, in order to define procedures useful in the mineralogical mapping for a better understanding of the pedologic environment.

6. ACKNOWLEDGMENTS

We would like to thank Dr. Robert Green and the colleagues of INPE, especially Moacir Godoy Jr., for their valuable assistance in atmospheric correction.

7. REFERENCES

Clark, R.N., G.A. Swayze, K. Heidebrecht, R.O. Green and A.F.H. Goetz, 1995, "Calibration to Surface Reflectance of Terrestrial Imaging Spectrometry Data: Comparison of methods", Summaries of the Fifth Airbone Visible/Infrared Imaging Spectrometer (AVIRIS) Workshop, JPL Publication 95-1, vol.1, Jet Propulsion Laboratory, Pasadena, CA, pp. 41-42.

Green, R.O., J.E. Conel, J.S. Margolis, C.J. Brugge and G.L. Hoover, 1991, "Na Inversion Algorithm for Retrieval of Atmospheric and Leaf Water Absorption from AVIRIS Radiance with Compensation for

Atmospheric Scattering", Proceedings of the Third Airbone Visible/Infrared Imaging Spectrometer (AVIRIS) Workshop, JPL Publications 91-28, Jet Propulsion Laboratory, Pasadena, CA, pp. 51-61.

Hlavay, H., K. Jonas, S. Elek and J. Inczedy, 1977, "Characterization of the Particle Size and Christallinity of Certain Minerals by Infrared Spectrophotometry and Other Instrumental Methods – I. Investigations on clay minerals", Clays and Clay Minerals, vol. 25, pp. 451-456.

Hunt, G.R., J.W. Salisbury and C.J. Lenhoff, 1971, "Visible and Near-Infrared Spectra of Minerals and Rocks: III. Oxides and hydroxides", Modern Geology, vol. 2, pp. 195-205.

Madeira Netto, J. da S., 1993, "Étude Quantitative des Relations Constituants Minéralogiques – Réflectance Diffuse des Latosols Brésiliens: Application à l'utilisation pédologique des données satellitaires TM (Région de Brasilia)", Éditions de l'ORSTOM, Paris, 236p.

Madeira Netto, J. da S., A. Bédidi, B. Cervelle, M. Pouget, N. Flay, "Visible Spectrometric Indices of Hematite (Hm) and Goethite (Gt) Content in Lateritic Soils: the application of a Thematic Mapper (TM) image for soil-mapping in Brasília, Brazil", Int. J. Remote Sensing, vol. 18, pp. 2835 – 2852.

Sherman, D.M. and T.D. Waite, 1985, "Electronic Spectra of Fe^{3+} Oxides and Oxide Hydroxides in the Near IR to Near UV", American Mineralogist, vol. 70, pp. 1262-1269.

Valeriano, M.M., J.C.N. Epiphanio, A.R. Formaggio, J.B. Oliveira, 1995, "Bi-directional Reflectance Factor of 14 Soil Classes from Brazil", Int. J. Remote Sensing, vol. 16, pp. 113 – 128.

INCORPORATING ENDMEMBER VARIABILITY INTO SPECTRAL MIXTURE ANALYSIS THROUGH ENDMEMBER BUNDLES

C. Ann Bateson, Gregory P. Asner, Carol A. Wessman

Cooperative Institute for Research in Environmental Sciences
University of Colorado, Boulder, CO 80302

1. INTRODUCTION

Variation in canopy structure and biochemistry induces a concomitant variation in the top-of-canopy spectral reflectance of a vegetation type. Hence, the use of a single endmember spectrum to track the fractional abundance of a given vegetation cover in a hyperspectral image may result in fractions with considerable error. One solution to the problem of endmember variability is to increase the number of endmembers used in a spectral mixture analysis of the image. For example, there could be several tree endmembers in the analysis because of differences in leaf area index (LAI) and multiple scatterings between leaves and stems. However, it is often difficult in terms of computer or human interaction time to select more than six or seven endmembers and any non-removable noise, as well as the number of uncorrelated bands in the image, limits the number of endmembers that can be discriminated. Moreover, as endmembers proliferate, their interpretation becomes increasingly difficult and often applications simply need the aerial fractions of a few land cover components which comprise most of the scene.

In order to incorporate endmember variability into spectral mixture analysis, we propose representing a landscape component type not with one endmember spectrum but with a set or bundle of spectra, each of which is feasible as the spectrum of an instance of the component (e.g., in the case of a tree component, each spectrum could reasonably be the spectral reflectance of a tree canopy). These endmember bundles can be used with nonlinear optimization algorithms to find upper and lower bounds on endmember fractions.

This approach to endmember variability naturally evolved from previous work (Bateson and Curtiss, 1996) in deriving endmembers from the data itself by fitting a triangle, tetrahedron or, more generally, a simplex to the data cloud reduced in dimension by a principal component analysis. Conceptually, endmember variability could make it difficult to find a simplex that both surrounds the data cloud and has vertices that are realistic endmember spectra with reflectances between 0 and 1.

In this paper, we create endmember bundles and bounding fraction images for an AVIRIS subscene simulated with a plant canopy radiative transfer model. The simulated subscene is spatially patterned after a subscene from the AVIRIS image acquired August, 1993 over La Copita, Texas. In addition, for comparison, we performed a traditional unmixing with image endmembers.

2. MODEL SIMULATION

A discrete ordinates plant canopy radiative transfer model was used to create AVIRIS-like image endmembers. Various aspects of the model are described in Iaquinta and Pinty (1994), Asner et al. (1997, 1998), and Asner and Wessman (1997). A brief summary description follows.

Single scattering is solved exactly while multiple scattering is simplified to a single-angle problem (zenith) (Iaquinta and Pinty, 1994). The model is designed explicitly for use with hyperspectral data, as wavelength-independent calculations (e.g. leaf angle distribution) are made only once per simulation, while those calculations requiring the leaf and stem optical properties (e.g. multiple scattering) are iterated by wavelength. The model produces top-of-canopy reflectance values from the following parameters: leaf and stem area index (LAI, SAI), leaf and stem angle

distributions (LAD, SAD), leaf and stem hemispherical reflectance and transmittance properties and soil reflectance, sun and view zenith and azimuth angles, and a hot-spot parameter for each vegetation component.

Scattering characteristics at the tissue and soil level are modeled as isotropic. Both leaf and non-photosynthetic vegetation (NPV) are included in the radiative transfer equation formulation. LAI and SAI are given on an m^2m^{-2} basis, and LAD and SAD can be modeled as erectophile, planophile, plagiophile, uniform, or as an ellipsoidal distribution with a given mean leaf angle (deWit 1965, Campbell 1986). For all analyses in this paper, solar zenith and azimuth angles were set at $20°$ and $0°$, respectively. View zenith and azimuth angles were both set to $0°$. The simulated image is based on the three dominant land-cover types found at La Copita: woody plant canopies, senescent grass canopies, and bare soil. The lack of a green grass component is realistic for La Copita in August, and has been documented in ground studies that found 95% of the graminoid biomass was dead in August 1993.

Leaf, woody stem, litter, and soil spectra gathered throughout the La Copita site were convolved to AVIRIS spectral response curves to produce 220 optical channels ranging from 400-2450 nm. LAI and mean leaf angle values gathered in August 1993 were used to constrain the range of canopy structural attributes for each simulated endmember. For each simulated AVIRIS pixel, LAI and mean leaf angle of an ellipsoidal distribution were randomly selected (Table 1). This created a range of reflectance spectra for each tree and grass endmember. A shade endmember was created based on the downwelling flux through the tree canopy (calculated in the radiative transfer model).

The tree, senescent grass, shade and bare soil endmembers were then linearly mixed by creating endmember cover fractions based on NDVI values computed for a 1993 AVIRIS subscene of La Copita. When NDVI was greater than 0.45, the tree fraction randomly varied from 70-90% cover; otherwise, it ranged from 0-69%. The shade fraction was 10% of the tree fraction. Soil and senescent grass fractions were randomly generated to sum all endmembers to 1 in each pixel. The fraction images used to direct the linear mixing of endmember spectra to produce the simulated AVIRIS image will be referred to in the sequel as the ground truth (GT) fraction images with one exception. Because the tree and shade fractions were perfectly correlated, it was not possible to derive a separate shade bundle. Hence, the image of their sum will be considered the GT tree image.

3. METHODS

3.1 Construction of Bundles

The simple scatterplot in Figure 1 illustrates the problem when pixels are mixtures of three components (Tree, Grass and Soil) with varying spectral signatures. An attempt to enclose the data in a minimal area triangle and interpret its vertices as endmembers (in this case, spectra T, G and S) will not yield spectral signatures and may in fact produce unrealistic spectra with reflectances not between 0 and 1.

What is needed is the delineation of the regions (referred to as bundles) labeled Tree, Grass and Soil in Figure 1. For the simulated La Copita scene, this delineation was done in five steps:

(1) A principal component analysis was performed on the simulated image and the data was reduced to two dimensions.

(2) Individual endmember spectra were selected automatically in the reduced dimension space using a simulated annealing algorithm. These endmembers (Figure 2) are analogous to T, G and S in Figure 1.

(3) The endmembers in (2) were significantly relocated using the manual endmember selection tool described in Bateson and Curtiss (1996) to the spectra in Figure 3, which are clearly recognizable as pure soil, tree and senescent grass. However, the data is not contained in the simplex they span.

(4) The endmembers in (3) were used as seeds to grow the soil, tree and senescent grass bundles in the

following way. Initially, each bundle contained its seed endmember. Nearby spectra were included in the bundle as long as their reflectance values ranged between 0 and 1 and they were sufficiently correlated (R=.99) to the seed endmember. Special care was taken to insure the bundles did not grow into each other and that no bundle grew into the smallest convex set containing the other bundles.

(5) In order to better contain the data within the convex hull of the three bundles, additional spectra were added to the senescent grass bundle.

The fact that realistic endmembers bounding the data cloud could not be found in steps (2) and (3) is symptomatic of endmember variability. In step (4), we limited the spectra in the tree, senescent grass and soil bundles to have reflectances bounded below by 0.02 and above by 0.5, 0.5 and 0.45 respectively. These limits were selected after examining the range of values in the image. Since the simulated image had a constant soil background, the soil bundle does not represent endmember variability but uncertainty in our knowledge of that endmember. The endmember bundles are shown in Figure 4.

3.2 Fraction Estimates

For each pixel P, we found upper and lower bounds on the tree fractional abundance by twice applying a constrained quasi-Newton algorithm to select from the bundles two sets of spectra. Each set contained one spectrum from each of the three bundles and in both cases P was contained within the triangle spanned by the spectra in the set. The first set was selected to maximize the fractional abundance of trees in P and the second set to minimize it. Repeating this procedure with soil and senescent grass, we obtained maximum and minimum images representing upper and lower bounds on endmember fractions based on the three bundles.

In addition, the simulated image was unmixed with the three image spectra having the largest fraction (~98%) of tree, senescent grass and soil in the GT fraction images. All images including the GT images are seen in Figures 6-8.

4. RESULTS

The minimum and maximum tree images (± 0.01) of Figure 8 bracket 98% of the pixels in the GT tree image. When the tree fractions computed with the image endmembers (Figure 5) were compared to the GT tree image, they had a small mean absolute error (.08). However, although the very best possible image endmembers were used to unmix the noise-free simulated scene, there were still 32 pixels with more than a 30% error in their tree fraction and 420 pixels with more than a 20% error. These large errors represent the effect that endmember variability can have on fraction estimates for individual pixels when only one spectrum is used to represent a complex landscape component like trees. In the maximum tree image, 380 of the corresponding 420 pixels differ from the GT tree image by less than 10% and in the minimum tree image 32 of the 420 pixels differ by less than 10%. Hence, the image endmember far more often underestimated than overestimated the tree fraction, but, more importantly, most of the time when large errors occurred in the tree fractions computed with the image endmembers, there was a selection of extreme endmembers from the bundles that would significantly decrease that error. Hence, the bundles approached a good characterization of endmember variability.

Soil and senescent grass minimum and maximum images (± 0.01) bracketed 94% and 99% respectively of the corresponding GT images. However, because of the low spectral contrast between soil and senescent grass, there was a close proximity between their bundles which forced their minimum images to be too small to be as useful as the Tree images.

5. CONCLUSIONS

Realistic variations in the structural attributes of trees and senescent grass together with realistic variations in tree and grass foliar optical properties are sufficient to cause errors in fractional estimates in excess of 30%.

Endmember bundles provide a conceptual framework both for understanding this variability and for quantifying the uncertainties it introduces into fractional estimates. Moreover, construction of the bundles may be accomplished without information ancillary to the AVIRIS image.

6. REFERENCES

Asner, G.P. and C.A. Wessman. 1997. Scaling PAR absorption from the leaf to landscape level in spatially heterogeneous ecosystems. Ecol. Mod. 101:145-163.

Asner, G.P., C.A. Wessman, and C.A. Bateson. 1998. Sources of variability in plant canopy hyperspectral data in a savanna ecosystem. Proc. 7th Annual JPL Airborne Earth Science Workshop.

Asner, G.P., C.A. Wessman, and J.L. Privette. 1997. Unmixing the directional reflectances of AVHRR sub-pixel landcovers. IEEE Transactions on Geoscience and Remote Sensing 35:868-878.

Bateson, C.A. and B. Curtiss, 1996. A method for manual endmember selection and spectral unmixing, Remote Sensing of Environment, 55:229-243.

deWit, C.T. 1965. Photosynthesis of leaf canopies. Agricultural Research Report 663, Pudoc Publications, Wageningen, The Netherlands.

Campbell, G.S. 1986. Extinction coefficients for radiation in plant canopies calculated using an ellipsoidal inclination angle distribution. Agricultural and Forest Meteorology 36:317-321.

Iaquinta, J. and B. Pinty. 1994. Adaptation of a bidirectional reflectance model including the hot-spot to an optically thin canopy. Proc. 6th Int'l Symp. Phys. Meas. Sign. Remote Sens., pp. 683-690.

7. ACKNOWLEDGEMENTS

This work was supported by NASA Innovative Research Grant NAGW-4689 and a grant under the NASA Earth Observing System (EOS) Interdisciplinary program (Grant NAGW-2662).

Table 1: Range of Parameter Values Used to Construct Tree and Senescent Grass Endmembers with Landscape Radiative Transfer Model.

	Range of LAI	Mean Leaf Angle of an Ellipsoidal Distribution
Tree	1.5 - 4.0	35 - 55°
Senescent Grass	1.0 - 3.0	55 - 70°

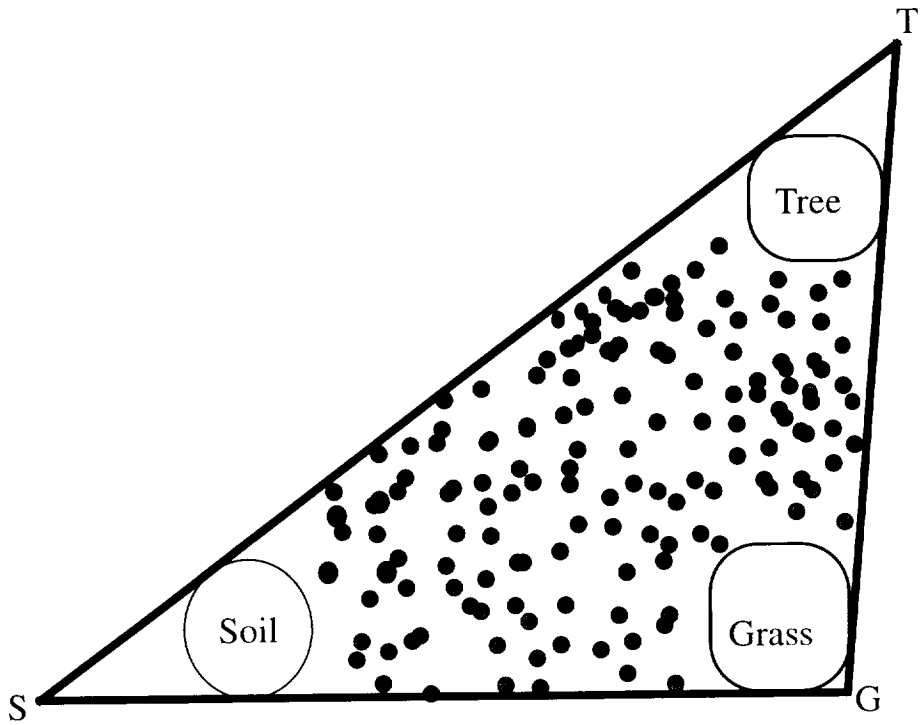

Figure 1. Scatterplot of spectral data viewed as points in the plane determined by two eigenvectors from a principal component analysis. This plot illustrates the effects of endmember variability on fitting a triangle to the data. Spectra representative of soil, trees and grass are contained within the labeled regions. The vertices, S, T and G of the smallest triangle containing the data are not within these regions and hence are not spectral endmembers. In fact, they may have unrealistic spectra with negative and superunity values.

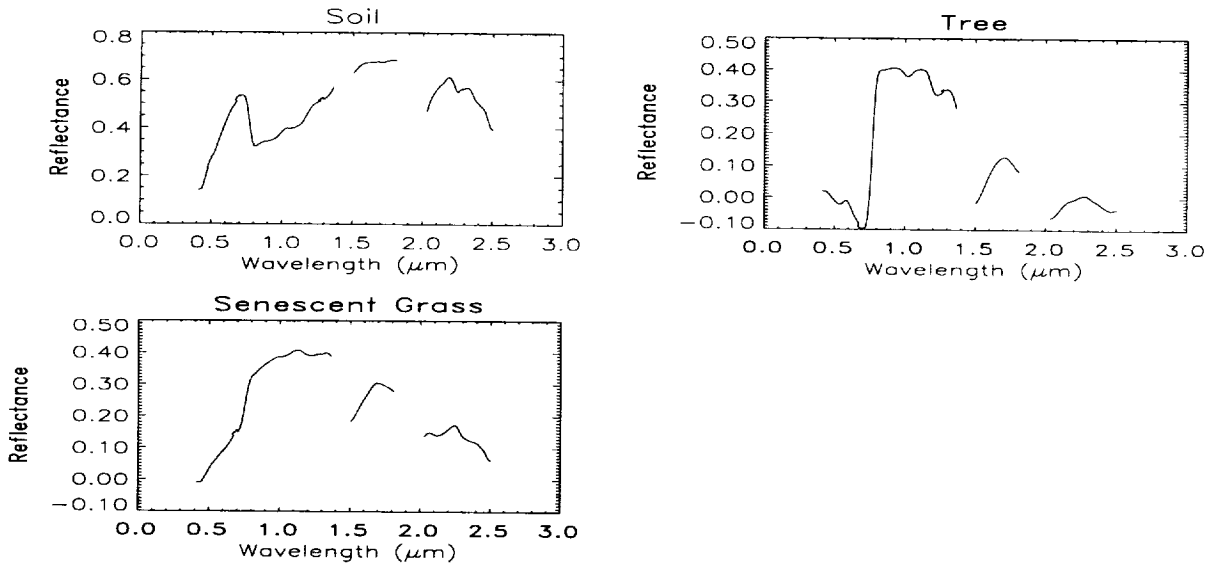

Figure 2. Endmembers automatically generated from the spectra of the simulated image. These endmembers are analogous to the vertices S, T and G in figure 1.

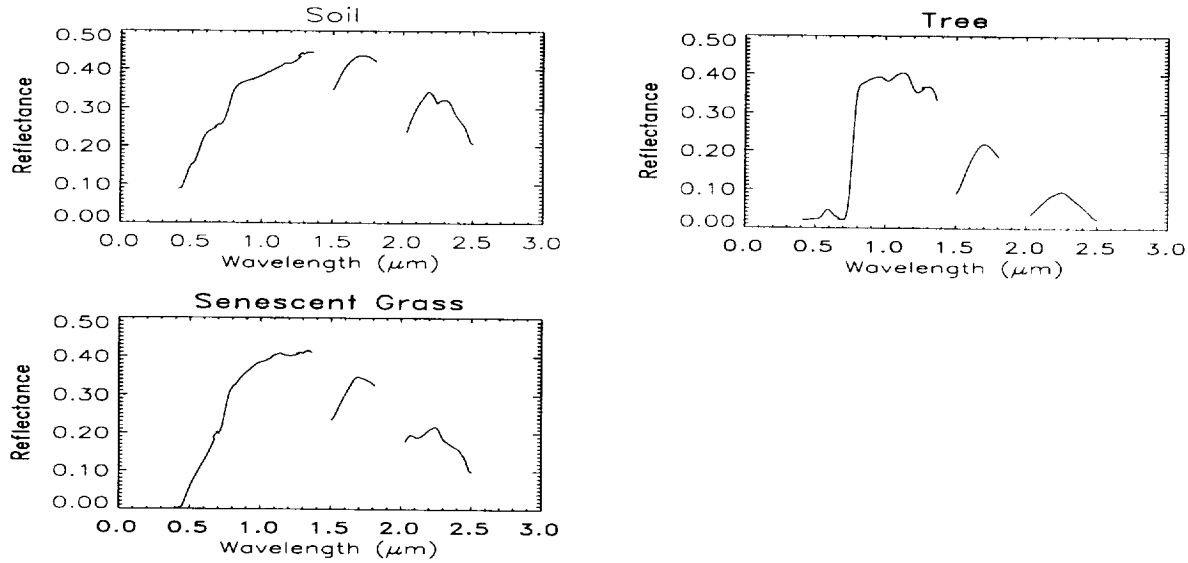

Figure 3. Endmembers selected with the manual endmember selection tool in a plane determined by two eigenvectors of a principal component analysis of the simulated image. These endmembers do not contain the data within the simplex they span.

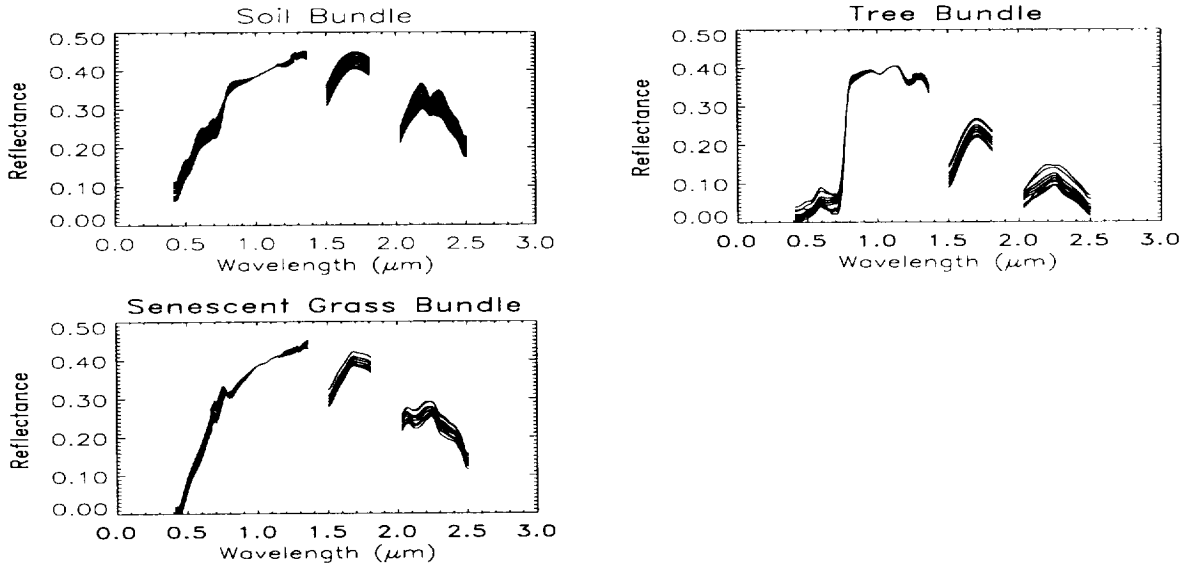

Figure 4. Endmember bundles: each bundle is grown from the corresponding endmember spectrum in Figure 3 by including nearby spectra when they are highly correlated to the seed spectrum (Pearson's correlation coefficient =.99)

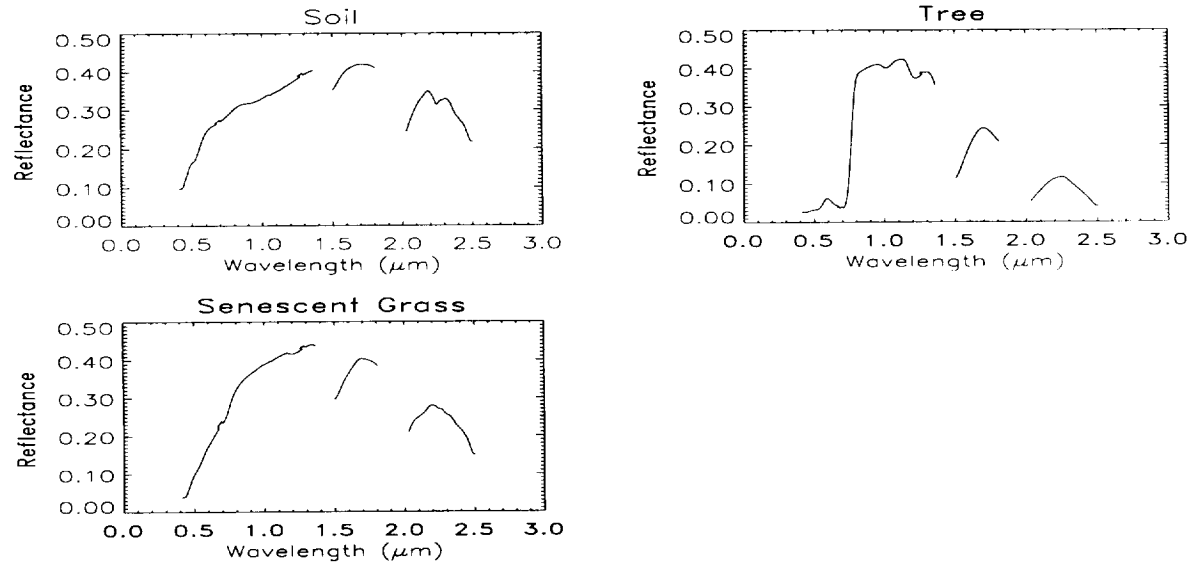

Figure 5. Endmember spectra selected directly from the image. Since these spectra are not dimension reduced through a principal component analysis, their appearance is slightly different from the spectra in figures 2-4.

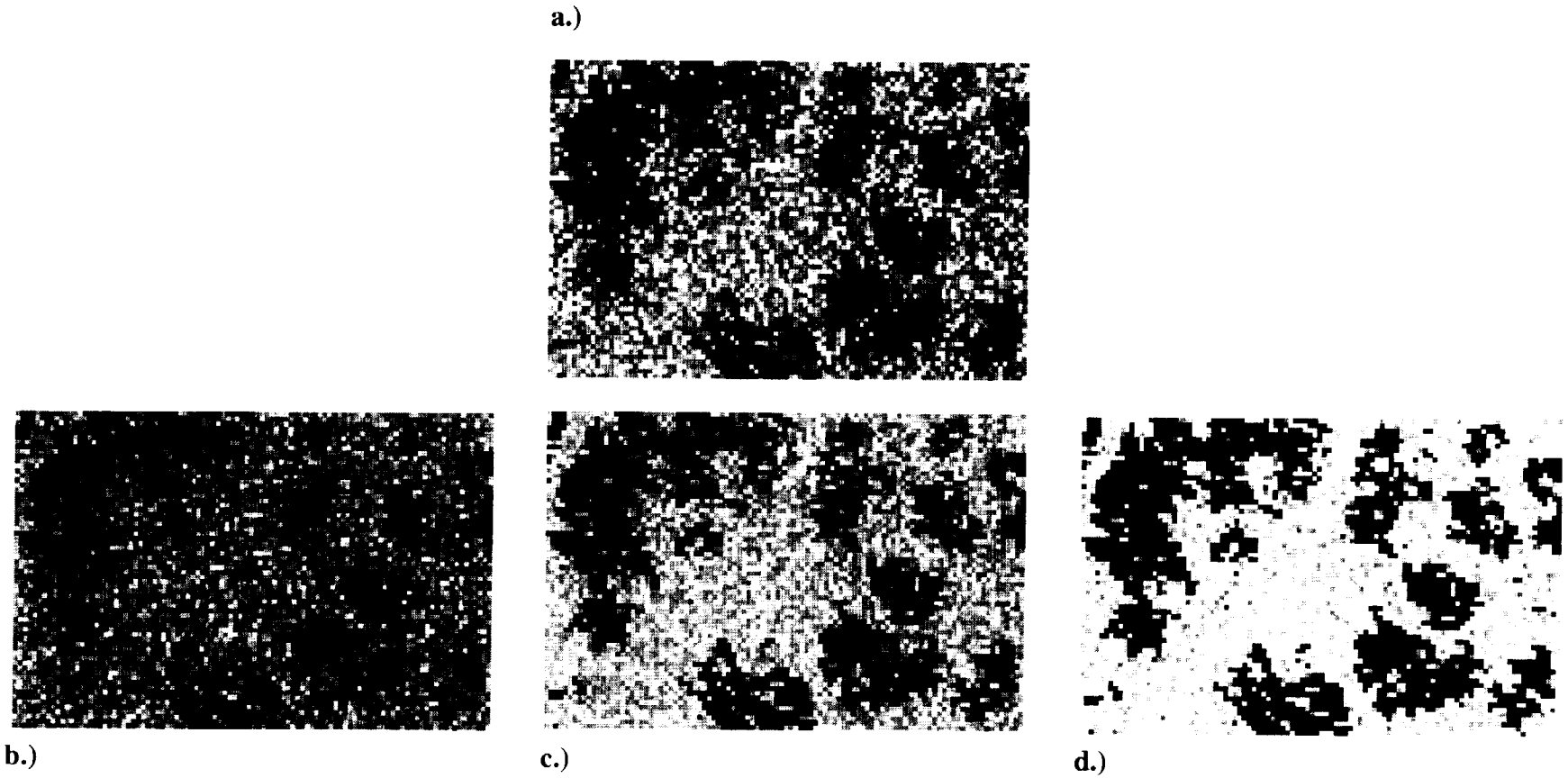

Figure 6. Tree Fraction Images: a) Fractions of the Image Tree Endmember, b.) Minimum Fractions Computed with Bundles c.) Ground Truth Fractions, and d.) maximum Fractions Computed with Bundles

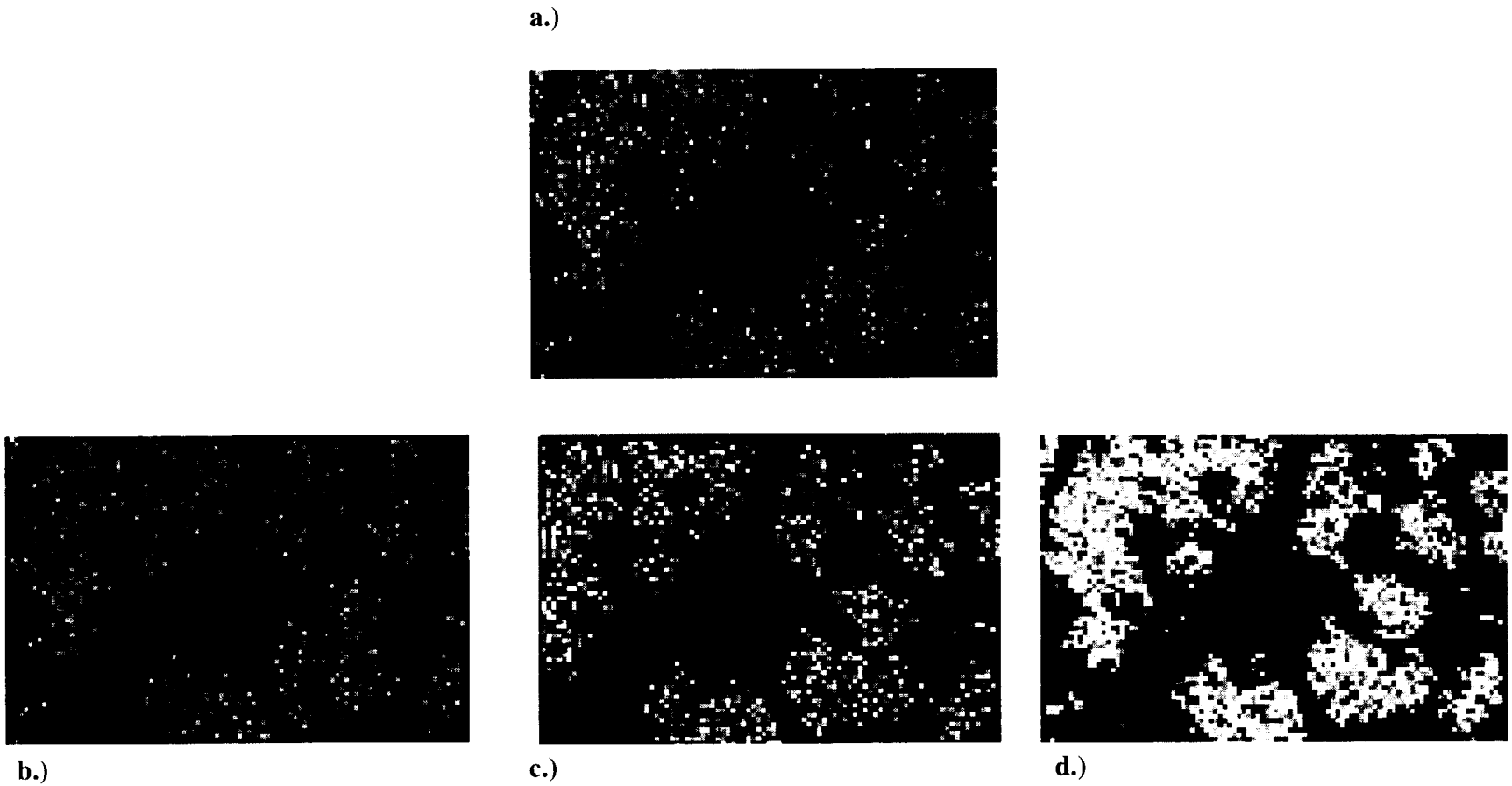

Figure 7. Soil Fraction Images: a) Fractions of the Image Soil Endmember, b.) Minimum Fractions Computed with Bundles c.) Ground Truth Fractions, and d.) Maximum Fractions Computed with Bundlles

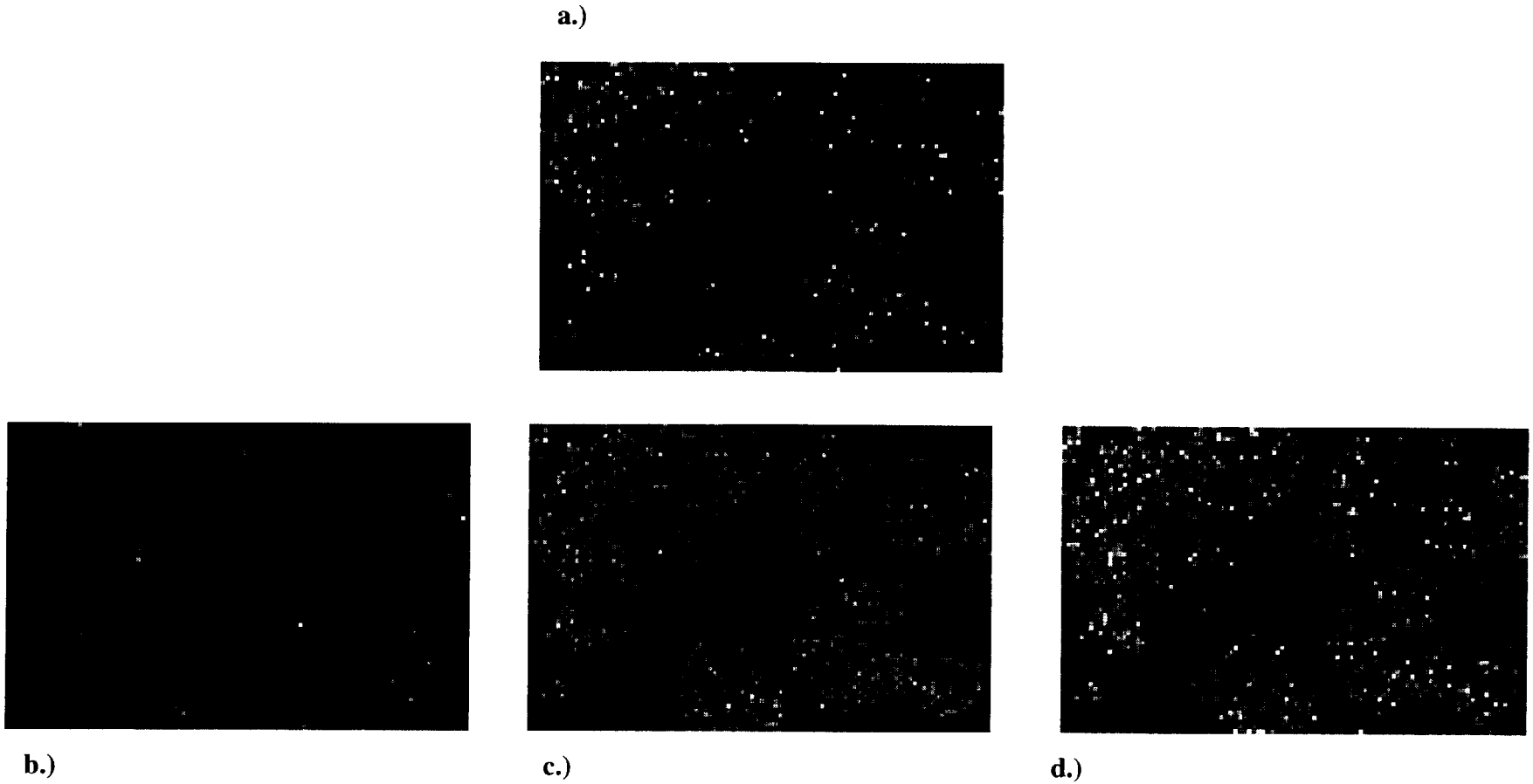

Figure 8. Senescent Grass Fraction Images: a) Fractions of the Image Senescent Grass Endmember, b.) Minimum Fraction Computed with Bundles c.) Ground Truth Fractions, and d.) Maximum Fractions Computed with Bundles

Post-ATREM Polishing of AVIRIS Apparent Reflectance Data using EFFORT : a Lesson in Accuracy versus Precision

Joseph W. Boardman
Analytical Imaging and Geophysics, LLC
Boulder, CO

boardman@aigllc.com

Since the focal plane refit before the 1995 flight season, AVIRIS has consistently produced calibrated spectral radiance data of extremely high precision. This high precision has not translated directly into high accuracy in the spectral radiance data or in the apparent surface reflectance spectra derived from them. The reason for this is the limited accuracy of the combined chain of absolute standards, calibrations, models and measurements that connect the high precision raw DN to the final output of relatively low accuracy apparent surface reflectance. Sources of error including: errors in the NIST standard bulbs; spectral and radiometric calibration uncertainty; in-flight system changes; solar irradiance model errors, inaccuracy in atmospheric parameter estimation; and radiative transfer code errors combine to limit the accuracy of the final apparent reflectance data to no better than several percent. Filtered by this relatively inaccurate signal processing chain, the very high precision (1 part in thousands) of the new AVIRIS data is underutilized. It is like a very high quality rifle in the hands of a near-sighted marksman, lots of precision but limited accuracy.

We have developed a process, EFFORT (the Empirical Flat Field Optimal Reflectance Transformation), to bootstrap a linear adjustment to the data to recover accuracy that matches the precision. It has its roots in the Empirical Line method, often used to reduce data from uncalibrated sensors using field measured spectra. However, in our application we use no ground data, and only apply the empirical gains and offsets after a theoretical data reduction has been done using the ATREM radiative transfer code. EFFORT asks a simple question, "Is there a mild linear transformation, a gain near unity and an offset near zero for each channel, that will make the spectra look more like real material spectra?". Since 1995, we have found that such a mild correction does exist and the application of these statistically insignificant adjustments, well within the error budget to the data calibration and reduction process, makes a profound improvement in the AVIRIS apparent reflectance spectra. It is like a guiding hand, gently steering our near-sighted marksman back to the bull's-eye. After EFFORT adjustment, comparison to library-based spectra is much improved. We believe that high quality imaging spectrometers will for ever more have precision that exceeds the accuracy of the atmospheric models needed to reduce them to reflectance. Thus, EFFORT seems sure to play a role in future applications requiring cutting-edge spectral fidelity.

Leveraging the High Dimensionality of AVIRIS Data for Improved Sub-Pixel Target Unmixing and Rejection of False Positives : Mixture Tuned Matched Filtering

Joseph W. Boardman
Analytical Imaging and Geophysics, LLC
Boulder, CO

boardman@aigllc.com

Much headway has been made by the direct application of the well-known signal processing technique of Matched Filtering to imaging spectrometry studies, especially applications involving detection and mapping of sub-pixel targets. The Matched Filter technique has long been used by electrical engineers for the detection of known signals in mixed backgrounds, especially in radio and radar applications. Its popularity derives from the proof that it is the optimal linear detector in such situations, maximizing the suppression of the background while simultaneously maximizing the target-to-background contrast. These dual properties make it appear to be the optimal detection method. However, in our case, the remote sensing mixed pixel case, it is most certainly not optimal. The underlying assumption of the "proof" used in radio and radar applications is one of unbounded superposition. Adding target signature in this case boosts the signal and one "hears" or "sees" the linear sum of the background and the target. This addition is wholly unbounded. In the imaging spectrometry case we have an undeniable and physically-meaningful bound on the signal: every pixel is only 100% full. As we add target material to a pixel it covers up some background, satisfying the unit-sum constraint. It does not add "area" to the pixel, as an additive radio signal adds "power" to its mixture. This simple but fundamental difference can be exploited to give an algorithm that then appears to have "super-optimal" performance, and shows the risk in a blanket application to remote sensing of techniques developed under different physical models and assumptions. We use these difference to our advantage in a technique called Mixture Tuned Matched Filtering (MTMF).

MTMF combines the best parts of the Linear Spectral Mixing model and the statistical Matched Filter model while avoiding the drawbacks of each parent method. From Matched Filtering it inherits the advantage of its ability to map a single known target without knowing the other background endmember signatures, unlike traditional Spectra Mixture modeling. From Spectral Mixture modeling it inherits the leverage arising from the mixed pixel model, the constraints on feasibility including the unit-sum and positivity requirements, unlike the Matched Filter which does not employ these fundamental facts. As a result MTMF can outperform either method, especially in cases of subtle, sub-pixel occurrences. In fact, using MTMF we have found a previously undetected, and very subtle, occurrence of ammonium minerals at the heavily studied site of Cuprite, Nevada! The MTMF method leverages the high dimensionality of AVIRIS data, using the high dimensional space to its advantage, to greatly increase detectability and selectivity. It routinely demonstrates single 3% to 5% abundance sub-pixel occurrences along with outstanding false-positive rejection and target selectivity. Question proofs of optimality.

Geometric Correction of AVIRIS Imagery Using On-Board Navigation and Engineering Data

by

Roger N. Clark, K. Eric Livo and Raymond F. Kokaly

U. S. Geological Survey, MS 964
Box 25046 Federal Center
Denver, CO 80225

(303) 236-1332
(303) 236-1371 FAX
rclark@speclab.cr.usgs.gov
http://speclab.cr.usgs.gov

Introduction

From 1989 through 1997 the NASA Airborne Visible and Infrared Imaging Spectrometer (AVIRIS) has been flown on multiple flights on an ER-2 aircraft at approximately 20 km altitude (e.g. see Vane *et al.*, 1984, Porter and Enmark, 1987, Chrien *et al.*, 1990). At the USGS, AVIRIS data have been used to make materials maps (e.g. see our web site http://speclab.cr.usgs.gov) but registration to a map base using classical control point registration methods with n-term polynomial or rubber sheeting image warping techniques has not fulfilled our expectations or needs, despite significant investment in people time. The Jet Propulsion Laboratory AVIRIS Data Facility delivers numerous engineering, aircraft state, and Global Positioning System (GPS) data sets that can be used to facilitate geometrical rectification of the imagery. Using the JPL data, combined with Digital Elevation Models (DEM), which can crudely, but adequately, be derived from atmospheric absorptions in the AVIRIS data, complete geometric correction appears possible. This paper derives the equations and compares the magnitudes of effects of the ER-2 plane motions on the AVIRIS imagery using example 1995 data over Arches National Park.

The AVIRIS scanner, similar to other "whisk broom" or "push broom" scanners has a relatively geometrically correct scan line that wanders around with the roll, pitch yaw, velocity and direction changes in the moving aircraft. The cross-track scan line dimension is geometrically excellent because the scan time is fast (8.3 msec) compared to plane motions.

This speed makes the AVIRIS scan line similar to that in a "push broom" sensor. Thus, AVIRIS geometric correction is a restricted problem that currently available commercial software that we have investigated does not consider. In this paper, we derive the equations for such a system using first principles and simple geometry.

To illustrate the problem, consider a stick (or rod) 1 meter long to represent the distance from the AVIRIS instrument to the ground. At the end of the meter-stick, attach a second stick 52 cm long whose length is at right angles to the length of the meter-stick. Attach the smaller stick at its center so the combined sticks look like the letter T. This smaller stick represents the AVIRIS cross-track scan and at a distance of 1-meter is close in appearance to the scan angle of AVIRIS. Hold the meter-stick so the small "cross-track" stick is near the floor and perpendicular to the direction you are facing. Now, walk forward adding slight twists and rotations to the meter stick, and move the meter stick up and down. The ER-2 aircraft does similar distortions because of irregularities in the atmosphere. From our examination of AVIRIS engineering and navigation data, the pitch (direction of the nose of the plane up and down), and yaw (direction of the nose of the plane left and right) vary by a couple of degrees on a typical flight. One degree corresponds to about 20 AVIRIS pixels, or 350 meters, so such plane motions drastically distort the imagery. Further, we often observe in the AVIRIS engineering data pitch and yaw variations of a degree in only 100 to 200 scan lines, corresponding to pixel offsets of about 20 pixels (10-20% local distortions in the imagery)! Unless the imagery includes linear or geometric features like roads or crop circles, such distortions are usually not apparent unless compared to geometrically correct maps. Further, variations in aircraft altitude and velocity (relative to the cross-track scanner sampling velocity) produce aspect-ratio differences in the pixels. We typically observe $\sim 10\%$ errors in the aspect-ratio of AVIRIS pixels.

Another effect in imaging data is that the distance from the aircraft to the ground is not constant because of the increasing distance due to topography, and when viewing off-nadir. Both of these effects are significant and require correction even if the aircraft stability and

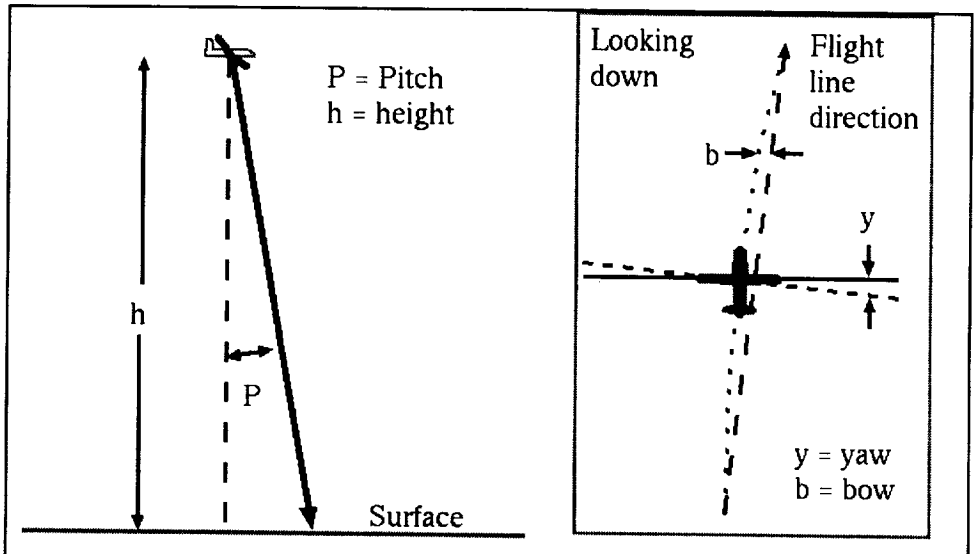

Figure 1. Conceptual geometry of an aircraft with a "wisk-broom" scanner.

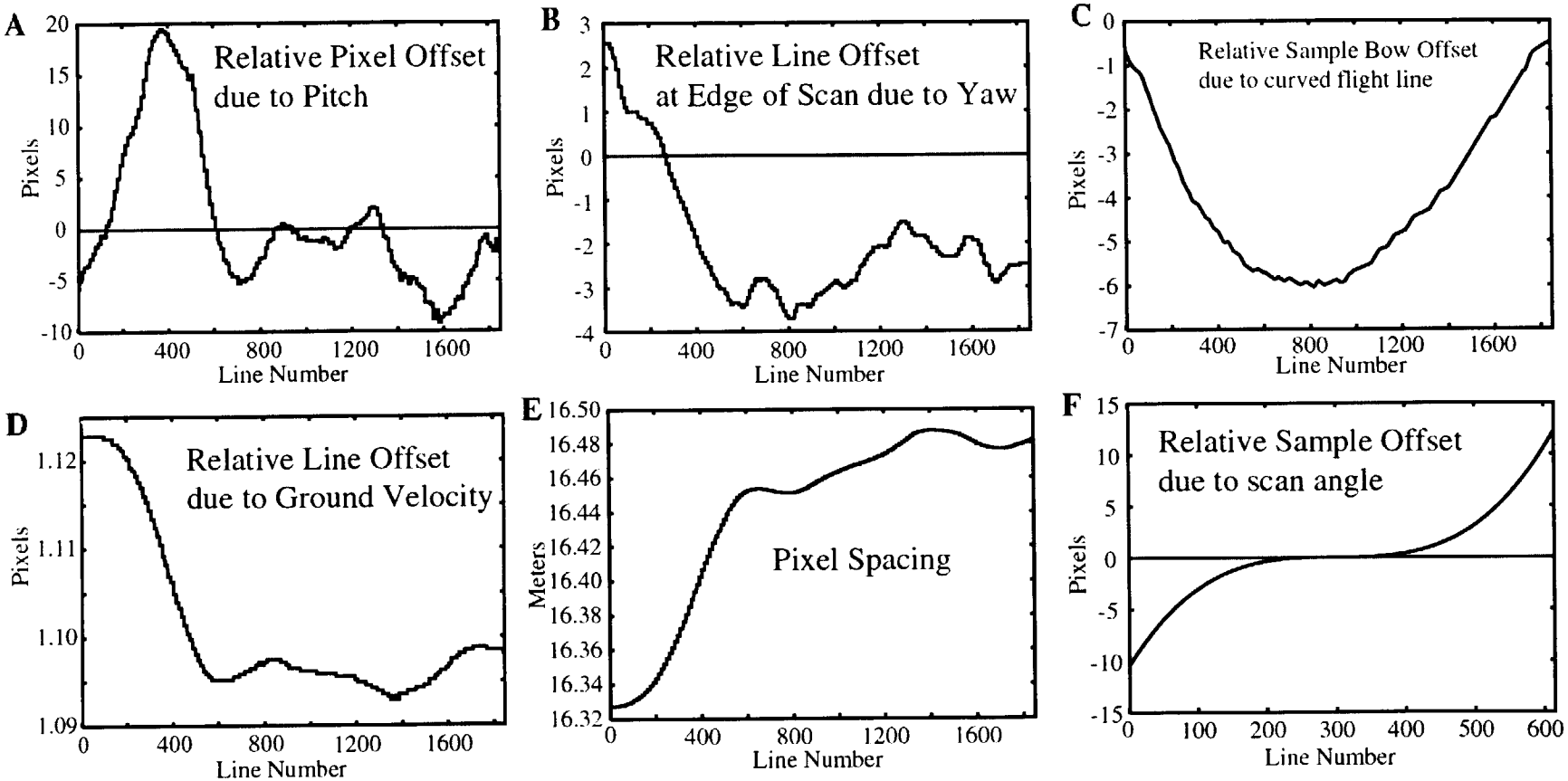

Figure 2. Example engineering data for an AVIRIS flight over Arches National Park on June 19, 1995

motions were ideal. Additionally, the aircraft may gain or lose altitude during the data acquisition.

Fortunately, the AVIRIS engineering and navigation data recorded on the airplane and distributed with the AVIRIS data can be used to correct most if not all of these distortions. The actual data recorded, how often it is sampled, and its format may vary from year to year. This paper examines data for 1995.

Geometric Correction Equations

Consider the airplane orientation in Figure 1, where the position of the aircraft is affected by roll, pitch, yaw, elevation, velocity and scan angle. First, we consider measurement over a flat plane (no topography). The AVIRIS scan width is not large, so curvature of the Earth may be ignored.

The offset distance on the ground due to pitch, d_p, is:

$$d_p = (h - e_o) \tan(pitch), \qquad \text{(eqn 1)}$$

where h is the height of the aircraft, e_o is the mean elevation of the scene, and *pitch* is the pitch angle (positive = nose up). The yaw angle of the aircraft equals the yaw angle of the scan line from the down-track direction of the flight. The magnitude of the yaw effect at any pixel is:

$$y_l = (x_c - center) \sin (yaw), \qquad \text{(eqn 2a)}$$

$$y_s = (x_c - center) \cos (yaw), \qquad \text{(eqn 2b)}$$

where y_l is the yaw offset along track (line) in pixels, y_s is the yaw offset cross track (sample) in pixels, *yaw* is the yaw angle (positive = nose to the left), x_c is the cross-track pixel and *center* is the center pixel of the cross-track scan (307 for AVIRIS). A positive yaw means the beginning of the scan line is behind the relative nadir point and the end of the scan line is ahead of nadir. The yaw and pitch effects are major effects to consider with AVIRIS on the ER-2, but yaw is not recorded. We derive yaw from the long term direction given by GPS and the true heading data:

$$lat\_avg = (latitude\_1 + latitude\_2)/2, \qquad \text{(eqn 3a)}$$

$$velocity\_heading = \arctan\{(longitude\_2 - longitude\_1)\cos(lat\_avg)/(latitude\_2 - latitude\_1)\}, \qquad \text{(eqn 3b)}$$

and

$$yaw = true\_heading - velocity\_heading, \qquad \text{(eqn 3c)}$$

where the _1 and _2 signifies the first and second positions. Example yaw data for an AVIRIS flight line are shown in Figure 2.

The AVIRIS instrument does a relative compensation for roll, meaning that once the data acquisition is started, any subsequent changes in the roll of the aircraft are compensated. That does not mean, however, that the center of the AVIRIS scan is pointed at nadir. It is pointed at the roll position, r_o, of the aircraft at the beginning of the data acquisition for that line. The roll compensation maximum is 2 degrees. Fortunately, we have not observed roll conditions that reached the limit in any of our data. Typically, the roll of the aircraft is less than a degree at the start of data acquisition and varies by only a few tenths of a degree in a flight line in the data we have examined.

The cross-track scan angle from nadir results in increasing pixel size and spacing away from nadir. The cross-track pixel offset, o_c distortion is given by:

$$o_c = (x_c - \textit{center})/\cos(a + r_o), \qquad \text{(units in pixels)}, \qquad \text{(eqn 4)}$$

where a is the cross-track angle. For AVIRIS, a increases to 15° at the edge of the scan, corresponding to approximately a 12 pixel offset (see Figure 2). The 614-pixel width of AVIRIS images becomes about 638 pixels when corrected for scan angle. The scan angle also means that objects, such as a mountain or cliff face, at the edge of the scan line will be viewed slightly on the side and not straight down on the top. Topography tends to "fall away" from the center of the scan line.

The relative topographic correction (in units of elevation, such as meters) due to scan and pitch angles is:

$$t_s = (e\text{-}e_o)\sin(a + r_o), \qquad \text{(eqn 5a)}$$

and

$$t_l = (e\text{-}e_o)\sin(p), \qquad \text{(eqn 5a)}$$

where t_s is the correction in the cross track pixel sample, t_l is the correction along track (line) direction, e is the elevation, and e_o is the mean elevation to which the data are corrected. Consider a 1000 meter tall mountain relative to the mean elevation of the image. If the mountain peak were at the edge of the scene, the viewing angle a is ~ 15 degrees and the mountain is displaced sin(15) = 0.259 times the mountain height, or 259 meters (about 15.2 AVIRIS pixels). If the mountain were anywhere in the image, and the pitch is 2 degrees, the mountain top would be displaced 2.0 pixels along track. Thus, topographic errors due to pitch are small, but should not be ignored in regions of large topographic variations.

The next correction considered is the scan velocity and the aircraft velocity. Topography plays a role here, too. If the plane travels along track with velocity v_l, and the cross track angular pixel spacing, a_c, the cross-track velocity, v_c, on the surface is:

$$v_c = (h - e_o)\tan(a_c)/\cos(a), \qquad \text{(eqn 6a)}$$

and

$$\textit{aspect\_ratio} = v_l / v_c. \qquad \text{(eqn 6b)}$$

The quantity a_c is 0.87 mrad, according to the AVIRIS engineering file, but is not of sufficient accuracy to project over 614 pixels (<0.0007 mrad is needed to assure errors < 0.5 pixel). The AVIRIS engineering team (Tom Chrien, personal communication) supplied a value of 0.8745 which seems to work well, but an even more precise number could slightly improve the results. (It might be derived empirically after additional corrections and experience are considered.) The image must be resampled in both along tract and across track to have the proper aspect ratio.

To account for relative offsets due to the aircraft velocity, the image must be resampled to a uniform grid:

$$l_g = [\{ \int_0^l v \} / i_l - g(l - 1)]/g, \qquad \text{(eqn 7a)}$$

where l_g is the line number offset sampled at grid spacing g (e.g. in meters) with the aircraft flying at velocity v for a time with a i_l lines per second. The integration is over the beginning of the flight line to line l. Similarly, cross-track scan must be resampled to the same uniform grid:

$$s_g = [\{ \int_0^s v_c \} / i_s - g(s - 1)]/g, \qquad \text{(eqn 7b)}$$

where s_g is the sample pixel offset, s is the cross track pixel, and i_s is the cross track pixels per second.

Combining all these effects, we derive the combined corrections:

$$p_s = y_s + o_c + t_s / s_p + s_g, \qquad \text{(eqn 8a)}$$

$$p_l = y_l + d_p / s_p + t_l / s_p + l_g, \qquad \text{(eqn 8b)}$$

where s_p is the pixel spacing (e.g. in meters) at the mean elevation at nadir.

The aircraft does not necessarily travel a straight line. The on board GPS data can be used to plot the aircraft motion. We do this relative to the end-points of the flight. Deviations from the flight line result in a "bow" in the image and the bow also changes the yaw. The GPS positions at the beginning and end of the flight line define a straight line of the ideal flight path. First we must compute the change in latitude and longitude per scan line using the beginning and ending GPS positions and the number of scan lines (nlines):

$$\text{del\_lat} = (\text{latitude\_2} - \text{latitude\_1})/\text{nlines}, \qquad \text{(eqn 9a)}$$
$$\text{del\_long} = (\text{longitude\_2} - \text{longitude\_1})/\text{nlines}, \qquad \text{(eqn 9b)}$$

The bow is the deviation from the straight line as compared to the actual GPS position along the

line. The equations are simple computations and are not shown here to conserve space. Given the GPS coordinates of the aircraft, the longitude and latitude of any pixel can be computed, but again, due to space limitations, the simple equations are not shown here.

All of the above corrections were applied to AVIRIS lines for our Arches National Park 1995 data as well as others. A typical result is shown shown in Figure 3.

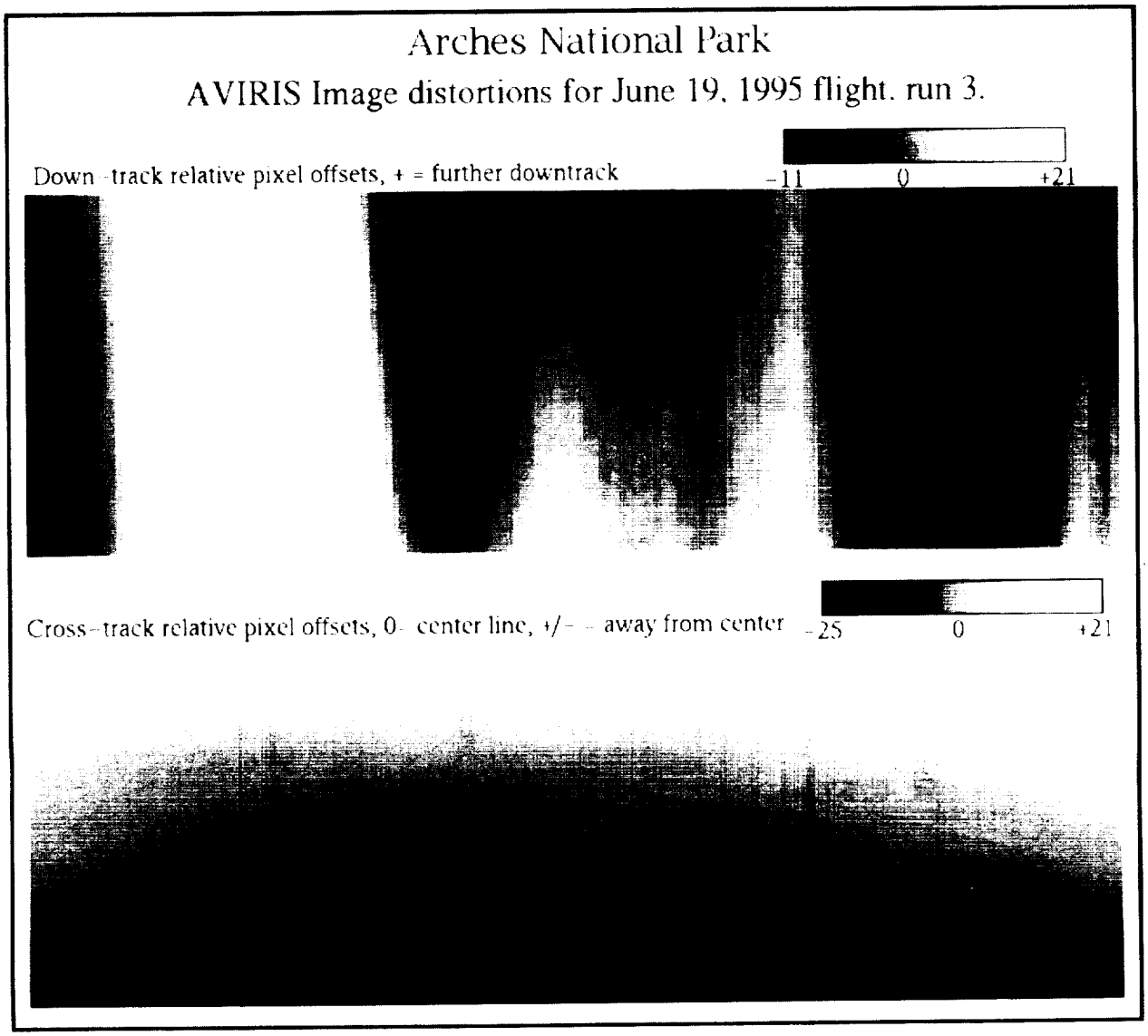

Figure 3. Combined pixel offsets due to pitch, yaw, bow, cross-track scan angle, veloocity and elevation variations of the ER-2 aircraft are shown for one flight line.

AVIRIS pixel spacing of ~17 meters corresponds to about 0.5 arc-second in longitude and latitude, and a 32-bit integer has a range of over $2x10^9$, so we plan to store the longitude and latitude for each pixel as two 32-bit integer image planes in arc-seconds times 1000, ensuring accuracy (~3 cm) for most existing and future conceivable data. This image data provides a lookup table for each pixel in the image cube.

Topography and Digital Elevation Models

In this study, we have not corrected our imaging data for topographic effects as described by equation 5 because we have not assembled digital elevation models. When looking straight down there are no corrections for topography, but as the scan angle off-nadir increases, relative pixel position shifts with topographic elevation changes (eqn 5). For example, consider two buildings, one at nadir, and one at the edge of the scan. The building at nadir is seen from the top and the roof and basement occur in the same pixel. But at the edge of the scan, the side of the other building is in view. The top of the roof occurs at a pixel further from nadir than the base of the building; it appears to be "falling" away from the nadir. Mosaicing adjacent flight lines will show this problem with topography.

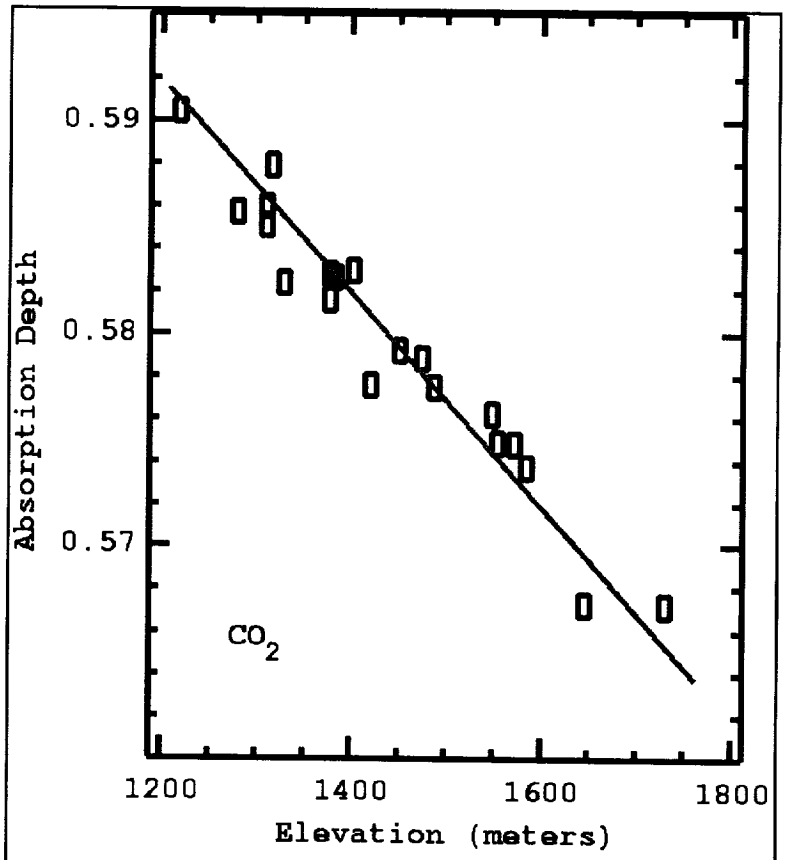

Figure 4. The 2.0 and 2.15-micron CO_2 bands combined absorption depth as a function of elevation for the Arches National Park AVIRIS data indicates that elevation can be derived to about 100 meters, at least in some cases.

Topographic corrections require a registered digital elevation model (DEM), but the AVIRIS data are not registered and corrections with a DEM requires an iterative solution. Elevations might be derived from the AVIRIS data directly using atmospheric absorptions and a few pixels with known elevations in the image to calibrate the absorption depths for the atmospheric conditions at the time of the flight. Such a calibration using atmospheric CO_2 is shown in Figure 4 where scatter of about 100 meters is seen (the pixels were averaged in a 5x5 pixel box), corresponding to an error about 1.5 pixels at the edge of the scan and smaller errors closer to nadir. Without such corrections errors would amount to about 9 pixels for the Arches data.

Conclusions

We have applied the equations presented in this paper to the registration of 3 overlapping AVIRIS lines over Arches National Park. We applied the corrections and printed 1:50,000 scale maps to overlay with existing published geologic and topographic maps of the Park. The printed maps overlaid well. Residuals occurred only where topography was significantly different than the mean. Printed maps of the uncorrected data, scaled to best fit the published maps showed large errors as indicated by the pitch and yaw data.

This paper, figures, additional images and software for making such corrections will be available on our web site: http://speclab.cr.usgs.gov.

References

Chrien, T. G., R.O. Green, and M. L. Eastwood, 1990, Accuracy of the Spectral and Radiometric Laboratory Calibration of the Airborne Visible/Infrared Imaging Spectrometer (AVIRIS), *Proceedings of the Second Airborne Visible/Infrared Imaging Spectrometer (AVIRIS) Workshop*, JPL publication 90-54, 1-14.

Porter, W. M., and H. T. Enmark, 1987, A system overview of the Airborne Visible/Infrared Imaging Spectrometer (AVIRIS), *Proc SPIE*, 834.

Vane, G, M. Crisp, H. Enmark, S. Macenka, and J. Solomon, 1984, Airborne Visible/Infrared Imaging Spectrometer: An Advanced tool for earth remote sensing, *Proc. 1984 IEEE Int'l Geoscience and Remote Sensing Symposium*, SP215, 751-757.

MINERAL MAPPING WITH IMAGING SPECTROSCOPY: THE RAY MINE, AZ

Roger N. Clark
U.S. Geological Survey, Mail Stop 964
Box 25046 Federal Center
Denver, Colorado 80225

J. Sam Vance
U. S. Environmental Protection Agency, Region VIII
Denver, Colorado 80202-2405
and
U.S. Geological Survey, Mail Stop 973
Box 25046 Federal Center
Denver, Colorado 80225

K. Eric Livo
U.S. Geological Survey, Mail Stop 964
Box 25046 Federal Center
Denver, Colorado 80225

and

Robert O. Green
Jet Propulsion Laboratory, MS 306-438
4800 Oak Grove drive
Pasadena, CA 91109

1. INTRODUCTION

Mineral maps generated for the Ray Mine, Arizona were analyzed to determine if imaging spectroscopy can provide accurate information for environmental management of active and abandoned mine regions. The Ray Mine, owned by the ASARCO Corporation, covers an area of 5700 acres and is situated in Pinal County, Arizona about 70 miles north of Tucson near Hayden, Arizona. This open-pit mine has been a major source of copper since 1911, producing an estimated 4.5 million tons of copper since its inception. Until 1955 mining was accomplished by underground block caving and shrinkage stope methods. (excavation by working in stepped series

usually employed in a vertical or steeply inclined orebody) In 1955, the mine was completely converted to open pit method mining with the bulk of the production from sulfide ore using recovery by concentrating and smelting. Beginning in 1969 a significant production contribution has been from the leaching and solvent extraction-electrowinnowing method of silicate and oxide ores. Published reserves in the deposit as of 1992 are 1.1 billion tons at 0.6 percent copper.

The Environmental Protection Agency, in conjunction with ASARCO, and NASA/JPL obtained AVIRIS data over the mine in 1997 as part of the EPA Advanced Measurement Initiative (AMI) (Tom Mace, Principal Investigator). This AVIRIS data set is being used to compare and contrast the accuracy and environmental monitoring capabilities of remote sensing technologies: visible-near-IR imaging spectroscopy, multispectral visible and, near-IR sensors, thermal instruments, and radar platforms. The goal of this effort is to determine if these various technologies provide useful information for environmental management of active and abandoned mine sites in the arid western United States. This paper focuses on the analysis of AVIRIS data for assessing the impact of the Ray Mine on Mineral Creek. Mineral Creek flows to the Gila River. This paper discusses our preliminary AVIRIS mineral mapping and environmental findings.

2. THE RAY DEPOSIT

Early geological studies of the Ray deposit were directed to the definition of reserves, optimizing mineral recovery techniques, and aiding mining practice. An ideal ore deposit is homogeneous and isotropic, permitting a standardized mining and milling practice. In contrast, the Ray geology is complicated by faulting, host rock variation, two known episodes of tilting, a complicated enrichment history, hypogene and supergene alteration and removal of a large portion of the original ore shell. Ray Deposit mineralization is controlled by rock type, position within the deposit, faulting and enrichment history.

The Ray Deposit, Figure 1, is a sulfide system developed in a variety of Precambrian rocks and in Laramide igneous intrusives. The oldest of the Precambrian rocks is the Pinal Schist. This is a sequence of metamorphosed shale, siltstone, sandstone and conglomerate with flows or plutons of a rhyolitic (?) porphyry (Phillips *et al.*, 1974). The Precambrian Ruin Granite, a coarsely crystalline quartz monzonite, intrudes the schist but postdates the metamorphism.

Overlying the Pinal Schist and Ruin Granite are the Pioneer Formation and Dripping Spring Quartzite of the upper Precambrian Apache Group. These are quartzitic clastic rocks ranging from tuffaceous mudstone to arkosic conglomerate.

A series of Laramide intermediate to acidic dikes and stocks intrude all older rocks. These include the Tortilla Quartz Diorite, the Teapot Mountain Porphyry quartz monzonite, and the Granite Mountain Porphyry. It is thought that these porphyry intrusives were the source of the hypogene copper mineralization and contemporaneous mineral alteration of the surrounding wall rock. (Phillips, et. al., 1974)

Two large faults cross the orebody, the Diabase-Ray-School Fault (the Diabase Fault) and the Emperor Fault (Phillips *et al.*, 1974). The Diabase Fault dips to the west and trends

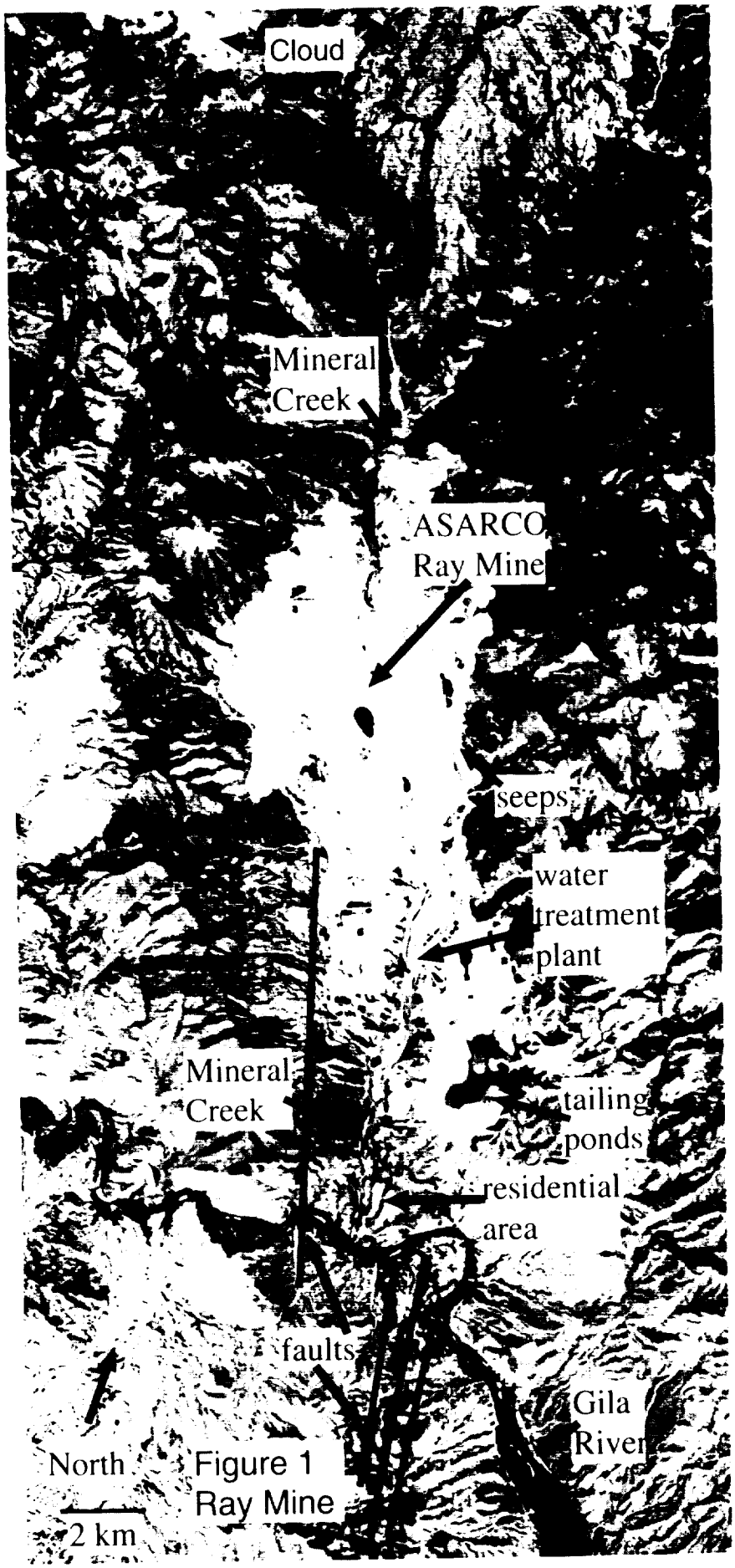

Figure 1. Ray Mine

northerly across the ore body separating the older rocks on the west from younger rocks on the east resulting in an apparent reverse movement. The Emperor Fault has shallow north or easterly dips and is considered to be a thrust. It is cut by the Diabase Fault and is known only on the west or hanging wall side of the Diabase Fault. The displacement on the Diabase Fault exceeds 1,500 feet, while the minimum movement on the Emperor Fault is about 3,000 feet with some very late movement indicated on both faults.

The zoning of Ray sulfide ore minerals is such that the central portion of the sulfide system is characterized by a low content of total sulfide and a high ratio of chalcopyrite to pyrite. The high copper zone is a "doughnut" surrounding the low-grade center and is comprised of a copper-rich chalcopyrite to pyrite mix. This is attributed to the increase in total sulfide content of this zone relative to the central portion of the deposit.

3. EPA AVIRIS PROJECT OVERVIEW

The EPA, during the analysis of risk posed to aquatic and terrestrial populations, has identified a number of contaminants in the Ray Mine Region. The primary contaminants and properties of concern to EPA are as follows: copper sulfate, copper carbonate, manganese oxide, iron oxide, arsenic, other sulfates, cadmium, temperature, pH and turbidity. Visible-near-IR imaging spectroscopy is unable to detect elemental forms of metals in a natural environment. However, previous studies in sulfide ore body settings (e.g. King *et al.*, 1995; Swayze *et al.*, 1998) show AVIRIS data can be used to map minerals that are associated with these metals, including hematite, ferrihydrite, goethite, jarosite, and alunite which are directly identifiable spectroscopically. Mineral maps can be used in the interpretation of individual mine-pile or mine operation's impacts to surface water quality and sediment composition.

AVIRIS is a useful remote-sensing tool that can be applied to accurately map diagnostic mineralogy of the Ray Mine and provide a regional geologic context for the surrounding area. This information provides both the regulator and the mining company with useful insight into the appropriate regulatory strategy. Furthermore, they provide a context in which to begin discussions on the impact of ASARCO's mining operation to the water and sediment quality in both Mineral Creek and in the Gila River. It is the synoptic understanding of the Ray Mine's contribution to regional water quality that will provide a balanced application of regulation and remediation to the environmental issues posed by mining in this region.

4. PRELIMINARY MINERAL MAPPING RESULTS

The AVIRIS data for the Ray Mine flight were converted to apparent surface reflectance using the radiative transfer methods of Green *et al.*, (1996 and references therein). The reflectance data were then mapped using the USGS Tricorder algorithm (Clark et al, 1990, 1991, 1993a, 1995) testing for the presence of 253 materials. These materials included mineral, mineral mixtures, water, vegetation, environmental pollutants, and other materials. The USGS library of materials is constantly being expanded in order to fully analyze the data provided by AVIRIS. The most significant materials identified were then assembled into color-coded mineral

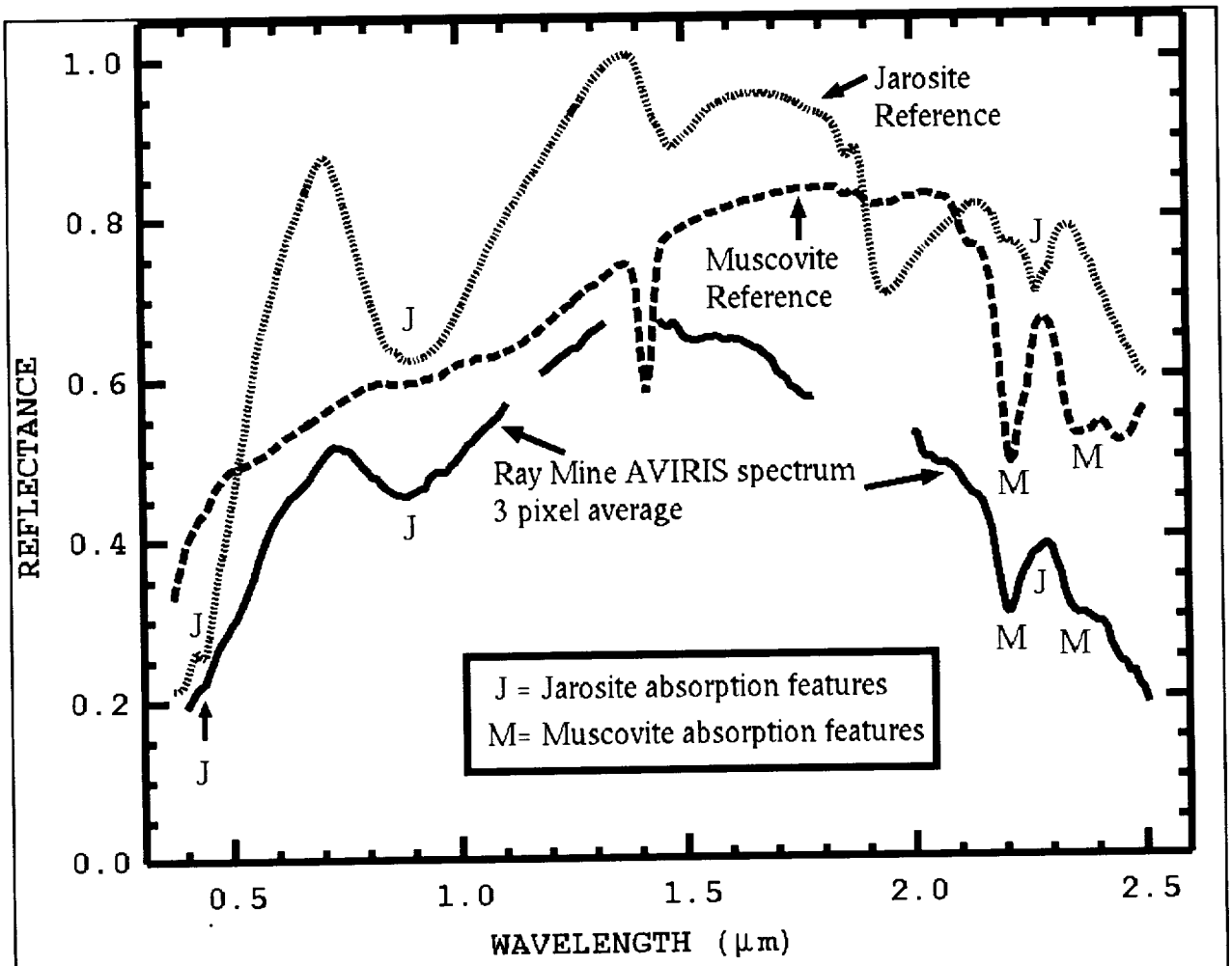

Figure 2. Spectra from the Ray Mine AVIRIS data set are compared to USGS reference spectral library (Clark et al.,1993b) data. Absorption features due to jarosite are indicated by a J and those from muscovite are indicated by an M. Note how the muscovite absorptions near 2.2 μm dominate the spectrum and only a very weak jarosite feature is present near 2.27 μm. A diagnostic jarosite feature is seen at 0.9 μm; the feature at 0.43 μm is indicative of iron sulfate, of which there are numerous forms, one being jarosite. Tricorder correctly mapped these pixels as a combination jarosite plus muscovite. The minerals in these pixels are in an intimate mixture, explaining why the muscovite features dominate the 2-μm region.

maps. Two maps have been assembled: those having electronic absorption features in the visible and 1-μm spectral regions (below called "1-μm maps"), and those having vibrational absorptions (typically due to OH, H_2O, and CO_3) which we call the "2-μm map." The current map is preliminary in the sense that we have had only a short time in the field to collect samples for verification. We have also confirmed the maps by extracting spectra and identifying spectral features. In general the spectra extracted from the data set confirms the mineral maps. Minor exceptions include edges of ponds where the rocks and soils are wet. An example AVIRIS pixel of a combination of jarosite and muscovite is shown in Figure 2, compared with library reference spectra. During field verification, jarosite plus muscovite was found to be a common occurrence, confirming our mineral maps.

4A. Geologic Results

Two regions mapped as calcite, both to the north and east of the mine, consistent with known geologic formations and verified in the field. Two small areas which mapped as calcite in the preliminary mapping run showed extracted spectra that appeared to be a combination of calcite and chlorite that we did not have in our spectral database. Upon field verification these areas were indeed found to contain a mixture of calcite and chlorite. Therefore the AVIRIS data is deemed reliable for mapping these units. Most of the mapped calcite correlates well with limestone units on the published geologic maps (Cornwall, *et al.*, 1971, Creasy, *et al.*, 1983), and the calcite-chlorite mixed pixels tended to be calcite float on chlorite rich bedrock.

The preliminary 1-μm mineral map results indicate high concentrations of iron-bearing mineralogy (Fe^{3+}-bearing minerals: hematite, goethite, jarosite, and Fe^{2+}-bearing minerals) in both the open-pit at the Ray Mine as well as in the region surrounding the mine. These initial findings are consistent with the published data on the regional and mine's geology and are considered accurate interpretations of the geologic setting. Examinations in the mine correlate well with the mapped mineralogy; however, because of mining operations, such field examinations were limited and probably always will be.

The most interesting feature within the 1-μm data is the partitioning of pyritic degradation mineralogy such that the secondary mineral jarosite was confined almost solely to the mine itself. Very few pixels of jarosite were found anywhere but within the mine. A few small outcrops of jarosite occur in the fault zones south of the Gila river. Data from similar high-acid, high-sulfide ore bodies suggests that this metal producing sequence is the single largest contributor to metal loading in streams and sediments (e.g. Swayze *et al.*, 1998). In this region, jarosite is expressed largely within the mine workings with none expressed in either Mineral Creek and only a few pixels were found in Gila River sand bars or shores. These features are most likely a result of sediment transport during the 1993 floods in the area which mobilized soils and tailings from the region into the Gila.

In the 2-μm mineral maps, we have identified clay and phyllosilicate minerals whose locations appear to portray well their locations within the areas we were permitted to examine within the mine itself. Published geologic maps (Cornwall et al, 1971, Creasy et al, 1983) and reports (Metz and Rose 1966, Phillips et al, 1974) describe lithology and hypogene and supergene alteration suites that generally contain abundant quantities of the minerals we have mapped using AVIRIS data. Our analysis finds that occurrences of three 2-μm minerals stand out (muscovite [sericite], montmorillonite, and kaolinite). Muscovite trends with occurrences of Pinal Schist. Some muscovite may be of metamorphic origin, but most is probably a result of quartz-sericite hypogene alteration. Montmorillonite is commonly found associated within high ore-grade diabase wall-rock. It may be associated with a high-grade hypogene potassic alteration (biotite-orthoclase). Metz and Rose, 1966) state that at least some of the montmorillonite and kaolinite occurring within this alteration suite is due to later supergene processes. Kaolinite in general appears to be associated with occurrences of Precambrian granite and Tertiary intrusive stocks. Its association with mineral alteration processes has not been examined in detail by this study. These findings are preliminary and correlated only with published information. Future studies may correlate our spectral analysis with detailed geologic mine maps and/or mine sampling. This is a dynamic

mine. The locations of mineral occurrences generally remain in the same place; however, transport of mine waste, processing waste and weathering products of these activities may alter the mapped locations of minerals significantly over time.

The mineral maps also display regional impacts of faulting as traced by mineral assemblages, permitting the location of both the Diabase Fault, and minor faults which surround these primary structures. Faults not indicated on published geologic maps are seen in the AVIRIS data. The maps have also portrayed the structural controls placed on both the Gila River and Mineral Creek as expressed in the morphology of both streams. Both Mineral Creek and the Gila River show evidence of structural control for their channel placement and meander features. Mineral Creek shows evidence of following an unmapped fault along its course from the exit of the mine to the Gila River. The Gila River shows meanders which appear to be controlled by a series of parallel faults trending north-south in that area.

4B. Preliminary Environmental Findings

Interpretation of the AVIRIS derived mineral maps for the Ray Mine and surrounding region show an interesting context of mining's environmental impact. While Mineral Creek does flow through the Ray Mine south to the Gila River which then flows west, there appears to be little or no jarosite contribution from the mine to the sediment or shores of either watercourse. Expanded views of both the imaging spectroscopy mineral maps along the shores and shoals of both waterways show very few pixels of jarosite outside the active mining operation. Field verification of this data indicate that there are tailings-sized materials deposited in these waterways. The single largest contributor to this lack of jarosite on in the waterways is the fact that the tailings-sized pyrite which is abundant in these sediments has had too little time to weather to its jarositic form. This lack of AVIRIS data detection indicates these deposits are below the 17-meter pixel detection of AVIRIS and that we are unable to map moderately low concentrations of unweathered sulfides. This is critical to understanding the limits to which AVIRIS is capable of indicating the release of metals to these streams. As Swayze et. al. have demonstrated, pyrite, weathering to jarosite, forms acidic waters which can leach metals (e.g. see Swayze *et al.*, 1998) contributing to poor environmental water quality. In this region, jarosite is nearly confined to the mine pit, above the water treatment plant. Goethite, another but lesser contributor to water quality degradation (depending on low pH), is more widespread and is identified at many of the headwaters of streams draining to the Gila. Its presence in the sediments of both Mineral Creek and the Gila is expected.

The mineral maps derived from AVIRIS data show both goethite and jarosite along a series of naturally occurring seeps on the eastern edge of the pit. This would be cause for some alarm to an environmental manager. However, research indicates these seeps predate the mine and the creek is, in most places, physically separated from the mine waste source rock of acid drainage (Neil Gambell, 1998, personal communication). It is in this area that Mineral Creek courses through the mine and comes in direct contact with these high metals and low pH-bearing waters. It appears that the effect to the sediments in Mineral Creek are confined to that portion of the creek which is contained within the pit. ASARCO operates a treatment facility at the southern end of the pit to treat these waters. Based upon AVIRIS data and derived mineral maps,

ASARCO appears to be fully treating this potential waste stream prior to discharge from the mining operation, caveated by the limited (17-meter) spatial resolution of AVIRIS. Preliminary AVIRIS data analysis suggests no evidence for large scale deposition of jarositic or goethitic sediments downstream from the mine. Whether or not this regional synoptic view from AVIRIS reflects small scale environmental effects would require additional detailed field research. Reconnaissance level field research indicates metals producing outcrops throughout the region. This indicates more than one source of water quality degradation to the Gila River. It is also important to remember that the Gila River is a gaining stream. Any groundwater which follows the faulting in the area is contributing metal loading to the stream as well as the mining operations at the Ray Mine and associated processing facilities upstream in Hayden, Arizona.

This preliminary study, appropriate images, follow-on studies and related research can be found at our web site: http://speclab.cr.usgs.gov.

5. ACKNOWLEDGEMENTS

This study was funded by the USGS imaging spectroscopy project, the EPA AMI program (RNC, JSV, and EKL) and by the Jet Propulsion Lab under contract with NASA (ROG).

Field verification sampling within the Ray Mine was provided through the direct cooperation of ASARCO employees whose knowledge of the operation and history of this mine proved invaluable to the understanding of the AVIRIS data.

A portion of the work described in this paper was carried out by the Jet Propulsion Laboratory, California Institute of Technology, under a contract with the National Aeronautics and Space Administration.

6. REFERENCES

Clark, R.N., A.J. Gallagher, and G.A. Swayze, 1990, Material Absorption Band Depth Mapping of Imaging Spectrometer Data Using a Complete Band Shape Least-Squares Fit with Library Reference Spectra, *Proceedings of the Second Airborne Visible/Infrared Imaging Spectrometer (AVIRIS) Workshop*. JPL Publication 90-54, 176-186.

Clark, R.N., G.A. Swayze, A. Gallagher, N. Gorelick, and F. Kruse, 1991, Mapping with Imaging Spectrometer Data Using the Complete Band Shape Least-Squares Algorithm Simultaneously Fit to Multiple Spectral Features from Multiple Materials, *Proceedings of the Third Airborne Visible/Infrared Imaging Spectrometer (AVIRIS) Workshop,* JPL Publication 91-28, 2-3.

Clark, R.N., G.A. Swayze, and A. Gallagher, 1993a, Mapping Minerals with Imaging Spectroscopy, *U.S. Geological Survey, Office of Mineral Resources Bulletin 2039,* pp. 141-150.

Clark, R.N., G.A. Swayze, A. Gallagher, T.V.V. King, and W.M. Calvin, 1993b, The U. S.

Geological Survey, Digital Spectral Library: Version 1: 0.2 to 3.0 μm, U.S. Geological Survey, Open File Report 93-592, 1340 pp.

Clark, R.N. and Swayze, G.A., 1995, Mapping Minerals, Amorphous Materials, Environmental Materials, Vegetation, Water, Ice and Snow, and Other Materials: The USGS Tricorder Algorithm. *Summaries of the 5th Annual JPL Airborne Earth Science Workshop*, Jan. 23-26, JPL Publication 95-1, Vol. 1, Jet Propulsion Laboratory, Pasadena, CA, pp. 39-40.

Cornwall, H.R., Banks, N.G., Phillips, C.H., 1971, Geologic Map of the Sonora Quadrangle, Pinal and Gila Counties, Arizona, USGS Quadrangle, GQ 1021.

Green, R.N., Roberts, D.A., and Conel, J.E., 1996, Characterization and Compensation of the Atmospheric for the Inversion of AVIRIS Calibrated Radiance to Apparent Surface Reflectance, *Summaries of the 6th Annual JPL Airborne Earth Science Workshop*, JPL Publication 96-4, Vol. 1, Jet Propulsion Laboratory, Pasadena, CA, pp. 135-146.

King, T.V.V., C. Ager, W.W. Atkinson, L.S. Balistrieri, R.J. Bisdorf, D. Bove, R.N. Clark, M.F. Coolbaugh, J.S. Erdman, L.P. Gough, P.V. Guerard, F.E. Lichte, W.F. Ortz, G.S. Plumlee, W.I. Ridley, K.S. Smith, G.A. Swayze, R.R. Tidball, K. Walton-Day, T.M. Yamosky, 1995, *Environmental Considerations of Active and Abandoned Mine Lands – Lessons from Sumitville, Colorado*. T.V.V. King, Ed., U.S. Geological Survey, Bulletin 2220, 38 p.

King, T.V.V., R.N. Clark, and G.A. Swayze, 1998, Application of Imaging Spectroscopy Data: A Case Study at Summitville, Colorado, *Methods in Environmental Geology: Remote Sensing*, Springer Verlag, in press.

Metz, R.A., and A.W. Rose, 1966, Geology of the Ray Copper Deposit, Ray, Arizona, *Geology of the Porphyry Copper Deposits, Southwestern North America*, Univ. of Arizona Press (Tucson, AZ), pp. 176-188.

Phillips, C.H., Gambell, N.A., Fountain, D.S., 1974, Hydrothermal Alteration, Mineralization, and Zoning in the Ray Deposit, *Economic Geology and the Bulletin of the Soc. of Economic Geologists*, Vol. 69, no. 8, pp. 1237-1250.

Swayze, G.A., Clark, R.N., Smith, K.S., Hagerman, P.H., Sutley, S.J., Pearson, R.M., Rust, G.S., Briggs, P.H., Meier, A.L., Singleton, M.J., Roth, S., 1998, Using Imaging Spectroscopy to Cost-Effectively Locate Acid-Generating Minerals at Mine Sites: An Example From the California Gulch Superfund Site in Leadville, Colorado, *Summaries of the 7th JPL Airborne Earth Science Workshop*, Jan. 12-16, JPL Publication 97-21, Vol. 1 (this volume), Jet Propulsion Laboratory, Pasadena, CA, pp. 385-389.

Hazard Characteristics of Hydrothermally Altered Rocks on Stratovolcanoes: A Remote Sensing Framework for Debris Flow Hazard Assessments

By

J. K. Crowley, and J. C. Mars, U. S. Geological Survey, Reston, Virginia 20192

D. R. Zimbelman, Natural Hazards Research and Applications Information Center, University of Colorado, Boulder

C. A. Finn, and R. O. Rye, U. S. Geological Survey, Denver, Colorado 80225

Abstract

Among the most devastating volcanic phenomena are large rock avalanches and debris flows that begin high on a volcano and surge for many tens of kilometers down the surrounding river valleys. Such events are closely linked to the presence and distribution of hydrothermally altered rocks, which serve both to weaken a volcanic edifice, and to produce clay-rich mudflows that travel especially long distances. For example, the Osceola Mudflow, which occurred approximately 5000 years ago, removed some 3 km^3 of rock from the summit of Mount Rainier, and traveled over 100 km downstream to Puget Sound. Catastrophic collapse events are not always triggered by eruptive activity, and many events appear to have taken place essentially without warning.

Airborne Visible/Infrared Imaging Spectrometer (AVIRIS) data acquired over nine Cascade stratovolcanoes have proven useful for mapping altered rocks based on associated clay and hydrous sulfate mineral spectral properties (Crowley and Zimbelman, 1997). These data, coupled with digital elevation models and ground-based mapping information, indicate that particular geomorphic features, including volcanic summits, ridges, amphitheaters, and breached craters, have distinctive hazard characteristics. For example, intensely altered summit rocks, present on Mount Rainier, Mount Adams, and Mount Shasta, have the potential to generate extremely large debris flows affecting any volcanic sector, i.e., the direction of flow is not constrained by the topography. In contrast, where altered rocks occur within breached craters, (e.g., Mount Baker, Mount Saint Helens, and Mount Hood), avalanches and debris flows are more likely to be constrained to the breach direction. Isolated ridges of altered rock would ordinarily be capable of generating flows of limited volume. However, where a ridge is contiguous to an altered summit, relatively small ridge failures might trigger a much larger summit collapse. Amphitheaters (arcuate cliffs) composed of altered rock are important debris flow source areas, and can be distinguished from glacial cirques, which have

a similar morphology, but different spectral characteristics. Amphitheaters seen on AVIRIS imagery of Mount Rainier and Mount Adams may signify preferred azimuths for major edifice failures. Amphitheaters also are a source of frequent smaller avalanches and debris flows, including an event at Mount Adams during 1997.

At least three distinct types of altered rock have been recognized with the Cascades AVIRIS imagery, including advanced argillic (sulfate-clay) and argillic (clay-silica) mineral assemblages in the Quaternary volcanics, and chlorite-quartz-sericite assemblages in surrounding Tertiary rocks. Although the lower rank argillic and Tertiary chlorite-quartz-sericite alteration forms may not be associated with large collapse events, their role as source areas merits further study. By examining the mineralogy of debris flow deposits and possible source rocks in a given watershed, it may be possible to link source areas with individual debris flows. This would aid in establishing how local structures and source mineralogy influence debris flow generation, and shape the size and sedimentological character of flows.

The combination of spatial and spectral information afforded by AVIRIS imagery provides a basic framework for making debris flow hazard assessments. Studies of the Cascade volcanoes will aid in extending this type of analysis globally as advanced satellite remote sensing data become available in the next decade.

Reference:

Crowley, J. K., and Zimbelman, D. R., 1997, Mapping hydrothermally altered rocks on Mount Rainier, Washington, with Airborne Visible/Infrared Imaging Spectrometer (AVIRIS) data: GEOLOGY, v. 25, p. 559-562

MAPPING OF ACID-GENERATING AND ACID-BUFFERING MINERALS IN THE ANIMAS WATERSHED BY AVIRIS SPECTROSCOPY

J. Brad Dalton, Trude V.V. King, Dana J. Bove,
Raymond F. Kokaly, Roger N. Clark, J. Sam Vance
and Gregg A. Swayze
U.S. Geological Survey, Mail Stop 973
Box 25046 Federal Center
Denver, Colorado 80225

1. INTRODUCTION

The Animas River Watershed is the site of a coordinated effort to characterize the extent and severity of environmental effects from acid water drainage. This water originates both from numerous abandoned mine sites that date as far back as the late 1800s, and from extensive areas of natural altered and mineralized outcrops. The headwaters of the Animas River are within the San Juan and Silverton calderas, which were responsible for creating large fractures and faults suitable for later mineralization. As part of the Abandoned Mine Lands (AML) Project of the United States Geological Survey (USGS), data were obtained over the San Juan Mountains and Animas Watershed using the Jet Propulsion Laboratory's Airborne Visible and InfraRed Imaging Spectrometer (AVIRIS) and are being used in conjunction with field geologic mapping, geochemistry and geophysics to determine the relative extent of natural and anthropogenic sources of acid water runoff, and its effect on water quality in the drainage.

2. THE AVIRIS DATASET

The Animas Basin AVIRIS data set is comprised of 14 AVIRIS scenes, approximately 10.5 km x 8 km apiece, extending from Hermosa Colorado to the headwaters of the Animas River north of Silverton, near the ghost town of Animas Forks. The 224 spectral channels cover a range from .37 to 2.51 μm, encompassing visible and near-infrared wavelengths suitable for mapping a wide variety of vegetation and minerals, including but not limited to the hydrothermally altered rocks of particular relevance to the San Juan Mountains. The 14 scenes are arranged in two overlapping lines parallel to and bounding the Animas river as it flows from its headwaters toward Durango, Colorado, including most of the Silverton caldera situated within the watershed. The data were acquired under cloud-free late morning conditions on June 18, 1996 in a 17-minute pass over the two lines. While yearly precipitation is normally quite high in the San Juan Mountains, the resulting thick vegetation still leaves significant large outcrops of exposed rock available for mapping analysis; in addition, at the time of acquisition of this dataset, the snowpack was greatly reduced due to melting.

3. REGIONAL GEOLOGY AND MINING ACTIVITY

The Animas watershed is located in the western part of the mid-late Tertiary age San Juan volcanic field (Lipman *et al.*, 1976). Here the local geology is largely comprised of lavas and related volcanic rocks associated with the San Juan caldera and the younger Silverton caldera (Steven and Lipman, 1976). Episodes of intense hydrothermal alteration and mineralization associated with dacitic to rhyolitic intrusion followed caldera formation by several million years (Casadevall and Ohmoto, 1977; Lipman *et al.*, 1976). More recent geologic activity has been dominated by uplifts during the Neogene (Steven *et al.*, 1995), followed by down-cutting and the formation of the Animas River and its tributaries, with brief episodes of deposition.

Gold was discovered in the San Juan Mountains in 1871 and upwards of a thousand mining claims were staked in the upper Animas River above Silverton within the next two decades. The Denver and Rio Grande railroad was extended from Durango to Silverton in 1882 and ore production continued at various levels until 1991 when the Sunnyside Mine directly upstream from Silverton was closed (Church, *et al.*, 1997). Remediation of private holdings in the region continues today, and the AML project is concerned in large part with evaluating remediation needs of the area, including the thousands of abandoned prospects and mines on both federal and private properties.

4. PRELIMINARY MINERAL MAPPING RESULTS

The AVIRIS data for the Animas Watershed were converted to apparent surface reflectance using the radiative transfer methods of ATREM (Gao *et al.*, 1993; Gao *et al.*, 1997) followed by calibration to ground reflectance using a path radiance correction (Clark *et al.*, 1993*a*). The reflectance data were then analyzed using Tricorder (Clark *et al.*, 1990, 1991, 1993*b*, 1995), testing for the presence of over 250 minerals, mineral mixtures, water, vegetation, and other materials of interest. The most significant materials detected were then assembled into color-coded mineral maps. For this investigation we focused our attention on the pyrite weathering sequence, wherein pyrite (Fe_2S) weathers to jarosite, which in turn weathers to goethite, and then hematite. Pyrite oxidation is the primary source of mining-related acidic runoff because sulfuric acid (H_2SO_4) is a product of this weathering reaction (Swayze *et al.*, 1996). Pyrite itself is difficult to detect directly using AVIRIS because of its extremely low reflectance; however its oxidation products are quite bright and have strong 1-μm absorptions due to Fe^{3+} in the matrix, making them easy to identify. These minerals are abundant in intensely mineralized regions such as in the Red Mountain area north of the Silverton mining district, and elsewhere throughout the watershed. Mine tailings in the San Juan Mountains are typically weathered to jarosite and goethite, and these surface expressions readily pinpoint mines and prospects in the AVIRIS scenes. Creeks carrying runoff from tailings piles and mineralized outcrops often have pH values as low as 1.8, and this high level acidity enables these streams to carry high concentrations of heavy metals such as zinc, copper, cadmium, arsenic, and mercury. Stream beds and edges typically display thick rinds of precipitated iron oxide materials, which also are quite evident in the Tricorder-processed AVIRIS mineral maps.

Recent work has shown that carbonate minerals in the San Juan Mountains may play an important role in the buffering of stream waters, reducing metal concentrations and carrying capacities (Church *et al.*, 1997). Calcite occurs in the San Juan Mountains both as sedimentary limestone, and as alteration products of primary minerals within volcanic rocks. While calcite within propylitically altered rocks may play a reduced role due to limited availability for buffering reactions, the importance of calcite in buffering reactions has been established in studies of limestones (Runnels and Rampe, 1989). Magnesium-bearing chlorites such as clinochlore may also provide some level of buffering of acidic stream reaches, however this has not yet been quantified (G. Desborough, private communication, 1997). Calcite has been identified in the Animas River watershed using imaging spectroscopy, and the presence of mapped calcite in particular stream reaches correlates with increased pH levels and attendant lowered heavy metal concentrations (Church *et al.*, 1997). Clear identification of calcite in the AVIRIS data is complicated by the spectral absorption bands of epidote and chlorite which overlap the 2.3-μm diagnostic calcite absorption. Epidote-chlorite-calcite-bearing lavas are widely distributed in the western San Juan Mountains. Samples of these have been obtained and work is underway to incorporate the complex spectral character of these mixtures into the Tricorder analytical database. As the comparative concentrations of epidote, chlorite and calcite vary in the lavas, the behavior of the 2.3-μm absorption band changes in ways that lend themselves well to mapping via spectral feature analysis. The possible revision of pixels previously mapped as calcite to primarily chlorite-epidote would still imply that they present some level of acid-buffering potential. The extent of this buffering capability, however, and improved mapping of these lavas, is an ongoing aspect of our current work.

5. UTILITY OF AVIRIS MAPPING

The distributions of major iron-bearing minerals, phyllosilicates, clays, carbonates, and acid-generating and acid-buffering materials, as determined by Tricorder analysis, have already been used to assist multi-disciplinary field investigations. During the 1997 field season, Tricorder maps of minerals were used to direct field geologists to outcrops of interest, assess the levels of acid generating potential of individual regions, and to locate mine tailings and associated abandoned mine sites. Biologists investigating heavy metal contamination of local waterfowl used Tricorder maps of acid-generating mineralogy to locate potentially compromised ptarmigan habitat, and EPA-mandated mine remediation sites were clearly identified on the Tricorder maps. The extent of naturally-occurring deposits of pyrite, jarosite and goethite within unmined areas suggests that acidity in the upper Animas River may have a sizable natural component. However the presence of potentially acid-buffering minerals within the watershed may play an important role in reducing acidity and metal concentrations as measured by field geochemical analyses (Church *et al.*, 1997). The AVIRIS maps also delineate regions where the river has deposited its sediment load containing iron-bearing precipitates and pyrite weathering products; curiously several of these sites correlate with influxes of potentially buffered water from tributaries that flow through the chlorite- and calcite-bearing structures. Though incomplete, Tricorder analysis of the Animas AVIRIS dataset has already demonstrated its usefulness and cost-saving capabilities, providing a unique regional coverage unavailable by other methods.

6. SUMMARY

Mapping of the 1996 Animas River Watershed using AVIRIS data and the USGS Tricorder algorithm continues to provide a wealth of important and cost-saving information. Improved field planning and insights into laboratory investigations of geochemical data are having direct impacts on interpretations of data collected to support the AML initiative. Synoptic mapping of the primary acid-generating minerals has been accomplished and extensively field-checked. Mapping of acid-buffering minerals, while incomplete, has been found to correlate with the findings of field geochemistry efforts from the 1997 field season. Efforts to further refine the mapping of these complex acid-buffering lithologies will continue in the 1998 field season.

This preliminary study, appropriate images, follow-on studies and related research can be found at our web site: http://speclab.cr.usgs.gov.

REFERENCES

Casadevall, T. and H. Ohmoto, 1977, Sunnyside mine, Eureka mining district, San Juan County, Colorado: Geochemistry of gold and base metal ore deposition in a volcanic environment: *Economic Geology,* v. 92, pp. 1285-1320.

Church, S.E., B.A. Kimball, D.L. Fey, D.A. Ferdener. T.J. Yager, and R.B. Vaughn, 1997, Source, Transport, and Partitioning of metals between Water, Colloids, and Bed Sediments of the Animas River, Colorado, U.S. Geological Survey Open File Report 97-151.

Clark, R.N., A.J. Gallagher, and G.A. Swayze, 1990, Material Absorption Band Depth Mapping of Imaging Spectrometer Data Using a Complete Band Shape Least-Squares Fit with Library Reference Spectra, *Proceedings of the Second Airborne Visible/Infrared Imaging Spectrometer (AVIRIS) Workshop.* JPL Publication 90-54, 176-186.

Clark, R.N., G.A. Swayze, A. Gallagher, N. Gorelick, and F. Kruse, 1991, Mapping with Imaging Spectrometer Data Using the Complete Band Shape Least-Squares Algorithm Simultaneously Fit to Multiple Spectral Features from Multiple Materials, *Proceedings of the Third Airborne Visible/Infrared Imaging Spectrometer (AVIRIS) Workshop,* JPL Publication 91-28, 2-3.

Clark, R.N., Swayze, G.A., Heidebrecht, K.B., Goetz, A.F.H., and R.O. Green, 1993a, Comparison of Methods for Calibrating AVIRIS Data to Ground Reflectance, *Summaries of the 4th Annual JPL Airborne Geosciences Workshop, Volume 1: AVIRIS Workshop*, JPL Publication 93-26, pp. 31-34.

Clark, R.N., G.A. Swayze, and A. Gallagher, 1993b, Mapping Minerals with Imaging Spectroscopy, *U.S. Geological Survey, Office of Mineral Resources Bulletin 2039,* pp. 141-150.

Clark, R.N. and G.A. Swayze, 1995, Mapping Minerals, Amorphous Materials, Environmental Materials, Vegetation, Water, Ice and Snow, and Other Materials: The USGS Tricorder Algorithm. *Summaries of the Fifth Annual JPL Airborne Earth Science Workshop,* January 23- 26,, Vol. 1: AVIRIS Workshop, R.O. Green, Ed., JPL Publication 95-1, p. 39-40.

Gao, B.C., Heidebrecht, K.B., and A.F.H. Goetz, 1993, Derivation of Scaled Surface Reflectances from AVIRIS Data, *Remote Sensing of Environment*, v. 11, 99. 1775-1795.

Gao, B.C., Heidebrecht, K.B., and A.F.H. Goetz, 1997, Atmosphere Removal Program (ATREM) Version 3.0 User's Guide, Center for the Study of Earth from Space, University of Colorado at Boulder.

Green, R.O., D.A. Roberts, and J.E. Conel, Characterization and Compensation of the Atmosphere for the Inversion of AVIRIS Calibrated Radiance to Apparent Surface Reflectance. *Summaries of the Sixth Annual JPL Airborne Earth Science Workshop*, March 4-8, 1996, JPL Publication 96-4, Vol. 1, AVIRIS Workshop, pp. 135-146.

Lipman, P.W., H.H. Mehnert, C.W. Naeser, R.G. Luedke, and T.A. Steven, 1976, Multiple Ages of mid-Tertiary mineralization and alteration in the Western San Juan Mountains, Colorado, *Economic Geology*, v. 71, pp. 571-588.

Runnells, D.D., and J.J. Rampe, 1989, Natural Clean-up of a Stream Contaminated by Mine and Mill Wastes: A Reaction Analogous to Liming in Water Treatment, *Proceedings of the 6th International Symposium on Water-Rock Interaction*, Malvern, 3-8 August 1989, Ed. D.L. Miles, pp. 597-598.

Steven, T.A., Hon, K., and M.A. Lanphere, 1995, Neogene Geomorphic Evolution of the Central San Juan Mountains Near Creede, Colorado, U.S. Geological Survey Map I-2504, Denver Colorado.

Steven, T.A., and P.W. Lipman, 1976, Calderas of the San Juan Volcanic Field, Southwestern Colorado: U.S. Geological Survey Professional Paper 958.

Swayze, G.A, R.N. Clark, R.M. Pearson, and K. Eric Livo, 1996, Mapping Acid-Generating Minerals at the California Gulch Superfund Site in Leadville, Colorado using Imaging Spectroscopy. *Summaries of the 6th Annual JPL Airborne Earth Science Workshop*, JPL Publication.

Swayze, G.A., Clark, R.N., Smith, K.S., Hageman, P.L., Sutley, S.J., Pearson, R.M., Rust, G.S., Briggs, P.H., Meier, A.L., Singelton, M.J., and S. Roth, 1997, Using Imaging Spectroscopy to Cost-Effectively Locate Acid-Generating Minerals at Mine Sites: An Example From the California Gulch Superfund Site In Leadville, Colorado. *Geological Society of America Abstracts with Programs*, October 20-23, 1997, v. 29, no. 6, pp. A-322.

X-RAY DIFFRACTION VERIFICATION OF AVIRIS CLAY MINERAL IDENTIFICATION, SUMMITVILLE AREA, SOUTHWESTERN COLORADO

W. S. Duncan[1], E.B. Ledger[1], and V. S. Whitehead[2]
[1]Dept of Geology, SFASU, Nacogdoches, TX
[2] Dept of Forestry, SFASU, Nacogdoches, TX

OBJECTIVES AND INTRODUCTION

The eastern San Juan Mountains of southwestern Colorado are the site of mid- and late-Tertiary volcanic activity. The volcanic activity had two effects on the state of Colorado. Some of the eruptions were extremely large, and magmas formed thick geologic rock units that contributed to the scenic nature of the area. The other effect was that magmas brought precious metals to the earth's near surface that could be exploited by mining.

In the last ten or twenty million years after most of the activity ended, the volcanic bedrock underwent extensive erosion due to the high relief, and chemical weathering of the volcanic rock produced clay minerals in the soil. The original mineralization also emplaced sulfide minerals (mostly non-ore minerals called gangue) that reacted to form very acidic conditions due to sulfide-to-sulfate reactions.

The clay minerals that form in such an environment depend on time (duration) of chemical reactions forming the clays, the parent volcanic rock composition and texture, and the present weathering conditions, including pH. Clay minerals are natural aluminosilicates that form at the earth's surface in response to chemical alteration of higher temperature minerals such as feldspars and mica. Feldspars and mica are K, Na, and Ca aluminosilicates that can form from magmas. They do not form at ambient temperatures, but rather alter to clay.

Analysis of clay minerals is not easy, because they are layer aluminosilicates that can change their structures (d-spacings) in response to their chemical environment, sometimes in a matter of seconds. Standard techniques have been developed over the last eighty or so years to identify various clay minerals using X-ray diffraction (XRD). Even with diagnostic chemical preparation in the controlled environment of the laboratory, clay minerals sometimes require elaborate means to get an unambiguous identification using XRD. A non-laboratory method of clay mineral identification is claimed by a group at the United States Geological Survey (USGS) that uses analysis of visible and near-infrared (NIR) spectra reflected from the ground, and detected from an airplane flying over the area of interest.

The purpose of this study is to analyze by traditional means claims regarding clay mineral identification using the AVIRIS system. A specific study of clay mineral interpretations was conducted on an image of the Summitville mine site in southwestern Colorado (Clark *et al.* 1995). This study centers on verifying clay mineral identifications made by Clark *et al.* (1995).

Most clay mineral structures were originally determined in the 1930s using XRD. This method was developed and applied to minerals by Nobel laureate Linus Pauling. We used XRD to analyze the mineral constituents in the area interpreted by Clark *et al.* (1995). The characterization of clay minerals as distinct crystalline materials as opposed to amorphous material was not proven until XRD was used to verify this in the 1930s. Since then XRD has remained the standard method of clay mineral identification. The objective of this study was to use XRD to attempt to verify a new method, imaging spectroscopy.

Clay Mineralogy

Clay minerals are hydrous aluminosilicates that have a layered structure, and are therefore classified as phyllosilicates. The layers are made of two modular units, tetrahedral and octahedral sheets. In the tetrahedral sheet the dominate cation is Si^{4+}, but Al^{3+} frequently substitutes for Si^{4+}, and Fe^{3+} substitutes occasionally. The chemical formula for all tetrahedral sheets can be represented as T_2O_5 where T represents the cation and O oxygen. Tetrahedral coordination is an atomic arrangement in which an ion is surrounded by four ions of opposite sign. The centers of the surrounding ions form the points of the tetrahedron around the central ion. In the case of clays, Si^{4+} or Al^{3+} and sometimes Fe^{3+}, are the central ions surrounded by O^{2-} ions. The tetrahedral sheets form as a result of individual tetrahedra resting on a tetrahedral face and sharing the oxygen on the three corners with three other tetrahedra. The fourth oxygen points upward, normal to the face on which the tetrahedron is resting and is referred to as the apical oxygen. The sheets that result from this repeated ordered arrangement are called tetrahedral sheets.

The octahedral sheet is a sheet of edge-linked octahedra, unlike the corner linked tetrahedra. The sheets are formed by two planes of closest-packed oxygen ions or hydroxyl ions, with cations occupying the resulting octahedral sites between the two planes. When the centers of six oxygen ions packed around an octahedral cation site are connected, an octahedron forms. When each of these octahedron connects to neighboring oxygen ions, an edge-linked sheet of octahedra forms.

Clay mineral structure is the result of linking these two modular units. The oxygen-to-oxygen or hydroxyl-to-hydroxyl ionic dimensions are approximately the same for the tetrahedral and octahedral sheets. This allows the apical oxygen of the tetrahedral sheets to replace two of the three hydroxyl ions in the octahedral sheet, thus linking the two. This assemblage of one tetrahedral sheet and one octahedral sheet is called a 1:1 layer silicate structure. When another tetrahedral sheet is inverted and placed on top of the 1:1 structure, a 2:1 layer silicate is formed. Because the sheets rarely fit neatly, distortions occur. Such distortions, and the cation/anion replacements that cause these distortions to the structure, give rise to the variety of distinct clay minerals or polytypes, all based on the 1:1 or 2:1 structures.

Weathering in volcanic environments, such as the San Juan Volcanic Field, tend to progress faster than in other environments. Factors such as the abundance of amorphous materials facilitate hydrolysis, and the presence of porous rocks such as pyroclastics enhance leaching and drainage. This rapid weathering can produce azonal distribution of clay minerals.

The clay minerals identified by remote sensing near the Summitville mine site include halloysite or a kaolinite-smectite mixture (Clark *et al.*, 1995). In general, these three minerals can be described as follows: Kaolinite has an assemblage of one tetrahedral sheet and one octahedral sheet and is a 1:1 layer silicate structure or layer type. It is a hydrous aluminosilicate with the chemical formula $Al_4Si_4O_{10}(OH)_8$. Kaolinite is one of the most widespread aluminosilicate minerals, forming as either a residual weathering product, or sometimes by hydrothermal alteration of other aluminosilicates, especially feldspars. Halloysite is a kaolin mineral, and like kaolinite, it has a single layer structure. The primary structural difference between kaolinite and halloysite is the habit. Halloysite has a fibrous habit instead of a platey habit. The smectites include all minerals formerly classified in the montmorillonite group of expansible layer silicates. Smectites have an octahedral sheet in coordination with two tetrahedral sheets in which oxygen atoms are shared. Cationic substitution occurs in the octahedral and tetrahedral sheets, and the corresponding differences in properties and chemical composition are used to classify the smectites (Dixon, 1977).

The formation of halloysite and kaolinite at low temperatures, and how they may be associated is discussed by Dixon (1977). A possible mechanism for the formation of halloysite is platey kaolinite rolling once interlayer hydrogen bonding has been weakened by hydration, thus forming halloysite (Singh and Mackinnon, 1996). Halloysite that formed as the result of the hydration of kaolinite would be occurring with kaolinite.

Fortunately, each of these three individual clay groups, as well as mixed layered clay minerals, can be distinguished by XRD. Both kaolinite and halloysite are single layer structures that yield strong reflections (Table

1). Heating kaolinite at 550 °C for one hour causes it to become amorphous, eliminating its diffraction pattern. Because of the fibrous habit of halloysite, crystals are not oriented in basal parallel fashion. This results in weak 00l reflections that are generally broad, compared to those of kaolinite, and strong nonbasal reflection between 20 - 30° 2θ. As a result halloysite has a diffraction pattern with a broad 00l and strong asymmetrical hk reflections. Smectites, such as montmorillonite, can be distinguished by their d-spacing reflections (Table 1). Randomly interstratified kaolinite/smectite mixtures are easily distinguished. Air dried samples will yield a peak of d = 7.4 - 8.3Å depending on the kaolinite/smectite ratio. When heat treated to 550° C the kaolinite becomes amorphous and its d-spacing will disappear. Collapsing the structure pulls in the mixed-layered reflection to a lower angle, larger d-spacing (Moore and Reynolds, 1989).

TABLE 1

Mineral	d-spacing	2θ
Kaolinite	7.1Å (001)and 3.57Å (020)	12.47° and 24.94°
Halloysite	10Å (001) and 7.4Å (001)	8.84° and 12.47°
Montmorillonite (Mg saturated)	17.6Å (001)	5.02°

The spectral signatures of the three individual clay groups can also be distinguished provided variations in the clay mineral spectral data are factored into interpretations. The spectral bands are related to the OH^- part of the crystalline structure of these minerals. These band frequencies consist of the sum of OH^- stretching and bending effects (Clark *et al.*, 1990) representing specific resonant bonds in a crystal structure, such as Al-OH bonding. The frequency of the bands varies as cation substitutions in the structure vary because different cation radii change bond lengths and alter the structural geometry (Post and Noble, 1993).

In addition to differences due to cation substitutions, properties of the individual clay minerals, such as the interaction of molecular water with smectites, will effect spectral signatures. Spectral absorptions due to molecular water in montmorillonite are influenced by both the interlayer cation and the moisture environment. Since the absorptions near 1.4 μm and 1.9 μm are composed of multiple, overlapping molecular water features, the band shape, the individual minima, and the band strengths are all important in laboratory spectral analysis and remote sensing of smectites (Bishop *et al.*, 1994).

The NIR Al-OH band position of dioctahedral smectites, muscovite, and other micas appears to be a linear function of Al content (Fig. 1). As the band frequency increases, the unit cell size decreases resulting in varied lower band frequencies (Post and Noble, 1993). Muscovite and kaolinite have NIR band positions that are close to each other, and because of chemical and structural similarities between kaolinite and halloysite it is possible that halloysite could lie in the same range of NIR band positions.

The limitation is in the fact that an interstratified mineral cannot be distinguished from a mixture of minerals. This limitation is evident since infrared spectroscopy probes short-range ordering (Srasra *et al.*, 1994). XRD can penetrate clay minerals enough to be used in distinguishing mixed-layered clay minerals, such as an ordered repeating sequence of kaolinite and montmorillonite, or an unordered repeating sequence as opposed to a mixture of kaolinite and montmorillonite crystals. It is possible that the short-range ordering limitation of NIR spectroscopy may also apply to the ability of the system to distinguish crystalline clay minerals from amorphous material.

GEOLOGIC SETTING

A complete explanation of the formation of the San Juan volcanic field has yet to be proposed. There are no other examples of huge stratovolcanoes, like the San Juans, that exist in the midcontinent. By means of stratigraphic field studies and gravimeter method studies, a general geology of the area has been described by Lipman, Steven, and Mehnert.

Volcanic activity began in late Eocene or early Oligocene time, between 40 and 35 Ma. The early rocks are mainly intermediate in composition, such as andesite, rhyodacite, and mafic quartz latite, erupted from many scattered stratovolcanoes. One such, the Summer Coon Volcano, has been dissected by erosion to reveal a highly symmetrical system of radiating dikes around a central intrusive area. The products derived from these volcanoes coalesced into a composite volcanic field covering more than 25,000 km^2 (Mertzman, 1971).

About 30 Ma the character of volcanic activity changed markedly to predominantly pyroclastic eruptions, and large volume quartz latite and rhyolitic ash flows spread widely from many centers. The earliest ash flows came from the Bonanza caldera in the northeast and the nested Platoro and Summitville calderas in the southern part of the San Juan volcanic field. These were erupted from clusters of early stratovolcanoes. Caldera collapse resulting from the ash flow eruptions largely destroyed the upper parts of these volcanoes (Steven and Lipman, 1976).

The sequence began when magma ascended, possibly from a large batholith, explosively along deep ring fractures into the volcano, destroying its edifice and venting as ash flows. Simultaneously, the structural block bounded by the ring fractures, subsided into the magma chamber, and displaced an amount of magma equal to that vented from the chamber. The result was thick intercaldera ash flow facies within the caldera and outflow facies outside (Ivosevic, 1984).

The materials that were airborne during the ash flow phase, were elutriated or density layered in the air. As the denser material fell, it landed on cooler ground to form glass. The next layer fell on top of the obsidian and formed welded tuff. Ash landed on the welded tuff to form an ash tuff.

In most of the calderas in the San Juan volcanic field, a resurgent dome was emplaced in the center of the caldera. Volcanic domes also formed along ring fractures and along intra caldera linear fractures. Often the caldera walls collapsed along rounded or scalloped faults that were subparallel to the ring fractures. Additional caldera subsidence developed a medial graben on the resurgent dome. These domes and the structures within them provided a host environment for mineral emplacement.

About 29 Ma ash flow eruptions began in the western part of the San Juan volcanic field. The first two of the calderas were largely covered and imperfectly understood. The last three formed much like those in the east. These five calderas formed in less than two million years.

As the activity in the western portion was developing, major pyroclastic eruptions began in the central San Juan volcanic field. This phase of development began about 28 Ma. The result was a sequence of eight major ash flow sheets. Caldera subsidence has been identified or inferred at all of the ash flow source areas. Ash flow activity ended in the central San Juan Mountains about 26.5 Ma.

In the early Miocene, about 25 Ma, the character of the erupted material changed from ash flow tuffs to basaltic material and high-silica alkali-rich rhyolite. This change occurred at approximately the same time as the basin and range faulting in the San Luis Valley segment of the Rio Grande trough. The basaltic eruptions continued intermittently until about 5 Ma. The only rhyolitic ash flow tuff, the Sunshine Peak Tuff, which formed during this period of basalt flows, formed about 22.5 Ma. It formed in and around the concurrently developing Lake City caldera, in the western portion of the San Juans (Lipman, 1975).

A total of 15 calderas are now known in the San Juan volcanic field, and indirect evidence suggests that at least two and perhaps three more exist. A major underlying batholith is indicated by a large Bouguer gravity anomaly that underlies the area containing most of the calderas. Sharp gradients at the margins of the anomaly suggest shallow emplacement of the top of the batholith. The change in eruptive material from the early intermediate composition rocks of the widely scattered stratovolcanoes, to the more silicic ash flows, probably took place as the batholith rose and differentiated beneath the central part of the field. As the roofs of the more gas-charged cupolas of the batholith failed, volumes of ash erupted rapidly, and unsupported segments collapsed to form the calderas. The sequential development of these calderas is believed to reflect the progressive emplacement of the different high level plutons of a composite batholith (Steven and Lipman, 1976).

METHODS OF STUDY

Field Methods

Samples were collected on the ground at Alum Creek in the imaged area. The location was identified on the image found in USGS Bulletin 2220, page 17. The scene was correlated with the USGS 7.5 minute Summitville Quadrangle. The area sampled was along Alum Creek, starting about 1.5 km from the confluence or joining of Alum Creek with the Alamosa River, and extending about 1 km downstream toward the Alamosa River. Samples were taken on slopes that were well exposed to aerial reconnaissance and showed little signs of disturbance or weathering, and were collected by scraping the surface of the slopes. About 10 kg total of sample was collected from the area.

Laboratory Methods

The analysis was performed to confirm the presence of certain minerals. Known peaks were used to identify clay minerals from diffractograms. The minerals to be confirmed were those listed as being imaged by the AVIRIS data and interpreted to be present in the USGS Professional Paper 2220, page 17.

The initial run was a box mount of the first sample collected, AC - 1. This was done to act as a control for the prepared samples. All other runs were slurry mounts used to confirm the presence of various clay minerals. Initially, a standard survey procedure was conducted to provide an estimate of the most abundant clay minerals present. Sufficient sample was used to yield 50-100 mg of clay. This 50-100 mg clay sample was dispersed by "vortexing" in pH 10 sodium carbonate solution. Using balanced centrifuge tubes, a "spin down" was run to separate the clay, what is referred to as the "2 μm cut". The turbid supernatant was decanted to another tube, Mg (II) solution was added, and another "spin down" was run. This resulted in a clear supernatant with clays at the bottom of the tube. The clear supernatant was decanted and discarded. Mg (II) solution was added while vortexing and another "spin down" was run. Again the supernatant was discarded and Mg (II) solution was added while vortexing, and another "spin down" was run. Next, 90% acetone in water was added while vortexing, and a "spin down" run, followed by decanting. Then 2 to 3 drops of 10% glycerol in ethanol was added with vortexing. While vortexing, distilled water was added drop by drop when necessary to achieve a slurry of proper viscosity. When the slurry had the proper viscosity, a Pasteur pipette was used to apply the clay slurry onto a clean, labeled petrographic slide. Slides were set aside to air-dry under a tilted watch glass.

The presence of the various clay minerals can be determined by their characteristic peaks that resulted after Mg saturation. Kaolinite at 7.1Å, montmorillonite at 17.6Å, and halloysite at 10Å. To confirm the presence of kaolinite, a sample can be heated at 550 °C for two hours, which causes the kaolinite to become amorphous and eliminates its diffraction pattern. Halloysite can be detected by looking for additional relatively weak nonbasal reflections that are strongest at about 20 to 35° 2θ. The 00l reflections are usually broader than those from kaolinite, and it will also give strong hk reflections despite efforts to achieve good preferred orientation. Further verification for halloysite can be achieved by gentle heating. This results in a peak of 7.1Å, because the 2.9Å layer of water has been driven out of the clay causing it to collapse to 7.1Å from 10Å.

RESULTS OF STUDY

The results, listed as d-spacings of increasing 2θ , are from X-ray diffractograms (Figs. 2-4) of samples acquired from Alum Creek. Those listed are peaks which had intensities significantly greater than background noise and are listed with associated minerals: h - halloysite, k - kaolinite, m - mica, mm - montmorillonite, j - jarosite, and o - orthoclase. Alum Creek Sample One, box mount, yielded peaks at the d-spacings of 9.88Å - (h,m), 7.11Å - (h,k), 5.92Å - (j), 4.98Å - (m), 4.45Å - (h,k), 4.23Å - (o), 3.56Å - (h,k,j), 3.33Å - (m,k,j), 3.07Å - (j), 2.55Å - (h,k,j), 2.37Å - (h,j), 2.28Å - (j,k), 2.12Å - (k), 1.97Å - (m,j), 1.54Å - (m), 1.43Å - (m), and 1.37Å - (m). Alum Creek Sample One slurry mount gently heat treated yielded peaks at the d-spacings of 16.70Å - (mm), 9.99Å - (h,m), 7.16Å - (h,k), 5.72Å - (j), 5.04Å - (m), 3.53Å - (h,k,mm), 3.33Å -

(h,m), 3.08Å - (j), 2.86Å - (j), 2.55Å - (h,k,m), 2.38Å - (h,k,mm), 2.28Å (k,j), and 2.00Å - (m,h). Alum Creek Sample One slurry mount heated at 550° C for two hours yielded peaks at the d-spacings of 10.01Å -(m), 4.99Å - (m), 3.33Å - (m), 2.70Å - (m), 2.51Å - (m), and 1.99Å - (m).

DISCUSSION

X-ray diffraction data on the samples from the Summitville site showed halloysite, kaolinite, mica, and minor montmorillonite. The determination of the halloysite is based on the sample with no heat treatment compared with those that were heat treated. Comparing AC-1 with gently heat treated AC-1 and AC-1 treated for two hours at 550° C, suggested the presence of both halloysite and kaolinite clay minerals as well as mica. The untreated sample, AC-1, yielded a strong peak at 9.9Å and 7.1Å. Both of these peaks, as well as others, suggested the presence of both kaolinite and halloysite. To further investigate this possibility, AC-1 was gently heated for several hours at 107° C. This intensified the 7.1Å peak and diminished the 9.9Å peak. This effect was not fully demonstrated because the sample had been glycerated, which may have inhibited collapsing of halloysite to 7.1Å spacing (Dixon, 1977). When the same sample was heated for two hours at 550° C, all of the peaks associated with kaolinite and halloysite disappeared, due to the mineral becoming amorphous. Furthermore, the 9.9Å peak narrowed to 10.1Å, due to the presence of mica in the sample. The mica and halloysite had formed a composite peak. The conclusion is that both halloysite and kaolinite were present and possibly formed as described by Singh and Mackinnon (1996).

The results indicated the presence of both kaolinite and halloysite and a slight amount of montmorillonite (Fig. 2-4). They also indicated a large amount of mica (Fig. 2-4), a common primary mineral associated with the volcanism. Mixtures of discrete clay minerals can cause interference with the identification of other clay minerals, especially dioctahedral smectite. The strong kaolinite band may overlap montmorillonite bands, and illite bands may overlap beidellite bands. The main band interference, for clays commonly found together, is from a mixture of kaolinite and montmorillonite (smectite) containing considerable Fe in the structure. Furthermore, the mica could easily be incorrectly identified as a clay, specifically kaolinite, according to the correlation of the primary Al-OH NIR combination bands and Al_2O_3 content for muscovite and kaolinite (Post and Noble, 1993). The correlation does not include halloysite which could also fall in the range close to muscovite.

CONCLUSION

The AVIRIS data used to image the Summitville site is available from JPL on 8 mm tape. They were obtained and yielded usable spectra with composite signatures, because of mixed pixels, which are those pixels with the spectra of more than one material. X-ray diffraction data of samples collected on the ground at Alum Creek in the Summitville area had halloysite, kaolinite, montmorillonite, and mica. The mica, which is from the original volcanic rocks, was much more abundant than the clay minerals.

Because clay minerals are difficult to determine, even in the laboratory, they represent the true test of a sensor's ability to distinguish materials. While the USGS group's interpretation of halloysite, kaolinite, and montmorillonite from AVIRIS data is correct, they fail to mention the abundant mica. This is significant because the similar spectra that mica produces can be confused with the spectra produced by clay minerals imaged. The problem still exists as to how the similar spectra of clay minerals and mica are distinguished from each other in composite signatures. Distinctions made between kaolinite and halloysite can possibly be due to the differences in Al-OH concentrations in muscovite and not to unique spectral signatures of clay minerals.

The purpose of this study was to confirm interpretations made of AVIRIS data by XRD. As a result of this study, mineral data has been produced that can be used to further assess the accuracy of AVIRIS. Scene PG03360-1 is an excellent test site in the continuing development of hyperspectral data. The head of the Alamosa River Basin provides a number of challenges to include several different clay minerals mixed with mica, that can be studied to enhance the abilities of AVIRIS. The conclusion of this study is that interpretations of clay minerals in volcanic environments need to be sensitive to the occurrence and resulting interference of mica, as well as properties of each clay mineral.

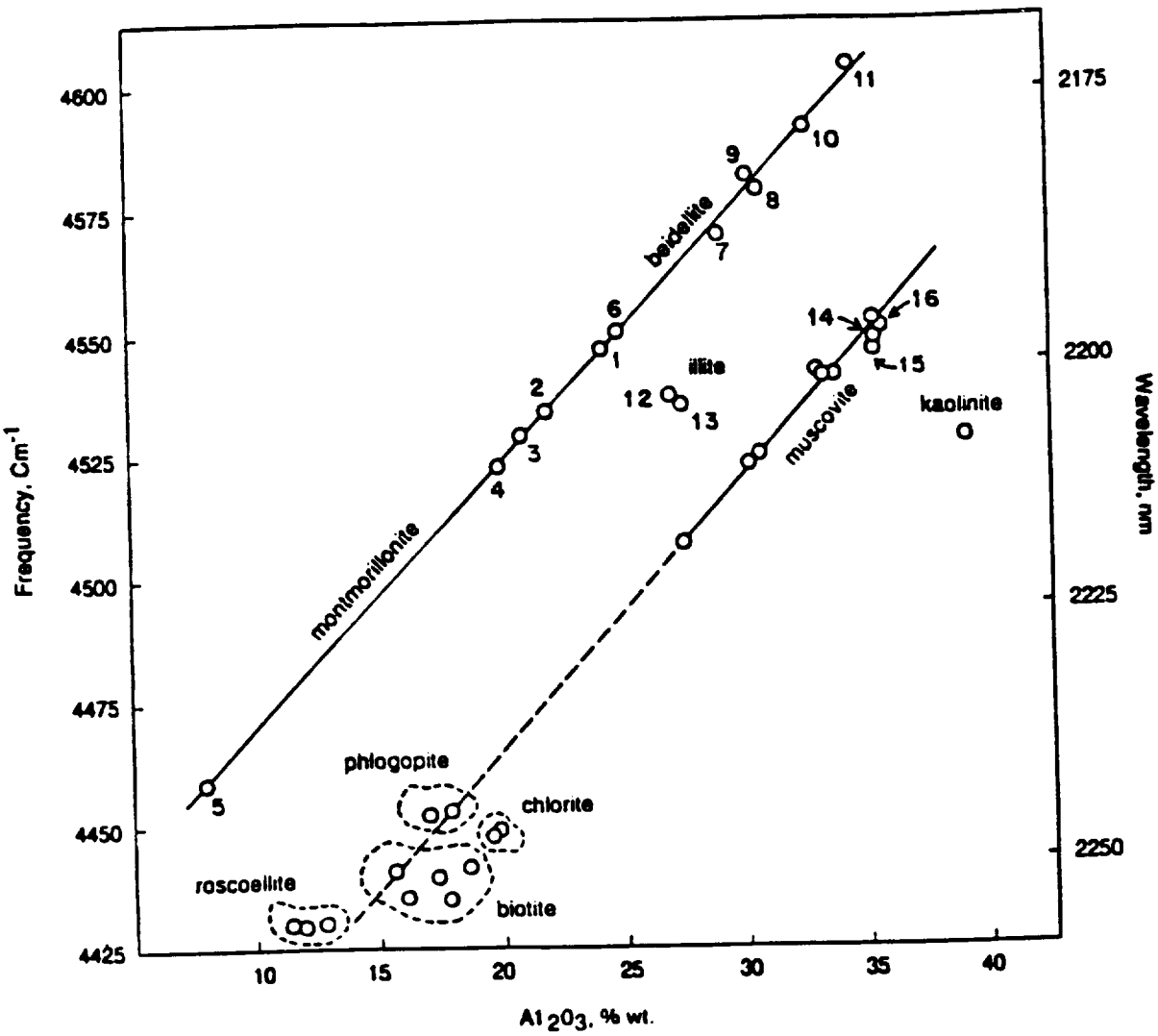

Figure 1. The correlation of the primary Al-OH NIR combination bands and the Al_2O_3 contents for different smectites and illites, plus muscovite, phlogopite, biotite, roscoelite, kaolinite, and chlorite (Post and Noble, 1993).

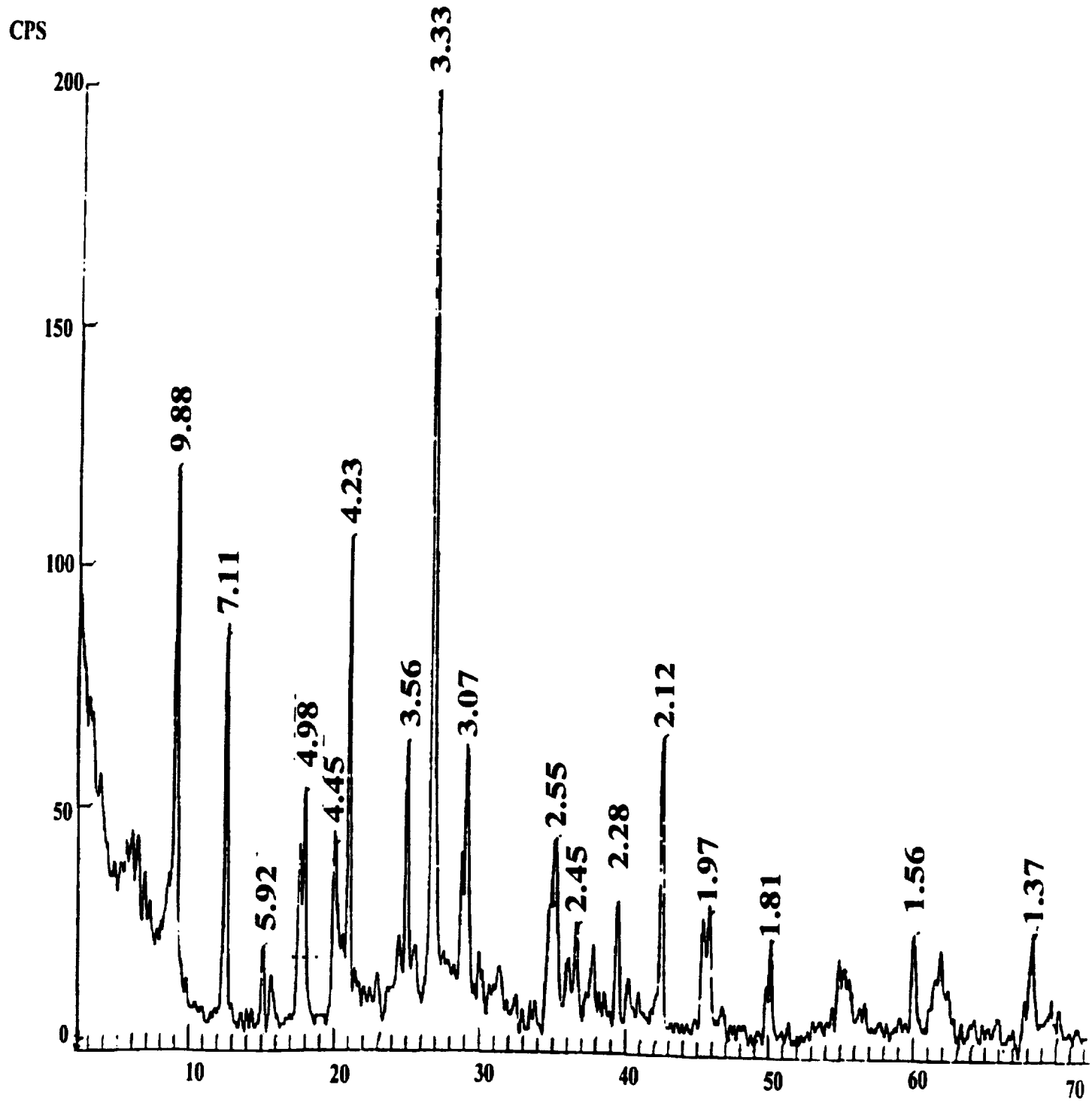

Figure 2. X-ray diffractogram of Alum Creek Sample One, box mount. The X-axis is the 2θ angle from the goniometer and the Y-axis is relative intensity. The 9.88 d-spacing is associated with halloysite and 7.11 d-spacing with kaolinite.

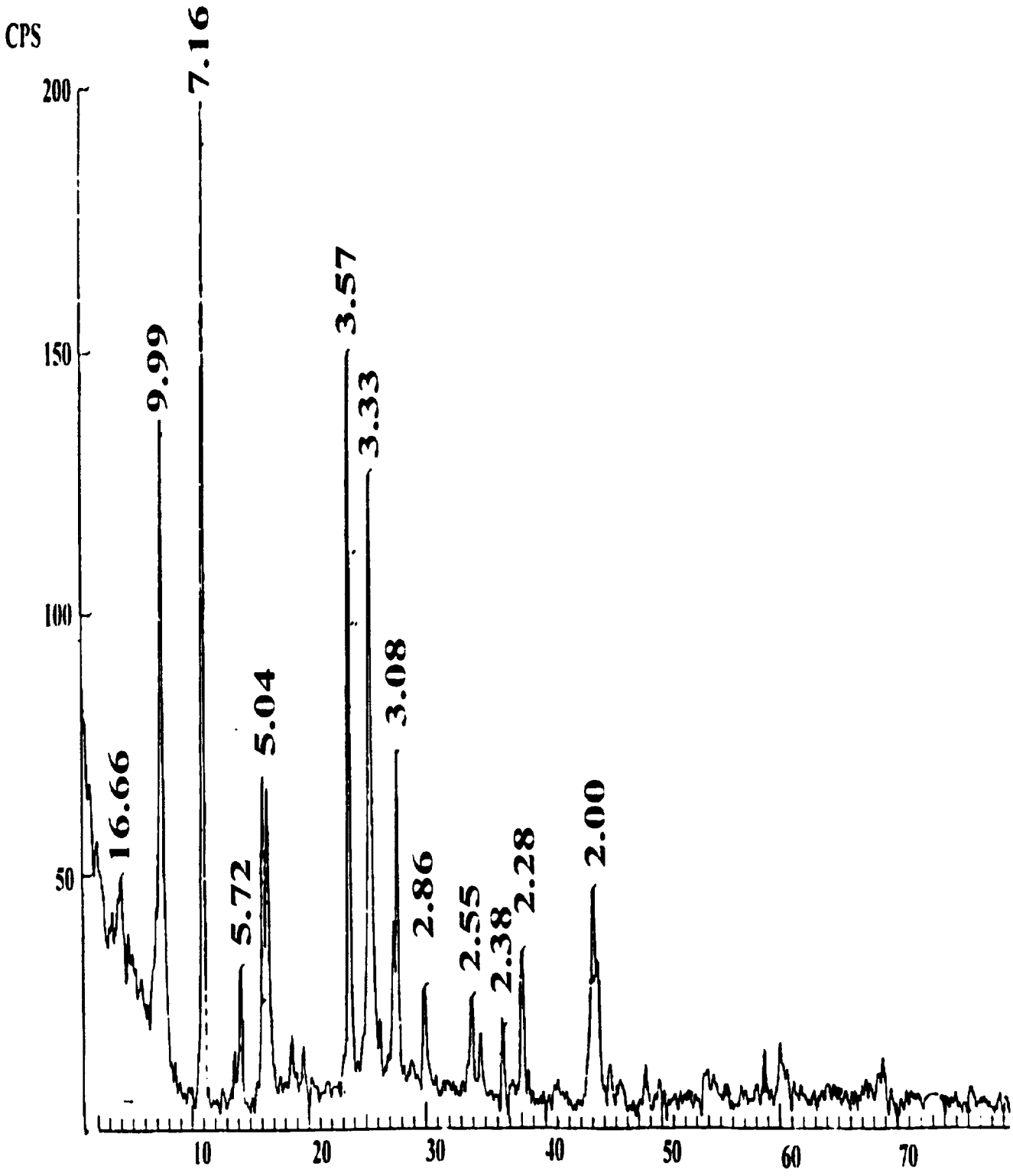

Figure 3. X-ray diffractogram of Alum Creek Sample One, slurry mount, heat treated at 107° C for twelve hours. The X-axis is the 2θ angle from the goniometer and the Y-axis is relative intensity. The 16.66 d-spacing is associated with montmorillonite, the 9.99 d-spacing with halloysite, and the 7.10 d-spacing with kaolinite. Gentle heating has intensified the kaolinite peak and diminished the halloysite peak.

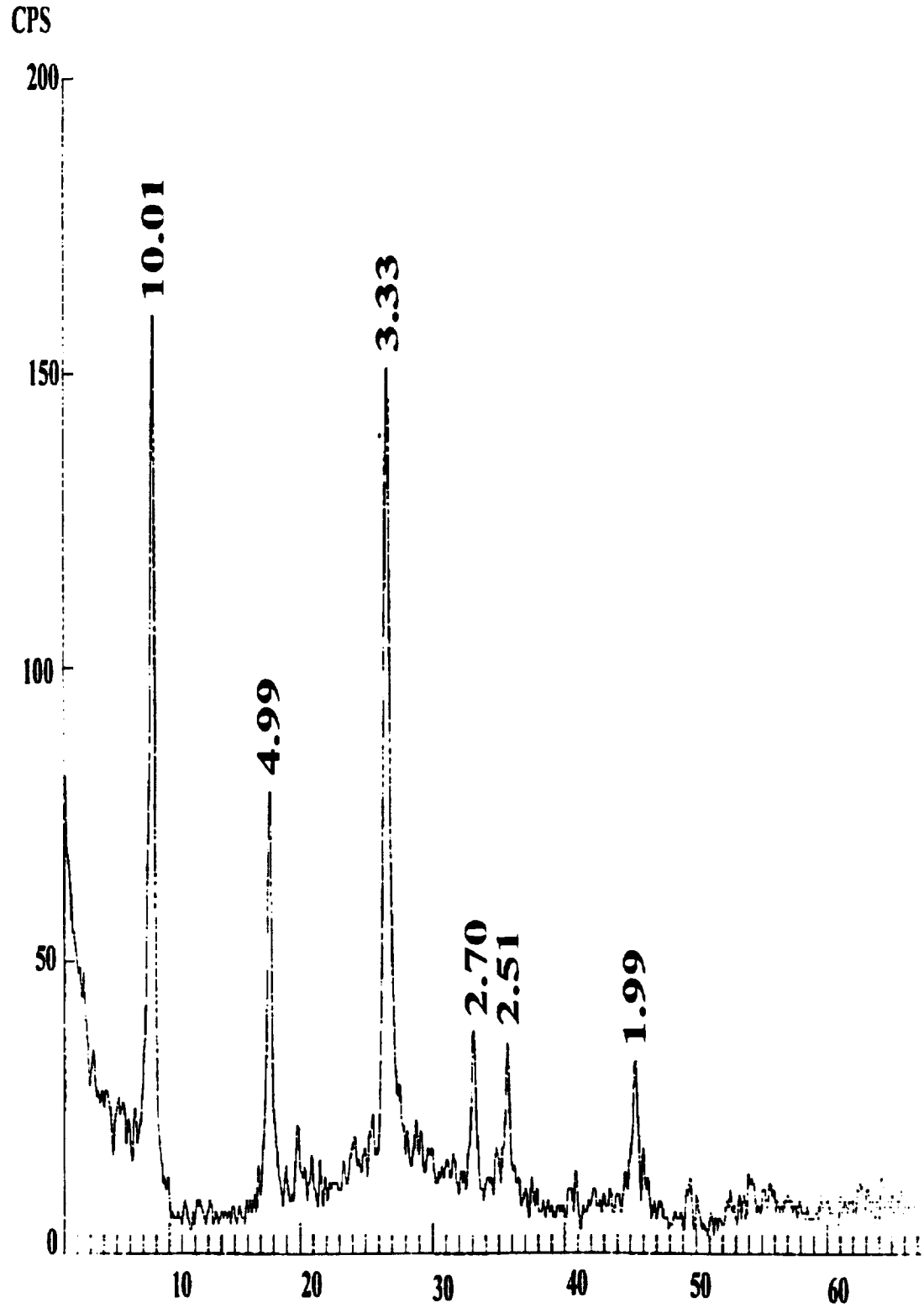

Figure 4. X-ray diffractogram of Alum Creek Sample One, slurry mount, heat treated at 550° C for two hours. The X-axis is the 2θ angle from the goniometer and the Y-axis is relative intensity. All d- spacings: 10.01, 4.99, 3.33, 2.70, 2.51, 1.99, are associated with mica.

REFERENCES

Bishop, J.L., C.M. Pieters, and J.O. Edwards, 1994, "Infrared Spectroscopic Analyses on the Nature of Water in Montmorillonite", Clays and Clay Minerals, Vol. 42, No. 6, pp. 702-716.

Clark, R.N., T.V.V. King, M. Klejwa, G.A. Swayze, and N. Vergo, 1990, "High Spectral Resolution Reflectance Spectroscopy of Minerals", Jour. Geophys. Research 95, No. 138, 12, 653-12, 680.

Dixon, J.B. and S.B. Weed, 1977, Minerals in Soil Environments, Soil Society of America. Madison, Wisconsin. ch. 9,11.

Ivosevic, S.W., 1984, Gold and Silver Handbook on Geology, Exploration, Economics of Large Tonnage, Low Grade Deposits. Stanley W. Ivosevic, Publisher.

King, T.V.V., 1995, "Environmental Considerations of Active and Abandoned Mine Lands Lessons from Summitville Colorado", U.S. Geol. Survey Bull. 2220, pp.38.

Lipman, P., 1975, "Evolution of the Platoro Caldera and Related Rocks, Southeastern San Juan Mountains, Colorado", U.S. Geol. Survey Prof. Paper 852, pp. 128.

Mertzman Jr., S.A., 1971, "Summer Coon Volcano, Eastern San Juan Mountains, Colorado", New Mexico Geologic Society, pp. 8.

Moore, D.M., and R.C. Reynolds, 1989, X-Ray Diffraction and the Identification and analysis of Clay Minerals. New York: Oxford Press. pp. 179-199.

Post, J.L. and P.N. Noble, 1993, "The Near-Infrared Combination Band Frequencies of Dioctahedral Smectites, Micas, and Illites", Clays and Clay Minerals, Vol. 41, No.6, pp. 639-644.

Singh, B. and I.D.R. Mackinnon , 1996, "Experimental Transformation of Kaolinite to Halloysite", Clays and Clay Minerals, Vol. 44, No. 6, pp. 825-834.

Srasra, E., F. Bergaya, and J.J. Fripiat, 1994, "Infrared Spectroscopic Study of Tetrahedral and Octahedral Substitutions in Interstratified Illite-Smectite Clay", Clays and Clay Minerals, Vol. 42, No. 3, pp. 237-241.

Steven, T.A. and P. Lipman, 1976, "Calderas of the San Juan Volcanic Field, Southwestern Colorado", U.S. Geol. Survey Prof. Paper 958, pp. 35.

Quantum Efficient Detectors for Use in Absolute Calibration

Jessica Faust, Michael Eastwood, Betina Pavri, James Raney
Jet Propulsion Laboratory
California Institute of Technology
Pasadena, CA 91109

ABSTRACT

The trap or quantum efficient detector has a quantum efficiency of greater than 0.98 for the region from 450 to 900 nm. The region of flattest response is from 600 to 900 nm. The QED consists of three windowless Hamamatsu silicon detectors. The QED was mounted below AVIRIS to monitor the Spectralon panel for changes in radiance during radiometric calibration. The next step is to permanently mount the detector to AVIRIS and monitor the overall radiance of scenes along with calibration.

BACKGROUND

The trap detector chosen has a quantum efficiency of greater than 0.98 for the region from 450 to 900 nm. The region of flattest response is from 600 to 900 nm. The model of trap detector chosen is the Graseby Optronics model QED-150 (see figure 1). The QED consists of three windowless Hamamatsu silicon detectors. The increased quantum efficiency is due to two factors. First, each detector has a deeper depletion layer (than a typical photodiode) allowing for more efficient collection of photons in the red to NIR region. Second, the detectors are arranged at 45° angles to allow photons not absorbed by the first detector to reflect off at an angle that allows absorption by the second detector. Photons not absorbed at the second detector are absorbed by the third. The third detector is aligned such that any photons not absorbed are re-directed back toward the second and then first detectors. Thus, this design allows the system to act as if five detectors are in the optical path, raising the quantum efficiency of the device.

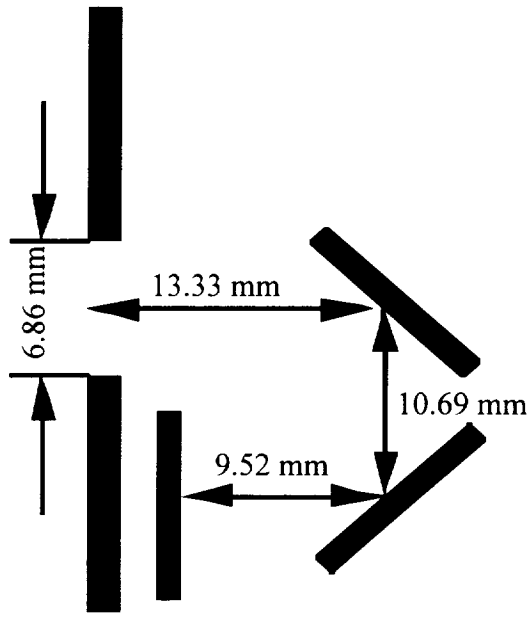

Figure 1. QED Detector Configuration

Two of the four AVIRIS spectrometers work within the range of the QED. Spectrometer A ranges from ~370 nm to 675 nm while spectrometer B's range is from ~665 nm to 1250 nm. A decision was made to limit the QED response to only one of the spectrometer ranges to better compare its data to the data from AVIRIS. The spectrometer data is integrated over the region for which the QED is filtered. Filters limiting the QED's response to the AVIRIS Spectrometer B wavelength range were chosen. A Melles-Griot bandpass (interference) filter with a 780±2 nm peak and 20±4 nm bandwidth limits the QED response. By the addition of RG695, a Schott cut-on filter, short wavelength leakage of 5% of the interference filter was reduced to 0.5%. Using a field spectrometer, the transmission of the each filter was measured to be 77.5% and 62% for the RG695 and Melles-Griot filters, respectively. In figure 2, a graph of the theoretical combination is given and shows a peak transmission of 58%.

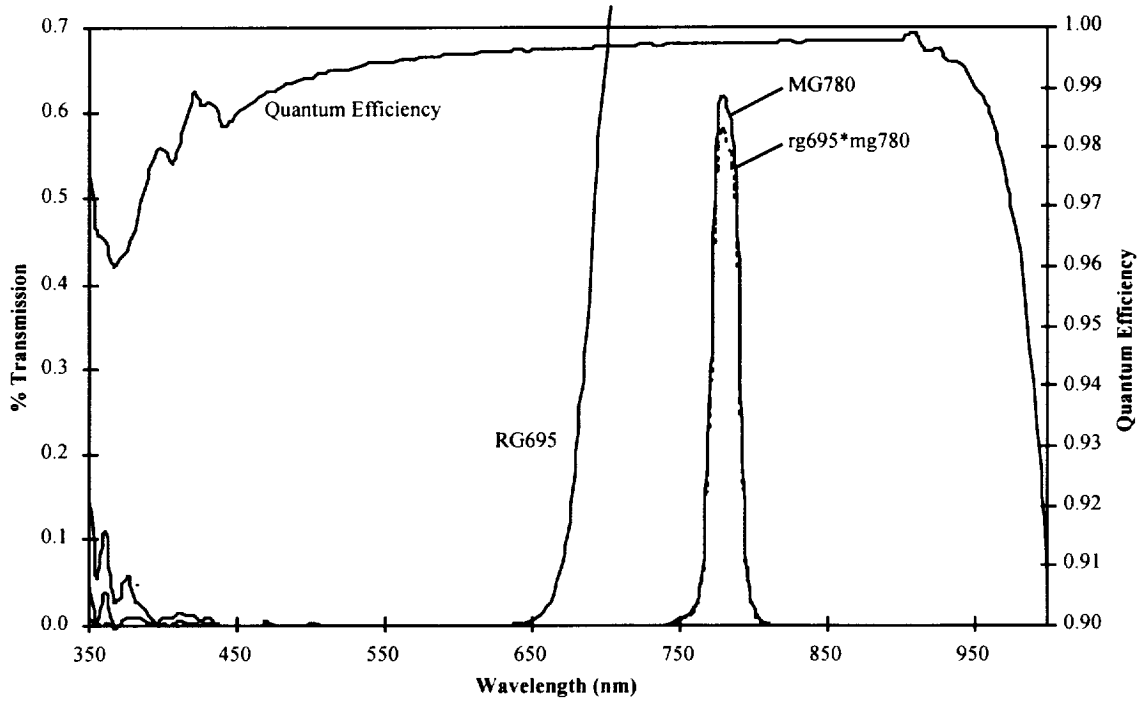

Figure 2. QED Response and Filter Transmission

A test was performed to determine the field-of-view of the QED without any apertures in place. The source --a 125 W bulb behind a diffuser and an aperture mask measuring approximate 5 mm in diameter— was placed upon an optical table with the QED a known distance above it. Measurements were taken as the source was moved carefully two perpendicular axes within the QED's field-of-view. The result was the spatial response function of the detectors. Using this information, the field-of-view of the QED was determined to be approximately 35° in the horizontal axis. In the vertical axis the field-of-view was 35° in the upward direction and 45° in the downward direction. The reason for the change in the vertical axis is the angle of the first detector (see figure 1).

This field-of-view is too large for our application. The QED is to observe a Spectralon target (a 99% reflectance target from Labsphere). The target is 30.5 cm by 30.5 cm and will be viewed from approximately 1.5 m; therefore, the spot diameter seen by the QED would be 94 cm.

SET-UP

The QED aperture has been limited to approximately 5.5° by the addition of a baffle assembly, which also serves as a filter retainer. The use of the first detector element was limited to the center 4-mm spot (of a 1-cm2 detector). The baffle assembly was designed with three precision beveled apertures to reduce stray light effects. (See figure 3.) This baffle design allows for a 14.1-cm spot diameter on the target.

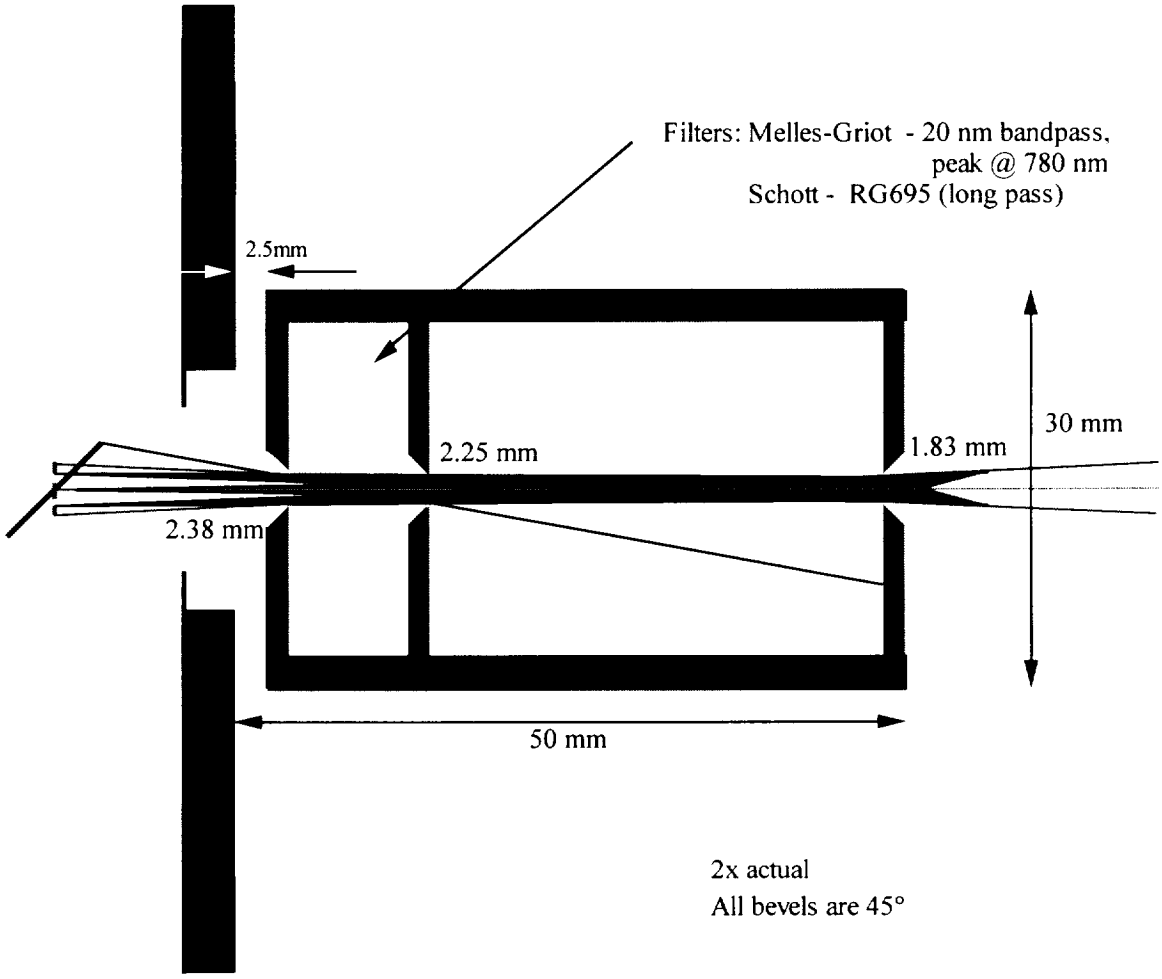

Figure 3. Field-of-View Reduction Baffle Assembly

During the 1997 flight season, the QED was removable and mounted on AVIRIS only during radiometric calibrations. This includes laboratory and field calibration. Figure 5 shows how the QED was put to use in monitoring the Spectralon target. The field target was carefully located beneath the AVIRIS, approximately 5° off the AVIRIS nadir looking view. For its initial use, the QED was aligned to the center of the target using a laser pointer (see figure 5) and locked into position (mounted to the QED). For all subsequent tests, it was mounted in the same orientation for each calibration and whenever calibration is performed the target is aligned using the laser pointer attached to the QED. As a quick check, a *crosstrack* scan was run using the ground system to make sure that the target was aligned to the AVIRIS instantaneous field-of-view.

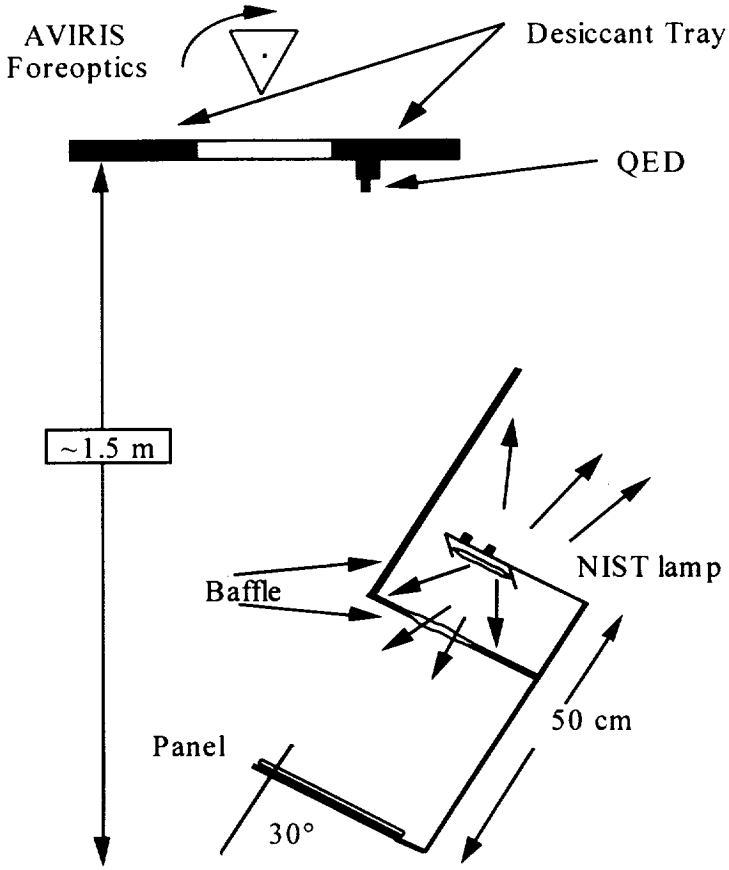

Figure 4. QED Current Configuration under AVIRIS

During the 1998 maintenance cycle, the QED will become a permanent part of the AVIRIS instrument. The QED will be hard mounted and incorporated into the AVIRIS data stream allowing for radiometric monitoring of calibration as well as flight scenes. The intent is that the QED will become an absolute radiometric calibration along with its current usage as a repeatable radiometric reference.

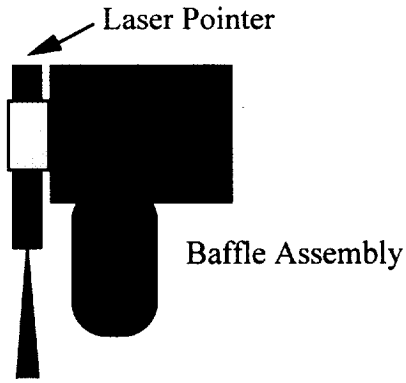

Figure 5. QED with laser pointer mounted

ANALYSIS and RESULTS

Graseby Optronics (now, UDT Sensors) provides a performance specification for the QED as follows:

$$R = QE * (\lambda / 1239.5) \qquad EQ.\ 1$$

$$I/P = QE * (\lambda / 1239.5) \qquad EQ.\ 2$$

$$P = I/[\,QE * (\lambda / 1239.5)\,] \qquad EQ.\ 3$$

where, R is responsivity of the detector in A/W,
P is the power input to the detector in watts,
I is the current output of the QED in amperes,
and λ is the wavelength of interest in nanometers.

Using the data taken with a point spectrometer, the transmission of the filter combination was approximated to a Gaussian shape. The transmission peak was at 780.5 nm, with a full width half maximum of 18.9 nm, and a peak transmission of 63.6%. According to the data sent to us with the detector, the quantum efficiency at 780.5 nm is approximate 0.9973. In table 1 below, these values were used with the average readings taken by the QED of the Spectralon panel when it was in place below AVIRIS.

Table 1. QED Measurement Results

DATE	Bulb	AVG Reading (A)	Flux (nW)
02/25/97	F-413	3.27E-09	5.2089
02/28/97	F-413	3.30E-09	5.2517
03/04/97	F-413	3.30E-09	5.2472
04/14/97	F-413	3.23E-09	5.1487
07/10/97	F-413	3.14E-09	4.9923
07/14/97	F-413	3.27E-09	5.2121
10/14/97	F-413	3.12E-09	4.9759
07/10/97	F-435	3.10E-09	4.9348
10/14/97	F-435	3.22E-09	5.1222
10/14/97	F-440	3.08E-09	4.9049

The theoretical values of flux are derived below by using the irradiance (E_{bulb}) and the reflectance (R_p) of the Spectralon panel. Equation 4 describes the relationship between radiance and irradiance for a Lambertian scatterer such as the Spectralon panel is assumed to be. The area of the detectors is defined by simple geometry and the radius (r) of the detector that has been illuminated is defined by the baffle described above. The area of the source is defined by the projection of the solid angle of the baffle where θ is the half field-of-view of the baffle and r_p is the radius of the panel seen by the detectors.

$$L_s = E_{bulb}(\lambda) * R_p(\lambda) / \pi \qquad EQ.\ 4$$

$$A_{det} = \pi * r^2 \qquad EQ.\ 5$$

$$A_{src} = \pi * r_p^{\,2} = \pi * z_{prime}^{\,2} * \sin^2(\theta) \qquad EQ.\ 6$$

$$\Phi = 1.05 \int_{740nm}^{810nm} \frac{L_s(\lambda)\,Area_{src}\,Area_{det}\cos\phi_1\cos\phi_2}{Z_{prime}^{\,2}} T_f(\lambda)d\lambda \qquad \text{EQ. 7}$$

In equation 7, the angles, $\phi 1$ and ϕ_2, represent the angles of the Spectralon target and the detectors to the normal (to the floor). The factor of 1.05 is the correction factor for the Spectralon target. Betina Pavri has characterized several panels and found that the calibration values that are increased by a factor of 5% when the panel is viewed at a 30° angle. The variable T_f represents the filter transmission at each wavelength. The integrated flux expressed in equation 7 represents the theoretical values of flux that the detector should receive and record. Table 2 shows the values calculated using our field target and three different NIST FEL 1000-W lamps.

Table 2. Theoretical Flux for Lamps Used in Field and Laboratory Calibrations

Lamp	Theoretical Flux (nW)
F-413	5.3662
F-435	5.7074
F-440	5.5930

RESULTS

The error between the theoretical QED response and the measured response is shown in figure 6. This chart reflects the error for all three FEL lamps.

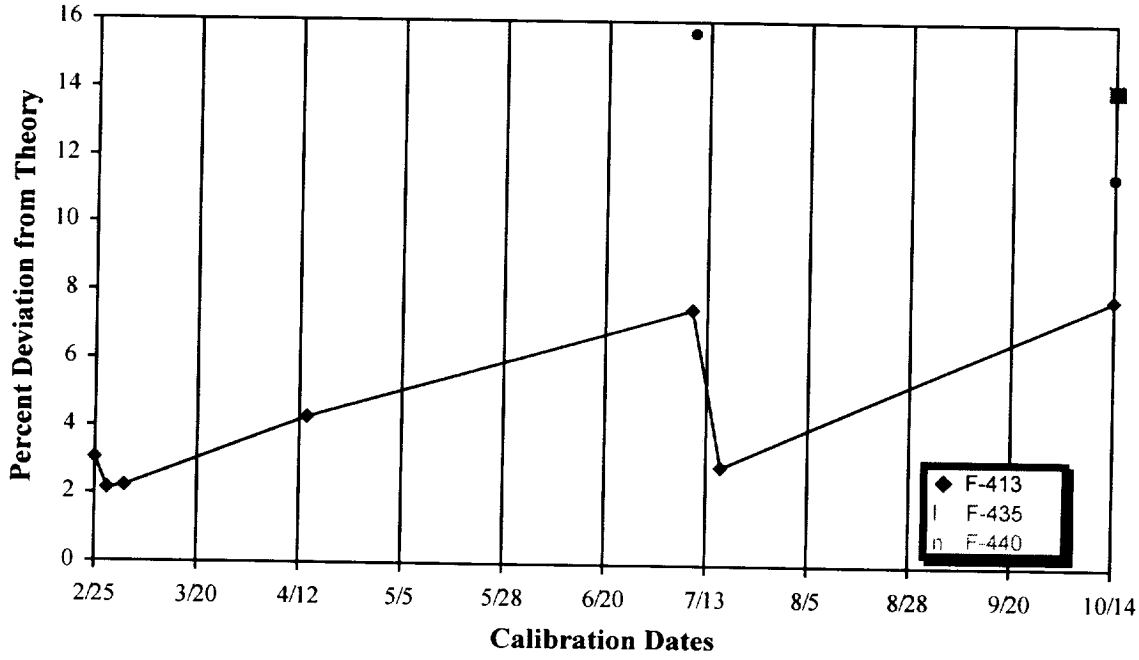

Figure 6. Error between theoretical and measured flux from QED for field calibrations

Several error contributions exist. The FEL lamps provided by Optronics are calibrated for use in the vertical position only. Using the lamps at a 30° angle to the vertical causes deterioration in the calibration numbers. The lamp's filament is not secured at both ends of the vacuum tube; therefore, when the lamp is used in a non-vertical position the filament sags. This causes the calibration of the lamps to be invalid after only a few hours of use was logged on each of them.

Another factor that contributes heavily to the errors seen with the F-413 bulb was the removal and replacement of the QED to its mounting each time it was used. The alignment procedure described above was used, but it was difficult to position the target exactly the same way each time. Part of this is a factor of how AVIRIS is looking at the target. If the ER-2 has a light load (i.e., not much fuel on-board) then AVIRIS will be a little higher off the ground at slightly inclined toward the front of the aircraft. If the fuel load is heavy, then the ER-2 will be lower because of the additional weight. This factor also has to do with the errors seen.

One change in the AVIRIS instrument occurred in late July that accounts for the larger errors seen for the October 14 data. The new foreoptics door was installed while AVIRIS was on deployment at Ames Research Center. New desiccant trays for the foreoptics came with this door. The QED mount was on the trays and moved to the new trays but placed differently than before. Because of this error, the data taken with the QED was not as reliable as it had been beforehand.

Another source of error may be in several of the assumptions. When the Spectralon panel is used at an angle, the calibration provided by Labsphere is off by a constant factor. This is mentioned in the Analysis and Results section. The Labsphere calibration is measured using an 8° hemispherical measurement at 45° to the normal of the target. A calibration of the reflectance is not possible unless the illumination were not normal to the panel, which is less than ideal. The 5% increase in reflectance values for a 30° use may need a slight adjustment because of this impossibility. This error contribution could be as much as 2-3 %.

Several activities are currently underway to ensure that these factors are reduced for the 1998 flight season. First, the use of the FEL lamps is being discontinued and NIST 200C lamps will be used once again. The 200C lamps are also 1000 W but are secured at both ends of the vacuum tube creating a tension in the filament that will keep it taut when in use. Second, the redesign of the field target is underway to ensure that AVIRIS and the QED will always be viewing it in the same geometry. Lastly, the QED will be hard-mounted and its data will be included in the data stream of AVIRIS.

ACKNOWLEDGEMENTS

The research described in this paper was carried out by the Jet Propulsion Laboratory, California Institute of Technology, under a contract with the National Aeronautics and Space Administration.

Thermal Stability of the AVIRIS On-Board Calibrator

Jessica Faust, Michael Eastwood, Chuck Sarture, Orlesa Williams
Jet Propulsion Laboratory
California Institute of Technology
Pasadena, California 91109

Introduction

The AVIRIS On-Board Calibrator (OBC) diagrammed in figure 1 provides essential data for refining the calibration of each AVIRIS data run. Annual improvement to the AVIRIS sensor and laboratory calibration accuracy has resulted in increasingly high demands on the stability of the OBC. Since the 1995 flight season, the OBC could track the stability of the spectrometer alignment to the 2% level, a significant improvement over previous years. The major contributor to this 2% stability was the conversion from a constant-current bulb power supply to an intensity-based active feedback power supply. Given the high sensor signal-to-noise ratio, improving the OBC to track 1% or 0.5% changes was highly desirable. Achieving stability better than 2% required an examination of the mechanisms affecting stability.

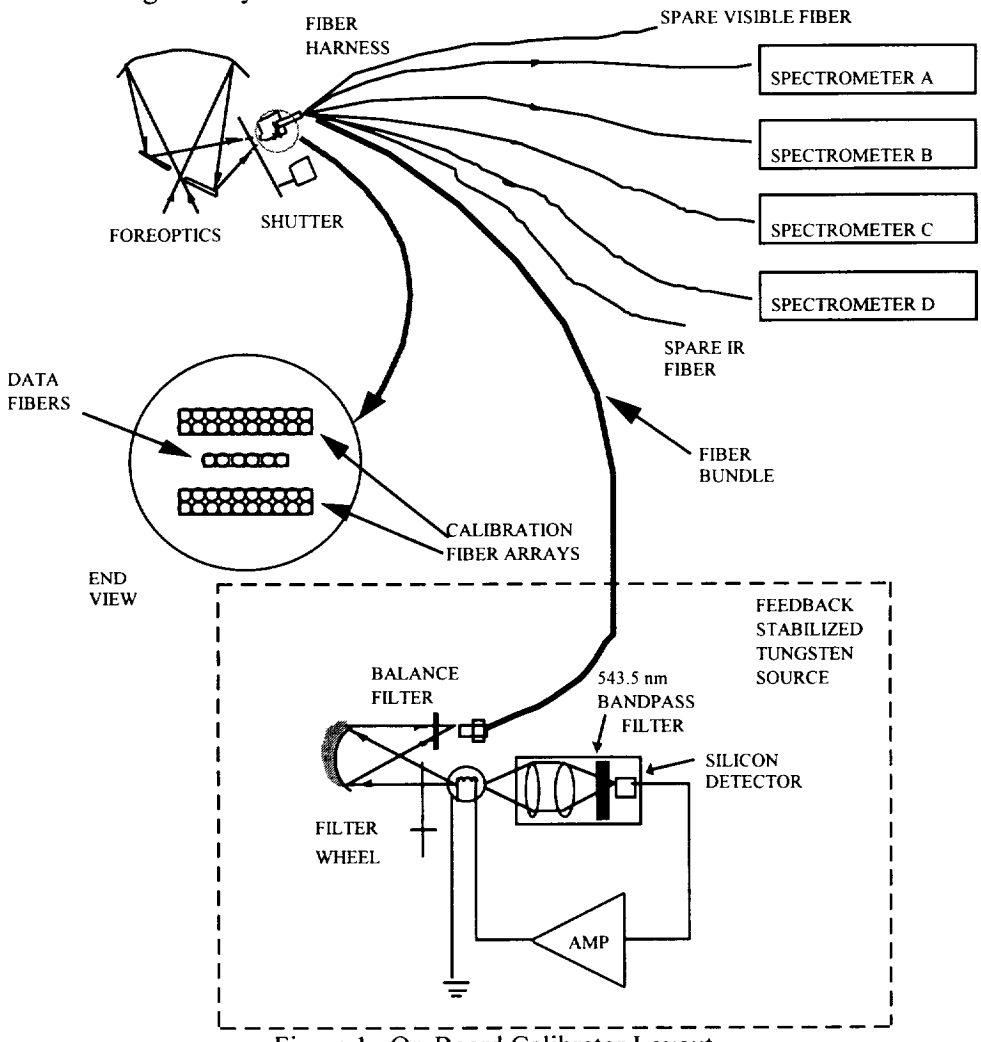

Figure 1. On-Board Calibrator Layout

Historically, the OBC temperature has ranged between +10°C and +50°C, in-flight minimum and in-laboratory maximum, respectively. Optical power variations caused by changes in the temperature of the OBC are seen by the AVIRIS spectrometers and degrade the utility of the OBC as a calibration source. The goal of thermal testing the AVIRIS OBC was to quantify any changes in the optical output from the optical fiber bundle as the temperature of its environment changes.

The on-board calibrator and its place in the AVIRIS sensor are shown in figure 1. When the foreoptics shutter is closed light from the feedback-stabilized tungsten source in the on-board calibrator is carried through a fiber bundle to the back of the shutter and reflected into the spectrometer data fibers. Fluctuations in the OBC temperature can distort the OBC structure, causing the tungsten lamp to mis-align and hence change the intensity of the light reaching the spectrometers. The change in temperature of the OBC in-flight has historically been as much as ±10°C.

Experimental Set-Up

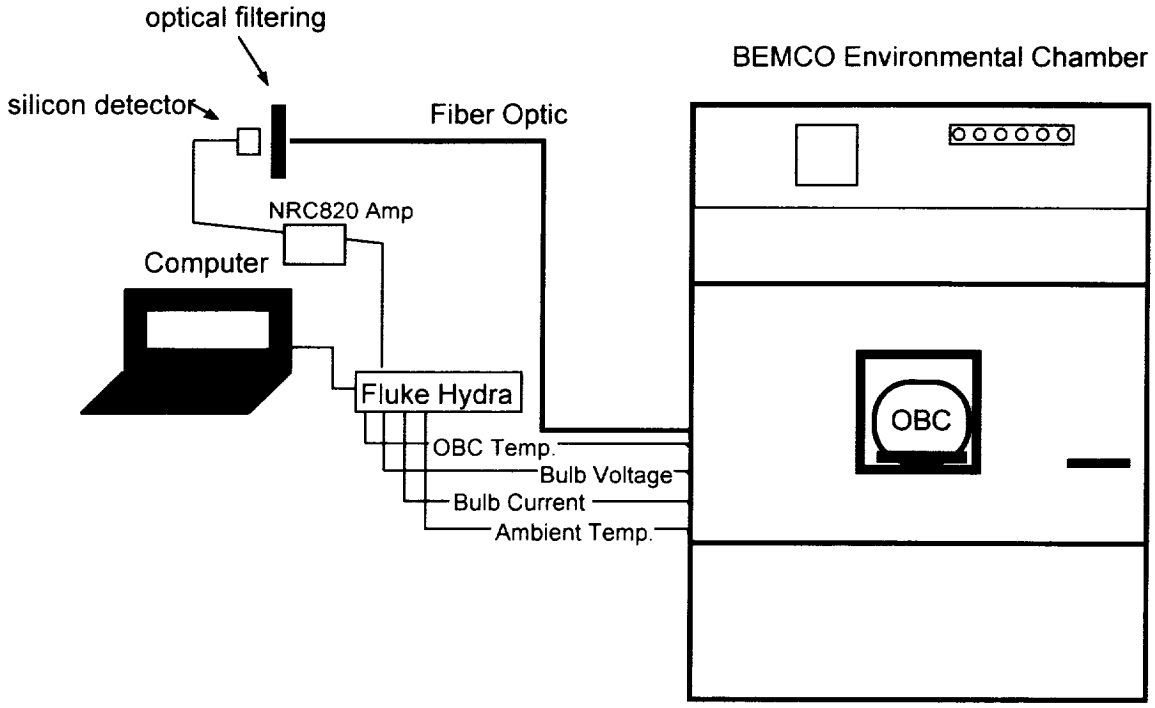

Figure 2. Experimental Set-Up

The OBC was placed in an environmental chamber such that thermal contact between the chamber floor and the calibrator was eliminated; therefore, chamber air provided the thermal transport as opposed to point contact with the cold chamber walls. (See figure 2.) Optical fiber and power cables were fed through an opening and attached to the OBC. Several OBC operating parameters were monitored, including light output through the optical fiber, voltage across the light bulb, voltage across a 0.1Ω resistor series (bulb current), plus both OBC structure and ambient temperature (10 mV/°C). Data was logged to an ASCII file using a Fluke Data Acquisition Unit. Optical power output was monitored by a model NRC820 silicon detector with an optical filter and stored to the data file (output was measured as volts DC on an arbitrary scale).

Procedure and Analysis

The test was performed four times with improvements to the set-up added each time. For the first run, the OBC was not mounted on an aluminum plate (as usually configured on AVIRIS) and the temperature range was 10°C to 50°C. In this run, the OBC output varied with small changes in temperature. Figure 3 shows oscillations in the OBC output over regions where the OBC structure temperature is fairly stable. The bulb voltage and current followed closely with the rise and fall of the temperatures and showed oscillations as well, but at significantly smaller magnitudes. The oscillations in the lamp current are 1 mA in 2000 mA and 2 mV in 5000 mV for the bulb voltage. This is a power variation of 2 parts in 10^7 while the optical flux at the output of the fiber bundle varied 3 parts in 10^3.

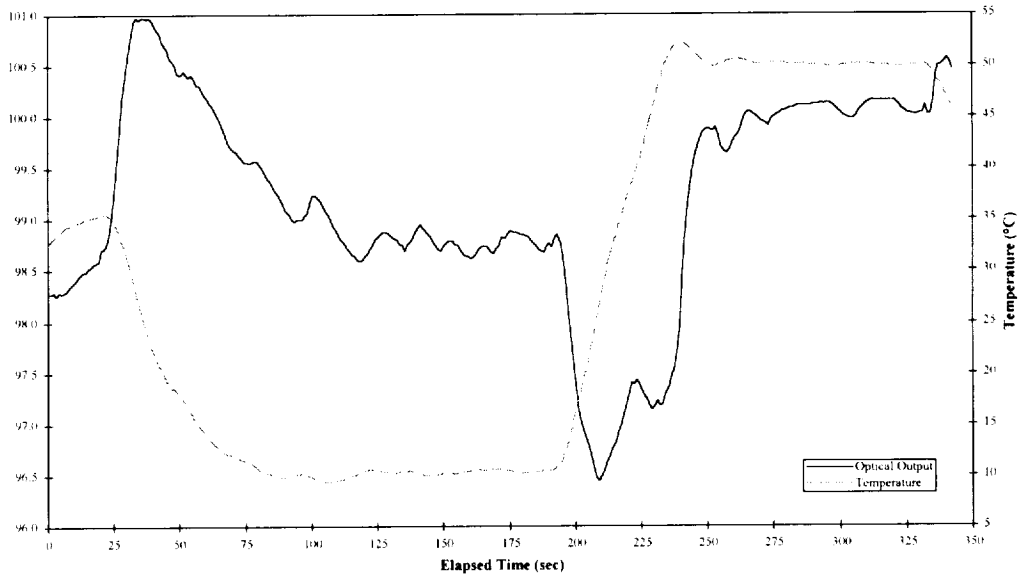

Figure 3. First Run: Optical Output and Temperature vs. Time for OBC without a shear plate

As shown in figure 1, the lamp output is imaged onto the fiber bundle by a spherical mirror after passing through the filter wheel. If the base plate of the OBC distorts, then the optical components will misalign, and the image of the bulb filament will move off the fiber bundle input. This is the most likely cause of the oscillations seen in figure 3.

For the second run, an aluminum plate was attached to the base of the OBC to more closely simulate the enhanced structural rigidity of the OBC baseplate when it is attached to the AVIRIS sensor's forward panel in the normal flight configuration. The test was terminated before completion because the temperature sensor readout became noisy and unstable. The addition of a filter to the circuit at the data acquisition unit eliminated this noise. The third test ranged in temperature from 20°C to 40°C (equilibrium was not achieved at 40°C). A 10 nm full-width-half-maximum (FWHM), 450 nm center wavelength bandpass filter was added to minimize any room temperature responsivity variations from the NRC820 silicon detector.

The fourth run was done over the same temperature range as the first run, adding another temperature equilibrium region at 30°C (See figure 4.). The equilibrium regions lasted for at least 45 minutes and did not show the oscillations that were visible in the first test. In this test, the OBC output was much more stable than in the first test.

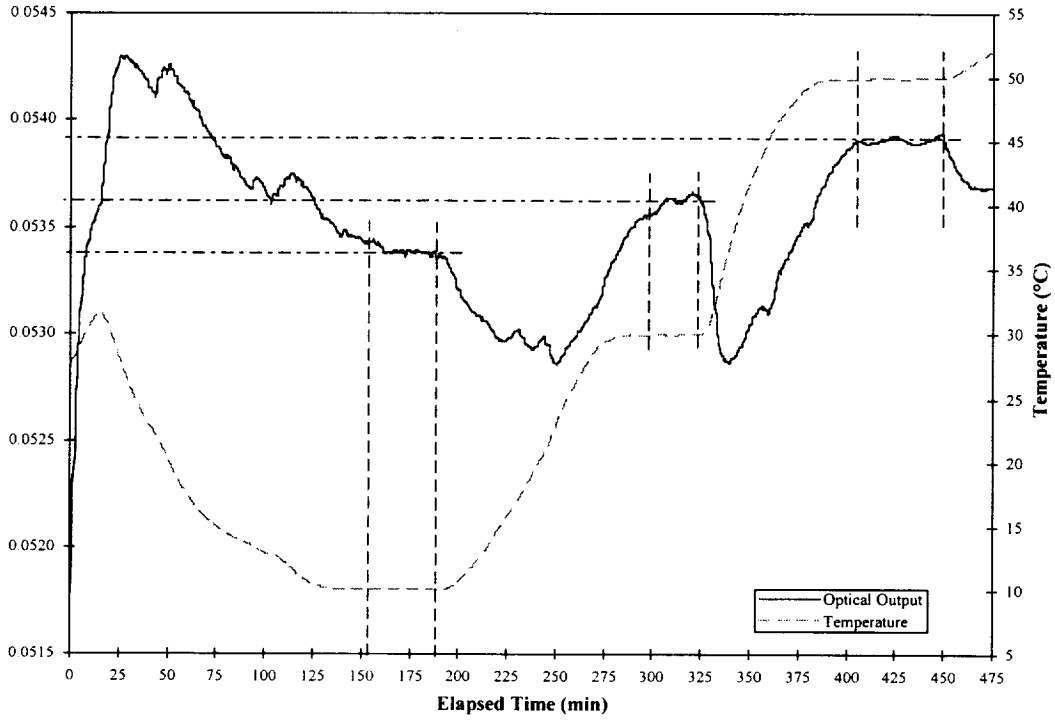

Figure 4. Fourth Run: Optical Output and Temperature vs. Time (with a shear plate)

Conclusion

A change in OBC structure temperature of 40°C leads to a change in optical output of approximately 4% at 450 nm. Last year, the in-flight temperatures ranged between 25°C and 45°C. If we assume AVIRIS will experience similar temperature variations in the future, the 20°C range would continue to yield an OBC light output uncertainty of 2%. However, for regions where the temperature is stable the optical output variation is far less than 2%. This is because temperature transients generate gradients that distort the OBC structure and misalign the optics. Once the OBC reaches thermal equilibrium, the optical alignment is re-established, as is evident in the fourth test where the output deviation was approximately 0.75% across each of the three temperature stable regions. Bulb voltage and current followed the temperature changes very closely, indicating that the 543.5 nm filtered silicon detector controlling the bulb has a residual output sensitivity to temperature, or that the structure holding the bulb in alignment with that detector is not perfectly rigid. (See figures 5 and 6.) From these results, we decided to implement a thermal control system to stabilize the OBC's internal temperature to 40°C. This thermal stabilization will further limit the variations in optical output to well below the 0.75% seen in the test.

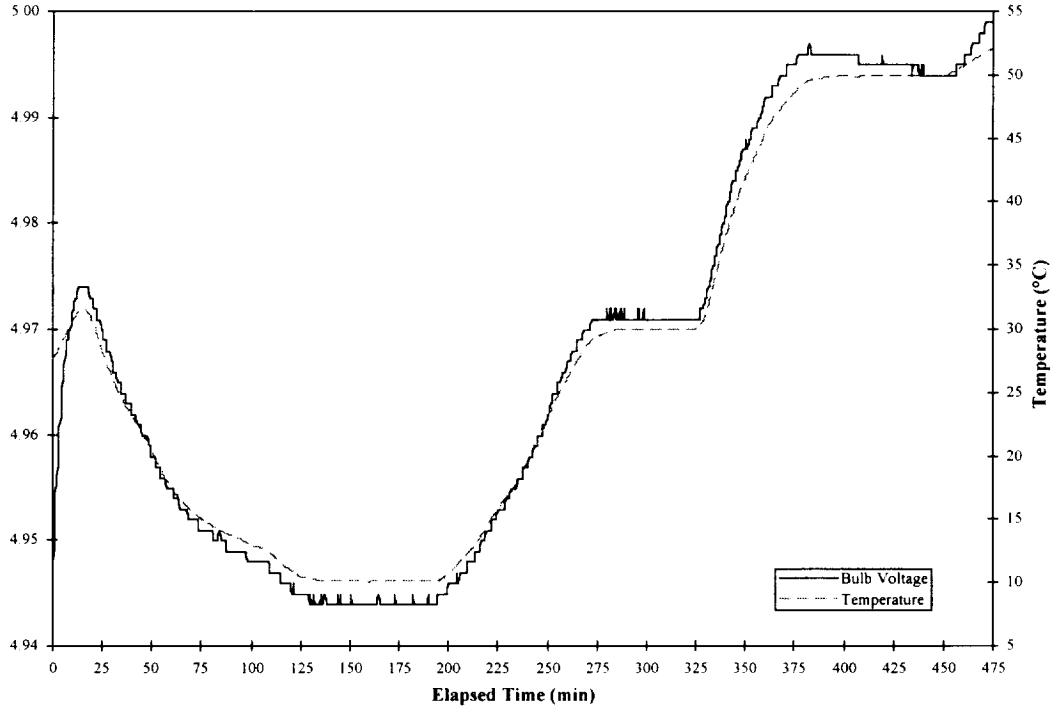

Figure 5. Bulb Voltage and Temperature vs. Elapsed Time

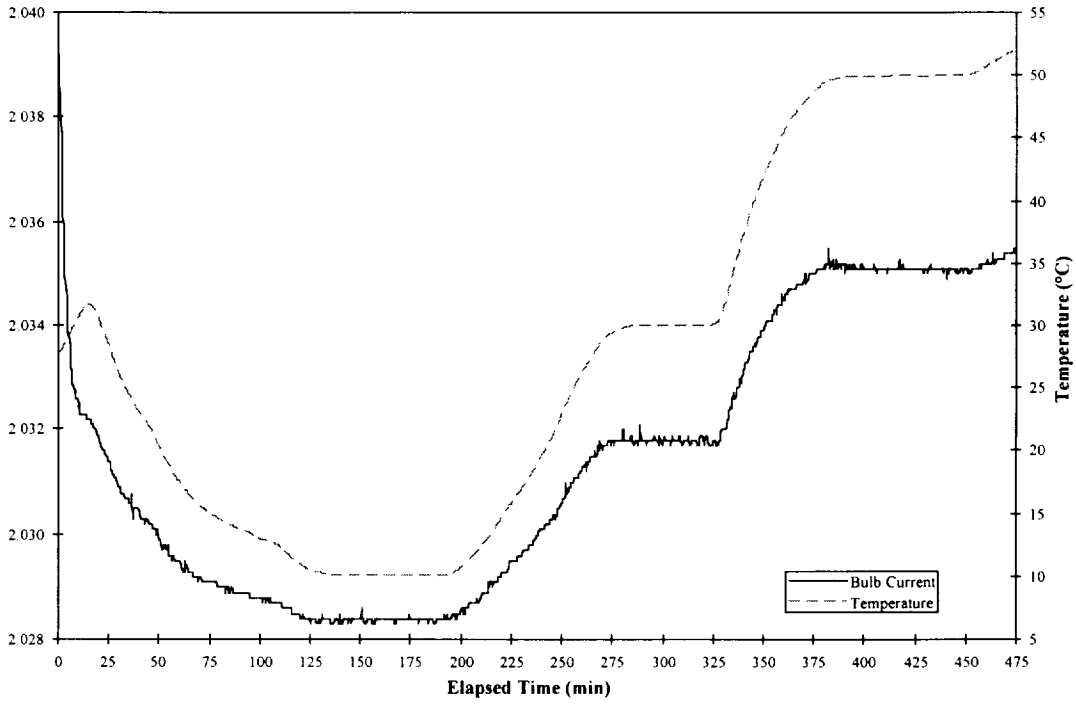

Figure 6. Bulb Current and Temperature vs. Elapsed Time

Data from the flight season, as seen in figure 7, shows that the variation in the lamp voltage was 0.47% while the lamp current varied by only 0.19%. This slow increase in bulb voltage and current could arise from the slowly decreasing bulb quartz envelope transmittance as tungsten is deposited on the inside of the envelope. The halogen cycle does minimize this deposition, but does not completely eliminate it. This increasing opacity would result in less light exiting the bulb for a given power level. The intensity-based closed-loop control compensates for this by increasing the power, thus the bulb output is maintained. A slight color temperature change also results, but is not significant for the variation seen here.

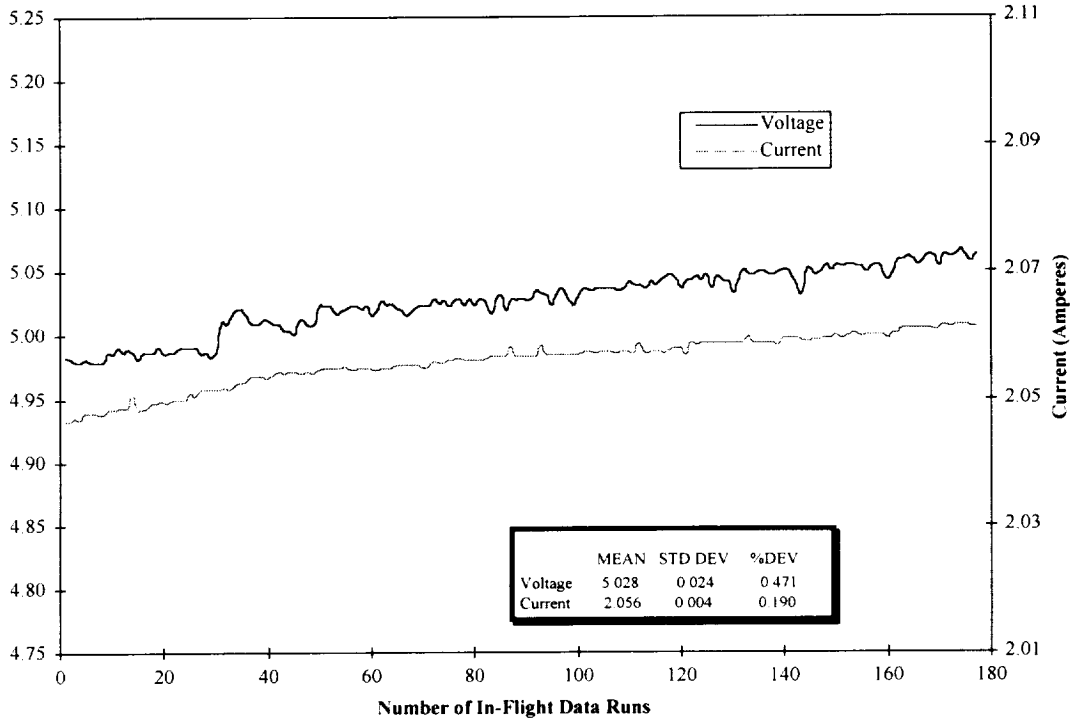

Figure 7. On-Board Calibrator Lamp Current and Voltage Trend for 1997 Flight Season

ACKNOWLEDGEMENTS

The research described in this paper was carried out by the Jet Propulsion Laborator- California Institute of Technology under a contract with the National Aeronautics and Space Administration.

REFERENCES

Chrien, Thomas G., Michael L. Eastwood, Charles M. Sarture, Robert O. Green, and Wallace M. Porter, "Current Instrument Status of the Airborne Visible/Infrared Imaging Spectrometer (AVIRIS)", Proc. Third AVIRIS Workshop, JPL Publication 91-28, Jet Propulsion Laboratory, Pasadena, CA, pp. 302-313, 1991.

Chrien, Thomas G., Michael Eastwood, Robert O. Green, Charles Sarture, Howell Johnson, Chris Chovit, and Pavel Hajek, "Airborne Visible/Infrared Imaging Spectrometer (AVIRIS) On-Board Calibration System", Proc.Fifth AVIRIS Workshop, JPL Publication 95-1, Jet Propulsion Laboratory, Pasadena, CA, pp.31-32, 1995.

A MULTI-SCALE SAMPLING STRATEGY FOR DETECTING PHYSIOLOGICALLY SIGNIFICANT SIGNALS IN AVIRIS IMAGERY

John A. Gamon[1], Lai-Fun Lee[1], Hong-Lie Qiu[2]
[1]Department of Biology and Microbiology
[2]Department of Geography and Urban Analysis
California State University, Los Angeles
Los Angeles, CA 90032

Stephen Davis
Natural Science Division
Pepperdine University
Malibu, CA 90263

Dar A. Roberts
Department of Geography
University of California, Santa Barbara, CA 93106

Susan L. Ustin
Department of Land Air and Water Resources
University of California, Davis, CA, 95616

1. INTRODUCTION

Models of photosynthetic production at ecosystem and global scales require multiple input parameters specifying physical and physiological surface features. While certain physical parameters (e.g., absorbed photosynthetically active radiation) can be derived from current satellite sensors, other physiologically relevant measures (e.g., vegetation type, water status, carboxylation capacity, or photosynthetic light-use efficiency), are not generally directly available from current satellite sensors at the appropriate geographic scale. Consequently, many model parameters must be assumed or derived from independent sources, often at an inappropriate scale (Hall et al. 1995, Sellers et al 1995).

An abundance of ecophysiological studies at the leaf and canopy scales suggests strong physiological control of vegetation-atmosphere CO_2 and water vapor fluxes, particularly in evergreen vegetation subjected to diurnal or seasonal stresses. For example hot, dry conditions can lead to stomatal closure, and associated "downregulation" of photosynthetic biochemical processes, a phenomenon often manifested as a "midday photosynthetic depression" (Tenhunen et al. 1984, 1985 and 1990). A recent study with the revised simple biosphere (SiB2) model demonstrated that photosynthetic downregulation can significantly impact global climate (Sellers et al. 1996). However, at the global scale, the exact significance of downregulation remains unclear, largely because appropriate physiological measures are generally unavailable at this scale (Prince et al. 1995, Sellers at al. 1996). Clearly, there is a need to develop reliable ways of extracting physiologically relevant information from remote sensing.

Narrow-band spectrometers offer many opportunities for deriving physiological parameters needed for ecosystem and global scale photosynthetic models. Experimental studies on the ground at the leaf- to stand- scale have indicated that several narrow-band features can be used to detect plant physiological status. One physiological signal is caused by xanthophyll cycle pigment activity, and is often expressed as the Photochemical Reflectance Index (PRI; Gamon et al. 1992, 1997; Peñuelas et al. 1995, 1997a). Because the xanthophyll cycle pigments are photoregulatory pigments closely linked to photosynthetic function (Demmig-Adams and Adams 1996), this index can be used to derive relative photosynthetic rates (Gamon et al. 1997). An additional signal with physiological significance is the 970 nm water absorption band, which provides a measure of liquid water content (Peñuelas et al. 1993, 1997b; Zhang et al. 1997; Sanderson et al. in press). This feature has been quantified both using a simple 2-band

ratio (900/970 nm, here referred to as the "Water Band Index" or WBI; Peñuelas et al. 1993, 1997b), and using the "continuum removal" method (Clark and Roush, 1984, as cited in Zhang et al. 1997 and Sanderson et al. in press). Current atmospheric correction methods for AVIRIS imagery also obtain quantitative expressions of surface liquid water absorption based on the 970 nm water band (Green et al. 1993, Roberts et al. 1997) and may be comparable to ground-based estimates of water content using this feature. However, physiological interpretations of both the PRI and the WBI are best understood at the leaf and canopy scales, where complications of atmospheric interference and complex stand and landscape features can be minimized, and where experimental manipulations can be readily applied.

Currently it is not known whether these physiological indices can be used to derive meaningful physiological information from AVIRIS imagery. In addition to the problem of atmospheric interference, another challenge is that any simple physiological index can be confounded by multiple factors unrelated to physiology, and this problem can become more severe at progressively larger spatial scales. For example, previous work has suggested that both the PRI (Gamon et al, 1995b) and the WBI (Peñuelas et al, 1993, 1997b), are strongly correlated with other optical measures of canopy structure (e.g., the Normalized Difference Vegetation Index or green vegetation fraction), indicating a confounding effect of structure on physiological signals at the larger, landscape scale. Furthermore, the normal operating mode of most imaging spectrometers does not allow simultaneous, ground truthing at a level of detail needed for physiological sampling. Additionally, manipulative experiments of physiology are difficult to apply at a geographic scale suitable for comparison with remote imagery, which often works at spatial scales that are several orders of magnitude larger than those typically used for physiological studies. These limitations require the consideration of alternative approaches to validating physiological information derived from AVIRIS data.

In this report, we present a multi-scale sampling approach to detecting physiologically significant signals in narrow-band spectra. This approach explores the multi-dimensional data space provided by narrow-band spectrometry, and combines AVIRIS imagery at a large scale, with ground spectral sampling at an intermediate scale, and detailed ecophysiological measurements at a fine scale, to examine seasonally and spatially changing relationships between multiple structural and physiological variables. Examples of this approach are provided by simultaneous sampling of the Normalized Difference Vegetation Index (NDVI), an index of fractional PAR interception and green vegetation cover (Kumar and Monteith 1981, Asrar et al. 1984, Hatfield et al. 1984, Sellers 1985, Bartlett et al. 1990, Gamon et al. 1995a), the Water Band Index (WBI, an index of liquid water absorption; Peñuelas 1993 and 1997b), and the Photochemical Reflectance Index (PRI, an index of xanthophyll cycle pigment activity and photosynthetic light-use efficiency; Gamon et al. 1992 and 1997, Peñuelas et al. 1995 and 1997a). By directly linking changing optical properties sampled on the ground with measurable physiological states, we hope to develop a basis for interpreting similar signals in AVIRIS imagery.

2. METHODS

All ground measurements presented here were made in 1997 at the Malibu Forestry Unit (Los Angeles County Fire Department) site, near Tapia Park in the Santa Monica Mountains, California, USA. This site, which is normally dominated by chaparral vegetation, burned in October, 1996, and was in early stages of secondary succession during 1997. In this first year following the fire, the landscape was covered by a diversity of species, ranging from reseeding annuals and perennials, to resprouting, perennial chaparral shrubs.

Spectral reflectance was measured from the ground using a prototype spectrometer constructed from a silicon photodiode detector (Zeiss MMS1, NIR enhanced, with VIS blaze, Hellma Cells, Forest Hills, New York, USA), fitted with a single fiber optic probe (15-0600 LTS-T39-P-2-SMA/SP, General Fiber Optics, Inc, Fairfield, New Jersey, USA) fitted with a tube that restricted the field-of-view to approximately 18 degrees. Reflectance was sampled at each meter along three transects, varying from 50 to 100 meters in length and covering both north- and south-facing slopes. Spectra were measured from a distance of approximately 1 m from the surface, so that each spectrum sampled a ground or canopy area of approximately 0.1 m^2. Reflectance measurements were made on April 12 and 18 ("spring"), July 4 and 5 ("summer") and October 5 ("fall"). The spring and fall dates matched within a few days the dates of three AVIRIS overflights.

Reflectance indices were derived from reflectance spectra using the following formulas:

$$NDVI = (R_{750}-R_{660})/(R_{750}+R_{660}) \quad (1)$$

$$WBI = (R_{900}/R_{970}) \quad (2)$$

$$PRI = (R_{531}-R_{570})/(R_{531}+R_{570}) \quad (3)$$

where R_{XXX} represents reflectance at the indicated wavelength (XXX, in nm).

Leaf water status was sampled with a pressure chamber (model 1001, PMS Instrument Co., Corvallis, Oregon), and expressed as pre-dawn water potentials, a common physiological measure of seasonally changing plant water status (Koide et al. 1989). Water potential samples from *Adenostema fasciculatum* ("chamise") resprouts and seedlings and from *Ceanothus crassifolius* seedlings were averaged to create representative values for this site. Because water potential values were not sampled on the same dates as reflectance, we averaged values from the dates closest to the reflectance sampling for this analysis to estimate water status comparable to reflectance measurements (table 1).

AVIRIS data tapes for this site and dates were not obtained in time for these proceedings. Consequently, we conducted our analysis using previously available AVIRIS images of Point Dume from fall of 1994 (May 9) and spring of 1995 (October 19), that closely matched the spring and fall dates of ground sampling, but on different years and on different locations. These scenes were expressed as surface reflectance using the atmospheric correction method of Green et al. (1993). Spectral mixture analysis, conducted using a commercial software package (ENVI, Research Systems, Inc., Boulder, Colorado, USA), allowed us to select spectrally uniform regions representing distinct, uniform vegetation types (riparian and oak woodland, coastal sage scrub, chaparral, and annual grassland). The identity of these vegetation types was then confirmed with field visits. For each date and vegetation type, spectra and reflectance indices were then extracted from the two image cubes. Reflectance indices were derived by selecting the AVIRIS bands closest to the wavelength values indicated in equations 1-3, above.

3. RESULTS

The WBI was strongly correlated with NDVI for all three ground sampling dates (figure 1). In this figure, low NDVI values represent bare soil, and high values indicate complete vegetation cover. Further analysis using analysis of covariance (ANCOVA) indicated that the slope of this relationship changed significantly between April and June ($p < 0.001$), but not between June and October (figure 1B). Similarly, predawn water potentials declined significantly between April and June, but not between June and October (table 1). Plots of PRI vs. NDVI for the same dates yielded similar patterns, indicating significant changes in slope between spring and summer, but not between summer and fall (figure 2).

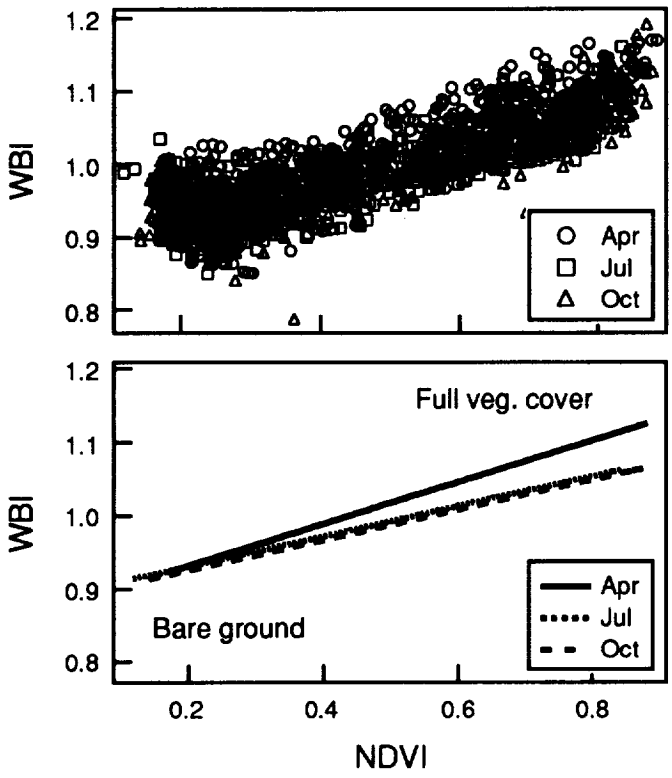

Figure 1. The Water Band Index (WBI) plotted against the Normalized Difference Vegetation Index (NDVI), both measured on the ground near Tapia Park, Santa Monica Mountains, California, in spring, summer, and fall, 1997. Each individual sampling point in panel A represents a surface area of approximately 0.1 m^2. Linear regressions (panel B) were highly significant ($p<0.0001$, Fisher's probability) and analysis of covariance indicated a significant change in slope between April and July, but not from July to October.

Date	mean Ψ (MPa)	SEM	range
April	-1.27	0.46	-0.40 to 3.32
July	-2.94	0.41	-2.13 to -3.19
October	-4.04	0.62	-1.75 to -5.14

Table 1. Mean, standard error of the mean (SEM), and range of predawn leaf water potential (Ψ) values near Tapia Park corresponding to the three reflectance dates in 1997. Mean values were estimated by averaging measurements of seedlings and resprouts of two species, as indicated in Methods. Lower values indicate drier leaves.

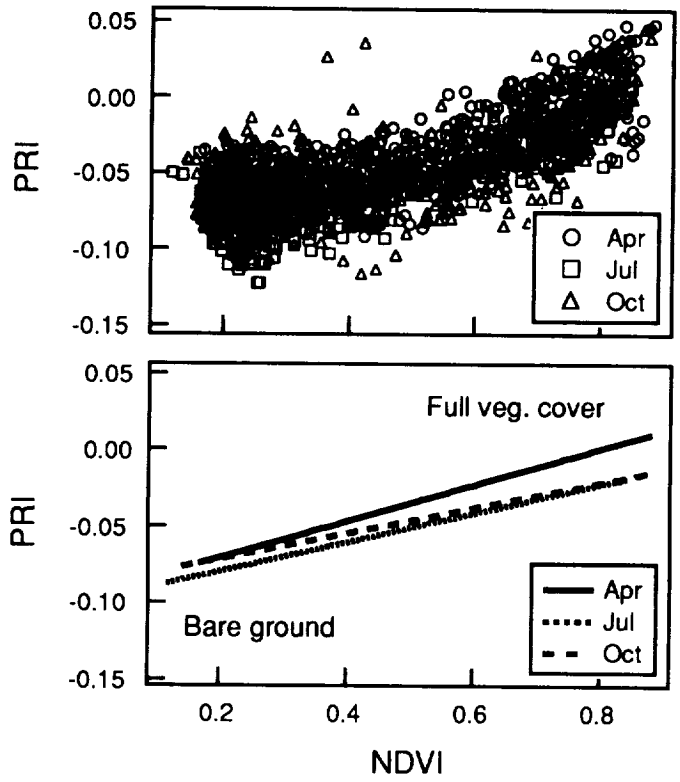

Figure 2. The Photochemical Reflectance Index (PRI) plotted against the Normalized Difference Vegetation Index (NDVI), both measured on the ground near Tapia Park, Santa Monica Mountains, California, in spring, summer, and fall, 1997. Each individual sampling point in panel A represents a surface area of approximately 0.1 m^2. Linear regressions (panel B) were highly significant ($p<0.0001$, Fisher's probability) and analysis of covariance indicated a significant change in slope between April and July, but not from July to October.

The plots of WBI vs. NDVI derived from AVIRIS are indicated in figure 3. As with the ground data, WBI was positively and strongly correlated with NDVI, and the relationship changed seasonally. For each vegetation type, both WBI and NDVI declined with the onset of summer drought, and this decline was most severe for the annual grassland and least severe for oak woodland. In contrast to these results, and in contrast to the pattern found on the ground (not shown), plots of PRI vs. NDVI derived from AVIRIS did *not* resemble the pattern found with the WBI. Unlike the results on the ground and in contrast to our expectations, the apparent PRI values derived from AVIRIS yielded a *negative* relationship with NDVI and *declined* from spring to fall (not shown).

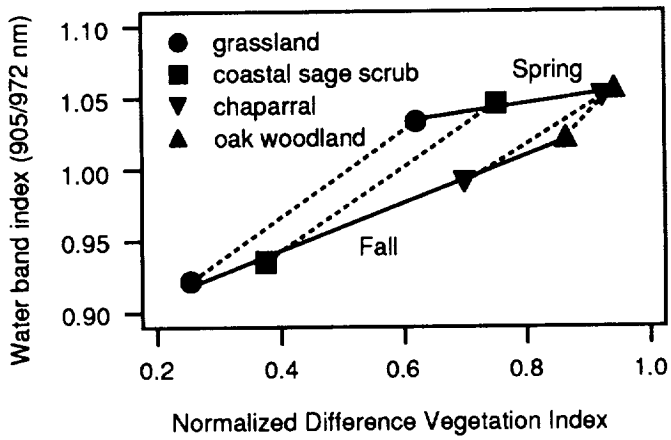

Figure 3. Values for the Water Band Index (WBI) vs. Normalized Difference Vegetation Index (NDVI) for different native vegetation types, derived from AVIRIS images of Point Dume (Santa Monica Mountains, CA). Each point represents the mean of 17 to 22 AVIRIS pixels (standard error bars are too small to see). Solid lines represent regression lines for samples selected from a single date in Spring, 1995 (top regression), or Fall, 1994 (bottom regression). Dashed lines represent hypothetical seasonal trajectories for each vegetation type in NDVI-WBI space.

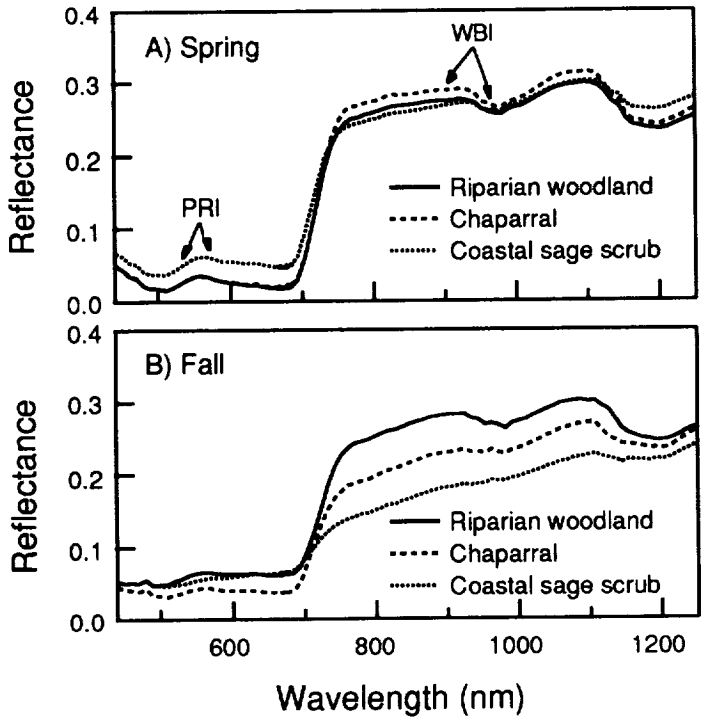

Figure 4. Apparent reflectance spectra for representative vegetation types derived from AVIRIS overflights of the Santa Monica Mountains, CA, in Spring, 1995 (panel A) and Fall, 1994 (panel B). Wavebands used for calculation of the Photochemical Reflectance Index (PRI) and the Water Band Index (WBI) are indicated on the top panel. Note aberrant patterns in apparent reflectance, particularly visible below 500 nm, which apparently confound accurate estimation of PRI for these scenes. Also, note the "flattening" of the 970 nm liquid water absorption feature from spring to fall, particularly for the drought-deciduous coastal sage scrub.

AVIRIS spectra for selected vegetation types are indicated in figure 4, along with the wavelengths used for calculation of the WBI and PRI. Note the "flattening" of the spectrum and concurrent loss of the 970 nm water absorption feature at the end of the summer drought, particularly for the drought-deciduous coastal sage scrub (compare 4A to 4B). Note also that the 400-550 nm region adjacent to PRI yields visibly distorted apparent reflectance spectra, visible as a steep slope in apparent reflectance (4A) or as small spikes in apparent reflectance (4B).

4. DISCUSSION

The finding of a positive relationship between the WBI and NDVI is consistent with several recent reports of a strong correlation between liquid water absorption and green canopy cover or leaf area as measured by NDVI (Peñuelas et al. 1997b, Roberts et al 1997), or green vegetation fraction (Roberts et al. 1997, Ustin et al. in press). This suggests that the WBI is largely functioning as a measure of green canopy cover or leaf area index. However, the significant changes in the WBI for a given value of NDVI (figures 1 and 3) illustrate a component of the 970 nm water absorption feature that appears to be independent of canopy structure and more directly related to leaf water concentration. This conclusion is consistent with a number of recent reports that suggest changing leaf or canopy water content can be detected with this feature (Peñuelas et al. 1993, 1997b; Zhang et al. 1997, Sanderson et al. in press). Seasonal patterns of leaf water potential gathered from single leaves on the ground (table 1) further support the hypothesis that the seasonal change in the WBI for a given NDVI indicates changing leaf water content. However, these leaf water potentials cannot provide a direct confirmation of this hypothesis for three reasons: 1) water potentials were not sampled on identical dates, canopies, or spatial scales as either ground or airborne reflectance sampling, 2) the units of water potential (pressure units, see Koide et al. 1989) are not linearly related to the units of liquid water content sampled with reflectance (more typically unitless, or expressed in microns of liquid water, see Roberts et al. 1997), and 3) the water potential samples were made before dawn, whereas AVIRIS flies near solar noon. Nevertheless, these preliminary results present qualitative support for the hypothesis that a component of the WBI and other similar measures of liquid water absorption (Roberts et al. 1997, Ustin et al. in press) is directly related to seasonally changing leaf water status. In mediterranean climate vegetation, where summer drought is a main factor limiting photosynthetic performance (Mooney et al, 1975, Tenhunen et al. 1984, 1985 and 1990, Gamon et al, 1995a), this component of the WBI may have direct physiological relevance, and may provide a means to remotely assess changing photosynthetic function. Further work is required before we can derive quantitative expressions of leaf water status or physiological function from this index, and better quantitative expressions of vegetation water content may emerge.

Even in the absence of quantitative solutions, the water absorption bands visible in AVIRIS spectra could be quite useful. The tendency for different vegetation types to occupy distinct trajectories in NDVI-WBI space (figure 3) suggests that it might be possible to develop functional classifications of vegetated landscapes entirely from imaging spectrometry using this approach. Similar vegetation classifications have been obtained with NDVI and surface temperature derived from AVHRR data (Nemani and Running, 1997). To our knowledge, classification of vegetation based on the water absorption features is relatively unexplored.

The similarity of the PRI-NDVI to the WBI-PRI patterns sampled from the ground (compare figures 1 and 2) provides further evidence that seasonal water limitations reduce photosynthetic fluxes in this drought-prone landscape. The finding of a decline in PRI for a given NDVI with the onset of summer drought (figure 2) is consistent with an abundance of reports indicating that ground-based PRI sampling can provide a useful indicator of photosynthetic function (e.g., Gamon et al. 1992 and 1997, Peñuelas et al. 1995 and 1997a, Filella et al. 1996). Furthermore, these transect samples traversing several AVIRIS pixels suggest that a meaningful PRI could be measured from AVIRIS if a good surface reflectance retrieval could be obtained. However, the same pattern of a seasonal decline in PRI for a given NDVI was not apparent in the AVIRIS imagery (not shown). Preliminary analyses suggest that radiometric or spectral calibration errors or insufficient atmospheric correction can lead to significant errors in PRI. In particular, atmospheric scattering was a likely source of error for these particular AVIRIS scenes due to a strong influence of marine aerosols. Complete atmospheric correction in this visible region of the spectrum remains a significant challenge, and is rarely attained without suitable ground calibration targets during the overflight

(Clark et al. 1993, Goetz et al., 1998). Simultaneous ground sampling during AVIRIS overflights could help solve this problem, but such simultaneous measurement is not always possible. Until this challenge can be resolved, PRI appears to be best sampled from close range where atmospheric interference is not a significant problem.

Because photosynthetic function and leaf water content are both very dynamic in time and space, and because physiological sampling and aircraft imaging spectrometry operate over vastly different spatial scales, it is extremely challenging to directly confirm any physiological interpretation AVIRIS reflectance spectra. Simultaneous sampling of reflectance at the stand scale from the ground would greatly help in confirming any quantitative interpretation of physiological signals derived from AVIRIS spectra. This would require closer coordination between AVIRIS flight crew and field sampling team, and a much larger investment of time and resources in field sampling than is usually the case. Extremely accurate spectral and radiometric calibration, and accurate retrieval of surface reflectance will also be essential for full evaluation of physiological signals in AVIRIS imagery. We are currently evaluating these issues with additional AVIRIS data from the Santa Monica Mountains.

5. ACKNOWLEDGMENTS

We wish to thank Meg Gardner (UC Santa Barbara) for assistance with atmospherically corrected AVIRIS scenes, Robert Green and Betina Pavri (Jet Propulsion Laboratory) for discussion of atmospheric correction methods, and Brandon Pratt and Kim Portwood for assistance with leaf water potential values. Access to the field site was provided by the Malibu Forestry Unit of the Los Angeles County Fire Department, and funding for the ground reflectance sampling was provided by the National Science Foundation. This is publication #3 of the Center for Spatial Analysis and Remote Sensing, California State University, Los Angeles, which is supported by funds from NASA.

6. REFERENCES

Asrar, G, M. Fuchs, E.T. Kanemasu, and J.L. Hatfield, 1984, "Estimating Absorbed Photosynthetic Radiation and Leaf Area Index from Spectral Reflectance in Wheat," *Agronomy Journal*. 76:300-306.

Bartlett, D.S., G.J. Whiting, and J.M. Hartman, 1990, "Use of Vegetation Indices to Estimate Intercepted Solar Radiation and Net Carbon Dioxide Exchange of a Grass Canopy," *Remote Sensing of Environment*. 30:115-128.

Clark, R.N., and T.L. Roush, 1984, "Reflectance Spectroscopy: Quantitative Analysis Techniques for Remote Sensing Applications," *Journal of Geophysical Research* 89(B7):6329-6340.

Clark, R.N., G. Swayze, K. Heidebrecht, A.F.H. Goetz, and R.O. Green, 1993, "Comparison of Methods for Calibrating AVIRIS Data to Ground Reflectance," *Summaries of the Fourth Annual JPL Airborne Geoscience Workshop*, October 25-29, 1993. JPL Publication 93-26 vol. 1. Jet Propulsion Laboratory, Pasadena, CA, pp. 35-36.

Demmig-Adams, B., and W.W. Adams III, 1996, "The Role of Xanthophyll Cycle Carotenoids in the Protection of Photosynthesis," *Trends in Plant Science* , vol. 1, pp. 21-26.

Filella, I., T. Amaro, J.L. Araus, and J. Peñuelas, 1996, "Relationship between photosynthetic radiation-use efficiency of barley canopies and the photochemical reflectance index (PRI)," *Physiol. Plant*, vol. 96, pp 211-216.

Gamon, J.A., C.B. Field, M.L. Goulden, K.L. Griffin, A.E. Hartley, G. Joel, J. Peñuelas, and R. Valentini, 1995a, "Relationships between NDVI, Canopy Structure, and Photosynthesis in Three Californian Vegetation Types," *Ecological Applications* 5(1), pp. 28-41.

Gamon, J.A., J. Peñuelas, and C.B. Field, 1992, "A narrow-waveband spectral index that tracks diurnal changes in photosynthetic efficiency," *Remote Sensing of Environment*, vol. 41, pp 35-44.

Gamon, J.A., L. Serrano, and J.S. Surfus, 1997, "The Photochemical Reflectance Index: an Optical Indicator of Photosynthetic Radiation Use Efficiency across Species, Functional Types, and Nutrient Levels." *Oecologia*, vol. 112 (2), pp. 492-501.

Gamon, J.A., R.O. Green, D.A. Roberts, and L. Serrano, 1995b, "Deriving Photosynthetic Function from Calibrated Imaging Spectrometry," pp. 55-60 in: Guyot, G. (ed.) *Proceedings of the International Colloquium. Photosynthesis and Remote Sensing*. 28-30 August, 1995. Montpellier, France.

Goetz, A.F.H., K.B. Heidebrecht, B. Kindel, and J.W. Boardman, 1998, "Using Ground Spectral Irradiance for Model Correction of AVIRIS Data," *Summaries of the Seventh JPL Earth Science Workshop*, January 12-16, 1998 (this volume).

Green, R.O., J.E. Conel, D.A. Roberts, 1993, "Estimation of Aerosol Optical Depth and Additional Atmospheric Parameters for the Calculation of Apparent Reflectance from Radiance Measured by the Airborne Visible/Infrared Imaging Spectrometer," In: *Summaries of the Fourth Annual JPL Airborne Geoscience Workshop*, Oct. 25-29, 1993, JPL Publication 93-26 Jet Propulsion Laboratory, Pasadena, CA, vol. 1, pp. 73-76.

Hall, F.G., J.R. Townshend, and E.T. Engman, 1995, "Status of Remote Sensing Algorithms for Estimation of Land Surface State Parameters," *Remote Sensing of Environment*, vol. 51, pp. 138-156.

Hatfield, J.L., G. Asrar, and E.T. Kanemasu, 1984, "Intercepted Photosynthetically Active Radiation Estimated by Spectral Reflectance," *Remote Sensing of Environment*. 14:65-75.

Koide, R.T., R.H. Robichaux, S.R. Morse, and C.M. Smith, 1989, "Plant Water Status, Hydraulic Resistance, and Capacitance," pp. 161-183, in: Pearcy R.W., J. Ehleringer, H.A. Mooney, and P.W. Rundel (eds), *Plant Physiological Ecology: Field Methods and Instrumentation*, Chapman and Hall, London.

Kumar. M, and J.L. Monteith, 1981, "Remote Sensing of Crop Growth," In: Smith, H (Ed) *Plants and the Daylight Spectrum*. Academic Press. London, England, pp. 133-144.

Mooney, H.A., A.T. Harrison, and P.A. Morrow, 1975, "Environmental limitations of photosynthesis on a California evergreen shrub," *Oecologia* vol. 19, pp 293-301.

Nemani. R., and S. Running (1997) "Land cover characterization using multitemporal red, near-IR, and thermal-IR data from NOAA/AVHRR," *Ecological Applications*, vol 7, pp. 79-90.

Peñuelas, J., I. Filella, and J.A. Gamon, 1995, "Assessment of Photosynthetic Radiation-Use Efficiency with Spectral Reflectance," *New Phytol*. vol. 131, pp. 291-296.

Peñuelas, J., I. Filella, C. Biel , L. Serrano, R. Savé, 1993, "The Reflectance at the 950-970 nm Region as an Indicator of Plant Water Status," *Int. J. Remote Sensing*, vol. 14, no. 10, pp. 1887-1905.

Peñuelas, J., J. Llusia, J. Piñol, and I. Filella, 1997a, "Photochemical Reflectance Index and Leaf Photosynthetic Radiation-Use-Efficiency Assessment in Mediterranean Trees," *Int. J. Remote Sensing*, vol. 18, pp. 2863-2868.

Peñuelas, J., J. Piñol, R. Ogaya, and I. Filella, 1997b, "Estimation of Plant Water Concentration by Reflectance Water Index WI (R900/R970)," *Int. J. Remote Sensing* , vol. 18, no. 13, pp. 2869-2875.

Prince, S.D., and S.N. Goward, 1995, "Global Primary Production: a Remote Sensing Approach," *Journal of Biogeography*, vol. 22, pp. 815-835.

Roberts, D.A., R.O. Green, and J.B. Adams, 1997, "Temporal and Spatial Patterns in Vegetation and Atmospheric Properties from AVIRIS," *Remote Sens. Environ.*, vol. 62, pp. 223-240.

Sanderson, E.W., M.H. Zhang, and S.L. Ustin, in press, "Geostatistical Scaling of Canopy Water Content in a California Salt Marsh: Bridging the Gap Between Ecology and Remote Sensing." *Landscape Ecology*.

Sellers, P.J., 1985, "Canopy Reflectance, Photosynthesis, and Transpiration," *International Journal of Remote Sensing*. 6:1335-1372.

Sellers, P.J., B.W. Meeson, F.G. Hall, G. Asrar, R.E. Murphy, R.A. Schiffer, F.P. Bretherton, R.E. Dickinson, R.G. Ellingson, C.B. Field, K.F. Huemmrich, C.O. Justice, J.M. Melack, N.T. Roulet, D.S. Schimel, and P.D. Try, 1995, "Remote Sensing of the Land Surface for Studies of Global Change: Models - Algorithms - Experiments," *Remote Sensing of Environment*, vol. 51, pp. 3-26.

Sellers, P.J., L. Bounoua, G.J. Collatz, D.A. Randall, D.A. Dazlich, S.O. Los, J.A. Berry, I. Fung, C.J. Tucker, C.B. Field, and T.G. Jensen, 1996, "Comparison of Radiative and Physiological Effects of Doubled Atmospheric CO_2 on Climate." *Science*, vol. 271, pp. 1402-1406.

Tenhunen, J.D., A. Sala Sera, P.C. Harley, R.L. Dougherty, and J.F. Reynolds, 1990, "Factors Influencing Carbon Fixation and Water Use by Mediterranean Sclerophyll Shrubs during Summer Drought." *Oecologia* 82:381-393.

Tenhunen, J.D., O.L. Lange, J. Geberl, W. Beyschlag, and J.A. Weber, 1984, "Changes in Photosynthetic Capacity, Carboxylation Efficiency, and CO_2 Compensation Point Associated with Midday Stomatal Closure and Midday Depression of Net CO_2 Exchange of Leaves of *Quercus suber*," *Planta* 162:193-203.

Tenhunen, J.D., O.L. Lange, P.C. Harley, W. Beyschlag, and A. Meyer, 1985, "Limitations Due to Water Stress on Leaf Net Photosynthesis of *Quercus coccifera* in the Portuguese Evergreen Scrub," *Oecologia* 67:23-30.

Ustin S.L., D.A. Roberts, J. Pinzón, S. Jacquemoud, M. Gardner, G. Scheer, C.M. Casteñada, A. Palacios-Orueta, in press, "Estimating Canopy Water Content of Chaparral Shrubs using Optical Methods," *Remote Sensing of Environment*.

Zhang, M, S.L. Ustin, E. Rejmankova, and E.W. Sanderson, 1997, "Remote Sensing of Salt Marshes: Potential for Monitoring." *Ecological Applications*. 7(3):1039-1053.

REMOVAL OF THIN CIRRUS PATH RADIANCES IN THE 0.4 - 1.0 μm SPECTRAL REGION USING THE 1.375-μm STRONG WATER VAPOR ABSORPTION CHANNEL

Bo-Cai Gao[1], Yoram J. Kaufman[2], Wei Han[3], and Warren J. Wiscombe[2]

[1]Remote Sensing Division, Code 7212, Naval Research Laboratory, Washington, DC 20375
[2]Climate and Radiation Branch, Code 913, NASA Goddard Space Flight Center, Greenbelt, MD 20771
[3]SFA, Inc., Largo, MD 20774

1. INTRODUCTION

Through analysis of spectral imaging data acquired with the Airborne Visible Infrared Imaging Spectrometer (AVIRIS) (Vane et al., 1993) from an ER-2 aircraft at 20 km altitude during several field programs, it was found that narrow channels near the center of the strong 1.38-μm water vapor band are very sensitive in detecting thin cirrus clouds. Based on this observation from AVIRIS data, a channel centered at 1.375 μm with a width of 30 nm was selected for the Moderate Resolution Imaging Spectrometer (MODIS) for remote sensing of cirrus clouds from space. The sensitivity of the 1.375-μm MODIS channel to detect thin cirrus clouds during the day time is expected to be one to two orders of magnitude better than the current infrared emission techniques. As a result, a larger fraction of the satellite data will likely be identified as containing cirrus clouds. In order to make better studies of surface reflectance properties, thin cirrus effects must be removed from satellite images. We have developed an empirical approach for removing/correcting thin cirrus effects in the 0.4 - 1.0 μm region using channels near 1.375 μm. This algorithm will be incorporated into the present MODIS atmospheric correction algorithms for ocean color and land applications and will yield improved MODIS atmospheric aerosol, land surface, and ocean color products.

2. BACKGROUND

Because of their partial transparency, thin cirrus clouds are difficult to detect in satellite images, particularly over land, both in the visible and in the 10–12 μm IR atmospheric window regions (Rossow et al., 1985). In order to illustrate the semi-transparent nature of thin cirrus clouds, we show in Figure 1 examples of images acquired with the Airborne Visible Infrared Imaging Spectrometer (AVIRIS) from an ER-2 aircraft at 20 km altitude during the NASA-sponsored First International Satellite Cloud Climatology Project Experiment Phase II Cirrus program (hereinafter FIRE II; cf. Starr et al., 1990) over Coffeyville in southeastern Kansas in December of 1991. From the 0.65-μm image in Fig. 1a, the streets of Coffeyville (in the upper right portion of the image), roads, and various surface fields, are clearly seen. Cirrus clouds are not obviously seen in this image. The 1.38-μm image in Fig. 1b shows only the upper level thin cirrus clouds; the surface features are not seen because atmospheric water vapor below the cirrus clouds completely absorbs the 1.38 μm sunlight. As a result, the 1.38-μm AVIRIS channel detected only the solar radiation scattered by the cirrus clouds. Without the 1.38-μm image, one would not know that the 0.65-μm image was contaminated by thin cirrus clouds. This same problem has affected all satellites used for land and ocean remote sensing; quantification of cirrus effects was not possible because of the lack of appropriate channels to detect thin cirrus clouds.

Based on the observation from AVIRIS data that narrow channels near the center of the strong 1.38-μm water vapor band are very effective in detecting thin cirrus clouds (Gao et al., 1993), Gao and Kaufman (1995) proposed to put a channel centered at 1.375 μm with a width of 30 nm on MODIS for detecting thin cirrus clouds from space. With strong support from the MODIS Science Team members and NASA Goddard Space Flight

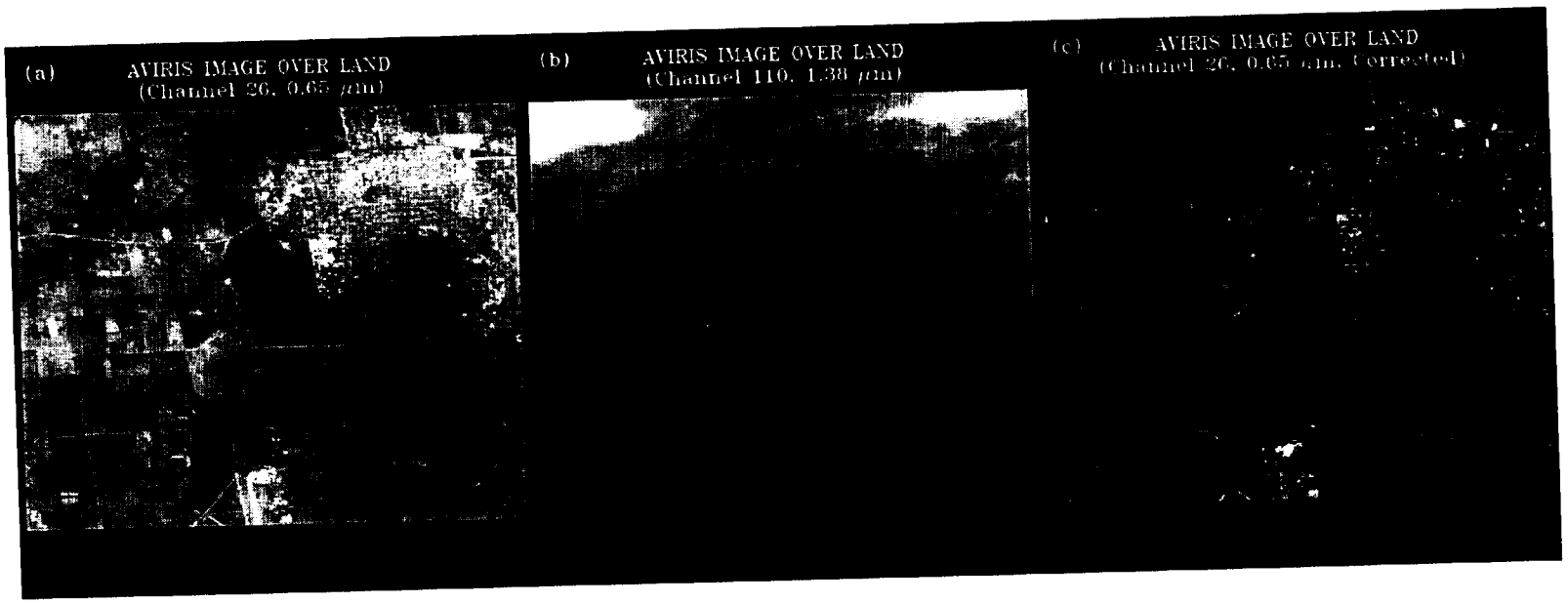

Fig. 1. AVIRIS 0.65 μm image (a), 1.38 μm image (b), and cirrus path radiance corrected 0.65 μm image (c) over Coffeyville in southeastern Kansas. The AVIRIS data were acquired on December 5, 1991.

Center management, the proposed channel was implemented on the MODIS instruments (Salomonson et al., 1989; King et al., 1992; Asrar and Greenstone, 1995) to be flown on the Earth Observing System (EOS) (Butler et al., 1987) AM and PM Platforms. The sensitivity of the 1.375-μm MODIS channel to detect thin cirrus clouds during the day time is expected to be one to two orders of magnitude better than the current infrared emission techniques (Gao and Kaufman, 1995). In this paper, we refer to ice clouds with reflectances in the visible spectral region of 0.1 or less as thin cirrus clouds.

In order to make better studies of reflectance properties of land and ocean surfaces, thin cirrus effects must be removed from satellite images. Therefore, there is a need to study radiative properties of thin cirrus clouds, so that a strategy for correction or removal of the thin cirrus effects, similar to the correction of atmospheric aerosol effect (e.g., Kaufman and Sendra, 1988), can be formed. In this paper, we describe an empirical approach for removing/correcting thin cirrus path radiances in AVIRIS images using channels near 1.375 μm.

3. CIRRUS PROPERTIES

Cirrus clouds consist of ice particles having different sizes and shapes. The "effective" particle sizes (radii of equivalent spheres) are usually greater than 5 μm. We illustrate the scattering and absorption properties of cirrus clouds through examples. Figure 2 shows two AVIRIS spectra (in reflectance units) acquired over areas covered by thick and thin cirrus clouds above Monterey Bay in California on September 4, 1992. The MODIS channels are also indicated. For each spectrum, the reflectances of ice particles in the 0.45 - 1.0 μm spectral region are nearly constant with wavelength, because ice particles are much larger than wavelengths and ice is non-absorbing. The larger apparent reflectances in the 0.45 - 0.6 μm region are due to Rayleigh scattering. Past 1.0 μm one finds several ice absorption bands, for example those centered near 1.5 and 2.0 μm. Weak ice absorptions occur near 1.24 μm and 1.375 μm; the imaginary parts of the ice refractive index are about the same at both wavelengths. The measured reflectances at 1.375 μm are smaller than reflectances in the 0.4–1.0 μm region mainly because of absorption by water vapor above and within the cirrus clouds. These upper-level water vapor absorption effects need to be accounted for before we can use the 1.375-μm channel for quantitative removal of cirrus effects in other channels.

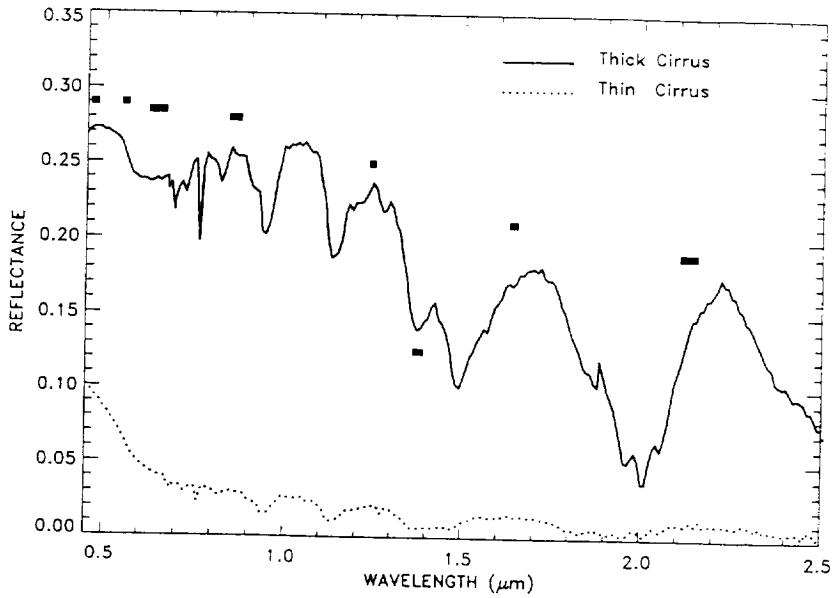

Fig. 2. Examples of AVIRIS spectra over thick and thin cirrus clouds.

At present, our knowledge of cirrus ice particle size, shape, and orientation distributions, spatial variability, and scattering phase functions is not sufficient for reliable, routine modeling of cirrus reflectivity (King, 1993; Shiobara and Asano, 1994). Cirrus spatial inhomogeneity and adjacency effects are difficult to treat properly

in radiative transfer models. In view of these difficulties, we have decided to use empirical relationships to characterize the main cirrus properties, and from these to develop an empirical cirrus removal technique.

4. THE EMPIRICAL APPROACH

For thin cirrus clouds, we assume that a homogeneous thin cirrus layer is located above a "virtual surface", which includes the effects of Rayleigh scattering and land or ocean surface reflection and scattering. Omitting for convenience the wavelength (λ) and cosine-solar-zenith-angle (μ_0) dependencies, we denote the "apparent reflectance" at the satellite as

$$\rho^* = (\pi L / \mu_0 E_0)$$

where L is the radiance measured by the satellite and E_0 is the extra-terrestrial solar flux. Then, accounting for transmission through the cirrus cloud and multiple reflections between cloud and the "virtual surface", we have the following relationship (similar to what is done for aerosol correction, e.g., Fraser and Kaufman, 1985):

$$\rho^* = \rho_0 + T_c\rho / (1 - S_c\rho) \quad (1)$$

where ρ_c is the reflectance of the cirrus cloud, T_c is the two-way transmission (direct + diffuse) through the cloud, ρ is the reflectance of the "virtual surface", and S_c is the cloud-base reflectance of upward radiation. Because $S_c\rho << 1$ for thin cirrus, Eq. (1) can be simplified to:

$$\rho^* = \rho_c + T_c\rho \quad (2)$$

In order to remove the cirrus effect from the satellite measurement ρ^*, namely to derive ρ based on (2), cirrus reflectance ρ_c and transmittance T_c must be known.

Analyzing AVIRIS data, we have found that cirrus reflectance ρ_c for AVIRIS channels between 0.4 and 1.0 μm is linearly related to ρ_c at 1.375 μm, i.e.,

$$\rho_c(\lambda) = \rho_c(1.375\ \mu m) / K_a, \quad 0.4 < \lambda < 1.0\ \mu m \quad (3)$$

where K_a is an empirical parameter derived from AVIRIS data themselves. It is essentially the 1.375-μm channel transmittance for water vapor above and within cirrus clouds. The weak ice absorption at 1.375 μm (see Fig. 2) also decreases slightly the K_a value. Substituting (3) into (2), we obtain:

$$T_c\rho = \rho^* - \rho_c(1.375\ \mu m) / K_a, \quad 0.4 < \lambda < 1.0\ \mu m \quad (4)$$

The image of $T_c\rho$ is referred to as the "cirrus-path-radiance-corrected" image in this paper. It is similar to the "virture surface" reflectance image of ρ because of the large transmittances of thin cirrus (T_c is usually greater than 0.9).

5. RESULTS

The technique described by Eq. (4) for removing cirrus path radiances, i.e, to derive images of $T_c\rho$, has been applied to several AVIRIS data sets acquired over different geographical regions during various NASA sponsored field programs. Results from AVIRIS data measured over the Gulf of Mexico, and over Coffeyville in southeastern Kansas are described below.

5.1 The Gulf of Mexico

AVIRIS data were acquired over the Gulf of Mexico on December 5, 1991 during the FIRE Phase II Cirrus Field Program. Figure 3a shows the 0.86-μm AVIRIS image, which reveals both the upper level extended cirrus clouds and the lower level cumulus clouds. Figure 3b shows the 1.38-μm image. Only the upper level cirrus clouds are seen in this image. Figure 4 shows the scatter plot of ρ^* (1.38 μm) versus ρ^* (1.24 μm) for all pixels in

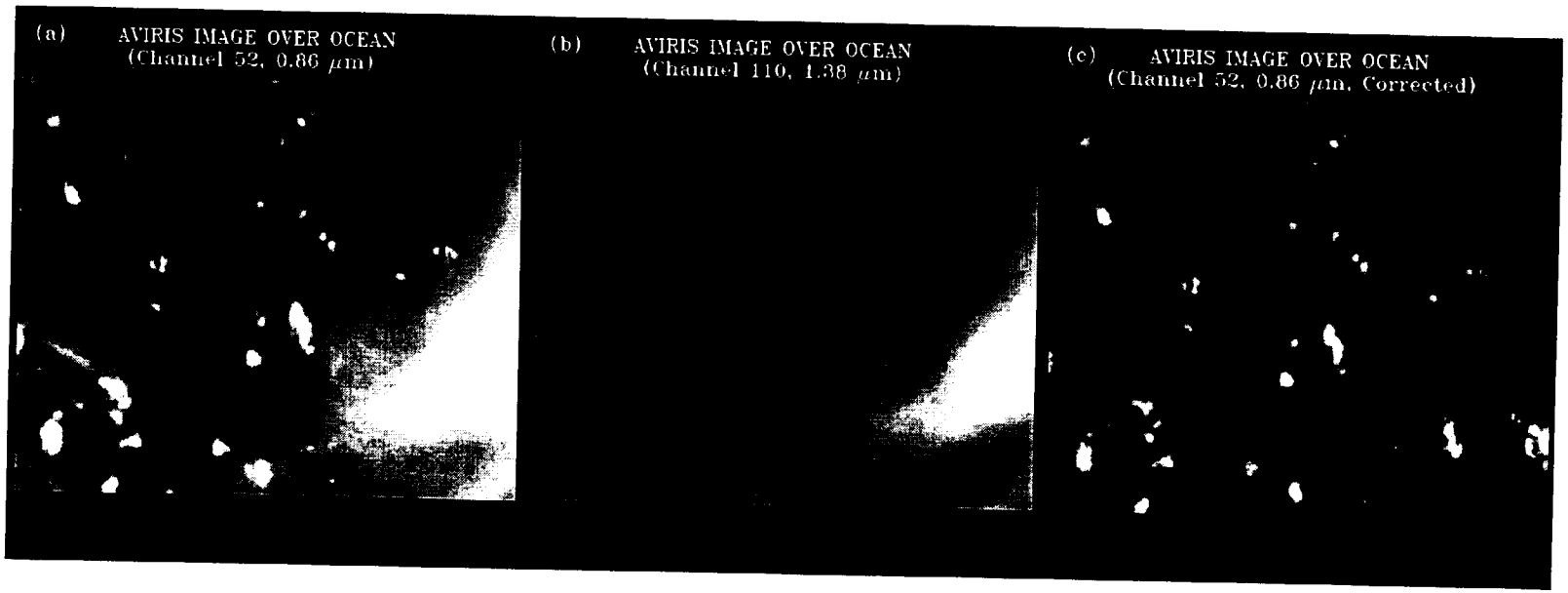

Fig. 3. AVIRIS 0.86 μm image (a), 1.38 μm image (b), and cirrus path radiance corrected 0.86 μm image (c) over the Gulf of Mexico. The AVIRIS data were acquired on December 5, 1991.

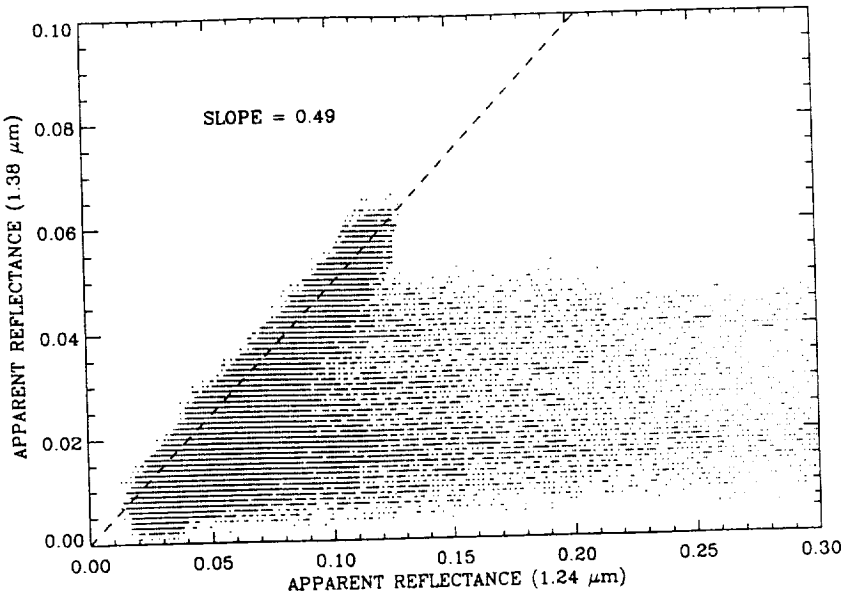

Fig. 4. A scatter plot of apparent reflectances at 1.38 μm versus those at 1.24 μm for the Gulf of Mexico scene.

the scene. We have found that the pixels covered by the upper level thin cirrus clouds are clustered around a straight line with a slope of 0.49 (see the dashed line). This slope is a good estimation of K_a (see Eq. (3)). Because cumulus clouds have higher reflectances at 1.24 μm and are invisible at 1.38 μm, the pixels containing both upper level cirrus and lower level cumulus are spread out to the right of the dashed line. Using the estimated K_a and based on Eq. (4), we have obtained a "cirrus-path-radiance-corrected" image, $T_c\rho$, which is shown in Figure 3c. Cirrus clouds are mostly removed while the cumulus clouds are still present in this image.

In order to have more quantitative descriptions of our cirrus removals, we show in Figure 5 several histograms for pixel reflectances. Fig. 5a shows this for the 0.86-μm image in Fig. 3a. The long tail to the right is typical of most cloudy images. Fig. 5b shows the histogram of the 1.38-μm image; the peak occurs at an "apparent" reflectance value of about 0.012. The maximum "apparent" reflectance value is approximately 0.06. These indicate that the cirrus clouds in the scene (see Fig. 3b) are very thin. The histogram also shows that there are almost no pixels with zero reflectances. Therefore, the entire scene is filled by thin cirrus. Fig. 5c shows the histogram of the "cirrus-path-radiance-corrected" 0.86-μm image, which peaks at a reflectance value of approximately 0.023. This value is what one would normally expect for the specular and waving water surfaces under clear conditions. At 0.86 μm, there is no upwelling radiance from beneath the air-water interface because of the strong sea water absorption of solar radiation. The histogram in Fig. 5c is similar to a gaussian curve, except for a long tail to the right due to small amounts of cumulus clouds in the scene (see Fig. 3c). When random noises are present in the measurements, the histogram for clear ocean pixels should follow a gaussian distribution. Therefore, the histogram in Fig. 5c indicates that our cirrus removal algorithm works reasonably well in this case.

5.2 Coffeyville, Kansas

AVIRIS data was acquired over Coffeyville in southeastern Kansas on December 5, 1991 during the FIRE Phase II Cirrus Program. The images of the 0.65 and 1.38 μm channels were shown in Figures 1a and 1b, respectively. The two bright areas in the upper left and upper right portions of Fig. 1b have apparent reflectance values between 0.05 and 0.06, indicating thin cirrus. The corresponding areas in Fig. 1a appear more blurred than the other areas covered by thinner clouds.

In order to use the 1.38-μm image for quantitative corrections of thin cirrus effects in the 0.65-μm image, we have to estimate the upper level water vapor transmittance, K_a (see Eq. 3). Because the land surface reflectances at 1.24 μm are quite variable spatially, the scatter plot method ρ(1.38 μm) versus ρ(1.24 μm)] for the estimation of

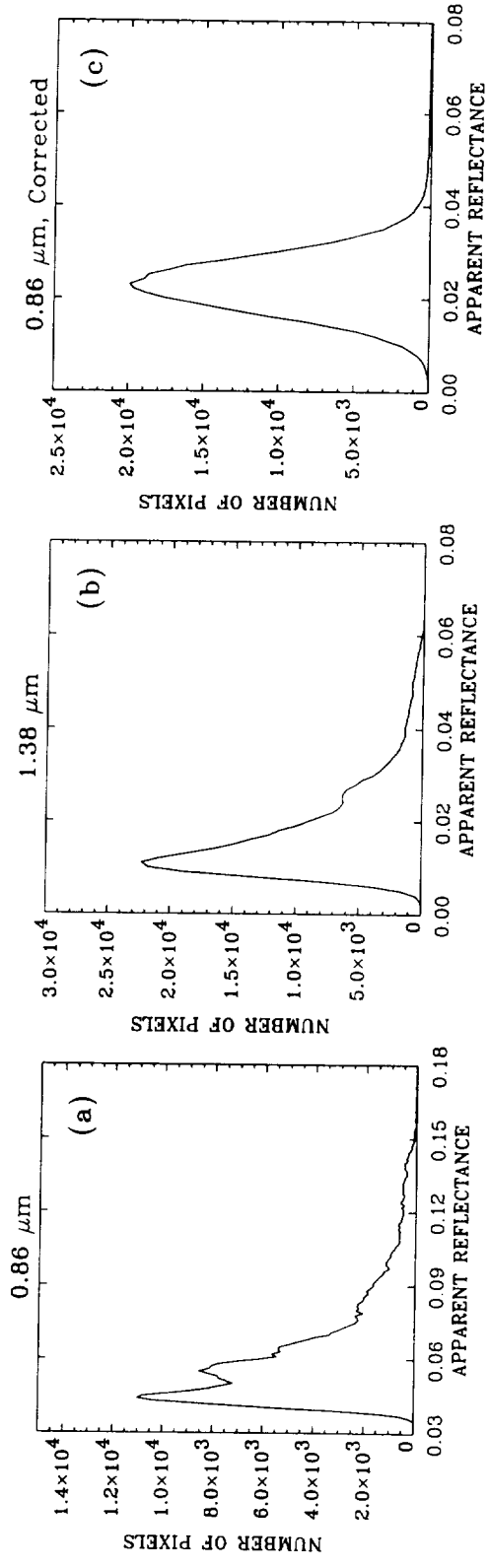

Fig. 5. Histograms corresponding to the 0.86 μm image (a), 1.38 μm image (b), and cirrus path radiance corrected 0.86 μm image (c) in Fig. 3.

K_a over water surfaces is not directly applicable to the land. Since green vegetation in the 0.64 - 0.67 μm spectral region has low and spatially uniform reflectances (~ 0.03), we used the scatter plot of ρ(1.38 μm) versus ρ(0.65 μm) for pixels covered by green vegetation (mainly winter wheat) in the estimation of K_a. The vegetated pixels are dark in Fig. 1a. The green vegetation pixels we used in the scatter plot have values of NDVI (the normalized difference vegetation index defined as $(\rho^*_{0.86\,\mu m} - \rho^*_{0.65\,\mu m}) / (\rho^*_{0.86\,\mu m} + \rho^*_{0.65\,\mu m})$ of 0.43 or greater. The estimated K_a is 0.7. Fig. 1c shows the path-radiance-corrected 0.65-μm image using this value of K_a. Surface features, particularly those in the upper left and upper right portions, are less blurred than those in Fig. 1a.

6. DISCUSSIONS

There are two kinds of errors introduced in our correction of cirrus path radiance effects in the 0.4 - 1.0 μm region. One kind of error is due to uncertainty in the estimated coefficient Ka from imaging data themselves. The other kind of error is the lack of correction for the cirrus transmittance factor, T_c. We expect that the combined errors introduced are smaller for thin cirrus over the dark ocean areas than for thick cirrus over brighter land areas.

Accurate corrections for the cirrus transmittances T_c in the 0.4 - 1.0 μm region are, in practice, more difficult than the corrections of path radiances. Because cirrus clouds are high in the atmosphere (typically 6 - 16 km above the sea level), the solar radiation on the two-way path (Sun-cirrus-surface-cirrus-sensor) encounters cirrus clouds at different spatial locations. If cirrus clouds are thick and their spatial distributions are not uniform, it is difficult to derive T_c from imaging data themselves due to the non-local nature of T_c. However, if cirrus clouds are thin and uniform, T_c can be considered to be equal to $[1 - \rho_c(1.375\,\mu m) / K_a]^n$, where n is a parameter with typical values in the range between 1 and 2. n depends on both the solar and view geometries. For the situation of thin cirrus clouds over the dark ocean, n should be close to 1. So far, we haven't found a reliable method to obtain n and therefore T_c from imaging data themselves for images acquired over land.

7. SUMMARY

We have developed an empirical technique that is successful in removing the cirrus path radiances in AVIRIS images between 0.4 and 1.0 μm. The same technique is being incorporated into the present MODIS atmospheric correction algorithms for ocean color and land applications and will yield improved MODIS atmospheric aerosol, land surface, and ocean color products.

8. ACKNOWLEDGMENTS

The authors are grateful to R. O. Green of Jet Propulsion Laboratory for providing AVIRIS data used in this study, and to A. F. H. Goetz at Department of Geological Sciences, University of Colorado at Boulder for useful discussions on radiative properties of thin cirrus clouds. This research is partially supported by a contract from NASA Goddard Space Flight Center in Greenbelt, Maryland to Naval Research Laboratory in Washington, DC.

9. REFERENCES

Asrar, G., R. Greenstone, (Editors), 1995: Mission to planet earth/earth observing system reference handbook, National Aeronautics and Space Administration, Goddard Space Flight Center, Mail Code 900, Greenbelt, MD 20771, USA, 277p.

Butler, D. M., et al., 1987, From pattern to process: The strategy of the earth observing system, in NASA Earth Observing System, Vol II, pp. 1-29, NASA, Washington D.C.

Fraser, R.S. and Y.J. Kaufman, 1985: 'The relative importance of aerosol scattering and absorption in remote sensing', *IEEE Trans. Geosc. Rem. Sens.*, GE-23, 525-633.

Gao, B.-C., A. F. H. Goetz, and W. J. Wiscombe, 1993, Cirrus cloud detection from airborne imaging spectrometer data using the 1.38 μm water vapor band, *Geophys. Res. Lett.*, 20, 301-304.

Gao, B.-C., and Y. J. Kaufman, 1995, Selection of the 1.375-μm MODIS channel for remote sensing of cirrus clouds and stratospheric aerosols from space,*J. Atm. Sci., 52*, 4231-4237.

Kaufman, Y.J. and C. Sendra, 1988: Satellite mapping of aerosol loading over vegetated areas. Ed. P. V. Hobbs and M. P. McCormick, *Aerosols and Climate,* A. Deepak Publ., Hampton, VA., 51-67.

King, M. D., Y. J. Kaufman, W. P. Menzel, and D. Tanre, 1992, Remote sensing of cloud, aerosol and water vapor properties from the Moderate Resolution Imaging Spectrometer (MODIS), IEEE Trans. Geosci. Remote Sens., 30, 2-27.

King, M. D., 1993, Radiative Properties of Clouds, in *Aerosol-Cloud-Climate Interactions*, (P. Hobbs editor), Academic Press, 123-149.

Rossow, W. B., F. Mosher, E. Kinsella, A. Arking, M. Desbois, E. Harrison, P. Minnis, E. Ruprecht, G. Seze, C. Simmer, and E. Smith, 1985, ISCCP cloud algorithm intercomparison, *J. Clim. Appl. Meteorol., 24*, 877-903.

Salomonson, V. V., W. L. Barnes, P. W. Maymon, H. E. Montgomery, and H. Ostrow, 1989, MODIS: Advanced facility instrument for studies of the earth as a system, *IEEE Trans. Geosci. Remote Sens., 27*, 145-153.

Shiobara, M., T. Hayasaka, T. Nakajima, and M. Tanaka, 1991, Aerosol monitoring using a scanning spectral radiometer in Sendai, Japan, J. Meteorol. Soc. Japan, 69, 57-70.

Starr, D. O'C., et al., 1990, FIRE Phase II: Cirrus Implementation Plan, can be obtained from the FIRE Project Office at NASA Langley Research Center in Hampton, Virginia.

Vane, G., R.O. Green, T.G. Chrien, H.T. Enmark, E.G. Hansen, and W.M. Porter, 1993, The Airborne Visible Infrared Imaging Spectrometer, *Remote Sens. Env., 44(2/3)*, 127-143.

A NEW AND FAST METHOD FOR SMOOTHING SPECTRAL IMAGING DATA

Bo-Cai Gao*, Ming Liu**, and Curtiss O. Davis*

*Code 7212, Naval Research Laboratory, Washington, DC 20375
**SAIC, Chantilly,VA 22021

1. INTRODUCTION

The Airborne Visible Infrared Imaging Spectrometer (AVIRIS) acquires spectral imaging data covering the 0.4 - 2.5 μm wavelength range in 224 10-nm-wide channels from a NASA ER-2 aircraft at 20 km. More than half of the spectral region is affected by atmospheric gaseous absorption. Over the past decade, several techniques (Goetz *et al.*, 1997) have been used to remove atmospheric effects from AVIRIS data for the derivation of surface reflectance spectra. An operational atmosphere removal algorithm (ATREM) (Gao *et al.*, 1993), which is based on theoretical modeling of atmospheric absorption and scattering effects, has been developed and updated (Gao and Davis, 1997) for deriving surface reflectance spectra from AVIRIS data. Figure 1 shows an example of a reflectance spectrum derived with ATREM from AVIRIS data acquired over Cuprite, Nevada in June, 1995. Due to small errors in assumed wavelengths and errors in line parameters compiled on the HITRAN database, small spikes (particularly near the centers of the 0.94- and 1.14-μm water vapor bands) are present in this spectrum. Similar small spikes are systematically present in entire ATREM output cubes. These spikes have distracted geologists who are interested in studying surface mineral features. A method based on the "global" fitting of spectra with low order polynomials or other functions for removing these weak spikes has recently been developed by Boardman (this volume). In this paper, we describe another technique, which fits spectra "locally" based on cubic spline smoothing, for quick post processing of ATREM apparent reflectance spectra derived from AVIRIS data. Results from our analysis of AVIRIS data acquired over Cuprite mining district in Nevada in June of 1995 are given. Comparisons between our smoothed spectra and those derived with the empirical line method are presented.

2. METHODOLOGY

In order to describe our smoothing technique, we first describe the commonly used cubic spline "fitting" technique, then we decribe the cubic spline "smoothing" technique.

2.1 Cubic Spline Fitting

The cubic spline fitting technique is a powerful numerical method and has been widely used in engineering and scientific computing. For example, Numerical Recipes (Press *et al.*, 1989) provides standard subroutines, using cubic spline fitting method, for interpolating data between points. In order to describe mathematically the cubic spline fitting technique, we consider an interval $a \le x \le b$, and subdivide it by a mesh of points corresponding to the location of the data at $a = X_0 < X_1 < \ldots < X_{j-1} < X_j \ldots < X_J = b$. An associated set of the observed data is prescribed by $y_o, y_1, \ldots, y_j, \ldots, y_J$. We seek an interpolating function *h(x)*, which is defined in the interval $[a,b]$. Its first and second derivatives are continuous on $[a,b]$ and it coincides

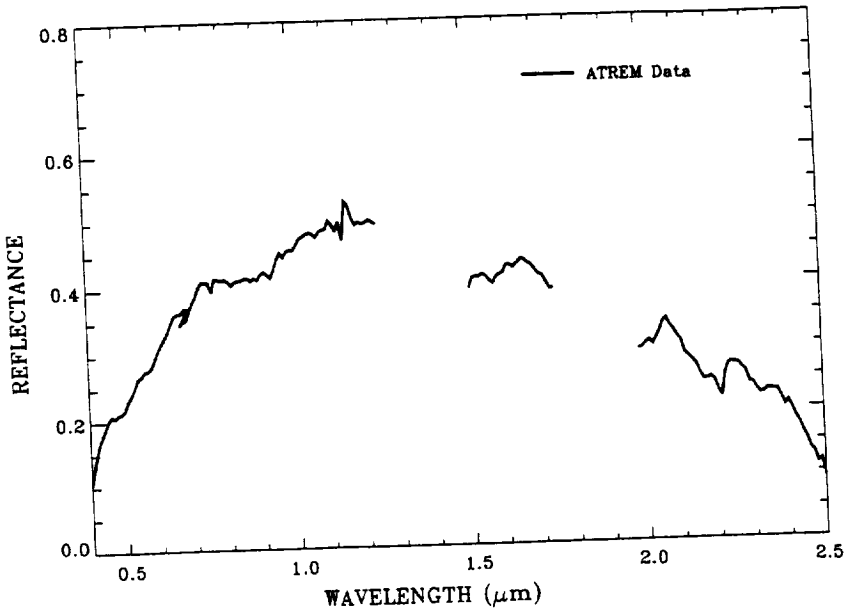

Fig. 1. An example of a reflectance spectrum derived with ATREM from AVIRIS data acquired over Cuprite, Nevada in June, 1995.

with a cubic polynomial in each subinterval $X_{j-1} \le x \le X_j$, and satisfies the relationship $h_j = h(X_j) = y_j$. Figure 2 illustrates the function *h(x)*. As adapted from Ahlberg (Ahlberg *et al.*, 1967), the function *h(x)* in the interval $X_{j-1} \le x \le X_j$ can be expressed as (for convenience, we assume the problem of equally spaced samples with a step size of Δ):

$$h(x) = \begin{cases} H_1(x) & X_0 \le x \le X_1 \\ \vdots & \vdots \\ H_j(x) & X_{j-1} \le x \le X_j \\ \vdots & \vdots \\ H_J(x) & X_{J-1} \le x \le X_J \end{cases}$$

where

$$H_j(x) = s_{j-1}\frac{(X_j - x)^3}{\Delta} + s_j\frac{(x - X_{j-1})^3}{\Delta} + \left[h_{j-1} - s_{j-1}\right]\frac{(X_j - x)}{\Delta} + \left[h_j - s_j\right]\frac{(x - X_{j-1})}{\Delta} \qquad (1)$$

$$X_j = X_0 + j\Delta$$

$$h_j = h(X_j); j = 0,1,2,..J$$

$\{s_j\}$, the spline coefficients, can be interpreted as the normalized second derivatives.

The polynomials (1) in adjacent segments are continuous at the knots:

$$H_j(X_j) = h_j = H_{j+1}(X_j).$$

The first derivative is continuous at the knot provided that

$$s_{j-1} + 4s_j + s_{j+1} = h_{j-1} - 2h_j + h_{j+1}. \qquad (2)$$

The second derivative is continuous at the knots

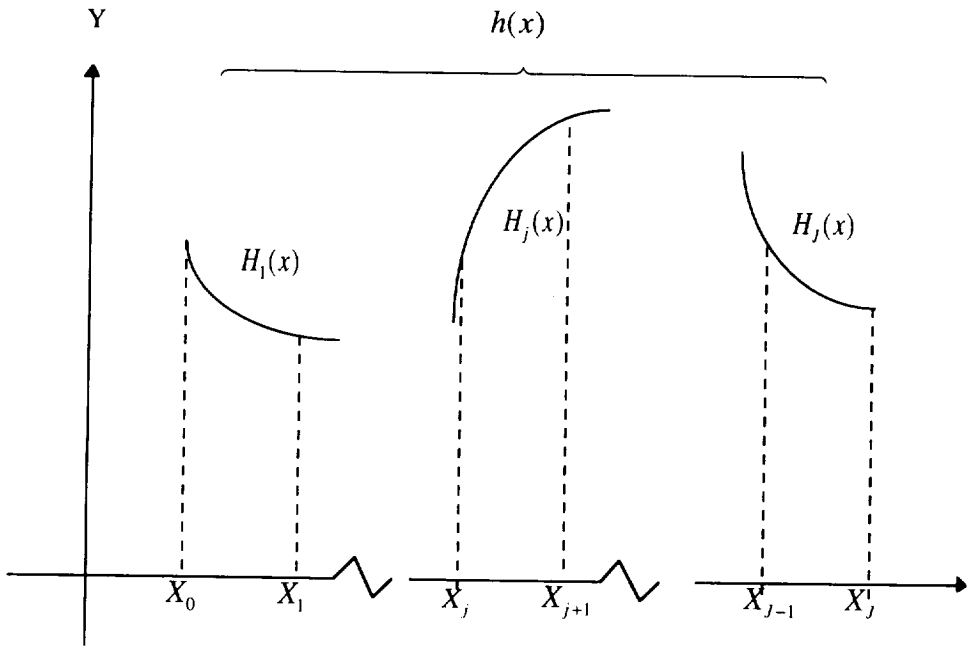

Figure 2: An illustration of the interpolating function *h(x)* .

$$H_j''(X_j) = H_{j+1}''(X_j) = \frac{6}{\Delta^2} s_j.$$

The polynomials (1) are determined by specification of $\{s_j\}$. The selection of these spline coefficients can involve any number of imposed weak constraints that characterize the spline fitting. One of the constraints is the minimization of the second derivative. Because

$$\int_{X_{j-1}}^{X_j} \left[H''(x)\right]^2 dx = \frac{12}{\Delta^3}\left[s_{j-1}^2 + s_j^2 + s_{j-1}s_j\right],$$

it follows that the quantity $\left[s_{j-1}^2 + s_j^2 + s_{j-1}s_j\right]$ is to be minimized in any kind of variational selections of $\{s_j\}$.

The simplest quadratic form to minimize is

$$\sum_{j=1}^{J}\left[s_{j-1}^2 + s_j^2 + s_{j-1}s_j\right].$$

However, this is not enough to guarantee continuity of the derivatives at the knots. A method to incorporate the condition

$$s_{j-1} + 4s_j + 4s_{j+1} - \left(h_{j-1} - 2h_j + h_{j+1}\right) = 0$$

must be found. This is done by introducing Lagrangian multipliers.

The simple spline formulation for the minimization is

$$E\left[\{s_j\}\right] = \sum_{j=1}^{J}\left[s_{j-1}^2 + s_j^2 + s_{j-1}s_j\right] + 2\sum_{j=1}^{J-1}\lambda_j\left[s_{j-1} + 4s_j + s_{j+1} - \left(h_{j-1} - 2h_j + h_{j+1}\right)\right] \tag{3}$$

where λ_js are the Lagrangian multipliers. These conditions are exactly satisfied upon completion of the minimization so that zeros are in effect added to the quantity to be minimized.

The procedure of solving those λ_js, therefore, the spline coefficients $\{s_j\}$, and the interpolating splines $\{h_j\}$, is similar to that of spline smoothing to be described in the next section.

2.2 Cubic Spline Smoothing

In the Spline fitting technique described above, the $\{h_j\}$ are taken to represent errorless data or observations, and the spline passes each point y_j. However, there can be circumstances that the observations are contaminated and unwanted noises are present. For example, in our case raw spectra exhibit coherent sawtooth like "noises". Under these circumstances, the data integrity condition should be relaxed. This can be done by adding a weak constraint term, $\sum_{j=0}^{J}\left[h_j - y_j\right]^2$ to Eq. (3), where y_j is the observed data, and only a "best fit" should be sought. The smoothed spline $\{h_j\}$ does not necessarily pass original observed data $\{y_j\}$, unlike the case of the spline fitting. An appropriate discrepancy sum can be formed as

$$\begin{aligned} E\left[\{s_j\},\{h_j\}\right] = \quad & \tau^2\sum_{j=1}^{J}\left[s_{j-1}^2 + s_j^2 + s_{j-1}s_j\right] + \sum_{j=0}^{J}\left[h_j - y_j\right]^2 \\ & +2\sum_{j=1}^{J-1}\lambda_j\left[s_{j-1} + 4s_j + s_{j+1} - \left(h_{j-1} - 2h_j + h_{j+1}\right)\right], \end{aligned} \tag{4}$$

where τ^2 is an adjustable weighting factor. As it increases, the tension of the spline smoothing increases, *i.e.*, the curve "flattens out". On the other hand, as it decreases, the observed data are reproduced more closely at the expense of increased curvature.

The variations on the spline coefficients are tabulated as:

$$\begin{array}{lcll} \delta s_0 & \tau^2\left(2s_0 + s_1\right) + 2\lambda & = 0 & \\ \delta s_1 & \tau^2\left(s_0 + 4s_1 + s_2\right) + 2\lambda_1 + 8\lambda_2 + 2\lambda_3 & = 0 & \\ \vdots & \vdots & \vdots & \\ \delta s_j & \tau^2\left(s_{j-1} + 4s_j + s_{j+1}\right) + 2\lambda_{j-1} + 8\lambda_j + 2\lambda_{j+1} & = 0 & j = 2,\ldots,(J-2) \\ \vdots & \vdots & \vdots & \\ \delta s_{J-1} & \tau^2\left(s_{J-2} + 4s_{J-1} + s_J\right) + 2\lambda_{J-2} + 8\lambda_{J-1} & = 0 & \\ \delta s_J & \tau^2\left(s_{J-1} + s_J\right) + 2\lambda_{J-1} & = 0 & \end{array} \tag{5}$$

The variations on the multipliers lead to

$$\delta\lambda_j: \quad s_{j-1} + 4s_j + s_{j+1} = h_{j-1} - 2h_j + h_{j+1}; \quad j = 1,(J-1) \tag{6}$$

Since the spline does not pass the data $\{y_j\}$, the $\{h_j\}$ are no longer fixed; their variations are listed below:

$$
\begin{array}{lcll}
\delta h_0 & 2(h_0 - y_0) - 2\lambda_1 & = 0 & \\
\delta h_1 & 2(h_1 - y_1) + 4\lambda_1 - 2\lambda_2 & = 0 & \\
\vdots & \vdots & \vdots & \\
\delta h_j & 2(h_j - y_j) - 2\lambda_{j-1} + 4\lambda_j - 2\lambda_{j+1} & = 0 & j = 2,\ldots,(J-2) \\
\vdots & \vdots & \vdots & \\
\delta h_{J-1} & 2(h_{J-1} - y_{J-1}) - 2\lambda_{J-2} + 4\lambda_{J-1} & = 0 & \\
\delta h_J & 2(h_J - y_J) - 2\lambda_{J-1} & = 0 &
\end{array}
\tag{7}
$$

Combining terms in (7), we have

$$
\left[h_{j-1} - 2h_j + h_{j+1}\right] - \left[y_{j-1} - 2y_j + y_{j+1}\right] = \lambda_{j-2} - 4\lambda_{j-1} + 6\lambda_j - 4\lambda_{j+1} + \lambda_{j+2} \tag{8}
$$

Each of the combinations $\left[s_{j-1} + 4s_j + s_{j+1}\right]; j = 1,\ldots,(J-1)$ in (5) can be replaced by their equivalents from (6) to obtain the following equations,

$$
\begin{array}{lcl}
\delta s_1 : & \tau^2(h_0 - 2h_1 - h_2) + 8\lambda_1 + 2\lambda_2 & = 0 \\
\delta s_j : & \tau^2(h_{j-1} - 2h_j - h_{j+1}) + 2\lambda_{j-1} + 8\lambda_j + 2\lambda_{j+1} & = 0 \\
\delta s_{J-1} : & \tau^2(h_0 - 2h_1 - h_2) + 2\lambda_{J-2} + 8\lambda_{J-1} & = 0
\end{array}
\tag{9}
$$

The $\left[h_{j-1} - 2h_j + h_{j+1}\right]$ in (9) can be replaced by the groupings in (8)

$$
\begin{array}{lcll}
\delta s_1 & \tau^2\left[\Delta^2 \aleph^2 y_1 + (6\lambda_1 - 4\lambda_2 + \lambda_3)\right] + 8\lambda_1 + 2\lambda_2 & = 0 & \\
\delta s_2 & \tau^2\left[\Delta^2 \aleph^2 y_2 + (-4\lambda_1 + 6\lambda_2 - 4\lambda_3 + \lambda_4)\right] + 2\lambda_1 + 8\lambda_2 + 2\lambda_3 & = 0 & \\
\vdots & \vdots & \vdots & \\
\delta s_j & \tau^2\left[\Delta^2 \aleph^2 y_j + (\lambda_{j-2} - 4\lambda_{j-1} + 6\lambda_j - 4\lambda_{j+1} + \lambda_{j+2})\right] + 2\lambda_{j-1} + 8\lambda_j + 2\lambda_{j+1} & = 0 & j = 3,\ldots,(J-3) \\
\vdots & \vdots & \vdots & \\
\delta s_{J-2} & \tau^2\left[\Delta^2 \aleph^2 y_{J-2} + (\lambda_{J-4} - 4\lambda_{J-3} + 6\lambda_{J-2} - 4\lambda_{J-1})\right] + 2\lambda_{J-3} + 8\lambda_{J-2} + 2\lambda_{J-1} & = 0 & \\
\delta s_{J-1} & \tau^2\left[\Delta^2 \aleph^2 y_{J-1} + (6\lambda_{J-3} - 4\lambda_{J-2} + \lambda_{J-1})\right] + 2\lambda_{J-2} + 8\lambda_{J-1} & = 0 &
\end{array}
\tag{10}
$$

where $\aleph^2 y_j = \dfrac{y_{j-1} - 2y_j + y_{j+1}}{\Delta^2}$

The $\{\lambda_j\}$ are then found as solutions of

$$
\mathbf{A}\,\lambda = \mathbf{y}'' \tag{11}
$$

where **A** is the pentadiagonal matrix

$$\begin{pmatrix} c & b & a & & & & & & \\ b & c & b & a & & & & & \\ a & b & c & b & a & & & & \\ & a & b & c & b & a & & & \\ & & a & b & c & b & a & & \\ & & & . & . & . & . & . & \\ & & & & . & . & . & . & . \\ & & & & & . & . & . & . \\ & & & & & & a & b & c & b & a \\ & & & & & & & a & b & c & b \\ & & & & & & & & c & b & c \end{pmatrix} \tag{12}$$

Here the matrix elements are constants and given by

$$\begin{aligned} a &= \tau^2 \\ b &= \left(2-4\tau^2\right) \\ c &= \left(8+6\tau^2\right) \end{aligned}$$

and

$$y'' = -\Delta^2\tau^2 \begin{pmatrix} \aleph^2 y_1 \\ \aleph^2 y_2 \\ . \\ \aleph^2 y_j \\ . \\ \aleph^2 y_{J-1} \end{pmatrix} \tag{13}$$

Given the $\{\lambda_j\}$, the $\{h_j\}$ can be determined directly from (8), and the spline coefficients $\{s_j\}$ can be found as a tridiagonal solution of (5).

3. POST PROCESSING OF ATREM REFLECTANCE CUBE

The small spikes, as seen in Fig. 1, are systematically present in all spectra in an ATREM output data cube. We hope to make mild "gain" adjustments to remove these small spikes during our post processing of the ATREM data cube. Specifically, we hope to find a gain function, g(λ), which contains all the weak spikes and which has a mean value close to 1. The multiplication of g(λ) to the ATREM output spectra should allow the removal of the systematic small spikes. Several steps are involved in our post processing of an ATREM output data cube. They are:

a). The cubic spline smoothing technique described in Section 2 is applied to each of the spectra in the ATREM data cube. As a result, an intermediate "smoothed" data cube is produced. Because the cubic spline smoothing technique fits a spectrum "locally", most of the smoothed spectra at this stage match quite well with the ATREM spectra. If the spectra were fit with low order Legendre polynomials "globally", only a minor fraction of the smoothed spectra would match well with the ATREM spectra.

b). The average reflectance, ρ_{avg}, is calculated for each of the spectra in the ATREM output data cube.

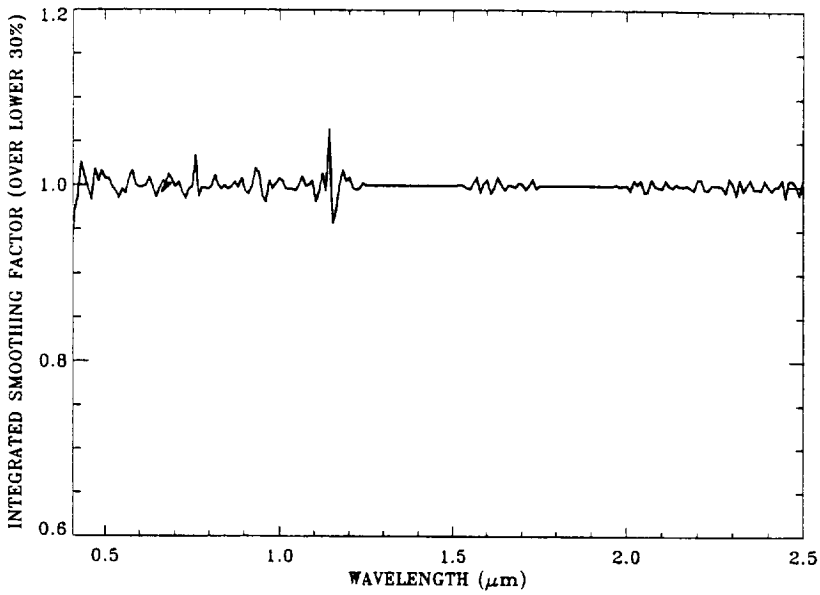

Fig. 3. A sample gain spectrum.

c). For each pixel, the standard deviation, σ, between the ATREM spectrum and the "smoothed" spectrum is calculated.

d). For an AVIRIS scene, a scatter plot of σ / ρ_{avg} v.s. ρ_{avg} is made. Pixels with σ / ρ_{avg} values in the lower twenty percentile are identified.

e). For each of the pixels identified in Step d, a ratio spectrum ("smoothed" spectrum / ATREM spectrum) is calculated. Our desired gain spectrum, $g(\lambda)$, is obtained by averaging all the ratio spectra. Figure 3 shows an example of a gain spectrum, which contains a number of weak spikes in the 0.4 - 2.5 μm spectral region.

f). The gain spectrum is applied to each of the spectra in the ATREM output data cube to obtain the "final" smoothed data cube.

Our algorithm for smoothing the ATREM output data cube is fast. It takes about 3 minutes on a SGI machine with a 150 MHz processor to process one complete data cube.

4. PRELIMINARY RESULTS

Results from one set of AVIRIS data acquired over the Cuprite Mining District in Nevada in June, 1995 are described below. Figure 4 shows a comparison among an ATREM reflectance spectrum over a single pixel , the smoothed spectrum, and the reflectance spectrum obtained with the well known empirical line method (Conel *et al.*, 1987). For clarity, the spectra in Fig. 4 are vertically displaced. The general shapes of these spectra in the 0.4 - 1.26 μm, 1.5 - 1.75 μm, and 2.0 - 2.5 μm wavelength intervals are very similar. Major mineral features in the 2.0 - 2.5 μm region are seen in all the spectra. The un-smoothed ATREM spectrum has quite a few weak spikes. These spikes are largely removed in the smoothed spectrum. The spectrum derived with the empirical line method shows weak inverse water vapor features near 0.94 and 1.14 μm. This indicates that the method results in a slight over-correction of atmospheric water vapor absorption effects for this pixel.

Figure 5 shows six ATREM reflectance spectra (vertically displaced for clarity). These spectra have distinct mineral absorption features in the 2.0 - 2.5 μm spectral region. Weak spikes (for example near 1.14 μm) are systematically present in all the spectra. Figure 6 shows the corresponding smoothed spectra, which look very similar to laboratory-measured reflectance spectra, particularly in the 2.0 - 2.5 μm spectral region. Weak spikes are all removed. A broad iron feature near 0.9 μm is seen nicely in one spectrum - the 4th spectrum from top. Figure 7

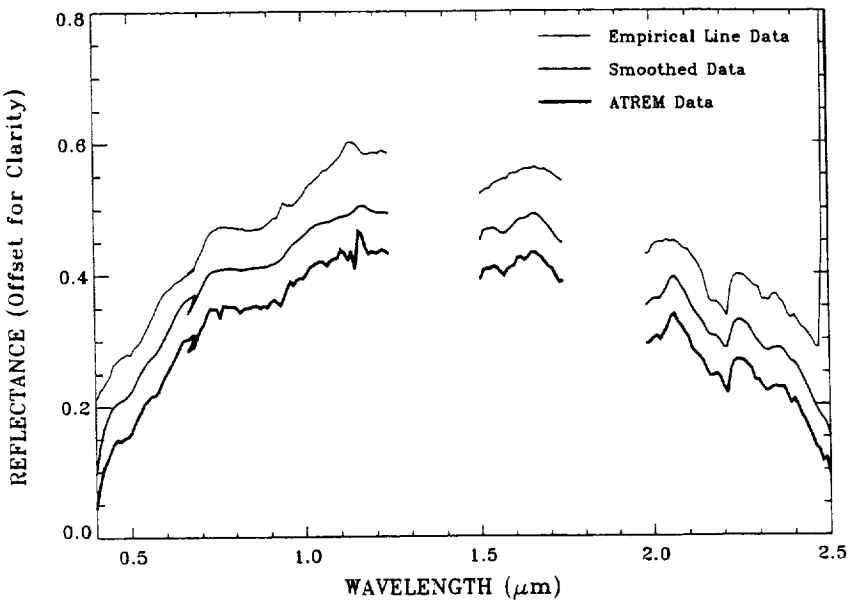

Fig. 4. A comparison among an ATREM reflectance spectrum, a smoothed spectrum, and a reflectance spectrum obtained with the empirical).

shows six spectra derived from the AVIRIS data with the empirical line method. Mineral features in the 2.0 - 2.5 μm region are recovered quite well with this method. However, water vapor features in the 0.94 and 1.14 μm regions are either over- or under- corrected. The broad iron feature in the 4th spectrum from the top is not clearly seen due to the over-correction of atmospheric water vapor absorption effects. By comparing Figures 5, 6 and 7, it is seen that major mineral features are preserved during our smoothing of the ATREM reflectance cube.

5. SUMMARY

We have described a technique, which fits spectra "locally" based on cubic spline smoothing, for quick post processing of apparent reflectance spectra derived from AVIRIS data using the ATREM code. Results from our analysis of AVIRIS data acquired over Cuprite mining district in Nevada in June of 1995 are presented. Very good agreement between our results and those of empirical line method in the 2.0 - 2.5 μm spectral region is obtained. It appears that the use of ATREM code for retrieving surface reflectance spectra from AVIRIS data plus the use of the smoothing technique described in this paper should yield surface reflectance spectra that look very similar to laboratory-measured reflectance spectra.

6. ACKNOWLEDGMENTS

The authors are grateful to J. W. Boardman of Analytical Imaging Geophysics, Boulder, Colorado for useful discussions, and to R. O. Green of Jet Propulsion Laboratory and Kathy Heidebrecht of Center for the Study of Earth from Space, University of Colorado at Boulder for providing AVIRIS data used in this study. This research is partially supported by a grant from NASA Headquarters in Washington, DC to Naval Research Laboratory in Washington, DC.

7. REFERENCES

Ahlberg, J. H., E. N. Nilson, and J. L. Walsh: The Theory of Splines and their Applications. Academic Press, New York, 9-13, 1967.

Conel, J. E., R. O. Green, G. Vane, C. J. Bruegge, R. E. Alley, and B. Curtiss, Airborne imaging spectrometer-2: Radiometric spectral characteristics and comparison of ways to compensate for the atmosphere, in *SPIE Proceedings, Vol. 834*, 140-157, 1987.

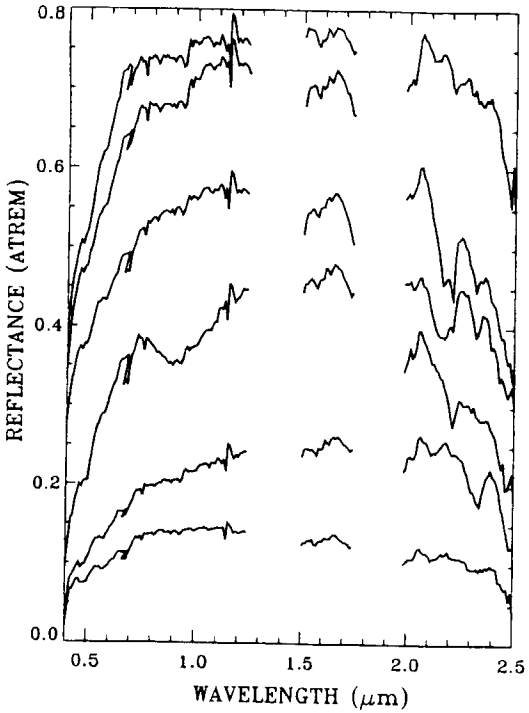

Fig. 5. Six reflectance spectra (displaced vertically for clarity) derived with ATREM from AVIRIS data acquired over Cuprite, Nevada in June, 1995.

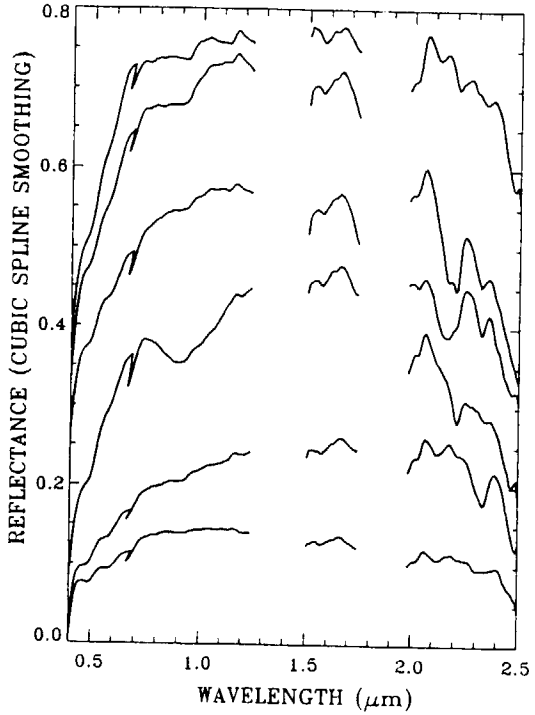

Fig. 6. Six smoothed reflectance spectra corresponding to those in Fig. 5.

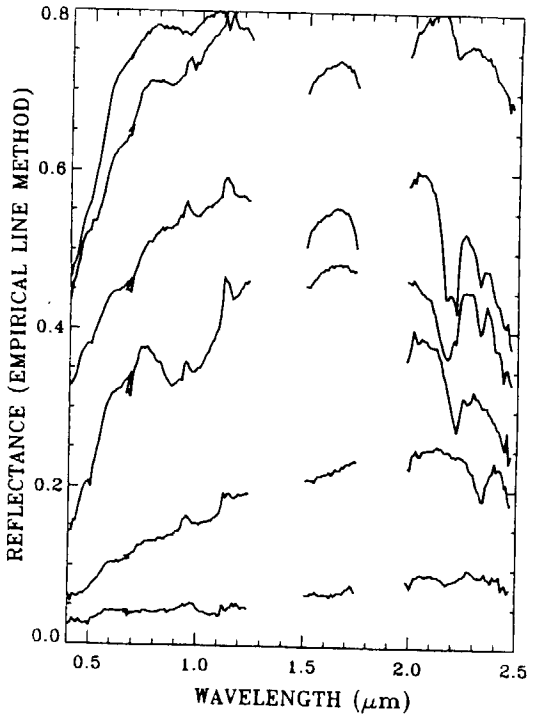

Fig. 7. Six reflectance spectra derived with the empirical line method.

Gao, B.-C., K. H. Heidebrecht, and A. F. H. Goetz, Derivation of scaled surface reflectances from AVIRIS data, *Remote Sens. Env., 44*, 165-178, 1993.

Gao, B.-C., and C. O. Davis, Development of a line-by-line-based atmosphere removal algorithm for airborne and spaceborne imaging spectrometers, in*SPIE Proceedings*, *Vol. 3118*, 132-141, 1997.

Goetz, A. F. H., J. W. Boardman, B. Kindel, and K. B. Heidebrecht, Atmospheric corrections: On deriving surface reflectance from hyperspectral imagers, , in*SPIE Proceedings*, *Vol. 3118*, 14-22, 1997.

Press, W. H., B. P. Flannery, S. A. Teukolsky and W. T. Vetterling, Numerical Recipes. Cambridge University Press, Cambridge CB2 1RP, 86-89, 1989.

IMPROVED ATMOSPHERIC CORRECTION FOR AVIRIS SPECTRA FROM INLAND WATERS

Mary Gastil and John M. Melack

Institute for Computational Earth System Science,
University of California, Santa Barbara, CA 93106-3060

1. INTRODUCTION

Remote sensing reflectance (Rrs) cannot be measured directly. Comparison of Rrs calculated from field measurements to Rrs calculated from AVIRIS spectra and the atmospheric radiative transfer model modtran provides a measure of the accuracy of our method. That and other comparisons are presented here as a validation of a method of retrieving Rrs from inland waters from AVIRIS radiance. The method of collecting field measurements for Rrs is described in Hamilton, 1993. Retrieval of Rrs from AVIRIS using modtran was developed from Carder, 1993. AVIRIS radiance is reduced by the path radiance modeled by modtran and divided by one-way transmission. Skylight, modeled by modtran, specularly reflected from the lake surface, is then subtracted from this radiance, leaving only that radiance which has come from under water. This water-leaving radiance is then normalized by the downwelling irradiance incident at the surface as modeled by modtran. Separate executions of modtran are made, in different modes, with the appropriate viewing geometry, to calculate the parameters of this equation:

$$Rrs = [\ (L_{AVIRIS} - L_{path})/T_{atm} - L_{sky}*\rho_{water}\ ]\ /\ E_d,$$

where L_{AVIRIS} is radiance measured by AVIRIS,
L_{path} is path radiance, indirect solar radiance at the view angle from nadir, at AVIRIS,
T_{atm} is atmospheric transmission, one-way,
L_{sky} is skylight, indirect solar radiance at the view angle from zenith, at the surface,
ρ_{water} is the Fresnel reflectance coefficient of water,
and E_d is the downwelling solar irradiance incident at the lake surface.

Our improved retrieval of Rrs has allowed us to fit a single curve to a set of 134 pairs of AVIRIS Rrs and measured chlorophyll gathered on eight experiments at Mono Lake. Previously, spectra from different surveys varied more due to lingering atmospheric effects and/or radiometric calibration imprecision than they varied due to chlorophyll.

2.0 USE OF MODTRAN

2.1 Modtran Model Inputs

The modtran version we used was shared with us by Robert Green (JPL); partly developed at JPL, an intermediate version between version 3 and 3.5, it is of circa 1993 vintage. It uses an updated solar spectrum and allows the user to specify gas amounts. In all cases we used 0.55 of nominal water vapor and 1.06 of nominal CO_2 specified in modtran. The effect of input H_20 vapor amount is limited to the water vapor absorption bands. This modtran version allows the surface albedo spectrum to be read from a file rather than using a scalar constant. The inclusion of 8-stream discrete ordinate scattering improved the modtran outputs' match to our measurements. For all cases the mid-latitude, rural model was used.

Some modtran inputs are less precise than the date, hour, viewing geometry and geographic location. These imprecisely defined inputs are used to optimize the match between modtran-retrieved Rrs and Rrs calculated from ground-based measurements. Of these, horizontal visibility has the greatest effect. Estimates of actual horizontal visibility at Mono Lake during AVIRIS experiments ranged from 100 to 200 km. The one date for which we have optical depths calculated from sun photometer measurements had a calculated visibility of 440 km. Modtran output is decreasingly sensitive to visibility as visibility increases.

2.2 View Angle Sensitivity

Path radiance, the largest part of the radiance measured at 20 km altitude over water, varies with view angle, as do T_{atm} and L_{sky}. The view angle of each survey station on the lake was calculated from its cross-track pixel location. Nominal values for an ER-2 altitude of 20 km and a scene total width of 11 km were assumed, understanding that any variation is a similar triangle to this geometry. A side scan of 16 degrees was assumed for the edges of the image; zero roll was assumed. Based on the regularity of the shoreline topography, we deduced that usually the roll was negligible.

Interpolating the modtran parameters L_{path}, T_{atm}, and L_{sky} to each station's specific view angle brought the same stations' spectra extracted from duplicate AVIRIS coverage into closer agreement. The effect of side-scan angle on the modtran parameters in the Rrs equation removed the largest part of the discrepancy between Rrs spectra of the same station in subsequent runs. All field measurements were done at zenith or nadir; Rrs is independent of view angle even though it is calculated from parameters dependent on view angle.

Modtran outputs for nadir and 15 degrees off nadir were used to linearly interpolate more precise L_{path}, T_{atm} and L_{sky} for each survey station. A good approximation is that L_{path}, L_{sky} and T_{atm} vary linearly with view angle. View azimuth was always 90 degrees from the solar plane because we requested the ER-2 fly directly at or away from the sun, so as to avoid sun glint. The left and right sides of the viewing geometry were treated symmetrically. Modtran was run with view azimuth to the east of the flight track.

3.0 VALIDATION

3.1 Skylight Comparison

Our intention was to choose a visibility for which the measured L_{sky} most closely matched the modtran output L_{sky}. Every field survey included sky spectra at zenith. However, the field measurements of skylight were variable, more so than changes in visibility. The modtran L_{sky} and that measured in the field are compared in Figure 1 for 7Oct92, but the choice of visibility is not obvious because the comparison is complicated by the different slope of the modtran modeled Lsky and field measured skylight spectra. Modtran models the skylight as more blue than was actually measured; the modtran skylight exceeds that measured in the blue end but is less than that measured in the red end. The modtran L_{sky} is theoretical, and so has an infintesimal fov. The fiber optic tip of the field spectrometer has a full width field of view (fov) of 22 degrees.

3.2 Downwelling Irradiance Comparison

Figure 2 shows that the downwelling irradiance modeled by modtran is less blue than that measured in the field, by either the gray card or the remote-cosine-reflector. The modtran modeled E_d is used in the denominator of the equation to retrieve Rrs from AVIRIS radiance. Modtran output E_d differs from that measured off the gray card by approximately a linear factor increasing from zero at 400 nm to 25 $\mu W/nm/cm^2$ at 800 nm. The effect of this difference in the denominator is to calculate a Rrs increasingly too low toward longer wavelengths. However, that is opposite to observed discrepancy between field measured and AVIRIS Rrs spectra.

3.3 Optical Depth Comparison

Atmospheric optical depth is the extinction integrated along the path. It varies with path length and concentration of molecules and aerosols. An atmosphere is well described by its optical depth. Optical depth may be partitioned into its separate contributors, but in this example we consider the total. A Reagan sun photometer was used to measure the intensity of direct solar radiance in nine channels as a function of time-of-day. From the curve of changing path length to the sun through the atmosphere, called a Langly plot, the optical depths were deduced. We collected sun photometer data successfully on most of our AVIRIS experiments but only one data set was reduced. We have optical depths for the 21Sep93 AVIRIS experiment.

Modtran calculates total optical depth, a unitless quantity. We used the optical depth from a modtran case for skylight at zenith and at 15 degrees off zenith for comparison to the sun photometer-measured optical depths. Figure 3 shows the modtran output as dots (so finely resolved that they appear almost continuous) and the sun

photometer channels' optical depths as diamonds. Figure 3 shows that optical depth is sensitive to the model used in modtran, and that the mid-latitude winter model is a better match for 21Sep93 than the mid-latitude summer.

3.4 Pumice Flats Comparison

Our land calibration site just 5 km south of Mono Lake is a 2 km wide, flat area covered with white pumice gravel named Pumice Flats. To improve the radiometric calibration (the factor of radiance over DN, where DN is digital number), the field spectra at Pumice Flats are ratioed to the spectra extracted from AVIRIS cubes at Pumice Flats. The field spectra are measured as DN over the pumice gravel and DN over the gray card to calculate reflectance, R_{PF}. This is radiance reflectance, not Rrs. To obtain the equivalent radiance that would be seen at 20 km altitude, the modtran outputs Lpath, Tatm, and Ed are used.

$$L_{PF} = R_{PF} * (E_d/\pi) / T_{atm} + L_{path}$$

In calculating a radiance-at-sensor (L_{PF}) from the field measurd reflectance (R_{PF}) we used modtran output irradiance rather than radiance. This method may produce a better L_{PF}. The gray card is Lambertian. The denominator in the field measured reflectance is E_d/π. The gravel in Pumice Flats is oriented at all angles so, although specular on each tiny surface, as an aggregate it will be somewhere between specular and Lambertian.

The AVIRIS radiance spectrum of Pumice Flats is the average of several hundred pixels. An average of three years' Pumice Flats field reflectance spectra is used in the numerator of all dates' radiance correction ratio. The spectra are resampled to the AVIRIS band center wavelengths of the year being processed. Radiance correction ratios calculated for six dates are graphed in Figure 4.

The total radiance AVIRIS measures at 20 km altitude is nearly all path radiance. If modtran has accurately modeled the path radiance, it should be less than the AVIRIS radiance. All variables in the equation below are positive.

$$L_{AVIRIS} = L_{path} + L_{sky}*\rho_{water} + L_{water}$$

When the AVIRIS radiance over the water is less than the modtran output path radiance, we know either the path radiance is incorrectly modeled or the AVIRIS radiance calibration is wrong. If the ratio from Pumice Flats brings the AVIRIS radiance above the path radiance, it could be correctly adjusting the radiometric calibration or mitigating inaccuracy in the modtran outputs.

If a lake spectrum was used instead of the Pumice Flats spectrum to create the radiometric calibration correction ratio, then that AVIRIS spectrum would be forced to agree with the field spectrum. This may be useful for making a chlorophyll map of one date, but this is counter to the purpose of finding the best predictive algorithm for multiple dates. The Pumice Flats reflectance has been found to be consistent over time-of-day and season.

3.5 Comparison of Same Station in Subsequent Overpasses

Two to three overpasses are required to cover Mono Lake, our ground control points on shore and land calibration site. On some dates these AVIRIS runs overlap, providing duplicated coverage of our stations on the lake. Comparison of spectra from the same station in subsequent overpasses has unexplained variability. AVIRIS spectra extracted as the average of a 10x10 bin of pixels centered on a station location (accurate to 2 to 4 pixels by georeferencing) should have near identical shape and magnitude. Their only differences are the 10 to 20 minute delay and resulting small sun angle change and drift of the lake water. A current on a calm day of 5 cm/s causes a drift of only 30 to 60 meters, which is only a fraction of a 200 m wide bin.

The small change in solar angle does affect modtran output measureably and so the time-of-day was input specific to each overpass. The time-of-day used was that where the ER-2 would be over the center of the stations covered in that overpass. Each scene of 512 lines takes 42 seconds to fly, so the ER-2 is over the lake for about 84 seconds on each pass.

A larger discrepancy between runs occurs when the ER-2 flies in the opposite direction (N->S then S->N). If there is stratospheric wind then the ER-2 must fly at a different altitude. Pixel area increases with altitude but the instantaneous field-of-view (ifov) remains constant. Because the stratosphere is so optically thin, a 0.5 km change

in ER-2 altitude does not affect the modtran outputs enough to explain the change in calculated Rrs. We have not determined the cause of the difference in brightness in overpasses flown from opposite directions.

3.6 Georeferencing Precision

The location of the stations on the lake was performed with care and with many more ground control points (GCP) than a second order transform requires. A set of 204 GCPs in the six topographic maps containing Mono Lake were measured which allowed ill-fit GCPs to be discarded until a rms error of less than 4 pixels was achieved in most scenes. A 10x10 bin of pixels was used to extract one average radiance spectrum at each survey station.

3.7 Rrs from AVIRIS Compared to Rrs from field spectra

In Figure 5 the Rrs calculated from field spectra and from AVIRIS spectra are overlaid for comparison on two dates. Eight dates were examined. The AVIRIS Rrs deviate most from the field spectra at the blue end, at wavelengths shorter than 440 nm, for most of these dates. At 490 nm the spectra are closer; and at 555 nm the field spectra and AVIRIS Rrs agree well; 17Aug94 is a counter-example of this. We attribute the differences mainly to an imperfect atmospheric correction but also partly to radiometric calibration of the blue wavelengths. The radiance ratio from Pumice Flats should compensate for most errors in the radiometric calibration. Because the ratio denominator was calculated with the same modtran outputs as were used to retrieve Rrs, the ratio partially compensates for those outputs' inaccuracy.

The field spectra within a survey do vary in amplitude, with close to identical shape. This is most evident in 20May94 spectra. This same phenomenon appears in AVIRIS spectra. This may be attributed to small fractions of a pixel (or fov of the field spectrometer) containing foam or flecks of sun glint from ripples. Only in the AVIRIS spectra can this raised amplitude be explained by stratospheric aerosols. In that case the Rrs(800nm) may be subtracted as a constant from the entire spectrum as a first approximation. This was done to the 1992 AVIRIS spectra.

4. OTHER SOURCES OF VARIABILITY AND ERROR

4.1 Coherent Noise

Two types of noise appear in AVIRIS images besides the random speckle caused by very low signal being digitized: diagonal stripes and horizontal swaths. The diagonal stripes became less a problem in each AVIRIS season as the instrument shielding and dynamic range improved. In years prior to 1995, when the roll-correction was done, the de-striping algorithms were thwarted because the images do not have the original time sequence in the signal. A simple boxcar smooth worsens the stripes unless the box is much larger than the stripes.

The second noise type, appearing as horizontal swaths, is caused by variation in dark current (DC). This effect was removed by averaging all lines of dark current in each scene before subtracting from raw DN. 1996 data are the first for which the DC vary less than one DN across a scene.

4.2 Shoreline Ghosts - 1996 Forward-looking Window Beam Split

The 1996 data had a unique error source. An internal refraction in the window was blamed for a split beam, resulting in the image 250 lines forward of nadir appearing also at nadir as a small fraction of the main beam's amplitude. This appeared in the image as a faint overlay of the same image, offset by 250 lines. Where the shore was many times brighter than the lake radiance, this ghost image caused a measurable error. Where stations were more than 250 lines before the shore, the error was not measurable. We detected this phenomenon in the 2Apr96 Mono Lake AVIRIS images, when the shore was exceptionally bright due to new snowfall.

5. SUMMARY

Comparisons between AVIRIS and field spectra have assessed our method of atmospheric correction. The radiance correction ratio calculated from AVIRIS radiance over a land calibration target significantly improved the agreement between field measured and AVIRIS Rrs for all but one survey. By varying modtran inputs to optimize the fit between AVIRIS and field spectra we have improved the consistency of our Rrs spectra of Mono Lake collected in eight surveys.

6. ACKNOWLEDGMENTS

This work was funded by NASA EOS contracts NAGW-2602 and NAGW-5185 and by NASA HIRIS contract NAS5-51713.

The AVIRIS field experiments at Mono Lake were a success due to team effort involving M. Embry, G. Dana, D. Heil and B. Jellison from 1992 through 1996. Sun photometer data was reduced at JPL by J.van den Bosch. The UCSB Maps and Imagery Laboratory provided access to ERDAS georeferencing software, training, and advice. R. Green provided the input/output shell for modtran and valuable discussions. Modtran was run on a DEC alpha at JPL. D. Roberts reviewed the methods and provided insight on modtran use.

7. REFERENCES

Carder, K.L., P. Reinersman, R.F. Chen, F. Muller-Karger, C.O. Davis, and M. Hamilton, "AVIRIS Calibration and Application in Coastal Oceanic Environments." Remote Sens. Environ. 44 (1993): 205-216.

Hamilton, M.K., C.O. Davis, W.J. Rhea, S.H. Pilorz, and K.L. Carder, "Estimating chlorophyll content and bathymetry of Lake Tahoe using AVIRIS data." Remote Sens. Environ. 44 (1993): 217-230.

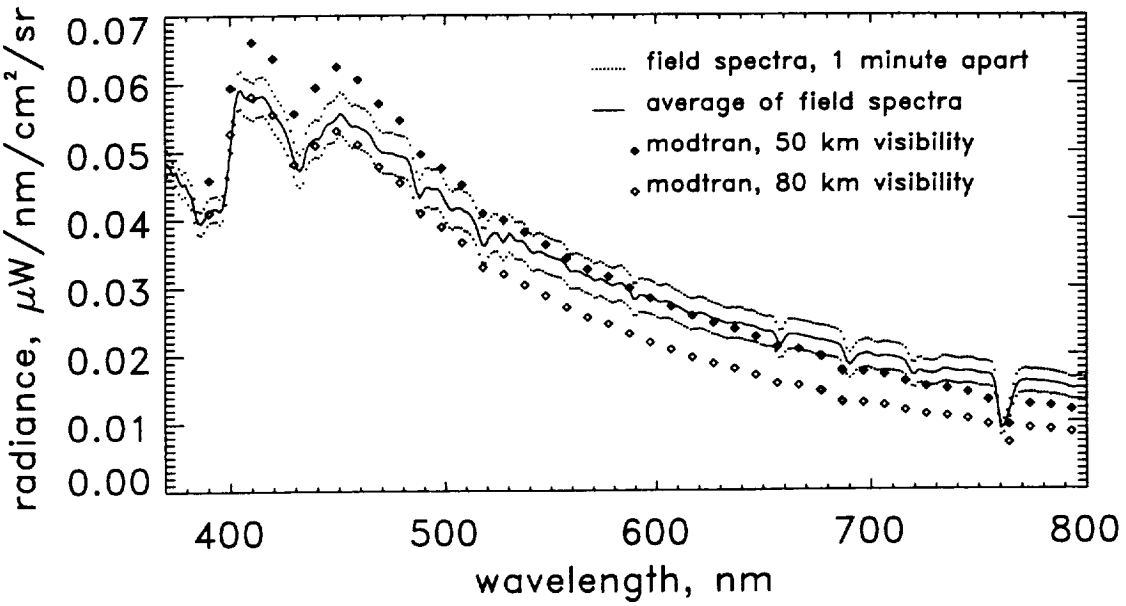

Figure 1. Measured skylight validates the modtran inputs.

The field measurement of skylight at zenith coincident with AVIRIS overflight can be used to select the modtran input visibility and to test the accuracy of the modtran model. The two field spectra, measured with the unbaffled fiber optic tip of a PS-II spectroradiometer (Analytical Spectral Devices) are plotted as one dot per 1.4 nm spaced waveband. The bands are so close that the spectrum shows fine atmospheric absorptions. Two skylight measurements are shown here, measured one minute apart. Their average is the solid line. The modtran simulated skylight at zenith is resampled to AVIRIS wavebands and plotted with a diamond at each band center. The solid diamond spectrum is from input visibility 50 km and the open diamonds from 80 km.

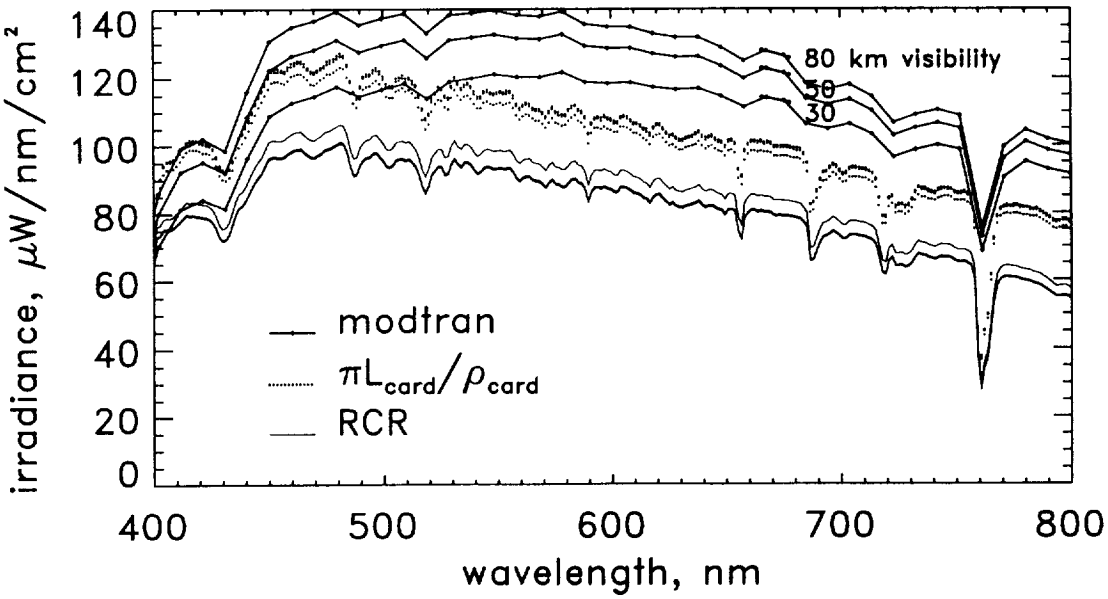

Figure 2. Modtran E_d compared to two field measurements of E_d.

Modtran models downwelling irradiance incident above the lake surface as brighter and less blue than we measured on the lake. E_d was measured directly using the remote cosine receptor (RCR) at the moment of AVIRIS overflight; three trials are graphed, solid curve. Rrs is calculated using the approximation of $\pi L_{card}/\rho_{card}$; radiance reflected off the gray card moments after overflight (dotted spectra) are brighter than measured with the RCR.

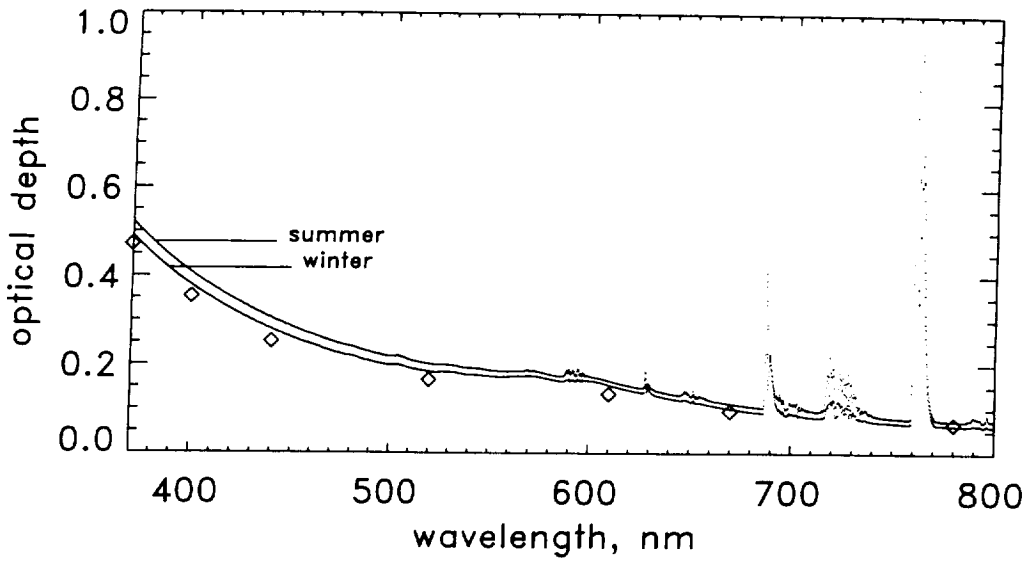

Figure 3. Modeled and measured atmospheric optical depth.

The optical depth output from the modtran model is graphed at high spectral resolution; inputs are specific to the 21Sep93 AVIRIS overflight conditions; summer and winter cases are compared. Optical depths calculated from sun photometer measurements on that day are graphed as diamonds. This comparison indicates a winter tropospheric temperature profile is appropriate.

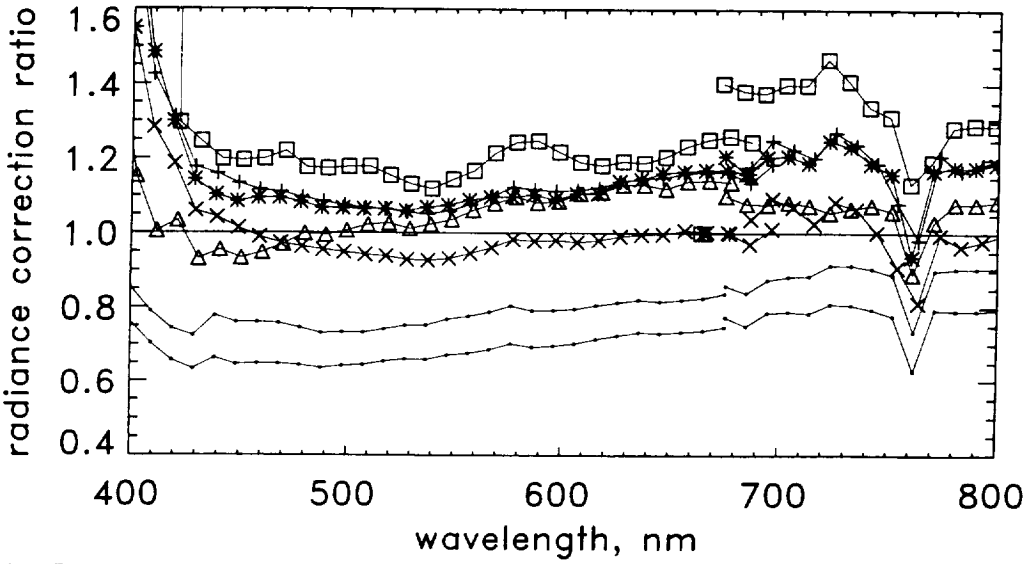

Figure 4. Radiance correction ratios for six AVIRIS dates.

For six overflights of Pumice Flats the ratio of field measured reflectance propagated to a radiance at 20 km over the AVIRIS radiance is graphed. For the spectral region of interest, about 440 nm to 710 nm for the purpose of predicting chlorophyll, these correction ratios vary from 0.9 to 1.3, with the exception of the 2Apr96 flight. On 2Apr96 Pumice Flats is covered in two overpasses; a correction ratio is calculated for each. These ratios, from 0.6 to 0.9, do not improve the match of AVIRIS Rrs to field measured Rrs. We speculate this is because for this date only the on-board calibration was already incorporated in the AVIRIS radiance. For all other dates, these correction ratios do improve the agreement between field measured Rrs and AVIRIS Rrs.

Plotting symbols:

• 2Apr96	□ 10Oct95	Δ 17Aug94
* 21Sep93	+ 7Oct92	x 1Sep92

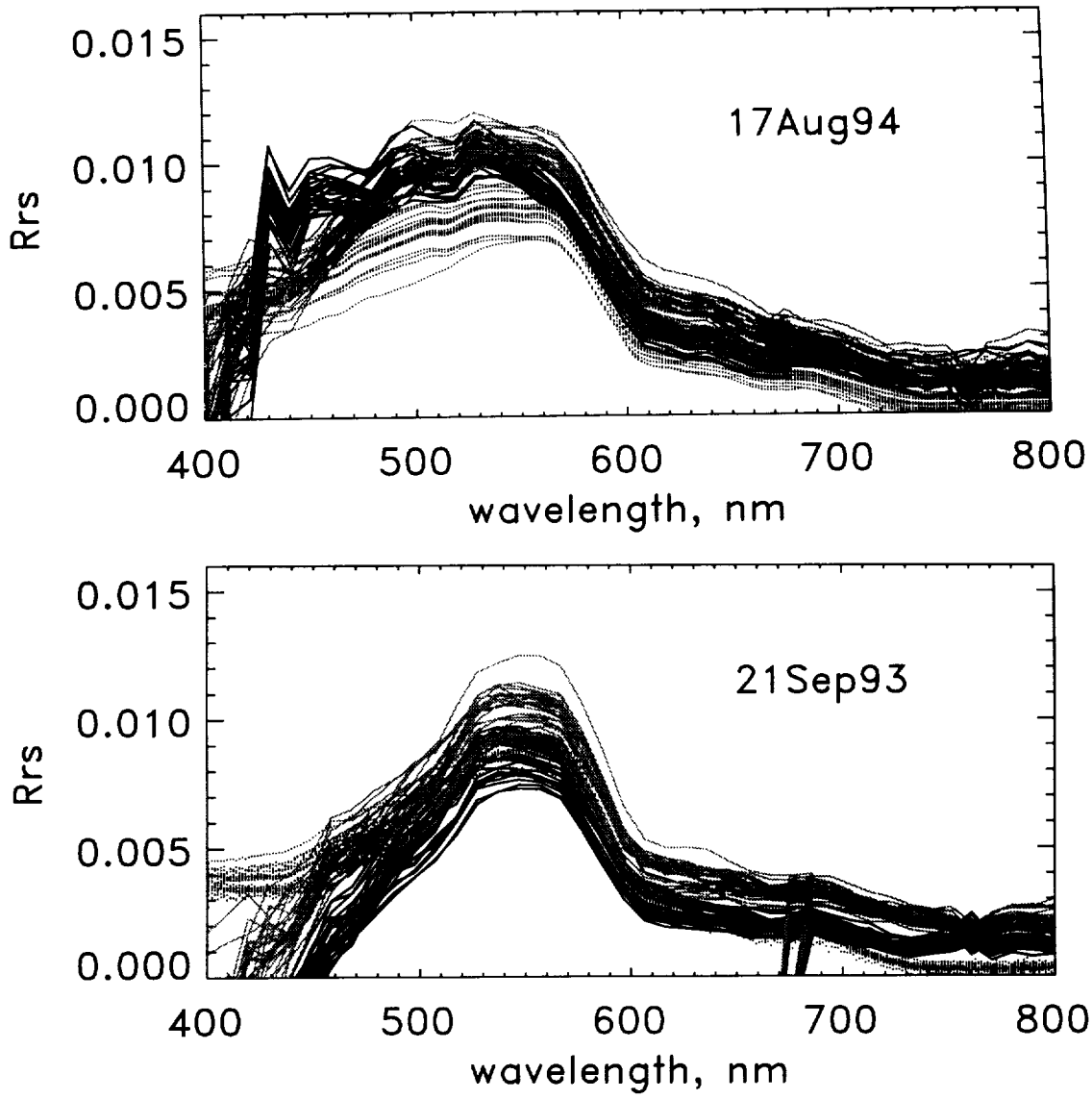

Figure 5. AVIRIS Rrs compared to field measured Rrs.

Rrs calculated from field spectra and from AVIRIS spectra are overlaid for comparison, separately for each of two dates. An 80 km visibility was input to modtran for both Rrs shown in this figure. The dotted curves are the field spectra, one dot per band. The solid black curves are the AVIRIS Rrs spectra without using the radiance ratio from Pumice Flats and the gray curves include that ratio in the Rrs calculation. The gray curves partially obscure the black curves and either solid curves obscure the dotted curves.

For the 17Aug94 AVIRIS spectra the radiance correction ratio smoothes the jags in the wavelengths shorter than 550 nm.

For the 21Sep93 the radiance correction ratio raises the AVIRIS Rrs. Even with the ratio applied, AVIRIS Rrs are negative below 440 nm. With ratio, AVIRIS is a better match to the field spectra up to 550 nm but at longer wavelengths the uncorrected spectra match more closely.

DOI Use of AVIRIS Data In Natural Resources Management - A Technology Transfer Project - Status Report

James R. Getter
United States Geological Survey
Reston, VA

Diane Wickland
NASA Headquarters
Washington, D.C.

Introduction

A meeting was held in December 1996, attended by representatives from Department of the Interior (DOI) and National Aeronautical and Space Administration (NASA) at the request of Department of the Interior Secretary, Bruce Babbitt and NASA, Administrator Director Dan Goldin, to discuss the use of hyperspectral systems and related remote sensing technologies in addressing environmental issues of environmental importance to the (DOI).

It was determined that NASA/DOI Coordination be established, comprised of representatives from each agency, designated to address the environmental issues and resulting technologies. A steering committee was formed consisting of representatives from NASA Headquarters, NASA PI's from University California-Davis, University of Colorado-Boulder, University of New Hampshire and DOI Bureaus (Indian Affairs, Land Management, Reclamation, National Park Service, and US Geological Survey).

Background

The steering committee provided three primary goals for the activities that were to and are taking place:

Goal 1) Provide technical and resource program personnel from DOI with scientific and technical information on hyperspectral systems and advanced technologies.

Goal 2) Focus on a limited number of resource issues or problems of interest to DOI that could potentially be addressed using hyperspectral, or complementary, remote sensing technologies.

Goal 3) Use of workshop format for DOI Resource Managers tutorial on hyperspectral and/or other advanced remote sensing technologies.

The steering committee solicited environmental issues believed to be most significant to DOI Bureaus as well as the identification of ecosystem areas, throughout the U.S., of importance to current DOI initiatives, to include technical and scientific interest thru a call for proposals, initiated in April 1997, to DOI Bureaus. It should be noted that there were no funds and/or resources to be provided interested parties other than the promise of limited NASA collects for the selected site(s) and a lot of hard work. Other constraints outlined in the solicitation were 1) a commitment from the bureau management that time and resources would be available to work on the project and 2) that there be baseline information readily available on the study site pertinent to the study proposed.

In May 1997, the committee selected four proposed study sites, of ten proposals received, that met the goals and constraints previously set by the committee and the proposal solicitation. All ten proposals were responsive to the solicitation but given the limited resource availability a ranking, rating and prioritization took place. The four selected study sites follow and are not listed in any specific priority order:

1- Mapping vegetation alliances, Congaree Swamp National Park, South Carolina.
2- Estimating the effect of invasive woody species on grasslands, Great Plains Basin.
3- Identify and map leafy spurge infestations, Theodore Roosevelt National Park, ND.
4- Mapping of mercury-containing mineral sources in the Owyhee Reservoir watershed, OR.

Mini-Workshop

In July 1997, the DOI and NASA PI's met in Denver, Colorado to discuss each of the selected proposals as it related to each of the studies problem statement to include, description of the area, existing baseline data, ancillary data collection efforts, analysis capability, knowledge of the technologies involved, milestones to be achieved, resource availability, logistics and expectations. Robert Green, NASA/JPL provided an overview of the AVIRIS platform, hardware, software and analysis capabilities along with an appreciation for flight planning logistics. The resulting actions of this two day workshop was to have the DOI and NASA PI's develop implementation plans defined well enough to carry out those activities necessary for the data collection, analysis and evaluation of hyperspectral technology on their respective environmental parameters to be measured. Planning efforts on flight line parameters were to be developed so that information could be transmitted to the NASA, Airborne Science and Applications Program flight control group for mission planning for 1998.

Transfer-Communications to Others

The entire project, including all technical and logistical aspects will be documented in a formalized report to the DOI, Science Board. It is also anticipated that results of this research will be published in an appropriate journal in the scientific literature. The results will also be available through the National Biological Information Infrastructure (NBII) at <http:// www.nbii.gov>.

A workshop is planned as a method for porting the technology to the DOI/Bureau technical line manager. The strategy is to use the experience of these selected studies to develop the curriculum for a workshop sponsored by NASA and DOI and probably held the USGS, EROS Data Center. The workshop agenda will provide for a tutorial of the advanced systems covering: 1) characterization of the hardware, software system, 2) characterization of the system data set, 3) exploitation and expectations of the data, and 4) data fusion, techniques, degree of difficulty in the use, known successes and failures in the use of the data and/or technology.
The US Geological Survey, Office of Biological Informatics and Outreach (OBIO) hosts a World Wide Web (WWW) page for this activity at <http://biology.usgs.gov/hwsc/>. The contents of this page consists of a steering committee membership list, the four implementation plans, a hyperspectral imaging searchable bibliography, a list of 200 URL's with hyperspectral

information, links to USGS Spectroscopy Lab, NASA AVIRIS Data Facility, AVIRIS flight line map and some University and vendor sites. It is the intent to use this page as a vehicle for communication to interested parties regarding these study efforts and outcomes.

1998 Study Activities

The study site implementation plans include methodologies and milestones consistent with both budget and personnel constraints of natural resource managers budgets. Milestones for each of the studies are listed with the particular study. The general activities to be performed are: 1) preparation and planning, which is currently on-going; 2) overflight collection with concurrent field observations, April through August 1998; 3) data preparation and analysis will occur as collects become available; 4) products development (ie., maps and stats) to include final study plans, which will be complete by January 1999.

Synopsis of DOI Studies

Mapping Vegetation Alliances at Congaree Swamp National Park South Carolina

Personnel:
PI's Mike Story and Rick Clark of the National Park Service and Dr. Mary Martin, University of New Hampshire.

Objectives:
The primary objective of this project is to incorporate the use of AVIRIS imagery with existing aerial photography and field collected vegetation data in order to evaluate the ability of the AVIRIS data to accurately map the variety of tree species found at COSW.

Background:
The COSW project includes approximately 30,000 acres of old-growth forest just Southeast of Columbia, SC. It contains a complex mosaic of wetland and upland communities. COSW is subjected to occasional hurricanes that can cause severe destruction to these communities. An important element of the NPS mission to manage the resources at COSW includes understanding the complex relationships of these communities and the changes that occur as a result of the destructive winds.

The NPS/BRD Vegetation Mapping Program initiated an effort at COSW in the summer of 1996. This effort includes the expertise of personnel from the National Park Service, USGS Biological Resources Division, Nature Conservancy, and the Savannah River Ecology Lab. To date, new CIR photography at 1:12,000 has been collected, initial interpretation of the photography has been completed, 125 vegetation plots have been located and data recorded representing approximately 31 Alliances.

This year, the plot data analysis will be completed followed by the final interpretation of the aerial photography. It is anticipated that the complex mosaics of forest types will be difficult to distinguish with the existing photography. It may be possible to make these distinctions by using the Hyperspectral capabilities of the AVIRIS system. By correlating the data from the known locations of the field sites with geocoded AVIRIS data, we should be able to train one of the spectral classifiers and classify the AVIRIS data into forest types.

Transition Plan:
The information gained from this project will be of immediate benefit to the Park and will be made available to them. Results from this project will help further the understanding of the capabilities of the AVIRIS system for mapping complex forests and will be made available to all interested parties.

Milestones:
Completed the analysis of field data by Sept. 1997.
Completed the final photo interpretation by Dec. 1997.
Obtain AVIRIS data of COSW in May 1998.
Complete normalization and geocorrection of the AVIRIS data by July 1998.
Complete the classification of the AVIRIS data by Sept 1998.

Estimating the Effect of Invasive Woody Species On Grasslands

Personnel:
PIs Dr. Dave Meyers, US Geological Survey, EROS Data Center and Dr. Carol Wessman, University of Colorado with The Nature Conservancy,Augustana College, North Dakota State University, the University of Toronto, the University of Nebraska, and Oklahoma State University.

Objectives:
The objective of this study will be to use spectral signature analysis and linear spectral mixing models to determine the degree to which a grassland spectral signature is influenced by woody species. Ultimately, these results will provide a means to quantify species gradients, allowing the isolation of the woody components in land cover mapping over the grasslands.

Background:
The proposed project is a continuation of extensive field, airborne and satellite data collection over several sites across the Great Plains of North America, initially funded by The Nature Conservancy, and later supported by grants from the Centre National d'Etudes Spatiales (CNES) to study the utility of the upcoming Vegetation Monitoring Instrument aboard the System Pour l'Observation de la Terre (SPOT) - 5 platform, and the National Aeronautics and Space Administration (NASA) to study the utility of the enhanced TM Plus (ETM+) system scheduled for launch on the Landsat-7 platform for the given application. This study also complements several projects under consideration for funding, including a study similar to those mentioned above, only using the Moderate Resolution Imaging Spectrometer (MODIS) aboard the Earth

Observing System's (EOS's) AM-1 platform, a grasslands carbon budget study submitted to the National Institute for Global Environmental Change (NIGEC), and a proposal submitted by a Northern consortium to study carbon and water budgets over the upper Missouri River Basin in consideration of the GEWEX/GCIP Northwest study area. EDC possesses the capacity for the management, processing, field validation and analysis of hyperspectral data, hence our requirements are only for data acquisition. We request two AVIRIS overflights at each of two grasslands test sites (4 total): two at the Tallgrass Prairie Preserve Oklahoma, within the Atmospheric Radiation Measurement program's Clouds and Radiation Testbed region (ARM/CART), a warm season tallgrass prairie in the southern Flint Hills; and two at the Niobrara Valley Preserve in Nebraska, partially within the Sand Hills, a prairie having a mixture of warm season and cool season grasses. The Tallgrass site is an area where tallgrass prairie has seen an increase in invasive oak species due primarily to changes in burning practices as lands are taken out of rangeland, and the study at this site will use linear mixture modeling to identify the degree to which these species are intruding into the grasslands. The Niobrara site serves two purposes: first, the identification of cedar and sumac species intruding into the Sand Hills grasslands, and also to determine the effect of the bright, sandy soils on vegetation species identification. At both sites, attempts will be made to identify nitrogen and lignin content and (indirectly) relationships between hyperspectral signatures and expressions of stable carbon isotope ratios as indicators of warm season or cold season grasses (C4 & C3 photosynthetic pathways).

Transition Plan:
The primary purposes of this study are to (1) improve the ability to characterize grasslands land cover, (2) determine the sensitivity of grasslands signatures to various influences, such as soil brightness, atmospheric conditions, and woody species invasion. It is anticipated that these findings will be applicable to the study of the effects of land management and climate on grasslands ecosystems function and species biodiversity.

Milestones:
summer 1997: overflight at Tallgrass prairie (peak greenness; late July to early August)
fall 1997: overflight at Tallgrass prairie (post greenness; late October to early November)
January 1, 1998: interim report on Tallgrass prairie
spring 1998: overflight at Niobrara (onset of cool season grasses; before May 1)
summer 1998: overflight at Niobrara (post cool-season, late June to early August)
January 1, 1999: final report on Niobrara study.

Detection and Mapping of Leafy Spurge at Theodore Roosevelt National Park and Vicinity Using AVIRIS Hyperspectral Imaging.

Personnel:
PI's are Dr. Ralph Root, USGS-BRD, Steve Hager, Theodore Roosevelt National Park, Gerald Anderson, Agricultural Research Service, Dr. Susan Ustin and Larry Costick, University of California - Davis, Jim Smith, NASA-GSFC, and Robert Green, NASA-JPL.

Objective:
The objective of this project is to determine the extent to which hyperspectral imaging can be used to develop automated methods for detecting and mapping the extent of the leafy spurge *(Euphorbia esula L.)* infestation in Theodore Roosevelt National Park

Background:
Leafy spurge *(Euphorbia esula L.)* is a troublesome invasive non-native plant on the Northern Great Plains of the United States. Current research shows that leafy spurge is a serious invader into the south unit of Theodore Roosevelt National Park (THRO) near Medora, North Dakota. This aggressive invasion has displaced many native plant species. In addition to destroying the rich species diversity unique to the badlands, significant ecological impacts are resulting. Infestations have grown from 13 ha. in 1972 to an estimated 702 ha. in 1993, 4% of the park's 18,680 ha. land base. Currently, leafy spurge is the number one resource threat to the park and environs. The Resource Management Plan of Theodore Roosevelt National Park identifies a requirement of intensive management to reduce and contain these infestations in keeping with the "preserve and protect" mandate of the National Park Service.

Geographic Information System (GIS) and remote sensing technologies have recently been integrated at THRO for a variety of natural resource applications, including mapping the distribution of non-native invasive plant species. Prior to 1993, mapping of leafy spurge was derived from ground estimates delineated on topographic maps. In 1993, Theodore Roosevelt National Park entered into a cooperative agreement with the Agricultural Research Service (ARS) in Weslaco, Texas to map the infestation using low-altitude aerial photographs. Interpretation of these photographs identified 702 ha. of leafy spurge and provided a digital product which was incorporated into the park's GIS in 1995. While this process produced a relatively accurate product, it required extensive preparation and personnel commitment. More automated techniques for monitoring the status of leafy spurge on a seasonal basis clearly would enhance the efficiency and effectiveness of control measures.

Transition Plan:
The resulting information will be incorporated into the park's GIS and used to develop Integrated Pest Management (IPM) strategies (chemical treatment and biological control) and evaluate control measures. These data will also support a major USGS-Biological Research Division (BRD) project at Theodore Roosevelt National Park designed to quantify the impact of leafy spurge on native vegetation and determine the effectiveness of Integrated Pest Management (IPM) techniques.

Milestones:
AVIRIS flight planning and mission execution, May-June, 1998.
Project preparation: January , May, 1998.
Ground data collection preparation, March-April, 1998.
Low altitude aircraft digital video data acquisition, March-June, 1998.
Ground spectrometer field work, May-June, 1998.
AVIRIS data pre-processing, June-July, 1998.
Data analysis, August - September, 1998.

Creation of map products and development of accuracy assessment, October - November, 1998.
Report preparation, June - November 1998.

Mapping of Mercury-containing Mineral Sources in the Owyhee Reservoir Watershed using AVIRIS Imaging

Personnel:
PI's Ron Pearson, Douglas Craft, and David Zimmer, Bureau of Reclamation, Dr. Roger N. Clark, U.S. Geological Survey, and Paul Seronko, Bureau of Land Management

Objectives:
This study proposes to include Landsat TM and AVIRIS mineral classification as a cost effective means for mapping the (largely) exposed surface mineralogy of the watershed and identifying source areas for naturally occurring Mercury containing minerals. Due to the areal extent of the Owyhee watershed, an initial assessment of tributary basins will be conducted using Landsat TM imagery to identify those tributary basins with geologic and mineralogic anomalies related to mining and geologic formations associated with mercury. AVIRIS data will then be acquired over those specific watershed tributaries and the reservoir basin to identify specific suspected sources at the much higher spectral and areal resolution of AVIRIS. The AVIRIS mapping will be used to develop land management plans and reservoir watershed management alternatives to limit the amount of Mercury influent to the reservoir.

Background:
Owyhee Reservoir was constructed during the 1930's by the Bureau of Reclamation, and covers approximately 13,900 acres over a lateral distance of 50 miles. Research projects and data collection activities have been limited. While anthropogenic Mercury source areas have been generally identified, very little is known regarding natural sources in the area. The Bureau of Reclamation is currently performing a baseline survey of Owyhee Reservoir for general chemistry and Mercury fate and transport. The reservoir study is evaluating the fate, transport, and transformation of Mercury in Owyhee Reservoir and inflow streams, and is interested in developing a more detailed knowledge of naturally occuring geologic Mercury source areas in the reservoir watershed. The natural and anthropogenic sources of Mercury in the watershed have produced Mercury bioaccumulation problems in local reservoirs, streams, and water bodies. Both Oregon and Idaho public health organizations have issued fish consumption advisories for Owyhee Reservoir, Antelope Reservoir, and several other watershed streams.

The Owyhee Basin is a large and remote watershed (approximately 11,000 km^2) located in southeastern Oregon (Malheur County), southwestern Idaho (Owyhee County), and a portion of northern Nevada (Elko County). The watershed geology is comprised primarily of igneous rocks: Quarternary and Tertiary silicic volcanic rocks, massive Tertiary tuffaceous sedimentary rocks with interbedding of basalts and

rhyolite, and older Miocene siliceous volcanics, mostly rhyolite and welded tuffs.

Mercury concentrations in watershed soils, measured to date, range from 0.1 - 565 mg/kg, and up to 6.2 mg/kg in rock samples. There are several small Mercury mining prospects in the general region. The Silver City area was also the site of extensive gold and silver mining, milling and extraction during the late 1800's, which introduced a significant anthropogenic source of Mercury to the watershed.

The primary occurrence of Mercury is in the mineral cinnabar, Mercury sulphide, which is associated with younger low-temperature hydrothermal systems in regions of late Tertiary orogeny and volcanic acitivity. Mercury deposits in the Owyhee Basin are located in altered tuff and tuffaceous lakebeds that have been silicified to opaline deposits. Erosion and transport of soils from these deposits may result in adsorption of Mercury onto suspended particles. In low pH environments, such as conditions produced in acid mine or acid rock drainage, or in natural low pH environments, inorganic Mercury is converted by anaerobic bacteria to methylmercury which is more mobile. Significant mining activity has occurred in the Jordan River watershed a major tributary to the Owyhee Reservoir.

The spectral resolution of AVIRIS is needed to discriminate the occurrences of natural deposits of Cinnabar and where Mercury is concentrated in the environment by other processes such as mining, or erosion, weathering and leaching of soils. Cinnabar has a very strong absorption in the visible due to a conduction band. The feature is a sharp step function that can be mapped with AVIRIS when concentration is high enough. Other low pH, secondary iron-minerals indicative of mining activity will also be mapped as indicators of possible sources of Mercury, as these same processes release methlymecury into the environment. These low pH, iron-bearing minerals have been successfully mapped and sources of acid rock drainage identified by USGS Spectroscopy Lab and Reclamation, using the Tricorder algorithm at the California Gulch Superfund Site in Leadville, Colorado. Due to the arid climate and volcanic bedrock at the surface, vegetative cover over most of the basin is very sparse and should not pose a significant problem in mapping mineralogy from the AVIRIS spectra..

Transition Plan:
This study will be conducted as a cooperative effort of the Bureau of Reclamation's Technical Service Center and Boise Regional Office, the Bureau of Land Management and the U.S. Geological Survey's Spectroscopy Laboratory. There are a number of other local and state agencies participating in the overall investigations and study of the Owyhee Reservoir watershed.

The ultimate application of AVIRIS imaging data for this project is to provide important information regarding identification and mapping of natural Mercury-source minerals that will be used to identify and implement strategies to reduce the Mercury bioaccumulation problems in this watershed.

This project is important because of several issues. First is the fact that natural mineral sources of Mercury may contribute directly to public heath concerns. Second, the size and remoteness of the watershed makes the application of AVIRIS technology a potentially cost effective mapping technique that may be more routinely applied in other volcanic rock watersheds besides the Owyhee Basin. Third, the mapping of volcanic rock and Mercury-containing minerals represents a scientifically legitimate research topic deserving further development. Finally, the remoteness of the reservoir watershed and lack of local population has produced a situation where funding for Mercury research is extremely limited. The addition of AVIRIS image data would certainly help existing modest programs attempting to provide the information needed to identify a reservoir or land management plan to reduce the Mercury public health impacts

Milestones:
Acquisition of Landsat TM imagery of entire watershed in 1997.
Mapping geologic anomalies using band ratios 5/7, 3/1, 4/5 of TM images.
Selection of tributary basin and reservoir area for AVIRIS flightline(s), early 1998.
Development and calibration of mineralogy using USGS "Tricorder" algorithm.
Analysis and mapping of AVIRIS data.
Publication of research results.
Incorporation of AVIRIS maps into GIS data base.
Assessment and development of watershed management options.
Publication of watershed management assessment.

USING GROUND SPECTRAL IRRADIANCE FOR MODEL CORRECTION OF AVIRIS DATA

Alexander F. H. Goetz[1,2], Kathleen B. Heidebrecht[1], Bruce Kindel[1],
[1]Center for the Study of Earth from Space/CIRES
[2]Department of Geological Sciences
University of Colorado, Boulder, CO 80309

Joseph W. Boardman
Analytical Imaging Geophysics, Boulder, CO 80301

1. Introduction

Over the last decade a series of techniques has been developed to correct hyperspectral imaging sensor data to apparent surface reflectance. The techniques range from the empirical line method (Conel et al, 1987) that makes use of ground target measurements to model-based methods such as ATREM (Gao et al, 1993) that derive parameters from the data themselves to convert radiance to reflectance, and combinations of the above (Clark et al, 1995). Here we describe a technique that combines ground measurements of spectral irradiance with existing radiative transfer models to derive the model equivalent of an empirical line method correction without the need for uniform ground targets of different reflectance.

2. Background

Hyperspectral imaging, with sensors such as AVIRIS, raises the expectation among novice users that a complete reflectance spectrum of the surface can be obtained after atmospheric correction. While this is a reasonable expectation, the reality is that extensive ground calibration at the time of overflight is necessary to derive the proper correction. The correction involves both an additive and a multiplicative term as seen in equation 1.

$$L_\lambda = \frac{\rho_\lambda T_\lambda E_\lambda \cos\theta}{\pi} + L_{p\lambda} \tag{1}$$

$$\rho_\lambda = \frac{\pi\left(L_\lambda - L_{p\lambda}\right)}{T_\lambda E_\lambda \cos\theta} \tag{2}$$

where ρ is the reflectance, E is the exoatmospheric solar irradiance, T is the atmospheric transmission and L_p is the path radiance, all a function of wavelength. The angle between the surface normal and the sun is θ. The reflectance is called "apparent reflectance" because of the uncertainty of the surface attitude (Gao et al, 1993). For simplicity, lambertian scattering from the surface is assumed.

A universally used technique that characterizes both the gain or transmission and the offset or path radiance is called the empirical line method (Conel et al, 1987). It consists of acquiring field reflectance spectra of a bright and dark target in the field, preferably large enough to encompass several pixels. A regression equation is created for each spectral band that provides a relationship between reflectance and raw radiance data. The result is a gain factor that consolidates all the multiplicative influences such as atmospheric transmission, solar irradiance and instrument response as well as an offset that is related to the sensor and the path radiance. The quality of the correction depends heavily on the availability of uniform ground targets of differing albedos located close together.

For the last decade, researchers have been concentrating on developing model-based techniques that derive all the necessary parameters from the image data themselves. These techniques rely on absolute radiometric calibration of the sensor and accurate knowledge of the exoatmospheric solar irradiance. The first attempt to make a rapid pixel by pixel correction (Gao and Goetz, 1990) only accounted for atmospheric transmission associated with water vapor. Later the ATMospheric REMoval Program (ATREM) was developed to account for other atmospheric gases and path radiance (Gao et al, 1993). Green et al (1996) applied the radiative transfer code MODTRAN-3 (Berk et al, 1989; Anderson et al, 1996) to correct for both transmission and path radiance. However, this technique is very computing intensive.

A combination of ATREM and the empirical line method was used successfully by Clark et al (1995) to correct the errors in ATREM by calculating the normalization factors for one pixel and then applying them to the rest of the ATREM-corrected image. While this solves the problem of errors in the model, it still requires well-understood, uniform calibration targets that are normally only found in desert environments.

The following is a description of a potential method, using a surface irradiance measurement at the time of overflight, that can be used to anchor a radiative transfer model for the sun-surface path to calculate the surface - sensor path transmission and scattering components.

3. Technique

3.1 Initial AVIRIS Comparison

The technique relies on determining atmospheric parameters from the spectral irradiance measurements made at the surface which in turn drive the MODTRAN model (Berk et al, 1989) to provide an at-sensor modeled radiance. In our first attempt, an ASD FieldSpec™-FR spectroradiometer (www.asdi.com), covering the region 350-2500 nm was used in the irradiance mode to receive sunlight with a remote cosine receptor. The irradiance spectra were acquired on June 28, 1996, 14:53 GMT at Harvard Forest, MA coincident with an AVIRIS overflight. The data were acquired in a grassy field and subsequently surface reflectance measurements were made with the same instrument. Figure 1 shows the relative coincidence of the irradiance spectra measured and modeled with MODTRAN. The general mismatch short of 600 nm is most likely the result of an improper scattering assumption. The major spikes in the ratio spectrum occur around deep atmospheric absorption features and are possibly the result of improper spectral calibration. The FieldSpec-FR has a wavelength calibration accuracy of ±1 nm.

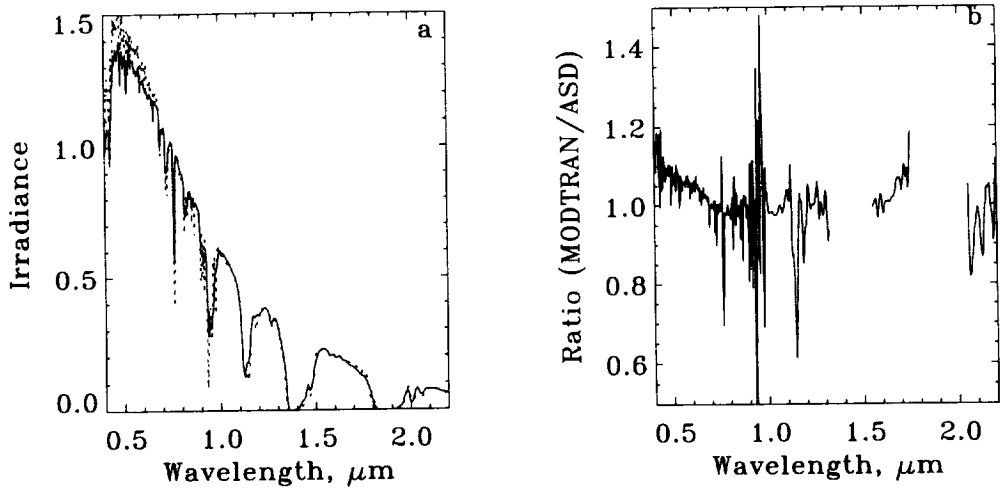

Fig. 1. Measured surface irradiance together with the nearest MODTRAN model (a). The figure (b) is a plot of the ratio between the MODTRAN model and the measured surface irradiance.

Figure 2 shows the surface reflectance derived from ATREM. Figure 3 shows the modeled MODTRAN radiance at AVIRIS altitude using parameters derived from the measured surface irradiance. The resulting reflectance spectrum of the 10-pixel grassy field closely matches the ground measured spectrum. The mismatch short of 600 nm comes from the fact that the scattering term was not correctly derived from the ground spectral irradiance measurements.

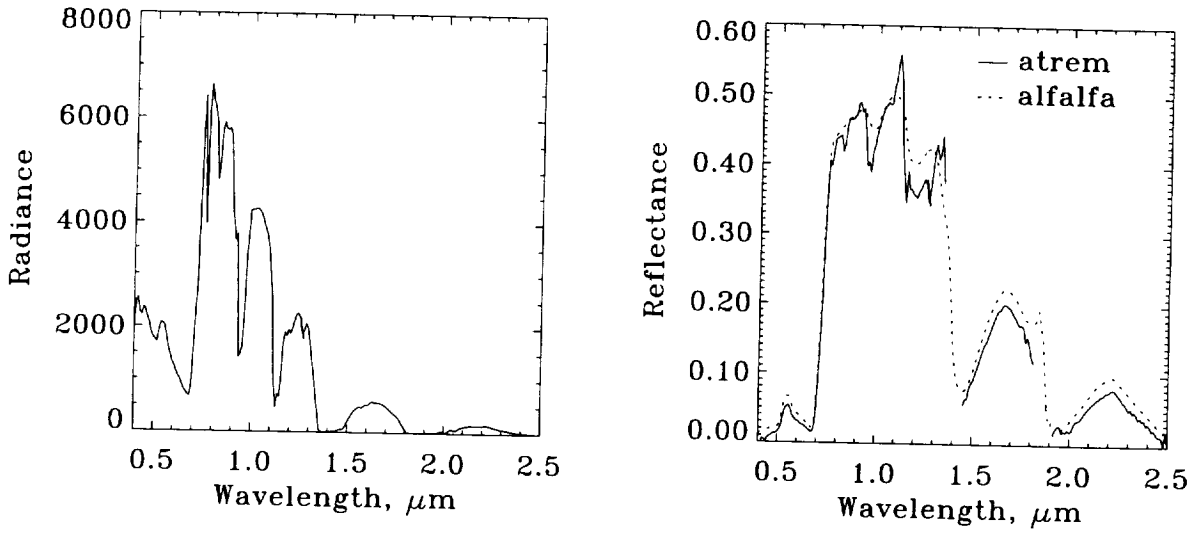

Fig 2. On the left is a plot of the average radiance received by AVIRIS from a group of 10 pixels over a vegetated field in Harvard Forest, MA. The right figure is a reflectance plot derived from ATREM.

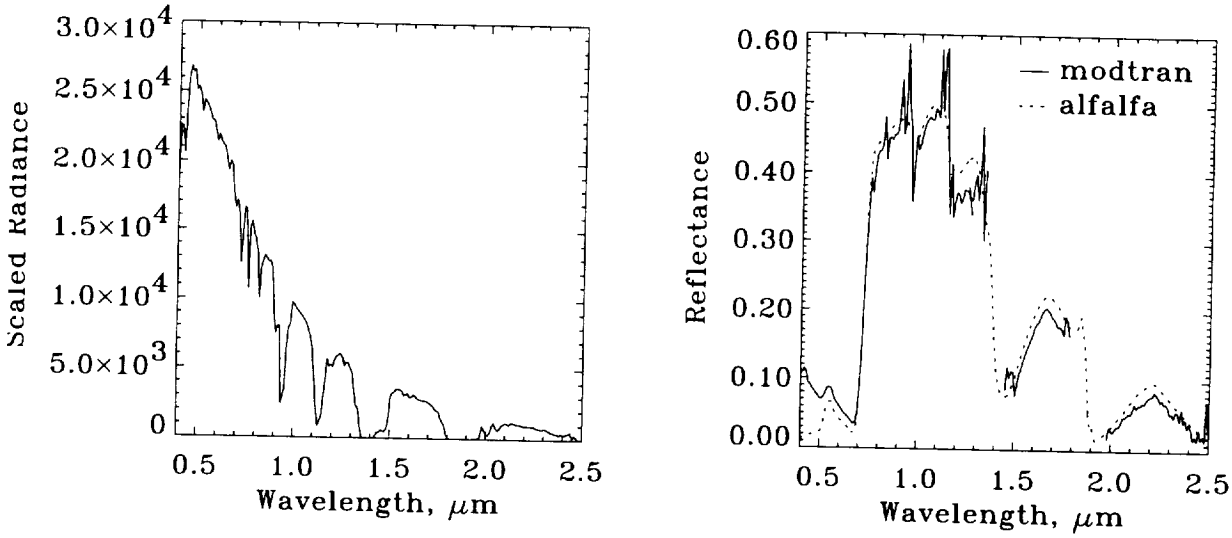

Fig. 3. On the left is the modeled radiance at AVIRIS altitude derived from MODTRAN and the measured surface irradiance. On the right is the reflectance derived from the model and superimposed is the field-measured spectral reflectance from an average taken over the 10-pixel field site. Scattering has not been accounted for, hence the disagreement in the visible region.

3.2 Radiance Databases

The initial attempts to find a MODTRAN model that would match the irradiance spectrum demonstrated that, for practical application, a method for rapid searching was required. Since multiple calculations of a radiative transfer code are too time consuming for pixel-by-pixel corrections, we decided to predetermine a multidimensional lookup table that relates atmospheric parameters to the image pixel radiance spectra. For this purpose, we developed two data bases, the first a set of measured irradiance spectra that includes over 8000 spectra acquired in the summer of 1997 in Boulder, Colorado under a variety of atmospheric conditions. The second data base consists of a series of 13,200 MODTRAN models incorporating combinations of variations in six parameters; zenith angle, water vapor, aerosol, cloud model, visibility and atmosphere profile. The parameters used are given in Table 1. The question remained whether the MODTRAN database represented actual atmospheric conditions.

Table 1: MODTRAN database parameters

ATMOSPHERE PROFILE	WATER VAPOR PROFILE	AEROSOL PROFILE	CLOUD PROFILE	VISIBILITY (km)	ZENITH ANGLE
tropical	tropical	rural	no clouds	5	0
mid-latitude summer	mid-latitude summer	maritime	cumulus	15	36.9
mid-latitude winter	mid-latitude winter	urban	stratus	23	60
subarctic summer	subarctic summer	desert	stratocumulus	50	72.5
subarctic winter	subarctic winter		standard cirrus model	100	84.3
1976 US Standard	1976 US Standard		sub-visual cirrus model		

3.3 Parameterization

The measured and modeled databases were resampled to AVIRIS resolution. A principal components transformation of each database reveals similarity in the dimensionality (fig. 4). Plots of individual eigenvectors show that beyond the first principal component the eigenvectors differ significantly (fig. 5). Mapping the intersection of subspaces revealed that the two data sets share a 10-dimensional spectral space (fig. 6) and that one can be transformed into the other. This property makes it possible to search for a model equivalent to an irradiance measurement rapidly and subsequently use the model parameters to calculate the surface-sensor atmospheric path corrections. Principal components transformation of the intersecting databases shows that the eigenvectors up to the 8th component are nearly identical, as seen in figure 7 and as predicted in figure 4.

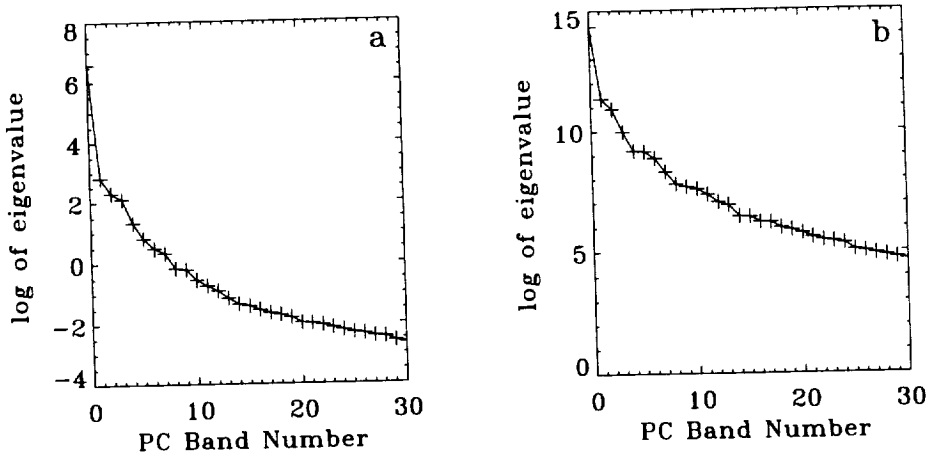

Fig. 4. Eigenvalue plot of the suite of field-measured irradiance spectra (a) and the MODTRAN database spectra (b).

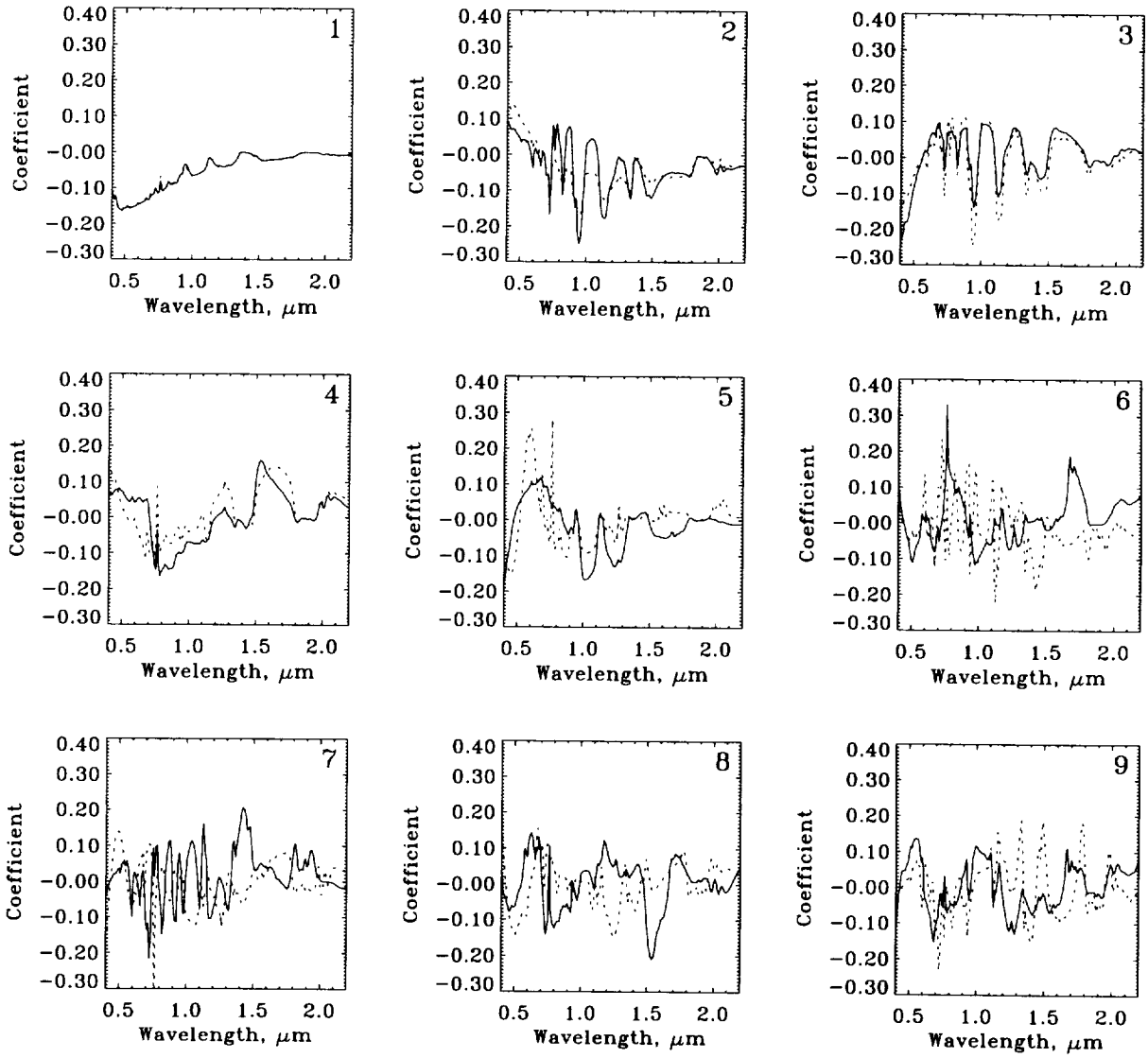

Fig. 5. Nine eigenvectors from the principal component transformation of the measured irradiance spectra (solid line) and the MODTRAN spectra (dashed line)

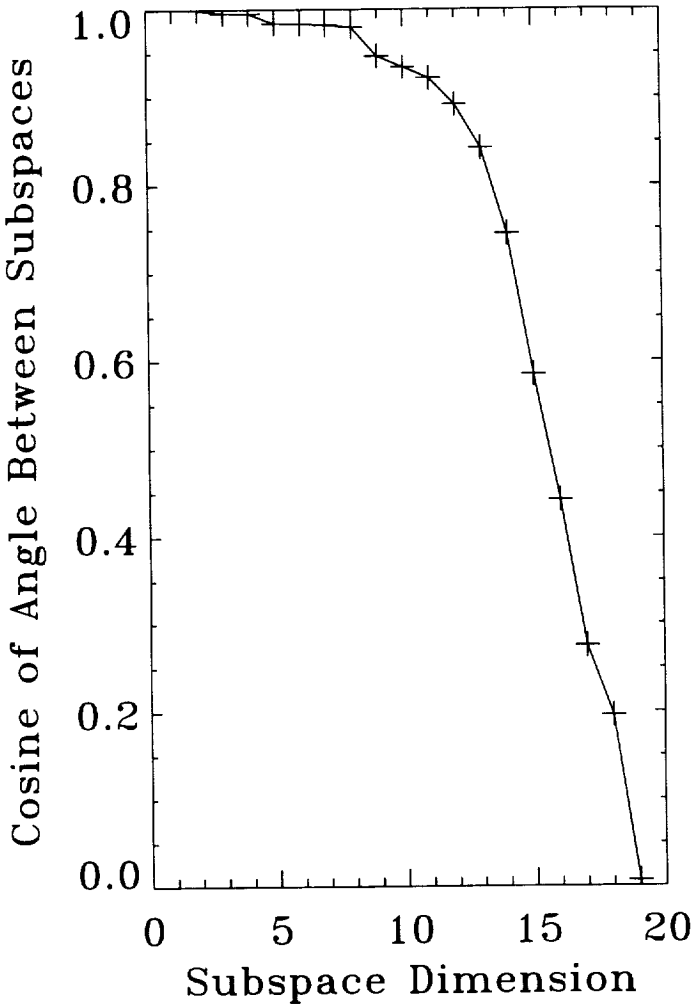

Fig. 6. The quality of match or overlap in 20 space of the irradiance and MODTRAN databases as measured by the angle between subspaces.

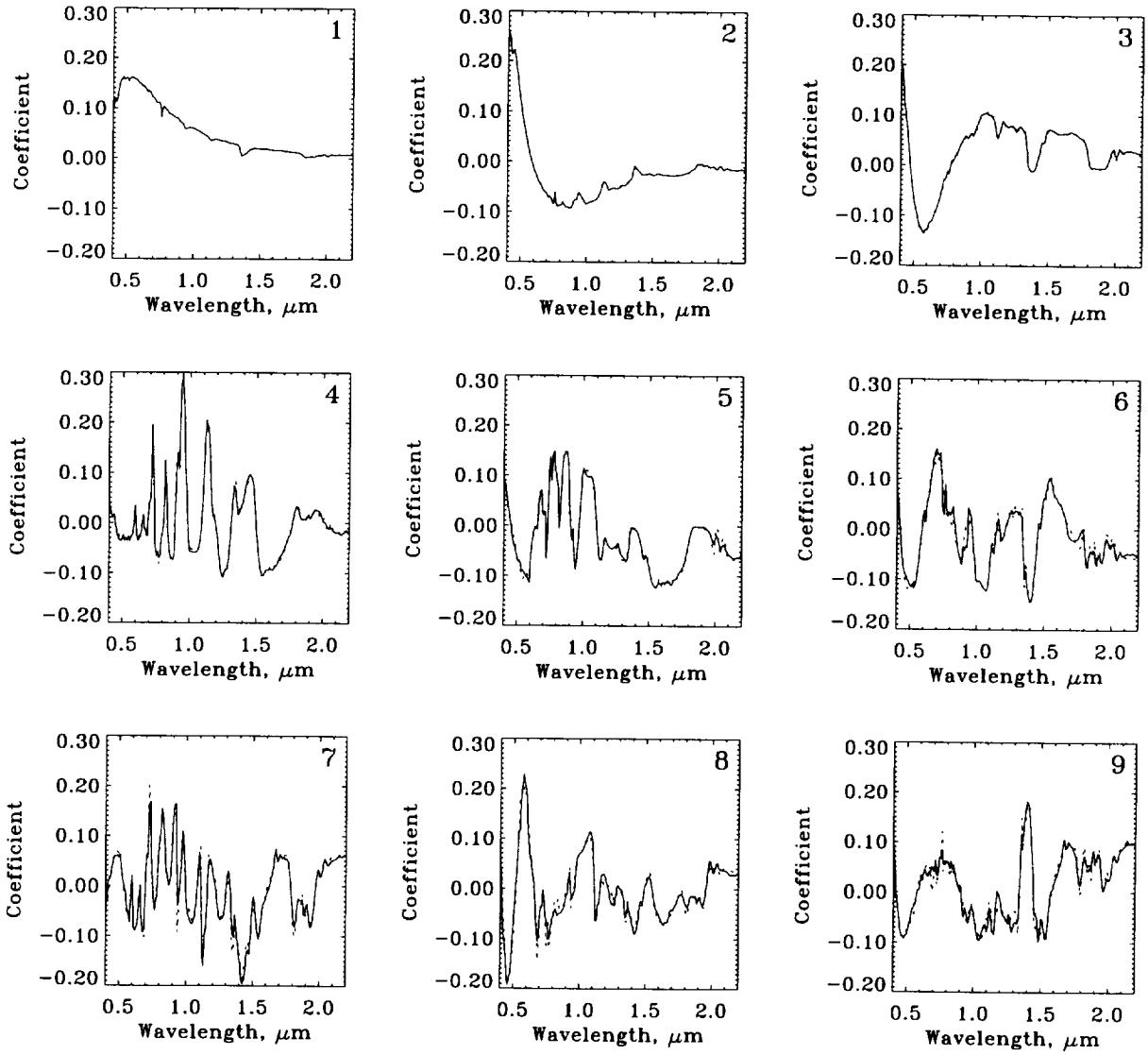

Fig. 7. Nine eigenvectors for the transformed databases. Compare with figure 5.

3.4 Model Search

From above we have shown that irradiance measurements can be compared to MODTRAN models using a statistical transformation. Therefore, spectra in each database can be matched, allowing for rapid searches for MODTRAN parameters that can be used to drive the calculation of the ground-sensor portion of the atmospheric path effects. Using spectra from the Boulder irradiance database, three spectra taken under different conditions were matched with spectra from the MODTRAN database in transform coordinates (fig. 8). The parameters obtained are given in Table 2.

Table 2. Retrieved MODTRAN parameters for 3 irradiance spectra

	Irradiance Spectrum		
MODTRAN parameter	bright	medium	dark
atmosphere	tropical	tropical	mid-latitude summer
water vapor	1.4 cm	1.4 cm	.85 cm
aerosol profile	maritime	desert	urban
cloud profile	sub-visual cirrus	cirrus	stratocumulus
visibility	15 km	100 km	15 km
solar zenith	0	60	0
Actual Conditions			
solar zenith	26.0	48.1	41.3
cloud profile	no clouds	medium cirrus	stratocumulus

The results shown in figure 8 are encouraging in that the values match well in the atmospheric windows. However, the intervals in solar zenith angle and atmospheric water vapor in the MODTRAN database are very coarse and that leads to compensation in other parameters chosen, such as cirrus cover. The MODTRAN modeled transmission in the wings of the water vapor absorption features does not agree with the irradiance measurements and the departures are similar to those seen in model-corrected AVIRIS data.

Analysis of the irradiance and model data sets reveals systematic departures from equivalence that can be ascribed to model inaccuracies in the wings of water vapor features and potential instrument radiometric calibration errors. The systematic errors are very similar to those seen in the gain coefficients derived from the empirical algorithm EFFORT (Boardman, 1998; Goetz et al, 1997).

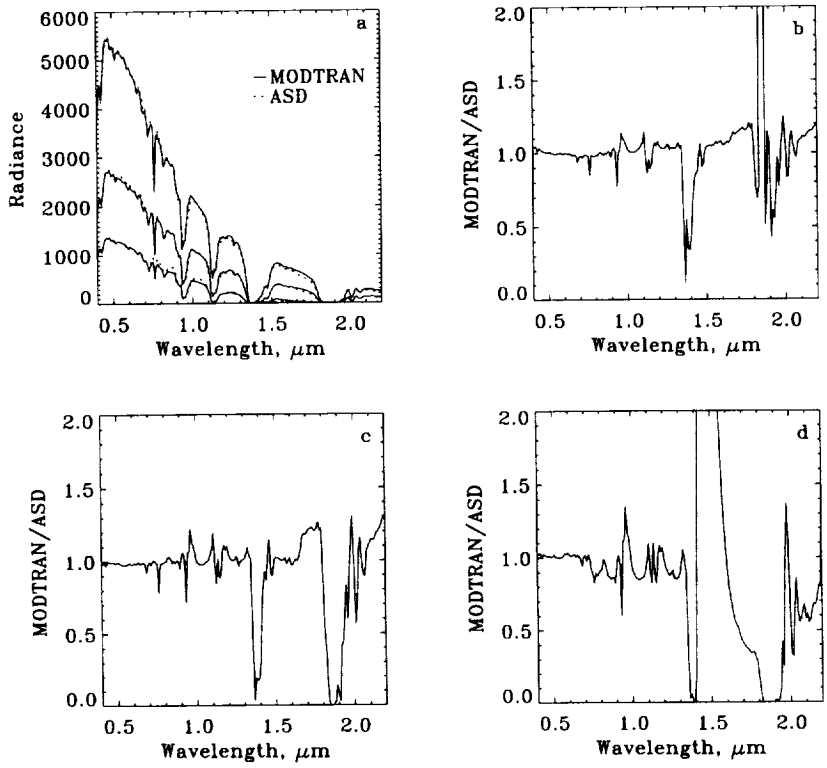

Fig. 8. Results of a search for the best match between 3 irradiance spectra and the MODTRAN database spectra (a). Ratios between the MODTRAN and measured irradiance spectra are shown in b,c,d.

4. Summary and Conclusions

Hyperspectral imaging requires that atmospheric corrections be made in order to be able to exploit the 60% of the 0.4-2.5 μm spectrum influenced by spatially-variable water vapor absorption and other absorbers and scatterers. A number of techniques have been developed to derive apparent surface reflectance from the data themselves. The quality of the results is approximately proportional to the amount of time and effort expended on the correction. Parameterization of the radiative transfer model database makes it possible to develop an ideal lookup table that allows a direct single pixel correction for solar irradiance, aerosol and molecular scattering and gaseous absorption. By utilizing a pixel-by-pixel correction with a rapid algorithm such as ATREM, the residual errors due to differential path length across a scene with topographic relief will be minimized. Furthermore, the processing time will be considerably reduced when compared to first-principles-based, non-linear inversion techniques.

This technique needs further work before it can be applied on a routine basis. Both the measured irradiance and the MODTRAN model databases need to be expanded. The measurement suite of irradiance spectra needs to include conditions of higher water vapor content and greater aerosol loading. These might be obtained from the DOE CART site at which a FieldSpec™FR is being installed to operate continuously. The MODTRAN database needs to be recalculated at a finer resolution in solar zenith angle and water vapor, and surface elevation needs to be added as a parameter.

5. Acknowledgments

This work was supported by NASA under contract no. NAG5-4447 from the Goddard Spaceflight Center and subcontract 95-B26 from the Desert Research Institute.

6. References

Anderson, G., J. Wang, and J.H. Chentwynd, 1995, MODTRAN3: An Update and Recent Validations Against Airborne High Resolution Interferometer Measurements, *Summaries of the Fifth Annual JPL Airborne Earth Science Workshop*, JPL Publication 95-1, Vol. 1, Jet Propulsion Laboratory, Pasadena, CA, 5-8.

Berk, A., L.S. Bernstein and C.C. Robertson, 1989, MODTRAN: A moderate resolution model for LOWTRAN 7, Final Report, GL-TR-0122, AFGL, Hanscom AFB, MA, 42p.

Boardman, J.W., 1998, Post-ATREM Polishing of AVIRIS Apparent Reflectance Using EFFORT: A Lesson in Accuracy Versus Precision, *in This Proceedings.*

Clark, R.N., G.A. Swayze, K.B. Heidebrecht, R.O. Green, and A.F.H. Goetz, 1995, Calibration to Surface Reflectance of Terrestrial Imaging Spectrometry Data, *Summaries of the Fifth Annual JPL Airborne Earth Science Workshop*, JPL Publication 95-1, Vol. 1, Jet Propulsion Laboratory, Pasadena, CA, 41-42

Conel, J.E., R.O. Green, G. Vane, C.J. Bruegge, R.E. Alley, and B. Curtiss, 1987, Airborne Imaging Spectrometer-2: Radiometric spectral characteristics and comparison of ways to compensate for the atmosphere, Proc. *SPIE* **834**, 140-157.

Gao, B.-C., K. B. Heidebrecht, and A. F. H. Goetz, 1993, Derivation of Scaled Surface Reflectances from AVIRIS Data, *Remote Sens. Environ.*, **44**, 165-178.

Goetz A. F. H., J. W. Boardman, B. Kindel and K. B. Heidebrecht, 1997, Atmospheric Corrections: On Deriving Surface Reflectance from Hyperspectral Imagers, Proceedings *SPIE*, **3118**, 14-22.

Green, R.O., D.A. Roberts and J.E. Conel, 1996, Characterization and compensation of the atmosphere for the inversion of AVIRIS calibrated radiance to apparent surface reflectance, in *Summaries of the Sixth Annual JPL Airborne Earth Science Workshop*, **1**, 135-146.

[Gao and Goetz, 1990 is probably:
Gao, B.-C., A.F.H. Goetz, 1990, "Column Atmospheric Water Vapor and Vegetation Liquid Water Retrievals from Airborne Imaging Spectrometer Data," J. Geophys. Res., Vol. 95, no. D4, 3549-3564.]

Issues in Absolute Spectral Radiometric Calibration: Intercomparison of Eight Sources

Alexander F. H. Goetz[1,2], Bruce Kindel[1],
[1]Center for the Study of Earth from Space/CIRES
[2]Department of Geological Sciences, University of Colorado, Boulder, CO 80309

Peter Pilewskie
NASA Ames Research Center, Moffett Field, CA

1. Introduction

The application of atmospheric models to AVIRIS and other spectral imaging data to derive surface reflectance requires that the sensor output be calibrated to absolute radiance (Green et al, 1996; Chrien et al, 1996; Gao et al, 1993). Uncertainties in absolute calibration are to be expected, and claims of ±2% accuracy have been published (Chrien et al, 1996). Measurements of accurate surface albedos and cloud absorption to be used in radiative balance calculations depend critically on knowing the absolute spectral-radiometric response of the sensor. The Earth Observing System project is implementing a rigorous program of absolute radiometric calibration for all optical sensors (Butler and Johnson, 1996a) Since a number of imaging instruments that provide output in terms of absolute radiance are calibrated at different sites, it is important to determine the errors that can be expected among calibration sites. Another question exists about the errors in the absolute knowledge of the exoatmospheric spectral solar irradiance (Nekel and Labs, 1984).

2. Data collection

In order to determine the extent of agreement among laboratory radiometric standards, we performed a round robin set of measurements with an Analytical Spectral Devices Inc. (ASD) FieldSpec™-FR spectroradiometer (www.asdi.com), that covers the range 350-2500 nm continuously to determine the agreement among radiometric sources at several NASA centers, Los Alamos National Lab and the University of Arizona. Both spheres and illuminated panels were measured and compared to the NIST-traceable radiance values documented for the sources.

2.1 Instrument calibration

The FieldSpec was calibrated using a NIST-traceable standard 1000 W quartz halogen lamp, controlled by a regulated power supply (Optronics Laboratories) placed 50 cm from a 10" x 10" Spectralon® (Labsphere Inc.) panel and viewed at 45° from the panel normal. The FieldSpec instrument feeds light through an optical fiberbundle with an acceptance angle of 25°. The irradiance from the bulb at the flat panel is not uniform because the bulb is emitting a spherical waveform. Instrument no. 607 was used throughout the study that extended from February through September 1997. Calibration at the ASD factory was repeated five times from October 1996 through September 1997. In September 1997, the error associated with the non-uniform panel illumination was discovered and the fiberoptic bundle was moved toward the panel until no further change in radiance was noted. The absolute error of the earlier measurements amounted to 3.5% and all these were corrected accordingly. The precision of the corrected measurements, as defined by the RMS error, was better than ± 2% at wavelengths greater than 500 nm. At shorter wavelengths, the error increased (fig. 1).

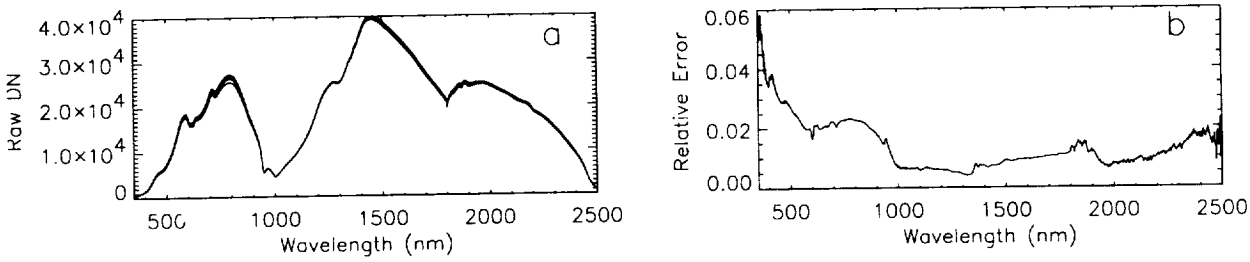

Fig. 1. (a) Raw DN plots of the five calibrations of FieldSpec no. 607 made between October 1996 and September 1997. (b) RMS calibration error derived from the five calibration spectra plotted in (a).

In each of the measurements described below, ASD calibration closest in time was used for comparison. The instrument was switched on at least 90 minutes before each measurement. A measurement consisted of an average of 50-100 ms spectra and 50 dark measurements. The VNIR data were corrected for the temperature-sensitive gain in the 750-1000 nm region with a parabolic fitting routine called "pcorrect" (www.asdi.com)

2.2 Los Alamos National Laboratory

Two visits on April 8 and May 29, 1997 were made to the DOE Los Alamos National laboratory (LANL) to measure the sphere being used to calibrate the MTI optical sensor. The 30 cm diameter sphere was constructed and calibrated by Labsphere Inc. and subsequently recalibrated by NIST. The FieldSpec fiberoptic was positioned 6 cm from the sphere entrance. The sphere was then rotated 14 degrees from normal to match the calibration configuration at both Labsphere and NIST. The sphere is continuously flushed with dry nitrogen. Figure 2 shows the ratio of the two different measurements made 51 days apart showing a precision of 1% or better at wavelengths longer than 600 nm.

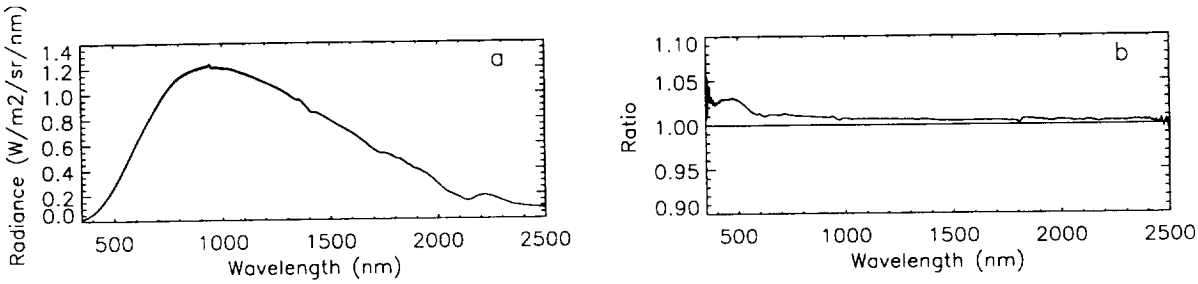

Fig. 2. (a) Radiance of the LANL sphere taken 51 days apart. (b) Radiance of the radiance spectra.

The absolute measurements, however, show greater differences. The calibration for the wavelengths covered are given for only 19 points chosen by NIST and Labsphere. In contrast the FieldSpec provides data at 1194 wavelengths before resampling to 1 nm intervals. Figure 3 shows the 19 values measured by Labsphere and NIST as well as the continuous spectrum measured with FieldSpec. The Labsphere and ASD measurements are nearly identical between 500 and 2300 nm. The greatest discrepancy between the ASD measurements and the NIST prediction is 5% between 500 and 2000 nm. The continuous spectrum shows significant departures from the values interpolated between the 19 points, particularly near 2200 nm.. These are associated with the spectral reflectance of Spectralon® and, if not accounted for, could cause the Spectralon spectral features to be superimposed on sensor data.

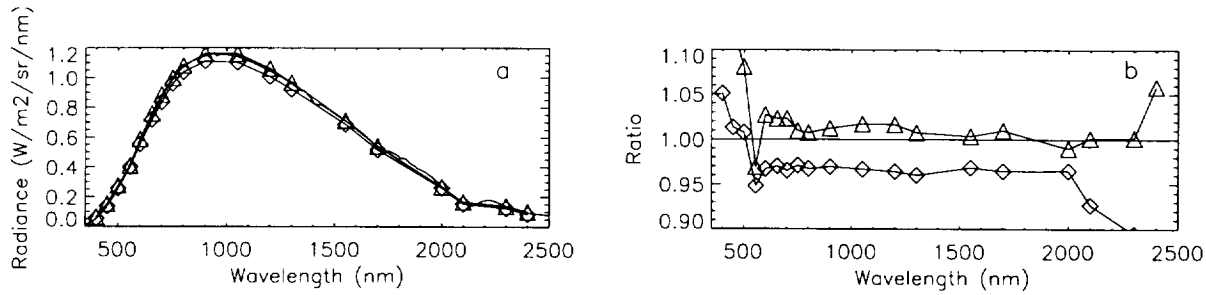

Fig. 3. (a) Radiance measured from the LANL sphere. Squares represent the NIST calibration, triangles the Labsphere calibration and the continuous curve the ASD FieldSpec. (b) Ratios of the Labsphere and NIST calibrations against the ASD FieldSpec measurement.

2.3 Jet Propulsion Laboratory

At the NASA Jet Propulsion Lab (JPL), measurements were made of the AVIRIS laboratory lamp and Spectralon standard on June 4, 1997. The setup, including lamp and power supply, is equivalent to the ASD calibration configuration. This setup differs in geometry from the AVIRIS ER-2 field calibration system (Chrien et al, 1996) and we were not able to measure the AVIRIS calibrator successfully. The comparisons of the JPL and ASD FieldSpec measurements are shown in figure 4. The agreement is better than 2% between 700 and 2500 nm but departs significantly at shorter wavelengths.

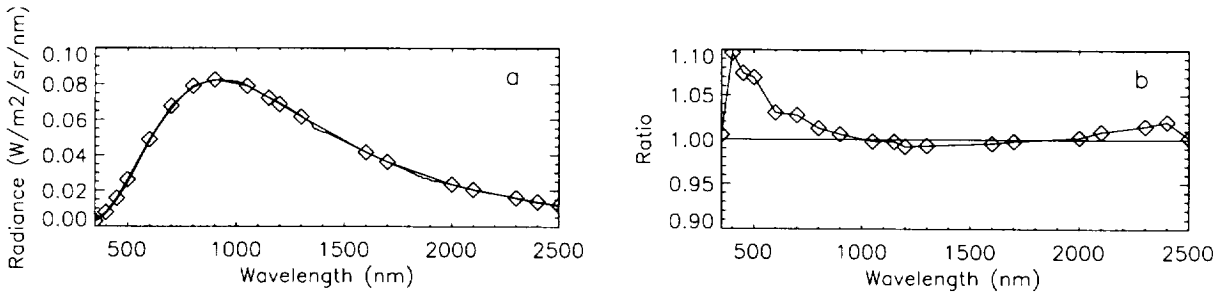

Fig. 4. (a) Radiance from the JPL lamp and Spectralon panel. The lamp calibration, traceable to NIST, is represented by squares and the continuous curve is the ASD FieldSpec measurement. (b) Ratio of the measurement and calibration values.

2.4 Goddard Space Flight Center

The Goddard Space Flight Center (GSFC) was visited on June 13, 1997. At GSFC there are three different spheres used for calibration of a variety of imaging instruments. The largest is approximately 1.8 m in diameter containing 12 lamps of 200W each, and coated with barium sulfate. The second is a 1.2 m diameter hemisphere, coated with barium sulfate and containing 12 lamps of 100 W each. The SeaWifs calibration sphere is 1.2 m in diameter and also coated with barium sulfate.

The 1.8 m sphere and the hemisphere have continuous calibration with wavelength, while the SeaWifs sphere is only calibrated to 1160 nm. The FieldSpec-measured and calibration values provided by GSFC are shown in figure 5. These spheres were not flushed with dry nitrogen and the effects of the humidity are dramatic. The fact that a photon that exits the sphere has been scattered off the sphere wall many times, adds as much as 50 m to the path the photon travels through the atmosphere. In the ratio plot of the 1.8 m sphere /FieldSpec comparison, the atmospheric O_2 absorption at 762 nm is visible. Water vapor features affect the majority of the SWIR spectrum which argues strongly for dry gas flushing of the large spheres. In both the sphere and the hemisphere plots, the

disagreements are greater than 5% in the visible region of the spectrum and greater than 10% in and around the water vapor absorption features.

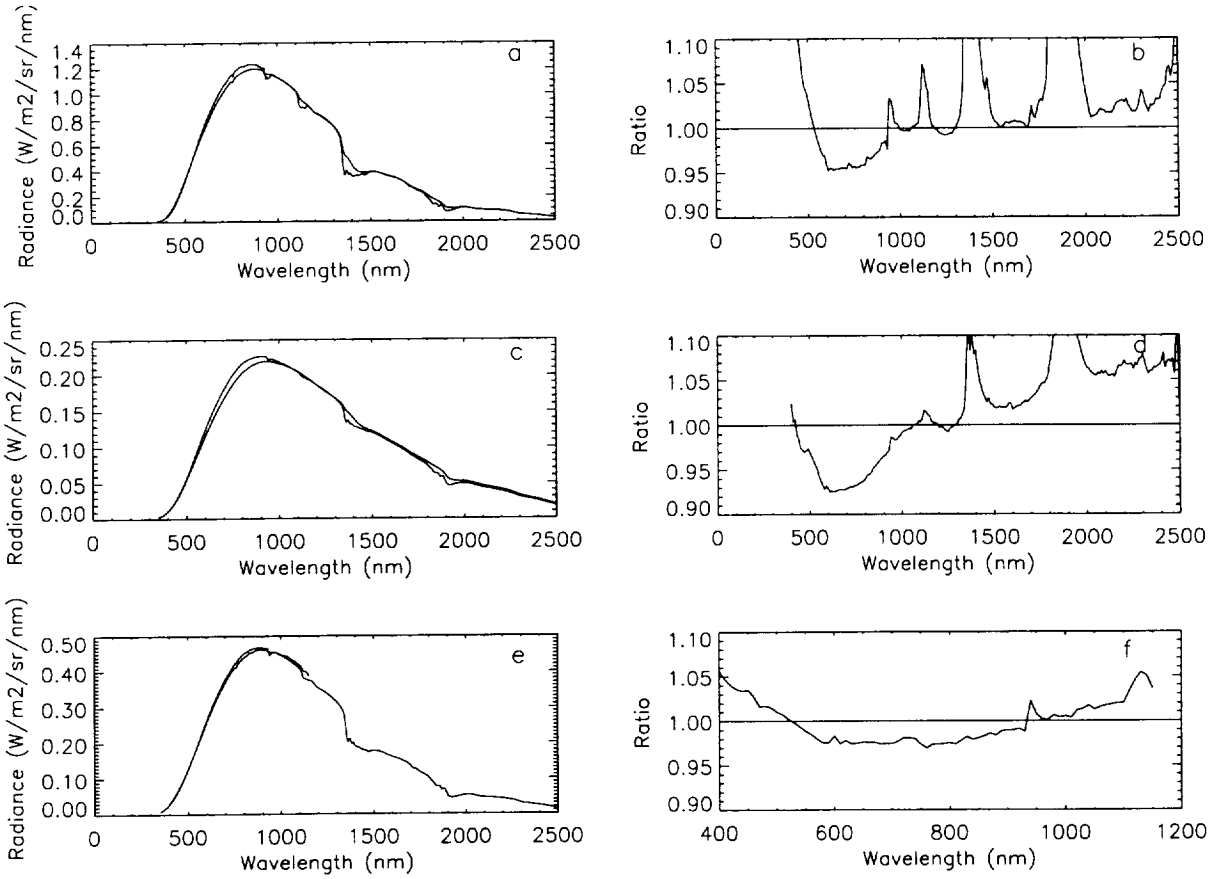

Fig. 5. Measurements of three GSFC spheres with the accompanying calibration values on the left and the ratio of the values on the right. The measurements were taken on a very humid day.

2.5 University of Arizona

The University of Arizona (U of A) calibration laboratory is located in the Optical Sciences Center. Measurements were made on September 22, 1997. The U of A sphere contains 10-150 W bulbs and two quantum efficiency transfer radiometers. This facility is one taking part in the EOS calibration round-robin (Butler and Johnson, 1996b). The laboratory is equipped with VNIR and SWIR filter radiometers that have been calibrated against a NIST standard bulb. Figure 6 shows the comparison of the sphere radiance as measured with the filter radiometers covering 16 wavelengths and the ASD Fieldspec. The ratio plot shows that there is a significant and consistent disagreement of 5 to 12% throughout the spectral region. The cause of this disagreement is not understood.

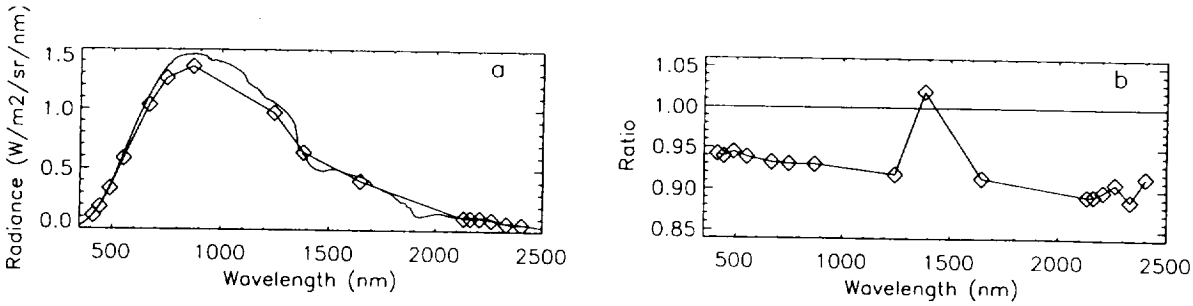

Fig. 6. (a) Measurements and calibration values for the University of Arizona sphere. (b) Ratio of the U of A values and the ASD FieldSpec measurements.

2.6 Ames Research Center

In February, 1997, 2 spheres and two standard lamp-panel combinations were measured. An Epply standard lamp calibration determined from the ASD FieldSpec measurement was used to calibrate the Solar Spectral Flux Radiometer (SSFR). Measurements of downwelling spectral irradiance at 21 km were made with the SSFR mounted in the ER-2. Figure 7 shows the measurement as compared to the MODTRAN-modeled irradiance (Anderson et al, 1995; Berk et al, 1989). For comparison, the top-of- atmosphere (TOA) irradiance is also plotted (Nekel and Labs, 1984). The agreement between the modeled and measured irradiances is better than 5% longward of 500 nm.

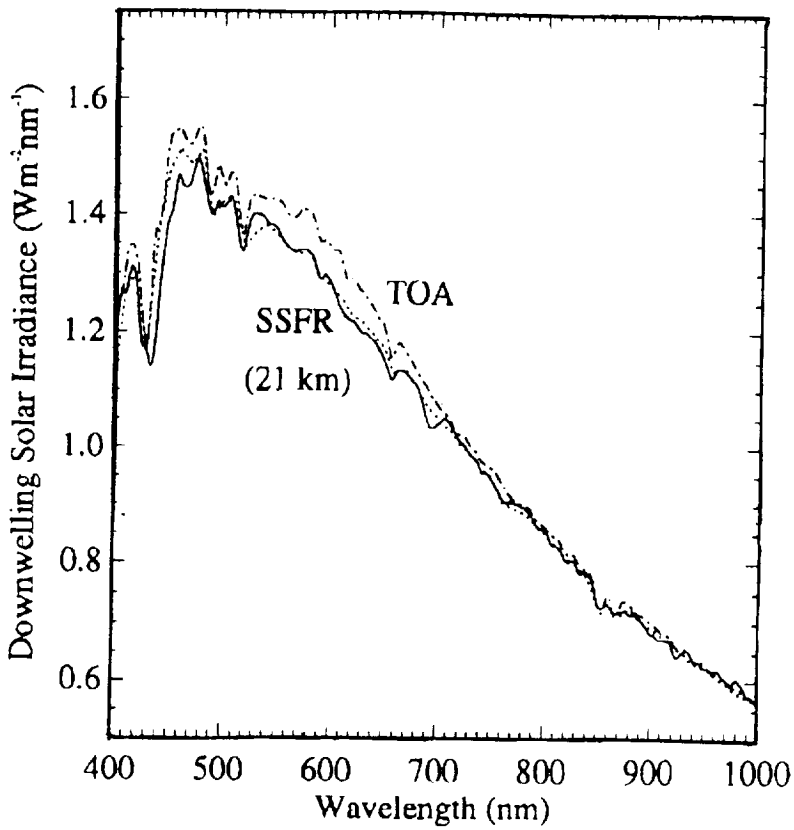

Fig. 7. Downwelling solar irradiance as measured from the ER-2 at 21 km altitude with the NASA Ames Research Center SSFR scanning spectrometer (solid). The dashed line is the exoatmospheric solar irradiance (Nekels and Lab, 1984) and the dotted line the MODTRAN modeled irradiance.

3. Summary and conclusions

The informal round robin measurement of radiometric sources conducted here shows the relative accuracy in absolute calibration of important sources for image sensor calibration is variable but usually within ±5% at wavelengths longer than 500 nm. However, interpolating radiance values between the NIST standard wavelengths can lead to significant errors for instruments like AVIRIS that cover the entire spectral range continuously. The measurements were made possible by the availability of a long-term precise, portable spectroradiometer.

Spheres, especially large ones, have variable output in the spectral regions affected by water vapor absorption. These spheres should be flooded with dry nitrogen to eliminate absorption and to keep water from being adsorbed in the barium sulfate coating. The discrepancies in the U of A sphere measurements have yet to be understood. Since all the other measurements were closer by approximately a factor of two, the discrepancy is particularly puzzling.

4. Acknowledgments

This work was supported by NASA under contract no. NAG5-4447 from the Goddard Spaceflight Center and subcontract 95-B26 from the Desert Research Institute. Particular thanks to Brian Curtiss and Dave Beal of Analytical Spectral Devices Inc. for the long-term loan of instrument 607 and for the 5 gratis calibrations. The authors wish to thank the personnel at each of the calibration facilities, in particular Steve Bender at LANL, Chris Chovit at JPL, Peter Abel and John Cooper at GSFC and Stuart Biggar at the University of Arizona.

References

Anderson, G.P., J. Wang, and J. H. Chentwynd, 1995, MODTRAN3: An Update and Recent Validations Against Airborne High Resolution Interferometer Measurements, *Summaries of the Fifth Annual JPL Airborne Earth Science Workshop,* **1**, 5-8.

Berk, A., L.S. Bernstein and C.C. Robertson, 1989, MODTRAN: A moderate resolution model for LOWTRAN 7, Final Report, GL-TR-0122, AFGL, Hanscom AFB, MA, 42p.

Butler, J. J. and B. C. Johnson, 1996a, Organization and Implementation of Calibration in the EOS Project, Part 1, *The Earth Observer,*. Vol. 8, No. 1.

Butler, J. J. and B. C. Johnson, 1996b, Calibration in the EOS Project Part 2: Implementation, *The Earth Observer,* Vol. 8, No. 2.

Chrien, T.G., R.O. Green, C.J. Chovit, M.L. Eastwood and C.M Sarture, 1996, Calibration of the Airborne/Infrared Imaging Spectrometer in the Laboratory, *Summaries of the Sixth Annual JPL Airborne Earth Science Workshop*, **1**, 39-48.

Gao, B.-C., K. B. Heidebrecht, and A. F. H. Goetz, 1993, Derivation of Scaled Surface Reflectances from AVIRIS Data, *Remote Sens. Environ.*, **44**, 165-178.

Nekel, H. and D. Labs, 1984, The Solar Radiation between 3300 and 12500 Angstroms, *Solar Physics,* **90,** 205.

Apparent Surface Reflectance of the DOE ARM SGP CART Central Site Derived from AVIRIS Spectral Images

Robert O. Green
Jet Propulsion Laboratory, California Institute of Technology

1.0 Introduction

The primary objective of the Department of Energy (DOE) Atmospheric Radiation Measurement (ARM) Program at the Southern Great Plains (SGP) Cloud and Radiation Testbed (CART) is to acquire in situ and remote sensing data to improve cloud and atmospheric radiative models and parameterizations. As a consequence of this program, a large number of atmosphere and surface measurements are being acquired at the ARM SGP CART central site. NASA's Airborne Visible/Infrared Imaging Spectrometer (AVIRIS) overflew this site on August 1, 1997. AVIRIS measures the upwelling spectral solar radiance from 400 to 2500 nm at 10-nm intervals. From 20 km altitude, these calibrated spectra are acquired as images of 11 by up to 800 km with 20-by-20 m spatial resolution. These data were acquired at the ARM SGP CART Central Site to first investigate derivation of atmospheric parameters from the measured spectra, second study the variation of these parameters, and third demonstrate the inversion of the calibrated radiance spectra to apparent surface reflectance. These objectives have been pursued with AVIRIS data at other sites for atmospheric water vapor (Conel et al. 1988, Gao et al. 1990, Green et al. 1991, Green et al. 1995) and derivation of apparent surface reflectance (Green et al. 1988, Green et al. 1990, Gao et al. 1993, Green et al. 1993, Clark et al. 1995, and Green et al. 1996).

2.0 AVIRIS data

On August 1, 1997, two intersecting AVIRIS flight lines were acquired over the ARM SGP CART Central Site (Table 1). Analysis has concentrated on the portion of the North-South flight line that includes the Central Site (Figure 1). This image contains agricultural fields both cleared and planted as well as roads, structures and sections of a river. A set of AVIRIS calibrated radiance spectra were extracted from vegetated and soil targets in this image (Figure 2). Both the atmosphere and surface cover are modifying the upwelling spectral radiance measured by AVIRIS near the top of the atmosphere and 20,000 m altitude. Atmospheric radiation measurement is the primary objective of the ARM program. Effects of atmospheric scattering dominate toward 400 nm, while atmospheric water vapor absorptions are present at 940, 1140, 1400, 1900 and 2500 nm. Surface reflectance modifies the upwelling radiance across the entire spectra in these clear sky AVIRIS measurements.

Table 1. Start and stop latitude, longitude and time for the AVIRIS flight lines.

Flight Date	Start Latitude	Stop Latitude	Start Longitude	Stop Longitude	Start Time	Stop Time
f970801	+036.800	+036.533	-98.033	-97.300	17.516	17.616
f970801	+036.350	+036.800	-97.566	-97.416	17.716	17.800

3.0 Characterization of the Atmosphere

The first objective of this investigation was to pursue the derivation of atmospheric parameters from the AVIRIS calibrated radiance. Water vapor is the principal atmospheric parameter of interest because of the range of variability through space and time as well as the strong absorption bands present in much of the solar reflected spectrum. An inversion algorithm that uses a nonlinear least squares fit between the measured AVIRIS spectrum with a MODTRAN (Kneizys et al. 1987, Berk et al. 1989, and Anderson et al. 1995) modeled spectra at the 940-nm water vapor band was applied. This algorithm simultaneously parameterizes the surface liquid water expressed in plant leaves, the background spectral reflectance as well as the water vapor. Close fits were achieved between the AVIRIS measured spectra and the MODTRAN modeled spectra with small residual errors (Figure 3). The algorithm operates on each spectrum and was applied to the entire DOE ARM SGP CART Central Site AVIRIS image (Figure 4). Total column water vapor amounts ranging from 38 to 41 mm precipitable water vapor were derived throughout the AVIRIS data set. The algorithm was not applied to regions with standing water present on the surface where the upwelling radiance at 940 nm approached zero. The second objective of this investigation was fulfilled by exploring the spatial variation of water vapor in the AVIRIS image. A histogram of the derived water vapor was calculated to show the range and frequency of water vapor derived from the AVIRIS spectra (Figure 5). A significant patchiness was measured in the water vapor image with gradients from 39 to 41 mm present at lateral scales of 500 m. This variation in water vapor provides the basis for the requirement to calculate the total column water vapor for every spectrum in the image. A single average value for the entire image is not sufficient.

In addition to the water vapor absorption at 940 nm, liquid water absorbs energy at 980 nm. To solve for the water vapor, the liquid water must be accounted for as a parameter in the nonlinear least square parameter fit (Green et al. 1991). If the liquid water was uncompensated, the water vapor would be over estimated in areas of vegetation. The image of liquid water derived from AVIRIS at the ARM SGP CART Central Site shows variation from 0.0 mm liquid water in cleared agricultural fields to 5.2 mm equivalent liquid water in some crops and in riparian vegetation (Figure 6).

4.0 Derived Apparent Surface Reflectance

The third objective of the investigation was to demonstrate the inversion of the calibrated AVIRIS radiance spectra to the apparent spectral reflectance of the surface. This inversion compensates for the atmospheric and solar irradiance components present in the total upwelling radiance measured by AVIRIS. The apparent reflectance is essential to derive surface material composition for research and applications based on the expressed molecular absorption and particle scattering characteristics. The apparent surface reflectance also contributes to the reflected radiance that is absorbed and scattered in the atmosphere and is therefore relevant to the ARM objectives. For this reflectance inversion, the radiance at AVIRIS is expressed in terms of the solar, surface and atmospheric contributions for a plane parallel atmosphere and surface (Equation 1). This equation is solved for surface reflectance with respect to a horizontal 100% Lambertian target (Equation 2). For each spectrum in the AVIRIS image, this equation is constrained by the latitude, longitude, time, and surface elevation. The equation is additionally constrained by the AVIRIS derived atmospheric water vapor. The well mixed gases of the atmosphere are constrained with the surface pressure height. Ozone is constrained by measurement from the TIROS Operational Vertical Sounder. Finally, aerosols are constrained regionally to be an estimate of the visibility with feedback from the AVIRIS water vapor fit. With these constraints the equation is solved for each spectrum in the AVIRIS image.

$$L_t = F_0\rho_a/\pi + F_0T_d\,\rho T_u/\pi\,/(1-S\rho) \qquad \text{Equation (1)}$$

L_t	total upwelling spectral incident at AVIRIS.
F_0	exoatmospheric solar irradiance.
ρ_a	atmospheric reflectance.
T_d	downward direct and diffuse transmittance of the atmosphere.
ρ	apparent lambertion surface reflectance
T_u	upward total atmospheric transmittance to the AVIRIS.

$$\rho_g = 1 / [\{(F_0T_dT_u/\pi) / (L_t - F_0\rho_a/\pi)\} + S] \qquad \text{Equation (2)}$$

For the ARM SGP CART Central Site, the apparent surface reflectance was calculated for all AVIRIS spectra. Spectra from different types of vegetation and soils show good compensation for the atmosphere (Figure 7). Vegetation spectra show the expected absorption of chlorophyll and ancillary pigments in the 400- to 700-nm region and the absorption of liquid water at 980, 1190, 1450, 2000, and 2500 nm. The soils show weak absorptions of chlorophyll from mixed vegetation in the 20- by 20-m spatial resolution. One example soil spectrum shows a strong carbonate absorption at 2300 nm in the solar reflected spectrum.

5.0 Conclusion

The objectives of this investigation were first to derive atmospheric parameters from AVIRIS calibration radiance spectra, second to examine the variability of the atmosphere, and third to invert the AVIRIS measured radiance to apparent surface reflectance. These objectives were achieved with respect to the atmospheric parameter of total column water vapor and apparent surface reflectance at the DOE ARM SGP CART Central Site. The water vapor images and derived apparent surface reflectance data are available to contribute directly to the ARM objectives at this site. Future research will pursue the derivation of atmospheric aerosols and investigation of the change in the atmosphere between the two AVIRIS flight lines.

6.0 Acknowledgments

The majority of the work described in this paper was carried out at the Jet Propulsion Laboratory, California Institute of technology, under contract with the National Aeronautics and Space Administration. A portion of the work was performed at the Institute for Computational Earth System Science, University of California, Santa Barbara, CA. I would like to express my appreciation for the efforts of the AVIRIS at the Jet Propulsion Laboratory.

7.0 References

Anderson, G. P., J. Wang, and J. H. Chetwynd (1995), "MODTRAN3: An Update And Recent Validations Against Airborne High Resolution Interferometer Measurements," Summaries of the Fifth Annual JPL Airborne Earth Science Workshop, Jet Propulsion Laboratory, Pasadena, CA, JPL 95-1, Vol. 1: AVIRIS Workshop, pp.5-8.

Berk, A., L. S. Bernstein, and D. C. Robertson, MODTRAN: A Moderate Resolution Model for LOWTRAN 7, Final Report, GL-TR-0122, AFGL, Hanscom AFB, MA, 42 pp., 1989.

Clark, R. N., G. A. Swayze, K. Heidebrecht, R. O. Green, and A. F. H. Goetz, "Calibration to Surface Reflectance of Terrestrial Imaging Spectrometry Data: Comparison of Methods," Summaries of the Fifth Annual JPL Airborne Earth Science Workshop, Jet Propulsion Laboratory, Pasadena, CA, JPL Pub. 95-1, Vol. 1: AVIRIS Workshop, 1995, pp. 41-42.

Conel, J.E., R.O. Green, V. Carrere, J.S. Margolis, R.E. Alley, G. Vane, C.J. Bruegge and B.L. Gary, Atmospheric Water Mapping with the Airborne Visible/Infrared Imaging Spectrometer (AVIRIS) Mountain Pass, California, Proceedings of the Airborne Visible/Infrared Imaging Spectrometer (AVIRIS) Performance Evaluation Workshop (G.Vane, Ed.), JPL Pub. 88-38, 1988, pp. 21-29.

Gao, B. C., and Goetz, A. F. H., "Column Atmospheric Water-Vapor And Vegetation Liquid Water Retrievals From Airborne Imaging Spectrometer Data," Journal of Geophysical Research Atmospheres, Vol. 95, No. D4, 1990, pp. 3549-3564.

Gao, B. C., Heidebrecht, K. B., Goetz, A. F. H., "Derivation of Scaled Surface Reflectances From AVIRIS Data", Remote Sensing of Environment, Vol. 44, No. 2-3, 1993, pp. 165-178.

Green, R. O., Retrieval of Reflectance from Calibrated Radiance Imagery Measured by the Airborne Visible/Infrared Imaging Spectrometer (AVIRIS) for Lithological Mapping of the Clark Mountains, California, Proceedings, Second AVIRIS Workshop, JPL Publication 90-54, Jet Propulsion Laboratory, Pasadena, CA, 1990, pp. 167-175.

Green, R. O., J. E. Conel, J. S. Margolis, C. J. Bruegge, and G. L. Hoover, "An Inversion Algorithm for Retrieval of Atmospheric and Leaf Water Absorption from AVIRIS Radiance with Compensation for Atmospheric Scattering," Proceedings, Third Airborne Visible/Infrared Imaging Spectrometer (AVIRIS) Workshop, JPL Publication 91-28, 1991, pp. 51-61.

Green, R. O., J. E. Conel, J. Margolis, C. Bruegge and G. Hoover, "An Inversion Algorithm for Retrieval of Atmospheric and Leaf Water Absorption from AVIRIS Radiance with Compensation for Atmospheric Scattering," Proceedings, Third AVIRIS Workshop, R.O. Green, ed., JPL Publication, 91-28, Jet Propulsion Laboratory, Pasadena, CA, 1991 pp. 51-61.

Green, R. O., J. E. Conel and D. A. Roberts, "Estimation of Aerosol Optical Depth and Calculation of Apparent Surface Reflectance from Radiance Measured by the Airborne Visible/Infrared Imaging Spectrometer (AVIRIS) Using MODTRAN2," SPIE Conf. No. 1937, Imaging Spectrometry of the Terrestrial Environment, 1993, p. 12.

Green, R. O., and J. E. Conel, "Movement of Water Vapor in the Atmosphere Measured by an Imaging Spectrometer at Rogers Dry Lake, CA," Summaries of the Fifth Annual JPL Airborne Earth Science Workshop, JPL Publication 95-1, Vol. 1: AVIRIS Workshop, R.O. Green, ed., Jet Propulsion Laboratory, Pasadena, CA, 1995, pp. 79-82.

Kneizys, F. X., E. P. Shettle, G. P. Anderson, L. W. Abrew, J. H. Chetwynd, J. E. A. Shelby, and W. O. Gallery, "Atmospheric Transmittance/Radiance; Computer Code LOWTRAN 7," AFGL, Hanscom AFB, MA, 1987.

Figure 1. A portion of the AVIRIS image flight lines of the DOE ARM SGP CART Central Site in Oklahoma. The image is a single channel from AVIRIS centered at 550 nm. The 11-km width and 20-km length in conjunction with the 20-m spatial resolution show the range of cover types present at this site.

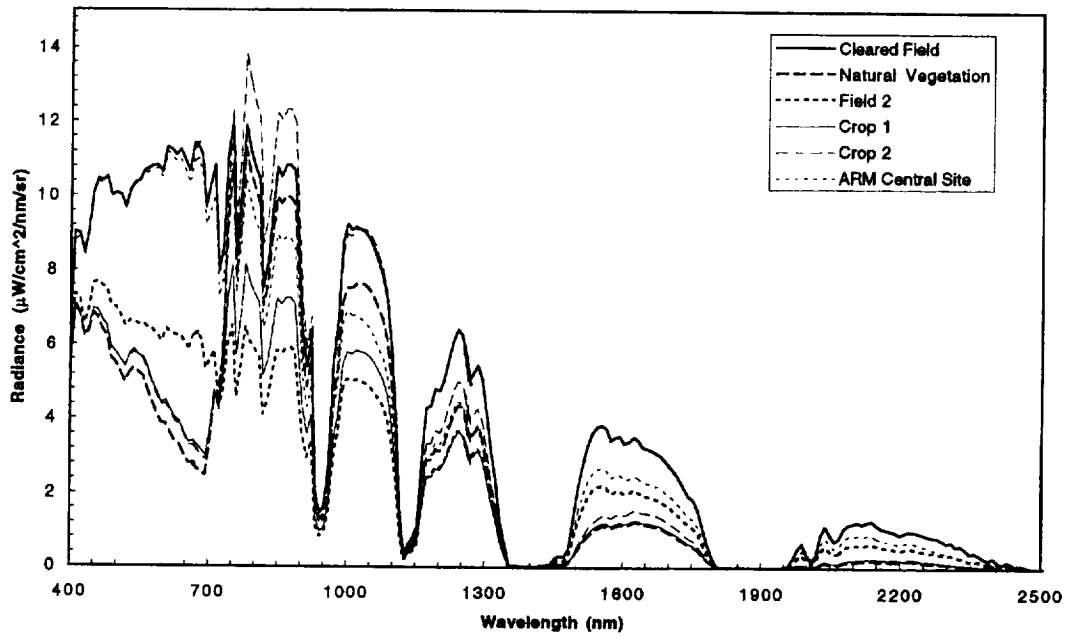

Figure 2. AVIRIS Radiance spectra from vegetation and soil targets in the DOE ARM SGP CART Central Site measured on August 1, 1997.

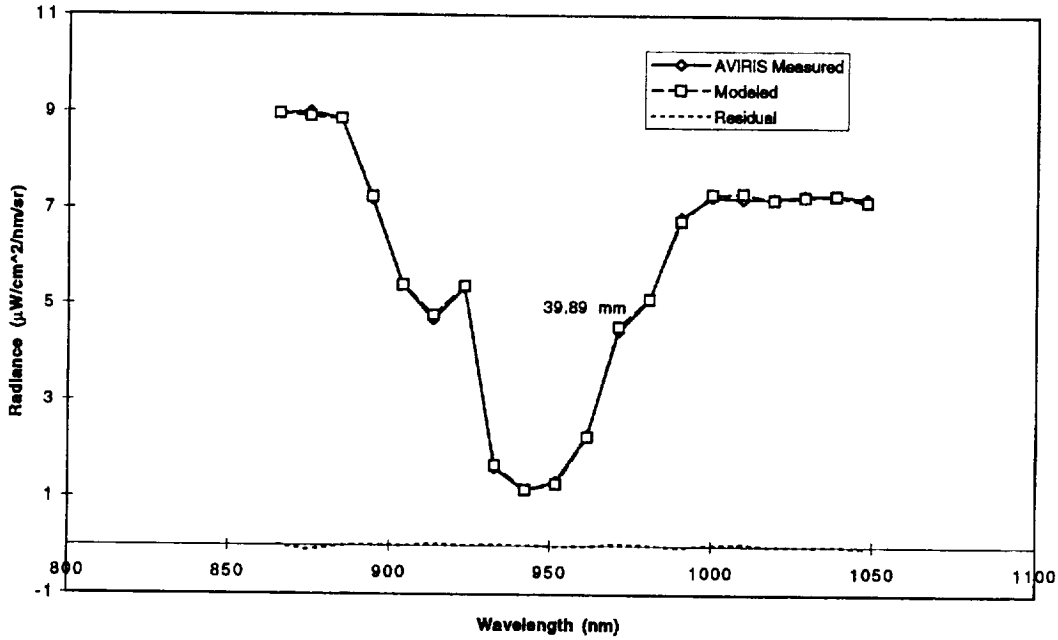

Figure 3. Water vapor inversion algorithm spectral fit for a target in the DOE ARM SGP CART Central Site AVIRIS spectral image.

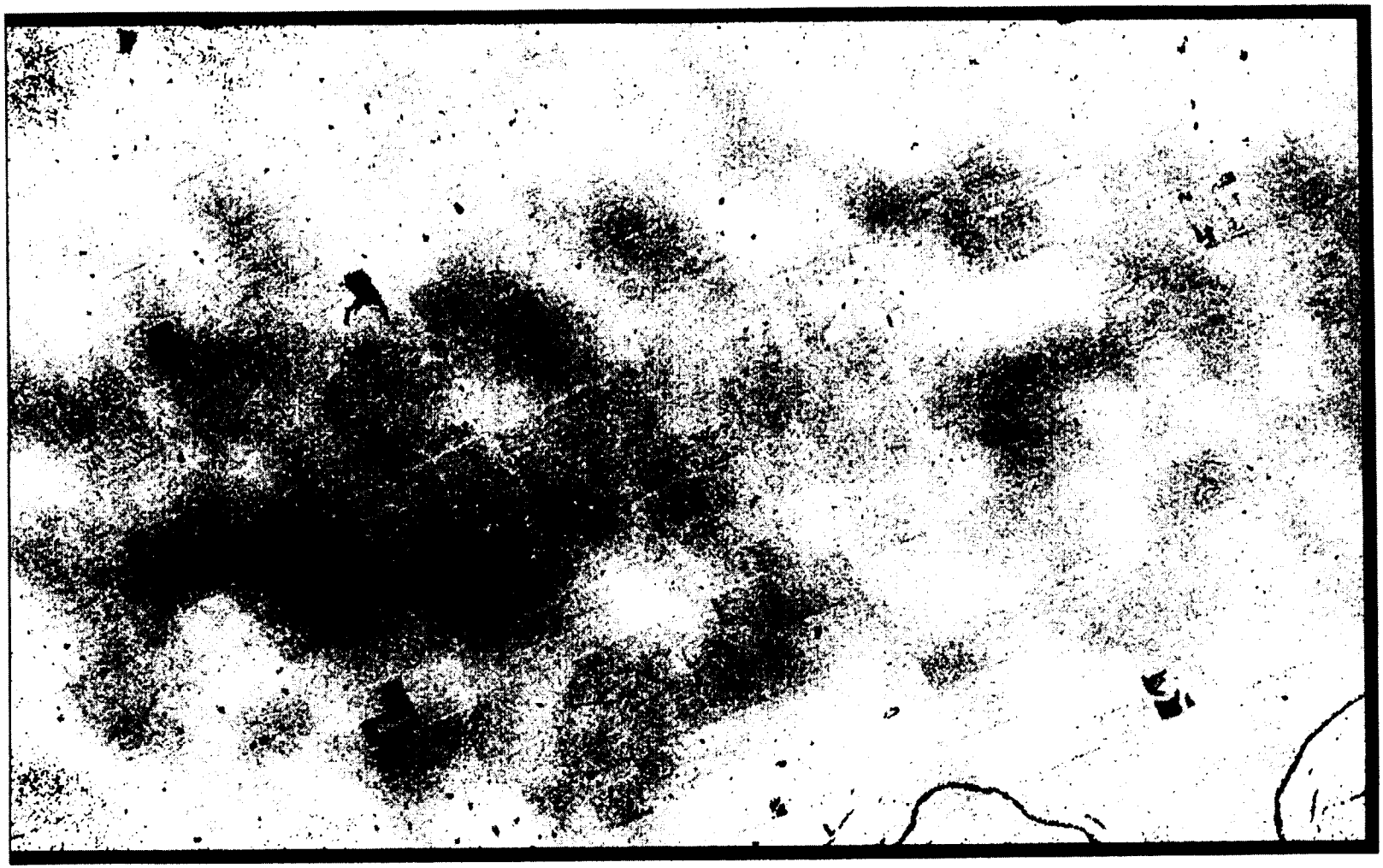

Figure 4. AVIRIS water vapor image for the DOE ARM CART Central site. The range is from 38 to 41 mm of precipitable water vapor. Areas of standing liquid water were excluded from the inversion and are shown as dark.

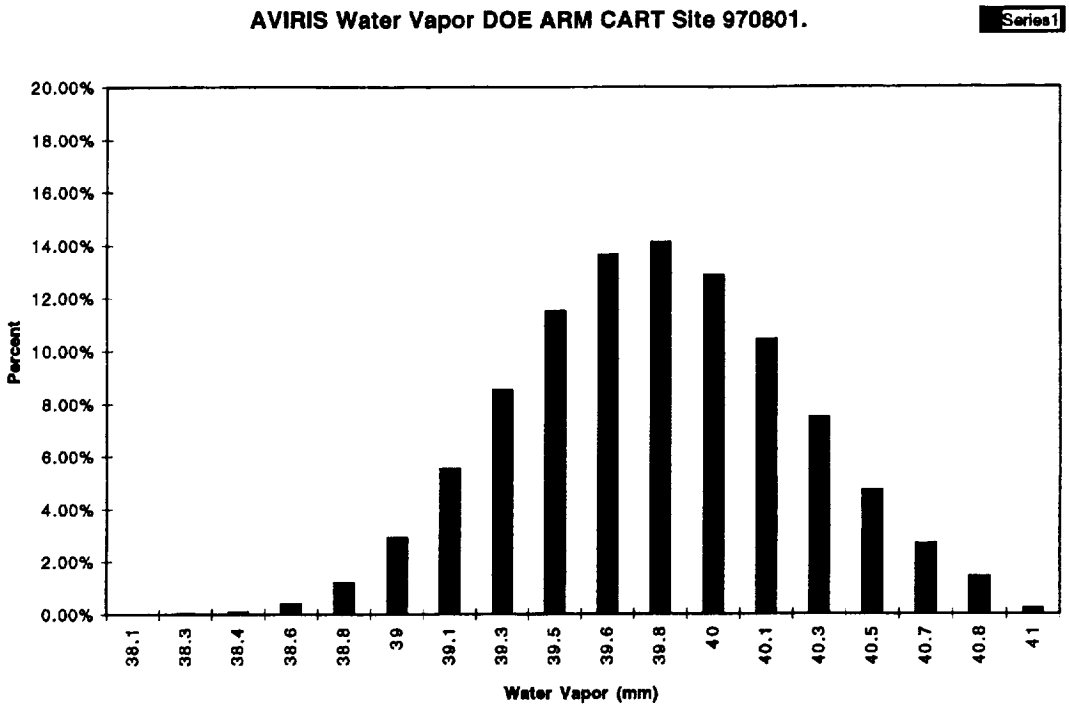

Figure 5. Histogram of the frequency distribution of water vapor derived from AVIRIS spectra of the DOE ARM SGP CART Central site on August 1, 1997.

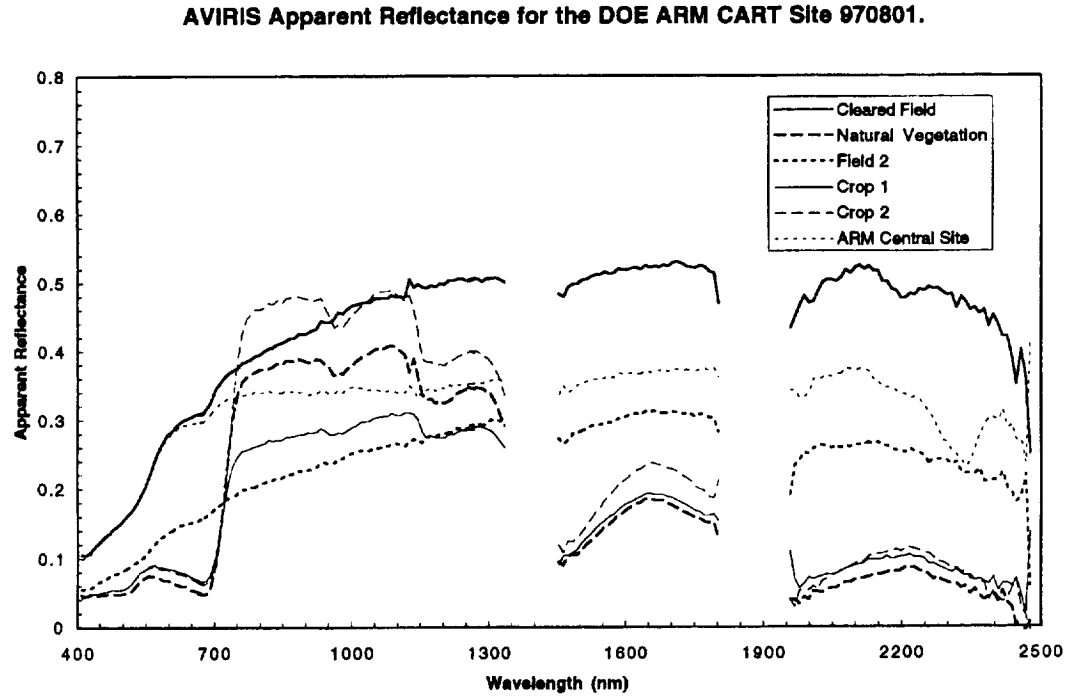

Figure 7. Apparent surface reflectance for soil and vegetation targets in the DOE ARM SGP CART Central Site on August 1, 1997.

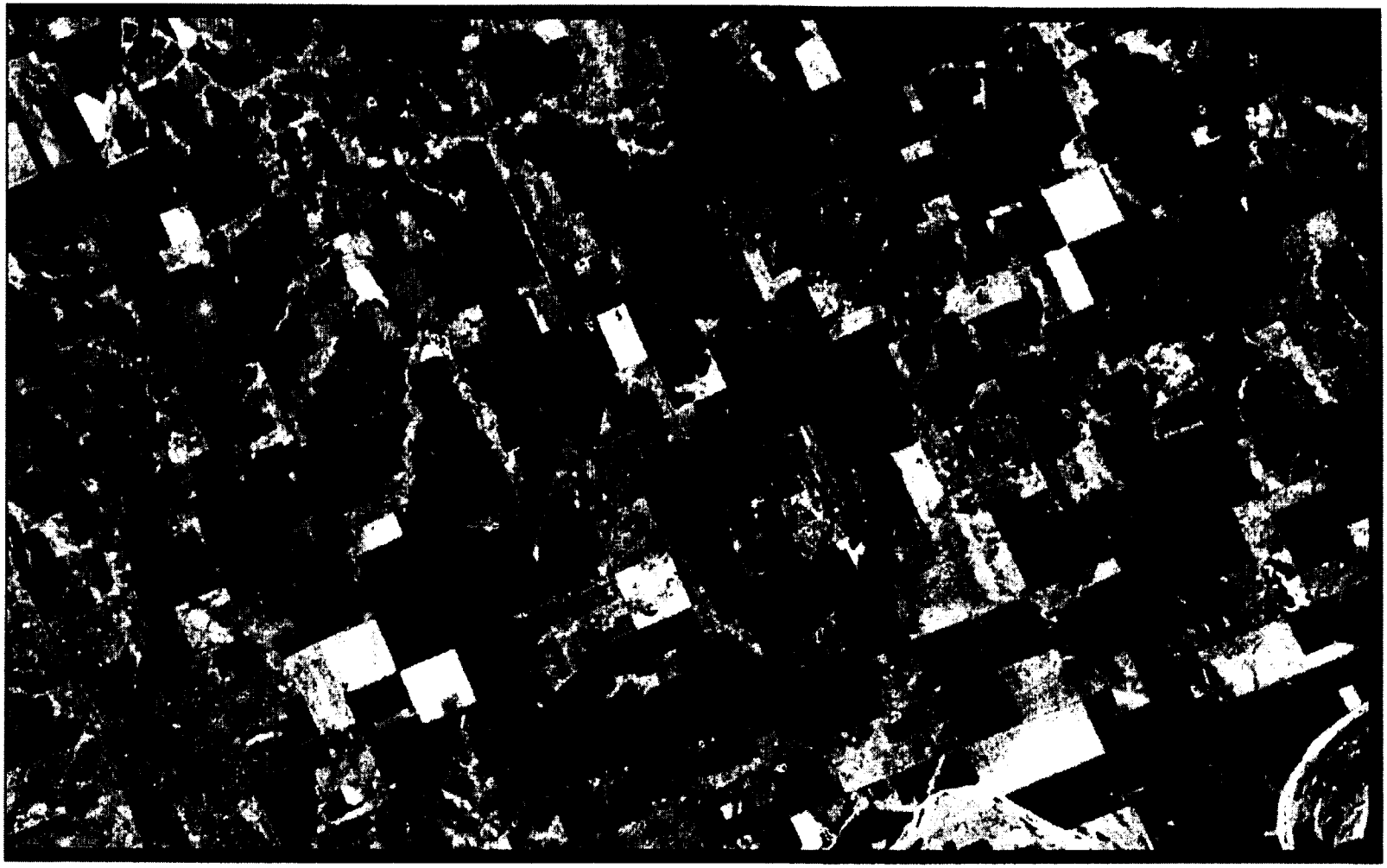

Figure 6. AVIRIS liquid water image for the DOE ARM SGP CART Central Site. The range is from 0.0 to 5.2 mm equivalent liquid water.

Minimum High Fire Temperatures Detected in AVIRIS Spectral Measurements from Brazil in 1995

Robert O. Green

NASA Jet Propulsion Laboratory, California Institute of Technology
Pasadena, CA 91109

1.0 Introduction

In August and September of 1995 the Airborne Visible/Infrared Imaging Spectrometer (AVIRIS) was deployed to Brazil as part of the NASA Smoke Cloud Aerosol and Radiation experiment in Brazil (SCAR-B). AVIRIS measures spectra from 400 to 2500 nm at 10-nm intervals. These spectra are acquired as images with dimensions of 11 by up to 800 km with 20-m spatial resolution. Spectral images measured by AVIRIS are spectrally, radiometrically, and spatially calibrated.

During the SCAR-B deployment, AVIRIS measured more than 300 million spectra of regions of Brazil. A portion of these spectra were acquired over areas of actively burning fires (Figure 1). Actively burning fires emit radiance in the AVIRIS spectral range as a function of temperature. This emitted radiance is expressed from the 2500-nm end of the AVIRIS spectrum to shorter wavelengths as a function of intensity and modeled by the Planck function (Figure 2). The objective of this research and analysis was to use spectroscopic methods to determine the minimum high temperature of the most intense fires measured in the SCAR-B AVIRIS data set.

Spectra measured by AVIRIS with hot sources have been previously examined for volcanic lava (Oppenheimer et al., 1993) and fires in Brazil (Green, 1996).

2.0 Data

AVIRIS measured 300 million spectra of 20- by 20-m spatial resolution for 8,000 km^2 area in Brazil in August and September of 1995. Spectra with actively burning fire are most easily identified by high radiance values in the 2000- to 2500-nm region of the spectrum measured by AVIRIS. The radiance values with burning fires vastly exceed those for reflected sunlight from a target with a reflectance of 1.0. For the more intense fire spectra, portions of the AVIRIS spectral range were saturated at the 12-bit digitization of the signal chain. To identify the most intense fires in the SCAR-B data set, an algorithm was developed to detect AVIRIS spectra that had saturated at the shortest wavelengths. This algorithm was applied to the 100 gigabytes of SCAR-B AVIRIS data.

A number of spectra near Alta Floresta, Brazil (latitude: -9.92, longitude: -55.80) acquired on the 23rd of August 1995 showed saturation of the AVIRIS spectrometers at 1000 nm in the spectral range (Figure 3). The saturation at 1000 nm shows this to be one of the most intense fires in the AVIRIS SCAR-B data set. However, even with this high intensity, at 500 nm wavelength the smoke in the Alta Floresta area dominates the AVIRIS image (Figure 4). At 1000 nm, as predicted by the spectrum, the intense fire is apparent in the upper right quadrant of the image (Figure 5). Also at 1000 nm, other surface features are apparent as some light is transmitted through the smoke particles. At the long wavelength end of the AVIRIS spectrum only the fires are expressed in the AVIRIS image of Alta Floresta on the 23rd of August 1995 (Figure 6). More than 50 fires were burning at the time these data were measured. For this research only the spectra from the most intense fire were analyzed to estimate the minimum high burning temperature.

3.0 Analysis and Results

The radiance of these most intense fire spectra derives from both solar reflected energy and fire emitted energy. To compensate for the solar reflected contribution, the radiance from an adjacent nonburning spectrum is subtracted from the intense fire spectra (Figure 7). This correction removes the scattered solar radiance contributed by the smoke. At 760 nm a small radiance peak is expressed in the spectrum that is attributed to hot oxygen in the fire and adjacent air. A simple estimation of the minimum high temperature of this fire is provided by comparing these solar corrected spectra to radiance spectra modeled for hot targets at various temperatures (Figure 8). This comparison leads to a minimum high temperature of 1175 K for these Alta Floresta spectra. This is a conservative estimate because the one-way transmittance of the atmosphere from the fire to AVIRIS has been ignored. Transmittance through the smoky atmosphere greatly reduces the radiance measured by AVIRIS compared to the fire source. To compensate for this transmittance loss, a calculation has been made using the MODTRAN radiative transfer code (Berk et al., 1989; Anderson et al., 1995) (Figure 9). This transmittance correction has been applied to the fire spectra and new Planck function spectra generated (Figure 10). This analysis shows a minimum high temperature of 1450 K. There is considerable uncertainty in this minimum high estimate due to the assumptions required in estimating the transmittance. For these analyses, the area of the burning fire has been assumed to fully fill the AVIRIS 20-m spatial resolution. Continuing research will focus on estimation of transmittance in these smoky atmospheres and assessment for fire area within the AVIRIS spatial resolution. However, both the 1175 K and 1450 K result give an initial range for the minimum high temperature for the fires measured by AVIRIS in Brazil.

4.0 Conclusion

A set of spectra from an extremely intense fire have been identified and extracted from the 300 million spectra measured during the deployment of AVIRIS to Brazil for the NASA SCAR-B experiment. A simple algorithm subtracting the radiance of an adjacent nonburning spectrum has been used to remove the solar-scatter contribution to the fire spectra. Comparison with modeled plank functions gives a conservative minimum high temperature of 1175 K for these spectra of a fire near Alta Floresta, Brazil, on the 23rd of August 1995. With a number of assumptions, the transmittance loss has been calculated and compensated for in these spectra. With this compensation, an estimated minimum high temperature of 1450 K has been derived. Additional work is required to validate and refine the transmittance correction. This research and analysis shows that for the SCAR-B data set, spectra measured by AVIRIS, enable new spectroscopic approaches for deriving properties of actively burning fires.

5.0 References

Anderson, G. P., J. Wang, and J. H. Chetwynd (1995), "MODTRAN3: An Update And Recent Validations Against Airborne High Resolution Interferometer Measurements," Summaries of the Fifth Annual JPL Airborne Earth Science Workshop, JPL Publication 95-1, Vol. 1; AVIRIS Workshop, R.O. Green, Ed., Jet Propulsion Laboratory, Pasadena, CA, 5-8.

Berk, A., L. S. Bernstein, and D. C. Robertson (1989), MODTRAN: A Moderate Resolution Model for LOWTRAN 7, Final Report, GL-TR-0122, AFGL, Hanscom AFB, MA, 42 pp.

Green, Robert O. (1996), Estimation of Biomass Fire Temperature and Areal Extent from Calibrated AVIRIS Spectra, Summaries of the Sixth Annual JPL Airborne Earth Science Workshop., March 4-8 1996, JPL Publication 96-4, Vol. 1: AVIRIS Workshop, JPL, Pasadena, California, 105-113.

Oppenheimer-C; Rothery-DA; Pieri-DC; Abrams-MJ; Carrere-V. (1993), "Analysis Of Airborne Visible/Infrared Imaging Spectrometer (AVIRIS) Data Of Volcanic Hot-Spots", International Journal Of Remote Sensing, 14, (16), 2919-2934.

6.0 ACKNOWLEDGMENTS

The majority of this research was carried out at the Jet Propulsion Laboratory, California Institute of technology, under contract with the National Aeronautics and Space Administration. A portion of the work was performed at the Institute for Computational Earth System Science, University of California, Santa Barbara, CA. In addition, I would like to express my appreciation for the efforts of the AVIRIS team at the Jet Propulsion Laboratory.

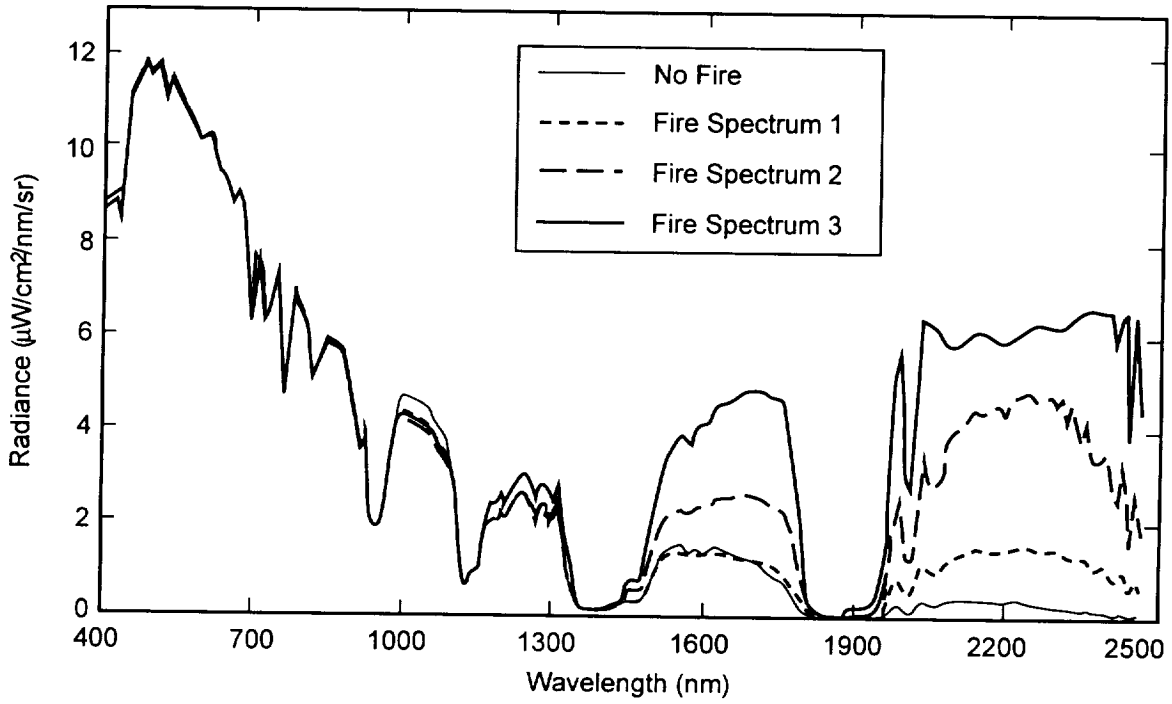

Figure 1. AVIRIS spectra from a fire measured during the 1995 deployment to Brazil. Four spectra are shown. Spectrum 1 is from unburned vegetation. Spectra 2, 3 and 4 are from active burning areas of increasing intensity. In these fire spectra, the radiance emitted by the fire dominates the 2000- to 2500-nm spectral range.

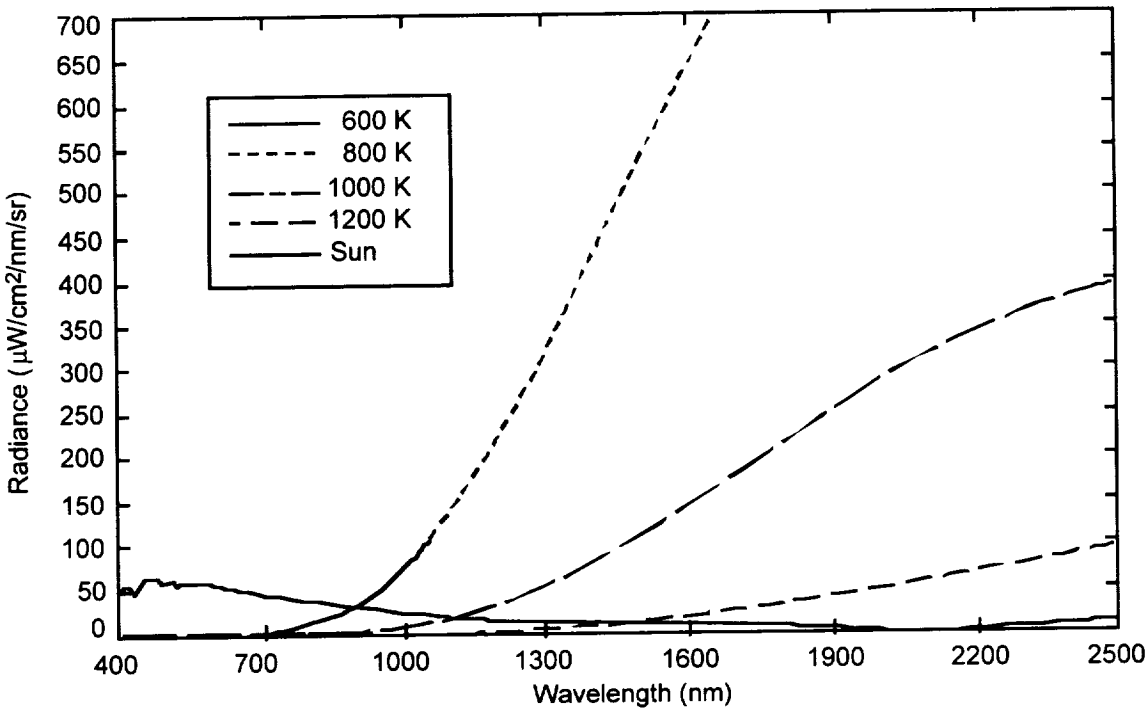

Figure 2. Planck function modeled radiance spectra from fires at several temperatures are shown. The radiance from the sun for a 1.0 reflectance target is also shown.

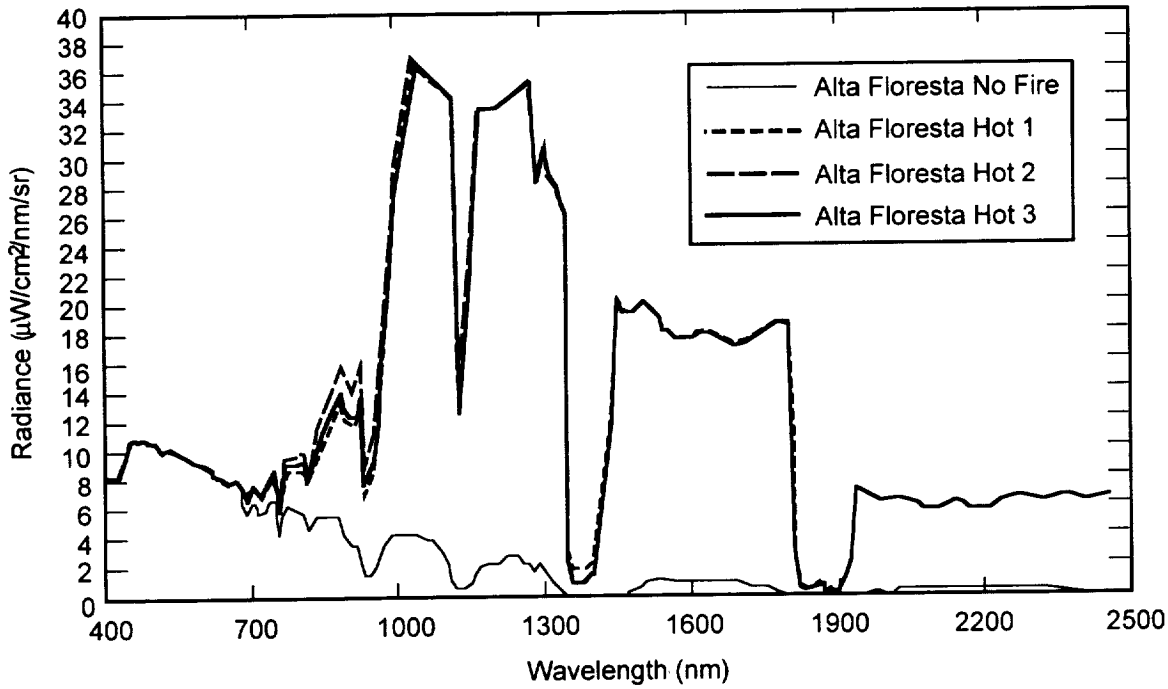

Figure 3. Four spectra from a fire near Alta Floresta acquired on the 23rd of August 1995. The first spectrum is from a nonburning area adjacent to the fire. The three fire spectra show a very intense fire with the AVIRIS spectrum saturated near 1000 nm.

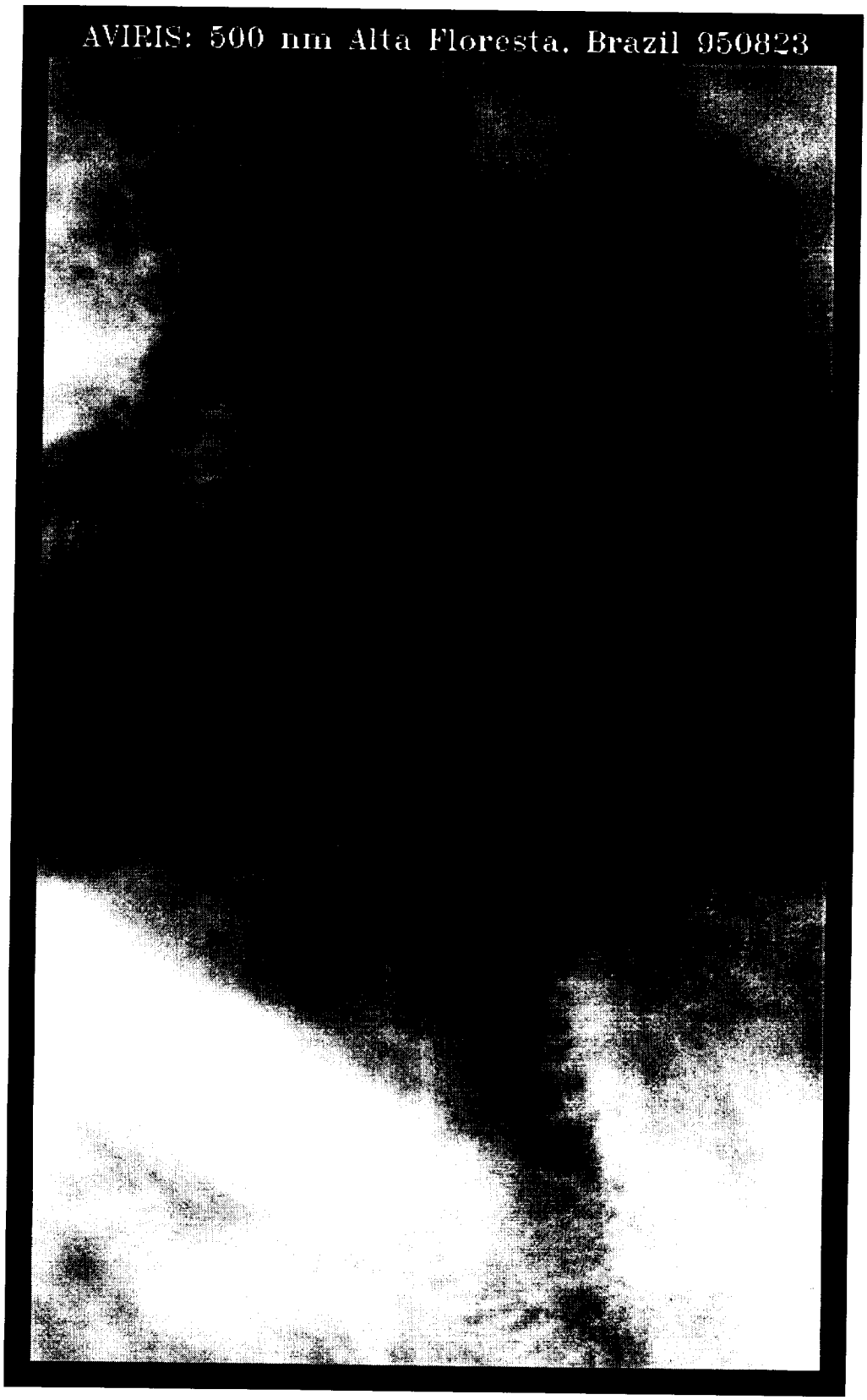

Figure 4. The AVIRIS 500-nm spectral image of the Alta Floresta region. Smoke from fire-dominates the entire image.

Figure 5. Alta Floresta AVIRIS spectral image at 1000 nm wavelength. Both solar reflected photons and photons emitted the intense fires penetrate fine particulate smoke. The most intense fire is expressed at the upper right quadrant of the image.

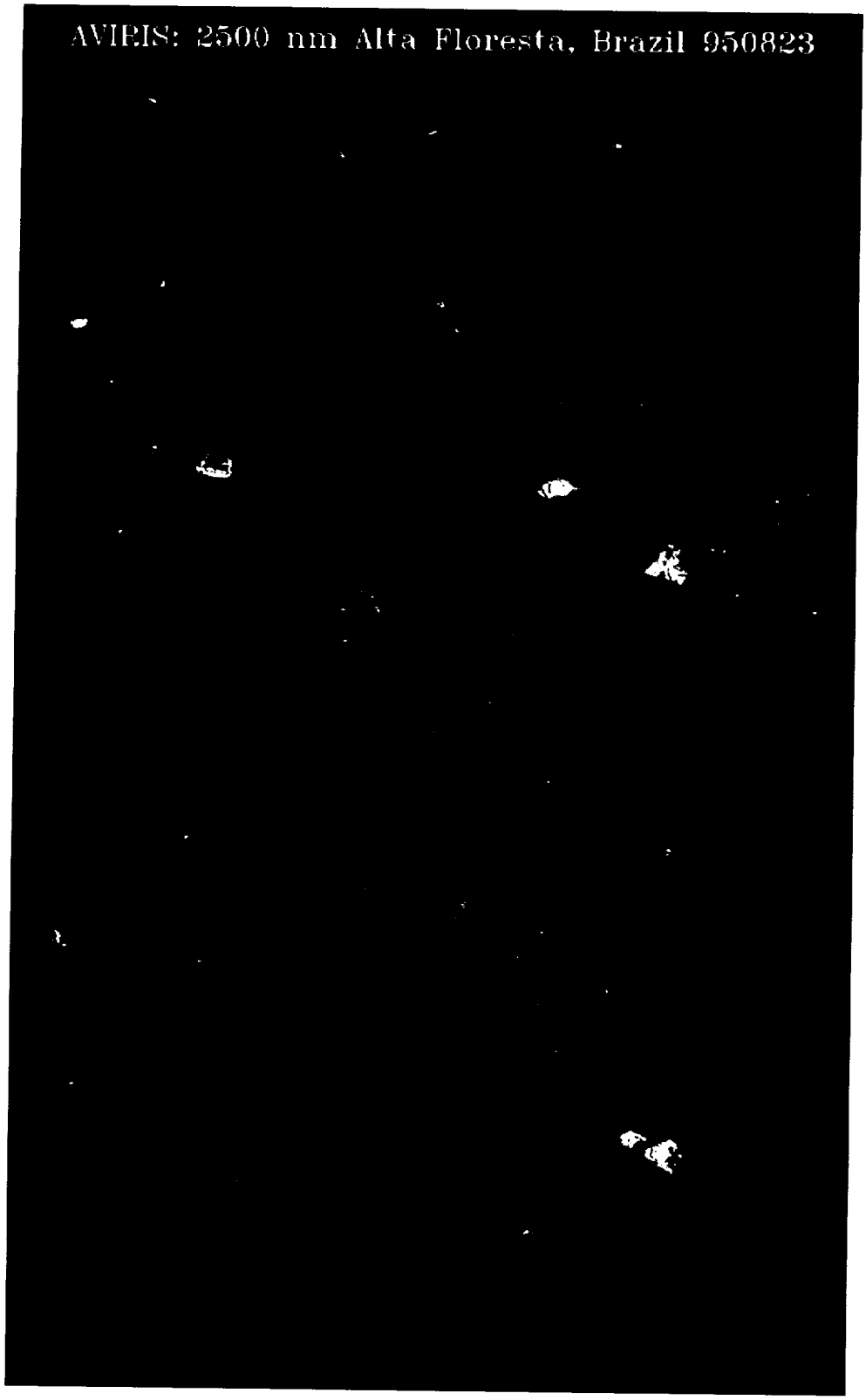

Figure 6. AVIRIS spectral image at 2500 nm wavelength. Only the photons emitted by burning fires penetrate the atmosphere and are measured by AVIRIS.

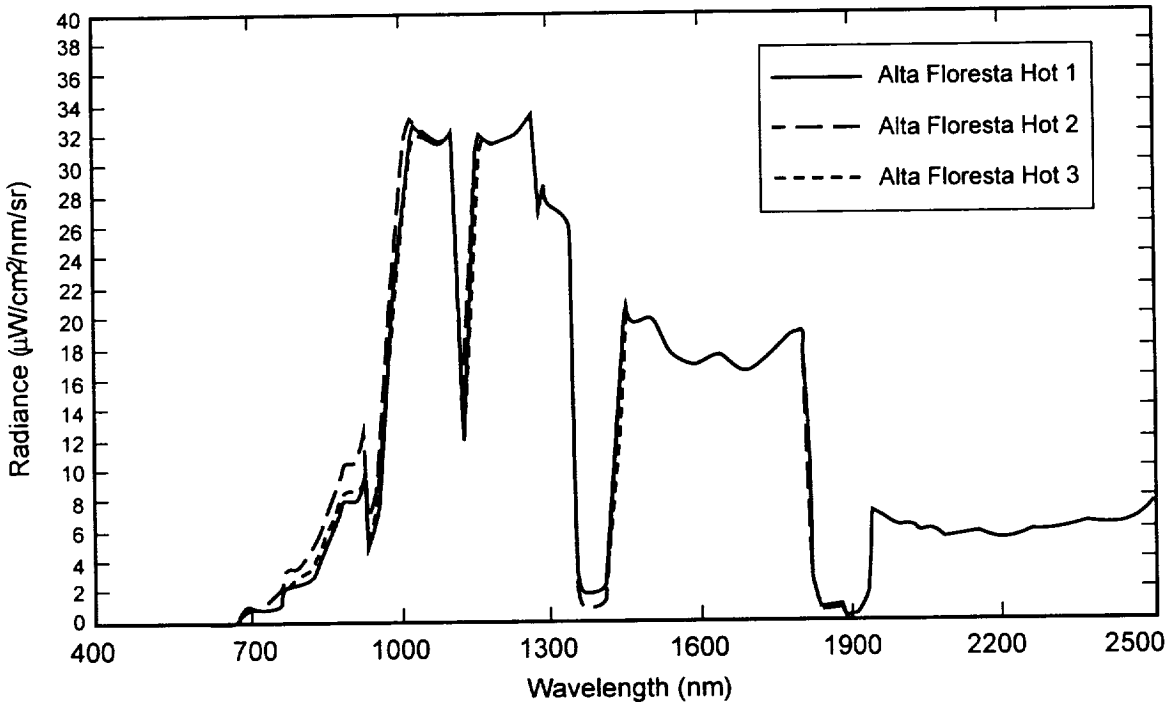

Figure 7. Alta Floresta fire spectra with adjacent nonburning spectrum subtracted.

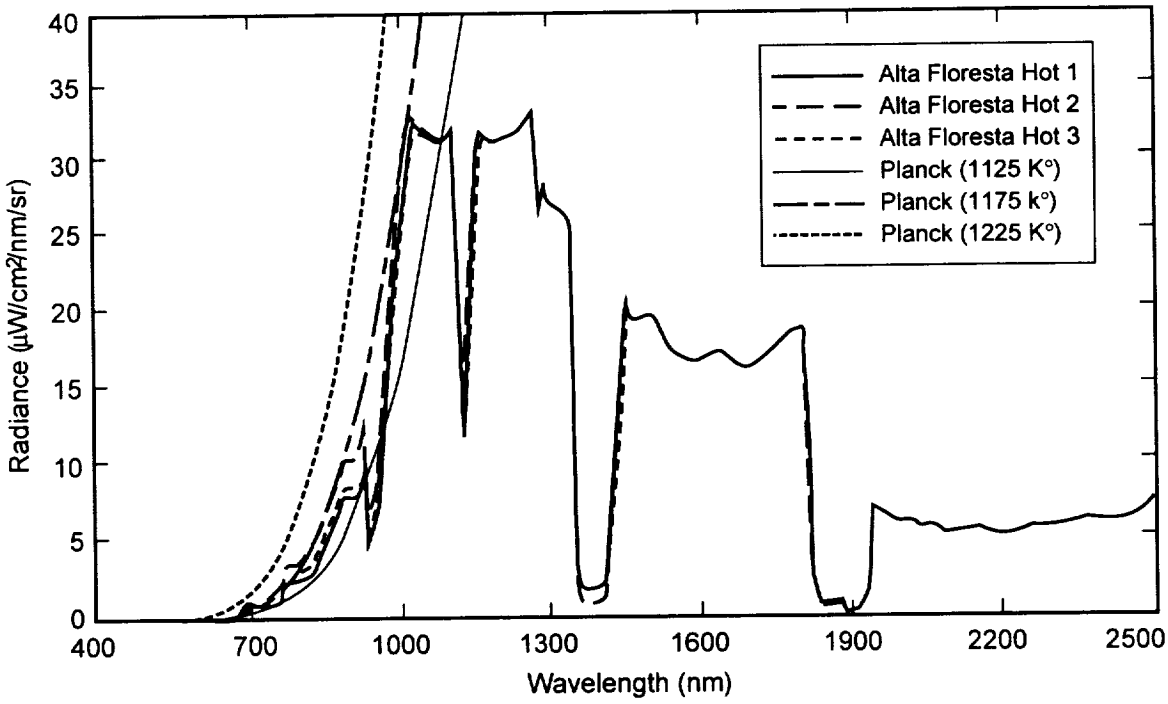

Figure 8. Planck function fit to solar compensated spectra. This gives an initial minimum high temperature of 1175 K.

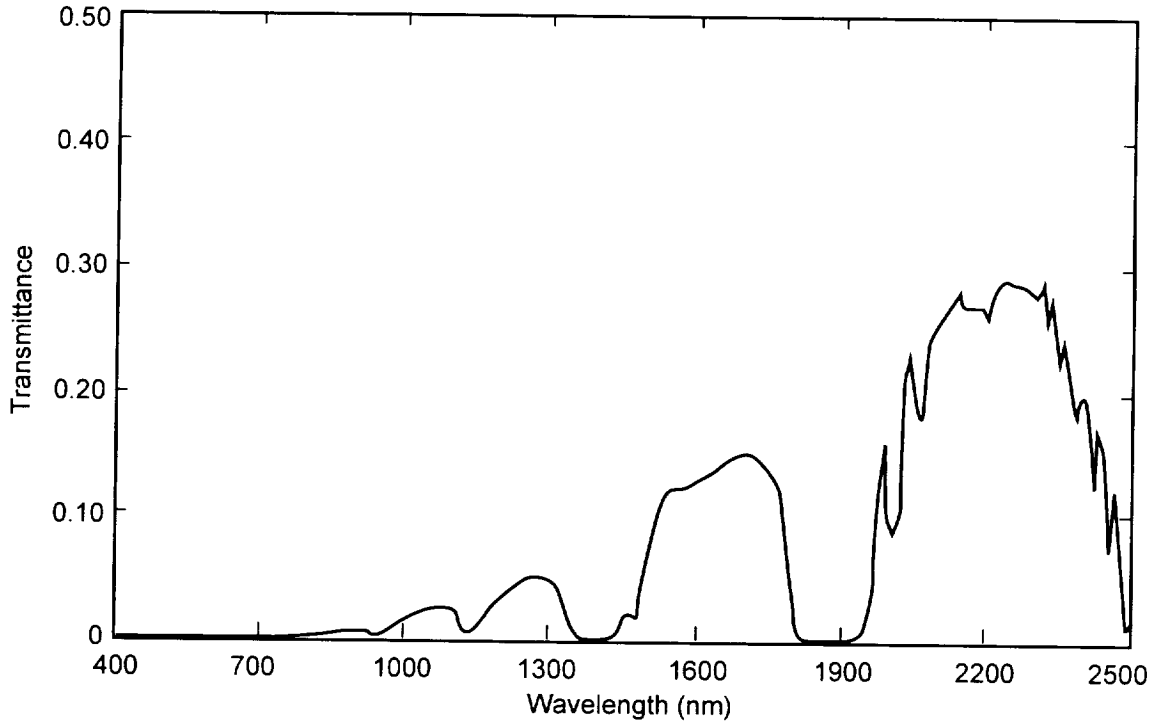

Figure 9. Calculated transmittance for the smoky atmosphere of the Alta Floresta data set.

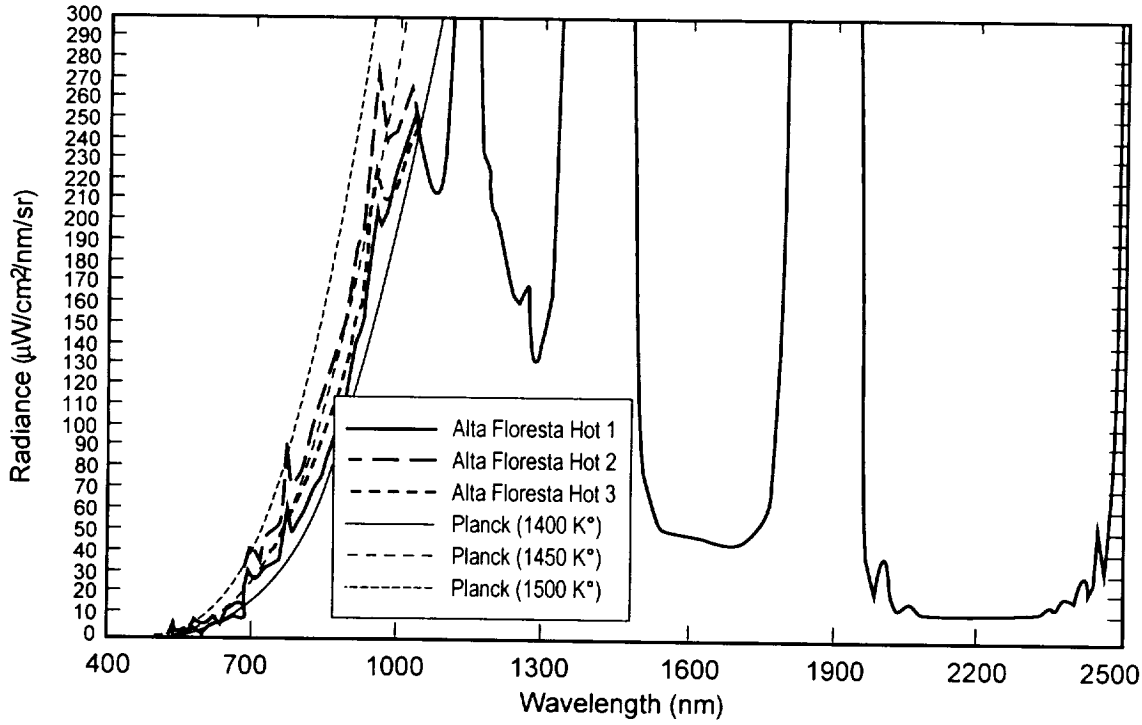

Figure 10. Transmittance compensated spectra and fit to plank functions. This gives an estimate of 1450 K for the minimum high temperature for these spectra.

Inflight Validation of AVIRIS Calibration in 1996 and 1997

Robert O. Green, Betina Pavri, Jessica Faust, Orlesa Williams and Chris Chovit
Jet Propulsion Laboratory
California Institute of Technology
Pasadena, CA 91109

1.0 Introduction

The Airborne Visible/Infrared Imaging Spectrometer (AVIRIS) measures spectral radiance in the solar reflected spectrum from 400 to 2500 nm (Figure 1). Spectra are measured through 224 spectral channels with nominally 10-nm sampling and 10-nm full width at half maximum (FWHM). From a NASA ER-2 aircraft flying at 20,000 m altitude, these spectra are acquired as images with an 11-km width by up to 800-km length. The spatial sampling is 17 m, and the instantaneous field of view (IFOV) 20 m. The objective of AVIRIS is to acquire calibrated spectra that are used to derive properties of the Earth's land, water, and atmosphere for scientific research and environmental applications. To achieve this objective, the AVIRIS spectra must be calibrated. The AVIRIS sensor is calibrated in the laboratory before and after each flight season (Chrien et al. 1990), however, the spectra acquired by AVIRIS for science investigators are acquired in the Q-bay of the ER-2 at 20 km altitude. The objective of the AVIRIS inflight calibration experiment is to validate the calibration of AVIRIS spectral images in the low pressure, low temperature operating environment of the ER-2. Inflight calibration experiments have been orchestrated for AVIRIS in every year of flight operations (Green et al. 1988, Conel et al. 1988, Green et al. 1990, Green el al. 1992, Green et al. 1993, Green el al. 1995. Green et al. 1996).

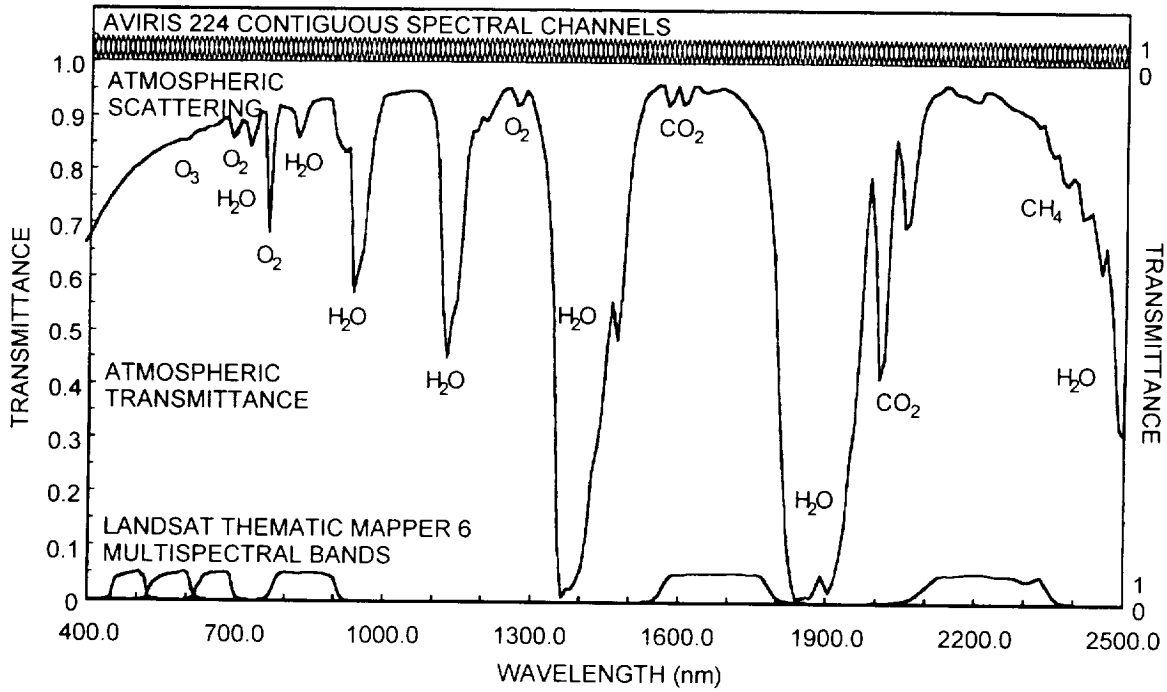

Figure 1. AVIRIS spectral coverage from 400 to 2500 nm at 10-nm spectral sampling. Also shown is a transmission spectrum of the Earth atmosphere and the six multispectral bands of the Landsat Thematic Mapper.

The approach to validate the calibration of AVIRIS is to independently predict the spectral upwelling radiance arriving at AVIRIS from a ground target and compare this prediction with the radiance measured by AVIRIS for the target. To implement the inflight calibration experiment, a homogeneous ground target is selected in an environment with clear, low humidity atmospheric conditions. At the time of the AVIRIS overflight, the surface spectral reflectance is measured for the target. In addition, atmospheric optical depths and total column water vapor are measured immediately adjacent to the target. These measurements are used to predict the radiance at AVIRIS with the MODTRAN radiative transfer code (Berk et al. 1989). Uncertainties in the radiative transfer prediction are estimated based on the uncertainty of the constraining surface and atmospheric measurements. The level of agreement between the MODTRAN predicted and the AVIRIS measured radiance is reported to validate AVIRIS calibration in flight. Inflight calibration experiments at the Ivanpah Playa, California are reported from the 1996 and 1997 flight seasons.

2.0 Field Measurements and Data

On June 15, 1996 and March 4, 1997, AVIRIS inflight calibration experiments were held at Ivanpah Playa, California (Figure 2). This dry lakebed is 740 m elevation above sea level and located at 35.515 degrees North latitude and 115.399 degrees West longitude in the Mojave Desert on the California and Nevada border. The elevation and desert environment lead to clear, dry weather for much of the year.

Surface calibration targets of 40 by 200 m dimension were designated on visually homogeneous portions of the playa surface. These targets are demarked with large blue plastic tarps at the ends of the target. The blue spectral characteristics of the tarps are easily measurable in the AVIRIS data. This provides unambiguous location for extraction of AVIRIS spectral data from the playa calibration target.

In the one-hour period centered on the AVIRIS overflight time, the surface spectral reflectance is measured. The field spectrometer used has an 8 degree field of view and measures the AVIRIS spectral range with better than 10-nm spectral sampling and FWHM. A reflectance standard is measured nominally every fifth measurement. Individual reflectance spectra of the playa calibration target are calculated as the ratio of the measurement of the playa ratioed to the measurement of the nearest standard multiplied by the spectral bidirectional reflectance of the standard. The average reflectance and standard deviation of the calibration target are calculated from all the measurements (Figure 3). Uncertainty in the reflectance of the 40- by 200-m calibration target is calculated as the standard deviation of the average of sets of five measurements. This suppresses the small scale variation not present in the 20-m AVIRIS IFOV.

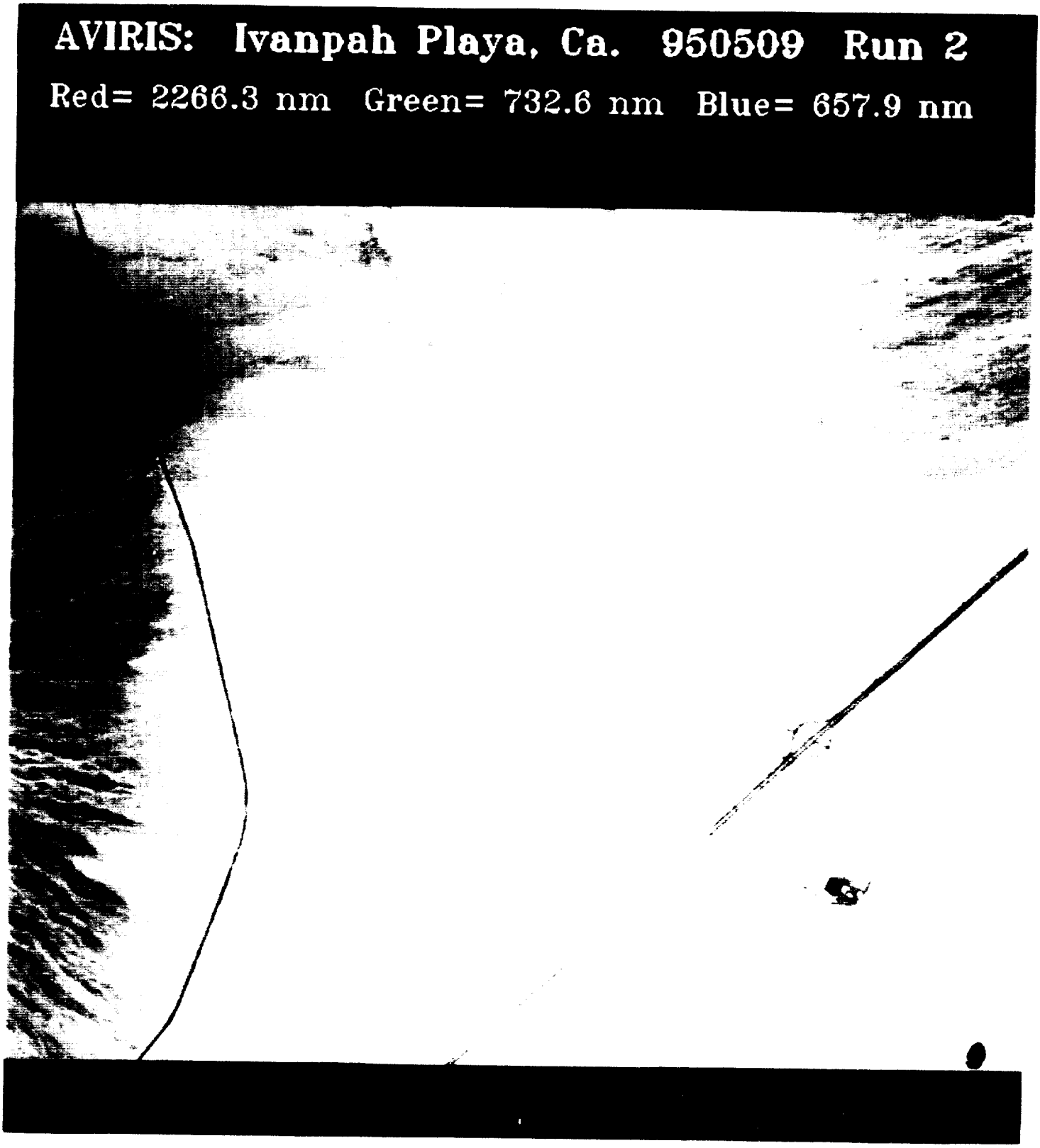

Figure 2. Image of Ivanpah Playa on the California and Nevada border. The width of the image is 11 km and the long axis is oriented roughly North to South

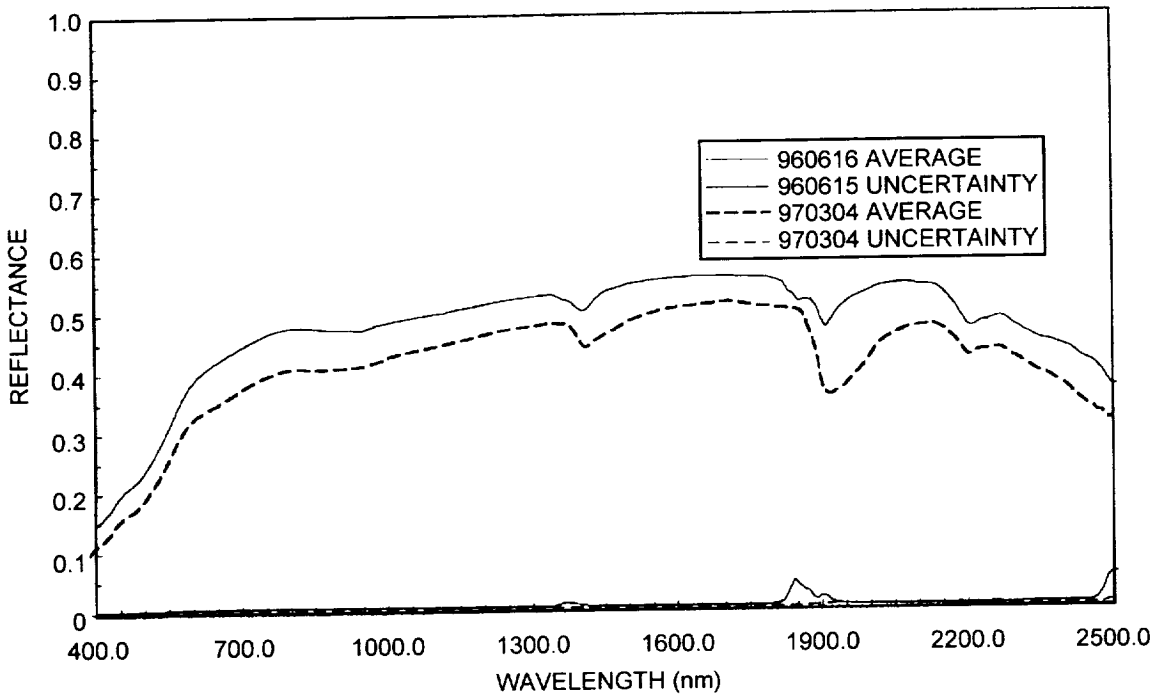

Figure 3. The average reflectance of the calibration targets on Ivanpah Playa measured on June 15, 1996 and March 4, 1997. Uncertainties are also shown.

Adjacent to the calibration target, sun photometer measurements are acquired from sunrise through one hour past the AVIRIS overflight time. These data in conjunction with the sun photometer calibration parameters are used to calculate the total optical depth nearest to the time of overpass (Table 1 and Table 2). Uncertainties in optical depth are calculated as the standard deviation of instantaneous optical depths in the one hour centered on the overflight.

The sun photometer data set contain a measurement acquired at 940 nm in an atmospheric water vapor absorption band. These data are used to calculate the instantaneous total column water vapor nearest the time of the AVIRIS overflight (Bruegge et al. 1990, Reagan et al. 1987). A value of 5.31 ± 0.30 mm was derived for June 15, 1996 and a value of 2.73 ± 0.16 mm was derived for March 4, 1997.

Ozone values are obtained from the TIROS Operational Vertical Sounder. A value of 315 ± 15 matm-cm was reported for June 15, 1996 and a value of 300 ± 15 matm-cm was reported for March 4, 1997.

Oxygen and carbon dioxide abundances are determined based on the pressure height of the Ivanpah Playa calibration site.

Table 1. Calculated total optical depths for June 15, 1996.

Wavelength (nm)	Optical Depth	Uncertainty
370	0.529	0.0098
400	0.444	0.0089
440	0.319	0.0079
520	0.204	0.0066
620	0.161	0.0049
670	0.108	0.0044
780	0.071	0.0042
870	0.056	0.0037
1030	0.045	0.0034

Table 2. Calculated total optical depth for March 4, 1997.

Wavelength (nm)	Optical Depth	Uncertainty
370	0.596	0.0047
400	0.482	0.0041
440	0.357	0.0040
520	0.223	0.0030
620	0.175	0.0028
670	0.120	0.0025
780	0.079	0.0023
870	0.064	0.0023
1030	0.055	0.0020

3.0 Calibration Validation Analysis

The field measurements and associated data are used to constrain the MODTRAN radiative transfer code and predict the radiance from the Ivanpah playa calibration target incident at the AVIRIS aperture. MODTRAN calculates radiance at a 1-wavenumber sampling of the radiative transfer band model. This high resolution data is convolved to the AVIRIS spectral characteristics (Figure 4). The AVIRIS spectral image of Ivanpah Playa is examined to locate the blue tarps and the spectrum extracted for the measured calibration target located between the tarps. The spectrum is calibrated to radiance based on the laboratory calibration and use of the AVIRIS onboard calibrator (Green et al. 1992, Green et al. 1993). For June 15, 1996 the average absolute agreement between the MODTRAN prediction and the AVIRIS measurement was 96.1 percent (Figure 5). On March 4, 1997 the average absolute agreement was 96.6 percent (Figure 6). The agreement calculation excludes the strong water vapor absorption bands at 1400 and 1900 nm where the radiance reaching AVIRIS approaches zero.

An additional parameter of interest for AVIRIS is the inflight signal-to-noise. This parameter is calculated from the onboard calibrator at the time of the AVIRIS calibration experiment. The onboard calibrator is a detector stabilized lamp on the AVIRIS sensor.

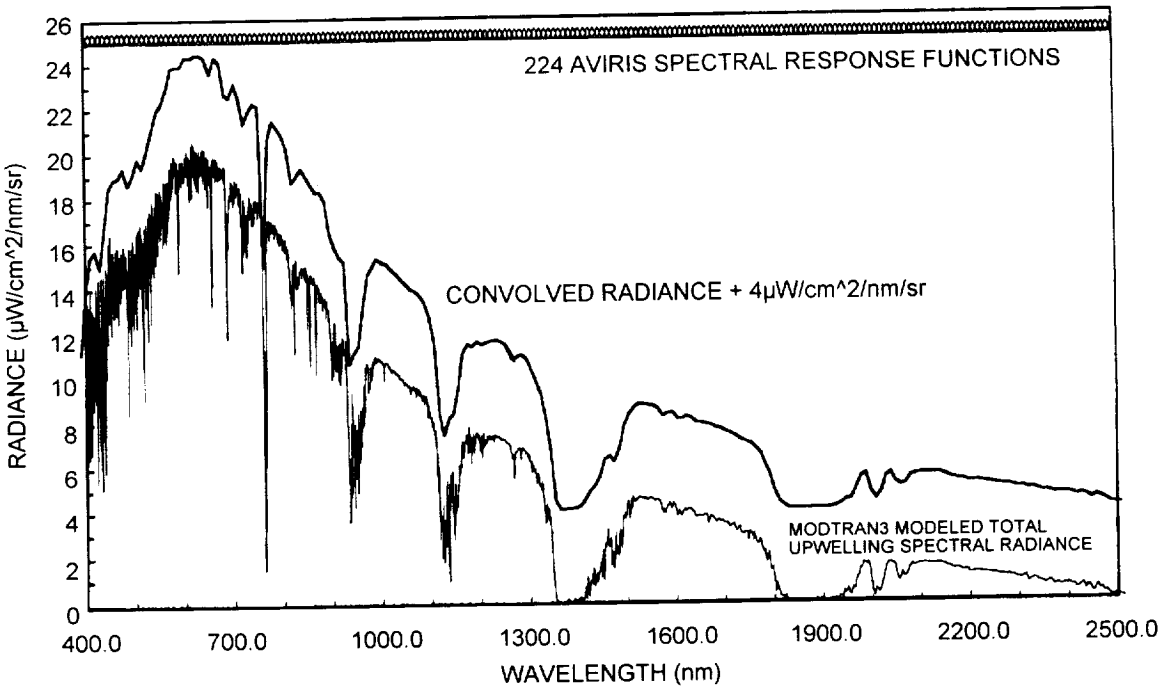

Figure 4. MODTRAN predicted radiance for June 15, 1996 at full resolution and convolved to the AVIRIS spectral characteristics.

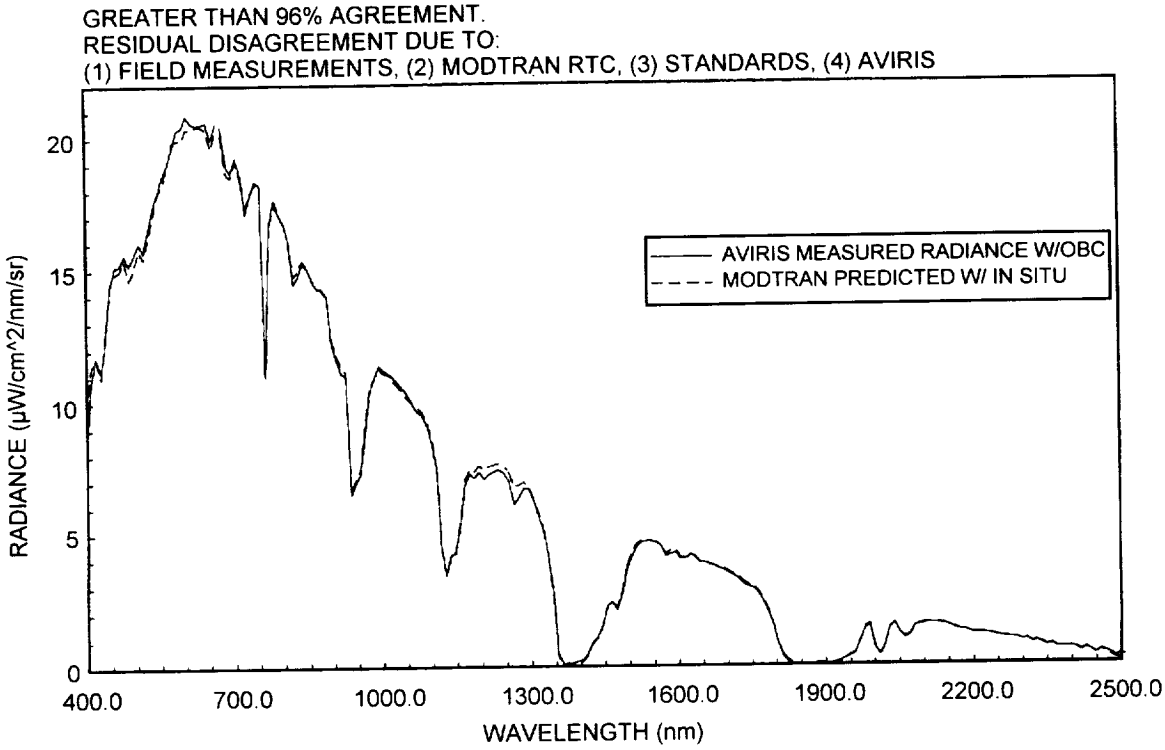

Figure 5. MODTRAN predicted and AVIRIS measured radiance for June 15, 1996. The average absolute agreement is better than 96 percent.

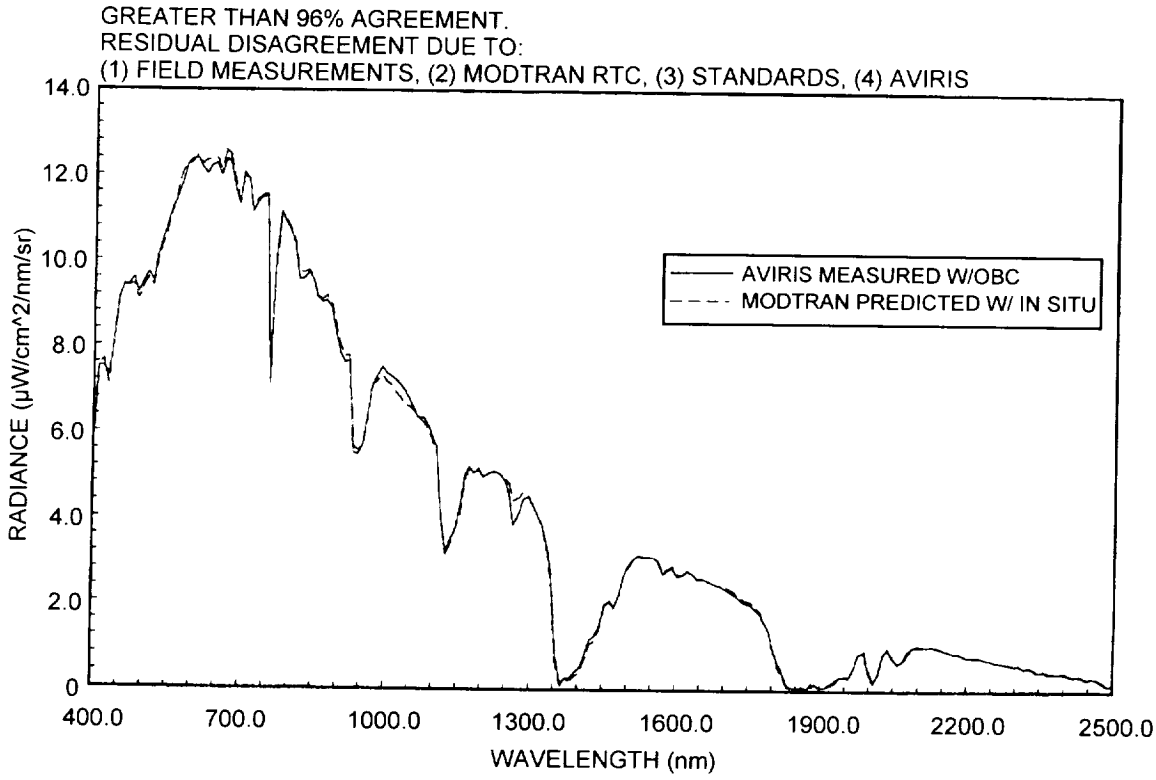

Figure 6. MODTRAN predicted and AVIRIS measured radiance for March 4, 1997. The average absolute agreement is better than 96 percent.

AVIRIS measures the radiance from the onboard calibrator before and after each science flight line. The average and standard deviation of 3000 dark and illuminated spectra acquired from the onboard calibrator are used to calculate the signal chain noise and signal dependent photon sampling noise. These noise components are used to calculate the signal-to-noise for the AVIRIS reference radiance (Figure 7 and Figure 8).

4.0 Uncertainty Analysis

AVIRIS is calibrated with a quartz-halogen lamp trace to the National Institute of Standards and Technology (NIST) with estimated uncertainty based on the calibration transfer process. The agreement between the AVIRIS measurement and MODTRAN prediction for 1996 and 1997 falls largely within the NIST-traced uncertainty of AVIRIS calibration (Figure 9).

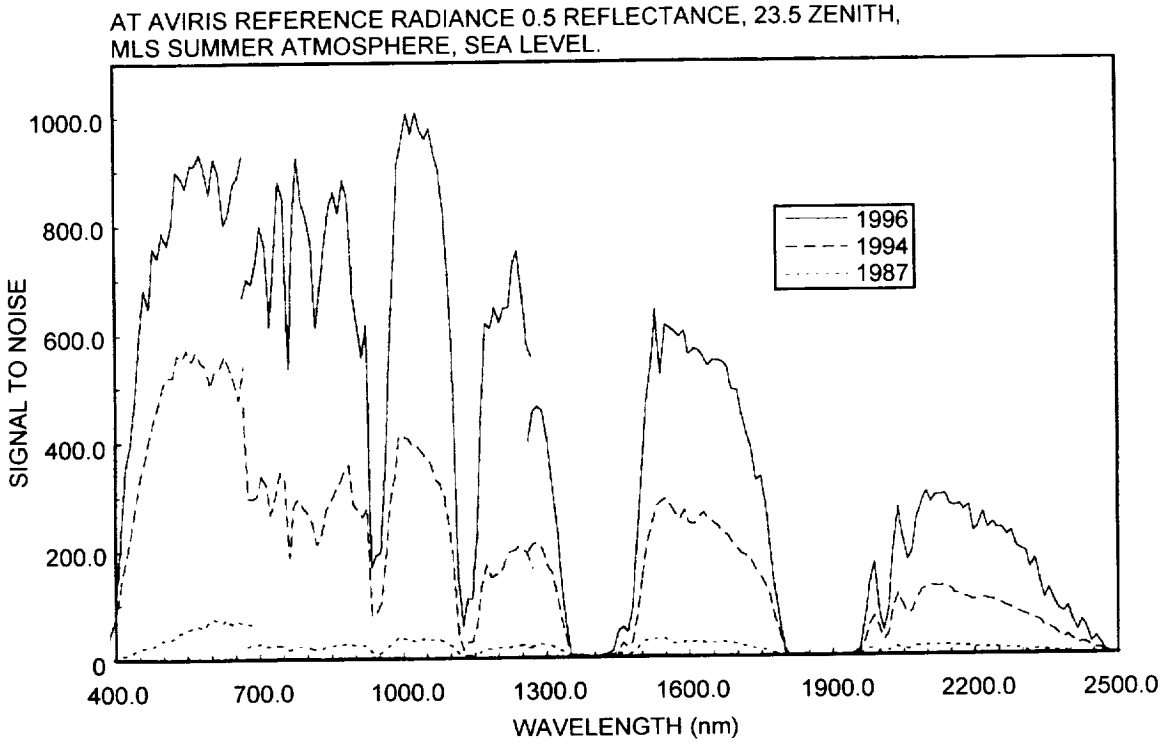

Figure 7. AVIRIS inflight signal-to-noise for June 15, 1996. Also shown are the AVIRIS signal-to-noise in 1987 and 1994.

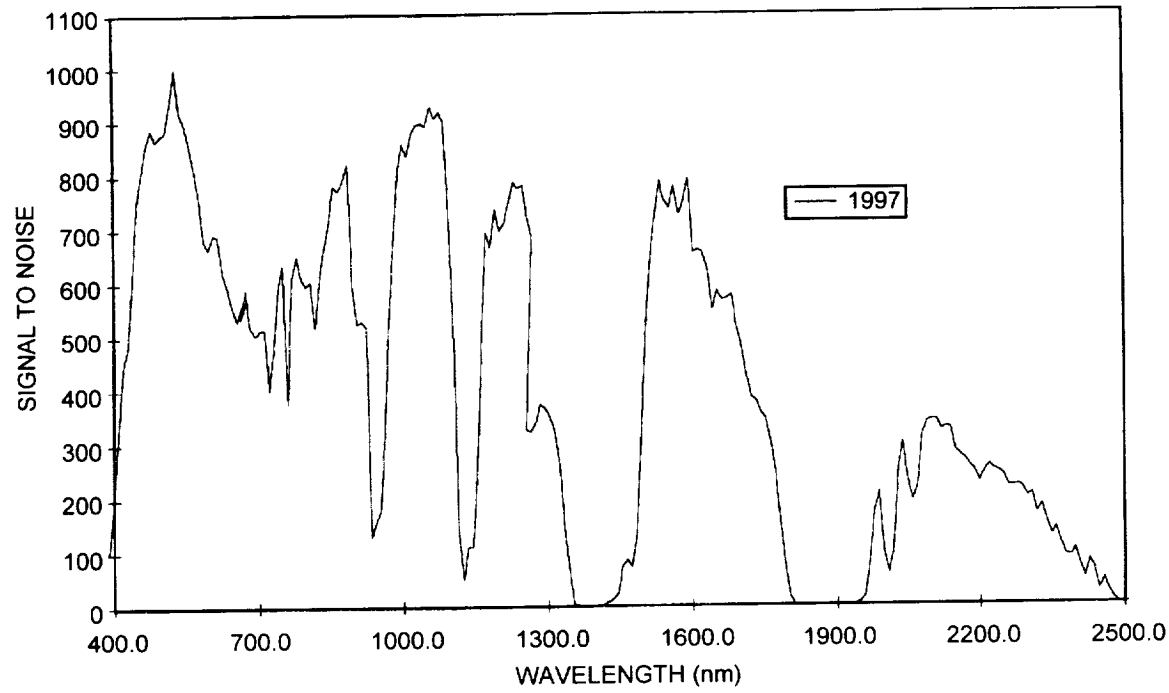

Figure 8. AVIRIS inflight signal-to-noise for March 4, 1997.

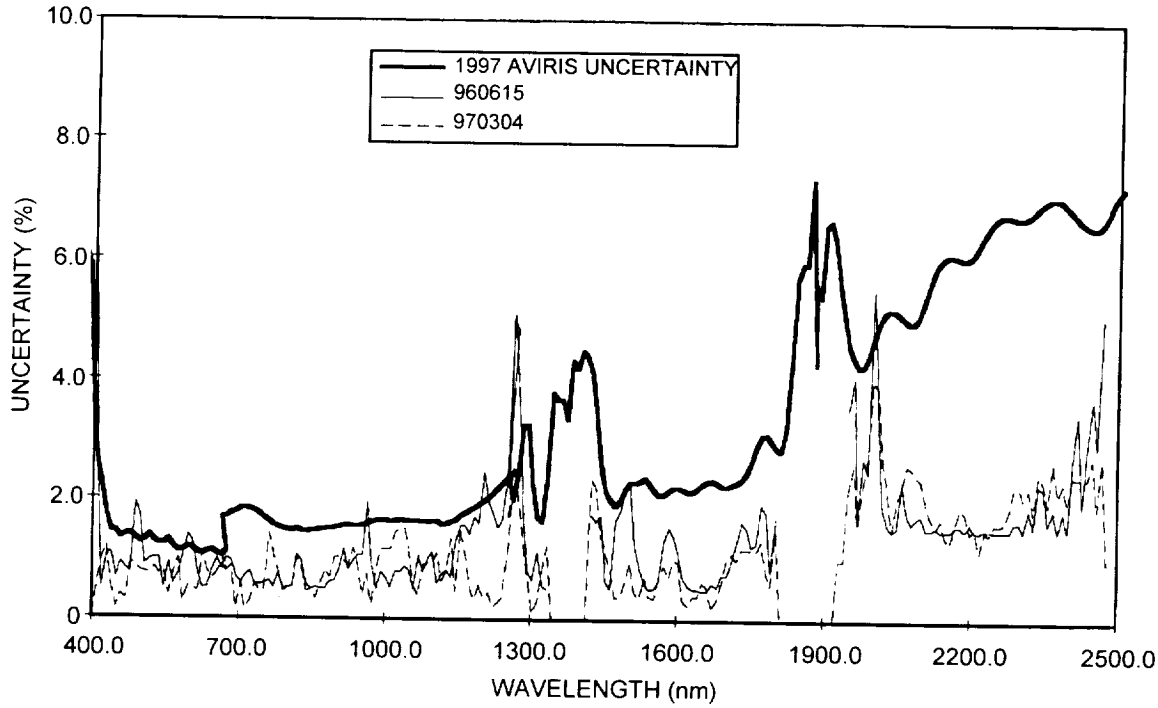

Figure 9. Uncertainty in AVIRIS NIST traced radiometric calibration and percent disagreement between AVIRIS measured radiance and MODTRAN predicted radiance for June 15, 1996 and March 4, 1997 inflight calibration experiments.

5.0 Discussion

Results from a calibration experiment in 1996 and 1997 are presented. These results show good agreement between the predicted radiance and measured radiance for the calibration targets. In each of these years, additional inflight calibration experiments where held at several times through the flight season. In all cases the agreement between the predicted and measured radiance was better than 96 percent for these years. In addition, the detector stabilized onboard calibrator was used to monitor AVIRIS radiometric stability for every flight line acquired in 1996 and 1997. Analysis of the onboard calibrator data set for these years shows AVIRIS to be stabilized at the 1 to 2 percent level over the 1996 and 1997 flight season.

6.0 Conclusion

Calibration experiments were held in 1996 and 1997 for the AVIRIS sensor. The objective of the experiments was to validate the calibration of AVIRIS in-flight. The experiment held on June 15, 1996 showed a 96.1 percent average absolute agreement between the predicted and measured radiance. The experiment on March 4, 1997 showed a 96.6 percent agreement. These experiments in conjunction with the calibration monitoring throughout the flight seasons in 1996 and 1997 validate the calibration of AVIRIS in this period. These results support the use of AVIRIS spectral images acquired in 1996 and 1997 for quantitative scientific research and environmental applications.

7.0 References

Berk, A., L.S. Bernstein, and D.C. Robertson, "MODTRAN: A moderate resolution model for LOWTRAN 7," Final Report, GL-TR-0122, AFGL, Hanscom AFB, MA, 42 pp., 1989.

Bruegge, C.J., J.E. Conel, J.S. Margolis, R.O. Green, G. Toon, V. Carrere, R.G. Holm, and G. Hoover, In-situ atmospheric water-vapor retrieval in support of AVIRIS validation, SPIE Vol. 1298, Imaging spectroscopy of the terrestrial environment, 1990.

Chrien, T.G., R.O. Green, and M. Eastwood, Laboratory spectral and radiometric calibration of the Airborne Visible/Infrared Imaging Spectrometer (AVIRIS), SPIE Vol. 1298, Imaging spectroscopy of the terrestrial environment, 1990.

Conel, J.E., R.O. Green, R.E. Alley, C.J. Bruegge, V. Carrere, J.S. Margolis, G. Vane, T.G. Chrien, P.N. Slater, S.F. Biggar, P.M. Teillet, R.D. Jackson and M.S. Moran, In-flight radiometric calibration of the Airborne Visible/Infrared Imaging Spectrometer (AVIRIS), SPIE Vol. 924, Recent advances in sensors, radiometry and data processing for remote sensing, 1988.

Green, R.O., G. Vane, and J.E. Conel, Determination of in-flight AVIRIS spectral, radiometric, spatial and signal-to-noise characteristics using atmospheric and surface measurements from the vicinity of the rare-earth-bearing carbonatite at Mountain Pass, California, in Proceedings of the Airborne Visible/Infrared Imaging Spectrometer (AVIRIS) Performance Evaluation Workshop, JPL Pub. 88-38, Jet Propulsion Laboratory, Pasadena, California, 162-184, 1988, pp. 162-184.

Green, R.O., J.E. Conel, V. Carrere, C.J. Bruegge, J.S. Margolis, M.Rast, and G. Hoover, "In-flight Validation and Calibration of the Spectral and Radiometric Characteristics of the Airborne Visible/Infrared Imaging Spectrometer (AVIRIS)," Proc. SPIE Conference on Aerospace Sensing, Imaging Spectroscopy of the Terrestrial Environment, Orlando, Florida, 16-20 April 1990, pp. 18-36.

Green, R. O., J. E. Conel, C. J. Bruegge, J. S. Margolis, V. Carrere, G. Vane and G. Hoover, "In-flight Calibration of the Spectral and Radiometric Characteristics of AVIRIS in 1991," Summaries of the Third Annual JPL Airborne Geoscience Workshop, JPL Publication 92-14, Vol. 1., AVARIS Workshop pp. 1-4, Jet Propulsion Laboratory, Pasadena, CA, 1992.

Green, R. O., S. Larson and I. Novack, "Calibration of AVIRIS digitized data", Proc. Third Annual Airborne Geoscience Workshop, JPL Pub 92-14, pp. 1992.

Green, R. O., J. E. Conel, M. Helmlinger, J. van den Bosch, C. Chovit and T. Chrien, "Inflight Calibration of AVIRIS in 1992 and 1993", Proc. Fourth Annual Airborne GeoScience Workshop, JPL Pub 93-26, 1993, pp. 69-72.

Green, R. O., "Use of Data from the AVIRIS Onboard Calibrator" Proc. Fourth Annual Airborne GeoScience Workshop, JPL Pub 93-26, 1993, pp. 69-72.

Green, R. O., J. E. Conel, M. Helmlinger, J. van den Bosch and P. Hajek, "Inflight Radiometric Calibration of AVIRIS in 1994", Proc. Fifth Annual Airborne GeoScience Workshop, JPL Pub 95-1, 1995, pp. 83-86.

Green, R. O., J. E. Conel, J. Margolis, C. Chovit and J. Faust, "InFlight Calibration and Validation for the Airborne Visible/Infrared Imaging Spectrometer (AVIRIS), Proc. Sixth Annual Airborne Earth Science Workshop, JPL Pub 96-4, 1996, pp. 83-86..

8.0 ACKNOWLEDGMENTS

The majority of this research was carried out at the Jet Propulsion Laboratory, California Institute of Technology, under contract with the National Aeronautics and Space Administration. A portion of the work was performed at the Institute for Computational Earth System Science, University of California, Santa Barbara, CA. I would like to express my appreciation for the efforts of the AVIRIS at the Jet Propulsion Laboratory.

On-orbit Calibration of ADEOS OCTS with an AVIRIS Underflight

Robert O. Green, Betina Pavri, Joseph W. Boardman, Masanobu Shimada and Hiromi Oaku

NASA Jet Propulsion Laboratory, California Institute of Technology
Pasadena, CA 91109

1.0 Introduction

The Ocean Color Temperature Scanner (OCTS) onboard the Advanced Earth Observation Satellite (ADEOS) was launched on August 17, 1996. Calibration of OCTS is required for use of the on-orbit measured data for retrieval of physical properties of the ocean. In the solar reflected portion of the electromagnetic spectrum, OCTS measures images with nominally 700-m spatial resolution through eight multispectral bands (Table 1). The objective of this research was to establish the absolute radiometric calibration of OCTS on orbit through an underflight by the Airborne Visible/Infrared Imaging Spectrometer (AVIRIS). AVIRIS is a NASA Earth-observing imaging spectrometer designed, built and operated by the Jet Propulsion Laboratory (JPL). AVIRIS acquires data from 20-km altitude on a NASA ER-2 aircraft, above most of the Earth's atmosphere. AVIRIS measures the solar reflected spectrum from 370 nm to 2500 nm through 224 contiguous spectral channels. The full width at half maximum (FWHM) of the spectral channels is nominally 10-nm. AVIRIS spectra are acquired as images of 11 km by up to 800 km extent with 20-m spatial resolution. The high spectral resolution of AVIRIS data allows direct convolution to the spectral response functions of the eight multispectral bands of OCTS (Figure 1). The high spatial resolution of AVIRIS data allows for spatial re-sampling of the data to match the ADEOS sensors spatial resolution. In addition, the AVIRIS high spatial resolution allows assessment of the scaling effects due to environmental factors of thin cirrus clouds, sub-pixel cloud cover, white caps, ocean foam, sun-glint, and bright-target adjacency. The platform navigation information recorded by AVIRIS allows calculation of the position and observation geometry of each spectrum for matching to the OCTS measurement. AVIRIS is rigorously characterized and calibrated in the laboratory prior to and following the flight season (Chrien et al., 1990, 1996). The stability and repeatability of AVIRIS calibration have been validated through an extensive series of inflight calibration experiments (Green et al., 1988,1996). In the OCTS portion of the spectrum, using pre- and post-flight runway calibrations of AVIRIS coupled with the on-board calibrator (Green et al. 1993, Chrien et al., 1995) an absolute calibration accuracy of better than 3% spectral (Green, 1995), 2% radiometric (Figure 2) and 5% spatial (Chrien and Green, 1993) has been achieved.

An analogous satellite underflight calibration experiment was performed with AVIRIS and the Optical Sensor (OPS) onboard the Japanese Earth Resources Satellite (JERS) (Green et al. 1993, 1997).

2.0 Data

On the 20th of May 1997 AVIRIS underflew the ADEOS OCTS sensor off the coast of Southern California near latitude 36.12 and longitude 128.25. The OCTS sensor was tilted to the Northeast to avoid sun glint. In order for the AVIRIS spectral images to overlap the area, the azimuth, and the zenith angles of the OCTS measurements, AVIRIS was flown in a circle (Figure 3) beneath OCTS (Figure 4). The AVIRIS scan angle (±15 degrees) plus the aircraft roll angle (15 degrees) assured overlap of both area and observation geometry. The data from the 20th of May 1997 flight were spectrally, radiometrically and spatially calibrated through the AVIRIS data system algorithms. The OCTS data were requested as uncalibrated digitized numbers at the sensor. Both the AVIRIS and the OCTS data sets included the position and pointing information at the time of acquisition. The simultaneous acquisition of the AVIRIS and OCTS with overlapping observation geometry provides the essential data set to complete the calibration objective.

Table 1. OCTS Visible to Near-Infrared Data Characteristics

SPECTRAL BAND	CENTER	FWHM
1	0.412 μm	20 nm
2	0.443 μm	20 nm
3	0.490 μm	20 nm
4	0.520 μm	20 nm
5	0.565 μm	20 nm
6	0.665 μm	20 nm
7	0.765 μm	40 nm
8	0.865 μm	40 nm
RADIOMETRIC		
Digitization	10 bits	
GEOMETRIC		
Field of view	40° (1500 km)	
Instantaneous FOV	0.85 mrad (~700 m)	

Table 2. AVIRIS Data Characteristics

SPECTRAL	
Wavelength range	370 to 2500 nm
Sampling	10 nm
Spectral response (FWHM)	10 nm
Calibration	<1 nm
RADIOMETRIC	
Radiometric range	0 to maximum Lambertian radiance
Sampling	~ 1 DN noise RMS
Absolute calibration	<= 96 %
Calibration Stability	<= 98 %
Polarization Sensitivity	<= 1 %
Noise	Exceeding NEdL/SNR requirement
GEOMETRIC	
Field of view	30 degrees (11 km)
Instantaneous FOV	1.0 mrad (20 m)
Calibration	<=0.1 mrad
Flight line length	800 km

3.0 Analysis

Determination of the areas of the OCTS and AVIRIS images with the same observation geometries requires projection of the data based on the position and pointing of the sensor. As a new set of algorithms was developed to calculate the azimuth (Figure 5) and zenith (Figure 6) angles of the AVIRIS spectra based on the Global Positioning System (GPS) and Inertial Navigation System (INS) information recorded from the ER-2 aircraft. For the geometric calculations, the GPS provided the latitude, longitude, and altitude of ER-2; and the INS provided the roll, pitch, and yaw of the ER-2 aircraft. The position of AVIRIS is known with respect to the ER-2 aircraft with some uncertainty introduced by the ±1.5 degree AVIRIS automatic roll correction. A related set of algorithms was developed and used to calculate the azimuth (Figure 7) and zenith angles (Figure 8) of the OCTS image. As with AVIRIS, the satellite sensors position and pointing information were supplied with the OCTS image data. With both the AVIRIS and OCTS image azimuth and zenith angles determined, the area of overlap was determined (Figure 9). This area contains the AVIRIS spectra and OCTS band of the same area on the surface with the same observation azimuth and zenith. The average AVIRIS spectrum from this area was extracted (Figure 10). A correction factor was applied for the transmittance from the 20-km AVIRIS altitude to the top of the atmosphere (Figure 11). This transmittance correction factor was calculated with the MODTRAN radiative transfer code (Berk et al., 1989, Anderson et al., 1995). The Ozone was constrained by the amount reported in the TOVS total ozone archive for the area of acquisition (http://nic.fb4.noaa.gov/products/stratosphere/tovsto/archive/np/). The corrected AVIRIS spectrum was convolved to the eight solar reflected OCTS multispectral bands (Figure 12). On-orbit radiometric calibration coefficients for OCTS were calculated as the ratio of the AVIRIS radiance propagated to the top of the atmosphere and the OCTS digitized numbers with dark signal subtracted (Table 3). Uncertainties were traced to the uncertainty in AVIRIS absolute radiometric calibration. The resulting on-orbit OCTS radiometric calibration coefficients were the objective of the AVIRIS underflight of OCTS and this research.

Table 3. ADEOS OCTS AVIRIS Based Radiometric Calibration Coefficients.

Band	OCTS DN	AVIRIS Radiance*	OCTS RCC**	RCC** Uncertainty
1	2.119E+03	7.673E+00	3.620E-03	1.086E-04
2	2.013E+03	7.220E+00	3.587E-03	7.174E-05
3	1.841E+03	5.661E+00	3.075E-03	5.535E-05
4	1.400E+03	4.254E+00	3.040E-03	4.864E-05
5	1.199E+03	2.787E+00	2.325E-03	3.720E-05
6	9.242E+02	1.383E+00	1.496E-03	2.842E-05
7	7.814E+02	7.174E-01	9.181E-04	1.653E-05
8	1.064E+03	5.008E-01	4.708E-04	8.004E-06

* μW/cm^2/nm/sr
** μW/cm^2/nm/sr/DN

4.0 Conclusion

The eight solar reflected multispectral bands of the OCTS sensor onboard the ADEOS satellite have been calibrated by an underflight of the AVIRIS imaging spectrometer. This calibration was enabled by the AVIRIS characteristics of: high spectral resolution; high spatial resolution; large image extent; accurate spectral, radiometric, and spatial calibration; high altitude flight, and accurate position and pointing knowledge. In addition, a new set of software modules has been developed to project AVIRIS spectra and satellite sensor multispectral data based on platform position and pointing information. These software modules will support future spaceborne sensor calibration efforts with AVIRIS.

This AVIRIS-based method is an important independent approach to establish the calibration of spaceborne optical sensors in the solar reflected spectrum. This approach calibrates the spaceborne sensor in the operational on-orbit environment with a signal level appropriate to the satellite sensor measurement objectives.

Increasingly rigorous calibration requirements are being established for Earth-looking satellite sensors to support physically based data analysis. Calibration is also required to support measurement and monitoring of the Earth system through time. The calibration of satellite sensors must be established and validated on orbit where the operational measurement objectives of the sensor are accomplished. The AVIRIS sensor characteristics, in conjunction with the AVIRIS rigorous calibration, enables a new strategy for the on-orbit calibration of satellite optical imaging sensors with a range of spatial, spectral, and radiometric resolutions in the solar reflected spectrum.

5.0 Acknowledgments

The majority of this research was carried out at the Jet Propulsion Laboratory, California Institute of technology, under contract with the National Aeronautics and Space Administration. A portion of the work was performed at the Institute for Computational Earth System Science, University of California, Santa Barbara, CA. I would like to express my appreciation for the efforts of the AVIRIS team at the Jet Propulsion Laboratory.

6.0 References

Anderson, G.P., Wang, J., Chrtwynd, J. H., (1995), MODTRAN3: An update and recent validation against airborne high resolution inferometer measurements, *Summaries of the Fifth Annual JPL Airborne Earth Science Workshop,* JPL Publication 95-1, Vol. 1: AVIRIS Workshop, R.O. Green, Ed., Jet Propulsion Laboratory, Pasadena, CA, 5-8.

Berk, A., L.S. Bernstein, and D.C. Robertson, MODTRAN (1989): A Moderate Resolution Model for LOWTRAN 7, Final report, GL-TR-0122, AFGL, Hanscomb AFB, MA., 42 pp.

Chrien, T.G., Green, R.O., Eastwood, M. L. (1990), Accuracy of the spectral and radiometric laboratory calibration of the Airborne Visible/Infrared Imaging Spectrometer, Proceedings of the Second Airborne Visible/Infrared Imaging Spectrometer (AVIRIS) Workshop., June 4-5, 1990, R. O. Green, Ed., JPL Publication 90-54, Jet Propulsion Laboratory, Pasadena, CA, 1-14.

Chrien, T.G.; Green, R.O. (1993), Instantaneous Field of View and Spatial Sampling of the Airborne Visible/Infrared Imaging Spectrometer (AVIRIS), Summaries of the Fourth Annual JPL Airborne Geoscience Workshop, October 25-29, 1993, R. O. Green, Ed., Vol. 1. AVIRIS, JPL Pub 93-26, Jet Propulsion Laboratory, Pasadena, CA, 23-26.

Chrien, T.G.; Eastwood, M.; Green, R.O.; Sarture, C.; Johnson, H.; Chovit, C.; Hajek, P. (1995), Airborne Visible Infrared/Visible Imaging Spectrometer (AVIRIS) Onboard Calibration System, Summaries of the Fifth Annual JPL Airborne Earth Science Workshop, Vol. 1. AVIRIS, Workshop JPL Pub 95-1, Jet Propulsion Laboratory, Pasadena, CA, 31-32.

Chrien, T.G; Green, R.O.; Chovit, C. J.; Eastwood, ML; Sarture, CM, 1996, Calibration of the Airborne Visible/Infrared Imaging Spectrometer in the Laboratory, Summaries of the Sixth Annual JPL Airborne Earth Science Workshop, March 4-8, 1996, Publication 96-4, Vol. 1: AVIRIS Workshop, R. O. Green, Ed., Jet Propulsion Laboratory, Pasadena, CA, 39-48.

Green, R.O., Vane, G. A., Conel, J. L., (1988), Determination of in flight AVIRIS spectral, radiometric, spatial, and signal to noise characteristics using atmospheric and surface measurements from the vicinity of the rare earth bearing carbonatite at Mountain Pass, California, Proceedings of the Airborne Visible/Infrared Imaging Spectrometer (AVIRIS) Performance Evaluation Workshop, June 6, 7, and 8, G. Vane, Ed., JPL Publication 88-38, Jet Propulsion Laboratory, Pasadena, CA, 162-184.

Green, R.O. (1993), Use of Data from the AVIRIS Onboard Calibrator, Summaries of the Fourth Annual JPL Airborne Geoscience Workshop, October 25-29, 1993, R. O. Green, Ed., Vol. 1. AVIRIS Workshop, JPL Publication 93-26, Jet Propulsion Laboratory, Pasadena, CA, 65-68.

Green, R.O.; Conel, JE; van den Bosch, J; Shimada, M. (1993), Use of the Airborne Visible/Infrared Imaging Spectrometer to Calibrate the Optical Sensor on Board the Japanese Earth Resources Satellite-1, Summaries of the Fourth Annual JPL Airborne Geoscience Workshop, Vol. 1. AVIRIS Workshop, R.O. Green, Ed., JPL Publication 93-26, Jet Propulsion Laboratory, Pasadena, CA, 77-80.

Green, R.O. (1995), Determination of the In-Flight Spectral Calibration of AVIRIS Using Atmospheric Absorption Features, Summaries of the Fifth Annual JPL Airborne Earth Science Workshop, Vol. 1. AVIRIS Workshop, R.O. Green, Ed., JPL Pub 95-1, Jet Propulsion Laboratory, Pasadena, CA, 71-74.

Green, R.O.; Conel, J.E.; Margolis, J.; Chovit, C.; Faust, J. (1996), In-Flight Calibration and Validation of the Airborne Visible/Infrared Imaging Spectrometer (AVIRIS), Summaries of the Sixth Annual JPL Airborne Earth Science Workshop, JPL Publication 96-4, Vol. 1: AVIRIS Workshop, R.O. Green, Ed., JPL: Pasadena, CA, 115-126.

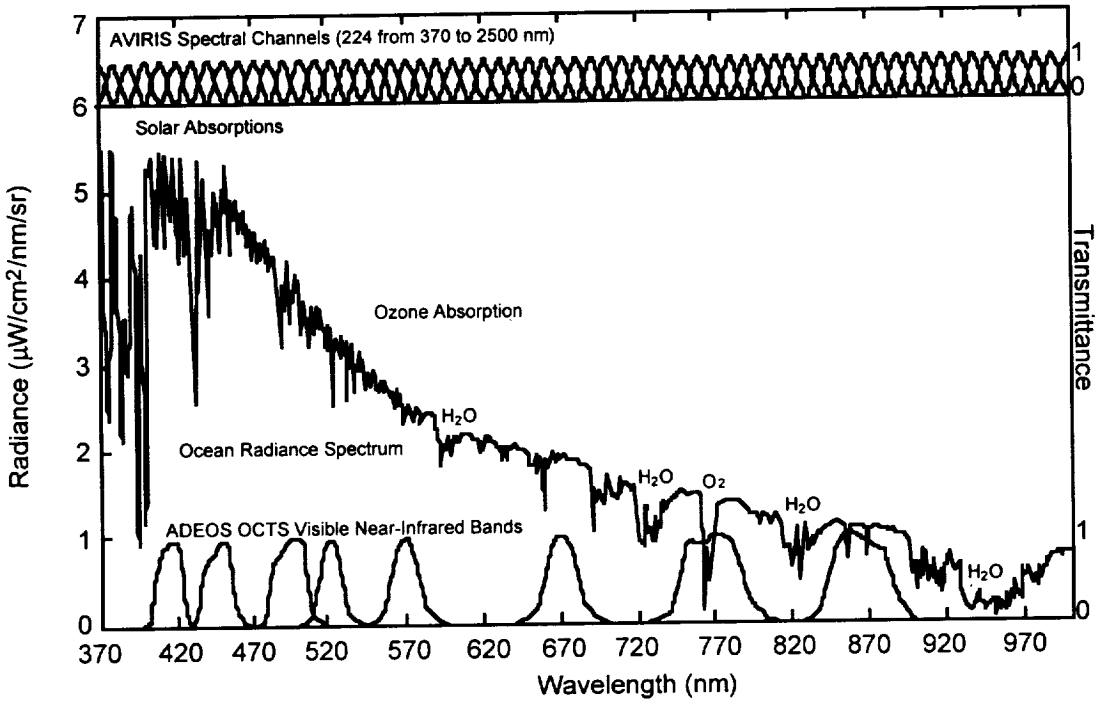

Figure 1. The OCTS bands and AVIRIS spectral channels for the spectral region from 400 to 1000 nm are shown. Also shown is a modeled high-resolution radiance spectrum for an ocean target.

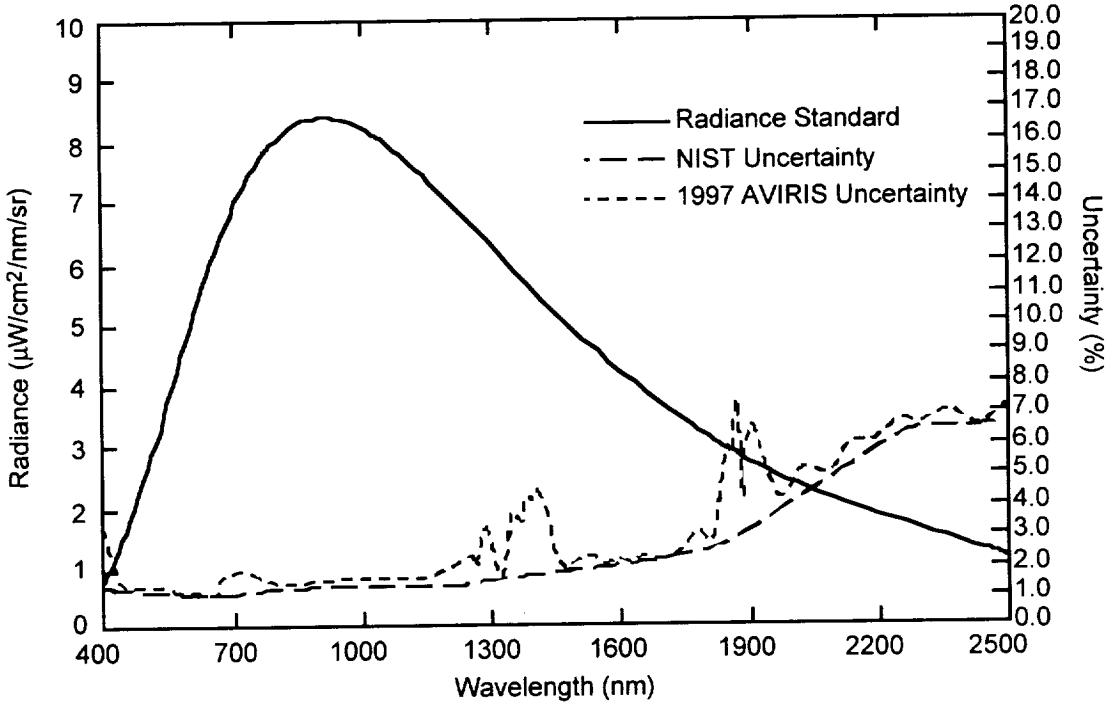

Figure 2. AVIRIS radiometric uncertainty based on the transfer of the radiance calibration standard to the AVIRIS sensor.

AVIRIS Data 970520
matching view geometry shown in green box
UTM zone 9 projection

Figure 3. AVIRIS flight circle under the ADEOS OCTS sensor on the 20th of May 1997.

OCTS Data D129000052000218.01
matching view geometry shown in green box
UTM zone 9 projection

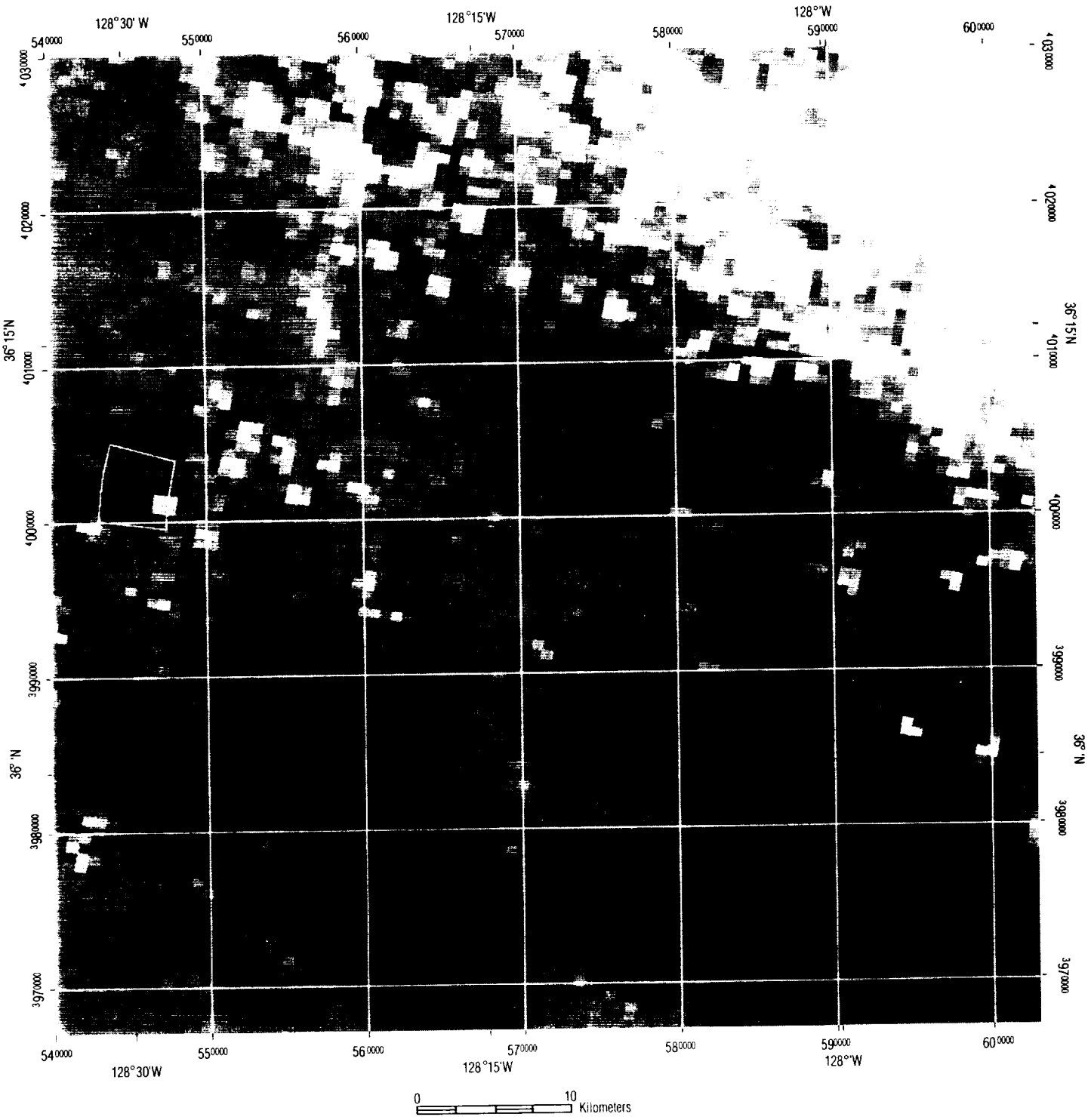

Figure 4. OCTS image for the 20th of May 1997.

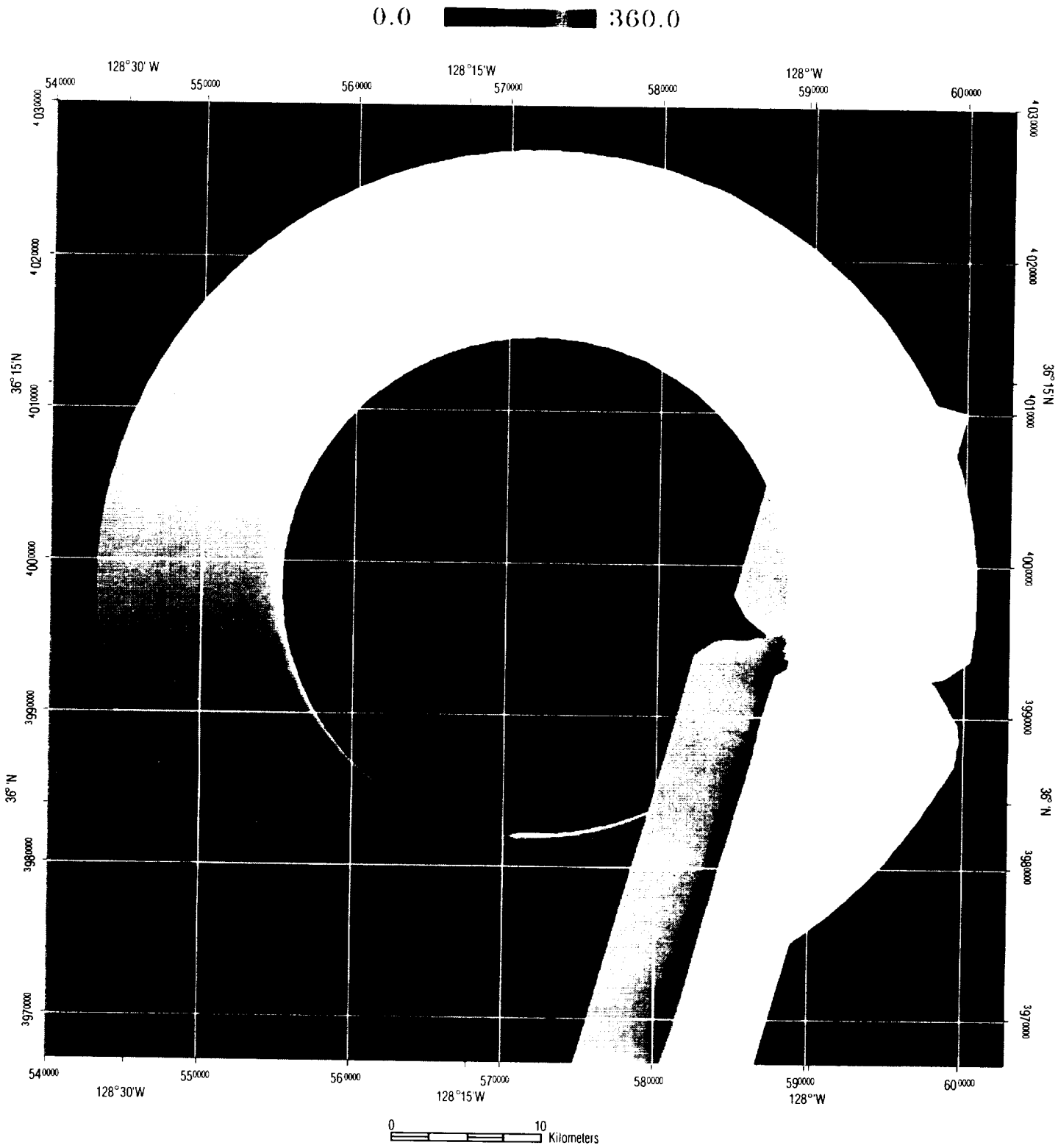

Figure 5. AVIRIS azimuth angles for the calibration data set.

AVIRIS Sensor Zenith Angle
UTM zone 9 projection

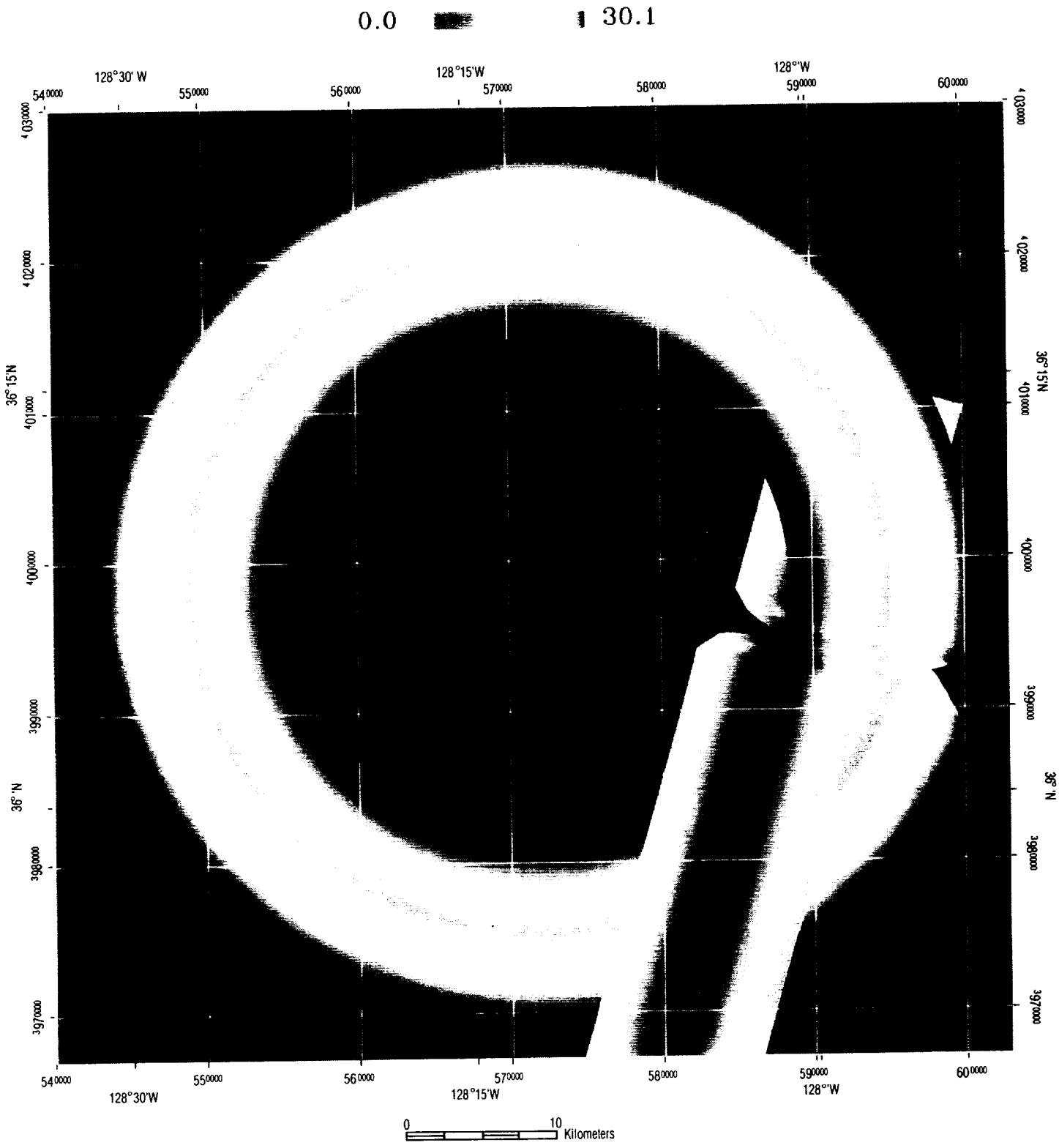

Figure 6. AVIRIS zenith angles for the calibration data set.

OCTS Sensor Azimuth Angle
UTM zone 9 projection

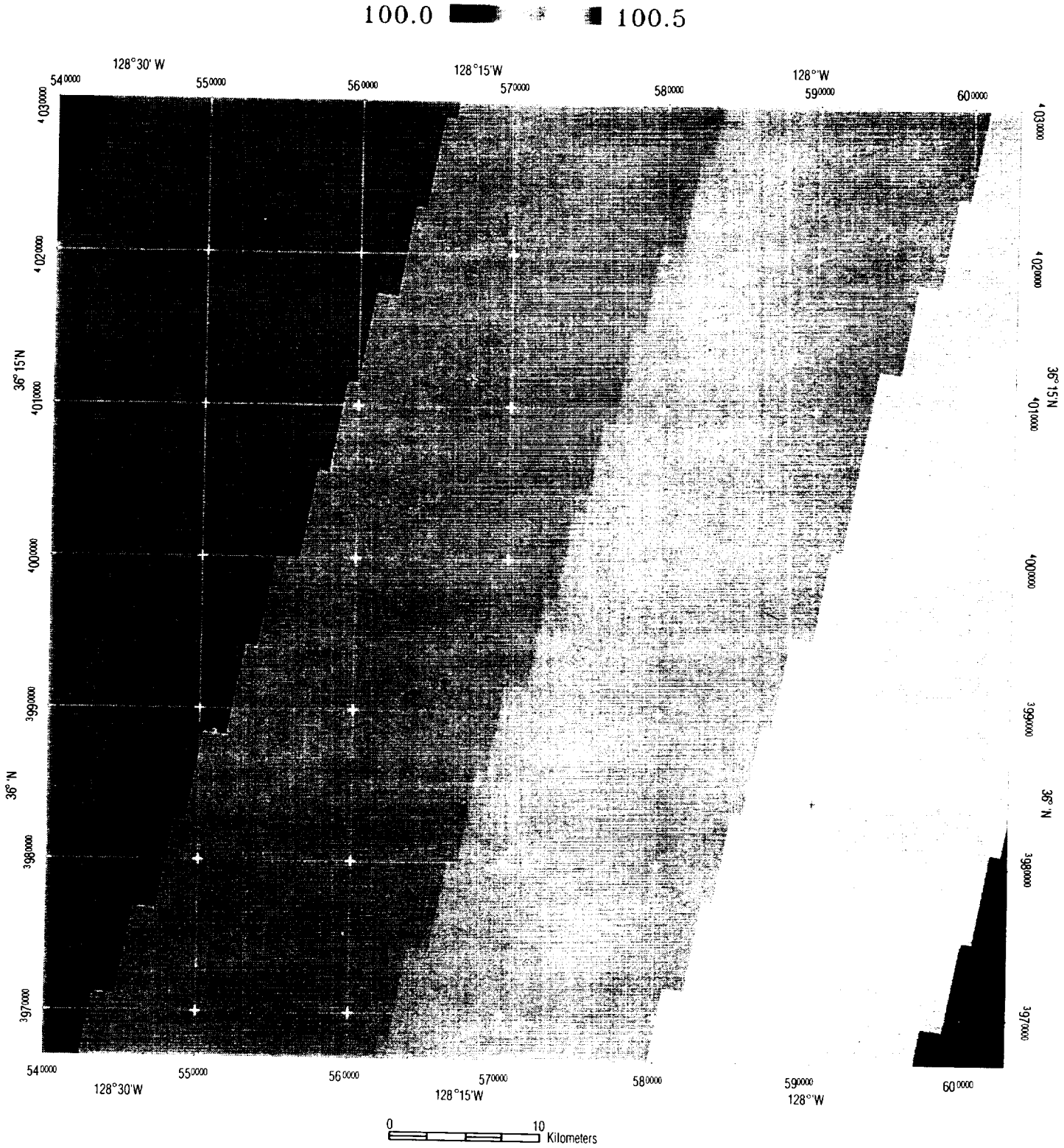

Figure 7. OCTS azimuth angles for the calibration data set.

OCTS Sensor Zenith Angle
UTM zone 9 projection

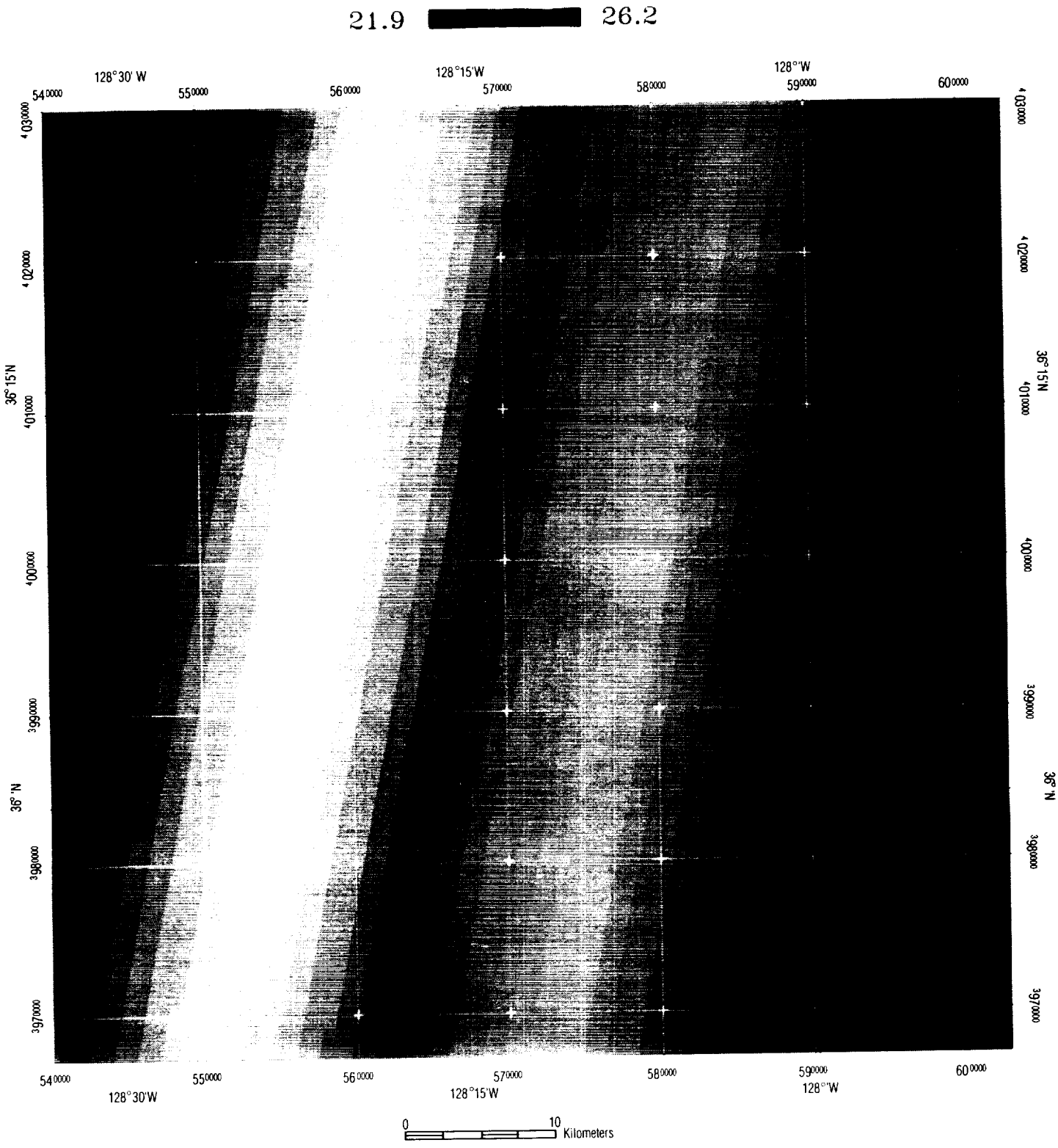

Figure 8. OCTS zenith angles for the calibration data set.

AVIRIS /OCTS Matching View Geometry
Zenith and Azimuth Within 5 Degrees
UTM zone 9 projection

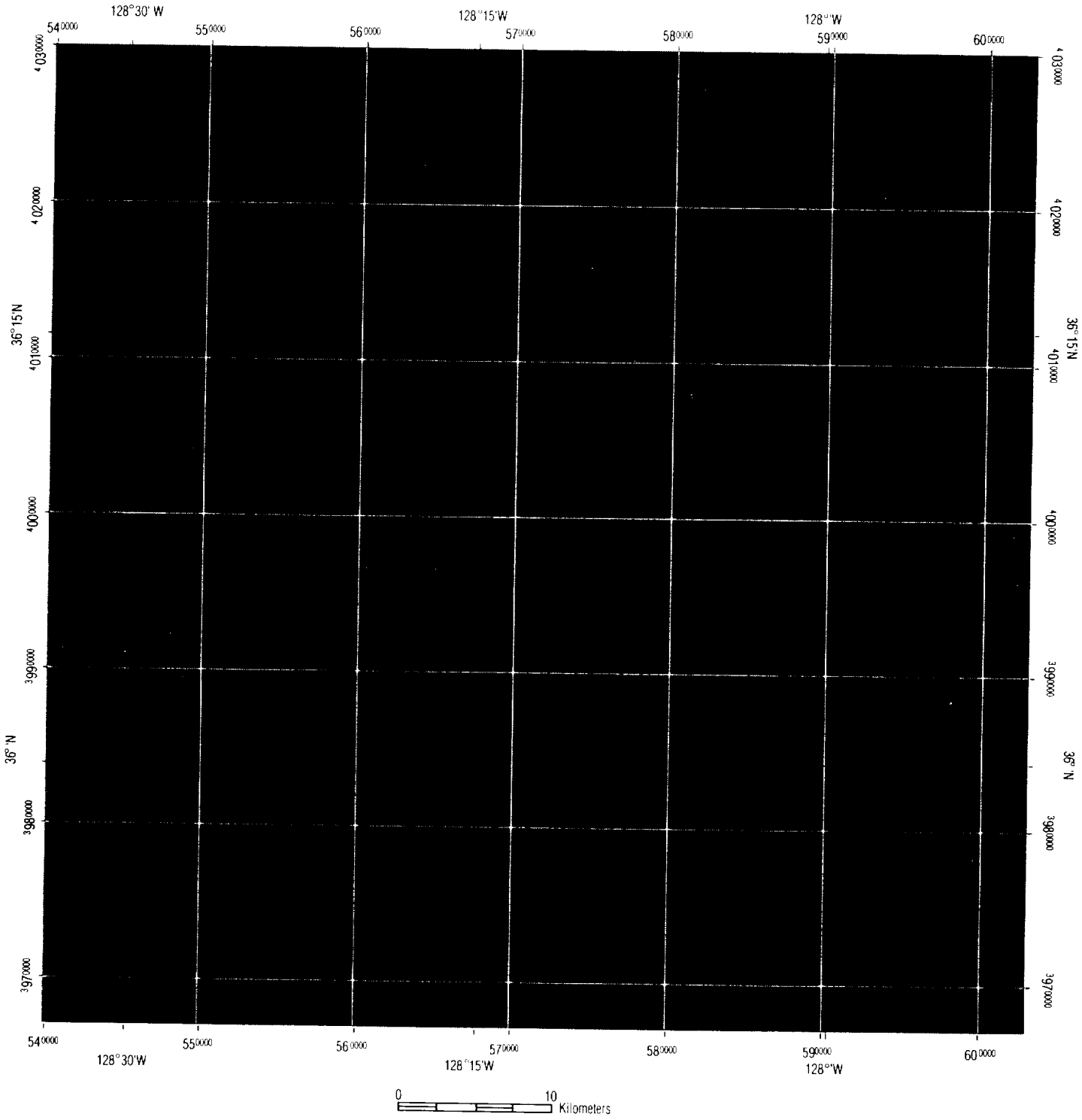

Figure 9. Area of overlap in azimuth and zenith angles between AVIRIS and OCTS for the 20th of May 1997 data set.

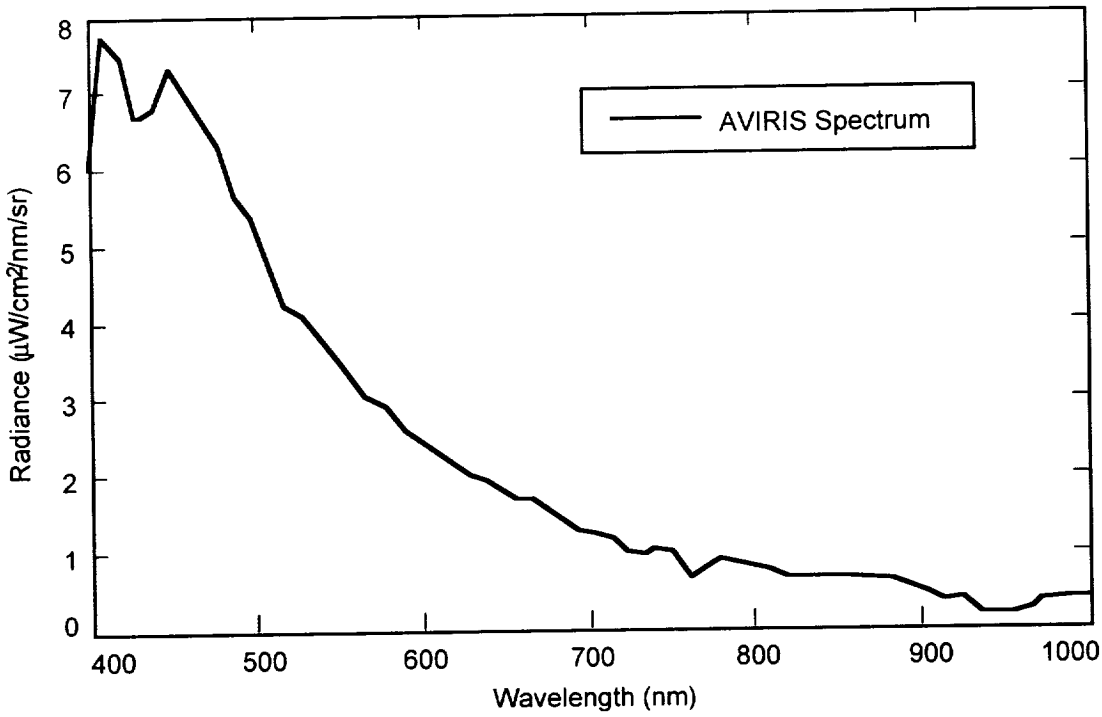

Figure 10. AVIRIS spectrum average for the area of geometric overlap between AVIRIS and OCTS .

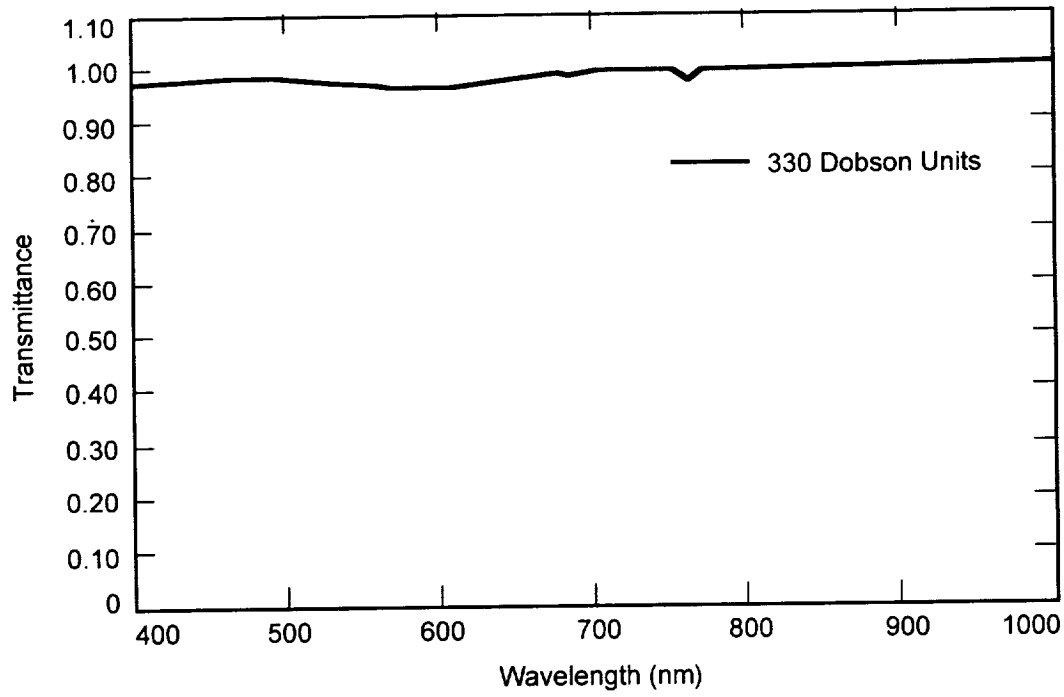

Figure 11. Transmittance from the AVIRIS altitude of 20 km to the top of the atmosphere.

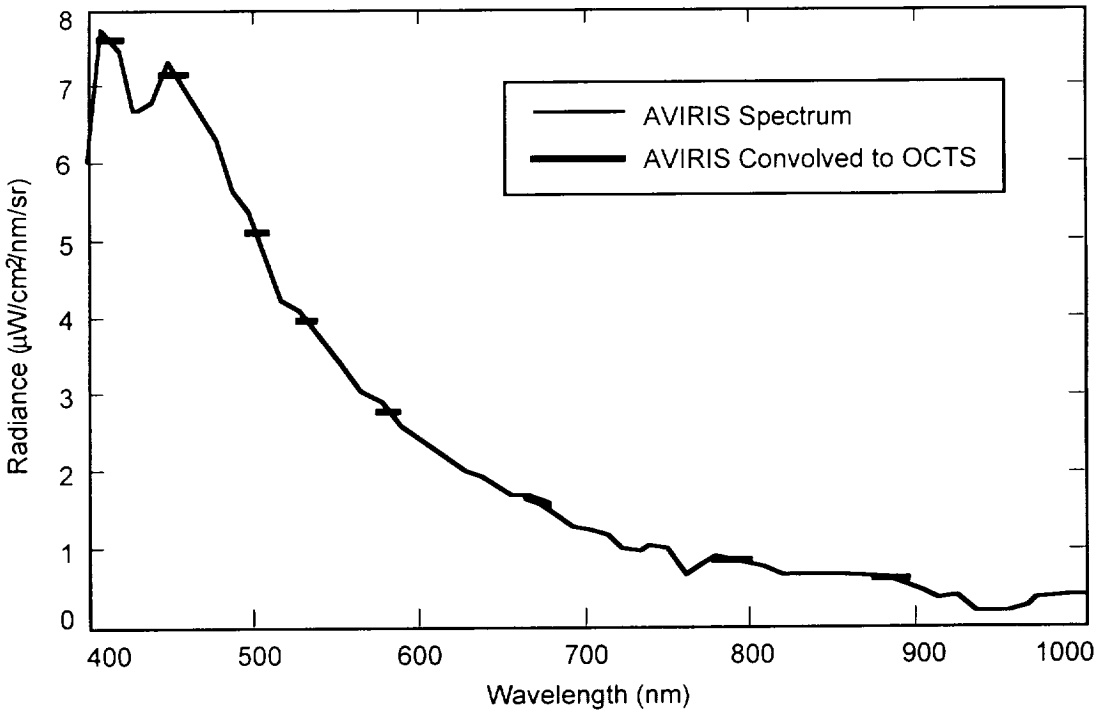

Figure 12. AVIRIS spectrum average convolved to the spectral response function of OCTS multispectral bands.

Mapping Agricultural Crops with AVIRIS Spectra in Washington State

Robert O. Green, Betina Pavri, Dar Roberts, and Susan Ustin

Jet Propulsion Laboratory, California Institute of Technology
Pasadena, CA 91109

1.0 Introduction

Spectroscopy is used in the laboratory to measure the molecular components and concentrations of plant constituents to answer questions about the plant type, status, and health. Imaging spectrometers measure the upwelling spectral radiance above the Earth's surface as images. Ideally, imaging spectrometer data sets should be used to understand plant type, plant status, and health of plants in an agricultural setting. An Airborne Visible/Infrared Imaging Spectrometer (AVIRIS) data set was acquired over agricultural fields near Wallula, Washington on July 23rd, 1997 (Figure 1). AVIRIS measures upwelling radiance spectra through 224 spectral channels with contiguous 10-nm sampling from 400 to 2500 nm in the solar-reflected spectrum. The spectra are measured as images of 11 by up to 800 km with 20-m spatial resolution. The spectral images measured by AVIRIS represent the integrated signal resulting from: the solar irradiance; two way trasmittance and scattering of the atmosphere; the absorptions and scattering of surface materials; as well as the spectral, radiometric and spatial response functions of AVIRIS. This paper presents initial research to derive properties of the agricultural fields near Wallula from the calibrated spectral images measured by AVIRIS near the top of the atmosphere.

2.0 Data and Atmospheric Correction

AVIRIS data are delivered as the calibrated spectral radiance measured at the sensor. Radiance spectra from five of the fields in the Wallula AVIRIS data set show differences, but are dominated by the solar source function and the absorption and scattering of the atmosphere (Figure 2). A radiance to reflectance inversion algorithm (Green et al. 1993) based in part on the MODTRAN radiative transfer code (Berk et al. 1989, Anderson et al. 1995) was used to derive the apparent surface reflectance of the Wallula data set. The algorithm compensates for atmospheric water vapor, Rayleigh scattering, aerosol scattering, as well as the absorption of well mixed gases and ozone. The surface reflectance is calculated based on the observational geometry of the AVIRIS sensor and the position of the sun. A horizontal surface appropriate for agricultural fields is assumed. Surface reflectance spectra for the five fields of the Wallula data set (Figure 3) show the the solar and atmospheric effects in the measured radiance spectra are compensated by this algorithm. Surface reflectance was not derived for narrow regions of the spectrum near 1400 nm and 1900 nm absorption due to the strong absorption by atmospheric water vapor. In the derived reflectance spectra, the absorption and scattering signatures of the important molecules and constituents of plants in the agricultural fields are expressed. At the reflectance level, the spectrum from each field is different from the others. This difference in reflectance provides the basis for deriving information about the different crops.

3.0 Analysis and Results

To isolate the different spectral characteristics of the agricultural fields, spectral fitting was used to derive the apparent abundance of different molecular constituents expressed in the spectrum. The first molecular constituent derived was the expressed liquid water absorption based on the 980-nm spectral feature. A spectral fitting algorithm was applied to assess the strength of the liquid-water absorption. A wide variation in expressed liquid water in plants is shown across the agricultural fields of the Wallula AVIRIS data set (Figure 4). Close examination of the liquid water image reveals fields that were being actively irrigated at the time of the AVIRIS acquisition. Bright, high-liquid water, radii appear in the crop circle with active irrigation caused by the liquid water drops

on the vegetation. A second spectral fit for liquid water was calculated based on the liquid water absorption expressed at 1180 nm in the spectrum. The light scattering of vegetation is reduced at 1180 nm relative to 940 nm; consequently, the expressed liquid water is dominated more by the top of the vegetation canopy. The 1180-nm liquid water image also shows a wide variation in the expressed liquid water abundance across the Wallula AVIRIS data set (Figure 5). The variation in expressed liquid water absorption within and between the two spectral regions provides information both about plant leaf water and the plant canopy scattering characteristic.

The most important molecule in plants is chlorophyll. A spectral fitting alogorithm was applied to the Wallula data set to assess the strength of the chlorophyll absorption in the 450- to 700-nm region of the spectrum. The expressed strength of the chlorophyll absorption varies over a wide range of values across the spectral image (Figure 6). The derived chlorophyll and the liquid-water absorption do not correlate strongly. This lack of correlation is due to actual differences in the chlorophyll and liquid-water content of the vegetation. In addition, the lack of correlation results from the enhanced expression of liquid water due to multiple scattering in the canopy at 980 nm and 1180 nm. The strong absorption of chlorophyll precludes significant multiple scattering. The liquid-water and chlorophyll images provide different, but complementary, information about the characteristics of the plants in the agricultural fields at Wallula, Washington.

The final molecular absorption assessed in the AVIRIS agricultural images was cellulose. Cellulose shows strong absorption features in the 2100-nm and 2300-nm regions of the spectrum. A spectral-fitting algorithm was applied to assess the combined strength of these absorptions across the Wallula data set (Figure 7). A range of cellulose values results from the spectral fitting analysis. The cellulose image is more noisy than that for liquid water or for chlorophyll. This increased noise results from the strong overprint of the liquid-water absorption on the cellulose absorption in the 2000-nm to 2500-nm spectral region. However, in the fields with uniform derived cellulose, the cellulose information contributes to characterization of the agricultural vegetation.

The expressed abundances of the different molecular constituents derived through spectral fitting were used to group the agricultural fields into similar crop types. A field visit after the AVIRIS data acquisition and after initial analysis of the data was used to attach labels to the different spectra and expressed molecular abundances (Figure 8). Identification of agricultural crop type is a required first step before extracting useful plant status and plant health information for the AVIRIS spectral images.

4.0 Summary

AVIRIS spectral images were acquired over a group of agricultural fields in the Wallula Washington area on the 23rd of July 1997. The calibrated AVIRIS radiance spectra were inverted from total upwelling spectral radiance to surface reflectance. In surface reflectance the inherent molecular absorptions and scattering characteristics of the agricultural plants are expressed. A spectral fitting algorithm was applied to the AVIRIS reflectance spectra to assess the expressed abundance of the molecules liquid water, chlorophyll, and cellulose in the agricultural vegetation. Wide variations in the expressed molecular absoprtions were found across the AVIRIS Walulla data set. For liquid water, two different portions of the spectrum were assessed with the spectral fitting algorithm. The expressed liquid water differed between the 980-nm and 1180-nm derivation. This is expected based on the differential penetration of the radiance into the plant canopy. The expressed chlorophyll absorption varied widely across the data set. Chlorophyll and liquid water absorption were found not to be strongly correlated. This is explained by the high level of multiple scattering at 980 nm compared to the chlorophyll-dominated portion of the spectrum. Finally, cellulose was assessed based on the absorptions at 2100 nm and 2300 nm. As with water and chlorophyll, variation in the expressed cellulose abundance was found across the image. The AVIRIS surface reflectance spectra and derived molecular abundance were used to

group the agricultural field in the Wallula data set. A field visit was used to establish and verify the plant type in several of the fields. Future work will focus on moving beyond identification of plant type and towards assessment of plant status and health.

5.0 References

Anderson, G.P., J. Wang, and J.H. Chetwynd (1995), "MODTRAN3: An Update And Recent Validations Against Airborne High Resolution Interferometer Measurements," Summaries of the Fifth Annual JPL Airborne Earth Science Workshop, JPL Publication 95-1, Vol. 1: AVIRIS Workshop, R.O. Green, Ed., Jet Propulsion Laboratory, Pasadena, CA, 5-8.

Berk, A., L.S. Bernstein, and D.C. Robertson (1989), MODTRAN: A Moderate Resolution Model for LOWTRAN 7, Final Report, GL-TR-0122, AFGL, Hanscom AFB, MA, 42 pp.

Green, R.O., Conel, J.E., Roberts, D.A. (1993), Estimation of aerosol optical depth and additional amospheric parameters for the calculation of the reflectance from radience measured by the Airborne Visible/Infrared Imaging Spectrometer, Summaries of the Fourth Annual JPL Airborne Geoscience Workshop., JPL Publication 93-26, Vol. 1, AVIRIS Workshop, R.O. Green, Ed, Jet Propulsion Laboratory, Pasadena, CA, 73-76.

6.0 ACKNOWLEDGEMENTS

The majority of this research was carried out at the Jet Propulsion Laboratory, California Institute of technology, under contract with the National Aeronautics and Space Administration. A portion of the work was performed at the Institute for Computational Earth System Science, University of California, Santa Barbara, CA. I would like to express my appreciation for the efforts of the AVIRIS team at the Jet Propulsion Laboratory.

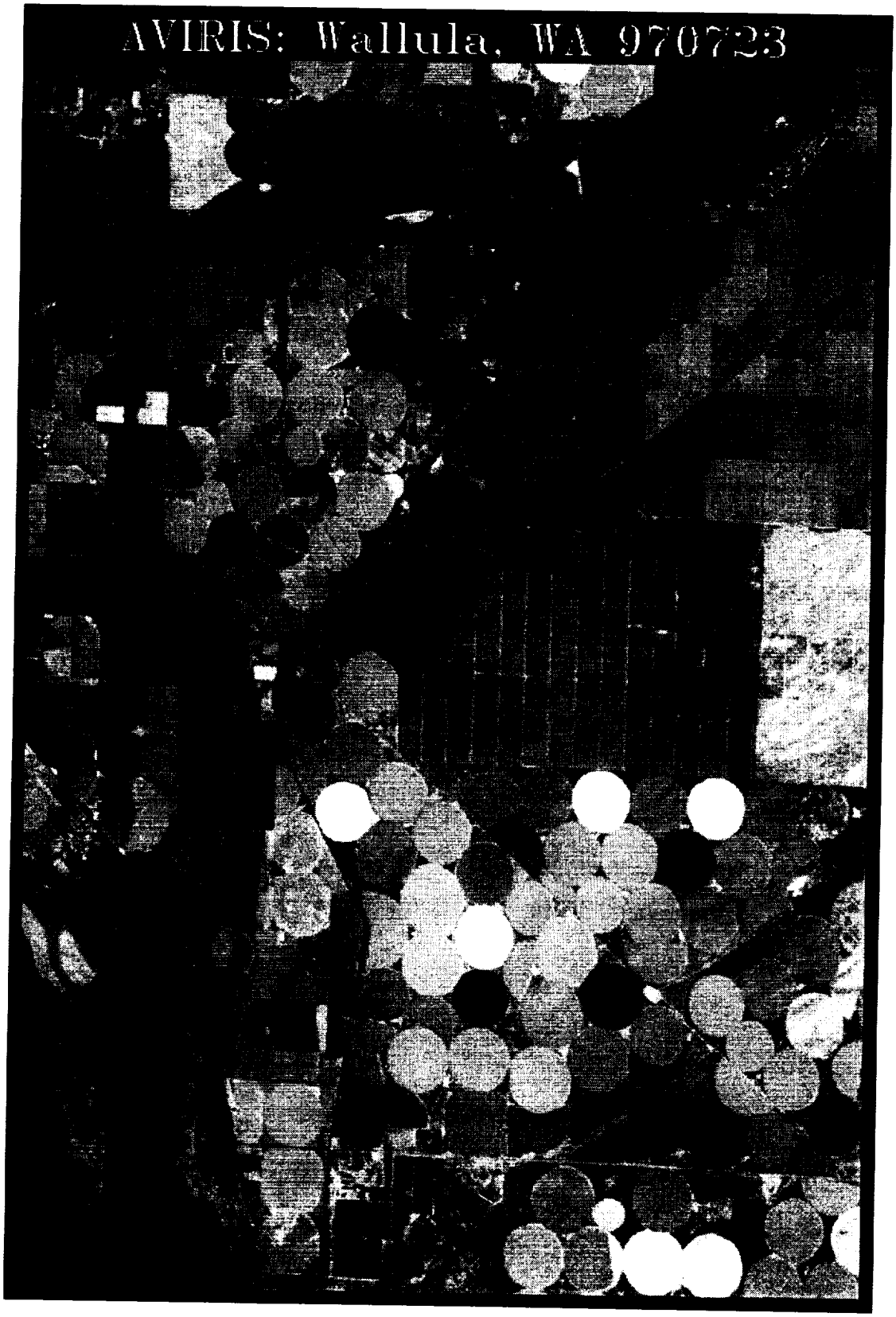

Figure 1. AVIRIS image of agricultural fields near Wallula, WA acquired on 23 July 1997.

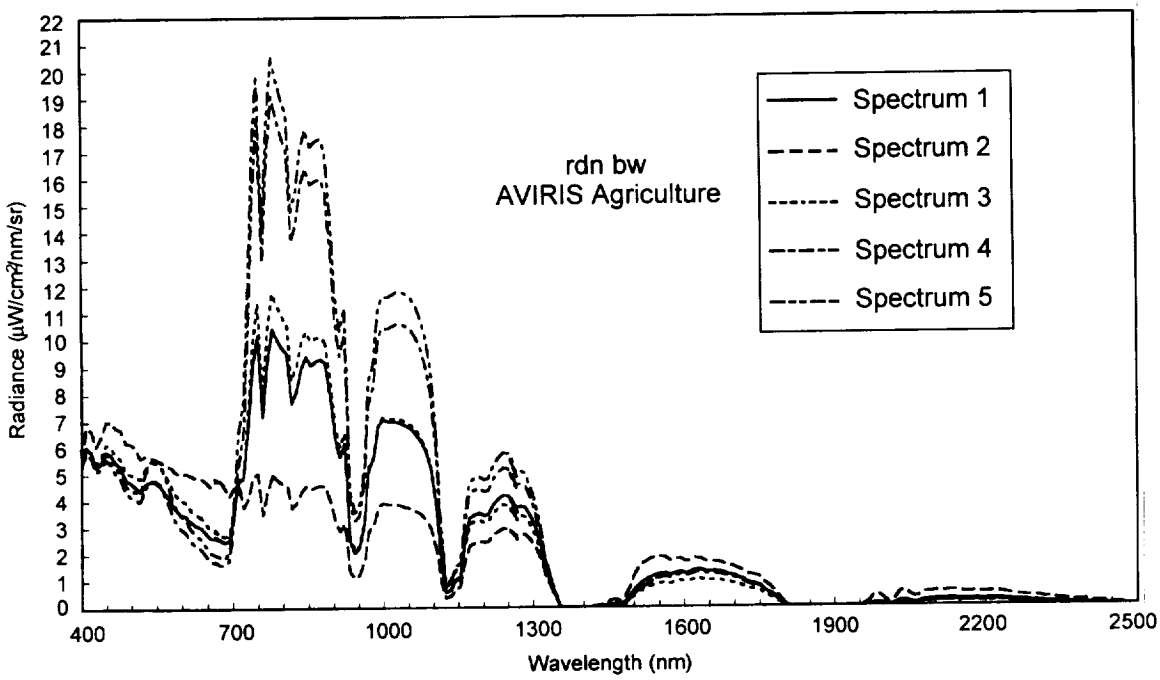

Figure 2. AVIRIS calibrated radiance spectra of agricultural fields and background areas.

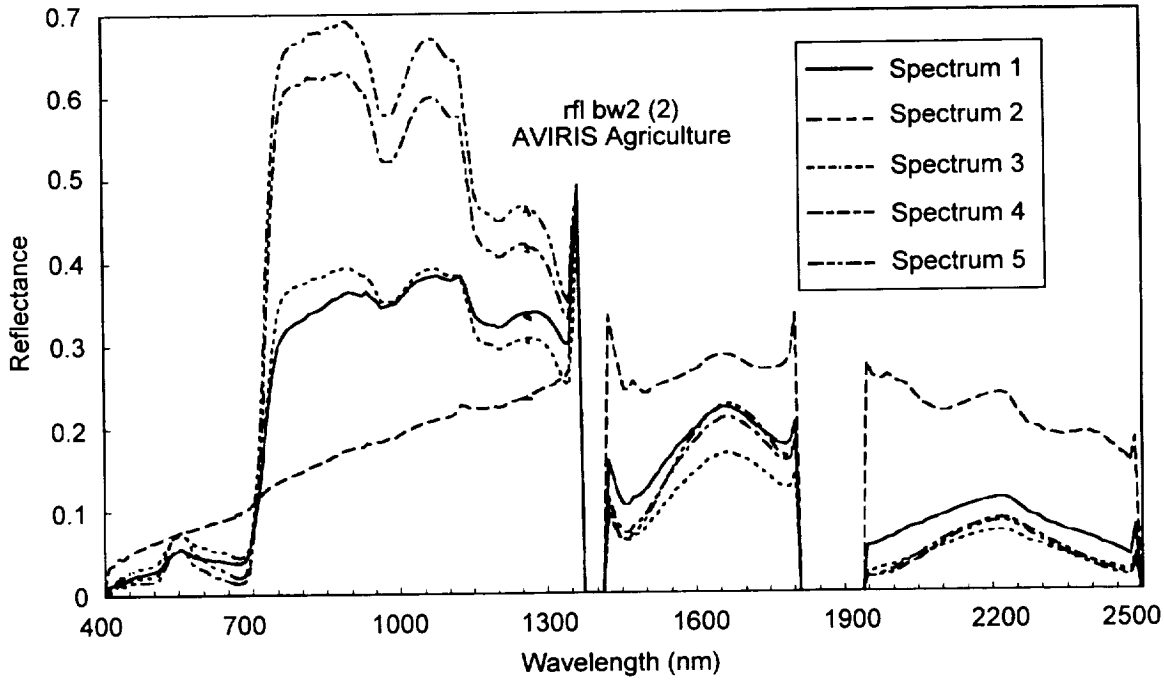

Figure 3. Derived surface reflectance spectra following radiance to reflectance inversion.

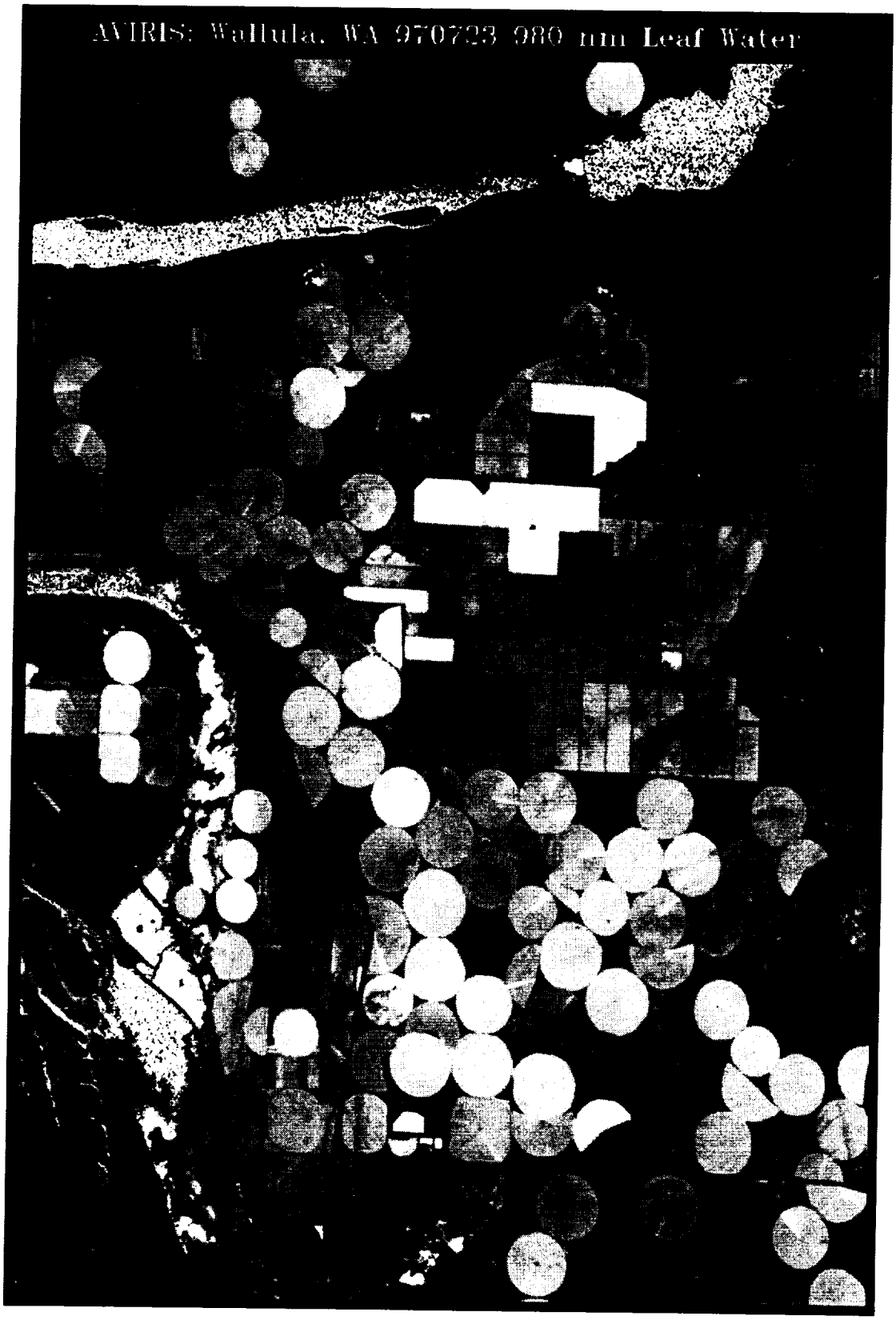

Figure 4. Spectral-fit 980-nm liquid-water image in equivalent transmittance microns. High liquid water is encoded as high image signal.

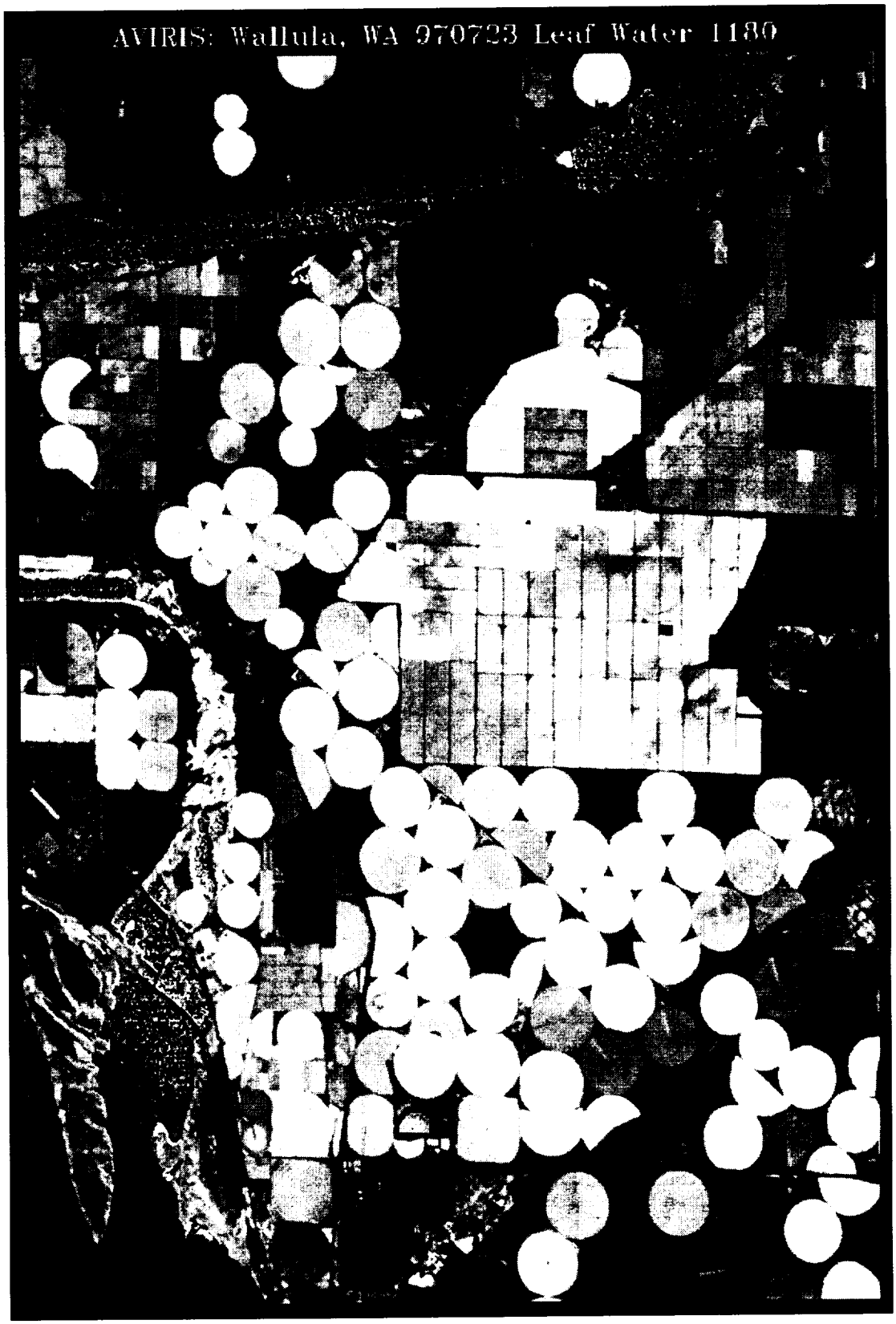

Figure 5. Spectral-fit 1180-nm liquid-water image in equivalent transmittance microns.

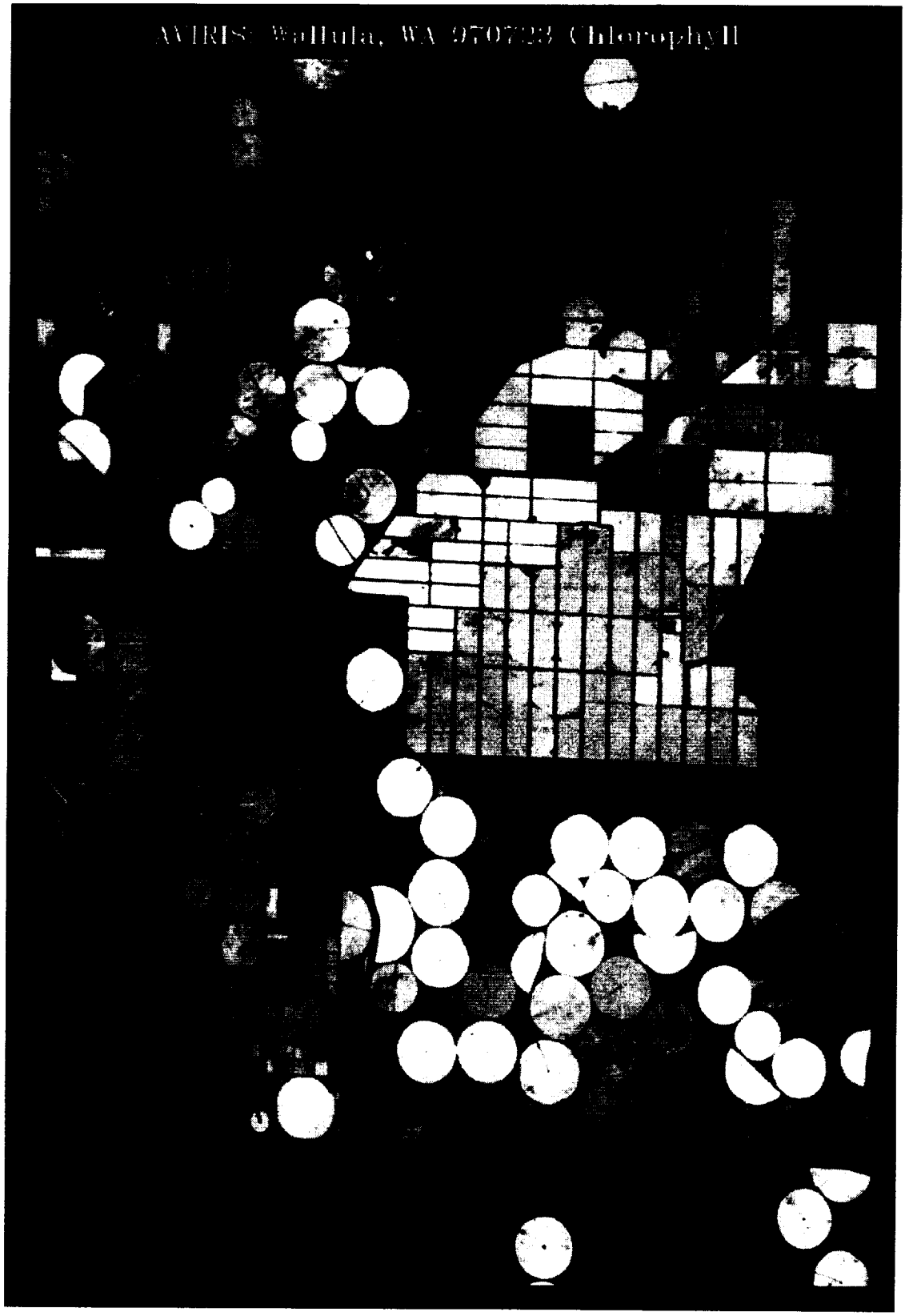

Figure 6. Spectral-fit chlorophyll image. High-chlorophyll absorption is encoded as bright image intensity.

Figure 7. Spectral-fit cellulose image. High-cellolose absorption is encoded as bright image intensity.

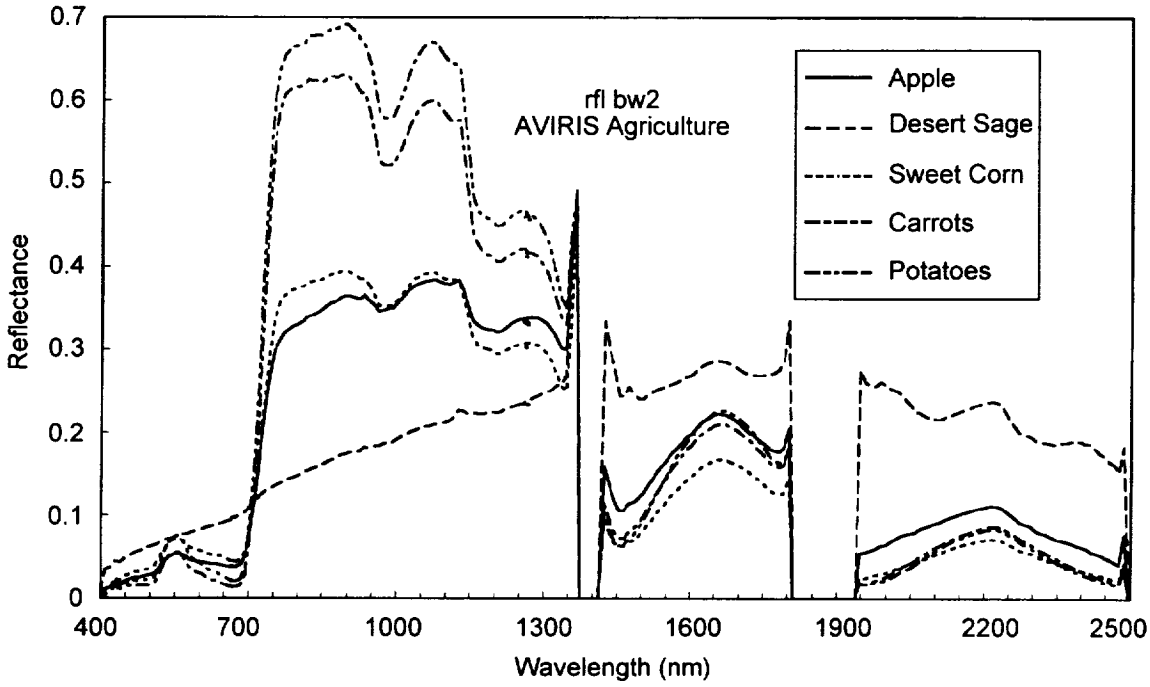

Figure 8. AVIRIS surface reflectance spectra of determined agricultural crops and background.

MONITORING OF VOLCANOGENIC CO_2-INDUCED TREE KILLS WITH AVIRIS IMAGE DATA AT MAMMOTH MOUNTAIN, CALIFORNIA

by
Brian P. Hausback
Mel Strong
Geology Dept., Calif. State Univ., Sacramento, 95819-6043
hausback@csus.edu
mel.strong@csus.edu

Chris Farrar
United States Geological Survey
Box 1360, Carnelian Bay, CA 96140
cdfarrar@usgs.gov

David Pieri
Jet Propulsion Laboratory, California Institute of Technology
MS 183-501, Pasadena, CA 91109
dave@etna.jpl.nasa.gov

Elevated cold CO_2 emissions from the flank of Mammoth Mountain volcano on the southwest rim of the Long Valley Caldera, eastern California, have been the cause of over 100 acres of dead trees in that area since 1990. The source of the CO_2 gas is thought to be from one or more magmatic intrusion(s) beneath Mammoth Mountain and is probably related to a period of seismic unrest that began in 1989 (Farrar et al., 1995). The gas rises to the surface probably from depths of a few kilometers, along faults and fracture zones.

The gas is at ambient temperature and diffuses from the soil rather than discharging from distinct vents. Typically, soil gas concentrations in tree-kill areas range from 10% to over 90% CO_2 by volume, as compared to normal background of <1% in healthy forest. The gas composition is predominantly CO_2 mixed with air (sulfur gases are not elevated), and C and He isotopic ratios are consistent with a magmatic origin for the gas (Sorey et al., 1993). The total CO_2 emission has been estimated at 1200 tons/day, comparable to the emissions at Kilauea. Some of the dead trees are as old as 250 years, suggesting that similar anomalous gas discharge has not occurred over the previous few hundred years. The delta C-13/12 ratio in the Mammoth Mountain CO_2 emission averages about -4.5 (PDB standard). This is consistent with a mantle source for the carbon. However, the large volume of the emission suggests that not all of the CO_2 is necessarily being generated from the 1989 intrusion. The voluminous gas could be leaking from a vapor-rich zone, capped by an impermeable layer, that was supplied CO_2 from degassing of many small magma bodies that intruded beneath the mountain over a period of decades or centuries. Earthquakes in 1989 could have fractured the capping layer and provided pathways for the escape of CO_2 to the surface. Alternatively, some of the CO_2 could be derived from contact metamorphism of carbonate rocks intruded by magma. Carbonate-bearing Paleozoic roof pendents crop out in close proximity to Mammoth Mountain. It is possible that similar rocks could occur at depth beneath Mammoth Mountain. and could have contributed CO_2 from thermal decomposition caused from recent intrusions. We hope to determine the C-13/12 ratio of a suite of samples to demonstrate if the carbonate rocks could be the source of at least part of the 1990-97 CO_2 emission.

To better understand the behavior of the CO_2 gas, we have used hyperspectral imagery data of Mammoth Mountain acquired from the Airborne Visual/Infrared Imaging Spectrometer (AVIRIS) to map out areas of dead trees. The areas of tree kill have increased in size from about 50 acres in 1994 to about 100 acres in 1997. Tree kill is the major surface manifestation of the carbon dioxide flux at Mammoth Mountain, is widely dispersed, and has been cursorily mapped by regular field mapping techniques in the area. Initial investigations using airborne digital imagery from the Thematic Mapper Simulator (NS001) and AVIRIS instruments have shown extremely encouraging results for complete delineation of the vegetation anomalies (de Jong, 1996). The most successful maps (when compared with ground truth) were developed using AVIRIS data with spectral angle mapper and matched filter algorithms with a data set that was reduced to maximum variance via the minimum noise fraction transformation. The result of this work is a series of maps that show the tree kill areas occurring in an halo-pattern surrounding the base of Mammoth Mountain. We are applying these same techniques to earlier AVIRIS images of Mammoth Mountain to examine the progression of the tree kill areas over time. Temporal maps of the tree kill areas may assist in constructing a picture of the structure beneath Mammoth Mountain.

References

de Jong, S. M., 1996, Surveying dead trees and CO_2-induced stressed trees using AVIRIS in the Long Valley Caldera, Summ. Sixth Ann. JPL Airborne Earth Sci. Workshop, Mar. 4-8, 1996, JPL Public 96-4, Vol. 1, Jet Propulsion Laboratory, Pasadena, CA, 67-74.

Farrar, C., M. Sorey, W. Evans, J. Howle, B. Kerr, B. Kennedy, C. King, J. Southon, 1995, Forest-Killing Diffuse CO_2 Emission at Mammoth Mountain as a Sign of Magmatic Unrest, Nature 376, 675-678.

Sorey, M., B. Kennedy, W. Evans, C. Farrar, G. Suemnicht, 1993, He isotope and gas discharge variations associated with crustal unrest in Long Valley Caldera, Ca., 1989-1992, JGR, 98, 15871-15889.

Acknowledgment

A portion of the work described in this paper was performed at the Jet Propulsion Laboratory, California Institute of Technology, under a contract with the National Aeronautics and Space Administration.

JOINT NASA/EPA AVIRIS ANALYSIS IN THE CHESAPEAKE BAY REGION: PLANS AND INITIAL RESULTS

Lee Johnson[1] , Peter Stokely[2] , Brad Lobitz[3], and Gary Shelton[4]

[1]CSUMB/ESSP, Ames Research Center, Moffett Field CA
[2]USEPA/EPIC, Region 3 Field Office, Reston VA
[3]JCWS Inc., Ames Research Center, Moffett Field CA
[4]NASA, Ames Research Center, Moffett Field CA

NASA's Ames Research Center is performing an AVIRIS demonstration project in conjunction with the U.S. Environmental Protection Agency (Region 3). NASA and EPA scientists have jointly defined a Study Area in eastern Virginia to include portions of the Chesapeake Bay, southern Delmarva Peninsula, and the mouths of the York and James Rivers. Several environmental issues have been identified for study. These include, by priority: 1) water constituent analysis in the Chesapeake Bay, 2) mapping of submerged aquatic vegetation in the Bay, 3) detection of vegetation stress related to Superfund sites at the Yorktown Naval Weapons Station, and 4) wetland species analysis in the York River vicinity.

In support of this project, three lines of AVIRIS data were collected during the Wallops Island deployment on 17 August 1997. The remote sensing payload included AVIRIS, MODIS Airborne Simulator and an RC-10 color infrared fim camera. The AVIRIS data were delivered to Ames from the JPL AVIRIS Data Facility on 29 September 1997. Quicklook images indicate nominal data acquisition, and at the current time an atmospheric correction is being applied.

Water constituent analysis of the Bay is our highest priority based on EPA interest and available collateral data, both from the surface and from other remote sensing instruments. Constituents of interest include suspended sediments, chlorophyll-a and accessory pigments. Analysis steps will include: verification of data quality, location of study sites in imagery, incorporation of relevant field data from EPA and other Chesapeake Bay cooperators, processing of imagery to show phenomenon of interest, verification of results with cooperators. By 1st quarter CY98 we plan to circulate initial results to NASA and EPA management for review. In the longer term we will finalize documentation, prepare results for publication, and complete any needed technology transfer to EPA remote sensing personnel.

A BRDF-RELATED BRIGHTNESS GRADIENT IN AVIRIS IMAGERY: LESSONS FROM AN EMPIRICAL COMPENSATION METHOD

Robert E. Kennedy*, Warren B. Cohen, and Gen Takao*****

1. INTRODUCTION

1.1 Goal of this paper

A brightness gradient was observed in the cross-track dimension of 1994 AVIRIS imagery acquired over a densely-forested study area in Oregon's Cascade Mountains. To compensate for the effect, Kennedy et al. (1997) tested four empirical methods based on simple quadratic fitting of the gradient. Interpretation of the fitting coefficients suggested that the gradient was caused primarily by vegetative bidirectional reflectance characteristics. In this paper, we discuss how the character of the brightness gradient may affect common analysis techniques of AVIRIS imagery such as classification, multi-image matching, and endmember selection.

1.2 Extent of problem

The 1994 AVIRIS imagery under study was collected with the aircraft heading nearly perpendicular to the solar plane, causing the scanning plane to closely parallel to the plane of the sun. These conditions accentuate bidirectional reflectance effects (Ranson et al, 1994) which Kennedy et al. (1997) suggested were the primary determinant of the brightness gradient. In an attempt to minimize the brightness gradient, 1996 AVIRIS images were collected with aircraft heading nearly parallel with the solar plane. Nevertheless, preliminary analysis showed that the effect was still present in the 1996 imagery (data not shown). The brightness gradient has also been reported in AVIRIS imagery at Harvard Forest, another densely-forested study area (Steve Newman, University of New Hampshire, personal comm.). Solar plane was slightly west of aircraft heading in one image and slightly east of aircraft heading in a second image, and the directional trend of the brightness gradient was reversed in the two images. The co-occurence of dense forests and the brightness gradient suggests that the effect may be an issue at other forested sites; the observance of the brightness gradient under a wide variety of sun-viewer geometries suggests the effect may occur with most flights at such sites and may be sensitive to solar position.

1.3 Interpretation of brightness gradient

The brightness gradient can be conceptualized as follows:

$$v(\alpha,\lambda) = [b \times f_{type}(\alpha,\lambda)] + C_{type}(\alpha,\lambda) \qquad \text{(Eq. 1)}$$

where $v(\alpha,y)$ is the brightness effect for a pixel at view-angle α and wavelength λ, b is some measure of that pixel's inherent brightness, f_{type} is a function describing the response to changes in view-angle for surface type equal to *type* at view-angle α and wavelength λ, and C_{type} is the additive function of view-angle effect for *type* and waveband λ (adapted from Kennedy et al., 1997).

The determinants of both $f_{type}(\alpha)$ and $C_{type}(\alpha)$ include the structure and physical features of the surface, the viewing geometry of the sun-surface-sensor configuration, and potentially atmospheric BRDF effects. The nature of the brightness gradient in the 1994 AVIRIS imagery utilized in this study suggested

* Department of Forest Science, Oregon State University, Forestry Sciences Laboratory, Corvallis, OR
** USDA/Forest Service, Pacific Northwest Research Stations, Forestry Sciences Laboratory, Corvallis, OR
*** Remote Sensing Laboratory, Forestry and Forest Products Research Institute, Ministry of Agriculture, Forestry, and Fisheries, Tsukaba, Japan

that the majority of the effect was related to the surface bidirectional effects of vegetation, not by atmospheric effects (Kennedy et al., 1997).

2. METHODS

2.1 Image processing and brightness gradient compensation

The image processing techniques are described in Kennedy et al. (1997). The AVIRIS image was acquired on July 19, 1994. Aircraft heading was nearly perpendicular to solar azimuth. ATREM (Gao et al., 1993) was used to convert radiance to apparent surface reflectance.

The brightness gradient compensation method used in this paper is the "multiplicative-classified" approach of Kennedy et al. (1997). Of the four methods tested, the multiplicative-classified technique appeared to best preserve spectral integrity of the data. The compensation process modeled $f_{type}(\alpha)$ and $C_{type}(\alpha)$ as a single quadratic equation (Brown et al., 1982; Leckie, 1987), and used a pixel's initial reflectance as an estimate for b, using three "BRDF" classes (see Kennedy et al., 1997 for a description of the classes).

2.2 Other processing techniques

To explore whether common AVIRIS imagery analysis techniques may be affected by the presence of a view-angle-related brightness gradient, we conducted two processing routines on the 1994 AVIRIS data.

The first exploratory routine was a comparison of spectral classifications before and after brightness-gradient compensation. A maximum likelihood classifier was used to partition each 154-band image into 20 classes. No ground data were used to ground-truth these classes. Instead, patterns in these classes were compared visually with an independently-derived and ground-truthed classification based on Landsat Thematic-Mapper (TM) data (Cohen et al., 1995).

The second exploratory routine was designed to understand how the character of a relatively stable spectral class could change as view-angle changed under brightness-gradient conditions. For the purposes of illustration, the spectral class ideally would be derived from an independent source unaffected by the brightness gradient. We used a TM-based image of percent conifer forest cover (Warren Cohen, *pers. comm.*). This image (separate from the TM-based classification used in the first exploratory routine) was independently ground-truthed, with an r^2 of prediction of 0.76. From this image, pixels with 99 or 100% conifer were chosen as a nearly-pure conifer-class, and their average reflectance by wavelength across scan angles for all spectral bands was calculated in the manner of Kennedy et al. (1997).

3. RESULTS

3.1 Classification

Classification appears to be influenced by the presence of the brightness gradient. Figure 1 shows the maximum likelihood classifications of the AVIRIS image before and after brightness-gradient compensation, with the TM-derived classification for comparison. To aid in interpretation and to lower visual confusion, the three darkest and the three brightest AVIRIS classes are lumped and displayed, and the 14 intermediate classes are omitted from the figure. Similarly, the TM classes roughly corresponding to the AVIRIS bright and dark lumped classes are displayed in the same tones, and the intermediate TM classes are omitted from the figure. Following the terminology of Cohen et al. (1995), the bright class displayed in Figure 1c as gray pixels corresponds to Open (0-30% mixed conifer and broadleaf cover) and Semi-open (30-85% mixed conifer and broadleaf cover) classes, and the dark class displayed as black pixels is Old-growth conifer (>85% old-conifer forest cover). The TM classes are not meant to correspond

in a one-to-one fashion with the AVIRIS unsupervised classes, but rather to serve as a visual indicator of patterns of light and dark classes on the landscape.

The distribution of bright and dark classes were quite different in the pre- and post-compensation AVIRIS classifications. In the pre-compensation AVIRIS classification, most of the dark class pixels were at the bottom half of the image (on the forward-scatter side of nadir) and few were in the top half of the image. The converse was true for the light class. In the post-compensation AVIRIS classification, the two classes were fairly evenly distributed between the top and bottom half of the image. The patterns of bright and dark classes displayed in the TM classification indicate that bright and dark classes are fairly evenly distributed across the landscape, suggesting that the post-compensation image more accurately reflects the patterning of classes on the landscape.

3.2. Changes in spectral class across view-angles

The character of the conifer forest class was also affected by the brightness gradient. Figure 2 shows the average reflectance for pixels in this class across scan angles. In order to illustrate the trend associated with scan angle, groups of 20 adjacent scan columns were lumped before display (Figure 2a). Because of misregistration errors and differing sensor characteristics between AVIRIS and TM, there is significant variability in the reflectances of these pixels across scan angles. Nevertheless, it is evident that the general trend is toward brighter pixels on the back-scatter side of nadir and darker pixels on the forward-scatter side of nadir. Figure 2b shows the ratio between the spectral reflectances of the scan angle furthest on the backscatter side to the scan angle furthest on the forward-scatter side of nadir. Not only is the backscatter spectrum as much as two and half-times as bright as the forward-scatter spectrum, but the ratio changes with wavelength.

The trend with scan angle in this class was consistent with trends observed in vegetative BRDF classes in Kennedy et al. (1997). Maximum reflectance for any given waveband was found at the scan angle furthest from nadir in the backscatter direction. Minimum reflectance was found at a point offset from nadir slightly in the forward-scatter direction.

4. DISCUSSION

4.1 Evaluating these examples

Neither example presented here was without potential problems. In the classification example, it was only certain that the pre- and post-classifications were different, not that one was better. It appeared that the post-compensation classification better represented the TM-image classification, but because of the different sensor types and the different years of acquisition, there can be no certainty. Similarly, the correspondence of TM-derived conifer pixels to spectra observed in AVIRIS imagery is not perfect, and thus the conifer class as tested likely included pixels from other classes. Additionally, the predicted conifer results in the TM scene, although good, were not perfect, further adding error. Finally, the compensation method itself was only designed a compensation, not a correction. There is error and miscompensation in the technique. A simple empirical technique cannot account for the infinite complexity of surface BRDF effects in a scene.

Despite their weaknesses, the results presented here strongly suggest that the brightness gradient could have an effect on many basic analyses of AVIRIS imagery. Classification techniques make use of variability in spectral space to determine placement of similar pixels into classes. They assume that pixels in a given class will have similar reflectance anywhere in the scene and that they will differ from other classes anywhere in the scene. The brightness gradient function modifies reflectance based on view-angle ($v(\alpha,\lambda)$), thus nullifying these latter assumptions by introducing a spatial component to the spectral variability. By extension, any technique that assumes that variation in spectral space is unrelated to position in the scene will be affected by the brightness gradient.

Similarly, any technique that uses spectral reflectance to predict a continuous variable will be affected by the brightness gradient. Although the conifer pixels used in the above example contained natural variability, it was evident that, on average, pixels with high percent coverage by conifer forest displayed a trend related solely to scan angle. A relationship between percent conifer coverage and spectral reflectance developed at one scan angle would provide erroneous values at most other scan angles. Similarly, spectral unmixing would be affected. The spectral variability introduced by the view-angle-effect would be translated into variability in fractions of endmembers, thus introducing error that would be based solely on scan angle.

4.2 Other affected image-processing techniques

The other major category of processing technique that would be affected by the brightness gradient would be multi-image comparisons. An obvious example would be comparing two images acquired over the same site, but with the aircraft heading in the second image rotated 90 degrees relative to the heading in the first image. The overlay of perpendicular brightness gradients would introduce significant spectral artifacts that would need to be accounted for before change detection could take place. Similarly, two scenes flown at the same heading, but imaged under different sun angle conditions, would be affected, especially if the sun moves to opposite side of nadir (e.g. the example from Harvard Forest described in Section 1.2). Finally, mosaicking images from adjacent flight lines would show an extremely pronounced image seam, since the overlap area would be on the backscatter side of nadir in one flightline and the forward-scatter side of nadir in the other.

4.3 Some potentially unaffected techniques

In the course of analysis, Kennedy et al. (1997) determined that spectral first derivative (Martin et al, 1994) was relatively unaffected by the compensation techniques. By inference, the first derivative image was apparently little affected by the brightness gradient. Because the first derivative as used by Martin et al (1994) relies on differences between adjacent bands, this resilience is likely explained by the fact that the change in brightness gradient from one band to the next at the same scan angle is relatively slight. Hence, analysis techniques that rely solely on first-derivative images may be little affected. Also, the ATREM procedure appeared to be relatively unaffected by the gradient. Kennedy et al. (1997) found that the same final image resulted when ATREM was run before view-angle compensation and when ATREM was run after view-angle compensation.

5. CONCLUSION

The exploratory examples presented here suggest that the view-angle-dependent brightness gradient evident in several AVIRIS images may affect spectral analysis. Analyses that may be affected are those that use some measure of scene-wide variability to predict or derive relationships: classification, unmixing, continuous variable prediction, etc. The gradient would manifest itself as increased variation unexplained solely by surface type. The problem existed in two years of imagery acquired for dense conifer forest of Oregon and existed in images from the mixed hardwood-deciduous forest of New England, and appeared to exist at a wide range of sun-object-viewer geometries. This suggests that other forested or densely vegetated systems may experience similar effects, and attention must be paid to this effect before analyses are conducted that rely on scene-wide measures of spectral variability.

References

Brown, R.J., Bernier, M.., and G. Fedosojevs, 1982, "Geometrical and atmospheric considerations of NOAA AVHRR imagery," In 1982 Machine Processing of Remotely Sensed Data Symposium, Purdue University Press, West Lafayette, IN, pp. 374-381.

Cohen, W.B., Spies, T.A., and M. Fiorella, 1995, "Estimating the age and structure of forests in a multi-ownership landscape of western Oregon, U.S.A.," Remote Sens. Env., vol. 16, no. 4, pp. 721-746.

Gao, B.-C., Heidebrecht, K.A., and A.F.H. Goetz, 1993, "Derivation of scaled surface reflectance from AVIRIS data," Remote Sens. Env., vol. 44, no. 2, pp. 165-178.

Kennedy, R.E., Cohen, W.B., and G. Takao, 1997, "Empirical methods to compensate for a view-angle-dependent brightness gradient in AVIRIS imagery," Remote Sens. Env., vol 62, pp. 277-291.

Leckie, D.G., 1987, "Factors affecting defoliation assessment using airborne multispectral scanner data," Photogramm. Eng. Remote Sens., vol. 53, no. 12, pp. 1665-1674.

Ranson, K.J., Irons, J.R., and D.L. Williams, 1994, "Multi-spectral bidirectional reflectance of northern forest canopies with the advanced solid-state array spectroradiometer (ASAS)," Remote Sens. Env, vol. 47, pp. 276-289.

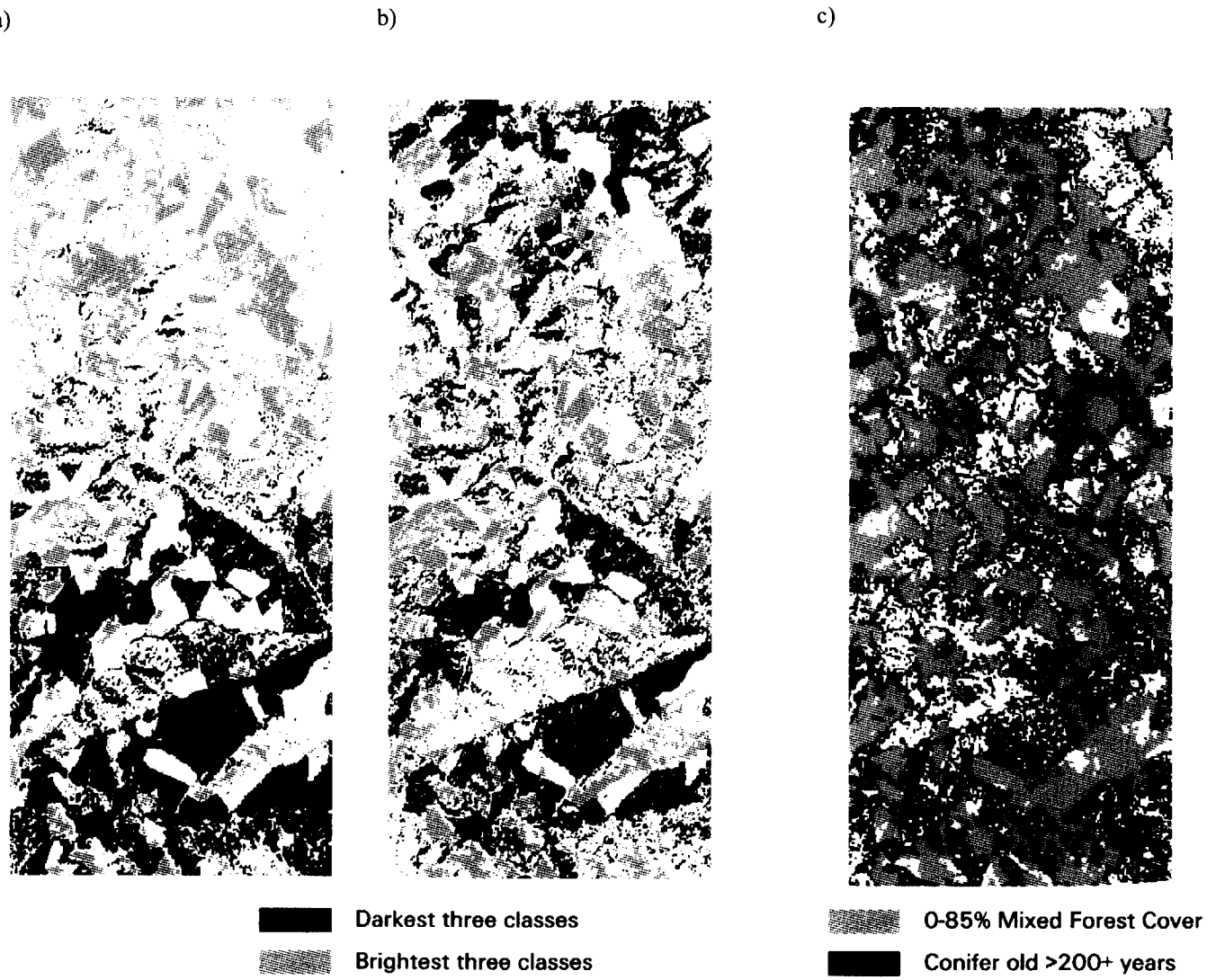

Figure 1.
Comparison of 20-class maximum likelihood unsupervised classification of AVIRIS data a) before and b) after view-angle compenation. The three darkest spectral classes are portrayed in black; the three brightest in grey. All intermediate classes in white. The nadir line runs horizontally across the middle of these two images.
c) For comparison, an independent, ground-truthed, TM-based classification for the same area (Cohen et al., 1995). Classes with 0 to 85% cover in the mixed forest category are displayed in gray; classes in the old-conifer category (>200 yrs.) are displayed in black. The post-compensation AVIRIS classification better mimics the distribution of bright and dark classes observed in the independent TM classification.

a)

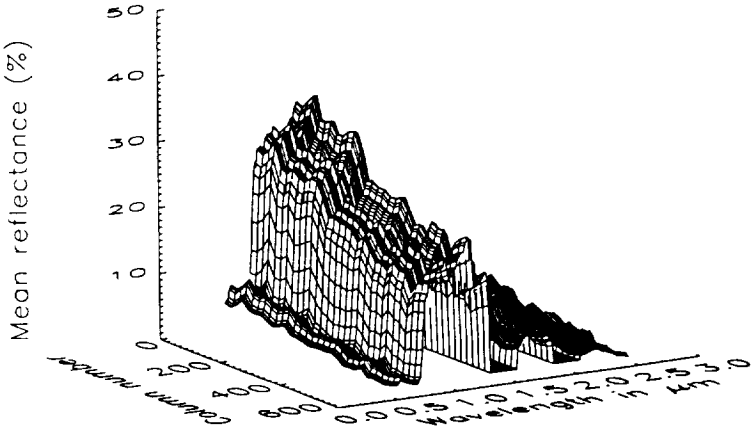

b)

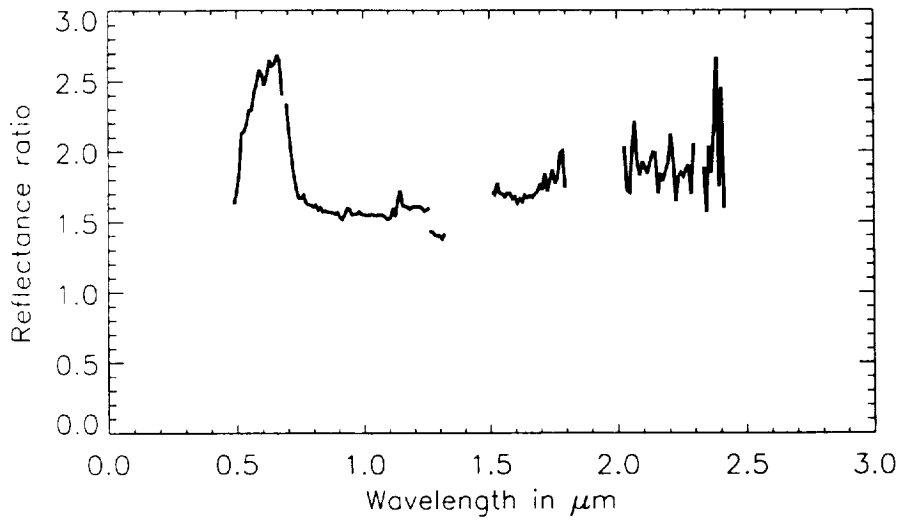

Figure 2. a) Average spectral reflectance of 99 and 100% conifer forest cover pixels across view-angles. Column number follows view-angle; nadir view is at column 306. b) The ratio of spectral reflectance of column 1 over column 614.

Automated Spectral Unmixing Using Unsupervised Classification

Minsu Kim
Institute for Resource Information System (IRIS)
453 Hollister Hall
Cornell University
Ithaca, NY 14853

Automated unmixing is one of the most interesting ideas in spectral analysis. We have data points in the reference space whose dimension is reduced by the principal component analysis or MNF transformation. Any kind of automated unmixing algorithm self-models the data system by finding endmember points solely based on the distribution of the data points in the reference space, so this algorithm was called a self-modeling technique in chemometrics of analytical chemistry.

The key is how to find the appropriate linear transformation matrix for the diagonal reference coordinate vectors of the reduced space. Many researchers suggested reasonable methods. In this paper, a few automated unmixing algorithms and related sensitivity analysis about the number of required data points to get significant results are suggested. In this algorithm, a transformation matrix is determined by the combination of unsupervised classification, regression analysis, and other intuitive methods to find appropriate facet hyperplanes.

Spectroscopic Determination of Leaf Biochemistry: Use of Normalized Band-Depths and Laboratory Measurements and Possible Extension to Remote Sensing Measurements

Raymond F. Kokaly and Roger N. Clark

U.S. Geological Survey, MS 973
Box 25046, Federal Center
Denver, CO 80225-0046
raymond@speclab.cr.usgs.gov

1. INTRODUCTION

Ecosystems play an important role in the exchange of water, energy and greenhouse gases between soil, vegetation, and the atmosphere. The ability to detect changes in ecosystem processes such as carbon fixation, nutrient cycling, net primary production and litter decomposition is an important part in defining global biogeochemical cycles and identifying changes in climate. These processes have been linked in models of forest ecosystems to canopy biochemical content, specifically to the nitrogen, lignin and cellulose concentrations in vegetation (e.g. Aber and Federer 1992, and references therein). However, measurements of canopy chemistry by traditional field sampling methods are difficult to perform for large regional and global studies. Therefore, remote sensing measurement of canopy biochemistry is crucial to studying changes in ecosystem functioning.

Several studies have suggested that estimates of canopy chemistry based on remote spectroscopic measurements may be possible (e.g. Card et al. 1988, Curran 1989, Wessman et al. 1989, and Martin and Aber 1997). These studies used stepwise multiple linear regression to predict canopy chemistry from derivative reflectance spectra. This methodology is based on laboratory techniques developed in the agriculture industry for rapid estimation of forage quality parameters, for example, crude protein content and digestibility (Norris et al. 1976 and Marten et al. 1989). The original applications stressed the importance of controlled laboratory methods for reducing noise levels and the limited application of regression equations to samples of the same type used in calibration (Marten et al. 1989). Recently, Grossman et al. (1996) found the use of regression techniques with derivative reflectance spectra to give inconsistent results between dry leaf and needle data sets for forest vegetation. Under the NASA Accelerated Canopy Chemistry Program, analysis using derivatives had also given inconsistent results between test sites (ACCP 1994). Furthermore, although recent studies have correlated plant canopy chemistry to imaging spectrometer measurements (Johnson et al. 1994, LaCapra et al. 1996 and Martin and Aber 1997), the results at leaf and canopy scales are inconsistent and the derived regression equations are applicable to only the study area and are not reliable predictors for other remotely-sensed data.

Because of site-specific results in wavelength selection by derivative analysis and the sensitivity of the technique to noise, we employed a different approach. Before applying the stepwise multiple linear regression, we utilized continuum-removal and band ratios, traditional methods of spectral analysis used in remote sensing by the terrestrial geology and planetary science disciplines. Absorption band-depths were calculated from continuum-removed spectral features in reflectance data. Since all band-depths in an absorption feature were ratioed to the maximum depth at the center of the feature we termed the result "normalized band-depths." Subsequently, we used a multiple stepwise linear regression algorithm applied to normalized band-depths to select wavelengths highly correlated to laboratory measurements of chemical concentrations. Wavelength selection was based on only two of the seven data sets used in this paper. Subsequently, the selected wavelengths were tested for correlation with the chemical concentrations of the five other data sets. To test the robustness of this approach, regression equations developed from a subset of the data were used to predict the concentrations in the remaining samples. Finally, since a broadly applicable method for dry leaves serves only as a foundation for a remote sensing algorithm, the method was tested for its extension to remote sensing measurements of plant canopies. The influences of leaf water content, sensitivity to noise in the reflectance spectra, sensor bandwidths, incomplete vegetation coverage, and atmospheric influences were considered.

2. METHODS

2.1 Data Sets

Data used in this study were comprised of reflectance spectra and foliar chemistry measured from specimens of dried and ground leaves. These samples were gathered and analyzed for the NASA Accelerated Canopy Chemistry Program (ACCP 1994). We examined data from seven sites: three eastern U.S. forests (Blackhawk Island, Wisconsin, Harvard Forest, Massachusetts, and Howland, Maine), a slash pine plantation near Gainesville, Florida, rice fields in California, Douglas-fir seedlings grown in a greenhouse, and a data set consisting of a variety of tissue types from a diversity of plants collected from Long Term Ecological Research (LTER) sites. More than 30 deciduous and coniferous tree species were represented by the 840 samples. Overall, the foliar chemistry covered a wide range: 0.22 to 3.51% nitrogen, 7.60 to 44.62% lignin and 23.69 to 74.73% cellulose.

2.2 Continuum Removal

Working with reflectance data, broad absorption features in the dry leaf spectra centered near 1730, 2100, and 2300 nm, shown for a dry leaf spectrum in Figure 1a, were selected for continuum analysis. Previous studies have shown that many of the chemical bonds in foliar constituents have vibrational absorptions in these bands (see the review by Curran 1989). The continuum is an estimate of the other absorptions present in the spectrum, not including the one of interest. Once the continuum line was established, continuum-removed spectra for the absorption features were calculated by dividing the original reflectance spectrum by the corresponding reflectance of the continuum line (Figure 1b). Although imaging spectrometers such as AVIRIS fully cover the wavelength range from 350-2500 nm, the analysis here excludes wavelengths near strong atmospheric absorptions, around 1400 nm and 1900 nm, and regions where the signal-to-noise ratio (S/N) is low due to water absorption and decreasing solar flux (wavelengths greater than 2400 nm). From the continuum-removed reflectance, the band depth (D) for each channel in the absorption feature was computed by:

$$D = 1 - R' \tag{1}$$

where R' is the continuum-removed reflectance (Clark and Roush, 1984).

2.3 Band Depth Normalization

Reflectance spectra of vegetation canopies vary with changing leaf biochemistry but remote sensing measurements are also affected by atmospheric absorptions, the size of leaf cells, the abundance of other absorbers in the leaf (such as water), and the fractional areal coverage of leaves in heterogeneous landscapes. Therefore, analytical methods for estimation of plant biochemistry must overcome any sensitivity to these extraneous factors. Normalization of continuum-removed reflectance spectra minimizes these influences. The normalized band-depth (D_n) at all wavelengths within the continuum-removed absorption feature is calculated by dividing the band-depth of each channel by the band-depth at the band center (D_c):

$$D_n = D / D_c \tag{2}$$

where the band center is the minimum of the continuum-removed absorption feature. Variations of D_n with wavelength describe the shape of the absorption feature. Resulting differences in the shapes of absorption features between samples are correlated to foliar biochemistry.

2.4 Stepwise Multiple Linear Regression

Normalized band-depth, D_n, values for all wavelengths in the three continuum-removed absorption features were analyzed using a stepwise multiple linear regression routine to determine wavelengths correlated with chemistry. The stepwise regression was run separately for each of the three leaf constituents: nitrogen, lignin, and cellulose. A stepwise regression routine in IDL (Interactive Data Language), STEPWISE, was used. This routine is

based on an algorithm by Afifi and Azen (1971).

3. RESULTS & DISCUSSION

3.1 Wavelength Selection

Two of the eastern U.S. forest data sets, Blackhawk Island and Harvard Forest, were used to derive wavelengths correlated with nitrogen, lignin and cellulose concentrations. Stepwise multiple linear regression was applied to the normalized band-depths of these data. Table 1 lists the locations of selected wavelengths. Five wavelengths were selected in the nitrogen regressions, all in the 2100 nm absorption feature. Lignin required six wavelengths, two in the 1730 nm and four in the 2300 nm absorption features. Eight wavelengths, a few in each of the three broad absorption features, were selected for the cellulose regression.

3.2 Application to All Sites of Wavelengths Derived from Blackhawk Island & Harvard Forest

Following wavelength selection using Blackhawk Island and Harvard Forest sites, linear regression was used to establish regression equations at each of the sites. The strengths of regressions are assessed on high R^2 (where R is the correlation coefficient and R^2 indicates the proportion of variance accounted for by the correlation) and low standard error of calibration (SEC). The SEC is the root mean square error (RMSE) between the chemical concentrations calculated from the regression equation and the values obtained by wet chemistry laboratory methods. Nitrogen correlations were very high (R^2 from 0.90 to 0.97) and SEC were low (0.06 to 0.17% nitrogen by dry weight). Relative to the mean nitrogen concentrations the SEC were less than 10%. In general, cellulose correlations were fairly good (R^2 from 0.75 to 0.93). Correlations for lignin were all significant (R^2 from 0.65 to 0.83) except for the rice field data which had a low R^2 of 0.32. The rice data set had a much lower average lignin concentration relative to the other data sets (approximately 25% lower). In fact, many of the samples in the rice data set were below the range of lignin concentrations present in the forest data sets. However, the error of the SEC relative to the mean lignin concentration for the data set was low, only 6.2%.

In summary, a set of wavelengths derived from an analysis of only the Blackhawk Island and Harvard Forest sites was found to be highly correlated with chemical concentrations for other data sets. These consistent results are significant considering that Grossman et al. (1996) found that wavelengths derived from any single data set were not able to reliably predict nitrogen concentrations in other data sets. Those tests were performed on log(1/R) and its first and second derivatives and only achieved low R^2 (.14-.49). In contrast, the results of this study, which used normalized band-depths describing the shape of absorption bands, show consistently high correlations and low errors across all data sets.

3.3 Predictive Ability of Regression Equations

Regression equations were tested for their ability to predict chemistry across data sets. Two-thirds of the samples from the eastern U.S. forest sites (Blackhawk Island, Harvard Forest and Howland, Maine) were used with the previously derived wavelengths to establish the coefficients in the regression equations. This calibration equation was then used to predict the chemical concentrations of the remaining validation data sets. The term Standard Error of Prediction (SEP) is commonly used to describe the prediction error. The SEP is the root mean square error between the chemical concentrations predicted from the regression equation and the values obtained by wet chemistry laboratory methods. As expected, correlations were highest and SEP lowest for the predictions of the remaining one-third of the eastern forest samples. The SEP in nitrogen estimates for slash pine and Douglas-fir data sets were slightly worse than the eastern forest validation set. The rice data set provided a test for the application of regression equations derived from forest foliage to non-forest vegetation. Nitrogen predictions were very good (R^2=0.83 and SEP=0.13%) The LTER data set also contained some sample tissues not present in the calibration data set: forest species different from the calibration set, grasses, bark, and roots. Nitrogen predictions were surprisingly good (R^2=0.93 and SEP=0.23%).

Similar to the nitrogen results, lignin and cellulose predictions for forest data were accurate. Cellulose estimates for the slash pine samples were good (SEP=2.60%, only a 7.2% error relative to the mean concentration).

The predictions of lignin and cellulose concentrations for the rice and LTER data were less accurate. Cellulose estimates for rice and LTER data have high errors of prediction (SEP of 7.49% and 6.88%, respectively) which might be influenced by structural or biochemical differences particular to these different vegetation types compared to all the other samples of tree foliage. Furthermore, mean concentrations for foliage constituents in the rice samples are significantly lower for nitrogen and lignin and much higher for cellulose than the other sites.

In order to be useful for remote sensing, an algorithm for predicting concentrations should be applicable over a wide variety of vegetation types. Nitrogen predictions were extremely robust for all new data sets. Rice and LTER predictions were good despite the fact that these tissues differ from the leaf and needle material of the calibration data. Lignin and cellulose predictions were good if the new samples were similar in type and concentration to those in the calibration data set. However, predictions for these biochemicals in non-forest tissues were not robust.

More generally applicable regression equations may be derived using a regression with all the samples. The results for regression constants and coefficients are given in Table 1. The results of regressions for nitrogen, lignin and cellulose gave R^2 values of 0.94, 0.64, and 0.83, respectively. The nitrogen results were excellent (SEC=0.17%) as shown in Figure 2. Given the wide range of concentrations and sample types in the 840 samples, these equations may be applicable to most dry leaf spectra obtained in future studies.

3.4 Remote Sensing Considerations

Schimel (1995) discusses the accuracy and precision required from remote sensing in order to map large scale variations in foliar nitrogen and lignin. Accuracy of ~0.5%(absolute) N is necessary to distinguish between ecosystems with differences in nitrogen large enough to affect photosynthesis. An accuracy of ~5.0% lignin concentration is needed to detect between-system gradients. The method used in this study has demonstrated errors below the required accuracy for nitrogen concentrations, even when extending predictions to different vegetation types (i.e., tree foliage to rice). However, accuracy will obviously degrade for extensions of this method to fresh, whole leaves or remotely sensed canopies. Additional complexities are encountered in vegetation spectra collected at the remote sensing scale, including: different instrument characteristics (S/N, sampling, and bandpass), atmospheric effects, leaf water, fractional vegetation coverage, and canopy architecture. This section of the paper addresses the effects of several, but not all, of these influences on this method.

3.4.1 Leaf Water

The largest difference between reflectance spectrum of a ground, dry leaf and a spectrum of a vegetation canopy is due to leaf water. Leaves in a plant canopy can be composed of 40 to 80% water by weight (Elvidge 1990). Because water is highly absorbing in the near infrared, and because the water comprises so much of the leaf, the spectral signatures of the other chemical components are, to a large degree, masked by the water. To test the sensitivity of our method to water we added water absorptions to dry leaf spectra. The spectrum of a dry leaf plus water was computed using the Hapke (1981) radiative transfer theory. We measured spectra of liquid H_2O on a Nicolet Fourier Transform Spectrometer. Using these data and the known index of refraction of water (Irvine and Pollack 1968), we added water to dry leaf spectra. The absorption coefficients of the dry leaf component were derived by inverting the Hapke equations (e.g. Clark and Roush 1984), assuming the index of refraction of water, and deriving the absorption coefficients as a function of wavelength. Given the optical constants (index of refraction and absorption coefficients as a function of wavelength), reflectance spectra of water plus dry leaf were computed for 10%, 20%, 30%, 40%, 50%, 60%, 70%, and 80% water added by weight to the dry leaf.

The dry leaf plus water calculations were made for five different samples from the data set. These samples were selected to span a range of biochemical composition and include different species: red oak, white pine, hemlock, and red maple. The effect of increasing water concentration on calculations of leaf biochemistry was investigated by comparing chemistry estimates from the spectra with added water to the estimates from the original dry leaf spectra. The average error for all five samples was computed at each level of added water. Errors in nitrogen estimation remained small for 10% and 20% water contents (0.21% and 0.19%, respectively). Errors in calculation of lignin were also small until a water content reached 30% (SEP = 2.54%). Cellulose calculations were

most sensitive to increasing water content. To apply the equations developed from laboratory data to fresh leaf or remotely sensed canopy spectra in order to estimate concentrations of nitrogen lignin and cellulose, the spectra must be synthetically/computationally "dried" to an accuracy of at least 10%.

The impact of leaf water content on our normalized band-depth approach was compared to the effect on derivative methods. Derivative calculations were made according to Bolster et al 1996. Table 2 shows how a 10% water content affects the calculation of leaf chemistry relative to the dry leaf calculation. Our method has an SEP of 0.21% for nitrogen, however, the errors from 1st and 2nd derivative methods are much higher, 0.52% and 0.50%, respectively. The results show the long observed fact that water has a dominant influence on the reflectance from fresh leaves and canopies for wavelengths greater than 1400 nm. In our study, we found that with a 10% residual water content we could still accurately estimate leaf chemistry. If a method for removing the spectral signature of water from fresh leaf and remote sensing data can be developed to this accuracy then we may be able to apply our regression equations to these data to predict biochemical concentrations.

3.4.2 Fractional Coverage

A common difficulty in remotely sensing canopy chemistry is incomplete coverage of the surface by the canopy. When vegetation cover is not 100%, other components, such as rocks, soil, water, or man-made objects will contribute to the remotely sensed signal. We tested how the reflectance signature of an incomplete canopy would compare to the complete canopy by adding a soil spectrum to a dry leaf spectrum. We used a soil spectrum that had no strong absorption features. We combined the spectrum of a dry leaf with soil in a 75% to 25% mixture. Errors between the incomplete and complete vegetation cover are presented in Table 2 for our method using normalized band depths and the methods of 1st and 2nd derivatives. The calculations of chemical concentration from the soil contaminated spectrum are nearly identical to the original dry leaf results for the normalized band depth approach (RMSE=0.11% Nitrogen). Normalizing the band-depth alleviates the soil influences on the spectrum. The commonly employed derivative approaches are slightly more sensitive to fractional coverage.

3.4.3 Atmospheric Effects (Residual Atmosphere Absorptions)

Atmospheric influences on remotely sensed vegetation canopy spectra that must be considered include the incomplete removal of atmospheric absorptions. Residual atmosphere absorption features due to water vapor and carbon dioxide are commonly observed in AVIRIS data. Methods for estimating canopy chemistry must not be sensitive to these residuals. In our analysis we restricted the absorption features examined to avoid strong atmospheric absorption regions (see Figure 1a). We recommend that all analyses should similarly avoid these wavelength regions.

Because the residual atmospheric absorptions partially overlap the absorptions due to leaf constituents, we tested our method for sensitivity to these residuals. We used MODTRAN (Berk et al, 1989) to calculate the transmittance spectra of a 30 m layer of atmosphere at an elevation of 8000 ft. A dry leaf spectrum was multiplied by the atmospheric transmittance of this layer. Calculations for chemistry were made using this "contaminated" spectrum and compared to the original dry leaf results. The average errors for the full data set are shown in Table 2 for our normalized band-depth approach and 1st and 2nd derivative methods. In general, all methods had small errors in nitrogen calculations. For the normalized band-depth approach, errors for all three estimates of concentrations were small. However, errors for 1st and 2nd derivative methods in the estimation of lignin and cellulose were larger.

3.4.4 Combined Effects of Atmosphere, Soil, and Leaf Water

In a final test for the sensitivity of these methods to influences encountered at the remote sensing level, we contaminated dry leaf spectra with 10% leaf water and added a soil background spectrum in a 75%/25% vegetation/soil combination. Next, we multiplied those spectra by the 30 m atmosphere residual. We performed these calculations for the five previously mentioned samples (see Section 3.4.1). The average errors for the estimates from the contaminated spectra are shown in Table 2. The advantage of the continuum removal and band normalization approach is evidenced in the much smaller errors as compared to the 1st and 2nd derivative methods. Nitrogen errors are doubled using the derivative approaches. Errors for lignin are extremely high for the 1st and 2nd

derivative methods, 15.52% and 28.72%, respectively.

4. CONCLUSIONS

Remote sensing algorithms are needed to measure canopy chemistry for large scale monitoring of ecosystem functioning. This paper examined the use of normalized band-depths calculated from continuum-removed reflectance spectra coupled with stepwise multiple linear regression to estimate leaf nitrogen, lignin, and cellulose concentrations. The method was designed with an awareness of the influences that will be encountered in remote sensing applications. A set of wavelengths highly correlated with leaf chemistry was determined. Independent applications of linear regression using normalized band-depths at these wavelengths to chemical concentrations of seven sites were accurately made. Furthermore, regression equations developed from a calibration set of data, including a variety of species from three eastern U.S. forests, were used to predict the chemical concentrations of slash pine, rice, and Douglas-fir samples. The method was consistent across independent data sets and a wide variety of species. The results of this study suggest that generally applicable equations can be developed to simply and rapidly estimate chemical concentrations in dry leaves from their reflectance spectra. These laboratory results are a necessary first step in establishing the validity of this empirical approach before analyzing remote sensing data. Although these results are encouraging, additional complexities must be considered for remote sensing data. Of all the influences on remotely sensed data that we considered, foremost is the effect of leaf water. In order for this method to work for fresh whole leaves or complete vegetation canopies, the influence of leaf water on spectral reflectance must be removed to within 10%. This presents a challenging problem and future research direction.

5. REFERENCES

ACCP, 1994, "Accelerated Canopy Chemistry Program Final Report to NASA-EOS-IWG," National Aeronautics and Space Administration, Washington D.C., 19 October 1994.

Aber, J.D., and Federer, C.A., 1992, "A generalized, lumped-parameter model of photosynthesis, evapotranspiration and net primary production in temperate and boreal forest ecosystems," *Oecologia,* vol. 92, pp. 463-474.

Afifi and Azen, 1971, *Statistical Analysis, A Computer Aided Approach*, Academic Press, London.

Berk, A., Bernstein, L.S., and Robertson, D.C., 1989, "MODTRAN, A moderate resolution model for LOWTRAN 7," Final Report, GL-TR-0122, AFGL, Hanscomb AFB, MA, 42 pp.

Bolster, K.L., Martin, M.E., and Aber, J.D., 1996, "Determination of carbon fraction and nitrogen concentration in tree foliage by near infrared reflectance: a comparison of statistical methods," *Canadian Journal of Forest Research*, vol. 26, pp. 590-600.

Card, D.H., Peterson, D.L., Matson, P.A., and Aber, J.D., 1988, "Prediction of leaf chemistry by the use of visible and near infrared reflectance spectroscopy," *Remote Sensing of Environment*, vol. 26, pp. 123-147.

Clark, R.N. and Roush, T.L., 1984, "Reflectance spectroscopy: Quantitative analysis techniques for remote sensing applications," *Journal of Geophysical Research*, vol. 89, pp.6329-6340.

Curran, P.J., 1989, "Remote sensing of foliar chemistry," *Remote Sensing of Environment*, vol. 30, pp. 271-278.

Elvidge, D.E., 1990, "Visible and near infrared reflectance characteristics of dry plant materials," *Remote Sensing of Environment*, vol. 11, pp. 1775-1795.

Grossman, Y.L., Ustin, S.L., Jacquemoud, S., Sanderson, E.W., Schmuck, G., and Verdebout, J., 1996, "Critique of stepwise multiple linear regression for the extraction of leaf biochemistry information from leaf reflectance data," *Remote Sensing of Environment*, vol. 56, pp. 1-12.

Hapke, B., 1981, "Bidirectional reflectance spectroscopy, 1: Theory," *J. of Geophys. Res.*, vol. 86, pp. 3039-3054.

Irvine, W.M., and Pollack, J. B., 1968, "Infrared optical properties of water and ice spheres," *Icarus*, vol. 8, pp. 324-360.

Johnson, L.F., Hlavka, C.A., and Peterson, D.L., 1994, "Multivariate analysis of AVIRIS data for canopy biochemical estimation along the Oregon transect," *Remote Sensing of Environment*, vol. 47, pp. 216-230.

LaCapra, V.C., Melack, J.M., Gastil, M., and Valeriano, D., 1996, "Remote sensing of inundated rice with imaging spectrometry," *Remote Sensing of Environment*, vol. 55, pp. 50-58.

Marten, G.C., Shenk, J.S., and Barton, F.E. II. Eds., 1989, *Near-Infrared Reflectance Spectroscopy (NIRS): Analysis of Forage Quality*, U.S. Dept. of Agric. Handbook 643, USDA, Washington D.C., pp. 1-96.

Martin, M. E. and Aber, J. D., 1997, "High spectral resolution remote sensing of forest canopy lignin, nitrogen and

ecosystem process," *Ecological Applications*, vol. 7, pp. 431-443.
Norris, K.H., Barnes, R.F., Moore, J.E., and Shenk, J.S., 1976, "Predicting forage quality by infrared reflectance spectroscopy," *Journal of Animal Science*, vol. 43, pp. 889-897.
Schimel, D., 1995, "Terrestrial biogeochemical cycles: Global estimates with remote sensing," *Remote Sensing of Environment*, vol. 51, pp.49-56.
Wessman, C.A., Aber, J.D., and Peterson, D.L., 1989, "An evaluation of imaging spectrometry for estimating forest canopy chemistry," *International Journal of Remote Sensing*, vol 10., pp. 1293-1316.

Table 1. Wavelengths correlated to leaf chemistry by regression with Blackhawk Island and Harvard Forest data and coefficient values determined by regression with all data.

Estimated Biochemical	Wavelength (nm) (selected by regression with subset of data)	Coefficient value (determined by regression with all data)
Nitrogen		6.6059 (constant term)
	2036	-34.3577
	2050	24.3511
	2078	-13.8809
	2152	-3.0247
	2180	3.3388
Lignin		-10.2775 (constant term)
	1666	9.3277
	1762	77.9044
	2246	105.1030
	2266	9.9582
	2324	-62.2543
	2346	28.4725
Cellulose		-49.3231 (constant term)
	1660	-76.2645
	1766	46.9154
	2066	32.1212
	2186	202.1462
	2202	-315.4317
	2266	45.8069
	2288	-44.6616
	2322	47.1973

Table 2. Errors in estimates of leaf biochemistry as caused by changes in leaf water content, soil background, atmospheric residuals and all effects combined.

Simulated Effect on Remote Sensing Data	Chemical Estimated	RMSE Error for "contaminated" data		
		Normalized Band-depth	1st Derivative	2nd Derivative
10% Leaf Water	Nitrogen	0.21	0.52	0.50
	Lignin	0.47	29.70	2.43
	Cellulose	3.20	26.86	3.23
25% Soil Background	Nitrogen	0.11	0.23	0.11
	Lignin	1.02	0.77	1.36
	Cellulose	3.56	4.27	4.14
Atmosphere Residual (30m)	Nitrogen	0.08	0.14	0.04
	Lignin	1.70	8.60	14.87
	Cellulose	0.77	6.38	3.02
Combined Effects	Nitrogen	0.21	0.43	0.43
- 10% Leaf Water	Lignin	1.70	15.52	14.36
- 25% Soil Background	Cellulose	2.68	28.72	3.19
- Atmosphere Residual (30m)				

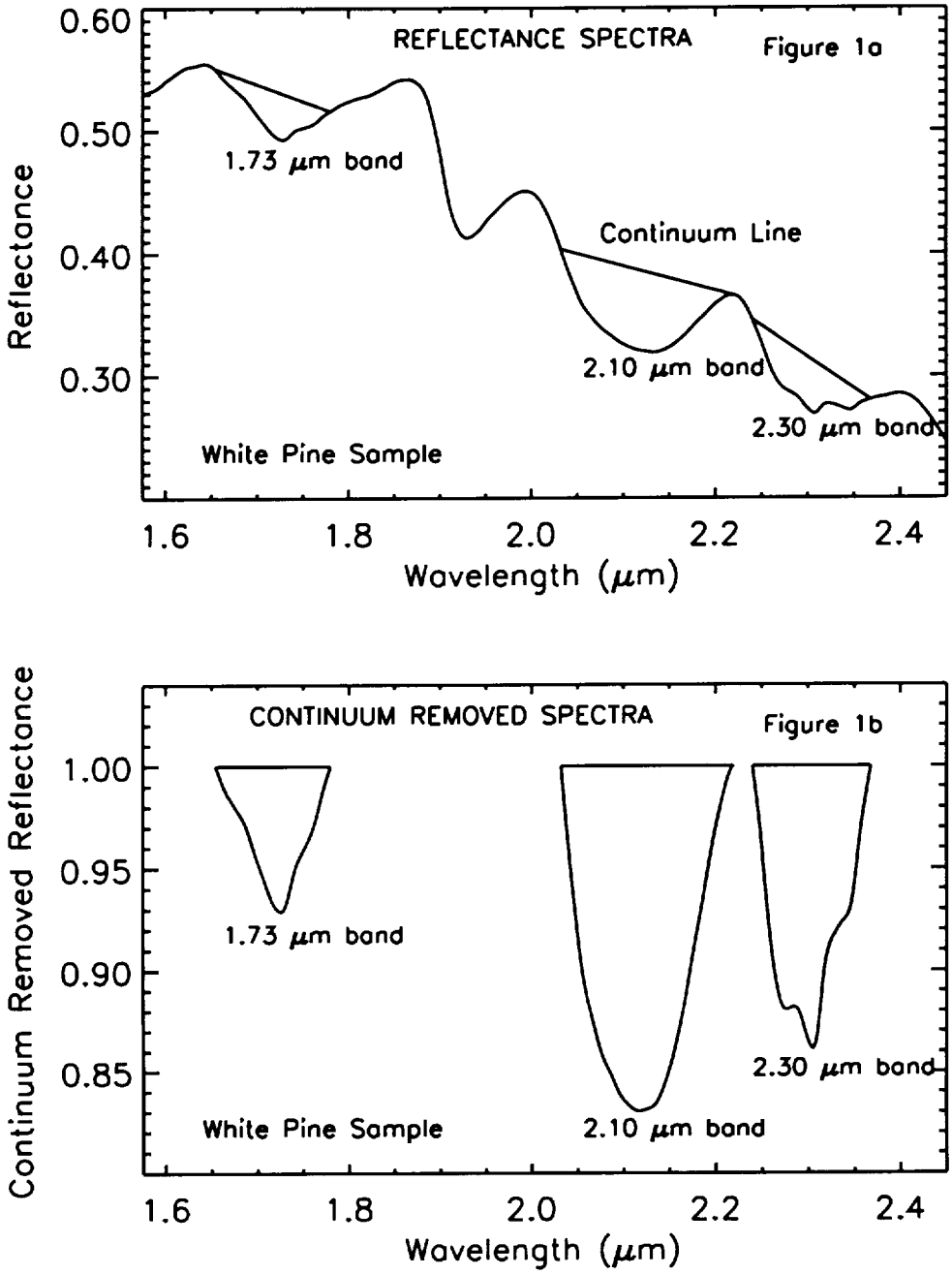

Figure 1. Example spectrum of white pine:
(a) reflectance spectrum with continuum lines
(b) continuum removed reflectance spectrum.

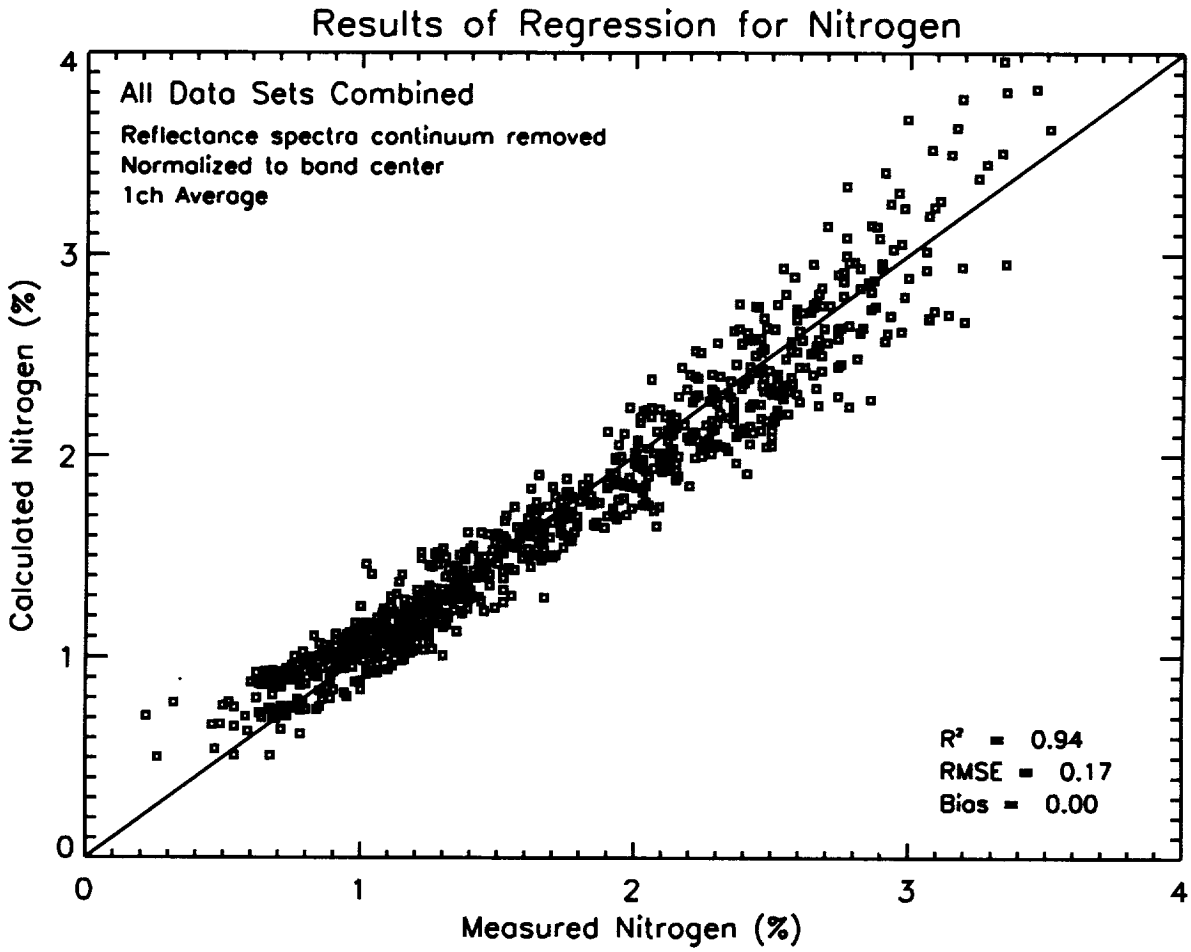

Figure 2. Regression results for nitrogen concentration using normalized band depths and all data sets combined (840 samples).

MAPPING THE BIOLOGY AND MINERALOGY OF YELLOWSTONE NATIONAL PARK USING IMAGING SPECTROSCOPY

Raymond F. Kokaly, Roger N. Clark, and K. Eric Livo

U.S. Geological Survey
Mail Stop 973, Box 25046
Denver Federal Center
Denver, Colorado 80225
raymond@speclab.cr.usgs.gov

1. INTRODUCTION

Yellowstone National Park preserves and protects unique geologic features and biologic systems. The area contains the world's largest assemblage of hot springs, geysers, and mud pots. Every year millions of visitors are drawn to see the active geysers, such as Old Faithful, and the colorful eroded remains of ancient hydrothermal systems in the Grand Canyon of the Yellowstone. Within the park, visitors also observe the activities of many large mammals, including bison, elk, moose, grizzly bears, and recently, wolves. The populations and movements of these animals are directly and indirectly influenced by the vegetation covering the park. The large fires of 1988 in Yellowstone demonstrated how dramatically and rapidly the vegetation and the state of the ecosystem can change. Although sometimes overlooked by park visitors, smaller organisms, the biota of the hot springs, are receiving increasing attention. These microorganisms are being researched by the biotechnology field for their potential benefits for the health of humans and the environment (Brock, 1994).

The U.S. Geological Survey (USGS), in cooperation with the National Park Service, is using imaging spectroscopy to advance the understanding of the geologic features and biologic systems in Yellowstone National Park. We are applying recent advances in remote sensing methods to detect and map the mineralogy of active and ancient hydrothermal systems, vegetation cover types, and hot springs microorganisms. These maps will be used to increase the understanding of the hydrothermal systems and to examine the links between the distribution of plant species and large mammal populations (specifically, the use of whitebark pine by grizzly bears). This paper presents the initial results of our efforts in mapping biology and mineralogy in Yellowstone National Park using imaging spectroscopy.

2. METHODS

2.1 AVIRIS Data Set

Spectroscopy is the science that deals with the interaction of electromagnetic radiation with matter. Imaging spectroscopy concerns spectral reflectance measurements made spatially over large areas by an airborne or spaceborne spectrometer. In contrast to broadband remote sensing instruments which measure reflectance in only a few channels over broad wavelength regions (e.g., Landsat Thematic Mapper), imaging spectrometers measure light that has been reflected from the surface in numerous continuous channels and using narrow bandwidths. For this study, the Airborne Visible and Infra-Red Imaging Spectrometer (AVIRIS) operated by NASA/JPL was used. AVIRIS collects reflectance data in 224 continuous channels of approximately 10 nanometer (nm) bandpass over the spectral wavelength range of 350 to 2500 nm (from visible light to near-infrared). AVIRIS collects 20 meter wide pixels at approximately 17 meter spacing. The sensor swath width is approximately 10.5 kilometers.

AVIRIS data were collected on August 7, 1996, in four flight lines that included the following areas: the Upper and Lower Geyser Basins, the Gallatin Mountain Range, Mammoth Hot Springs, Norris Geyser Basin, the Grand Canyon of the Yellowstone, and the Lamar Valley. These areas were selected in consultation with National Park Service personnel to target areas of primary geologic and biologic interest. Figure 1 shows the outlines of the

AVIRIS flight lines on a base of Landsat imagery.

2.2 AVIRIS Data Calibration

In order to convert AVIRIS data from radiance to reflectance, the data had to be corrected for the influence of several variables, including solar irradiance, atmospheric gas absorptions, and path radiance (Clark et al, 1993a). We employed a two-step procedure for this conversion: 1) primary atmospheric correction using the ATREM algorithm (Gao et al, 1993 and 1997), and 2) correction of residual features using ground calibration. The ground calibration was used because, although the ATREM program corrected most atmospheric effects, residual atmosphere absorptions remained in the data and the atmospheric path radiance for wavelengths shorter than 500 nm was overcorrected. A ground calibration site was selected by field survey as having the properties of being fairly large, homogenous, and not containing material with strong absorption features. A gravel staging area, located near Norris Geyser Basin, was utilized for calibration. On the day of the AVIRIS flight, reflectance measurements of this site were made with an Analytical Spectral Devices Full-Range field spectrometer. AVIRIS data over the calibration site were used with the field measurements to generate a multiplicative correction for the entire AVIRIS data set. An additive path radiance correction was derived using vegetation covered area in shadow (this area had a reflectance in the ultraviolet of less than 1%). Following the initial correction using ATREM, these additive and multiplicative corrections were applied to each pixel of AVIRIS data to derive surface reflectance.

2.3 Mineral Mapping

The USGS Tricorder algorithm was used to identify and map distributions of minerals in the AVIRIS data (Clark et al., 1990, 1991, 1993b, and 1995). The Tricorder algorithm is an expert system which compares the absorption features present in each pixel of AVIRIS data to the characteristic absorptions of more than 300materials, including minerals, mineral mixtures, vegetation, water, snow, and man-made materials. The reference spectra are contained in the USGS spectral library (Clark et al, 1993c) and in our research library. The algorithm uses continuum removal to isolate specific absorptions and remove the effects of changing slopes and overall reflectance levels (Clark and Roush, 1984). Tricorder compares the wavelength position and shape of absorptions in the AVIRIS data with those in each reference sample of the library. A modified least-squares fitting algorithm is used to assess the closeness of the match. The Tricorder expert system makes further refinements to select the closest match using threshold values, continuum slope constraints and other methods.

2.4 Vegetation Mapping

All vegetation contain the same basic constituents: chlorophyll and other pigments, water, proteins, starches, waxes, and structural biochemical molecules, such as lignin and cellulose (Elvidge, 1990). All of these components contribute to the reflectance spectra of vegetation. Figure 2 shows laboratory reflectance spectra of vegetation foliage in both the fresh state and after being dried in an oven for 24 hours. The wavelength regions in which the basic plant components have strong absorptions are indicated on this plot. In dry vegetation, the strong absorption of water is absent and the absorptions due to protein, lignin, and cellulose become apparent in the spectrum.

Since all vegetation contains the same basic materials, their reflectance spectra are similar. However, different plants contain varying amounts of each leaf component which causes subtle changes in the shapes of absorption features. On this basis, we developed a strategy to detect and map the distribution of vegetation cover types in Yellowstone National Park using imaging spectroscopy. Figure 3 shows the reflectance spectra of two vegetation cover types found in Yellowstone National Park, Engelmann spruce/subalpine fir and lodgepole pine. Their overall spectral profiles are similar. However, differences can be seen in the chlorophyll absorptions (400 to 680 nm) and also in the absorptions arising from water within the conifer needles (at 970 and 1190 nm). The pigments present in the lodgepole pine give it a yellow-green color (higher reflectance in the green and red areas of the visible spectrum relative to the blue region). In comparison, the spruce/fir needles appear blue-green. Their reflectance spectrum shows a relatively high reflectance in the blue region that due to the presence of waxy coatings on the needles and different amounts of pigments as compared to lodgepole pine. The water absorptions (970 and 1190 nm) differ in depth and shape between the two vegetation types. We believe that several factors influence

reflectance spectra in this range of wavelengths, including the amount of water in the needles and the structure of the forest canopy.

Using our knowledge of the biological factors influencing vegetation spectra, we developed the following method to map vegetation. First, we identified the major cover types in Yellowstone National Park during a field survey. We located pixels in the AVIRIS data covering these sites and averaged spectra for each of the cover type areas. Nearly 30 such training sites were identified. These sites included all major forest cover types, including lodgepole pine, whitebark pine, Douglas-fir, and a mixed Engelmann spruce/subalpine fir category. Since lodgepole pine covers the greatest area in the park and is the major colonizing species on recently disturbed ground, several age classes of this type were used. In addition, training sites for many types of nonforest vegetation were identified. These nonforest types included sagebrush, willow, grasslands, lush sedge habitats, and wetland areas. The average AVIRIS spectra for the vegetation cover types were assembled into a reference library. Finally, we used Tricorder to compare the spectrum from each pixel of AVIRIS data to the library reference spectra. Using the chlorophyll (660 nm) and leaf water absorptions (970 and 1190 nm), Tricorder detected and mapped the distribution of the vegetation cover types. This paper discusses the results of forest and nonforest cover type mapping for two areas in the park, Mammoth Hot Springs and Mount Washburn.

In addition to vegetation cover, spectra of hot springs biota were included in the reference library. During field surveys we measured the reflectance spectra of hot springs bacteria and algae and found the shapes to be unique compared to vegetation. Figure 4 shows a spectrum of a common hot springs bacteria (*Synechococcus*). The chlorophyll absorption is narrow and the water absorptions very strong. The strength of the water absorption is due to a thin layer of hot water running over the surface of the bacteria.

3. RESULTS & DISCUSSION

3.1 Mineral Maps

Mineral maps were produced for the following areas: Upper and Lower Geyser Basins, Norris Geyser Basin, the Roaring Mountain hydrothermal area, and Mammoth Hot Springs. The maps made using the USGS Tricorder algorithm reveal the presence of minerals that are commonly associated with hydrothermal areas: calcite, siliceous-sinter, montmorillonite, kaolinite, and alunite. The mineral maps show a change in mineralogy for the different areas revealing both alkaline and acidic hydrothermal areas. By analyzing the mineral maps in conjunction with known geological relationships, we can speculate about the water chemistry, environment of deposition, and sources for the minerals and waters within these active hydrothermal areas.

In the Mammoth area, AVIRIS mineral maps reveal an abundance of calcium carbonate. The large tracts of carbonate travertine are derived from dissolution of underlying limestone and subsequent transport to the surface by moderately hot, alkaline waters (White et al, 1988).

To the south of Mammoth is the Roaring Mountain geothermal field. AVIRIS maps show alunite in the center of the area surrounded by kaolinite and halloysite with minor outcrops of montmorillonite and siliceous-sinter on the perimeter of the area. White et al (1988) associated alunite and kaolinite in this area with hot acidic, slightly reducing waters derived from steam and hydrogen sulfide (H_2S) gas above a water table interface. The H_2S gas is oxidized to form sulfates (e.g. alunite) near the surface and the clay minerals form by mineral alteration of the rhyolite country rock (White et al, 1988). We believe this indicates that at Roaring Mountain a hotter more acidic hydrothermal system is exposed at the surface as compared to Mammoth.

In contrast to Roaring Mountain, mineral maps of Norris Geyser Basin reveal large outcrops of siliceous-sinter and montmorillonite with lesser occurrences of kaolinite and halloysite outcrops and only a few pixels of alunite. White et al (1988) proposed that the montmorillonite and siliceous-sinter are formed from neutral pH waters high in chlorine and quartz (SiO_2). The water table is at or near the surface with relatively high flow of water derived from distant sources (White et al, 1988). The fringes of the basin, where the AVIRIS maps show kaolinite and alunite, are regions above the water table with less fluid flow and high temperatures where surficial acid sulfate alteration occurs, similar to that found at Roaring Mountain.

Mineral maps for the Upper and Lower Geyser Basins show broad regions of siliceous-sinter mixed with montmorillonite and very minor amounts of halloysite and kaolinite. This indicates that these areas are the least acidic areas of those mapped in the park because of the dominant presence of siliceous-sinter which is formed in neutral to alkaline conditions and because of the very minor occurrences of the sulfate and clay minerals common to acid systems.

3.2 Hot Springs Biota Maps

The characteristic spectral signature of hot springs bacteria and algae in the AVIRIS remote sensing data were used to map hot springs biota. The results show that the narrow chlorophyll absorption and strong water absorption in the reflectance spectra of the hot springs biota are not confused with the spectra of vegetation. The maps of hot springs biota complement the information in the mineral maps made from AVIRIS. For the Norris Geyser Basin, maps created for both the minerals and hot springs biota were compared. Together these maps show the overall extent of the hydrothermal area. In some areas the mineral signature was weak but the bacteria signature was very strong. Because the thermophilic microorganisms require areas of hot running water to live in, we interpret these areas as having thriving microbial mats covering the underlying material and masking the mineral signature in the reflectance spectra. Thus, using the mineral and hot springs biota maps in combination shows not only the overall extent of thermal areas but also which parts had actively flowing water at the time of the overflight.

Each hot springs microorganism requires certain conditions for its growing environment (i.e., specific water temperature and pH) (Brock, 1994). Future work will be conducted to distinguish between the several bacterial and algae communities in Yellowstone using field spectral measurements and to extend this ability to the AVIRIS data. However, the controlling environmental conditions can change rapidly over small distances. The current 17 meter spacing of AVIRIS means that each pixel may contain many different bacterial or algal communities. Higher spatial resolution data would be more useful in identifying individual species and their related environmental conditions in the hydrothermal areas. AVIRIS is proposed to fly on a different platform in the next year that will give higher spatial resolution. Other imaging spectrometers can also collect data at higher spatial resolutions. High spatial resolution maps would provide useful information for the study of the hot springs bacterial and algal communities. In addition, multi-temporal images of this type could be used to study seasonal and long-term changes in the hydrothermal systems.

3.3 Vegetation Maps - Forest Cover

Using imaging spectroscopy, forest cover maps were produced which reveal the distributions of conifer species, including whitebark pine. Different age classes of lodgepole pine were also distinguished based on their spectral signature. For initial validation of the results, we compared the forest cover type maps derived from AVIRIS data to maps created from air photos by Despain (1990).

Whitebark pine was mapped along the slopes of Mount Washburn indicating areas where grizzly bears forage for food. The link between whitebark pine and grizzly bears is provided by red squirrels which store cones from the trees in middens; these middens are raided by grizzly bears in the fall season (Mattson, 1992; Mattson et al 1997). The distribution of whitebark pine as mapped using the AVIRIS data were in general agreement with air photo interpretations.

The map from produced for the AVIRIS scene that includes Mammoth Hot Springs shows that the forest cover is predominately lodgepole pine of various age classes. In the northern part of the scene, around Mammoth Hot Springs, stands of Douglas-fir were detected and mapped. These stands are also indicated in the air photo interpretations. Within the Mammoth scene, the distribution of various age classes of lodgepole pine were mapped. Although the majority of lodgepole consist of young seedlings reestablishing after the 1988 fires, a triangular shaped patch of older lodgepole pine was clearly indicated in the southeast corner of the Mammoth scene. The trees in this stand were identified by the Tricorder analysis as falling into two age categories: 50-150 year old small diameter, dense lodgepole and 150-300 year old lodgepole with some understory development (these age categories are defined by Despain, 1990). The maps of lodgepole pine made from AVIRIS data match the distributions of these classes in the air photo interpretations. However, for the youngest age class of lodgepole pine, lodgepole

regrowth from fires (less than 50 years of age), differences exist between the AVIRIS maps and the air photo interpretation. The air photo interpretation represents all young lodgepole as a single class while AVIRIS maps further discriminate between areas with slow, moderate, and vigorous regrowth. We suspect that areas of slow regrowth are dominated by a grass cover rather than lodgepole seedlings since in the AVIRIS images these pixels were mapped as grasslands by the Tricorder algorithm. Areas of vigorous regrowth were detected in the AVIRIS data and these will be field checked to determine the species composition of these sites and to determine the causes of favorable growing conditions in these areas.

Our preliminary results show that imaging spectroscopy data can discriminate a great number of vegetation cover types using chlorophyll and leaf water absorption features. The forest cover maps produced using Tricorder agree with air photo interpretations. The agreement is remarkable considering that these maps were produced using very different techniques: spectral analysis of AVIRIS data compared to the identification of texture, color, and crown shape patterns in air photos. In addition to comparisons with the air photo interpretations, we will conduct field work to verify the vegetation cover maps.

3.4 Vegetation Maps - Nonforest Cover

Nonforest vegetation cover types were also mapped in the park using AVIRIS data. The preliminary maps show reasonable distributions based on coarse field surveys. Sagebrush was mapped at low elevations in the north part of the image covering Mammoth Hot Springs and in some higher elevation areas. Willow and wetland areas were mapped along streams and rivers. Grasses were mapped along the north base of Mount Washburn as observed in the field. In the future, we will refine these maps and include more nonforest cover types. Maps of nonforest cover types produced from AVIRIS data could have important application by National Park Service personnel for assessing winter grazing resources for the large mammals in the park, for example the bison and elk. These maps could lead to a better understanding of the movements of mammal populations within and beyond the park boundaries.

4. CONCLUSIONS

Maps generated from AVIRIS data using the USGS Tricorder algorithm reveal the presence of minerals commonly associated with hot springs. The mineral maps show the difference between alkaline geyser basins like the Old Faithful area and hotter, more acidic thermal areas such as Roaring Mountain.

Field measurements revealed a spectral signature of the hot springs microorganisms which is not confused with the reflectance spectra of higher plants. Maps of hot springs biota were produced from AVIRIS data. These maps complement the information in mineral maps by showing the areas where hot water is flowing on the surface. Future work will include efforts to discriminate and map individual species of bacteria and algae in the hydrothermal areas. However, since bacterial and algal communities change rapidly over short distances, we suggest that higher spatial resolution imaging spectroscopy data would be more effective for studying these areas.

The results from identifying and mapping the distribution of vegetation using AVIRIS were very encouraging. Fine discriminations between vegetation types were made, including identifying whitebark pine, important for understanding grizzly bear habitat, and age classes of lodgepole pine. Initial comparisons with older maps produced from air photos confirm our results. Nonforest vegetation was also mapped using imaging spectroscopy. The method of using both the chlorophyll and water absorptions found in plant spectra was successful in identifying the vegetation cover. This demonstrates the power of using more than one region of the electromagnetic spectra to distinguish between vegetation types. As a result, future efforts will include an extension of the method to include the 2-micron region of the spectrum.

The advantage of imaging spectroscopy over other remote sensing methods was demonstrated by its ability to address many issues with one data set: detection of hot springs biota, mineral mapping to reveal differences in hydrothermal systems, mapping of forest cover types and lodgepole age classes, and discrimination of nonforest vegetation types. In summary, imaging spectroscopy was used to map minerals, vegetation and hot springs biota for selected parts of the park. In the future, this information will be acquired and analyzed over more areas to increase

the understanding of the geologic features and biologic systems in Yellowstone National Park .

5. REFERENCES

Brock, T. D., 1994, Life at High Temperatures, Yellowstone Association for Natural Science, History & Education, Inc., Yellowstone National Park, Wyoming.

Clark, R. N. and T.L. Roush, 1984, "Reflectance Spectroscopy: Quantitative Analysis Techniques for Remote Sensing Applications," *Journal of Geophysical Research*, vol. 89, pp. 6329-6340.

Clark, R.N., A.J. Gallagher, and G.A. Swayze, 1990, "Material Absorption Band Depth Mapping of Imaging Spectrometer Data Using a Complete Band Shape Least-Squares Fit with Library Reference Spectra," *Proceedings of the Second Airborne Visible/Infrared Imaging Spectrometer (AVIRIS) Workshop.* JPL Publication 90-54, 176-186.

Clark, R.N., G.A. Swayze, A. Gallagher, N. Gorelick, and F. Kruse, 1991, Mapping with Imaging Spectrometer Data Using the Complete Band Shape Least-Squares Algorithm Simultaneously Fit to Multiple Spectral Features from Multiple Materials, *Proceedings of the Third Airborne Visible/Infrared Imaging Spectrometer (AVIRIS) Workshop,* JPL Publication 91-28, 2-3.

Clark, R.N., G.A. Swayze, Heiebrecht, K.B., Goetz, A.F.H, and Green, R.O., 1993a, "Comparison of Methods for Calibrating AVIRIS Data to Ground Reflectance," *Summaries of the 4th Annual JPL Airborne Geosciences Workshop, Volume 1: AVIRIS Workshop*, JPL Publication 93-26, pp. 31-34.

Clark, R.N., G.A. Swayze, and A. Gallagher, 1993b, Mapping Minerals with Imaging Spectroscopy, *U.S. Geological Survey, Office of Mineral Resources Bulletin 2039,* pp. 141-150.

Clark, R.N., Swayze, G.A, Gallagher, A.J., King, T.V.V., and Calvin, W.M., 1993c, "The U.S. Geological Survey, Digital Spectral Library: Version 1: 0.2 to 3.0 microns," U.S. Geological Survey Open File Report 93-592.

Clark, R.N. and Swayze, G.A., 1995, "Mapping Minerals, Amorphous Materials, Environmental Materials, Vegetation, Water, Ice and Snow, and Other Materials: The USGS Tricorder Algorithm," *Summaries of the Fifth Annual JPL Airborne Earth Science Workshop,* January 23- 26, R.O. Green, Ed., JPL Publication 95-1, p. 39-40.

Clark, R.N., G.A. Swayze, and T.V.V. King, 1998, "Imaging Spectroscopy: A Tool for Earth and Planetary System Science Remote Sensing with the USGS Tricorder Algorithm," in preparation, to be submitted to *Science.*

Despain, D. G., 1990, Yellowstone Vegetation: Consequences of Environment and History in a Natural Setting, Roberts Rinehart Publishers, Santa Barbara.

Elvidge, D.E., 1990, "Visible and near infrared reflectance characteristics of dry plant materials," *Remote Sensing of Environment*, vol. 11, pp.1775-1795.

Gao, B.C., Heidebrecht, K.B., and Goetz, A.F.H., 1993, "Derivation of Scaled Surface Reflectances from AVIRIS Data," *Remote Sensing of Environment*, vol. 44, pp.165-178.

Gao, B.C., Heidebrecht, K.B., and Goetz, A.F.H., 1997, "Atmosphere Removal Program (ATREM) Version 3.0 User's Guide," Center for the Study of Earth from Space, University of Colorado at Boulder, pp. 1-27.

Mattson, D.J., Blanchard, B.M., and Knight, R.R., 1992, "Yellowstone grizzly bear mortality, human habituation, and whitebark pine seed crops," Journal of Wildlife Management, vol. 56, pp. 432-442.

Mattson, D.J., and Reinhart, D.P., 1997, "Excavation of red squirrel middens by grizzly bears in the whitebark pine zone," *Journal of Applied Ecology*, vol. 34, pp. 926-940.

White, D.E., Hutchinson, R.A., and Keith, T.E.C., 1988, "The geology and remarkable thermal activity of Norris Geyser Basin, Yellowstone National Park, Wyoming," U.S. Geological Survey Professional Paper 1456.

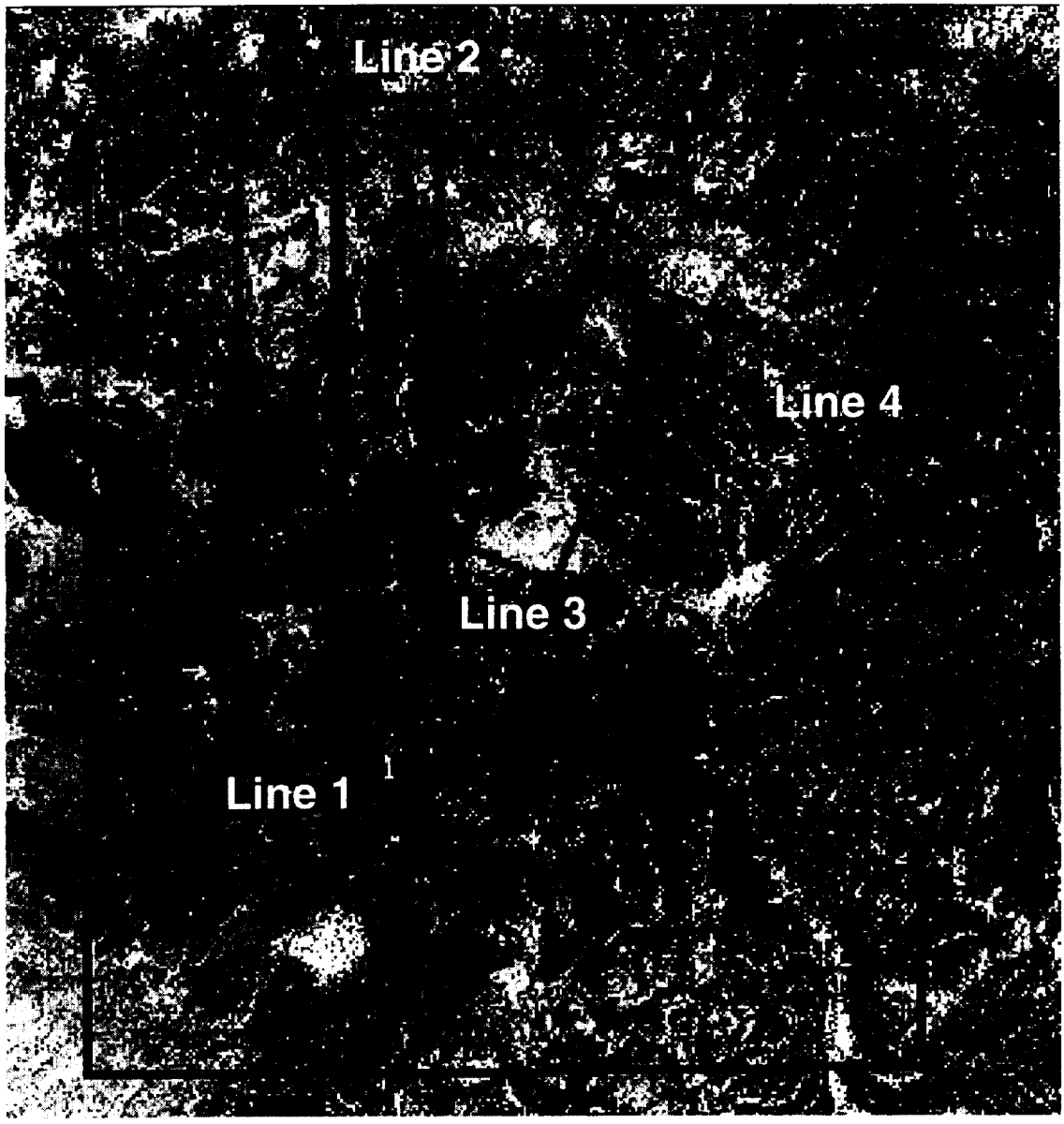

Figure 1. AVIRIS coverage for Yellowstone National Park collected on August 7, 1996, overlaid on Landsat TM imagery. Areas covered in each line include:
1) from the Old Faithful area north along the Gallatin Range to Electric Peak,
2) from Norris Geyser Basin north to Mammoth Hot Springs and Gardiner, Montana,
3) from Hayden Valley northeast along the Grand Canyon of the Yellowstone to Tower Junction,
4) from Tower Junction southeast along the Lamar Valley.

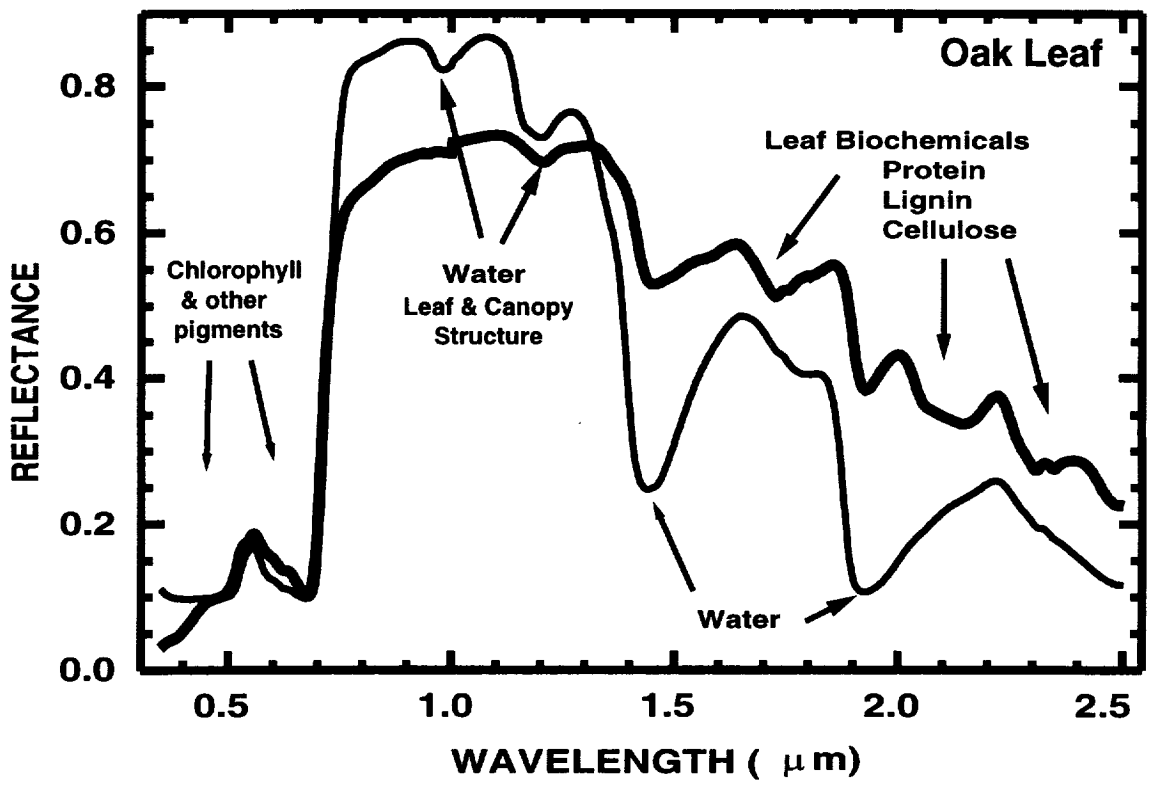

Figure 2. Laboratory reflectance spectra of an oak leaf in a fresh state (thin line) and after being dried (thick line). Because the strong absorptions due to water are absent, the dried leaf spectrum shows the protein, lignin and cellulose absorption features in the 1.5 - 2.5 micron region.

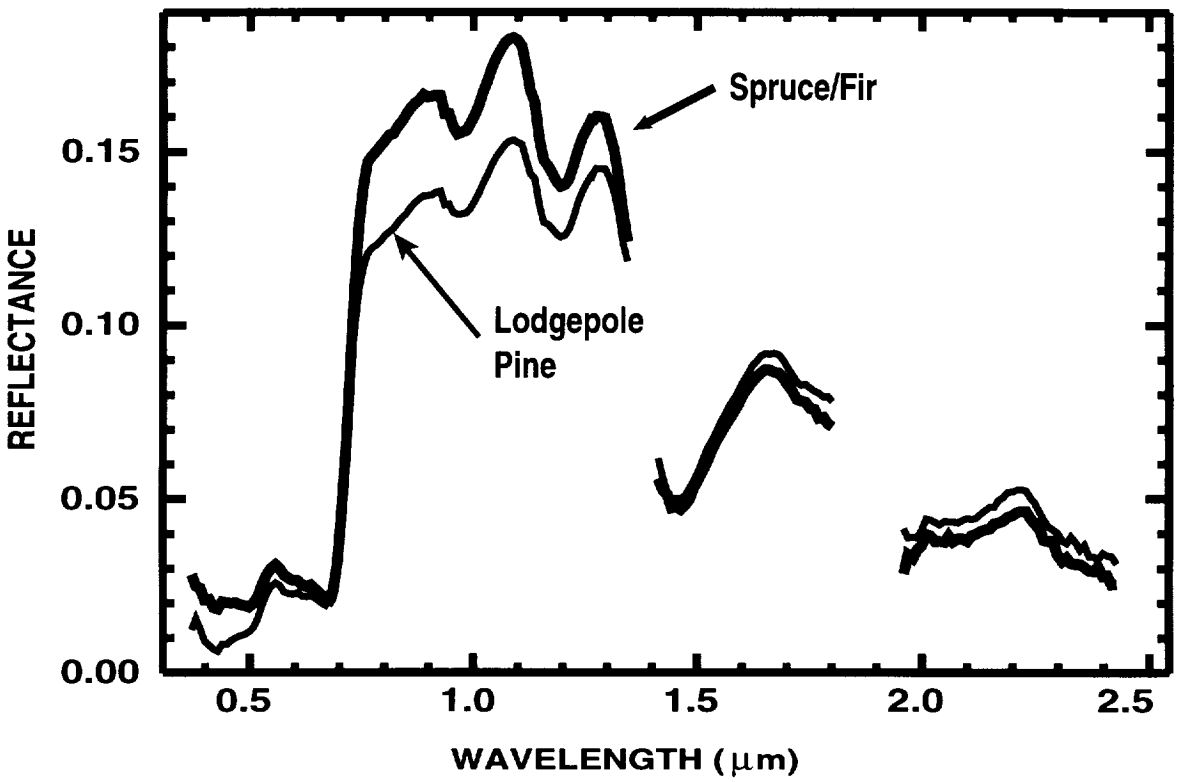

Figure 3. Reflectance spectra of two forest cover types from calibrated AVIRIS reflectance data over Yellowstone National Park, lodgepole pine (thin line) and Engelmann spruce/subalpine fir (thick line) cover tpes.

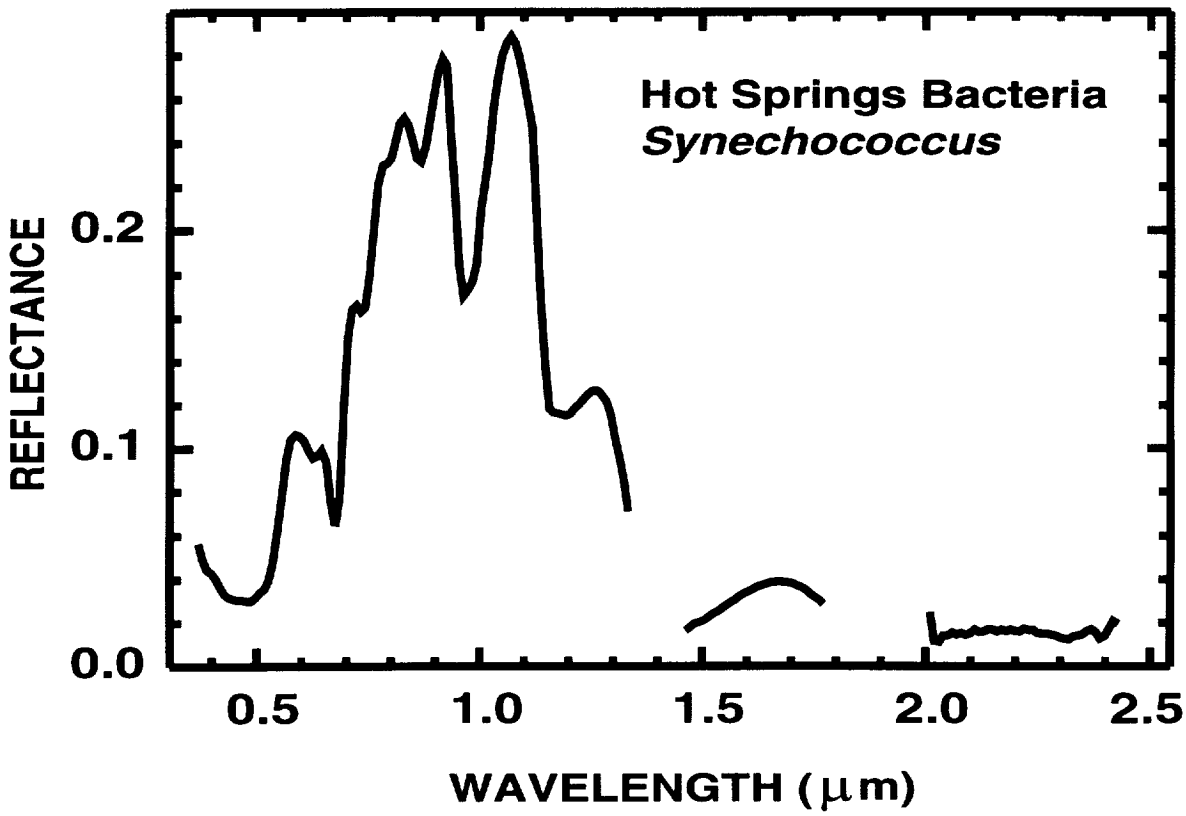

Figure 4. Field measured reflectance spectrum of thermophilic bacteria found in Yellowstone National Park hydrothermal systems.

MAPPING ACTIVE HOT SPRINGS USING AVIRIS AND TIMS

F. A. Kruse

Analytical Imaging and Geophysics LLC, 4450 Arapahoe Ave, Suite 100
Boulder, Colorado, USA, 80303, kruse@aigllc.com

ABSTRACT

This research is studying the occurrence and characteristics of both active and fossil hot springs systems using Thermal Infrared Multispectral Scanner (TIMS) and Airborne Visible/Infrared Imaging Spectrometer (AVIRIS) data to provide insights into the origins of hydrothermal systems and precious metal ore deposits. At Steamboat Springs, Nevada, TIMS delineates the silica sinter associated with active alkaline-type hot springs, while AVIRIS data map alteration minerals including alunite, kaolinite, and hydrothermal silica associated with inactive acid-sulfate hot springs. Sites studied at Yellowstone National Park, Wyoming, include Mammoth Hot Springs, consisting of several ages of travertine terraces as well as glacially-transported travertine material. Hot springs in the Firehole River basin, include active hydrothermal areas associated with the Upper, Midway, and Lower geyser basins, with mineralogy characteristic of the both the alkaline and acid-sulfate type hot springs, including hydrothermal silica, alunite, and kaolinite. Surface exposures in Hayden Valley and in the Norris and Gibbon Geyser Basins indicate predominantly acid-sulfate alteration, along with smaller occurrences of silica sinter. Study of the nature and spatial distribution of specific hydrothermal alteration minerals at active hot springs using hyperspectral remote sensing provides insight into the geochemistry of these systems, and to the occurrence and characteristics of hot springs systems in the fossil record. These findings potentially could lead to new and/or improved exploration methods for epithermal ore deposits.

SPECTRAL IDENTIFICATION OF IMAGE ENDMEMBERS DETERMINED FROM AVIRIS DATA

F. A. Kruse

Analytical Imaging and Geophysics LLC, 4450 Arapahoe Ave, Suite 100
Boulder, Colorado, USA, 80303, kruse@aigllc.com

ABSTRACT

Experienced scientists can easily identify materials based on their visible/infrared reflectance spectra using field or laboratory instruments. Imaging spectrometry (hyperspectral data) also allow identification of materials using spectroscopy; however, these data typically consist of hundreds-of-thousands of spectra, so which spectra do you identify? Some researchers have taken the approach of matching every spectrum in an image to a spectral library. This works well when pure materials are present on the ground and all of the materials are contained in the library. In real-world situations, however, where materials are spatially or intimately mixed, only the strongest features are matched. In this case, it's also not possible to have all of the possible mixtures in the library, and thus the above approach will only "identify" the predominant material, if any material at all. The research described here concentrates on identifying only the purest spectra extracted from the hyperspectral data. After applying data reduction and endmember extraction methodologies, the endmember spectra are used in an automated identification procedure based on analysis of spectral features. This approach has an improved likelihood of success because 1) the best endmember spectra have already been extracted for analysis, 2) the extracted endmembers are mean spectra and thus have improved signal-to-noise over single spectra, 3) these spectra are typically one material (no mixing), 4) not every spectrum in the image needs to be analyzed. Once the individual endmembers have been identified, then a variety of mapping methods can be used to map their spatial distributions, associations, and abundances.

CHARACTERIZATION AND MAPPING OF KIMBERLITES AND RELATED DIATREMES USING AVIRIS

F. A. Kruse and J. W. Boardman

Analytical Imaging and Geophysics LLC, 4450 Arapahoe Ave, Suite 100
Boulder, Colorado, USA, 80303, kruse@aigllc.com, boardman@aigllc.com

ABSTRACT

Airborne Visible/Infrared Imaging Spectrometer (AVIRIS) data are being used to study the occurrence and mineralogical characteristics of kimberlite diatremes at several sites in Utah and in the State-Line district of Colorado/Wyoming. The Utah kimberlites are well exposed and provide an excellent case history of mineralogical mapping of kimberlite mineralogy and abundant xenoliths of country rock. Two different mineral associations have been observed; 1) dolomite, minor calcite and illite, and an association of kaolinite and goethite at the Mule Ear and Cane Valley diatremes, and 2) serpentine matrix with dolomite xenoliths at the Moses Rock Dike site. The Moses Rock Dike appears to be spatially zoned. The State-Line kimberlites are deeply weathered, poorly exposed, and the AVIRIS data are dominated by green and dry vegetation, presenting a challenge to remote sensing technology. Identification of characteristic kimberlite minerals is difficult except where exposed by current mining; however, sub-pixel analysis methods have been successfully used to map the mineralogy of exposed mine areas, to locate similar areas, and to map the distribution of potential new exploration targets. Minerals identified in the State-Line district using the AVIRIS data include dolomite, calcite, phlogopite, and kaolinite. This work is in progress, with the goal of determining methods for characterizing subtle mineralogic changes associated with kimberlites and developing exploration models valid for a variety of geologic terrains.

Environmental study of the Bonanza Mining District, Colorado using AVIRIS, aircraft, satellite, and terrain data

K. Eric Livo, Ken Watson, Dan H. Knepper, Jr., and Susanne Hummer-Miller
U. S. Geological Survey
Denver, Colorado, USA

INTRODUCTION

The objective of this study was to describe the mineralization, altered rock, and mining impacts on the environment of the Kerber Creek drainage within the Bonanza Mining District, Colorado, using several types of remotely sensed data. Several types of data set were analyzed, including imagery, map data, and point data. These data were assembled into a coregistered database where features were correlated between layers visually and/or combined through masking.

BONANZA MINING DISTRICT

The Bonanza Mining District is located at the headwaters of Kerber Creek, within the San Juan Mountains 120 miles southwest of Denver, Colorado. It is situated within the Bonanza caldera with mountains forming three sides of the drainage basin. Kerber Creek water is used for crop irrigation and drinking water 15 miles downstream in the San Luis Valley.

DATA SETS

Data sets used were a digitally scanned reconnaissance geologic map, Digital Elevation Model (DEM), Thematic Mapper Simulator (TMS), National Uranium Resource Evaluation (NURE), and Airborne Visual and Infra-Red Imaging Spectrometer (AVIRIS). All data were georeferenced to a Systeme Probatoire d'Observation del la Terre (SPOT) image. Lithology and structure as mapped and compiled by Knepper (1974) after Burbank (1932) and information from a literature review were used as ground truth as well as local checking of several spectral anomalies with an Analytical Spectral Devices (ASD) field spectrometer and by hand-sample examination.

The airborne TMS sensor covers 12 broad-band channels with reflectance coverage from 0.42 to 2.35μm and thermal coverage from 8.5 to 14μm. These data were acquired on August 28, 1992 under cloud-free conditions from a NASA ER-2 simultaneously with the 1992 AVIRIS data. DEM point-elevation data and gridded NURE radiometric data were acquired from the U.S. Geological Survey. The NURE gamma-ray spectrometry data were flown on a one-quarter-mile spacing in the mid 1970's with radioactive uranium, thorium, and potassium counts recorded. AVIRIS data were acquired in 1992 (west north-south line) and on October 11, 1994 (east north-south line) with 70% overlap. The two flightlines were processed separately; the 1992 mineral mapped coverage which fell outside the 1994 flightline was added to the 1994 mineral maps. These reflectance data were measured in 224 channels from .45 to 2.45μm.

GEOLOGY

The pre-volcanic basement upon which the middle Tertiary volcanic rocks of the Kerber Creek area (Bonanza volcanic field) were deposited, consist of Precambrian crystalline rocks and

Paleozoic sedimentary strata containing sandstone, shale, and carbonate units. Rocks of Mesozoic age that are presumed to have once covered the area were completely eroded (Burbank, 1932) following the uplift of the region during the late Cretaceous-Eocene Laramide orogeny (Knepper and Marrs, 1971).

Oligocene volcanic rocks (Bonanza volcanic sequence) are exposed over a large portion of the Kerber Creek drainage basin. These rocks consist of flows, intrusives, and lava domes varying from mafic to silicic in composition. The alteration and mineralization in the Kerber Creek drainage basin are associated with this period of volcanic activity and are mostly hosted by rocks of this volcanic sequence. After the eruption of the ash-flows and during and after eruption of younger andesites and latites, the central portion of the Bonanza volcanic center collapsed forming the asymmetric Bonanza caldera (Burbank, 1932; Marrs, 1973). The caldera is the dominant structural feature of the Kerber Creek drainage basin and is directly responsible for most of the present-day topographic configuration of the area.

Following the eruption of the andesites and latites, small plutons and lava domes were emplaced in the Bonanza volcanic sequence. Post-volcanic deposits in the Kerber Creek drainage basin are limited to Pleistocene and Holocene alluvial fans, terraces, and channel deposits.

MINERALIZATION/ALTERATION

Mineralization and hydrothermal alteration of rock at Bonanza is considered a Creede type epithermal vein deposit (figure 1). The Bonanza District has quartz-adularia alkali-chlorite polymetallic vein deposits with silver-lead-zinc-copper ore (Burbank, 1932; Mosier and others, 1986). The ore occurs in sub-vertical quartz-pyrite-base metal sulfide veins hosted in felsic to intermediate volcanics (rhyolite-latite-andesite). The veins are structurally controlled within the caldera's concentric and radial faults which localize the ore shoots and grade of altered minerals.

Deposits within the district have their mineralogy vertically and laterally zoned (from top to bottom or center outward). Deposit tops contain a massive silicification and acid-sulfate cap (kaolinite and/or alunite), followed by quartz+/-kaolinite+montmorillonite+/-zeolites+/-barite+/-calcite, at mid-level with quartz+sericite+pyrite (QSP), and at depth with quartz+chlorite+adularia (potassic alteration). A distal propylitic assemblage of chlorite+epidote+calcite+pyrite is pervasive throughout the district.

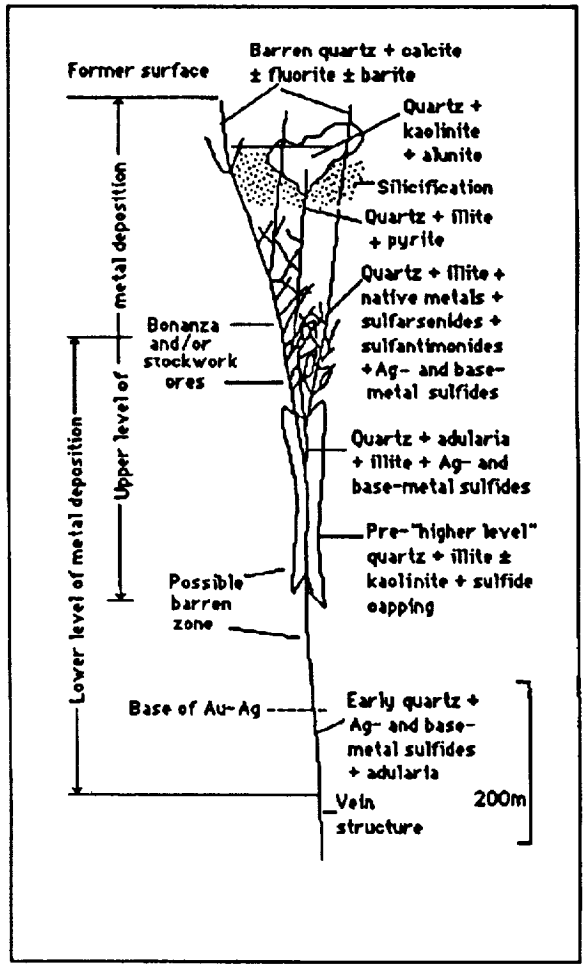

Figure 1. Schematic cross section of mineral deposit model 25b (Mosier and others, 1986).

RESULTS

TMS Image of Inferred Iron Oxides and Clay

An iron oxide and clay image was formed through the selection of a specific Digital Number (DN) interval for iron oxide (band ratio 9/10 gray-scale image) and a DN interval for clay (band ratio 5/2 gray-scale image) after visually analyzing color hue ranges from a color-ratio-composite (CRC) image. The band ratios for the CRC were bands 9/10, 5/2, and 5/7, which are equivalent to the Landsat TM ratios 5/7, 3/1, and 3/4. A CRC hue range was visually selected which represents the dominate color range for iron oxide and for clay (Knepper and Simpson, 1992), then the gray-scale image DN intervals were measured for the same spatial regions. The iron oxide and clay theme image was also masked for vegetation generated from an vegetative index theme image. Clays, micas, carbonates, and sulfates form one group of altered minerals while iron oxides and hydroxides form the other.

DEM Image of Ground Slope

The DEM data were used to generate a ground slope image. Relative steepness was assessed and a minimum steepness threshold DN measured. Slope steepness, combined with bare areas rich in clay were used to characterize areas susceptible to ground failure and potential release of heavy metals.

Radiometric Image

A radiometric image of uranium and thorium was formed similarly to the TMS image. A color-composite image of uranium, thorium, and potassium was generated to visually aid in selecting regions anomalously radioactive, with DN intervals measured from the uranium and potassium gray-scale images. Thorium within the Bonanza District is highly correlated with uranium and was not utilized further. Uranium was found to be associated with thick regions of the Bonanza Tuff while potassium is associated with the younger latite volcanic flows. Sedimentary rocks are low in radioactive potassium. A zonation was also found between uranium and potassium where potassium anomalies trend further from the caldera than the uranium anomalies.

AVIRIS Mineral Suite Images

Mineral maps were formed which identify iron bearing minerals and clay, mica, and carbonate minerals. The data were corrected for atmospheric path radiance using the program ATmosphere REMoval (ATREM) version 1.1 from the Center for the Study of Earth From Space (CSES), University of Colorado (Gao and others, 1992), then further calibrated to relative ground reflectance using field spectra acquired from a ground calibration site with an ASD field spectrometer. Several dozen identified mineral images were generated from these data using the U.S.G.S. goodness-of-fit program (Clark and others, 1990; Swayze, 1997), which correlates the fit of diagnostic absorption bands of pixel spectra (continuum removed) to mineral spectra from the U.S.G.S. library database (Clark and others, 1993). Mineral maps were assembled from selected mineral images which had visible mineral anomalies, pixels with high goodness-of-fit numbers, and moderate to strong absorption band depths. Pixels which did not meet these criteria were not mapped. Vegetation obscured a significant portion of the area, which also was not mineralogically mapped. Mineral identification was confirmed by visual examination of mapped

pixel spectra within the AVIRIS image cube, by field examination of hand specimens, and for a few mineral anomalies, by measurement with an ASD field spectrometer. Iron-bearing minerals individually identified and mapped using AVIRIS data were goethite, hematite, jarosite, and two varieties of ferrous iron minerals. The mapped Clay- and carbonate minerals were kaolinite, montmorillonite, several spectrally distinct varieties of muscovite/sericite/illite, paragonite, calcite, and dolomite. Maghemite has been spectrally identified, but is most likely the mineral hematite.

Eight types of altered mineral suites and a carbonate suite (table 1) have been characterized using the AVIRIS mineral maps.

Table 1: Altered mineral suites (1-8) and carbonate suite (9)

Suite	Primary minerals	Location
1	montmorillonite-goethite-Fe^{+2} bearing minerals	Superior and Rawley Mills, Kerber Creek tailings ponds south of Bonanza; fluvial sediments downstream from Greenback Gulch, which also contain maghemite and hematite.
2A	sericite-montmorillonite +/- kaolinite-jarosite-goethite +/- hematite	Cocomongo-Bonanza, Minnie Lynch, and Rawley Mines dumps, and Hayden Peak - Elkhorn Peak. The latter area also contains goethite, but lacks jarosite.
2B	montmorillonite-sericite +/- kaolinite-iron oxides	Sheep Mountain (with jarosite-goethite-hematite), Antora Meadows (with maghemite and/or hematite), and Flagstaff Mountain (Fe^{+2}-goethite surrounded by maghemite).
3	sericite-kaolinite-hematite-goethite	Greenback Gulch - Express Gulch
4	sericite-Fe^{+2} bearing minerals	On ridge southwest from Hayden Peak
5	maghemite ?	Kerber Creek - Little Kerber Creek intersection and Eagle Gulch-Chloride Gulch
6	sericite-hematite	Kerber Creek - southern part of district
7	kaolinite-Fe^{+2} bearing minerals	Kerber Creek - southeastern part of district
8	kaolinite-Fe^{+2} bearing minerals with lesser goethite-jarosite	Section 11, southwest of Porphyry Peak
9	dolomite and calcite (lithologic, no mineral alteration).	Kerber Creek - southern and southeastern part of district

CONCLUSIONS

Areas within the Kerber Creek drainage that can have significant impact on environmental factors locally or more distant include mined and mineralized but unmined ground, flood plains, creek bottoms, and regions with natural alkali conditions. The impact of areas may be detrimental, or in the case of country rock that can neutralize acid waters, beneficial.

Mine dumps and mill tailings occur throughout the district, but are concentrated near the town of Bonanza. Several mills dumped tailings into ponds along Kerber Creek, which have since been breached, spreading clay, powdered rock, and heavy metals throughout the flood plain. Clay and silt erosion 'trains' are seen in the AVIRIS mineral maps of Kerber Creek.

Heavy metals (Pb-Zn-Cu), acid waters, and iron are derived from oxidation of sulfide rich rock that occur as mined material discarded on surface, mineralized rock exposed within mined workings, or mineralized rock exposed through erosion. This material is introduced into Kerber Creek where natural buffering capacity of the country rock (limestone and propylized volcanic rock) begin to neutralize the acidity of the transported material, and thus precipitate the iron and heavy metals. The clays, which carry these precipitates, are deposited along the stream banks and flood plains. Moran and Wentz (1974) have found that the combination of high iron content, low pH, and toxicity effect of high metal concentrations (Pb, Zn, Cu) eliminate all occurrences of aquatic macroinvertebrates and fish. Dissolved metals within the water exceed drinking water quality standards for 20 miles downstream.

Radioactive uranium and potassium occur throughout the district, but are most commonly associated with the caldera rim. Uranium also occurs within thicker parts of the Bonanza Tuff and at a local volcanic complex (Greenback Gulch).

Regions with potential impact on environmental factors are mineralized areas which are susceptible to slope failure. These are areas of steep, bare, mineralogically altered (clay rich) ground which may contain Pb-Zn-Cu and possibly uranium mineralization. A location map of these areas (figure 2) was generated using the DEM slope map, the TMS vegetation mask, the AVIRIS mineral maps, and the Uranium theme image.

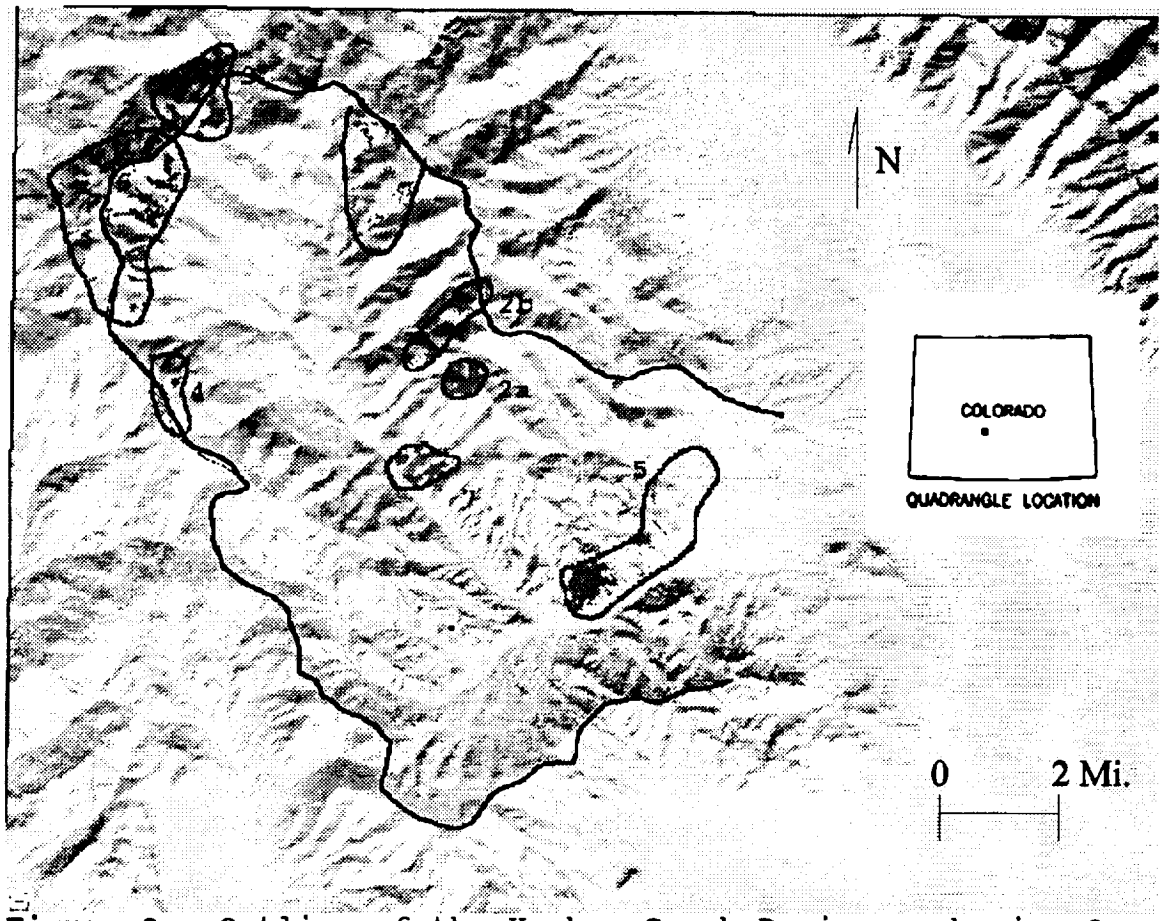

Figure 2. Outline of the Kerber Creek Drainage showing 8 regions of detected altered ground. Dark gray zones within the mineralized areas are classified as steep, bare, clay-rich areas that may be susceptible to slope failure.

REFERENCES

Burbank, W.S., 1932, Geology and ore deposits of the Bonanza mining district, Colorado: U.S. Geological Survey Professional Paper 169, 166 p.

Clark, R.N., Gallagher, A.J., and Swayze, G.A., 1990, Material absorption band depth mapping of imaging spectrometer data using a complete band shape least-squares fit with library reference spectrum, *in* Proc. Second Airborne Visible/Infrared Imaging Spectrometer (AVIRIS) Workshop, Jet Propulsion Laboratory, Pasadena, CA, Pub. 90-54, p. 176-186.

Clark, R.N., Swayze, G.A., Gallagher, A.J., King, T.V.V.,and Calvin, W.M., 1993, The U.S. Geological Survey, Digital Spectral Library: Version 1: 0.2 to 3.0μm: U.S. Geological Survey Open File Report 93-592.

Gao, B.C., K.B. Heidebrecht, A.F.H. Goetz, 1992, Atmospheric REMoval Program (ATREM) User's Guide, version 1.1, Center for the Study of Earth from Space, University of Colorado, Boulder, CO, 24p.

Knepper, D.H., Jr., 1974, Tectonic analysis of the Rio Grande rift zone, central Colorado: Colorado School of Mines Ph.D. Thesis T-1593, 237 p.

Knepper, D.H., and Marrs, R.W., 1971, Geological development of the Bonanza-San Luis Valley-Sangre de Cristo Range area, south-central Colorado, *in* New Mexico Geological Society Guidebook 22d Field Conference, San Luis Basin, Colorado, 1971: New Mexico Geological Society, p. 249-264.

Knepper, D.H., and Simpson, S.L., 1992, Remote sensing, in Geology and mineral resources of the Altiplano and Cordillera Occidental, Bolivia: U.S. Geol. Survey Bull. 1975 p. 47-55.

Marrs, R.W., 1973, Application of remote-sensing techniques for the geology of the Bonanza volcanic center: Colorado School of Mines Ph.D. Thesis T-1531, 279 p.

Moran, R.E,.and Wentz, D.A., 1974, Effects of metal-mine drainage on water quality in selected areas of Colorado, 1972-1973: Colorado Water Resources Circular No. 25, 107p.

Mosier, D.L., Sato, Takeo, Page, N.J., Singer, D.A., and Berger, B.R., 1986, Descriptive model of Creede epithermal veins, *in* Cox, D.P. and Singer, D.A., eds., Mineral deposit models: U. S. Geological Survey Bulletin 1693, p. 145-149.

Swayze, G.A., 1997, The hydrothermal and structural history of the Cuprite Mining District, southwestern Nevada: an integrated geological and geophysical approach: University of Colorado Ph.D. Thesis, 399 p.

MINERAL MAPPING USING AVIRIS DATA AT RAY MINE, AZ

Ian McCubbin[1, 2], Harold Lang[2], Robert Green[1, 2] and Dar Roberts[1, 2]

[1] University of California, Santa Barbara
Geography Department
Santa Barbara, CA 93106

[2] Jet Propulsion Laboratory, California Institute of Technology
4800 Oak Grove Drive
Pasadena, CA 91109

1. Introduction

Imaging Spectroscopy enables the identification and mapping of surface mineralogy over large areas. This study focused on assessing the utility of Airborne Visible/Infrared Imaging Spectrometer (AVIRIS) data for environmental impact analysis over the Environmental Protection Agency's (EPA) high priority Superfund site Ray Mine, AZ. Using the Spectral Angle Mapper (SAM) algorithm to analyze AVIRIS data makes it possible to map surface materials that are indicative of acid generating minerals. The improved performance of the AVIRIS sensor since 1996 provides data with sufficient signal to noise ratio to characterize up to 8 image endmembers. Specifically we employed SAM to map minerals associated with mine generated acid waste, namely jarosite, goethite, and hematite, in the presence of a complex mineralogical background.

2. Background

If left unmonitored waste products from mineral extraction can create long term environmental problems for both government and industry. Currently the EPA's Advance Measurement Initiative (AMI) is using remote sensing instruments such as AVIRIS to collect data that can be used for detection of pollutants associated with mining operations (EPA, 1997). Releases of these pollutants into the environment tend to be associated with natural disasters and/or processes, even though the mine operator has attempted to prevent release under normal conditions. Imaging spectroscopy could provide the mineral extraction industry and the EPA a new synoptic tool for monitoring mining operations. Enhanced monitoring will allow for better understanding of the materials present within an open pit mine. Determining the locations of high-risk materials could contribute to the prevention of future unnecessary accidents. Furthermore, the synoptic view offered by remote sensing can provide the mining industry an improved understanding of the surface geology within a region of interest for exploration or mine development.

This type of AVIRIS-based target endmember determination was demonstrated by Swayze et al. (1996) who documented a method for identifying and characterizing acid generating materials associated with hard rock mining. Pyrite is one of the main source minerals for acid drainage. The weathering of pyrite causes sulfide oxidization. Low pH water, created during the weathering process, reacts with pyrite to release heavy metals, such as Pb, As, Cd, Ag and Zn into the environment. From these weathering processes the secondary mineral jarosite is created. Although it is not possible to identify pyrite with imaging spectroscopy it is possible to map jarosite because of the crystal field absorption due to the presence of Fe^{++} (~900 nm) and SO_4 (~2280 nm) in the jarosite crystal structure (Hunt, 1980). Using hyperspectral data analysis to identify and map the abundance of this mineral, it is possible to identify pyrite oxidation zones. Heavy metals can substitute for Fe in the secondary mineral and can be transported into watersheds downstream from mining operations. Once in the watershed the jarosite mixes with higher pH water and the heavy metals precipitate out.

3. Methods

AVIRIS data was acquired in April 1996 as part of an AMI pilot study of Ray Mine, AZ, a copper producing open pit mine. Approximately 65 kilometers east of Phoenix, AZ, the mine is located within the

Mineral Creek drainage, a tributary of the Gila River. Copper deposits are associated primarily with a Tertiary hydrothermal alteration zone in Precambrian schist (Creasy et al., 1983, Metz et al., 1968, Phillips et al., 1971, Ransome 1919). Except in the area of excavation for mining operations and grading for roads, the Ray Mine region has vegetation cover that approaches 50%. Ray Mine, a high priority site for EPA Region 9, was selected as a demonstration site by AMI to evaluate the use of remote sensing instruments for characterizing and monitoring mine generated waste products. We used a scaled down version of the Analytical Imaging and Geophysics (AIG) standardized methodology of Kruse & Boardman (1997) for processing of AVIRIS data as summarized below.

3.1 Conversion to Apparent Reflectance

Initial radiance data was inverted to apparent reflectance using a set of radiative transfer spectral feature fitting algorithms and in situ field spectra (Green et al. 1996). Use of a radiative transfer model was necessary to correct for atmospheric effects, so the AVIRIS data was comparable to the spectral library reflectance data.

3.2 Spatial Spectral Browsing

Once in apparent reflectance, it was possible to use spatial/spectral browsing of the image to compare and contrast spectral differences within the spatial domain of the image. Of particular interest was the open pit and associated mine tailings at Ray Mine itself, as well as the watersheds of Mineral Creek and the Gila River.

3.3 Spectral Library Rebuilding

Due to differences in spectral resolution between AVIRIS and the USGS spectral library it was necessary to convolve the spectral library from 420 bands to match the coarser resolution of AVIRIS data at 224 bands. Furthermore AVIRIS spectral calibration data is in nanometers whereas the spectral library was in micrometers, so we chose to convert the spectral library to the same units as the AVIRIS data.

3.4 Target Endmember Selection

The library spectra shown in Table 1 were selected as endmembers for mapping using SAM. All reference endmember spectra were from the USGS mineral spectral library that is included with the commercial, off-the-shelf ENVI software package. In addition, a SAM classification was done using only the jarosite endmembers.

Spectral Library File Name	Mineral Identification
Jarosit6.spc	Jarosite JR2501 K
Jarosit8.spc	Jarosite WS368 Pb
Chlorit4.spc	Chlorite SMR-13.c 45-60 μm
Dolomit2.spc	Dolomite COD2005
Hematit1.spc	Hematite 2% + 98% Qtz GDS76
Gypsum2.spc	Gypsum SU2202
Kaolini4.spc	Kaolinite KL502 (pxyl)
Montmor5.spc	Montmorillonite CM27

Table 1. Spectral Library Used For SAM Classification

3.5 SAM Classification

Mapping the spatial abundance of the jarosite endmembers was done using the SAM supervised classification algorithm over the entire 400 - 2400 nm region covered by AVIRIS. However, the 1200 - 1400 nm and 1800 -1900 nm intervals effected by atmospheric water absorption were excluded. SAM is a vector-based approach that identifies pixels that have spectra that best match spectra in the reference endmember spectral library. It compares the "spectral angle" between two spectra and classifies pixels that have the best match. As well as a classified image showing pixels that are the same spectrally, a rule image is created which shows the differences between the reference and image spectra in radians (Kruse and Huntington, 1996). Figures 1& 2 shows the rule image for jarosite 8 endmember compared to a band 150 image that has a band center at 1782 nm. The SAM algorithm only identifies the spectrally pure pixels, and does not address the issue of mixed pixels.

Figure 1: Band 150 (1782 nm) Image of Ray Mine.

Figure 2: Sam Rule Image of Jarosite abundance within the scene. Lighter pixels are areas classified as jarosite.

4. Results

Initial analysis of the AVIRIS data set using the SAM supervised classification has mapped large areas of jarosite within Ray Mine. However, these areas are well within the controlled region of the mining operation and do not appear to be entering into the Gila River watershed. A small region has been mapped outside of Ray Mine (near the bottom right central part of figure 2). This area is a defunct mining operation circa 1919, and is not associated with Ray Mine. The proximity of the abandoned operations and the Gila River Watershed might allow transport of jarosite into the Gila River. Though the SAM algorithm allowed for identification of pixels that were predominately jarosite, the inability to classify mixed pixels is a drawback. Not mapping all pixels that may contain only a fraction of jarosite prevents a complete understanding of the spatial distribution of all possible zones of weathering pyrite. Future analysis of the Ray Mine data set using the Partial Unmixing technique (Boardman et al., 1995) should allow identification of smaller quantities of jarosite within a pixel.

5. Conclusion

The SAM supervised classification results allowed for identification of possible areas of pyrite oxidation within Ray Mine. These preliminary results show that within Ray Mine there are areas of high jarosite concentrations attributed to pyrite alteration. These areas are restricted to the mine confines indicating that acid-generating waste from active operation at Ray Mine is not entering the Gila River via the Mineral Creek drainage. These results show that imaging spectroscopy is a useful tool for the mining

industry and environmental regulators. It provides an efficient method for mapping surface mineralogy at open pit mine sites. Understanding the spatial distribution of materials such as jarosite helps mine operators prevent releases of environmental contaminants. Beyond the scope of environmental impact prevention and/or analysis, industry may see the use of remote sensing instruments, such as AVIRIS, as a cost saving mineralogical mapping tool for exploration and mine development.

6. Acknowledgments

This study presents preliminary results from an initial stage in the EPA's AMI and NASA's Geology and Natural Hazards Research Program analysis of Ray Mine, and we would like to thank the project's Principal Investigator Dr. Tom Mace. A majority of the research described in this paper was performed at the Jet Propulsion Laboratory, California Institute of Technology, under a contract with the National Aeronautics and Space Administration. The balance was performed at The Remote Sensing Research Unit (RSRU), University of California, Santa Barbara. We would like to thank Dr. Jack Estes and his RSRU Group at UCSB for the use of their facilities. Thanks to Boardman and Kruse of Analytical Imaging and Geophysics for their valuable discussions, and Research Systems Incorporated for the use of the ENVI software package. Thanks to Dr. Roger Clark at USGS Spectroscopy Lab for his guidance. Furthermore, a huge thanks to Dr. Leal Mertes of the UCSB Geography Department.

7. References

Boardman, J.W., F.A. Kruse, and R.O. Green, 1995, Mapping Target Signatures Via Partial Unmixing of AVIRIS Data, *Summaries of the Fifth Annual JPL Airborne Earth Science Workshop,* JPL Publication 95-1, Vol. 1, AVIRIS Workshop. Jet Propulsion Laboratory, Pasadena, CA, pp. 23-26.

Creasy, S.C., D.W. Peterson, and N.A. Gambell, 1983, Geologic Map of the Teapot Mountain Quadrangle, Pinal County, Arizona: USGS 1:24,000 Scale Geologic Quadrangle Map.

Environmental Protection Agency, 1997, Advanced Measurement Initiative: Discrimination and Screening of Problem Mine and Extractive Industry Waste, *Environmental Protection Agency AMI Home Page,* http://www.epa.gov/ami/raymine.html.

Green, R.O, D.A. Roberts, and J.E. Conel, 1996, Characterization and Compensation of the Atmosphere for the Inversion of AVIRIS Calibrated Radiance to Apparent Surface Reflectance, *Summaries of the Sixth Annual JPL Airborne Earth Science Workshop,* JPL Publication 96-4, Vol. 1, AVIRIS Workshop. Jet Propulsion Laboratory, Pasadena, CA, pp. 135-146.

Hunt, G.R., 1980, Electromagnetic Radiation: The Communication Link in Remote Sensing, *in Siegal, B.S. and Gillespie, A.R., eds, Remote Sensing in Geology,* New York, John Wiley, pp. 5-45.

Kruse, F.A., and J.W. Boardman, 1997, Hyperspectral Data Analysis and Image Processing Workshop Handbook, Analytical Imaging and Geophysics, LLC, pp. 305-380.

Kruse, F.A., and J.F. Huntington, 1996, The 1995 AVIRIS Geology Group Shoot, *Summaries of the Sixth Annual JPL Airborne Earth Science Workshop,* JPL Publication 96-4, Vol. 1, AVIRIS Workshop. Jet Propulsion Laboratory, Pasadena, CA, pp.155-164.

Metz, R.A., C.H. Phillips, and C.R. Caviness, 1968, Recent Developments in the Geology of the Ray Area: *Southern Arizona Guidebook III,* Arizona Geological Society, pp. 173-146

Phillips, C.H., Cornwall, H.R., and M. Robin, 1971, A Holocene Ore Body of Copper Oxides and Carbonates at Ray, Arizona: *Economic Geology,* V.66, pp. 495-498.

Ransome, F.L., 1919, The Copper Deposits of Ray and Miami, Arizona: U.S.G.S. Professional Paper 115, 192 p.

Swayze, G.A., R.N. Clark, R.M. Pearson, and K.E. Livo, 1996, Mapping Acid-Generating Minerals at the California Gulch Superfund Site in Leadville, CO using Imaging Spectroscopy, *Summaries of the Sixth Annual JPL Airborne Earth Science Workshop,* JPL Publication 96-4, Vol. 1, AVIRIS Workshop. Jet Propulsion Laboratory, Pasadena, CA, pp. 231-234, http://speclab.cr.usgs.gov.

Analysis of volcanic fields near Popocatepetl, Mexico, from AVIRIS data

Erzse'bet Mere'nyi, U of Arizona, Lunar and Planetary Lab, and
Brian S. Penn, Pan-American Center for Earth and Environmental Studies, U of Texas at El Paso

We investigate the compositional distribution of tephras over a volcanic field approximately 50 km south of Popocate'petl. The surface mineralogy is expected to reveal some of the eruptive history of the field. AVIRIS was flown over this area on November 23, 1994. The resulting 224-band image has been provided for us by Dr. Harold Lang of JPL.

Popocate'petl (5452 m) is a stratovolcano located 60 km SE of Mexico City in the eastern portion of the WNW trending 1,000 km long Trans-Mexican Volcanic Belt (TMVB). The presence of three successive debris-avalanche deposits fanning southward documents the previous existence of other large volcanic edifices destroyed by gravitational collapse. The present cone consists of inter-layered lavas and pyroclastic deposits of intermediate to silicic composition. Such volcanoes usally result in violent phreato-magmatic eruptions (e.g., Mt. Saint Helens), due to the viscous nature of the magmas, which also tends to restrict lava flows to within a few kilometers of the vent. Ash-flow and/or air-fall deposits, on the other hand, can spread very far. Small cinder cones of more basic composition were also found east and west of Popocate'petl. During the last 20,000 years, at least seven Plinian eruptions occured near Popocatepetl, producing pumice-fall and ash-flow deposits as far away as Mexico City (Siebe et al. 1995). The volcanic field in our AVIRIS image has presumably preserved a lot of the dynamic geologic history related to Popocatepetl and other volcanoes active in the past in the TMVB.

VIS-NIR reflectance spectrometry is very sensitive to different extents of alteration in basaltic tephras (Farrand, 1991). AVIRIS images can potentially differentiate between many stages of alteration between highly palagonitized tephras and unaltered ones because of the high spectral resolution. This is partly due to the fact that many volcanic products (e.g., basaltic tuffs) have not one characteristic mineral with an associated absorption feature that can be used to map their distribution. The overall shapes of the reflectance spectra have proven more diagnostic, which hyperspectral images provide in great detail. Using the power of AVIRIS-class imagery it is possible, for example, to look for multiple hydroclastic and/or dry vents and try to reconstruct the eruptive/hydrologic history of the volcanic field. Relatively few works have dealt so far with the detection of either active or inactive volcanic features from AVIRIS data. Hot spots and gas emanations were investigated by, e.g., Oppenheimer et al. (1993), DeJong et al. (1996). Thorough analysis of compositional distribution of tephras has been done for the Lunar Crater Volcanic Field in a number of works by Farrand and co-workers (Farrand 1991, Farrand and Harsa'nyi 1994, 1995) and Mere'nyi et al. (1996a,b). We will present a detailed spectral classification of the volcanic field near Popocatepetl and attempt mineralogic interpretation based on eariler works and laboratory spectra. In a subsequent phase, field work is also planned, which will help interpretation. It will also further refine our knowledge of reflectance spectra of pyroclastic and hydroclastic volcanic products and their recognition from AVIRIS images.

The relevance of this investigation is emphasized by its spatial and genetic relationships to Popocate'petl, which has been showing activities in the past two years. The fact that the largest eruption in 50 years occurred on July 1, 1997 makes this work extremely timely.

References

Farrand, W.H. 1991. VIS/NIR Reflectance Spectroscopy of Tuff Rings and Tuff Cones, Ph.D. Thesis, University of Arizona

Farrand, W.H. and Harsanyi, J.C. 1994. Mapping distributed geological and botanical targets through constrained energy minimization. Proc. Tenth Thematic Conference on Geologic Remote Sensing, San Antonio, TX, 9--12 May 1994. I. pp 419-429

Farrand, W.H. and Harsanyi, J.C. 1995. Discrimination of poorly exposed lithologies in imaging spectrometer data. JGR, 100, pp 1565-1578

De Jong, S. M., and Chrien, T. G. 1996. Mapping Volcanic Gas
Emissions in the Mammoth Mountain Area Using AVIRIS. Summaries of the Sixth Annual JPL Airborne Earth Science Workshop, Pasadena, CA, March 4-8, 1996, Vol. 1: AVIRIS Workshop, Ed. R.O. Green

Merenyi, E., Taranik, J.V., Minor, T.B., and Farrand, W.H. 1996. Quantitative Comparison of Neural Network and Conventional Classifiers For Hyperspectral Imagery. a) Summaries of the Sixth Annual JPL Airborne Earth Science Workshop, Pasadena, CA, March 4-8, 1996, Vol. 1: AVIRIS Workshop, Ed. R.O. Green b) submitted to Remote Sens. Environ.

Oppenheimer, C.D. et al. 1993. Analysis of Airborne Visible/Infrared Imaging Spectrometer (AVIRIS) data of volcanic hot spots. International Journal of Remote Sensing, 14, 2919-2934

Siebe, C., Macias, J. L., Abrams, M., Rodriguez, S., Castro, R., and Delgado, H. 1995. Quanternary Explosive Volcanism and Pyroclastic Deposits in East Central Mexico: Implications for Future Hazards. In Geological Society of American Annual Meeting 1995, New Orleans, Louisiana, Field Trip Guide Book #1, pp 1-47.

MONITORING COMMUNITY HYSTERESIS USING SPECTRAL SHIFT ANALYSIS AND THE RED-EDGE VEGETATION STRESS INDEX

Ray Merton
Department of Geography
University of Auckland
Private Bag, Auckland
New Zealand
email: r.merton@auckland.ac.nz

1. INTRODUCTION

The red-edge, centered at the largest change in reflectance per wavelength change, is located between two of the most widely used wavelength regions used for broad band vegetation studies, the red trough and the NIR plateau. The vegetation red-edge in Airborne Visible/Infrared Imaging Spectrometer (AVIRIS) data comprises eight contiguous spectral bands between 0.6852 - 0.7523μm.

The aim of this study focuses on the development of simple techniques to identify and model multi-temporal red-edge geometry changes in disparate vegetation communities at Jasper Ridge Biological Preserve, Palo Alto, California. This study examines the design and performance of selected measures for monitoring community stress from early spring to late autumn. Defining complex red-edge symmetry through a range of geometric and statistical measures has potential for seasonal and long-term vegetation monitoring.

Second-derivative calculations are applied to the measurement of red-edge inflection point shifts. Derivative spectra are also used to identify variations in red-edge geometry associated with apparent stress in communities and changing environmental variables and to determine bands for inclusion in the Red-edge Vegetation Stress Index (RVSI). Patterns of community hysteresis based on multi-temporal changes in spectral shifts, the RVSI, and other important vegetation indices are examined.

1.1 Vegetation Communities

Seven communities are selected to identify an environmental gradient that spans the mesic to near-xeric environments found in the Jasper Ridge Biological Preserve. By including a selection of disparate communities along this gradient, it is possible to more fully interpret spectral and multi-temporal trends. As ongoing research focuses on biogeochemical stress analysis, many communities located on Jasper Ridge retain the nomenclature representative of the underlying geology/soil (Merton, 1994).

The following is a brief description of communities. *Serpentine community*: restricted to the main serpentine deposit as a narrow-endemic tolerant of high geochemical toxicity and near-xeric conditions. Representative species include *Stipa pulchra* and *Eschscholzia californica*. *Sandstone community*: predominantly annual grassland species located on a sandstone substrate. Representative species include a range of annual grasses especially *Bromus rigidus*. *Halo community*: located in the moderate toxicity zone (geochemical halo) is influenced by mobile serpentine geochemicals. This distinctive community is regarded as an intermediate between the serpentine and sandstone communities. *Chaparral community*: a fire-climax community situated on dry southwest facing slopes containing chamise chaparral, *Prunus* chaparral, and *Baccharis* shrub. *Woodlands community*: an open canopy community situated predominantly on northwest slopes containing a range of oaks, buckeyes, and laurels. *Delta community*: a willow (*Salix lasiolepsis*) dominated community located in the swampy deltaic areas at the southern margin of Searsville Lake. *Redwood community*: dense stands of *Sequoia sempervirens* are located adjacent to San Francisquito Creek to the north of Jasper Ridge.

1.2 AVIRIS Datasets

Five AVIRIS datasets are selected to construct a near-consecutive multi-temporal database. Chronological five-date imagery is not available in any one year. Therefore, two spring datasets from 5 April 1996 and 30 April 1994 are combined with the consecutive 1992 datasets of 2 June, 1 September, and 6 October. Non-sequential datasets are substituted into the beginning of the series as spring is not normally associated with vegetation stress. This disparity between datasets, although not ideal, provides valuable indicator information of early season stress responses. Additionally, environmental variables such as precipitation and temperature did not vary significantly between dataset years. However, to reduce annual difference between datasets, environmental variables were recalculated as merged datasets combining data from intervals prior to image acquisition dates. The period between 2 June and 1 September is the largest with a 91 day interval. Ideally, another dataset in this period would provide additional information on summer trends.

2. METHODS

Eight band high spectral resolution (8.4nm FWHM) data encompassing the red-edge can be used to describe community phenological response through time as a function of changes to red-edge symmetry. Analyses such as Guyot (1992), focusing on the measurement of reflectance change, have endeavored to define the red-edge as a single quantifiable variable. My aim is to identify an appropriate single red-edge descriptor for vegetation stress analysis, defined not only by statistic techniques but by the identification and measurement of common red-edge geometric points.

2.1 Calculating Red-Edge Inflection From Second-Derivative Spectra

The red-edge is a relatively featureless waveform and does not display abrupt peaks or troughs between adjacent bands on which geometric analyses can be readily based. This section describes techniques for the calculation of red-edge inflection (re_i) based on spectral symmetry. The calculation of the red-edge inflection wavelength (λ_i) provides a standard reference for monitoring spectral shifts between communities through time.

Second-derivative data are used to identify red-edge inflection wavelengths for Jasper Ridge communities. Second-derivative curves amplify changes in spectral reflectance slope between consecutive red-edge bands. As most vegetation exhibits increasing reflectance values between the red trough and the NIR plateau, the first- (ρ') and second-derivative (ρ'') transformations emphasize subtle absorption/reflection features as deviations along the otherwise near-linear central red-edge. Deriving red-edge spectra as single values reduce spectral data and generate a time-series. Identifying red-edge spectral shifts through derivative analysis permits the comparison of seasonal intra- and inter-community change.

Second-derivative calculations define λ_i as the wavelength where ρ'' values cross zero. The identification of λ_i enables the tracking of wavelength displacements through time as spectral shifts. Red-shifts denote changes to longer wavelengths and blue-shifts to shorter wavelengths. Spectral shifts of λ_i can be correlated to changes in leaf chlorophyll concentrations, leaf area index, leaf inclination angle, moisture deficit stress, heat stress, and changes in other environmental factors (Guyot *et al.*, 1992; Merton *et al.*, 1997).

2.2 Red-edge Vegetation Stress Index

The application of second-derivative spectral analysis in this study permitted the identification of anomalous community red-edge reflectance spectra not conforming to established descriptions of an asymptote shape. Red-edge reflectance spectra for vegetation generally exhibit concave lower red-edge curves and convex upper red-edge curves. However, calculations and plots of first- and second-derivative data show spectral anomalies in upper red-edge curve shape. A critical "break-point" was identified occurring mid-way (~0.716μm) along the red-edge. Below this mid-point, red-edge curves displayed predominantly concave shapes with lower geometric

variability. At longer wavelengths beyond the break-point, curves either: *1.* displayed increasing reflectance (nominal "asymptote curve"), *2.* continued as near-linear curves (anomalous "near-linear curve"), or *3.* exhibited decreasing reflectance followed by a marked increase (strongly anomalous "cuspoid curve"). Additionally, the degree of concavity for each community appeared to vary over time in response to changes in environmental stress. Comparisons with radiance data confirmed that these features were not an artifact of user error or reflectance calibration. Further analysis showed that anomalous spectra were not restricted to one or two datasets, nor to a distinct "data year".

The Red-edge Vegetation Stress Index (RVSI) was developed in this study to identify inter- and intra-community trends based on spectral changes in upper red-edge geometry. The RVSI derives measures of spectral concavity as a displacement in reflectance between a "modeled" linear mid-point (defined as the mean reflectance of two bisecting points; the red-edge break-point (~0.716μm) and the start of the NIR plateau) and the "data" mid-point value. The difference between the two modeled and data mid-point values can then be expressed as positive or negative values. The RVSI is defined as:

$$RVSI = \left(\frac{\rho_{714} + \rho_{752}}{2} \right) - \rho_{733}$$

Equation 1 Red-Edge Vegetation Stress Index

where: ρ = reflectance at wavelength centers (nm)

Concave curves produce positive displacements from the data mid-point to the modeled mid-point value position (Figure 1). As this index is designed to measure stress, positive index values indicate increased degrees of relative stress. Conversely, negative index values are calculated for convex upper red-edge curves. A zero value marks a probable transition between stressed and non-stressed values. Figure 1 illustrates examples of convex and concave upper red-edge spectra.

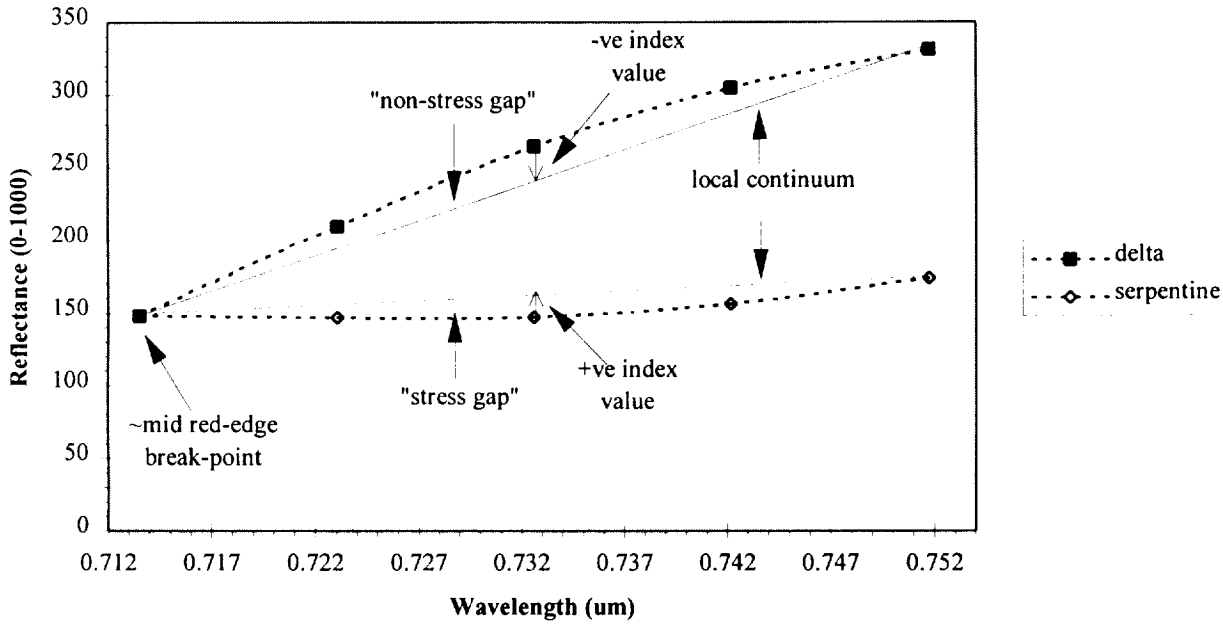

Figure 1 Upper Red-Edge Spectra For The "Low Stress" Delta Community (30 April) And "High Stress" Serpentine Community (1 September). *Note:* examples are selected to illustrate convex (non-stress) and concave (stress) curve shapes.

In Figure 1, the stress/non-stress "gaps" indicate the area under or over the max. - min. bisect line. An "area under the curve" integration could also be applied as an alternate measure of stress. However, the RVSI is designed to be sensitive to data variations by calculating reflectance shifts near the point of maximum displacement. Secondly, the RVSI does not directly incorporate measurements from the two data tails, which more closely fit the modeled linear min-max relationship. Thirdly, this research aims to produce a simple index that can be readily interpreted. Particular emphasis is given in this paper to the interpretation of RVSI multi-temporal trends.

2.3 Red-Edge Hysteresis

This component of the research attempts to plot data values as multi-temporal hysteresis trends to gain an understanding of the seasonal dynamics of calculated red-edge parameters as discrete intra- and inter-community patterns. By plotting two variables against each other, subtle seasonal hysteresis relationships can be readily interpreted.

Hysteresis is a form of analysis commonly used in geology to model multi-event data. Hysteresis is a term 'borrowed from the study of magnetism and used to describe a bivariate plot, which evidences a looped form' (Goudie, 1994, p269). In a simple elastic hysteresis event, forces act on an body causing data values to displace along a trajectory. The subsequent removal of forces may produce a return to the original values along the reciprocal or an alternate cyclic trajectory path. The direction of cyclic hysteresis is commonly described as either clockwise or anti-clockwise.

Plotting patterns of hysteresis between data points is achieved through the application of 'exponential smoothing'(Microsoft, 1997) to extrapolate data as spline lines. This technique predicts a value based on the forecast for the prior period, adjusted for the error in the prior forecast. Exponential smoothing uses a smoothing constant, the magnitude of which determines how strongly forecasts respond to errors in the prior forecast. Spline lines are used as "indicators only" and assist in interpretation as extrapolated trends between calculated values.

2.4 Vegetation Indices

A selection of five indices developed for vegetation studies are correlated with RVSI values. The indices are used in this study to identify possible associations with key biochemical and biophysical canopy parameters. The following is a brief description of indices selected.

•*Percent Lignin* (Aber and Martin, 1995): an index used to derive a canopy lignin concentration. Canopy lignin is particularly important ecological indicator as a very strong relationship exists between canopy lignin concentration and annual net nitrogen mineralisation, or nitrogen cycling.

•*Moisture Stress Index* (MSI) (Miller, Elvidge, Rock, and Freemantle, 1990): is used here to quantify the relative amount of canopy moisture in each vegetation community. The sensitivity of the MSI is related to total canopy water content. Moisture stressed canopies have a higher ratio value compared to non-stressed canopy sites.

•*Normalized Difference Vegetation Index* (NDVI): a widely used broad-band canopy greenness indicator. The NDVI is substituted with single AVIRIS wavelengths (667nm and 831nm) to form a narrow-band equivalent.

•*Percent Nitrogen* (Aber and Martin, 1995): an index to estimate canopy nitrogen concentrations from AVIRIS spectra at 764nm and 1640nm. Chlorophyll content in foliage is highly correlated with total protein, and therefore total nitrogen content. 1640nm is a first overtone of a C-H absorption band.

•*Photochemical Reflectance Index* (PRI) (Gamon, Roberts, and Green, 1995): is derived from reflectance at 531nm and 570nm from AVIRIS datasets. PRI varies with photosynthetic capacity, radiation-use efficiency, and vegetation type. Vegetation types exhibiting chronically reduced photosynthesis during periods of stress invest proportionally more in photoprotective processes than vegetation with high photosynthetic capacity.

3. RESULTS

3.1 Red-Edge Inflection From Second-Derivative Spectra

Red-edge inflection wavelength values (λ_i) calculated by the second-derivative technique for seven Jasper Ridge communities are plotted in Figure 2.

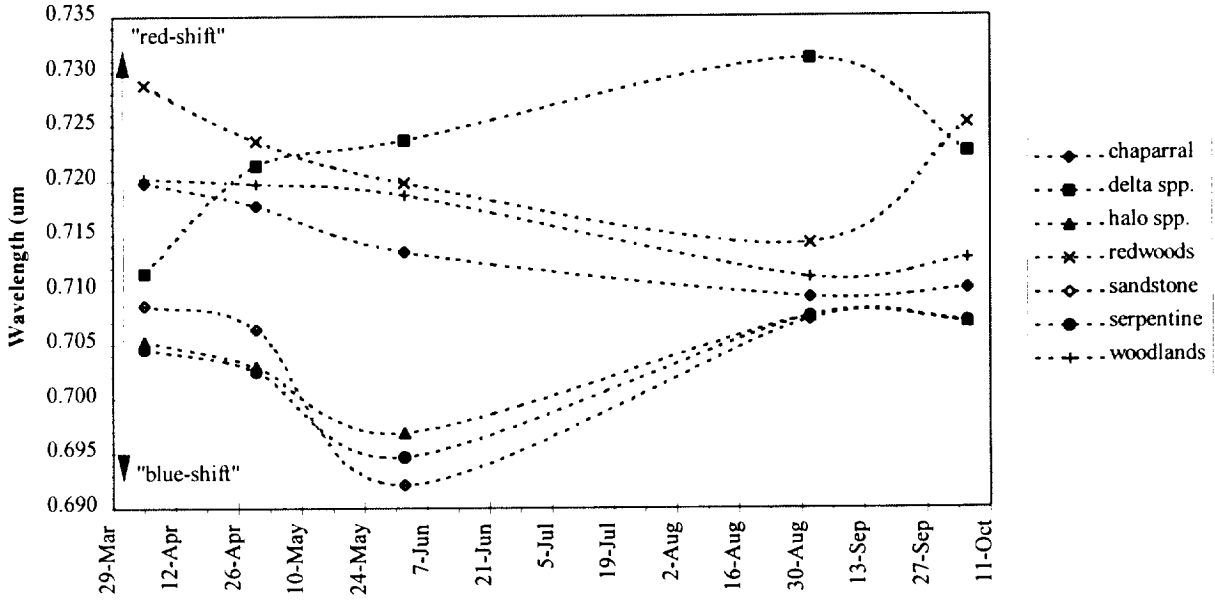

Figure 2 Mean Community Red-Edge Inflection Wavelength Values (λ_i) Plotted As Time-Series Data. *Note:* Spline lines between data values are exponentially smoothed to indicate data trends only.

From multi-temporal λ_i values displayed in Figure 2, three distinct community "clusters" can be identified. The first community cluster consists of redwoods, woodlands, and chaparral communities. Figure 2 displays these communities with steadily decreasing λ_i values from early spring to early autumn. Early autumn to late autumn is characterized by a red-shift, particularly evident in the redwood community. For these communities, a blue-shift can therefore be associated with increasing environmental stress. Additionally, late season red-shifts indicate a reduction in environmental stress associated with decreased heat and moisture deficit stress.

The second cluster contains the delta community. This community is characterized by consistently increasing λ_i values from early spring to early autumn, interpreted as a response to increasing leaf chlorophyll and increasing LAI, a result of a seasonally high water table. The abrupt blue-shift in late autumn is likely to be a direct stress response to lowering of the water table and to the reduction in both LAI and leaf chlorophyll associated with the onset of senescence. Interestingly, the trends between the first and second clusters are reversed, indicating a strong difference between these two community clusters and their environments.

The third cluster is represented by the sandstone, halo and serpentine communities. Figure 2 displays λ_i value trends for these communities as gradually decreasing to shorter wavelengths between early and late spring. The subsequent period to summer exhibits an abrupt increased blue-shift associated with maximum environmental stress. This stress maxima occurs earlier than first cluster communities resulting from the onset of mid summer senescence and advanced seed set. Autumn λ_i values approximate those experienced during spring, indicating a return to lower stress conditions and the emergence of new growth.

3.2 Red-Edge Vegetation Stress Index

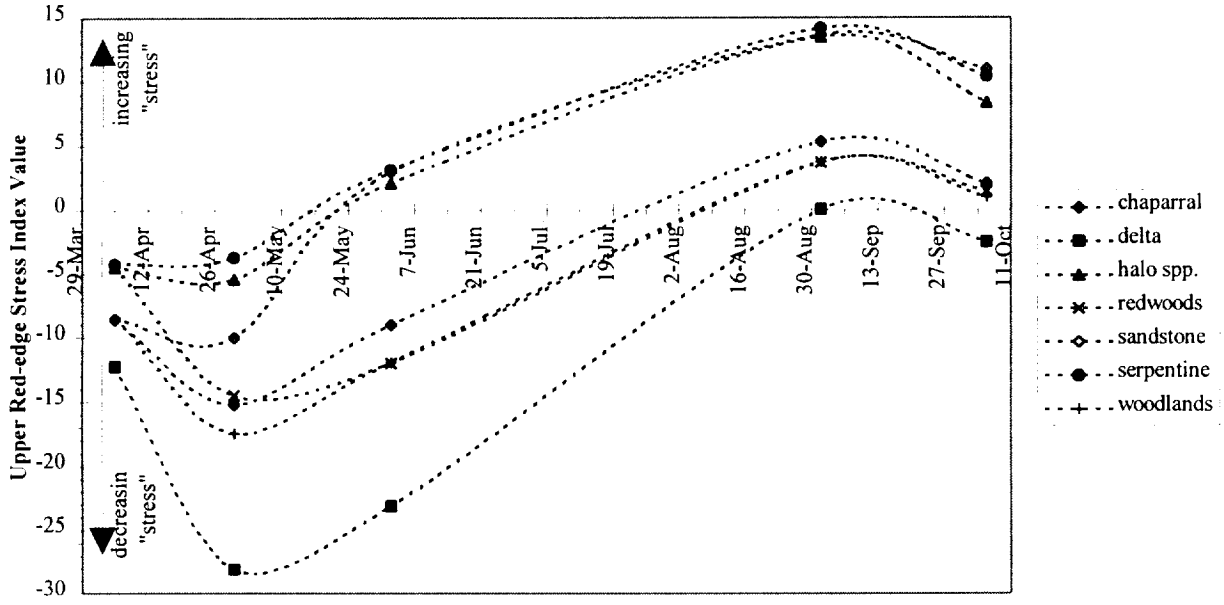

Figure 3 Mean Community RVSI Values Plotted As Time-Series Data. *Note:* Low stress = negative values, high stress = positive values. Spline lines between data values are exponentially smoothed to indicate data trends.

RVSI values for each community are plotted in Figure 3 to provide a graphical representation of data trends. Selected interpretations from Figure 3 are summarized as follows. All community data values on 5 April and 30 April have low stress (-ve RVSI) values. In contrast, 1 September values indicate high stress (+ve RVSI) values. Intermediate dates provide good comparative indicators for the timing and magnitude of community-specific stress. The time-series plot (Figure 3) shows decreasing RVSI values for all communities during the 5 April to 30 April period related to an early spring vigorous growth phase. Environmental conditions produce near-optimal growth conditions around 30 April resulting in lowest stress values for most communities. Data values and spline lines indicate that the peak of this optimal phase is likely to be centered in early to mid May. Community spectra shift from negative to positive RVSI values by 1 September in response to seasonal environmental stress. Positive RVSI values indicate an early onset of environmental stress for serpentine, halo, and sandstone communities occurring from mid-May.

With the onset of hot/dry summer conditions, environmental stress on plants increase. The period between 30 April and 2 June shows a general increase in RVSI values for all communities. Major differences in the rate of value change between communities is evident. The abrupt increase in RVSI values for the annual sandstone grassland community can be interpreted as early spring growth to the early onset of late summer senescence. The redwood community by contrast, shows the lowest rate of change between 30 April and 2 June, possibly reduced by the north facing microclimatic conditions.

All communities except the delta community show a similar increase in RVSI values over the period 2 June to 1 September. The delta community displays a relatively steep rate of change between the two dates becoming only marginal stressed (RVSI = 0.05) by 1 September. The period 1 September to 6 October shows decreasing RVSI values for all communities, a response to decreasing environmental stress associated with cooler autumn conditions. Total rainfall during this period is not however significantly higher than summer.

3.2.1 *Correlation Of RVSI Values To Selected Environmental Variables and Vegetation Indices*

Figure 4 illustrated the relationship between multi-temporal RVSI values and two important environmental variables, precipitation and temperature. The plot combines two independent sets of correlation results as a graphical summary.

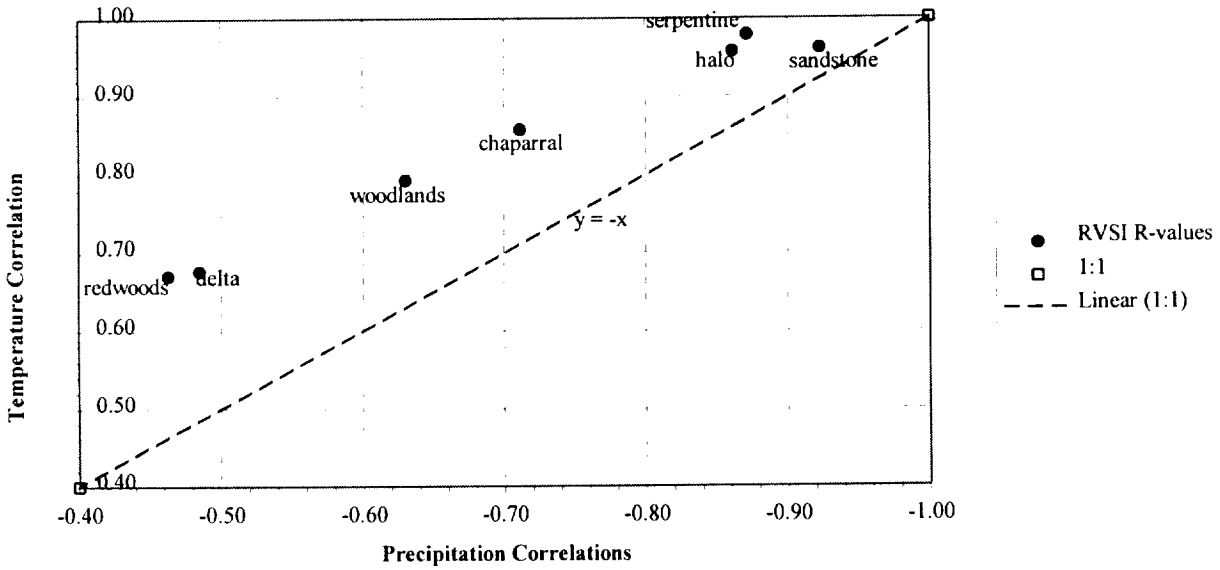

Figure 4 Correlation Of RVSI Values To Precipitation And Temperature. *Note:* This plot indicates the relative importance between two key environmental variables to RVSI multi-temporal correlation trends. Precipitation = daily precip, temperature = daily max. temp. Refer to Table 1 for correlation values.

Communities with high negative correlations between RVSI values and precipitation are associated with patterns of decreasing rainfall and increasing vegetation stress. Similarly, increasing temperatures indicate increasing RVSI values. A near-linear gradient of community correlation trends can be identified. A modeled linear (1:1) regression line is fitted to indicate which of the two variables is more highly correlated to RVSI value trends. Community RVSI values are more highly correlated to patterns of temperature than to precipitation.

Community correlation trends are not parallel to the linear (1:1) regression line but converge towards higher correlations. Sandstone community correlations have similar precipitation values (R = -0.923) and temperature values (R = 0.962), indicating a comparable response to both variables. Conversely, the redwood community has dissimilar precipitation (R = -0.463) and temperature (R = 0.671) correlations, indicating that this community may be more strongly influenced by temperature than precipitation. However, for communities with decreased correlation values such as redwoods and delta, this observation may be less significant.

Correlation analysis is also performed to compare RVSI values with important biochemical and biophysical indices such as percentage nitrogen (Aber *et al.*, 1995), percentage lignin (Aber *et al.*, 1995), Moisture Stress Index (MSI) (Miller, *et al.*, 1990), NDVI, and the Photochemical Reflectance Index (PRI) (Gamon, *et al.*, 1995). Correlations between RVSI and indices for each community are summarized in Table 1.

Results show that individual indices are not consistently highly correlated to RVSI values, indicating that RVSI is not a facsimile of another index. The closest consistent match for all communities exists between RVSI and NDVI, consistent with the decay of the red-edge reflectance. Similar correlation trends between communities may indicate community-specific and community clustered relationships. Community gradients can also be identified based on R value ranking. For example, MSI correlated to RVSI can be ranked to provide a community gradient:

redwoods (-0.623), delta (-0.586), woodlands (0.611), halo (0.815), chaparral (0.890), sandstone (0.891), serpentine (0.913). Community gradients can be used to compare the relative influence of biochemical and biophysical indices for each community.

Table 1 Community Correlation Values Calculated Between RVSI And Selected Environmental Variables and Vegetation Indices.

RVSI	*Precip.*	*Temp.*	*Lign.*	*MSI*	*NDVI*	*Nitro.*	*PRI*
chaparral	-0.711	0.858	0.512	0.890	-0.712	-0.342	-0.051
delta	-0.485	0.677	0.699	-0.586	-0.562	-0.790	-0.405
halo	-0.862	0.958	-0.736	0.815	-0.730	0.820	-0.009
redwoods	-0.463	0.671	0.869	-0.623	-0.446	-0.869	-0.172
sandstone	-0.923	0.962	-0.792	0.891	-0.880	0.890	-0.125
serpentine	-0.872	0.979	-0.734	0.913	-0.730	0.732	0.076
woodlands	-0.630	0.793	0.874	0.611	-0.711	-0.863	-0.045

3.3 Red-edge Hysteresis

The section contains a selection of hysteresis plots followed by brief interpretations of key points. Patterns of hysteresis for red-edge inflection and RVSI are plotted against the NDVI to assist interpretation.

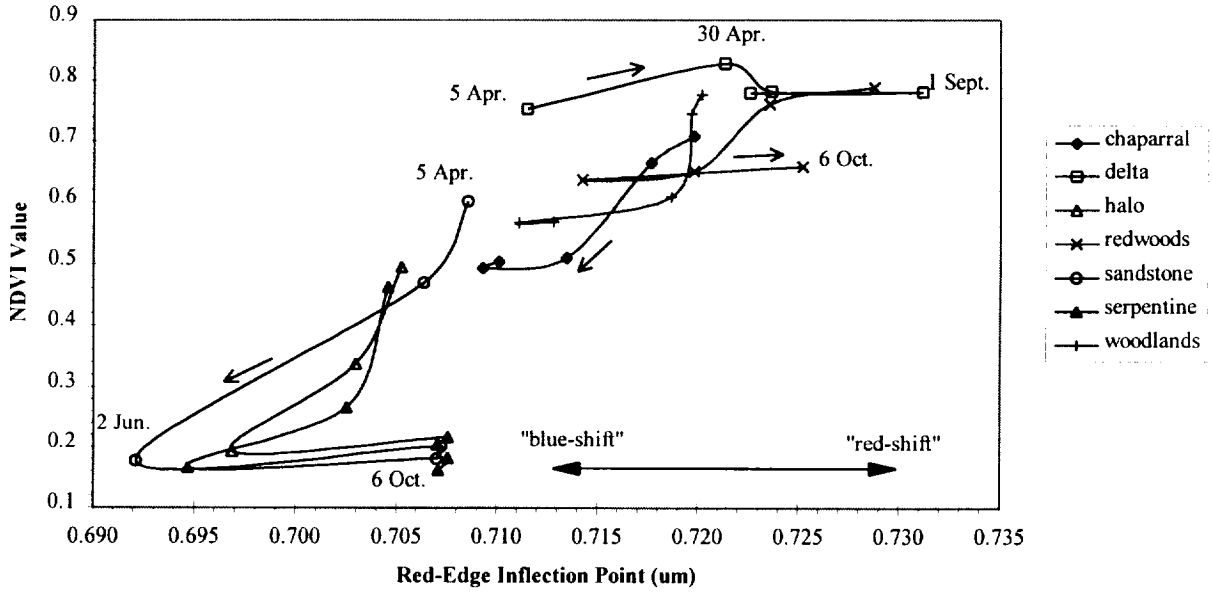

Figure 5 Hysteresis Plot Showing The Multi-Temporal Relationship Between The Red-Edge Inflection Point (λ_i) And NDVI Values. *Note:* arrows indicate the direction of hysteresis. Dataset dates: 5 April, 30 April, 2 June, 1 September, 6 October. Spline lines between data values are exponentially smoothed to indicate data trends. Wavelength is plotted on the x axis.

Figure 5 plots λ_i values against NDVI in a graphical representation of temporal hysteresis trends. Note the division of tree communities from grassland and serpentine-related communities. Serpentine, halo, and sandstone, communities display a significantly blue-shift from 5 April to 2 June and a red-shift from 2 June onwards producing an anti-clockwise hysteresis. In contrast to other communities, delta displays a large red-shift from 5 April to 1 September, followed by a blue-shift to 6 October.

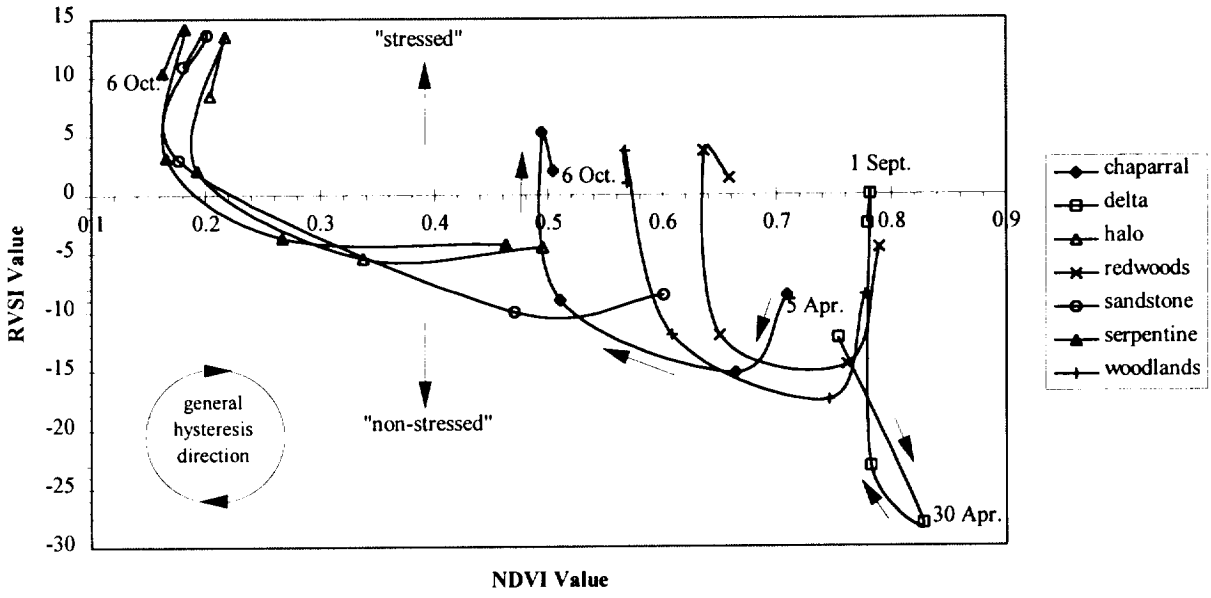

Figure 6 Hysteresis Plot Showing The Multi-Temporal Relationship Between RVSI Values And NDVI Values. *Note:* refer to Figure 5 for explanation.

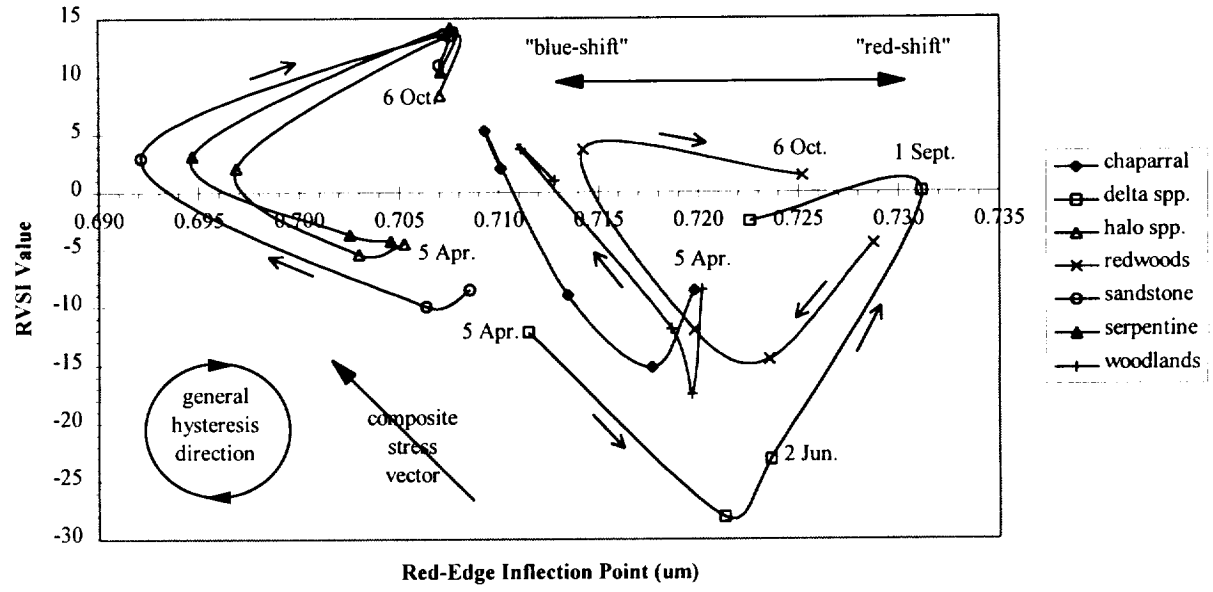

Figure 7 Hysteresis Plot Showing The Multi-Temporal Relationship Between The Red-Edge Inflection Point (λ_i) And RVSI Values. *Note:* refer to Figure 5 for explanation. The pattern of hysteresis for the redwoods community provides a satisfactory initial reference for interpreting trends.

Most communities in Figure 6 display a clockwise direction of hysteresis between RVSI and NDVI values. A general trend from serpentine to delta communities is evidenced by decreasing RVSI values and increasing NDVI values. Additionally, a decrease in the width of community hysteresis trajectories with increasing NDVI is also apparent along this trend.

Figure 7 combines RVSI values and λ_i values for an assessment of two vegetation stress red-edge indicators. Patterns of multi-temporal stress hysteresis appear to be strongly cyclic. All communities except the delta community exhibit a general clockwise hysteresis. Plots identify the sandstone grassland and serpentine-related communities as disparate. RVSI and red-edge inflection appear to be indicators of distinct components of vegetation stress. The relationship between the two variables is complex.

4. CONCLUSIONS

This research has applied a selection of analyses including, red-edge inflection calculations, derivative spectra, RVSI values, and hysteresis plots to an assessment of vegetation community stress. Red-edge inflection and the RVSI performed well as indicators of multi-temporal stress at the community scale.

Main research findings can be summarized as follows: Asymptote and near-linear curves generally appear in early season. Cuspoid spectra are associated with mid- to late season community phenology. Upper red-edge concavity is correlated to seasonal changes in precipitation and temperature. Upper red-edge cuspoid curves become increasingly concave during periods of increasing environmental stress. The RVSI performed satisfactorily as an indicator of changing phenology and environment-induced vegetation stress. Hysteresis plots assist in the clarification of relationships between a range of red-edge measures. Community clusters can be identified from the shape and trajectory of multi-temporal hysteresis curves.

Current research focuses on the biotic and abiotic factors influencing vegetation red-edge geometry and relationships to spectral shifts. Additionally, increasing the number of datasets may improve the accuracy of mapping multi-temporal trends. Analyzing annual patterns of hysteresis may also prove a useful tool for long-term studies of environmental and ecosystem change.

5. REFERENCES

Aber, J.D., Martin, M.E. (1995). High Spectral Remote Sensing of Canopy Chemistry, In: *Summaries of the Fifth Annual JPL Airborne Earth Science Workshop*, Vol. 1, AVIRIS Workshop (Ed: R.O. Green), January 23-26, 1995. NASA Jet Propulsion Laboratory publication 95-1, Vol.1, p1-4.

Gamon, J.A., Roberts, D.A., Green, R.O. (1995). Evaluation of the Photochemical Reflectance Index in AVIRIS Imagery, In: *Summaries of the Fifth Annual JPL Airborne Earth Science Workshop*, Vol. 1, AVIRIS Workshop (Ed: R.O. Green), January 23-26, 1995. NASA Jet Propulsion Laboratory publication 95-1, Vol.1, p55-58.

Goudie, A, (1994). *The Encyclopedic Dictionary of Physical Geography*. Blackwell, Cambridge, Mass, 611p.

Guyot, G., Baret, F., Jacquemoud, S. (1992). Imaging Spectrometry for Vegetation Studies. In: *Imaging Spectroscopy: Fundamentals and Prospective Applications*, (Ed: Toselli and Bodechtel), Kluwer Academic Publishers, The Netherlands, 145-166.

Merton, R.N. (1994). *Hyperspectral remote sensing of environmental and biogeochemical stress at Jasper Ridge, California.* MSc.(Hons) Thesis. Department of Geography, University of Auckland, New Zealand. 135p.

Merton, R.N., Harvey, L.E. (1997). Analysis of Seasonal Changes In Jasper Ridge Vegetation Biochemistry And Biophysiology Using Multi-Temporal Hyperspectral Data. *ASPRS Conference*, Seattle, WA. 6-10 Apr 1997.

Microsoft Corporation, (1997). *Microsoft Excel, Vers. 7.0a*, Seattle WA. USA.

Miller, J.R., Elvidge, C.D., Rock, B.N., Freemantle, J.R. (1990). An Airborne Perspective on Vegetation Phenology From the Analysis of AVIRIS Data Sets Over the Jasper Ridge Biological Preserve. In: *Proceedings of the IEEE Geosciences and Remote Sensing Society/URSI 1990 Conference.*

DIVERSE SPECTRAL PROPERTIES IN A TEMPERATURE ESTUARY: FIRST RESULTS FROM NARRAGANSETT BAY, RHODE ISLAND

John F. Mustard and Warren Prell
Department of Geological Sciences, Brown University, Providence RI 02912

1.0 INTRODUCTION

Coastal embayments and estuaries are important ecosystems containing a number of critical habitats and resources. They are currently threatened by changes to their surrounding watersheds. Although there has been a wealth of new knowledge generated over the last decade about these ecosystems, the spatial and temporal patterns of biologic and physical processes, as well as anthropogenic influences are not fully understood. Remotely sensed data offer a unique perspective on these processes because of the synoptic view and that quantitative algorithms can be used to extract geophysical and biophysical information from them. We are conducting a number of investigations using remotely sensed data to develop a better understanding of the visible-near infrared reflectance of water, substrate, and land components that will be used to develop algorithms and analytical tools for analysis of processes in the near shore and estuarine environment (patterns of productivity, spatial and temporal patterns of algal blooms, turbidity, etc.).

The study area for our work is Narragansett Bay, Rhode Island (Figure 1). The bay and coastal salt ponds are Rhode Island's premier natural resource and provide the state with numerous jobs ranging from tourism to shellfishing. The objectives of this proposal are complementary to many Bay Project initiatives and thus support a number of high quality goals. These include: effects of land use and land use change on estuarine systems, links between existing data sets for Narragansett Bay and coastal salt ponds with regional perspectives of remote sensing, and a better understanding of the relationships between physical and biological processes.

Visible-near infrared reflectance spectra of coastal and estuarine waters are a complex convolution of the optical properties of water, phytoplankton, gelbstoff, dissolved organic matter, and suspended sediment. Our long term goals are to develop quantitative methods for extraction of the physical abundances of these contributing constituents to the observed reflectance spectra. The work consists of observations with airborne sensors such as AVIRIS and insitu measurements using water samples, towed salinity, temperature, and fluorescence sensors, and field spectra obtained with portable spectrometers. In this abstract, we report on the first results of data obtained by AVIRIS on August19, 1997. The data discussed here were obtained at 11:22 EDT on a flight path from the north to the south along the eastern border of the bay (Figure 1). The solar zenith angle was 55.5° and the solar azimuth was 141°.

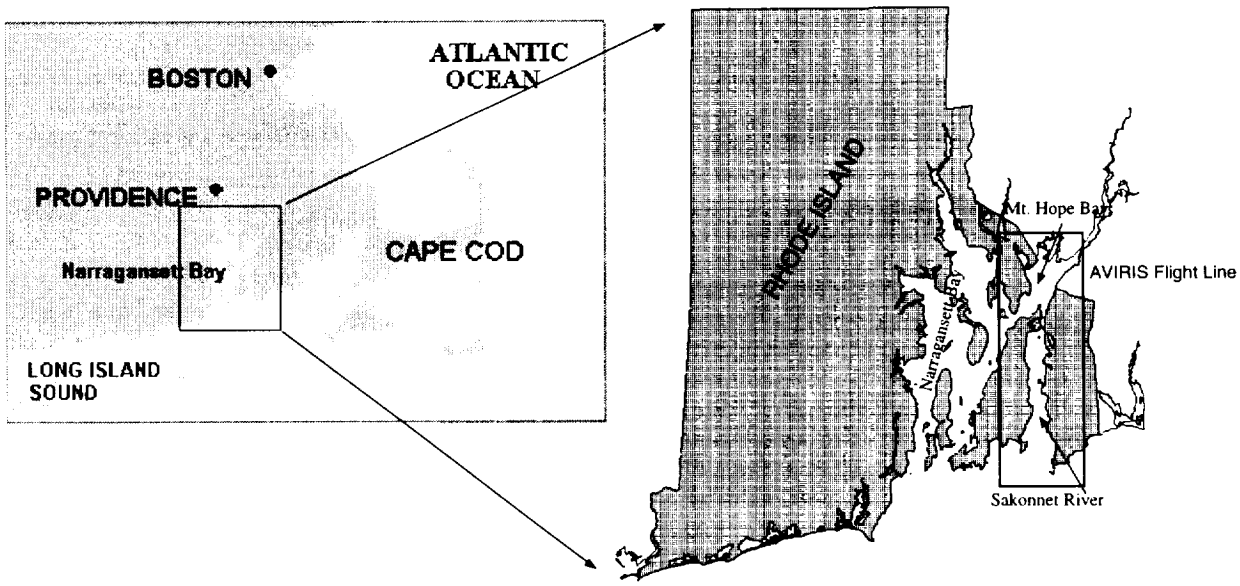

Figure 1. Location of Narragansett Bay and the AVIRIS flight line.

2.0 PHYSICAL CHARACTERISTICS OF MT. HOPE BAY

The Narragansett Bay estuary runs northward from the Rhode Island Coast into Rhode Island and Massachusetts (Figure 1), and has a drainage area of 4660 km^2 [Kremer and Nixon, 1978]. Its 2.6 X 10^9 m^3 of water are spread over an area of almost 350 km^2, with a mean depth of 7.8 m [Chinman and Nixon, 1985]. The mean tidal prism is much greater than the mean volume of river flow into the bay during an equivalent period of time, so that the estuary is generally well mixed, although occasionally stratified (measured by salinity gradients) in the upper bay [Kremer and Nixon, 1978]. The semi-diurnal tide ranges from 0.8 to 1.6 m [Chinman and Nixon, 1985], but the prevailing winds, northwest during the winter and southwest during the summer, frequently dominate short-term circulation patterns [Kremer and Nixon, 1978]. Water temperatures throughout the year range from below freezing up to the mid-20s (°C), and the annual water temperature cycle tends to lag solar radiation by about 40 days [Kremer and Nixon, 1978]. The Narragansett Bay ecosystem is phytoplankton based, and usually experiences a bay-wide winter-early spring bloom, several localized short term blooms throughout the summer, and a late summer bay-wide bloom [Kremer and Nixon, 1978]. The bay is inhabited by many commercially important fish species, and the benthos is dominated by clams which are harvested in limited areas. The Narragansett Bay ecosystem is significantly impacted by industrial and sewage-treatment effluents, as well as runoff from its intensely populated watershed.

3.0 AVIRIS DATA CALIBRATION

A number of approaches were examined for reducing the AVIRIS calibrated radiance data to reflectance. The ATREM model was applied, but due to lack of adequate characterization of the atmosphere, the resulting spectral shapes were unsatisfactory. Though typical land cover units exhibited realistic spectral shapes (e.g. vegetation, soils), the spectra for the estuary were unlike any field spectra that we had obtained to date. An empirical line calibration was attempted. However, this resulted in systematic features in the water spectra unrelated to the spectral properties of water. In essence, the gain and offset corrections were weighted towards the noise statistics of the low albedo calibration target. Projection to the even lower albedo properties of water resulted in the unacceptable spectral features.

Fortuitously, several small low altitude cumulous clouds were present in the AVIRIS flight line. These cast shadows over both land and water. Radiance spectra were extracted from shadowed and unshadowed regions of approximately similar terrain cover and analyzed. Regardless of terrain cover, all the shadowed spectra exhibited a consistent spectral shape between 0.4-0.8 μm, and ratios of the various shadowed terrains to shadowed water produced a relatively flat ratio spectrum. Thus we propose that shadowed water can provide a first order estimate of path radiance. The cumulous clouds scatter light very efficiently in the 0.4-0.8 μm region without any significant absorptions. They can therefore provide a first order estimate of solar radiance. To provide a first order estimate of reflectance we therefore simply subtract the spectrum of shadowed water, with a small reduction to account for reflected sky irradiance (basically attenuate the spectrum by a factor of 0.95) from every pixel in the scene, and divide by the spectrum of a homogeneous cloud, which also has had the estimate of path radiance removed. Carder et al (1992) presented an approach based on the same concept but with a more thorough development of the radiance contributions for all sources. This was used to constrain a radiative transfer model for the calculation of reflectance and they showed the cloud-shadow approach has merit in the calibration of hyperspectral data in aquatic environments.

3.1 ASSESSMENT OF CALIBRATION

Simply put, the extremely simplistic approach to calibration provided remarkably clean spectra of the estuary that are highly consistent with reflectance spectra measured in situ. This is illustrated in Figure 2. The AVIRIS spectra are 3x3 pixel averages selected from regions representative of the typical estuarine waters. The field spectra were acquired with ASD portable spectrometers using a 20% reflective Spectralon target as a standard and corrected for the absolute reflectance of the standard. We see that the AVIRIS spectra reproduce the main important characteristics of the field spectra of the estuary: strong chlorophyll absorption between 0.4 and 0.55 μm, strong drop in reflectance after 0.58 μm due to increased water absorption, and the presence of a small chlorophyll absorption near 0.67 μm. These spectra are also comparable to estuarine spectra collected by other researchers (e.g. Roesler and Perry, 1995).

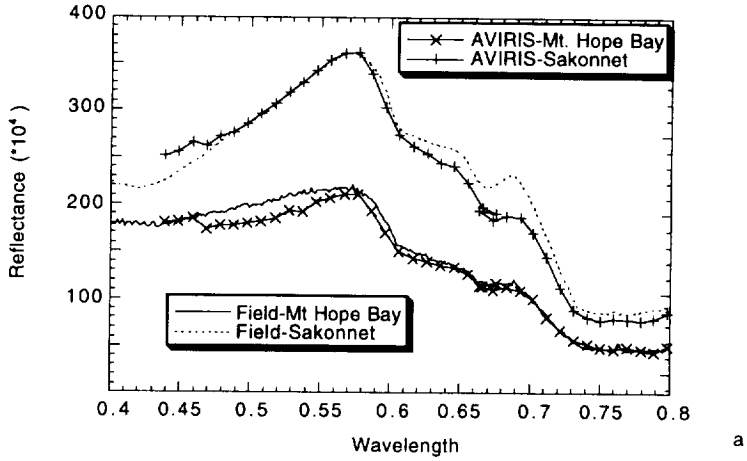

Figure 2. Comparison between AVIRIS apparent reflectance spectra and field spectra acquired with an ASD FieldSpec FR.

4.0 ANALYSIS

We have only just begun the analysis of these data, and many of the approaches will require refinement. Our objective is to use a number of approaches and compare them to in situ data of water optical and physical properties. Spectral ratios that are well known and used in the processing of ocean color sensors such as SeaWIFS will be used as the simple methods. However, such models are well known to have sensitivity problems in turbid inland waters. Since the AVIRIS data are of such high quality, we also plan to use more spectrally based approaches such as mixture modeling. Typical mixture models that are widely used in the analysis of terrestrial data (e.g. Adams et al, 1993) are not directly applicable to aquatic spectra and will have to be modified. One such approach that we are pursuing is the model of water reflectance presented by Roesler and Perry (1995) that relates the primary backscattering constituents to the primary absorbing constituents. Ultimately we plan to integrate these results into a 3-dimensional hydrodynamic model that has been successfully applied in our thermal modeling of Narragansett Bay (Mustard et al., 1997).

To illustrate the diversity in spectral properties in this estuary, and to point to the remarkable quality of the AVIRIS data, Figure 3 shows the reflectance at 560 nm of the eastern portion of Narragansett Bay covered by the AVIRIS flight line with the spectral properties of several distinct regions indicated on the left side of the diagram. We can clearly see a number of important spectra features related to the water constituents. The middle graph shows the spectra of two fresh water ponds which have extremely strong and well developed absorptions due to chlorophyll. The strength of the absorptions are variable, and related to the relative abundance of phytoplankton in these ponds. These are clearly eutrophic. In the upper plot, spectra from Mt. Hope Bay are shown. The most notable feature here is the variable in the 0.4-0.55 chlorophyll absorption, and the spectrum from waters affected by the sewage effluent along the eastern portion of the bay. This spectrum is relatively dark, but shows a high degree of backscatter as evidenced by the overall flat continuum properties. In the lower plot, the transition from the high phytoplankton abundance in the Narragansett Bay to the lower phytoplankton abundance in the coastal ocean is clearly seen. The coastal ocean spectrum is very bright in the blue with little chlorophyll evident. However, this spectrum is quite a bit darker than typical open ocean or blue water spectra (e.g. Roesler and Perry, 1995).

5.0 SUMMARY

The first analysis of data from the Narragansett Bay estuary are extremely promising. We recognize all the major water absorbing constituents related to chlorophyll and backscattering components. Though there are no riverine sources of suspended sediment, it is clear from many of the spectra that sediment has been suspended off the bottom. This will provide excellent data to attempt to remove the effects of suspended sediment from inland water spectra. There are dramatic variations in chlorophyll concentration, varying from the eutrophic ponds to the relatively chlorophyll-poor coastal ocean. The simple calibration approach employed here is remarkably good for revealing the relative spectral properties of these constituents. We are planning a number of analysis approaches to quantitatively extract physical and biophysical properties from these high quality spectral data acquired by AVIRIS.

Acknowledgments: This research is supported by a NASA grant NAG13-39 from the Stennis Space Center.

6.0 REFERENCES

Adams, J. B., M. O. Smith, and A. R. Gillispie. 1993, "Imaging Spectroscopy: Interpretations Based on Spectral Mixture Analysis." *Remote Geochemical Analysis: Elemental and Mineralogical Composition (C. M. Pieters and P. A. Englert, Eds.)*, 145-166.

Carder, K. L., P. Reinersman, and AR. F. Chen, 1992, AVIRIS calibration using the cloud-shadow method, Summaries of the Fourth Annual JPL Airborne Geoscience Workshop, (R. O. Green, ed.) JPL Publication 92-14, vol. 1, 26-28.

Chinman, R.A. & S.W. Nixon. 1985. Depth-Area-Volume Relationships in Narragansett Bay. Graduate School of Oceanography, the University of Rhode Island. NOAA/Sea Grant Marine Technical Report 87.

Kremer, J.N. & S.W. Nixon. 1978. A Coastal Marine Ecosystem. New York: Springer-Verlag Berlin Heidelberg.

Mustard, J. F., A. Sen, C. Swanson, D. Mendelsohn, and C. Deacutis, 1997, Integration of remotely sensed data and hydrodynamic modeling into a GIS to assess the impacts of thermal effluent in an estuary, in *Proc. 4th International Conference on Remote Sensing for Marine and Coastal Environments*, Environmental Research Institute of Michigan, Ann Arbor, MI, II 34-II 43.

Roesler, C. S. and M. J. Perry, 1995, "In situ phytoplankton absorption, fluorescence emission, and particulate backscatter determined from reflectance", J. Geophys. Res. v. 100, 13,279-13,294.

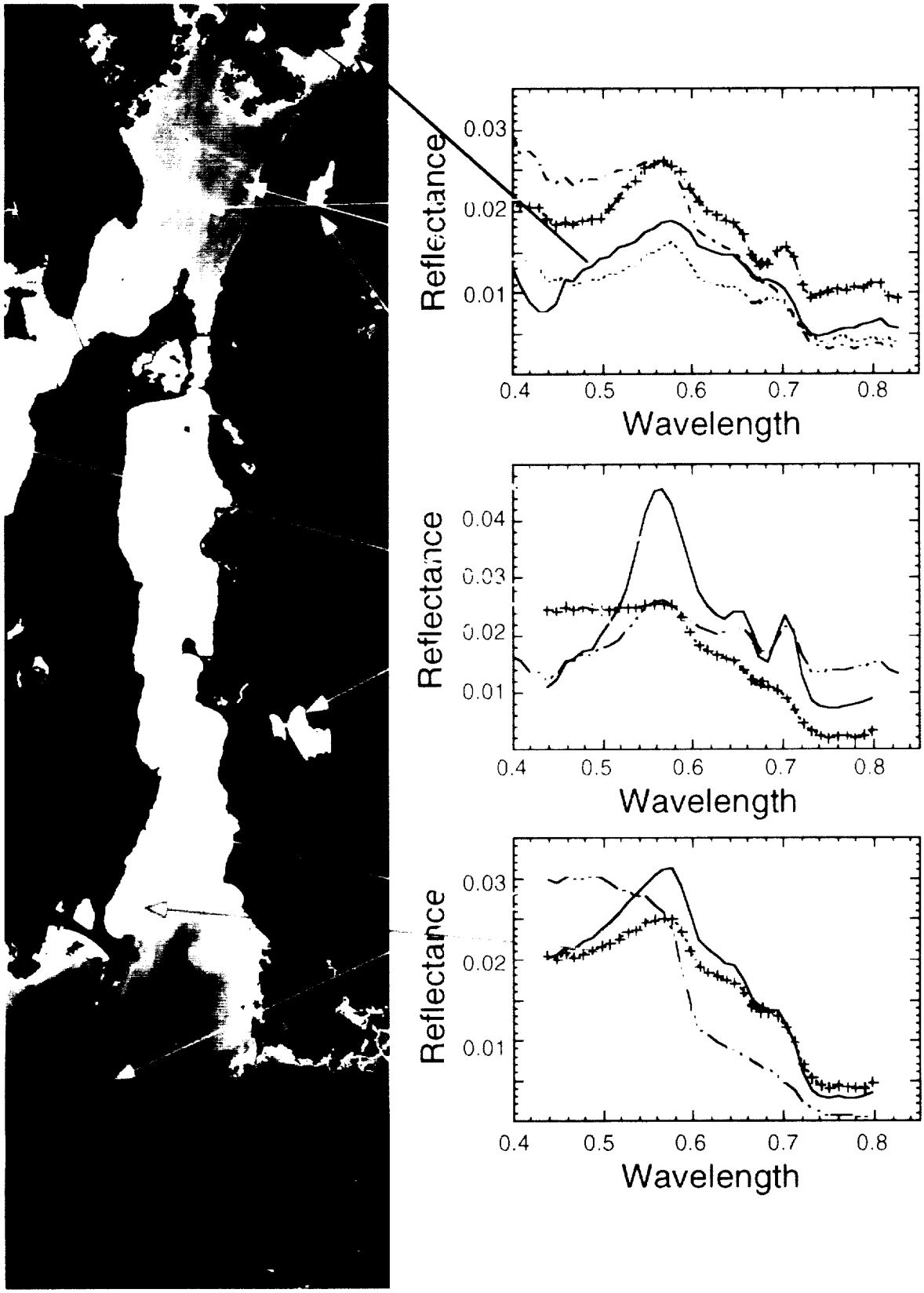

Figure 3. Reflectance at 560 nm (left) and representative reflectance spectra for a number of diverse regions covered by the scene.

MULTIPLE ENDMEMBER SPECTRAL MIXTURE ANALYSIS:

APPLICATION TO AN ARID/SEMI-ARID LANDSCAPE

Gregory S. Okin [1]
William J. Okin [2]
Dar A. Roberts [2]
Bruce Murray [1]

[1] Division of Geological and Planetary Sciences, 170-25
California Institute of Technology, Pasadena, CA, 91125

[2] Department of Geography, University of California
Santa Barbara, CA 93106

1. INTRODUCTION

As the Earth's human population increases and once-fertile areas become less so, human activities are bound to spread into areas that once were considered barren and unworkable, namely our planet's arid and semi-arid regions. Worldwide, this process already has begun. As a result, these fragile areas are being put under stresses that are leading to severe landscape damage and hence, a decrease in usefulness to humans. This process of "desertification" is already widespread, and although many people frequently consider desertification to be a problem unique to arid and semi-arid Africa, it is in fact occurring on all continents except Antarctica.

Desertification is actually a complex suite of phenomena that occur in arid and semi-arid environments which can be triggered by human land use, interannual climate variability or long-term climate change. Many interrelated processes on sub-canopy to regional spatial scales are included, but the dominant form of desertification in the southwestern U.S. is the conversion of grasslands to shrublands (Sears, 1935; Buffington and Herbel, 1965; Mabbutt and Floret, 1980). The processes involved frequently occur as "runaway" phenomena which are not reversible or remediable on human timescales for reasonable cost (Schlesinger *et al.*, 1990). As a result, monitoring of arid regions is critical in any attempt to short-circuit these land degradation processes.

Remote monitoring using current or anticipated satellite remote sensing is the most time- and cost-efficient way to proceed with arid region monitoring in the future. Unfortunately, interpretation of remote sensing data from arid regions is particularly difficult. Three factors are thought to contribute to this. First, arid and semi-arid regions are often characterized by large soil background, in many cases swamping out the spectral contribution of plants (Huete *et al.*, 1985; Huete and Jackson, 1988; Smith *et al.* 1990; Escafadel and Huete, 1991). Second, light rays reaching sensors from desert plants are often polluted by additional interactions with desert soils (Huete, 1988; Ray and Murray, 1996). Finally, due to evolutionary adaptations to the harsh desert environment, desert plants are spectrally dissimilar to their humid counterparts, lacking in many cases a strong red edge, exhibiting reduced leaf absorption in the visible, and displaying strong wax absorptions around 1720 nm (Ehleringer, 1981; Ray, 1995).

Many of the early applications of remote sensing to arid and semi-arid regions suggest that present remote sensing techniques, including most brightness and greenness indices, are susceptible to over- or underestimation of vegetation cover simply due to variations in soil color and low vegetation cover (Huete *et al.*, 1985; Huete and Jackson, 1987; Huete and Jackson, 1988; Escafadel and Huete, 1991; Pickup *et al*, 1993) although Musick (1984) found a correlation between total vegetation cover and Landsat MSS band 5 brightness. None of theses studies were able to accurately and reliably discern shrubs from grasses in arid and semi-arid environments, which is probably the most important means by which to identify desertification (Schlesinger *et al.*, 1990). Later work by Franklin *et al.* (1993) and Duncan *et al.* (1993) using SPOT wavebands and greenness and brightness indices found these indices to be sensitive to vegetation type as well as cover. High variance in these studies, however, suggests that even in cases where landscape components were determined to be significantly different, it may not be possible to accurately retrieve the contribution of these components to spatially averaged reflectance measurements. This characteristic is presumably due to the low spectral resolution of the SPOT wavebands and the effect of nonlinear mixing under low

cover conditions, as well as the typically high spectral variability found in desert plants.

Despite the lackluster performance of remote sensing in arid regions, there are have been a few studies that suggest there is potential for doing accurate and reliable remote sensing in arid and semi-arid regions. Smith *et al.* (1990) applied a mixing model that employed laboratory and field spectra to Landsat TM data from the Owens Valley, indicating that mixture modeling can facilitate mapping and monitoring of sparse vegetation cover. Roberts *et al.* (1993) have used linear mixture analysis of AVIRIS data to map green vegetation, nonphotosynthetic vegetation (NPV), and soils at the Jasper Ridge Biological Preserve, CA. It is a natural next step, therefore, to apply spectral mixture analysis to arid and semi-arid regions in the hope that this will overcome previous difficulties in accurate and reliable landscape assessment by remote sensing in these areas. The purpose of this study is to determine if multiple endmember spectral mixture analysis will accurately and reliably characterize arid and semi-arid region vegetation and soils from AVIRIS data. The ultimate goal of this work is to develop tools for remote sensing of arid regions that make the best use of current and near-future remote sensing technology to monitor these environments.

2. METHOD

2.1 Study Site Description

This study was conducted at the Jornada Long Term Ecological Research (LTER) site 23 miles northeast of Las Cruces, NM in the Chihuahuan Desert ecosystem. It is located on the Jornada del Muerto plain, which is bounded by the San Andres Mountains on the east and by the Rio Grande Valley and the Fra Cristobal-Caballo Mountain complex on the west. Elevation varies from 3,900 to 4,500 feet. The Jornada Plain consists of unconsolidated Pleistocene detritus. This alluvial fill from the nearby mountains is 300 feet thick in places and the aggradation process is still active. Coarser materials are found near foothills along the eastern part of the study area. The topography of the study area consists of gently rolling to nearly level uplands, interspersed with swales and old lake beds (Buffington and Herbel, 1965).

The climate of the area is characterized by cold winters and hot summers and displays a bimodal precipitation distribution. Winter precipitation usually occurs as low-intensity rains or occasionally as snow and contributes to the greening of shrub species in the basin in the early spring. Summer monsoonal precipitation, usually in the form of patchy, but intense, afternoon thunderstorms, is responsible for the late-summer greening of grasses. The average annual precipitation between 1915 and 1962 in the basin was 23.1 cm, with 52% falling between July 1 and September 30 (Paulsen and Ares, 1962). The average maximum temperature is highest in June, when it averages 36°C, and lowest in January, when it averages 13°C (Buffington and Herbel, 1965).

The principal grass species in the study area are burrograss (*Scleropogon brevifolius*), several species of *Aristida*, and tobosa grass (*Hilaria mutica*) while major shrubs are creosote (*Larrea tridentata*), mesquite (*Prosopis glandulosa*), and tarbush (*Florensia cernua*). Soils in the basin are quite complex but generally range from clay loams to loamy fine sands, with some areas being sandy or gravelly (Soil Conservation Service, 1980).

2.2 Image Acquisition and Processing

AVIRIS data were acquired over the Jornada Basin on May 27, 1997. After they were acquired, data were radiometrically corrected at the AVIRIS data facility. Apparent surface reflectance was retrieved using a technique developed by Green *et al.* (1993; 1996; Roberts *et al.* 1997a). This technique uses MODTRAN 3.5 to generate look-up tables for path radiance and reflected radiance for water vapor at a range of values for a specified date, time, location, meteorological visibility, and surface elevation. Modeled radiance is fitted to the 940 nm atmospheric water band of measured upwelling radiance by using a nonlinear least-squares-fitting routine on a pixel-by-pixel basis. Apparent surface reflectance is calculated for each pixel by modeling total upwelling radiance at the sensor as the sum of the path radiance and atmospherically-attenuated reflected surface radiance.

2.3 Multiple Endmember Spectral Mixture Analysis

Spectral mixture analysis (SMA) is based on the assumption that the reflectance spectrum derived from an air- or spaceborne sensor can be deconvoluted into a linear mixture of the spectra of ground components, frequently called spectral endmembers. The best-fit weighting coefficients of each ground component spectrum, which must sum to one, are interpreted as the relative area occupied by each component in a pixel. Multiple endmember spectral

mixture analysis (MESMA) is simply a SMA approach in which many possible mixture models are analyzed in order to produce the best fit (Gardner, 1997; Roberts *et al.*, 1997b; Painter *et al.* 1997). In the MESMA approach, a "spectral library" is defined which contains spectra, convolved to the 224 AVIRIS bands, of plausible ground components. A set of mixture models with n ($n \geq 2$) endmembers from the library is defined, with shade always present as one endmember in the model. The weighting coefficients (fractions) for each model and each pixel are determined such that the linear combination of the endmember spectra produces the lowest RMS error when compared to the apparent surface reflectance for the pixel. Weighting coefficients are constrained to be between zero and one, and a valid fit is restricted to a maximum preset RMS error. Models that meet these constraints are recorded, which typically yields several possible models for each pixel. As an optional final step, the one model for each pixel with the lowest RMS can be identified. It is these best-fit models which are discussed below.

This approach requires an extensive library of field or image spectra, where each plausible ground component is represented at least once. Including more than one spectrum of a ground component allows for the considerable spectral variability often found in desert vegetation, thus overcoming a difficulty identified by Franklin *et al.* (1993) of doing remote sensing in arid regions.

2.4 Methods Used in This Study

In this study two-, three-, and four-endmember models were run on the apparent surface reflectance retrieval from an AVIRIS scene which includes the headquarters of the Jornada LTER site (flight 970527 run 2, scene 6).

Warren and Hutchinson (1984) correctly suggested that the phenological stages of arid and semi-arid region plants would affect their spectral characteristics. This "spectral phenology" is a further complication of arid region remote sensing and suggests that SMA will be most effective when field spectra taken at the same time as the acquisition of remote sensing data are used in mixture models. Field spectra collected in the Jornada LTER site during May 24-25, 1997 were incorporated into the spectral library in this study in order to make as direct an identification of landscape components as possible. Field spectra were collected from 350 nm to 2500 nm using an ASD Full Range portable spectroradiometer (Analytical Spectral Devices, Inc., Boulder, CO) on loan from the Jet Propulsion Laboratory. With a 100% reflective Spectralon panel, spectra can be displayed and recorded in real-time as reflectance.

A total of 36 field spectra were chosen to be included in the spectral library for this study. This includes spectra of nine soils, nine grasses (three species), seven creosote, four tarbush, and seven mesquite. Representative spectra are shown in Figure 1. Soil spectra were given the names of the sites at which they were collected. Four soil spectra that appeared to model soils in the basin are: *M-rab*, a dark red loamy fine sand soil of aeolian origin from a mesquite duneland, *P-tabo*, a clay loam from a gypsiferous playa, and *T-east* and *G-basn*, clay loam to fine sandy loam soils found on basin floors and toe slopes of fans (Soil Conservation Service, 1980). Grasses at this time of the year were by and large senesced. Spectra used in three- and four-endmember models were chosen to minimize computation time and to maximize spectral variability using the method outlined by Gardner (1997). In this library analysis, each spectrum in the spectral library is modeled by every other spectrum in the library, coupled with shade, and constrained by the constraints that will be used in the final analysis. This approach allows spectra to be compared to one another, and redundant or unique spectra to be identified. Spectra were chosen that 1) modeled other spectra of the same type, 2) were not modeled by other spectra of the same type, and 3) were not confused with spectra of other types.

For the two-endmember models, the entire 36-member spectral library was used in MESMA modeling. For the three-endmember models, all soil + grass + shade, soil + shrub + shade, grass + shrub + shade combinations of a reduced library (spectra of seven shrubs, six grasses, and six soils) were used, resulting in a total of 144 different models. Finally, for the four-endmember models, four soil spectra, six grass spectra, and six shrub spectra were used to define a total of 146 soil + grass + shrub + shade models. Each of the models was run twice: once with a maximum RMS threshold of 2.5% and once with a maximum RMS threshold of 2.0%.

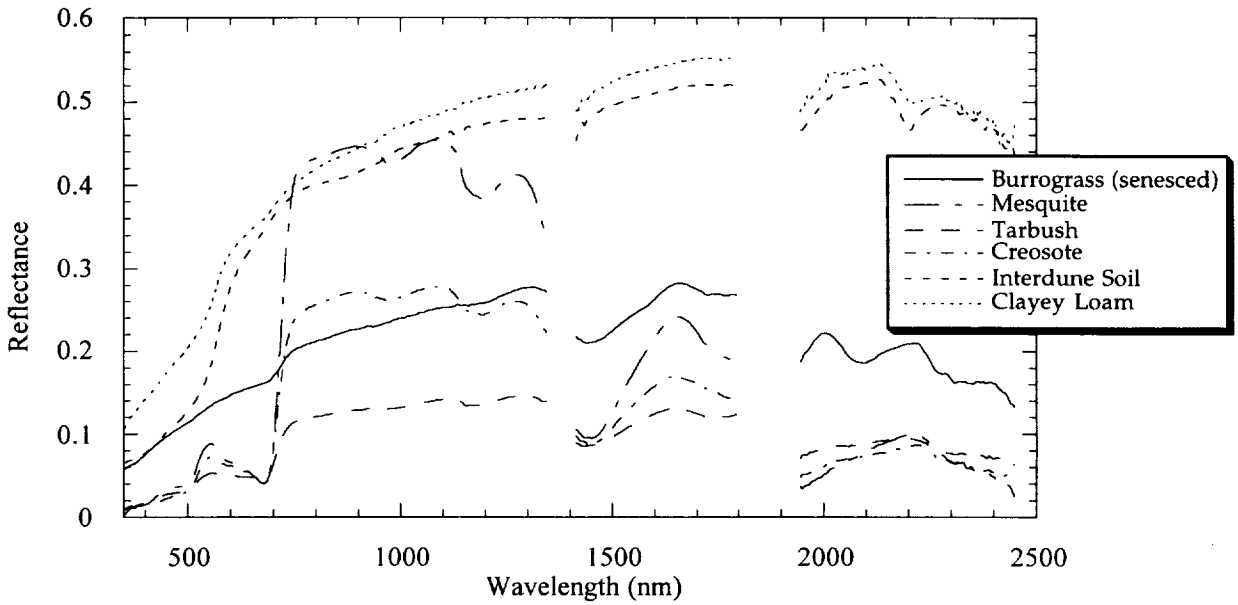

Figure 1. Representative spectra used in MESMA of AVIRIS image

3. RESULTS AND DISCUSSION

3.1 Two-Endmember Models

Two endmembers modeled only 24% of the AVIRIS scene within the 2.5% RMS constraints. The only endmembers that successfully modeled the image were soils, mainly *T-east* and *P-tabo*. This result implies primarily that the first-order signal in the image is soil, which is to be expected in an arid environment and indeed confirms other authors' results that soil is the major spectral contributor to remote sensing data in arid and semi-arid regions (Huete *et al.*, 1985; Huete and Jackson, 1988; Smith *et al.*, 1990; Escafadel and Huete, 1991). This result also suggests that since the soil signal is so strong, it might be very difficult to get much information about vegetation in the scene.

Although a quarter of the scene was modeled using just soil and shade, examinations on the ground suggest there are very few areas in this region that are pure soil. Virtually all of the pixels probably contain some vegetation. Clearly, two-endmember models are inadequate for use in this environment, where soil is the major, but not only, contributor to pixel-wide spectral averages. Reducing the maximum RMS constrain to 2.0% efficiently eliminated the two-endmember models from consideration, with less than 2% of the entire scene meeting the constraints. This is further evidence that two-endmember models cannot accurately be used to model reflectance in this scene.

3.2 Three-Endmember Models

Figure 2 is a map of fencelines within the AVIRIS scene taken from ground data acquired from Barbara Nolen at the Jornada LTER office, New Mexico State University. This map is at the same scale as all Figure 3 images and is to be used as a geographical comparison. Features of note in this image are the square exclosure on the western side of the map, the southwest-northeast trending fenceline southeast of the exclosure, and the Jornada LTER Headquarters north of the exclosure.

The three-endmember models were divided into three categories: soil + shrub + shade, soil + grass + shade, and shrub + grass + shade. With an RMS constraint of 2.5%, 90% of the image was modeled, whereas a 2.0% RMS constraint reduced this fraction to 30%. The shrub + grass + shade category modeled virtually none of the image, a testament to the strength of the soil signal and its importance in any SMA models for this environment. Figure 3b shows pixels that were best modeled by soil + shrub + shade as gray, and those best

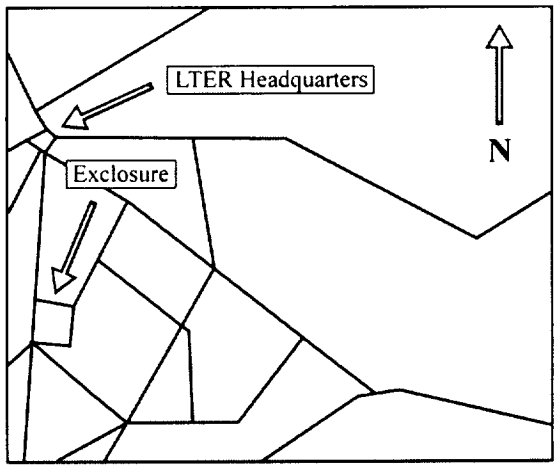

Figure 2. Fencelines in AVIRIS scene used in this study.

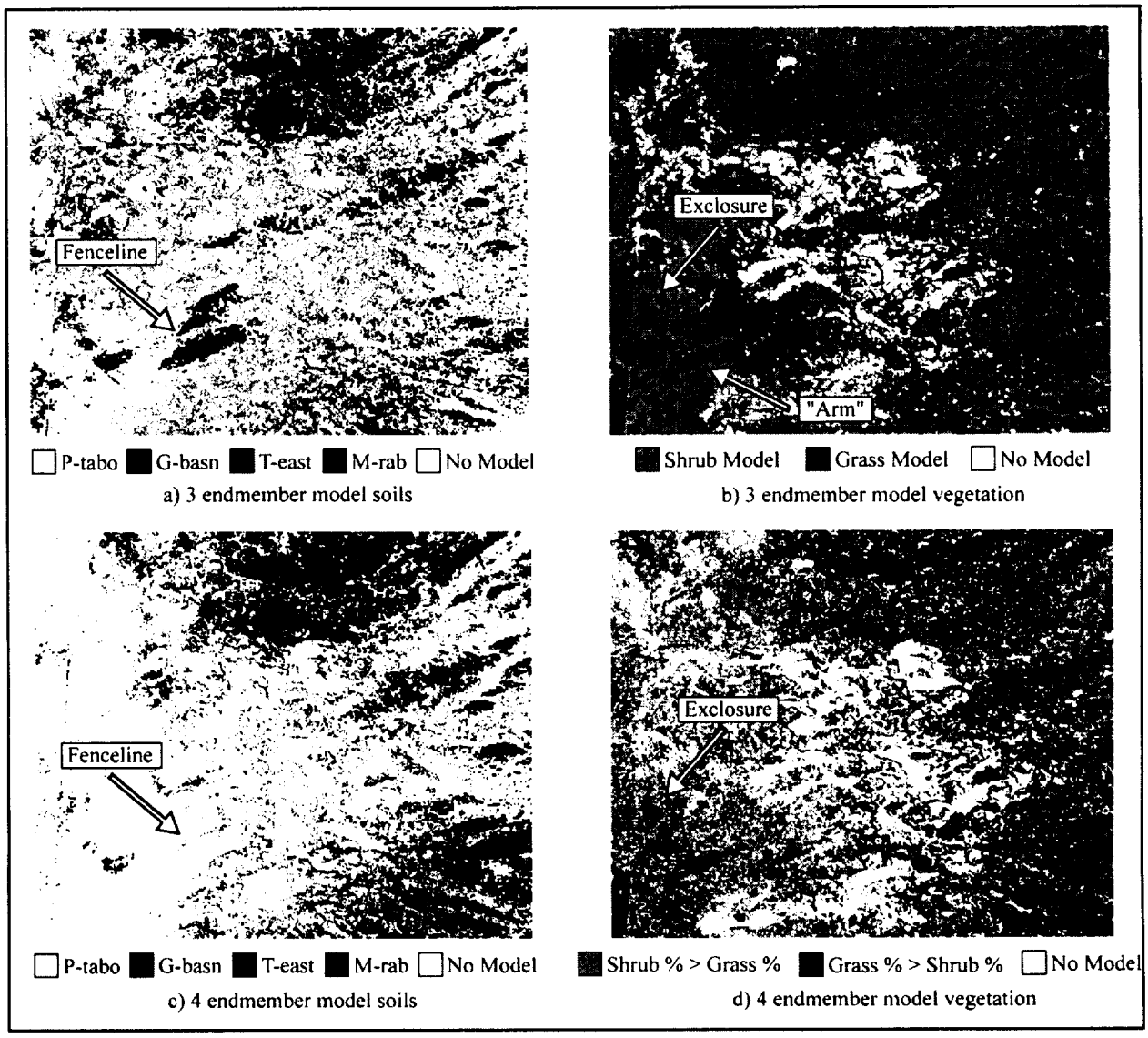

Figure 3. Results of MESMA for 3- and 4-endmember models with maximum RMS of 2.5%.

modeled by soil + grass + shade as black. Most of the scene was modeled by soil + shrub + shade, giving the impression that shrubs dominate the environment. The most successful shrub spectra in the three-endmember models were of creosote and tarbush. This result is certainly reasonable given preliminary examination of the environment which suggests that these shrubs are dominant in this area. A significant part of the image was not modeled by any three-endmember model at the chosen RMS constraints. This result suggests that a prominent and unique endmember is missing from the spectral library, which corresponds to some obvious bright features in apparent surface reflectance found in the central part of the scene (not shown).

The areas where the grass models are chosen imply that the three-endmember approach is able to capture some of the true vegetative variability in the scene. Most obviously, the square exclosure in Figure 3b and the "arm" adjacent to it are clearly visible in the image as a sea of grass models amidst an ocean of shrub models. This indicates a clear spectral change across fencelines which may by due to a real change in vegetation. Preliminary ground observations suggest that these areas are indeed dominated by grass.

Figure 3a shows the four soils which dominate the three-endmember results. *P-tabo* is the most prominent soil, spanning the entire image, and accounting for most of the soil in the left side of the image. *M-rab* shows several contiguous features, especially a large portion of the top of the image and a long linear feature across the middle of the image. It also appears in the exclosure and the "arm". *G-basn* is spread across the image, and has a spurious look to it, since it is quite fragmented and frequently borders unmodeled portions of the image. *T-east* shows up in the same regions as *M-rab*, but with much less frequency.

The frequency of *P-tabo* in successful three-endmember models is not geologically sensible: *P-tabo* is a gypsiferous playa soil, but the areas best modeled by it are not playas. On the other hand, areas best modeled by *M-rab* are sensible: *M-rab* is an interdune soil and areas best modeled by it are aligned with the dominant southwest-northeast trending wind direction in the basin and also correspond to areas mapped as highly susceptible to wind erosion (Soil Conservation Service, 1980). Few pixels are best modeled by *T-east,* which was collected just off the southwestern edge of the scene. This might be interpreted as an erroneous result. However, the Soil Conservation Service soil map (1980) of the basin does place a boundary between the southwest corner of this image and the *T-east* site in both soil type and texture, suggesting that despite its proximity, the *T-east* soil type is not present in the scene.

One geographical feature in particular stands out in the image to suggest that three-endmember models may not be optimal everywhere in an arid environment: the change of soil model across the fenceline in Figure 3a (cf. Figure 2 for fencelines). Although there are means by which a soil may change across a fenceline, this is unlikely in this case. More likely is a change in vegetation, from grass-dominated to shrub-dominated, across the fenceline due to differential livestock grazing. Since only three endmembers are being used for these models, however, this change in vegetation can't be modeled explicitly, and the difference appears as a change in the soil endmember. This fenceline soil feature can be expected to disappear in the four-endmember models.

Despite the problems with the three-endmember models mentioned above, these results suggest that MESMA may have some success in modeling apparent surface reflectance in arid and semi-arid regions. The fact that grasses are modeled in areas known to be grass dominated-- the exclosure and the "arm"-- as well as the spatial contiguity of the modeled endmembers suggests that MESMA is responding to real spectral variation and may be capable of accurately and reliably modeling soils and vegetation in arid and semi-arid regions. Nonetheless, it is clear that four-endmember models may be required under certain circumstances to deconvolute soils and plant signatures.

3.3 Four-Endmember Models

In this arid region of New Mexico, there are two basic vegetation types: shrubs and grasses. Since the two- and three-endmember modes have shown that soil is the dominant signal in the image, a soil endmember must be included in any mixture model in this region. Thus, to capture the two vegetation types, four endmembers will often be needed-- soil, shrub, grass, and shade. Since four soils dominated the three-endmember models, these soil spectra were combined with six grass spectra and six shrub spectra to define 146 soil + grass + shrub + shade four-endmember models. With an RMS constraint of 2.5% the four-endmember models fitted 80% of the image while at 2.0% RMS, 34% of the image was modeled. A significant part of the image was not modeled by any four-endmember model at the chosen RMS constraints. These unmodeled areas correspond to the same areas in the three-endmember models that were unmodeled, further indicating that a prominent and unique endmember is

missing from the spectral library. The fact that more pixels were modeled at a maximum RMS of 2.5% in the three-endmember models instead of the four-endmember models is likely due to the significant reduction in the size of the spectral library which was needed to make MESMA computation time reasonable.

Displaying pixels with a greater fraction of grass than shrubs and vice-versa in Figure 3d gives the impression that there is much more grass in the region than implied by the three-endmember models. Preliminary ground observations indicate that this is probably the case. Again, forcing only one vegetation endmember on an environment with two distinct vegetation types may be causing erroneous results. The exclosure and the "arm" are still apparent, although the contrast at the fencelines isn't as great as it was in the three-endmember vegetation image (Figure 3b). As hypothesized, the questionable change in soil type across the fenceline noted in Figure 3a has disappeared in Figure 3c, and Figure 3d does suggest that a change in vegetation across this fenceline may be responsible for the apparent soil change noted in the three-endmember results.

Unfortunately, *P-tabo* shows up in the four-endmember results just as it did in the three-endmember results. Once again, this is probably a spurious result. The greater spatial contiguity of the areas mapped as *P-tabo* may suggest, nonetheless, that the four-endmember model really is more successful at disentangling soil from vegetation contributions to apparent surface reflectance. Loss of *M-rab* as the best fit soil in the southeastern portion of the image may also be erroneous.

4. CONCLUSIONS

It was the purpose of this study to determine if the MESMA approach can provide an accurate and reliable means to characterize arid and semi-arid region vegetation and soils from AVIRIS data. The results presented here indicate that MESMA can successfully capture some of the most important landscape features, such as shrub-to-grass ratios, that are relevant for desertification monitoring. Two-endmember models are inadequate for mixture modeling of arid and semi-arid environments. Although MESMA can be forced to model AVIRIS data from these areas using only two endmembers, these results are not convincing. The fact that two-endmember models fail to characterize a significant portion of the image indicates the MESMA is responding correctly to landscape structure. Application of three-endmember models indicates that these models might introduce some errors into the results due to the fact that there is an inadequate amount of variation in the vegetation endmembers to capture real variation on the ground. Four-endmember models provide enough flexibility to account for some of the complexity of this arid environment, but may not be applicable everywhere. It is clear from our results that a combination of three- and four-endmember models will be required to apply MESMA accurately and reliably to arid and semi-arid regions. Given the fact that the same areas were modeled with both three and four endmembers, the criterion for this choice in arid regions can not be minimum RMS. Another method must be found, and might take advantage of the spectral phenology encountered in arid and semi-arid regions.

5. FUTURE RESEARCH

Although the results of this study are promising, there are some sources of error that must be addressed before this research can proceed further. First and most importantly, the reflectance inversion used in this work has suffered due to the fact that modeled reflectance was not adjusted to a known target reflectance of any one pixel in the scene. This procedure allows refinement of all apparent surface reflectance spectra in the scene and may greatly improve mixture modeling. There are few targets in this study area which are homogenous enough to use for this refinement, but one must be found in order to proceed with confidence. Second, these results must be field-checked. We suggest the use of a stratified random sampling scheme to do this. In addition, some obvious gaps in the ability to model the image arose from some conspicuous missing endmembers. In the future, improved models might result from a larger and more complete spectral library for this region.

Finally, an improved method must be found for choosing between three- and four-endmember models in arid and semi-arid environments. It is proposed that this method might take advantage of the large spectral changes in plants during their different phenological stages. Since grasses will show much more variation in greening and senescence than shrubs and also green at different times than shrubs, seasonal differences may give additional information to differentiate between these vegetation types. The ability to determine whether a three-endmember model or a four-endmember model is more appropriate for a given pixel is a crucial step that must included in the definition of a robust methodology for modeling arid environments using MESMA.

6. REFERENCES

Buffington, L.C., and Herbel, C.H., 1965, "Vegetational changes on a semidesert grassland range from 1858 to 1963", Ecological Monographs, v. 35, p. 139-164.

Duncan, J., Stow, D., Franklin, J., and Hope, A., 1993, "Assessing the relationship between spectral vegetation indices and shrub cover in the Jornada Basin, New Mexico", International Journal of Remote Sensing, v. 14, p. 3395-3416.

Ehleringer, J., 1981, "Leaf absorptances of Mohave and Sonoran Desert plants", Oecologia, v. 49, p. 366-370.

Escafadel, R., and Huete, A., 1991, "Improvement in remote sensing of low vegetation cover in arid regions by correcting vegetation indices for soil "noise"", C. R. Academie des Sciences Paris, v. 312, p. 1385-1391.

Franklin, J., Duncan, J., and Turner, D.L., 1993, "Reflectance of vegetation and soil in Chihuahuan desert plant communities from ground radiometry using SPOT wavebands", Remote Sensing of the Environment, v. 46, p. 291-304.

Gardner, M., 1997, Mapping Chaparral with AVIRIS Using Advanced Remote Sensing Techniques, Master of Arts thesis: Department of Geography, University of California, Santa Barbara, CA.

Green, R.O., Conel, J.E., and Roberts, D.A., 1993, "Estimation of aerosol optical depth and additional atmospheric parameters for the calculation of apparent surface reflectance from radiance measured by the Airborne Visible/Infrared Imaging Spectrometer", *in* Green, R.O., ed., Fourth Annual JPL Airborne Geoscience Workshop, Volume 1, JPL Publication 93-26, Jet Propulsion Laboratory, Pasadena, CA, p. 73-76.

Green, R.O., Roberts, D.A., and Conel, J.E., 1996, "Characterization and compensation of the atmosphere for the inversion of AVIRIS calibrated radiance to apparent surface reflectance", *in* Green, R.O., ed., Sixth Annual JPL Airborne Earth Science Workshop, Volume 1, JPL Publication 96-4, Jet Propulsion Laboratory, Pasadena, CA, p. 135-146.

Huete, A.R., Jackson, R.D., and Post, D.F., 1985, "Spectral response of a plant canopy with different soil backgrounds", Remote Sensing of Environment, v. 17, p. 37-53.

Huete, A.R., and Jackson, R.D., 1987, "Suitability of spectral indices for evaluating vegetation characteristics on arid rangelands", Remote Sensing of the Environment, v. 23, p. 213-232.

Huete, A.R., 1988, "A soil-adjusted vegetation index (SAVI)", Remote Sensing of Environment, v. 25, p. 295-309.

Huete, A.R., and Jackson, R.D., 1988, "Soil and atmosphere influences on the spectra of partial canopies", Remote Sensing of Environment, v. 25, p. 89-105.

Mabbutt, J.A., and Floret, C., 1980, "Case Studies on Desertification", United Kingdom, United Nations, Scientific and Cultural Organization.

Musick, H.B., 1984, "Assessment of Landsat Multispectral Scanner spectral indices for monitoring arid rangeland", IEEE Transactions on Geoscience and Remote Sensing, v. GE-22, p. 512-519.

Painter, T.H., Roberts, D.A., Green, R.O., and Dozier, J., 1997, "Improving mixture analysis estimates of snow covered areas from AVIRIS data", Remote Sensing of Environment, *in press.*

Paulsen, H.A., Jr., and Ares, F.N., 1962, "Grazing values and management of black gramma and tobosa grasslands and associated shrub ranges of the Southwest", Technical Bulletin 1270, U.S. Forest Service.

Pickup, G., Chewings, V.H., and Nelson, D.J., 1993, "Estimating changes in vegetation cover over time in arid rangelands using Landsat MSS data", Remote Sensing of Environment, v. 43, p. 243-263.

Ray, T.W., 1995, Remote Monitoring of Land Degradation in Arid/Semiarid Regions, Ph.D. thesis: Division of Geological and Planetary Sciences, California Institute of Technology, Pasadena, CA.

Ray T.W., and Murray, B.C., 1996, "Nonlinear spectral mixing in desert vegetation", Remote Sensing of Environment, v. 55, p. 59-64.

Roberts, D.A., Smith, M.O., and Adams, J.B., 1993, "Green vegetation, nonphotosynthetic vegetation, and soils in AVIRIS data", Remote Sensing of the Environment, v. 44, p. 255-269.

Roberts, D.A., Green, R.O., and Adams, J.B., 1997a, "Temporal and spatial patterns in vegetation and atmospheric properties from AVIRIS", Remote Sensing of Environment, v. 62, p. 223-240.

Roberts, D.A., Gardner, M.E., Church, R., Ustin, S.L., Scheer, G., and Green, R.O., 1997b, "Mapping chaparral in the Santa Monica Mountains using multiple endmember spectral mixture models", Remote Sensing of Environment, *in press.*

Smith, M.O., Ustin, S.L., Adams, J.B., and Gillespie, A.R., 1990, "Vegetation in deserts: I. a regional measure of abundance from multispectral images", Remote Sensing of Environment, v. 31, p. 1-26.

Schlesinger, W.H., Reynolds, J.F., Cunningham, G.L., Huenneke, L.F., Jarrell, W.M., Virginia, R.A., and

Whitford, W.G., 1990, "Biological Feedbacks in Global Desertification", Science, v. 247, p. 1043-1048.
Sears, P.B., 1935, Deserts on the March: Norman, Oklahoma, University of Oklahoma Press.
Soil Conservation Service, 1980, "Soil survey of Dona Ana County area, New Mexico", United States Department of Agriculture.
Warren, P.L., and Hutchinson, C.F., 1984, "Indicators of rangeland change and their potential for remote sensing", Journal of Arid Environments, v. 7, p. 107-126.

Automated subpixel snow parameter mapping with AVIRIS data

Thomas H. Painter[1,2], Dar A. Roberts[1,2], Jeff Dozier[2,3], Robert O. Green[1,2,4]

[1]Department of Geography, University of California, Santa Barbara 93106

[2]Institute for Computational Earth System Science, University of California, Santa Barbara 93106

[3]Donald Bren School of Environmental Science and Management, University of California, Santa Barbara 93106

[4]Jet Propulsion Laboratory, California Institute of Technology, Pasadena, CA 91109

ABSTRACT

We describe an automated algorithm (MEMSCAG) for mapping subpixel snow covered area (SCA) and snow grain size with AVIRIS data. The algorithm is based on the multiple endmember approach to spectral mixture analysis in which the spectral endmembers and the number of endmembers can vary on a pixel-by-pixel basis. This approach accounts for surface cover heterogeneity within a scene. The mixture analysis runs on endmembers from a spectral library of snow, vegetation, rock, soil, and lake ice spectra. Snow endmembers of varying grain size were produced with a radiative transfer model. All non-snow endmembers were collected with a portable field spectrometer. Mapping is performed through sequential 2-endmember, 3-endmember, and 4-endmember mixture model runs, each subject to constraints on RMS, residuals, fractions and priority. Grain size is determined by the grain size of the snow endmember used in the optimal mixture model. We apply MEMSCAG to AVIRIS data collected over Mammoth Mountain, CA and the northern site of the BOREAS in Manitoba, Canada. MEMSCAG produces appropriate snow covered area estimates in all regions. A preliminary comparison of grain size estimates from MEMSCAG with field measurements demonstrates high accuracy.

INTRODUCTION

Maps of snow covered area and grain size provide initialization, validation, and re-initialization for distributed climatologic and snowmelt models. Snow cover is likely to be a sensitive indicator of climate change. Snow grain size is a dominant control over the spectral albedo, hence its spatial distribution can strongly influence the surface net radiation at a range of scales.

The spectral signature of pure snow is primarily sensitive to grain size (Figure 1). With an increase in particle size, visible reflectance remains unchanged while near infrared and short wave infrared reflectance decrease. This is due to a six order of magnitude change in the imaginary part of the complex index of refraction of ice across the solar spectrum. Mountainous regions frequently exhibit grain size gradients driven

by gradients in air temperature and incident solar radiation. Due to the sensitivity of the spectral signature to particle size, snow exhibits a gradient in spectral signature along the grain size gradients.

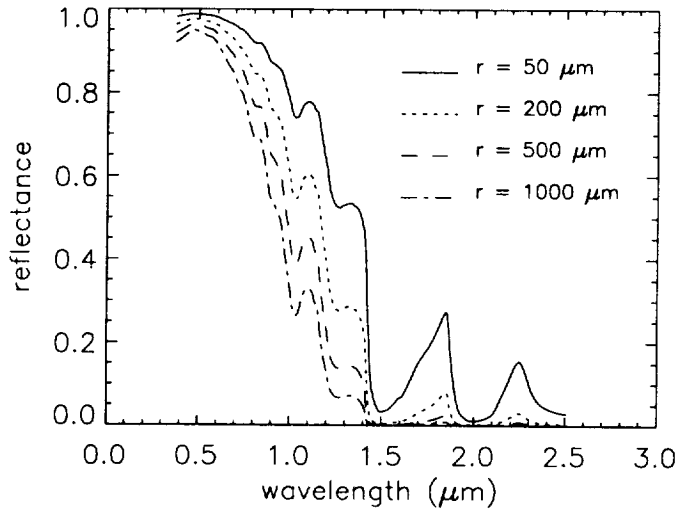

Figure 1. Directional-hemispherical reflectance of snow for varying grain size.

The efficacy of spectral mixture analysis in mapping subpixel surface cover has been shown for snow (Nolin *et al.*, 1993; Rosenthal and Dozier, 1996), vegetation (Roberts *et al.*, 1993), and geology (Adams *et al.*, 1986). In previous work (Painter *et al.*, 1996; Painter *et al.*, 1998), we demonstrated that a suite of snow endmembers varying with grain size is required to accurately map snow covered area and grain size with spectral mixture analysis. Roberts *et al.* (1998) presented multiple endmember spectral mixture analysis (MESMA), in which endmembers and the number of endmembers are allowed to vary pixel by pixel. This approach can better account for surface cover heterogeneity than ordinary spectral mixture analysis in which a suite of endmembers is selected to model the entire scene.

ALGORITHM

The automated algorithm MEMSCAG (Multiple EndMember Snow Covered Area and Grain size) is based on the MESMA approach. We created a spectral library of snow, vegetation, rock, soil, lake ice, and vegetation-shaded snow spectra. Snow spectra were generated using a two stream radiative transfer model (Wiscombe and Warren, 1980). The Mie scattering parameters were generated for ice spheres of radii ranging from 50 to 1500 μm (Wiscombe, 1980). Vegetation, rock, soil, lake ice, and vegetation-shaded snow spectra were acquired in the central Sierra Nevada with an Analytical Spectral Devices FieldSpec FR field spectroradiometer. Field spectra were subsequently convolved to AVIRIS bandpasses. AVIRIS calibrated radiance was converted to

apparent surface reflectance using the nonlinear least squares water vapor fitting of Green *et al.* (1993).

The algorithm flow is shown in Figure 2. We run suites of n endmember models in which the first n-1 endmembers are physical constituents (snow, vegetation, rock, etc.) and the nth endmember is photometric shade. For example, a two endmember model could consist of snow (r = 750 μm) and shade, and determines if the pixel is pure snow with grain size of 750 μm. In order for a model to be accepted for a pixel, the model must meet the following constraints: RMSE < 2.5%, no 7 consecutive residuals can exceed 2.5%, and spectral fractions must be between –0.01 and 1.01. For each n, some pixels have multiple models that meet the constraints (overlapping models). To select the optimal model, we use the minimum RMSE as a metric. This produces best fit SCA and grain size images for each n. In order to select from overlapping models across varying n, we use priority selections. Priorities were initially established, from highest to lowest, as two, three, and four endmembers. For example, if a pixel is modeled in the two, three, and four endmember case, its SCA and grain size derive from the values of the two endmember case.

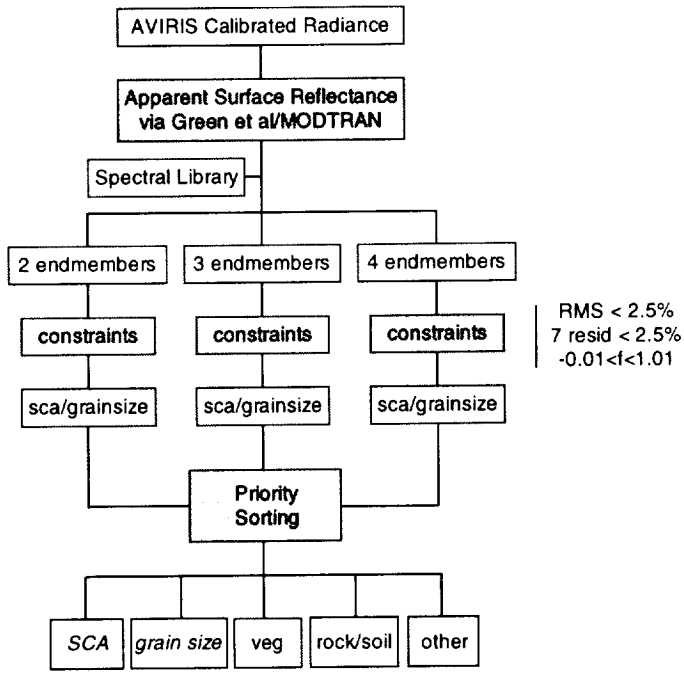

MEMSCAG = Multiple Endmember Snow Covered Area and Grain Size

Figure 2 Flowchart of MEMSCAG algorithm.

The establishment of priorities deserves further attention in order to preserve geographic and physical consistency. A likely geographic and spectral scenario is snow mixed spatially with rock, whereas an unlikely scenario is that of snow mixed with illuminated vegetation. Vegetation vertical relief dictates that the latter mixture includes vegetation-shaded snow, a third physical constituent. Hence, the four endmember model (snow, vegetation, vegetation-shaded snow, and shade) is more realistic than the three endmember model.

RESULTS

We applied MEMSCAG to AVIRIS data acquired over Mammoth Mountain, CA and the northern BOREAS site, Manitoba, Canada on April 5, 1994 and April 20, 1994. Figures 3 and 4 show SCA and grain size results for Mammoth Mountain and BOREAS,

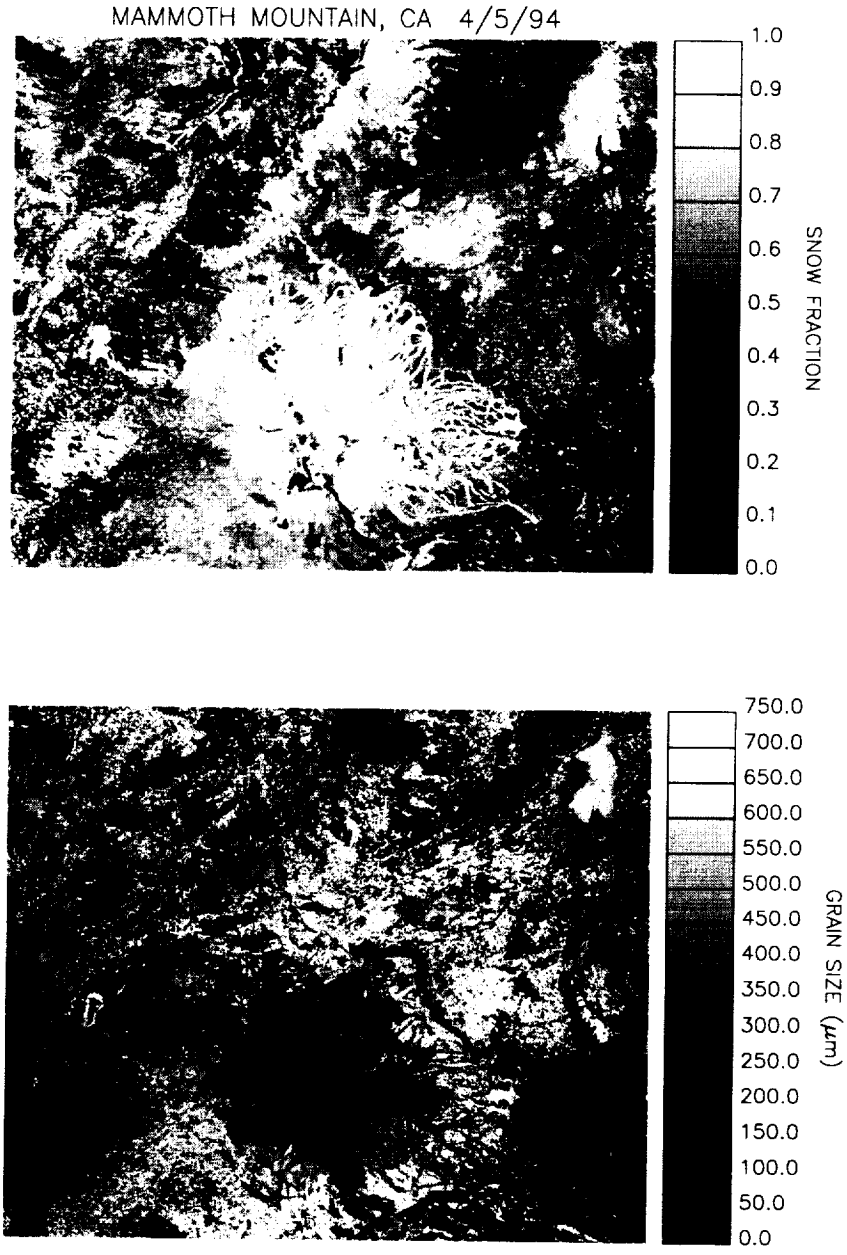

Figure 3 Subpixel snow covered area and grain size for Mammoth Mountain, CA - 4/5/94.

respectively. SCA results were appropriate for both regions, exhibiting high snow cover above timberline and in large forest openings. Lower snow cover fractions corresponded

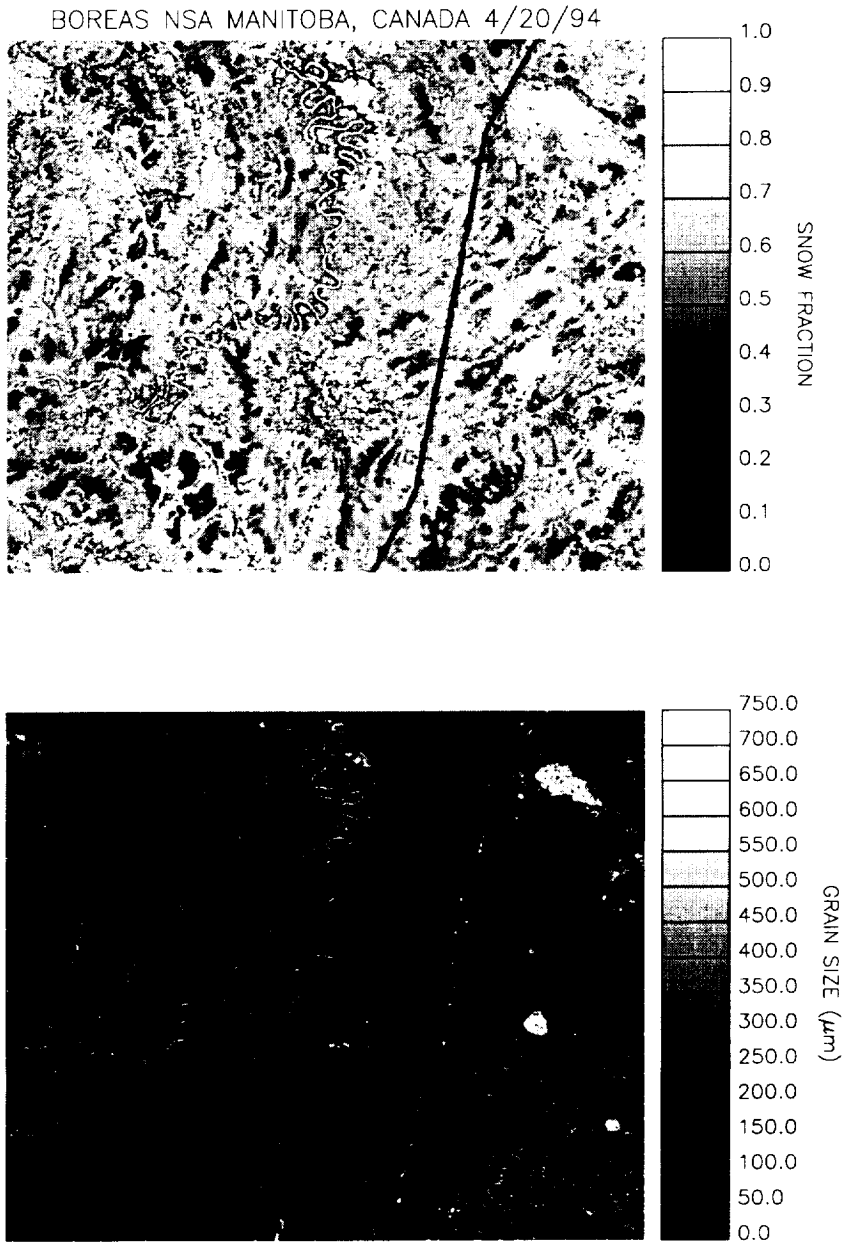

Figure 4 Subpixel snow covered area and grain size for BOREAS northern site - 4/20/94.

to timbered regions, and exposed rock outcrops, roads and lake ice. Surface grain sizes in the boreal forest vary according to canopy closure, with larger grains in openings exposed to greater temporally-integrated solar irradiance. Grain sizes in the boreal forest as retrieved by MEMSCAG were qualitatively consistent with field measurements. Table 1 presents a preliminary comparison of grain sizes retrieved by MEMSCAG with those

retrieved from stereological (Davis *et al.*, 1987) analysis of snow samples collected on Mammoth Mountain. Though not statistically significant, the results demonstrate potentially high accuracy. Root mean squared error for this sample is 23.6 μm.

Mammoth Mtn. 4/5/94	MEMSCAG grain radius (μm)	STEREOLOGY grain radius (μm)
Back Chair 23	124.1	130.5
Boundary	240.7	281.1
Climax	80.4	81.4

Table 1 Comparison of MEMSCAG and stereology grain size results for Mammoth Mountain, CA - 4/5/94.

ACKNOWLEDGMENTS

This work was sponsored under NASA EOS MTPE grant NAGW-5185 and performed at the University of California, Santa Barbara and the Jet Propulsion Laboratory, Pasadena, CA. We thank Robert E. Davis of the U.S. Army Corps of Engineers Cold Regions Research and Engineering Laboratory for processing snow samples.

REFERENCES

Adams, J. B., M. O. Smith, and P. E. Johnson, 1986, Spectral mixture modeling: A new analysis of rock and soil types at the Viking Lander 1 site, *J. Geophys. Res.* 91(B8):8098-8112.

Davis, R. E., J. Dozier, and R. Perla, 1987, Measurement of snow grain properties, in *Seasonal Snowcovers: Physics, Chemistry, Hydrology*, H. G. Jones and W.J. Orville-Thomas, eds., pp 63-74, NATO ASI Series, D. Reidel Publishing Company.

Green, R. O., J. E. Conel, and D. A. Roberts, 1993, Estimation of aerosol optical depth and calculation of apparent surface reflectance from radiance measured by the Airborne Visible/Infrared Imaging Spectrometer (AVIRIS) using MODTRAN2, *SPIE Conf. No. 1937, Imaging Spectrometry of the Terrestrial Environment*, p.12.

Nolin, A. W., J. Dozier, and L. A. K. Mertes, 1993, Mapping alpine snow using a spectral mixture modeling technique, *Ann. Glaciol.* 17:121-124.

Painter, T. H., D. A. Roberts, R. O. Green, and J. Dozier, 1996, Subpixel snow covered area and snow grain size from mixture analysis with AVIRIS data, *Summaries of the Sixth Annual JPL Airborne Earth Science Workshop, R. O. Green, editor, JPL Publication 96-4, Vol. 1*, 185-188.

Painter, T. H., D. A. Roberts, R. O. Green, and J. Dozier, 1998, Improving spectral mixture analysis of snow covered area with AVIRIS data, *Remote Sens. Environ.*, in press.

Roberts, D. A., M. O. Smith, and J. B. Adams, 1993, Green Vegetation, Non-photosynthetic Vegetation, and Soils in AVIRIS Data, *Remote Sens. Environ.* 44(2/3):255-269.

Roberts, D. A., M. Gardner, R. Church, S. Ustin, G. Scheer and R. O. Green, 1998, Mapping chaparral in the Santa Monica Mountains using multiple endmember spectral mixture models, *Remote Sens. Environ.*, in press.

Rosenthal, W., and J. Dozier, 1996, Automated mapping of montane snow cover at subpixel resolution from the Landsat Thematic Mapper, *Water Resour. Res.* 32(1):115-130.

Wiscombe, W., and S. G. Warren, 1980, A model for the spectral albedo of snow I. Pure snow, *J. Atmos. Sci.* 37:2712-2733.

Wiscombe, W., 1980, Improved Mie scattering algorithms, *Applied Optics* 19:1505-1509.

REMOTE SENSING OF SOILS IN THE SANTA MONICA MOUNTAINS: HIERARCHICAL FOREGROUND AND BACKGROUND ANALYSIS

Alicia Palacios-Orueta[1], Jorge E. Pinzón[2], Susan L. Ustin[1], and Dar A. Roberts[3]
[1]Department of Land, Air, and Water Resources, [2]Department of Applied Mathematics, University of California, Davis, CA 95616, USA; [3]Department of Geography, University of California, Santa Barbara, CA

1. INTRODUCTION

The extreme spatial and temporal variability of surface processes makes soil properties extremely variable and therefore, difficult to measure. Since soil and ecosystem processes occur at different scales, it is necessary to work at sufficiently large spatial resolution and coverage for generalizations to be made. Organic matter is a soil property closely related to soil quality, not only as an indicator of soil erosion and degradation, but also as a regulating factor of processes such as nutrient availability, water holding capacity, and permeability. Because values of organic content are highly variable and react very quickly to external changes (Gerrard, 1992), decomposition rates show high spatial variability. The spatial distribution of organic matter content can be an indicator of the rate of decomposition and other processes happening on the soil surface, such as differences in deposition and erosion rates or microclimate factors.

Imaging spectrometry offers a potential way to map certain soil properties that are relevant to surficial processes at the landscape scale. In the last few years the analysis of hyperspectral data and image processing techniques have improved to the point that they offer the potential for direct analysis of soil properties. Several multispectral sensors have already been used for discrimination between soils (Lewis et al, 1975; Agbu et al, 1990; Coleman et al, 1993). Specifically, there are several studies where organic matter has been analyzed in terms of its reflectance properties (Stoner and Baumgardner, 1981; Henderson et al, 1989). Hyperspectral data, specifically Advanced Visible Infrared Imaging Spectrometer (AVIRIS) data has been shown to be useful for improved discrimination of minerals (Clark et al, 1990; Kruse et al, 1990). Also, several other studies have dealt with soil identification and discrimination directly or indirectly using AVIRIS data (Smith et al, 1990; Roberts et al, 1993; Palacios-Orueta and Ustin, 1996, 1998b).

A significant problem for soil analysis is the presence of vegetation in most pixels. Because the signatures of soils and vegetation are so different, the lesser variability contained within the soil component is not significant enough for soil discrimination when vegetation is also present in the pixel. HFBA (Hierarchical Foreground and Background) (Pinzón et al, 1988) is a new steerable analytic technique where the Foreground and Background Analysis (FBA) equation (Smith et al, 1994) is applied at several levels in a hierarchical way, thus, the variability contained in the data set is confined at each step, making it possible to extract subtle absorption features. For this model FBA was modified to project the spectra into a property-specific axis of continuous variation. To examine the application of this method to extract and improve detection of soil properties using an imaging spectrometer, we applied it to map the spatial distribution of organic matter content from samples in two watersheds in the Santa Monica Mountains Recreation Area. In earlier work, Palacios-Orueta and Ustin (1988a) found that soils from each valley could be discriminated based on organic matter and iron content and that these could be spectrally estimated with reasonable accuracy in soil samples. The purpose of this work was to test the performance of HFBA (Hierarchical Foreground and Background Analysis) applied to AVIRIS data for the discrimination of these soils and soil properties.

2. METHODS AND MATERIALS

2.1 Study Sites, Soils, and Geologic Materials

The soils are from two south-to-north trending watersheds, La Jolla Valley and Serrano Valley, within the Point Mugu State Park in the western (coastal) region of the Santa Monica Mountains National Recreation Area, between Ventura and Los Angeles Counties, California. The climate is typically Mediterranean with dry summers and mild winters. In late 1993 a wildfire removed most of the vegetation in both valleys making it possible to

observe soils with minimal vegetation cover. Further description of this area is found in Palacios-Orueta (1997) or Palacios-Orueta and Ustin (1988a). La Jolla Valley soils are formed from weathered sandstone and shale while Serrano Valley soils are derived from basic igneous rock. The soil moisture regime in both valleys is xeric and the soil temperature regime is considered thermic. The steep terrain and the distance to the ocean create different microsite environments which consequently result in high soil variability (Edwards et al, 1970).

2.2 Field Soil Data Collection

Seventy-four soil sample composites were collected from the valleys. Samples were selected to represent the range of aspect, slope, elevation and parent materials within the area, although this goal could not be completely achieved due to the roughness of the terrain. The locations of the soil samples were identified using a Global Positioning System unit (Trimble Navigation PROXL) with +/- 1 meter accuracy after differential correction.

2.3 Physico-chemical laboratory analyses

The soil samples were analyzed by the DANR (Division of Agriculture and Natural Resources) Analytical Laboratory at U.C. Davis for organic matter, iron content, and texture. Organic matter content was significantly higher in La Jolla Valley although variances were similar in both valleys (Palacios-Orueta and Ustin, 1988a). The soil sample preparation for spectrometry followed the standardized procedure from Henderson et al (1992). Further information about this procedure, spectroscopic technique and soil characteristics can be found in Palacios-Orueta (1997).

2.4 Spectroscopic Analysis

The spectral data set includes laboratory reflectance spectra (400-2500 nm) measured in a Varian Cary 5E spectrophotometer, and two AVIRIS scenes acquired April 11, 1994.

2.5 Geographic Information Systems Database

The geographic information was organized in a GIS (Arc/Info) database. The AVIRIS scenes were georeferenced using control points and combined in the database with ancillary information composed of a Digital Elevation Model, vegetation map, and the digitized geologic map. The organic matter content was also included in the database. The AVIRIS imagery used for this study was acquired approximately six months after the wildfire and at the end of the winter precipitation period. Two adjacent image scenes were used for this analysis. Apparent surface reflectance retrieval used a radiative-transfer based atmospheric model (MODTRAN 2) that accounts for spatial variation of the atmospheric conditions (Green et al, 1993).

3. METHODOLOGY

HFBA was developed by Pinzón et al (1995) as an improvement of FBA (Smith et al, 1994). The approach taken (Fig. 1) was to narrow the variance by stratification of the soil population into small but reliable ranges of soil variability that can be consistently detected. This process is done by first discriminating the soils between the valleys, and second, by investigating the variability related to organic matter content within each group. A smaller range of spectral variability is found in the second level. These vectors are calculated using a training set derived from laboratory data and Singular Value Decomposition (SVD) is used to solve the HFBA equation at each level in the analysis. The performance was tested with the whole laboratory spectral data set and then applied to the AVIRIS image. Each pixel was classified as being of the soil type of one of the two valleys or into a class level of organic matter content. The analyses were done in Matlab (1994).

4. RESULTS AND DISCUSSION

4.1 First Level of Soil Classification: Vector Training

Although other sources of variability between the soils at these two locations are likely, the spectral variability due to the combination of organic matter is summarized in this step. HFBA uses a supervised

classification scheme where each valley was represented by a scale of values in which Serrano type soils ranged from 0 to 7 and La Jolla from 7 to14. Then, spectra in the training set were projected by the HFBA vector to the center of each class. Figure 2 shows the mean spectra for each valley and the HFBA vector that yielded the best discrimination between valleys. It can be observed that the two spectral areas most important for discrimination between the valleys were near 1000 nm and 2200 nm. Although the greatest weights were given to the band at 2200 nm, an area between 700 and 1400 nm and centered on 1000 nm was consistently negatively weighted. This means that a wide area around 1000 nm is important in the discrimination while only a few bands around 2200 nm are significant. Palacios-Orueta and Ustin (1988a) found that reflectance around 1000 nm was not only related to organic matter content but also iron, thus low reflectance in this band by itself is not sufficient to determine the organic matter content. From the mean spectra, it is observed that the reflectance at 1000 nm is significantly different between valleys. The absorption bands centered at 2200 and 2300 nm are most likely due to the presence of OH-Al and Mg-OH in dioctahedral and trioctahedral clays respectively (Hunt and Salisbury, 1970). The differences in geologic parent materials could produce this effect. These results combined with the analysis of error (Table 1) support the idea that although there must be other sources of variability, organic matter and iron contents play a critical role in the spectral discrimination between valleys.

4.2 Second Level: Organic Matter Content

At the second HFBA level, the analysis focused on extracting information related to the biogeochemistry. In order to do this, two analysis tools were used: the quantization of the chemical data into ranges and the selection of the soil samples for the training set. In each group defined at the first level, two new vectors were trained to classify spectral samples for organic matter. Vectors **a** and **b** (Fig. 3 a,b) were trained with the soils classified either as Serrano or La Jolla types. Both HFBA vectors show a concave shape around the 700 nm region although in La Jolla the minimum value is slightly shifted towards 800 nm. In these soils the weights increase until reaching the highest value at 1400 nm. The band at 2200 nm is highly weighted in Serrano, while in La Jolla the band centered at 2300 nm has highly positive weights. In La Jolla, the vector is smoother over a wider range of wavelengths, possibly due to the higher organic matter and lower iron contents in this valley. Organic matter characteristics are stronger and their features are more clearly observed. Table 2 shows the quantization levels for organic matter content, and the number of samples in the whole data set and in the training set. Figure 4 shows the distributions of the measured and the predicted values for both valleys. The continuous line represents the predicted values and the dashed line represents the measured data. The r^2 from the regression analysis is 0.72, and only five samples were outside of one standard deviation. The distributions of the predicted and the measured data follow similar patterns assigning more samples to the centrally placed values.

4.3 Classification between valleys

The first vector was trained to assign each pixel a classification value that will locate it in one of the two soil types. Since many pixels are not pure soils they are classified outside the range of the original classes (0-14). Although the area under study was recently burned in a major wildfire there was a considerable amount of revegetation in some areas, mainly in the moister valley bottoms. Because the image was acquired following the wildfire and winter storms we expected the amount of dry vegetation to be low, thus, decreasing the possibility of confusion with soil.

There are also some terrestrial areas in the image that were not affected by the wildfire and remained vegetation covered. Masking the vegetation using an NDVI threshold is an arbitrary decision and pixels with small but undetermined amounts of vegetation still remain. Our interest lies in discriminating soil properties in pixels over a range of partial vegetation cover. Since the vectors are trained with pure soils, we expect that pixels having some vegetation will still show soil characteristics while pixels with higher levels of vegetation cover will be out of the range of the predicted soil property values. This allows an *a posteriori* decision about vegetation cover that is derived from the soil information rather than an *a priori* vegetation-based decision. The NDVI (Fig. 9a) is shown as a reference and used to compare the spatial distribution of the vegetation derived from the HFBA but it was not used directly to mask vegetation in the analysis. Our results showed that the negative values projected by the classification vector were pixels with high NDVI (>0.5), providing some confirmation of the methodology.

A histogram of the results (Fig. 5) shows that the AVIRIS distribution forms a long tail with only a few

pixels having values higher than 21. Nearly all pixels with values higher than 14 were located in the ocean, therefore we used this criteria to remove them from further consideration in the soil analysis. All pixels with values less than 0 were classified as vegetation. The remaining "potential soil" pixels in the image were classified at several levels. Pixels with values between 0 and 7 were assigned to Serrano type soil class, i.e., have the physicochemical properties of Serrano Valley soils, and pixels with values between 7 and 11 have the physicochemical characteristics of soils from La Jolla Valley soil type. Pixels with values between 11 and 14 are located in the beach areas, and although they have soil properties, due to the high albedo of the sand they are projected in the high extreme of the soil range. The Serrano soil type is assigned a light gray and soils classified as La Jolla are assigned dark gray in Figure 9b. Comparing these results with the NDVI shows that areas with NDVI > 0.5 (black) follow the same spatial pattern as the pixels that were not classified (white) in Figure 9b. The image the La Jolla soil type pixels are clustered in patches, and the pixels classified as Serrano soil type are distributed more continuously over most of the image.

The first level of classification allowed us to select pixels classified as Serrano or La Jolla soil types. Only pixels with enough spectrally expressed soil to fall within the laboratory data range were analyzed in the second step. Thus the variability due to soils alone is identified and this variability is divided into that produced by La Jolla and Serrano soil types. This hierarchy optimizes the application of the organic matter vector.

4.4 Organic Matter Content Determination

Organic matter was estimated applying the vectors trained with laboratory data. Vector **a** was used to predict organic matter content in pixels classified as Serrano type soils in the first level classification and Vector **b** was used for pixels classified as La Jolla type soils (Fig. 6). Although the predicted organic matter values range from –15 to 10%, the range most pixels are found within the 1 - 6%, the same range as laboratory data. Pixels where soil is not the primary component show projected values outside this range. The ocean pixels have extreme high projected values of organic matter content and pixels having high NDVI (> 0.5) are projected to low or negative values of organic matter content, thus making it straight forward to remove them from consideration. The distribution of the AVIRIS soil organic matter for the two soil types (Fig. 7) followed the same trend as the laboratory data; the range is the same although the distribution is different. Figure 9c shows the results of the analysis for AVIRIS pixels having a high soil component (i.e. organic matter between 0 – 6%). The light gray indicates low and dark gray indicates high organic matter, white indicates pixels out of range in the first classification level or had negative organic matter content values. Soils with high organic matter content are not uniquely associated with La Jolla Valley and it is observed that the pixels mapped as La Jolla type soils (Figure 9b) show high organic matter content in Figure 9c (e.g., northeast area). This pattern agrees with our laboratory soils data. The spatial distribution of organic matter was related to the aspect (Fig. 8). North and east facing aspects are generally cooler and more humid and characteristically accumulate higher levels of organic matter. It can be seen that high values are predominant on north facing aspects while lower values are predominant on south facing slopes. AVIRIS is not simply mapping soils in separate valleys but the distribution of organic matter as a continuous variable. The spatial variation in organic matter is probably related to the steep terrain and aspect. This property is not unique to the respective valley and because variability within the valleys is high it is representative of the larger region. Palacios-Orueta and Ustin (1998b) found spatial variability in iron content was independent of the organic matter content but the variation in the valleys was sufficient to map the larger region.

5. CONCLUSIONS

HFBA was found to be a suitable method for soil analysis to determine relative changes in organic matter content because it is sequentially structured so that soil properties can be quantized into different ranges of variance. There are a combination of features that makes this spectral model work more efficiently than standard classification methods:

1. It is a mixture model therefore it can use continuous data over the whole spectrum.
2. It is steerable model, maximizing variability between classes and minimizing variability within classes, optimizing the amount of information extracted.
3. As a supervised classification algorithm, it can be focused on specific soil properties.
4. The Singular Value Decomposition equation efficiently discriminates between foreground soil properties and background environmental conditions.

5. The hierarchy reduces variability at each step allowing subtle absorption features to be extracted.

The results obtained when training the vectors with the laboratory data showed that the organization of the system and the singular value decomposition transformation work effectively in predicting organic matter from spectral data. Although the classified soils were not uniquely associated with either valley, the predictions of organic matter content from the image agreed with the soil characteristics from the field sampling locations. This methodology is based on a hierarchical analysis, which implies that variability is reduced at several steps, each time becoming more specific. The use of HFBA provides a mechanism to efficiently reduce the number of field measurements, or to use a vector developed from an area having similar soil variability. HFBA would be very useful for identifying changes in soil properties in a temporal framework. To understand landscape soil processes more completely, the data could be further analyzed in a geographic context, e.g., using a relational GIS database.

6. REFERENCES

Agbu, P.A., D.J. Fehrenbacher, and I.J. Jansen, 1990, "Statistical Comparison of SPOT Spectral Maps with Field Soil Maps," Soil Sci. Soc. Am. J., vol. 54, no. 3, pp. 812-818.

Clark, R.N., A.J. Gallagher, and G.A. Swayze, 1990, "Material Absorption Band Depth Mapping of Imaging Spectrometer Data using a Complete Band Shape Least-Squares Fit with Library Reference Spectra," Proceedings of the Second Airborne Visible/Infrared Image Spectrometer (AVIRIS) Workshop, Pasadena, California, pp. 176-186.

Coleman, T.L., P.A. Agbu, and O.L. Montgomery, 1993, "Spectral Differentiation of Surface Soils and Soil Properties - Is It Possible from Space Platforms?" Soil Sci., vol. 155, no. 4, pp. 283-293.

Edwards, R.D., D.F. Rabey, and R.W. Kover, 1970, "Soil Survey, Ventura Area, California," United States Department of Agriculture, United States Soil Conservation Service, 148 pp.

Green, R.O., J.E. Conel, and D.A. Roberts, 1993a, "Estimation of Aerosol Optical Depth and Calculation of Apparent Surface Reflectance from Radiance Measured by the Airborne Visible-Infrared Imaging Spectrometer (AVIRIS) using MODTRAN 2," SPIE Conf. 1937, Imaging Spectrometry of the Terrestrial Environment, 12 pp.

Henderson, T.L., M.F. Baumgardner, D.P. Franzmeier, D.E. Stott, and D.C. Coster, 1992, "High Dimensional Reflectance Analysis of Soil Organic Matter," Soil Sci. Soc. Am. J., vol. 56, no. 3, pp. 865-872.

Henderson, T.L., A. Szilagyi, M.F. Baumgardner, C.T. Chen, and D.A. Landgrebe, 1989, "Spectral Band Selection for Classification of Soil Organic Matter Content," Soil Sci. Soc. Am. J., vol. 53, no. 6, pp. 1778-1784.

Kruse, F.A., K.S. Kiereinyoung, and J.W. Boardman, 1990, "Mineral Mapping at Cuprite, Nevada with a 63-Channel Imaging Spectrometer," Photogramm. Eng. and Remote Sens., vol. 56, no. 1, pp. 83-92.

Lewis, D. T., P.M. Seevers, and J.V. Drew, 1975, "Use of satellite imagery to delineate soil associations in the sands hills region of Nebraska," Soil Sci. Soc. Am. Proc., vol. 39, no. 2, pp. 330-335.

Matlab (1994). The MathWorks, Inc.

Palacios-Orueta, A. 1997, "Soil Discrimination with Laboratory Spectra and Airborne Imaging Spectrometer Data (AVIRIS)," Department of Land, Air and Water Resources. Davis, University of California, 120 pp.

Palacios-Orueta, A. and S.L. Ustin, 1996, "Multivariate Classification of Soil Spectra. Remote Sens. Environ., vol. 57, no. 2, pp. 108-118.

Palacios-Orueta, A. and S.L. Ustin, 1998, "Remote Sensing of Soil Properties in the Santa Monica Mountains: I. Spectral Analysis," Remote Sens. Environ., (in press).

Pinzón, J.E., S.L. Ustin, C.M. Castaneda, and M.O. Smith, 1998, "Investigation of Leaf Biochemistry by

Hierarchical Foreground/Background Analysis," IEEE Trans. Geosci. and Remote Sens., (in press).

Pinzón, J.E., S.L. Ustin, Q.L. Hart, S. Jacquemoud, and M.O. Smith, 1995, "Using Foreground/Background Analysis to Determine Leaf and Canopy Chemistry," Summaries of the Fifth Annual JPL Airborne Earth Science Workshop: AVIRIS Workshop, vol. 1, pp. 129-132.

Roberts, D.A., M.O. Smith, and J.B. Adams, 1993, "Green Vegetation, Nonphotosynthetic Vegetation, and Soils in AVIRIS Data," Remote Sens. Environ., vol. 44, nos. 2/3, pp. 255-269.

Smith, M.O., D.A. Roberts, J. Hill, W. Mehl, B. Hosgood, J. Venderbout, G. Schmuck, C. Koechler, and J. Adams, 1994, "A New Approach to Quantifying Abundances of Materials in Multispectral Images," Institute of Electrical Electronics Engineering, Int. Geosci. Remote Sens. Trans., IGARSS '94, California Institute of Technology, Pasadena, CA (CD), vol. 4, pp. 2372-2374.

Smith, M.O., S.L. Ustin, J.B. Adams, and A.R. Gillespie, 1990, "Vegetation in Deserts I. A Regional Measure of Abundance from Multispectral Images," Remote Sens. Environ., vol. 31, no. 1, pp. 1-26.

Stoner, E.R. and M.F. Baumgardner, 1981, "Characteristic variations in reflectances of surfaces soils." Soil Sci. Soc., Am. J., vol. 45, no. 6, pp. 1161-1165.

Table 1. Table of classification errors after first level classification step from spectral analysis of soil samples.

		Number of soil samples that belong to:		
		La Jolla	**Serrano**	**Total**
Number of soil samples classified in:	**La Jolla**	34	1	35
	Intermediate	5	2	7
	Serrano	3	29	32
	Total	42	32	74

Table 2. Quantization levels (R1-R4) for ranges of soil organic matter content and number of samples in the training set and in the whole laboratory soil sample data set.

	Organic Matter (%)							
	La Jolla Valley				**Serrano Valley**			
	R1	**R2**	**R3**	**R4**	**R1**	**R2**	**R3**	**R4**
Range Center	0.98	2.33	3.68	5.03	1.1	2.04	2.99	3.93
Training Set	3	6	3	3	2	8	1	2
Complete Data Set	4	15	13	10	7	13	7	5

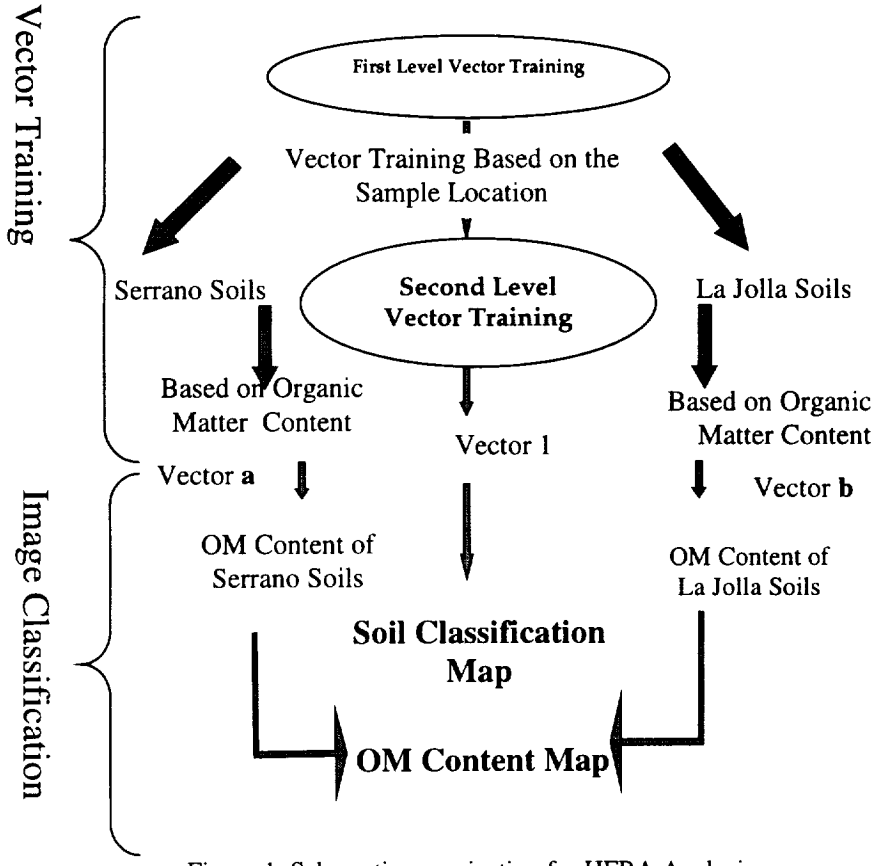

Figure 1. Schematic organization for HFBA Analysis.

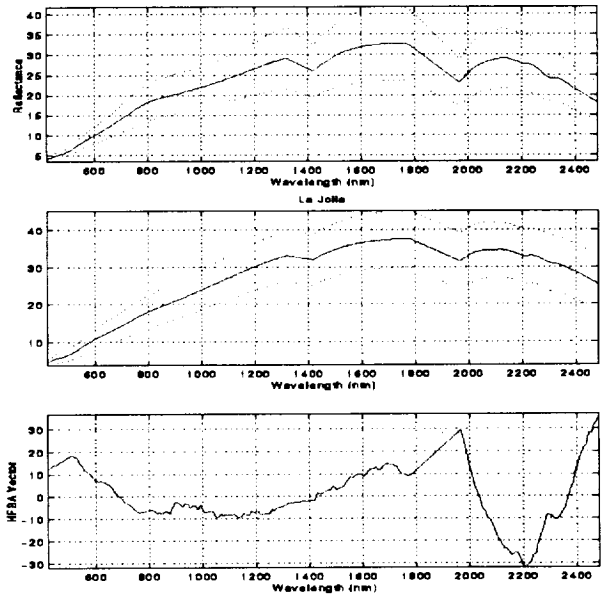

Figure 2. Mean reflectance spectra for La Jolla (a), Serrano Valleys (b) and HFBA vector (c) for first level of classification.

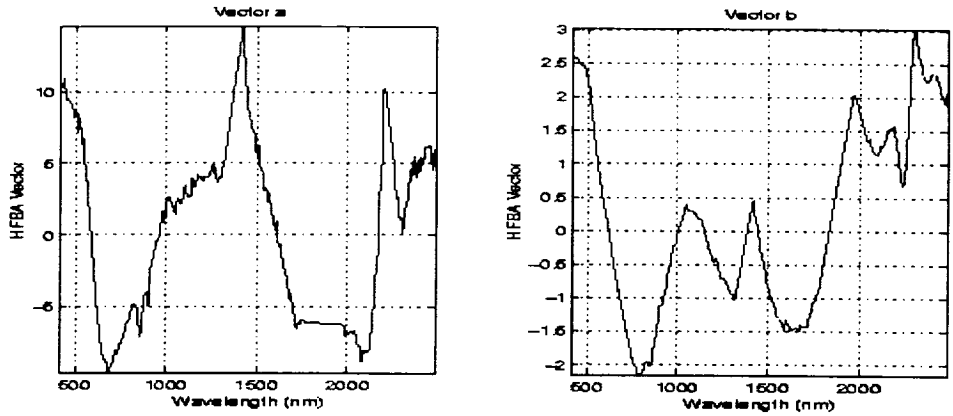

Figure 3. HFBA training vector weightings for predicting organic matter content. Vector *a* corresponds to Serrano and vector *b* to La Jolla type soils.

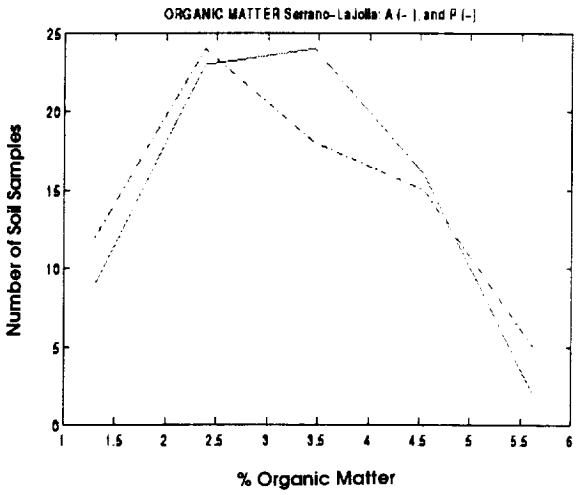

Figure 4. Distributions of the predicted and the measured data for organic matter content for laboratory soil samples. The continuous line represents the predicted values and the dashed line represent the measured values.

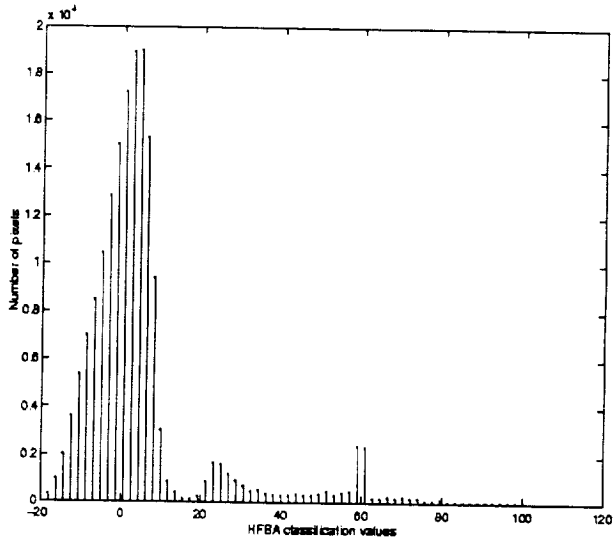

Figure 5. Histogram of the distribution of AVIRIS soils after applying the classification vector at the first level.

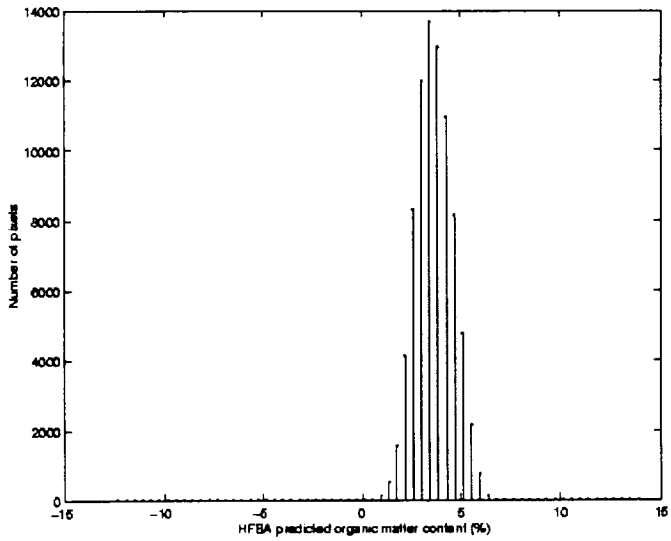

Figure 6. Predicted organic matter content distribution from AVIRIS data.

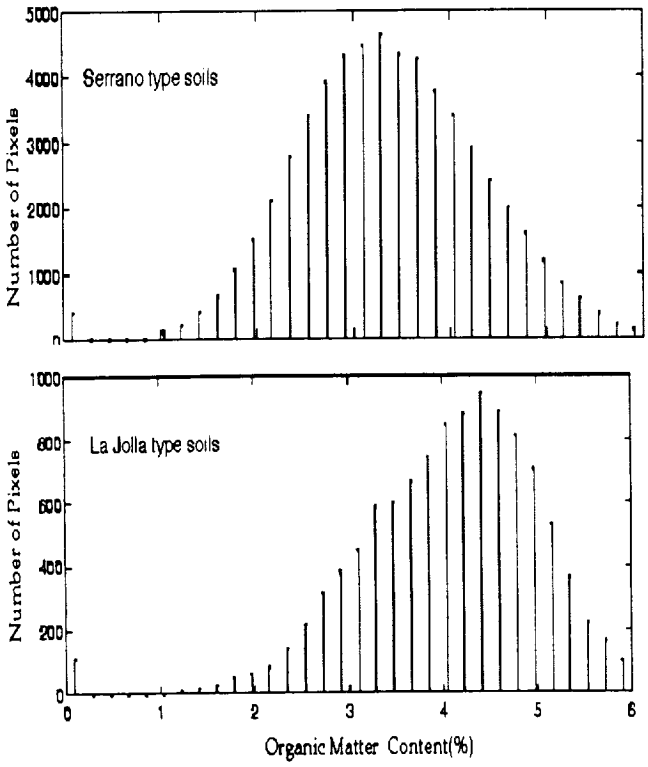

Figure 7. Predicted organic matter content distributions for soils having characteristics of Serrano and La Jolla type soils.

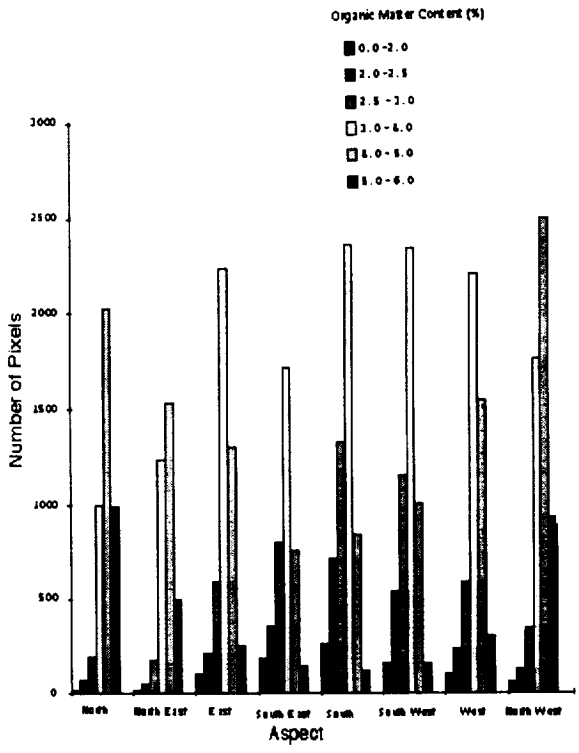

Figure 8. Predicted distribution of organic matter content for different aspects from AVIRIS data.

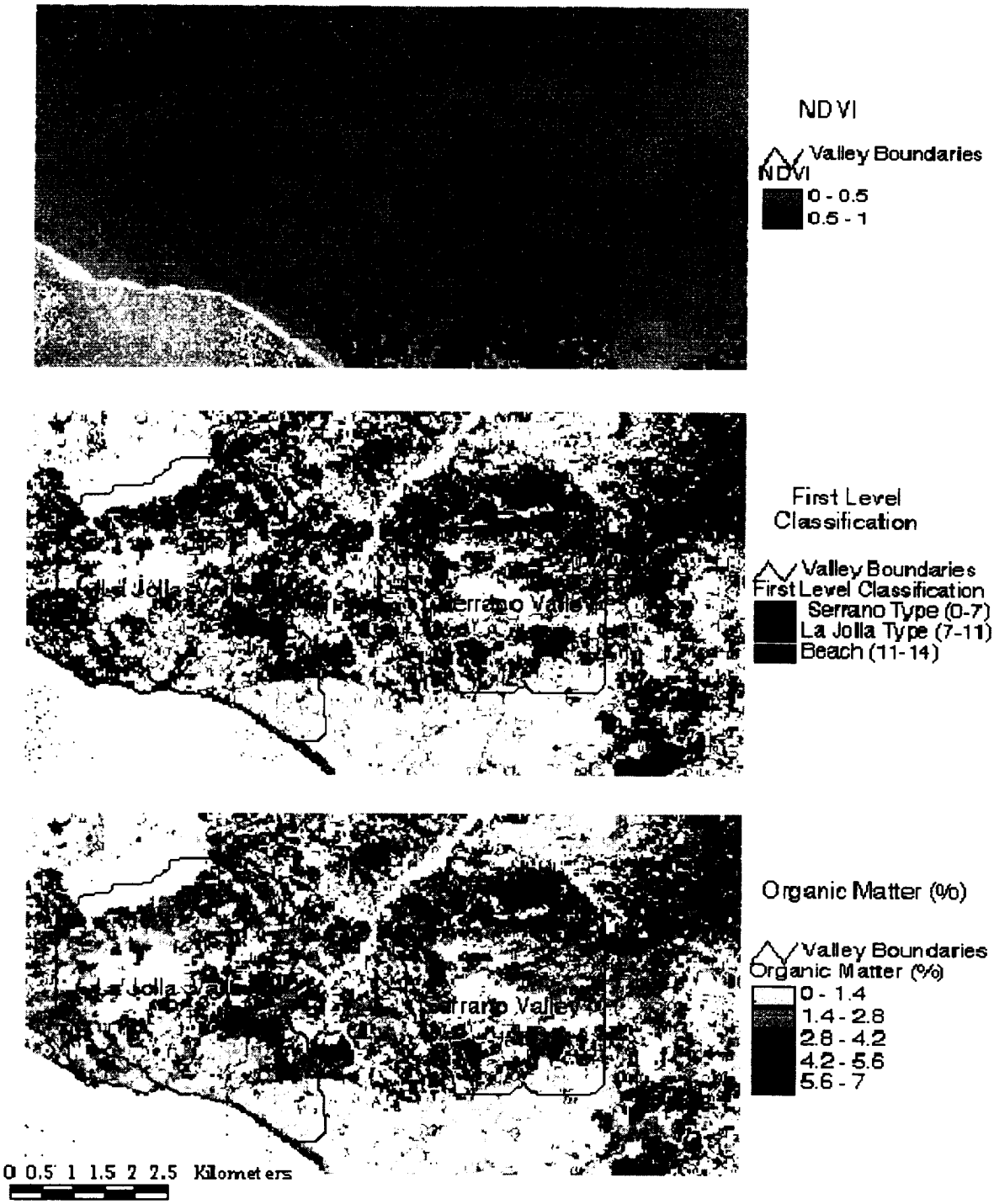

Figure 9a. AVIRIS NDVI results showing location of vegetated pixels. Black indicates high vegetation (NDVI>0.5), light gray indicates the low vegetation cover. Figure 9b. Classification results at the first level. White corresponds to ocean and vegetation dominated pixels. Light gray corresponds to Serrano type soils, dark gray to La Jolla type soils and black to the beach areas. Figure 9c. Predicted organic matter ranges for pixels having low vegetation cover. Black and dark gray correspond to high levels and light gray corresponds to low levels, while to ocean and vegetation dominated pixels.

Calibration Targets of the Southwest:
Albedo and Homogeneity Comparisons Using AVIRIS Data

Betina Pavri and Robert Green
Jet Propulsion Laboratory[1]
California Institute of Technology
Pasadena, CA 91109

Abstract: Various locations in the southwestern U.S. are used to calibrate remote sensing instruments. This study shows how some of these targets compare in terms of albedo and homogeneity, and records the variation of these factors for a single location (Ivanpah Playa) over a period of one year. Results indicate that there is a great deal of variation among these targets in albedo, spectral flatness, and surface uniformity, and that these factors can change throughout the year.

Introduction: The targets chosen for this study are listed in Table 1.

Table 1: Targets included in study

playa name	date of image	latitude	longitude
Ivanpah Playa	960408	35°32'30"	115°23'40"
	960615		
	961101		
	970304		
Lunar Lake	940405	38°23'41"	115°59'37"
Rogers Dry Lake (Edwards AFB)	930518	34°55'19"	117°50'30"
	970228		

These playas have been chosen for AVIRIS radiometric calibration experiments because of their size, high albedo, spectral flatness, and homogeneity. These factors are critical for a variety of reasons. First, large target is easily located in the final image, and a gives the field team a good selection of possible sites to set up. Second, a bright target provides good signal/noise for a radiometric calibration, while spectral flatness guarantees that detectors in all bands receive sufficient signal/noise for calibration. Finally, spatial homogeneity in the calibration area ensures that the field data and remotely sensed data can be compared with minimal concern about sampling issues. If the region were not homogeneous, it would be difficult to be sure if the spectra collected by the field team were representative of the calibration region as a whole.

Figure 1 illustrates spectral data for the three playas, and emphasizes their spectral flatness in comparison to White Sands National Monument.

[1] *The research described in this paper was carried out by the Jet Propulsion Laboratory under a contract with the National Aeronautics and Space Administration.*

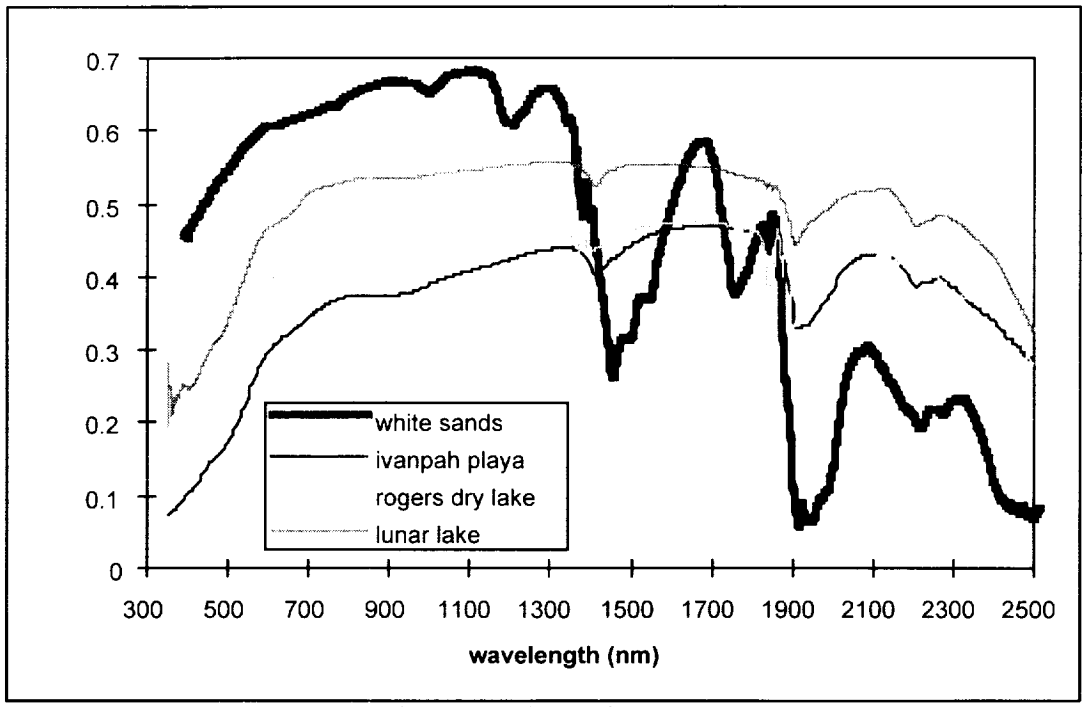

Figure 1: Reflectance of various calibration targets as measured by a field spectrometer. Note how albedo and spectral " flatness" compare to another popular remote sensing target, White Sands National Monument.

Method: AVIRIS data at 20m resolution was used to evaluate the homogeneity of each target. Bands from 710 - 870nm were averaged for the analysis. To simulate the resolution of some proposed spaceborne instruments, the pixels in each image were binned into 13x13 and 51x51 groups, so that homogeneity was measured on two scales: 260m and 1020m (Figure 2). Homogeneity was quantified by the following equation:

$$\text{homogeneity factor} = \frac{\text{average radiance (AVIRIS pixels)}}{\text{standard deviation of radiance (AVIRIS pixels)}}$$

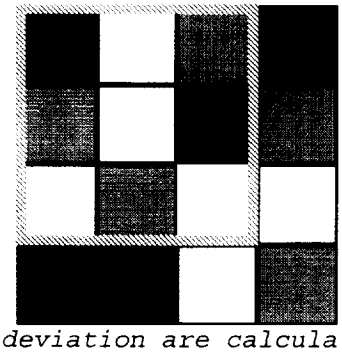

Figure 2: Mean and standard deviation are calculated for a group of 20m AVIRIS pixels. Group is defined by scale on which homogeneity is to be calculated; the statistics for the group are used to calculate the homogeneity factor for the central pixel.

In the resulting images, regions homogeneous on the scale of interest appear brighter than non-homogeneous ones. The ratio is independent of albedo.

Statistics were extracted for a sample region in each homogeneity image. Evaluation areas did not include the entire playa surface, but were contiguous regions specifically chosen to exclude anthropogenic structures such as roads, runways, and buildings. This was done on the assumption that only the most homogeneous regions of each target would be used for calibration purposes. The same area of each playa was used for the evaluation at both the 260m and 1020m scales. For Ivanpah Playa, a single region was evaluated for different times throughout one year.

Results: The results of the homogeneity transformation are shown in Figure 3. Note that the locations of the most homogeneous (brightest) regions vary with scale, and that features at the scale of interest are emphasized (runways in the 260m scale image and large-scale drainage patterns in the 1020m scale image).

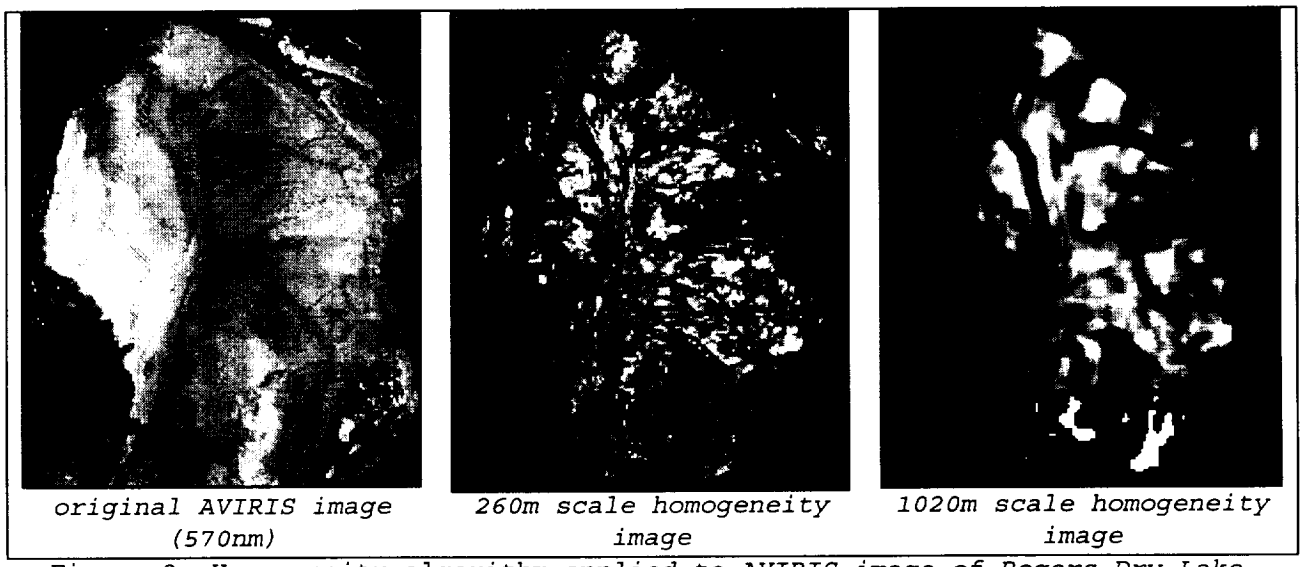

original AVIRIS image (570nm) | *260m scale homogeneity image* | *1020m scale homogeneity image*

Figure 3: Homogeneity algorithm applied to AVIRIS image of Rogers Dry Lake. Note how runways, roads, and drainage patterns are emphasized.

In Figure 4, note that average homogeneity values as well as the range of homogeneity values vary with the playa chosen. Lunar Lake has the highest overall homogeneity values, but few of them, as its average homogeneity value is slightly lower than that of Rogers Dry Lake. At the 1020m scale, Rogers Dry Lake has both the greatest homogeneity value of the three playas and the largest mean value as well. According to this analysis, Lunar Lake might be superior for high spatial resolution instruments, but would probably be a poor choice for instruments with coarser resolutions on the order of 1km.

Figure 5 shows that Ivanpah playa varies in both its average homogeneity value and the range of values over one year. Not only do the values change, but the locations of the most homogeneous regions change as well, depending on weather and other factors such as off-road vehicle use since the last rain.

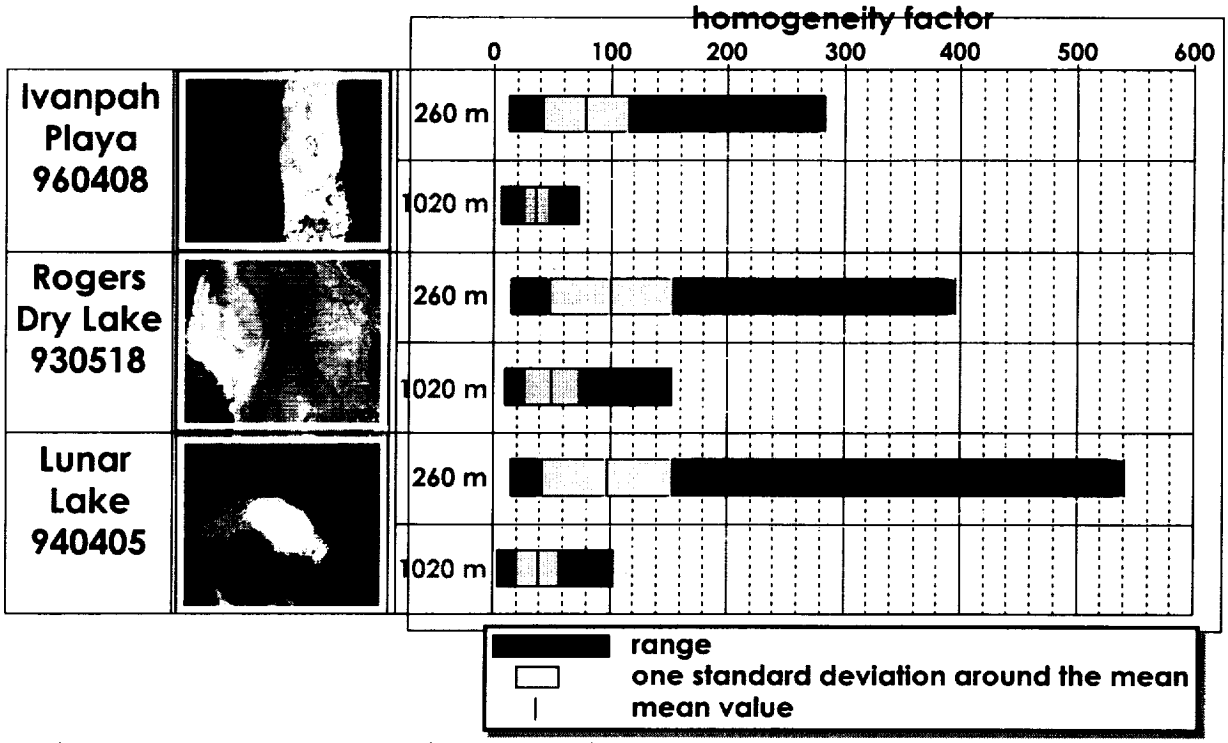

Figure 4: Playa homogeneity comparisons. All AVIRIS images are single band images, not homogeneity images, and are shown at the same scale (11 km wide).

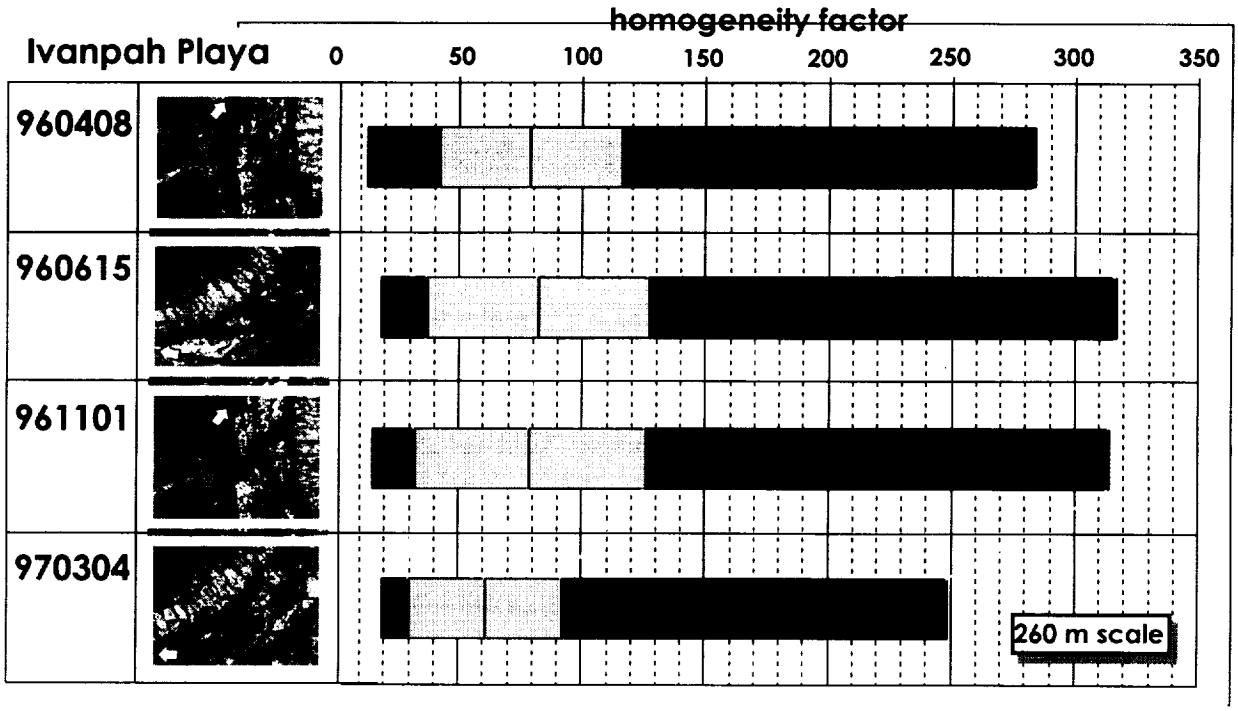

Figure 5: Seasonal variation in homogeneity of Ivanpah Playa. Homogeneity images shown on left. Note that 960615 and 970304 images are perpendicular to 960408 and 961101 data. White arrows indicate north in each image.

Conclusions: Choosing a good calibration experiment target involves balancing issues such as accessibility and facilities with the desire for a pristine, homogeneous surface on which to work. Lunar Lake may be homogeneous, but is remote and often flooded; Ivanpah Playa gets some offroad vehicle use, but is close to the highway, and has hotel facilities close by. Rogers Dry Lake is relatively pristine, but requires access to Edwards Air Force Base -- access which can be revoked on short notice. The inter-playa comparison indicates the following: first, playas vary not only in overall (average) homogeneity, but also in the range of the homogeneity factors observed. Second, the targets most homogeneous on a small scale are not necessary the most homogeneous on larger scales, so it may be necessary to choose a target based on the spatial resolution of the instrument to be calibrated. Further, the homogeneity and brightness of a playa, as well distribution of homogeneous regions within it, varies with time. As a result, analyses such as this can provide guidelines on good places to work, but a field team needs to make an evaluation of the best location to set up at the time of a radiometric calibration experiment.

ROBUST FEATURE EXTRACTION FOR HYPERSPECTRAL IMAGERY USING BOTH SPATIAL AND SPECTRAL REDUNDANCIES

Jorge E. Pinzón[1], Susan L. Ustin[2], John F. Pierce
[1] Dept. of Applied Mathematics, [2] Dept. of Land, Air, and Water Resources,
University of California Davis, CA, 95616
[3] [2]KT-Tech, Inc., 9801 Greenbelt Road, Suite 314, Lanham MD 20706

1 INTRODUCTION

As we move into the next century, a wide range of new satellites and airborne sensors will become available with a variety of interesting problems for data analysis and signal processing. In particular, hyperspectral sensors with both, a large set of spatially contiguous spectra and a large set of spectrally contiguous images will require new techniques that ideally would treat the spatial and spectral patterns in the data simultaneously. Resolving the significant spectral and spatial properties associated to ecological processes and interactions is critical to successful interpretation of remote sensing data.

In hyperspectral images is desirable to classify images within the conventional frame of reference of field and laboratory observations with methods that avoid intrinsic singular problems. In this respect, spectral mixture analysis (**SMA**) has become a well established procedure for analyzing imaging spectrometry data (Ustin et al., 1993; Ustin et al., 1994; Roberts et al., 1990; Sabol et al., 1990; Gamon et al., 1993). SMA is a structured and integrated framework that simultaneously addresses the mixed-pixel problem, calibration, and variations in lighting geometry and displays the results in terms of proportions of endmembers that can be related easily to standard ecological observational units (e.g., cover). The general form of the SMA equation for each band is expressed as:

$$R_b = \sum_{em=1}^{N_e} F_{em} R_{em,b} + E_b \tag{1}$$

where R_b is the radiance at band b, F_{em} is the fraction coefficient of each endmember R_{em} weighting their radiance at band b, and E_b is an error term accounting for the unmodeled radiance in band b. Endmembers are chosen to explain the spectrally distinct materials that form the convex hull of the spectral volume. This approach works best when describing a few spectral types that, in various mixtures, can account for most of the variance in an image data set. It does not mean, however, that it is possible to identify any specific material. SMA works less well when the spectral features of interest are minor components of the total variance. In fact, SMA has the disadvantage, at least for this application, of approximating linearly the natural (non-linear) complexity of materials represented by the mixture of endmembers. This produces a non-unique mixing model to identify and quantify materials that occur at the sub-pixel scale (Sabol et al., 1992). In summary, the technique is relatively insensitive to subtle absorption features, and produces significant quantification errors due to endmember variability from linear and nonlinear mixtures (e.g. from scattering, and lighting geometry) in a pixel.

Boardman (Boardman, 1994), used a geometric approach based on the convex hull of the spectra projected into the mixing space to find a solution that minimized spectral variation for some features while accentuating others. His technique is still a SMA approach that automatically derives the number of

endmembers and estimates their pure spectral composition (Boardman, 1994), but it is suboptimal in the presence of multiple mixing. More recently, Harsanyi and Chang (Harsanyi and Chang, 1994) developed a mixture technique that rejects undesired interference by performing an orthogonal subspace projection (**OSP**). This technique simultaneously reduces data volume and emphasizes the presence of a signature of interest. Bolster et al. (Bolster et al., 1996) seeking the same goals, instead use the first difference partial least squares regression (**PLS**) that is based on a singular value decomposition (**SVD**) of the whole spectrum data set. SVD reduces noise-related interference, common in a first difference analysis, and reduces the analysis into a smaller set of independent variables. Both, OSP and PLS, achieve good performance in detecting material abundances at low levels for a particular scenario by incorporating the variability of the material abundance into the more important independent variables (factors) but they are unable to extend the application to other scenarios. In order to develop a directed search methodology to locate the desired robustness (analytic) property, Smith et al. (Smith et al., 1994) proposed a revised SMA technique, that they termed Foreground/Background Analysis (**FBA**). Harsanyi's approach shares the properties of orthogonal space projection and a similar rationale with the FBA technique. In this technique, spectral measurements are divided in two groups of foreground and background spectra that comprise a selected subset of spectra which emphasizes the presence of a signature of interest. In defining both groups they do not include intermediate mixtures between foreground and background. In that way, FBA vectors should be sensitive to minor sources of foreground spectral variation and insensitive to background spectral variation. The goal of FBA is to project spectral variation along the most relevant axis of variance that maximizes the spectral differences between the foreground and background, while minimizing spectral variation within each group. Their FBA approach defines a weighting vector $w = (w_1, w_2, \ldots, w_{Nb})$, with components w_b at each channel $b = 1, \ldots, Nb$, such that all foreground spectral vectors, $R_f = (R_{f,1}, R_{f,2}, \ldots, R_{f,Nb})$, are projected to 1 while background spectral vectors, R_b, to 0. This property is defined by the FBA system of equations:

$$\sum_{b=1}^{Nb} w_{F,b} R_{F,b} + T = 1 \qquad foreground \tag{2}$$

and

$$\sum_{b=1}^{Nb} w_{B,b} R_{B,b} + T = 0 \qquad background$$

where T provides a translation that is typically required to optimize the FBA system. As stated FBA is in essence another linear classifier of the spectra that can be applied to identify low and high material abundances. Pinzón et al. (Pinzón et al., 1994; Pinzón et al., 1995) modified the FBA linear system to project a subset of spectra into relevant axis of continuous property variation, like chemical content.

In this paper, we present a supervised classification technique that discriminates broad categories of materials of the surface in terms of ground truth features, such as vegetation characteristics, and soil properties. The actual relationships between these two ecological units are often difficult to resolve with respect to understanding which of many potential interacting factors is significant in a particular locality. We decompose the interaction between the spatial and spectral domains associated to these units by using wavelet tools and a hierarchical foreground background analysis (HFBA). Wavelets provide spatial coherence information that should allow us to generalize the results from the spectral features extracted by HFBA.

2 METHODS

For most purposes the problem of supervised classification can be formulated as follows: given an *input space* X and a desired property in an *output space* Y, there is an unknown (functional) relationship, F, between X and Y that is represented by a subset of m samples, from which one wants to guess the

$X - Y$ relationship. In general, F takes the form of a deterministic function + noise. One is given the training set of m samples and the guess functional $\widehat{F}$, the problem is to guess, using $\widehat{F}$, what output space value, $\widehat{y}$, is the most appropriate for a given input x. The precise meaning of "appropriate" can be difficult, and is measured through loss functions. A popular choice is the quadratic error function:

$$\epsilon(X,Y) \;=\; \sum_{i=1}^{m}(\widehat{F}(x_i) - y_i)^2 \tag{3}$$

The loss function and the way it is minimized determine the method used and its ability to generalize. Under this definition the problem of supervised classification has been identified by many other names, such as inductive inference, regression, statistical inference, model inversion, etc.

2.1 HFBA

Pinzón et al. (Pinzón et al., in press; Pinzón, 1996) modified the FBA system to project a subset of spectra into the most relevant axis of variation of a desired property. In this case, the system of equations is given by

$$\sum_{b=1}^{Nb} w_b R_{i,b} \;+\; T \;=\; c_i \tag{4}$$

That is, the reflectance matrix R times the FBA weighting vector w is equal to the desired ground characteristic C. The goal of this system is to relate spectral and ground variation along the most relevant axis of spectral variance. The general form of the FBA system has the form of a generic Finite Impulse Response (**FIR**) filter equation in time domain (Smith et al., 1996):

$$y(t) \;=\; \sum_{j=1}^{n} h(k)x(t - k/f_s)$$

where f_s is the sampling frequency and $h(k)$ are the Fourier series coefficients of the frequency response of the FIR filter, $H(f)$. Therefore, solving the FBA system plays similar role as the design process of a FIR filter.

To improve the detection of minor sources of spectral variation, we can apply the process iteratively obtaining a system of equations that works at different levels of accuracy. We stop at the level of the system noise. Solving each equation in the iteration system is the so called hierarchical FBA technique (**HFBA**) which derives sequentially a series of FBA vectors, with different general discriminating features. In essence, the HFBA system is an iteratively decimation process which extracts details in each of the levels.

The power of the HFBA method becomes apparent as we begin to catalogue more precisely the performance of the SVD in energy-packing and avoidance of overfitting problems due to its stability properties. First, r, the rank or dimension of the matrix R, could be estimated by examinating the number of non-zero singular values (Golub and Van Loan, 1989). Second, the decomposition $R = U\Sigma V^*$ provide an approximation of the matrix R by a sum of rank-one matrices (Golub and Van Loan, 1989). That is,

$$R \;=\; \sum_{j=1}^{r} \sigma_j u_j v_j* \tag{5}$$

Here, r is the rank of the matrix R, and σ_j its singular values, u_j, and v_j the left and right singular column vectors respectively. This is easily shown by noticing that Σ can be written as a sum of r matrices $\Sigma \;=\; \sum j = 1^r \Sigma_j$, where each Σ_j has just one nonzero entry σ_j . Then Equation 5 follows. One can find a very large number of different representations of R as a sum of rank-one matrices. However, Equation 5 represents the best approximation of R. That means that the hyper-ellipsoid with principal axis of

length σ_j's, provides a very important property: the q-th partial sum captures as much of the detail of R as possible (Golub and Van Loan, 1989). That is, the best least squared approximation of a matrix R by matrices of lower rank q ($q < r$), is given by $R_q = \sum_{j=1}^{q} \sigma_j u_j v_j*$. Third, when solving the FBA equations at each level with spectral matrices R close to rank-deficient, it turns out that most of the standard algorithms used to solve such systems have ill conditioned stability properties. In such cases, SVD is a good stable alternative (Golub and Van Loan, 1989). Computationally, SVD is more expensive than the standard methods, but more accurate and stable. This is the principle advantage of using SVD in the solution of the FBA equations: a stable method to process hyperspectral (rank-deficient) matrices R.

2.2 Wavelets

Wavelets are mathematical functions that split data (image or signal) into different scale components that provide the best approximation at each scale. The wavelet analysis starts with a function $\psi(x)$, called mother wavelet that is well localized and oscillating. By localization, we mean $\psi(x)$ decreases rapidly to zero as x tends to infinity. Oscillating requires that ψ behaves as a wave, that is, integrals of ψ and its firsts k moments be zero.

In summary, a wavelet decomposition can be seen as an application of a pair of complementary low and high pass filters, H and G respectively. Thus, a generic wavelet transform is depicted in Figure 1.

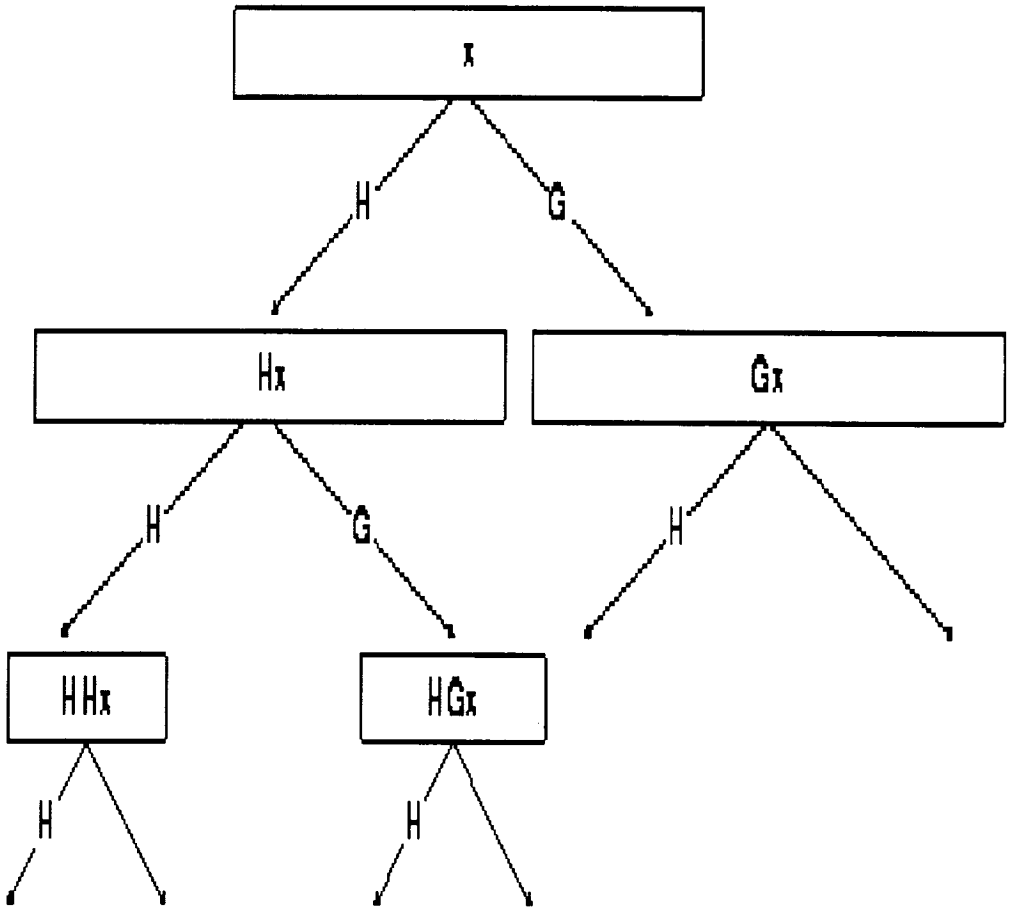

Figure 1. Discrete generic wavelet transform. From (Wickerhauser, 1994).

The properties of the wavelets are determined by the properties of the filters H and G, and by the

properties of the signal being analyzed. The construction of wavelets then begins by designing the filters that could be a basis of the space we want to transform. To lead to high compression and get coherent information we use a coiflets with 4 vanishing moments, avoiding at the same time to include noise into the estimated generalization functional, $\widehat{F}$.

3 Results

We present two applications of the HFBA: 1) retrieval of biochemical properties using laboratory spectra and chemical content of fresh leaves samples, and 2) discrimination of soil in the Santa Monica Mountains.

3.1 Retrieval of biochemical properties

For this application, we have fresh leaf samples from 3 different sites: from Santa Monica Mountains, CA, from Joint Research Center, Ispra, Italy, and from Jasper Ridge Biological Preserve at Stanford University. The samples are botanically very heterogenous, specially those in JRC. We have trained each HFBA vector with 20% of the samples from JRC and validated the results with the remaining data set. Three levels of detection were obtain, the first discriminates monocots from dicots, the second low water content from high water content and finally the actual chemical content was predicted (here we present nitrogen and water results). Monocot and dicot samples are identified by their spectral features in the visible region, where monocots are brighter due to their higher chlorophyll (a and b) content. That property is precisely the characteristic manifested in the HFBA vector, Figure 2(a). Similarly, low and high water contents are spectrally discriminated by the main water absorption features at 1400 nm and 1900 nm and their interaction in the blue visible region, Figure 2(b).

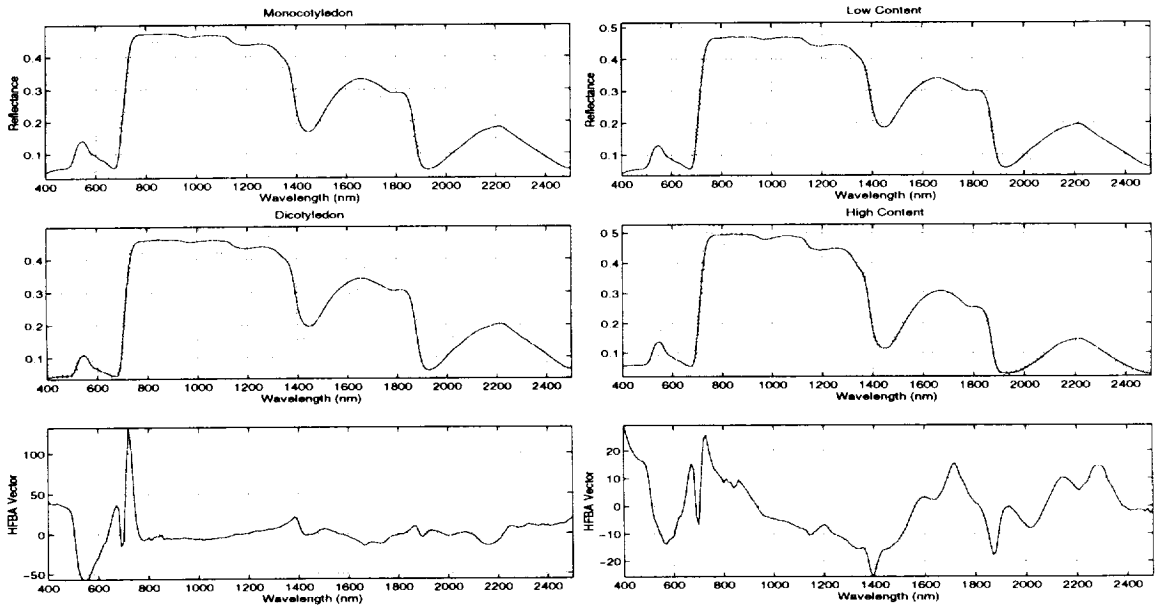

Figure 2. Classification step: (a) monocots vs dicots (b) high vs low water content

The statistics of the prediction indicates the good performance of HFBA at the laboratory level: regressions of 0.71 and 0.75 with good fit of the distribution of actual data, Figure 3.

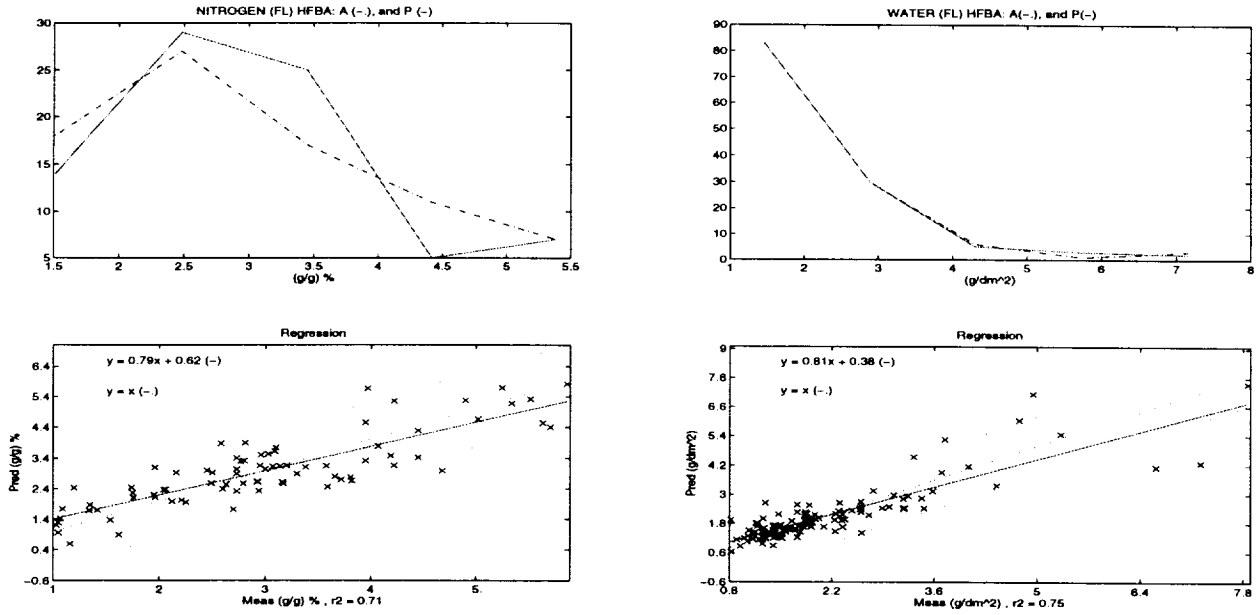

Figure 3. Retrieval of biochemical properties: (a) nitrogen concentration (b) water content.

3.2 Discrimination of Soil in the Santa Monica Mountains

We have used two levels of HFBA to discriminate soils and soil properties from two valleys in the Santa Monica Mountains (Serrano and La Jolla) using AVIRIS data. The region is highly susceptible to erosion and wildfires due to the xeric soil moisture regime typical of Mediterranean climates, as well the steep terrain. The combination of all these factors markedly increases heterogeneity in the distribution of soil properties. Large coverage and sufficient spatial resolution are required to understand soil pattern differences. AVIRIS satisfies these two requirements. The classification vector discriminates soils with high organic matter from those with low organic matter (see Figure 4). Ninety four percent of the samples were correctly classified. The other six percent show intermediate organic matter contents.

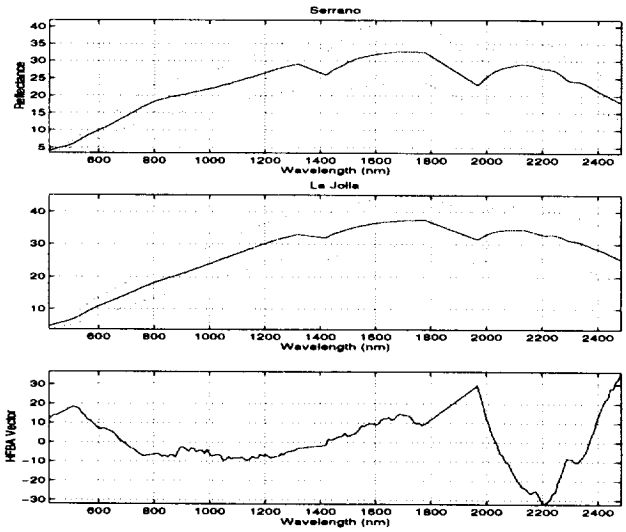

Figure 4. HFBA classification vector.

It can be observed that the two spectral areas most important for discrimination are between 1000nm and 2200nm (OH-AL and Mg-OH absorptions). The characteristic of the vector between 600 and 800 nm also could be used to detect vegetation and it will work like NDVI for this purpose. The first image in Figure 5 shows the HFBA spatial distribution. After applying coiflet wavelets (Figure 5, second row), the spatial coherence is manifested and this allows noise reduction and improves the performance of HFBA vectors. The final classification allows a better interpretation of the ecological processes involved. Image classification follows known spatial characteristics. Finally, Figure 6 shows the organic matter spatial distribution from AVIRIS data predicted by HFBA and coiflet noise reduction. High values are concentrated near ridges of the mountains as expected. It can be observed that the pixels mapped as La Jolla soils in the classification image also show high content of organic matter which agrees with our laboratory data.

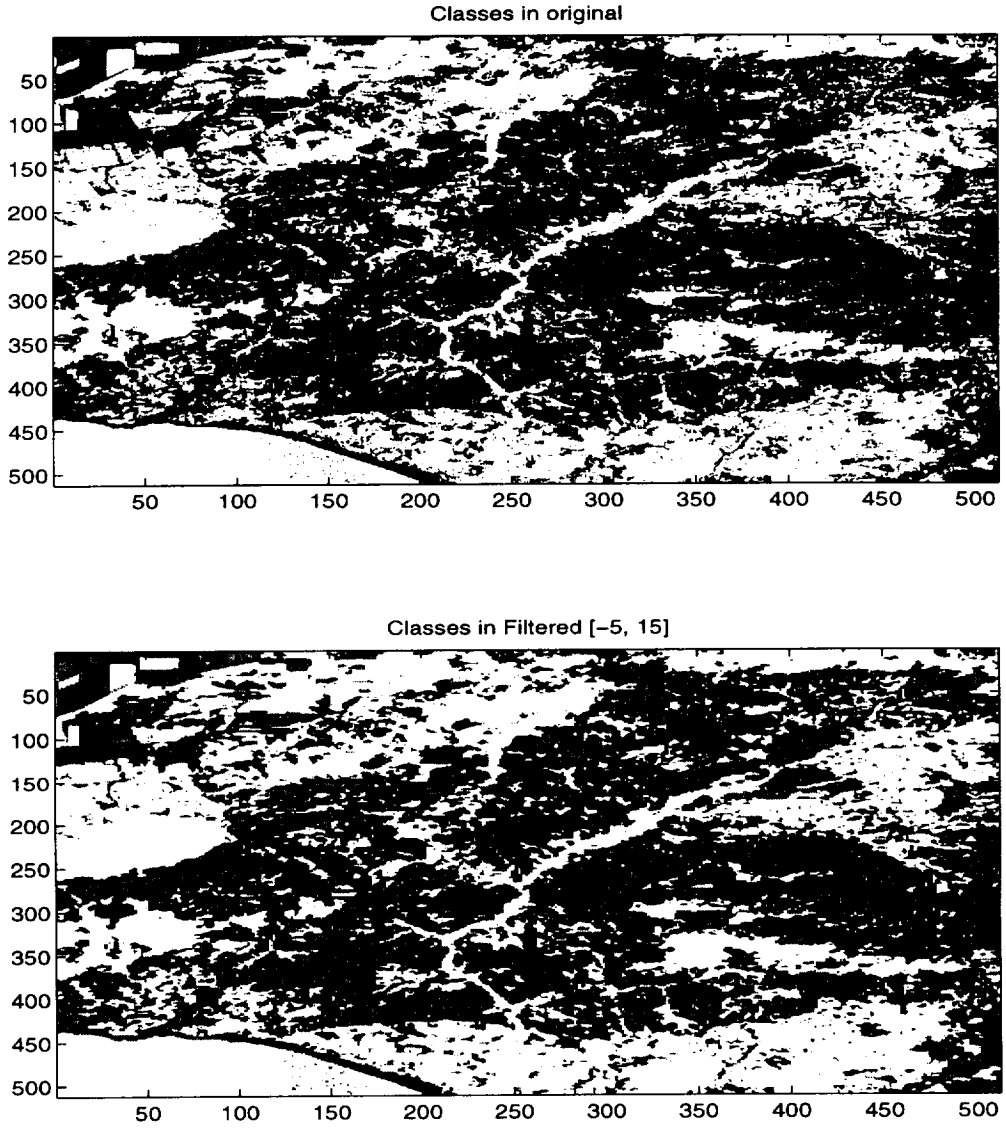

Figure 5. (a) HFBA classification and (b) spatial coherence manfested after coiflet noise reduction.

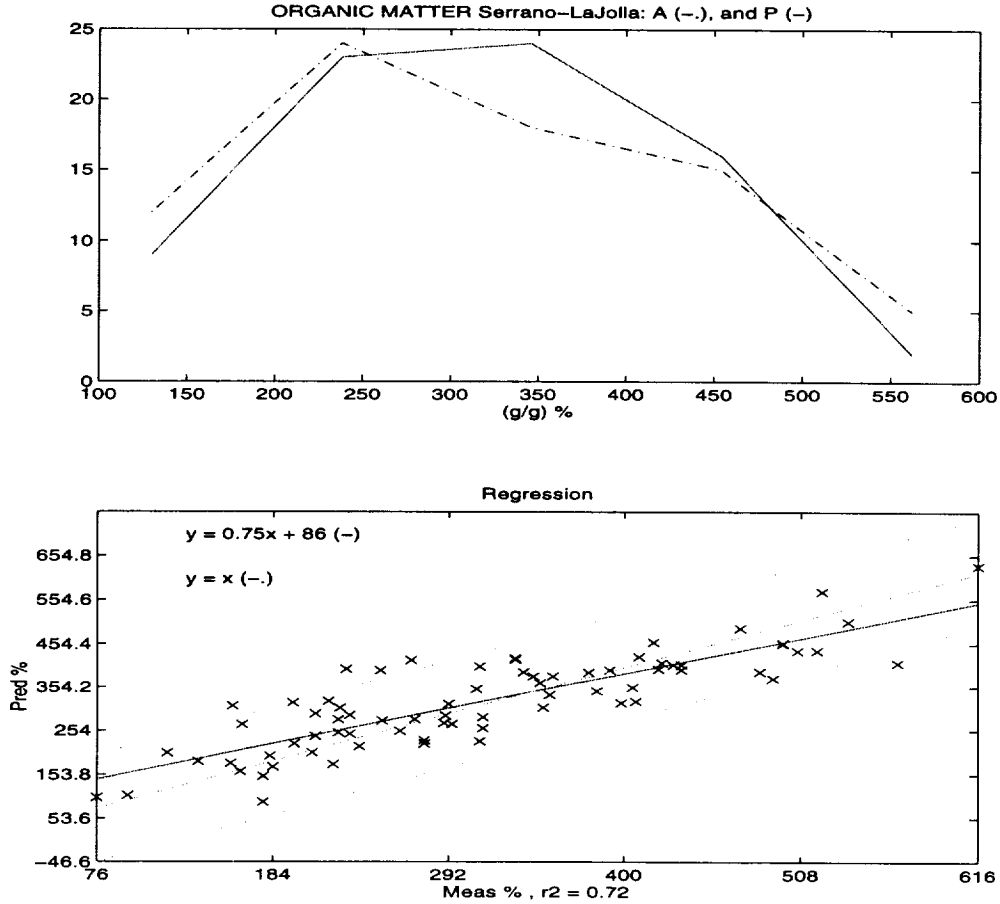

Figure 6. (a) HFBA classification and (b) spatial coherence manfested after coiflet noise reduction.

4 Conclusions

A new robust approach for the detection and classification of materials was developed and tested. The technique uses a combination of an iterative hierarchical application of a modified FBA technique and coifle noise reduction to detect functional relationships between spectra and ground truth features at different levels of accuracy.

The power of the HFBA technique is based on the attractive properties of the SVD transform in information packing and avoidance of overfitting problems by minimizing extraneous noise in the analysis. The technique was trained over laboratory data and applied to AVIRIS images. It is clear from the above experiments that the proposed approach is promising.

By the iterative hierarchical procedure we force the system to account for important non-linear dependencies directly related to spectral scaling. In that respect, one of the strong points of the proposed method is that we can group together samples with similar anatomical properties manifested spectrally. However, if the distribution of these properties is continuous, samples near the boundaries of the discriminant regions could be misclassified weakening the helpfulness of the classification step. In particular, as spatial variation of vegetation is high, the selection of a training set that explains the mixing presented at different spatial scales is critical. This process seems to be a key factor for understanding the good performance of HFBA dealing with sub-pixel scaling issues in this application, although HFBA was not properly equipped to deal directly with these spatial issues. There are more appropriate image analysis methodologies concerning spatial scaling problems such as wavelet transforms. The wavelet decomposition gives a better representation of spatial distribution (at different scales) of the data, and especially a better

description of the properties of samples near to discriminant boundaries. Clearly, these points have to be further investigated to identify the relationship between spatial-spectral scales.

As a conclusion, we consider that a combination of HFBA and wavelets or other spatial scaling transforms has significant potential and certainly deserves further investigation. There are many aspects for the discrimination among materials that still need investigation. The aspects we have in mind are aptly illustrated by Yves Meyer in his book *Wavelets: algorithms and applications* (Meyer, 1993): "It is notable that Mandelbrot used the word *describe* and not *explain* or *interpret*. We are going to follow him in this, ostensibly, very modest approach. This is our answer to the problem about the objectives of the choices: *Wavelets, whether they are of the time-scale or time-frequency type, will not help us to explain scientific facts, but they will serve to describe the reality around us, whether or not it is scientific.* Our task is to optimize the description. This means that we must make the best use of the resources allocated to us to obtain the most precise possible description."

References

Boardman, J. W.: 1994, in *IGARSS 94: Procedings International Geosciences Remote Sensing Symposium*, Vol. 4, pp 2369–2371

Bolster, K. L., Martin, M. E., and Aber, J. D.: 1996, *Can. J. For. Res.* **26**, 590

Gamon, J. A., Field, C. B., Roberts, D. A., Ustin, S. L., and Valentini, R.: 1993, *Remote Sensing of Environment* **44(2)**, 239

Golub, G. H. and Van Loan, C. F.: 1989, *Matrix Computations*, John Hopkins University Press, Baltimore, Maryland

Harsanyi, J. C. and Chang, C. I.: 1994, *IEEE Transactions on Geoscience and Remote Sensing* **32(4)**, 779

Meyer, Y.: 1993, *Wavelets: Algorithms and Applications*, SIAM press, Philadelphia

Pinzón, J. E.: 1996, *Master's thesis*, University of California, Davis, Master degree

Pinzón, J. E., Ustin, S. L., Castañeda, C. M., and Smith, M. O.: In press, *Investigation of Leaf Biochemestry by hierarchical Foreground/Background Analysis*, IEEE Transactions on Geoscience and Remote Sensing

Pinzón, J. E., Ustin, S. L., Hart, Q. L., Jacquemoud, S., and Smith, M. O.: Jan 23-27, 1995, in R. O. Green (ed.), *Proc. 5th. annual JPL Airborne Earth Science Workshop: AVIRIS Workshop*

Pinzón, J. E., Ustin, S. L., Hart, Q. L., Jacquemoud, S., and Smith, M. O.: Reno, Nevada, Nov 9-10, 1994, in *Spectral Analysis Workshop: The Use of Vegetation as an Indicator of Environmental Contamination*

Roberts, D. A., Adams, J. B., and Smith, M. O.: 1990, *Remote Sensing of Environment* **34**, 1

Sabol, D. E., Adams, J. B., and Smith, M. O.: 1990, in *Proceedings of the IEEE International Geoscience Remote Sensing Symposium 1990*, Vol. 2, pp 967–970

Sabol, D. E., Adams, J. B., and Smith, M. O.: 1992, *Journal of Geophysical Research* **97(E2)**, 2659

Smith, M. O., Roberts, D. A., Hill, J., Mehl, W., Hosgood, B., Venderbout, J., Schmuck, G., Koechler, C., and Adams, J.: 1994, in *IGARSS 94: Procedings International Geosciences Remote Sensing Symposium*, Vol. 4, pp 2372–2374

Smith, M. O., Weeks, R., and Gillespie, A.: 24-27 June, 1996, in *ERIM 96: Second International Airborne Remote Sensing Conference and Exhibition, San Francisco*, Vol. 1

Ustin, S. L., Hart, Q. J., Scheer, G., and Duan, L.: 1994, in *IGARSS 94: Procedings International Geosciences Remote Sensing Symposium*, Vol. 2, pp 1211–1212

Ustin, S. L., Smith, M. O., and Adams, J. B.: 1993, in J. R. Ehleringer and C. B. Field (eds.), *Scaling Physiological Processes: Leaf to Globe*, pp 339–357, Academic Press, San Diego

Wickerhauser, M. V.: 1994, *Adapted wavelet analysis from theory to software*, A K Peters, Ltd., Wellesley, MA

INVESTIGATING THE RELATIONSHIP BETWEEN LIQUID WATER AND LEAF AREA IN CLONAL POPULUS

Dar Roberts[1], K. Brown[2], R. Green[13], S. Ustin[4] and T. Hinckley[2]

1. Department of Geography, EH3611, University of California, Santa Barbara, CA 93106
2. College of Forestry, University of Washington, Seattle, WA 98195
3. Jet Propulsion Laboratory, California Institute of Technology, 4800 Oak Grove Dr., Pasadena, CA 91109
4. Department of Land, Air, and Water Resources, University of California, Davis, CA, 95616,

1 Introduction

Leaf Area Index (LAI) is one of the most commonly employed biophysical parameters used to characterize vegetation canopies and scale leaf physiological processes to larger scales. For example, LAI is a critical parameter used in regional scale estimates of evapotranspiration, photosynthesis, primary productivity, and carbon cycling (Running et al., 1989; Dorman and Sellers, 1989; Potter et al., 1993). LAI is typically estimated using ratio-based techniques, such as the Normalized Difference Vegetation Index (NDVI: e.g. Tucker 1979; Asrar et al., 1989; Sellers 1985, 1987). The physical basis behind this relationship depends on the high spectral contrast between scattered near-infrared (NIR) and absorbed red radiation in canopies. As the number of leaves present in a canopy increases over a unit area, NIR reflectance increases, while red reflectance decreases, resulting in an increase in the ratio. Through time series and image compositing, NDVI provides an additional temporal measure of how these parameters change, providing a means to monitor fluxes and productivity (Tucker et al., 1983). NDVI, while highly successful for agriculture and grassland ecosystems has been found to be less successful in evergreen chaparral and forested ecosystems (Badhwar et al., 1986; Gamon et al., 1993; Hall et al., 1995). Typically, the relationship between NDVI and LAI becomes progressively more asymptotic at LAI values above three (Sellers, 1985), although linear relationships have been observed in conifers at LAIs as high as 13 (Spanner et al., 1990).

In this paper, we explore an alternative approach for estimating LAI for remotely sensed data from AVIRIS based on estimates of canopy liquid water. Our primary objective is to test the hypothesis that the depth of the liquid water bands expressed in canopy reflectance spectra at 960, 1200, 1400 and 1900 nm increases with increasing LAI in canopies. This study builds from work by Roberts et al. (1997), in which liquid water was shown to increase following a gradient of increasing LAI ranging from grasslands to coniferous forests. In that study, it was observed that forests, which showed little variation in NDVI, showed significant variation in liquid water. In order to test this hypothesis, we analyzed field spectra measured over *Populus* resprouts of known LAI and monitored changes in liquid water in young *Populus* stands as they aged over a 4-year time span. The study was conducted in south-central Washington, in a clonal *Populus* fiber farm owned and operated by Boise-Cascade near the town of Wallula.

2 Background

2.1 Estimation of Liquid Water in Canopies

Green et al. (1991, 1993) developed techniques for retrieving apparent surface reflectance, mapping column water vapor and liquid water from AVIRIS using a modified version of Modtran radiative transfer code. In order to separate water vapor in the atmosphere from liquid water in the landscape, Green et al. (1993) incorporated a simple model for the expression of liquid water in a reflectance spectrum. This model makes the assumption that the depth of the liquid water band across the 865 to 1035 nm region can be approximated using Beer-Lambert's law for exponential extinction in an absorbing or scattering medium. Based on this model, the depth of the water band will vary as a function of the strength of the absorber (described by the absorption coefficient for liquid water) and the pathlength of light within an absorbing/ scattering element. While this simple model was originally developed primarily to improve water vapor retrievals from AVIRIS, recent studies by Roberts et al. (1997) and Ustin et al. (1998) have shown that the liquid water maps that result may be one of the most products available from AVIRIS.

In order to simulate AVIRIS liquid water retrievals in field spectra, a Beer-Lambert model was developed that duplicates the approach used in AVIRIS. This approach is shown schematically in Figure 1. In the upper two frames, two formulations of the Beer-Lambert law are presented, one that models light attenuated as it passes through an absorbing (or scattering) medium, and one in which part of the light is partially blocked. In the example shown on the left, the natural log of transmittance (or reflectance) can be modeled as a linear function that passes through the origin and has a slope equal to the pathlength. Addition of a blocking factor adds an intercept to the equation. In the central frames, two leaf reflectance spectra are shown on the left, with a plot of the absorption coefficient of liquid water on the right. The lowest frame shows a plot of the natural logarithm of reflectance (ln(R)) plotted against the absorption coefficient for two wavelength regions. Liquid water thickness is derived from the slope of the line.

Figure 1. Methodology: Modified Beer-Lambert

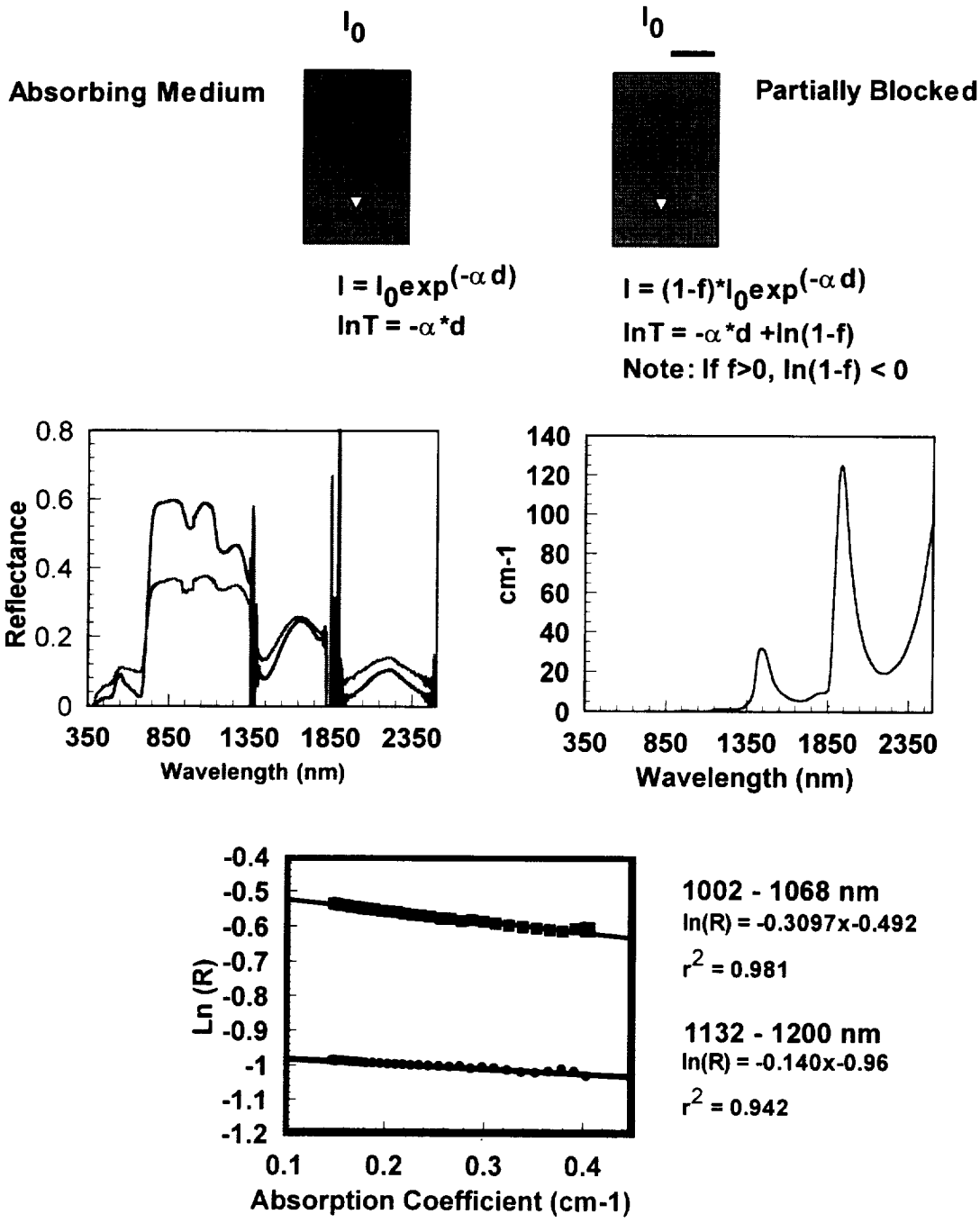

3 Methods

3.1 Study Site

The study was conducted in the vicinity of Wallula, Washington (46° 4' N, 118° 54' W), located several km southeast of the confluence of the Snake and Columbia Rivers. The area has a semi-arid, steppe climate, characterized by minimum monthly temperatures slightly below freezing between the months of December and February and peak summer temperatures above 30° C in July and August (NOAA, 1994; 1996). Total annual precipitation ranges between 200 and 350 mm, falling primarily between November and February, but extending through all months except July and August. The dominant natural vegetation is sagebrush scrub (*Artemisia tridentata*), although the region has extensive agricultural coverage of potatoes, corn, and other agricultural crops. Field research and image analysis were concentrated at the Boise-Cascade Wallula fiber farm, a plantation consisting primarily of *Populus trichocarpa, nigra,* and *deltoides* clones (Fig. 2). *Populus* clones in the area begin to leaf out in April, reach peak leaf display by June then senesce by mid-October, varying slightly interannually depending on temperature pattern. Spectral differences between *P. trichocarpa-deltoides* (TxD) and *P. deltoides-nigra* (DxN) can be attributed primarily to architectural differences between TxD with more horizontally oriented leaves and DxN with more vertical leaf displays (Roberts et al., 1995; Heilman et al., 1996).

3.2 Field Study

The field study was designed to test the LAI/liquid water hypothesis using field spectra of DxN clones at the Wallula fiber farm. Field work was conducted at the farm between July 20th and July 25th, 1997 during the time of an AVIRIS overflight. Seventy-six young stump sprouting plants, ranging between 10 and 60 cm in height were located and flagged in a 6-year old stand that had been recently harvested. Reflectance spectra were measured above each plant using an Analytical Spectral Devices (ASD) full range instrument on loan from JPL (Analytical Spectral Devices, Boulder, CO). Field spectra were standardized to spectralon (Labsphere, Inc. North Sutton, NH) measured at approximately 10-minute intervals. At least three replicates were measured for each plant. One to four sets of spectra were measured at each plant depending on the size of the resprout at a height of 0.5 m above the canopies.

For destructive harvesting the plants were stratified into five height classes: < 19 cm, 20-29 cm, 30-37 cm, 38-48 cm, and 48-60 cm. Five plants were randomly sampled from each height class for detailed analysis. Measurements of plant height and diameter along the major and minor axes were collected for each of the sampled plants for later determination of ground area and plant volume. In order to determine leaf area of each of the sample plants, every stem was destructively harvested then measured with calipers to determine stem diameter. In order to develop a linear equation that relates leaf area to stem diameter, one of every ten stems was stored in a plastic bag and cooled for later laboratory analysis. In the laboratory, leaves from each stem were harvested, measured for leaf area, then regressed against stem diameter. Once this relationship had been developed, it was combined with the resprout stem data to calculate total leaf area for each resprout, then divided by the areal projection of each resprout (in meters) to determine LAI. An example for plant 6-7 (row 6, 7th plant), which consisted of 353 stems is shown in Figure 3.

Liquid water was determined from leaf spectra using the approach described in the background section, modified to account for differences between AVIRIS spectra and the field spectra. The most notable difference occurs in the transition between the VNIR and SWIR1 detectors in the instrument used in the field. Instrumental problems between the VNIR (350-1000 nm) and SWIR1 (1000-1800 nm) regions, tend to create a discontinuity between the two detectors in reflectance spectra (Fig. 1). As a result, it was not possible to apply the same wavelength range as used in AVIRIS to the field spectra. As a solution, the liquid water fits were restricted to the long-wavelength end of the liquid water band, ranging from 1002-1068 nm rather than the 865- to 1065-nm region used in AVIRIS. To test whether AVIRIS and ASD data gave similar results in a wavelength region that did not have instrumental artifacts, fits were also extended to the 1132-1200-nm range and applied to both field and AVIRIS reflectance spectra.

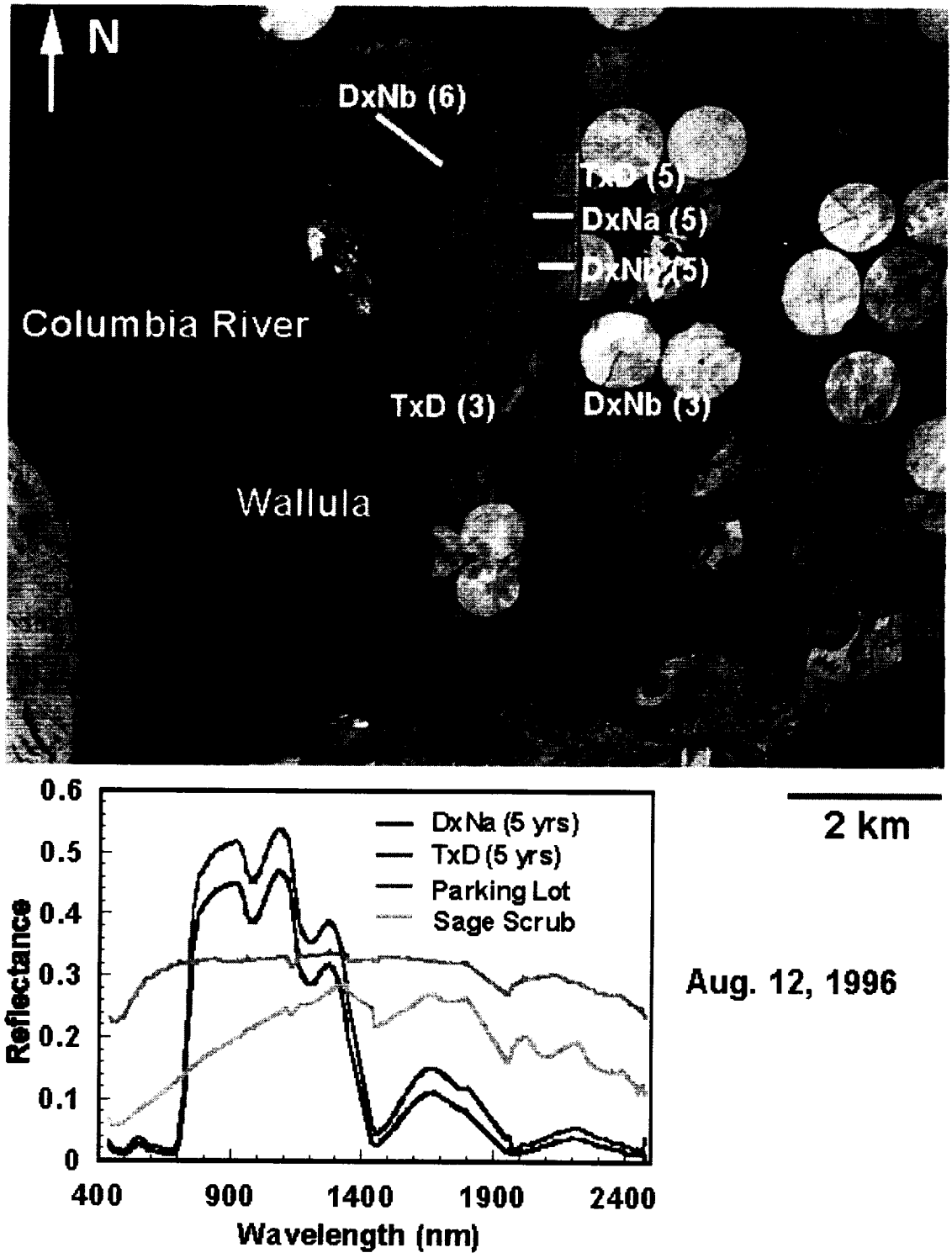

Figure 2. Index map of Wallula fiber farm. Reflectance spectra are displayed for DxN, TxD clones, sage scrub and a parking lot, which was used as a temporally invariant target for calibration.

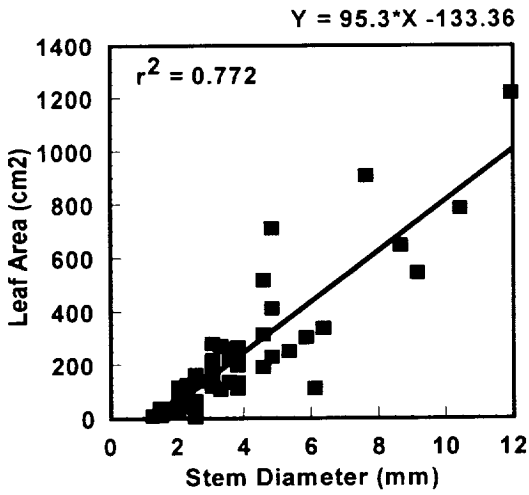

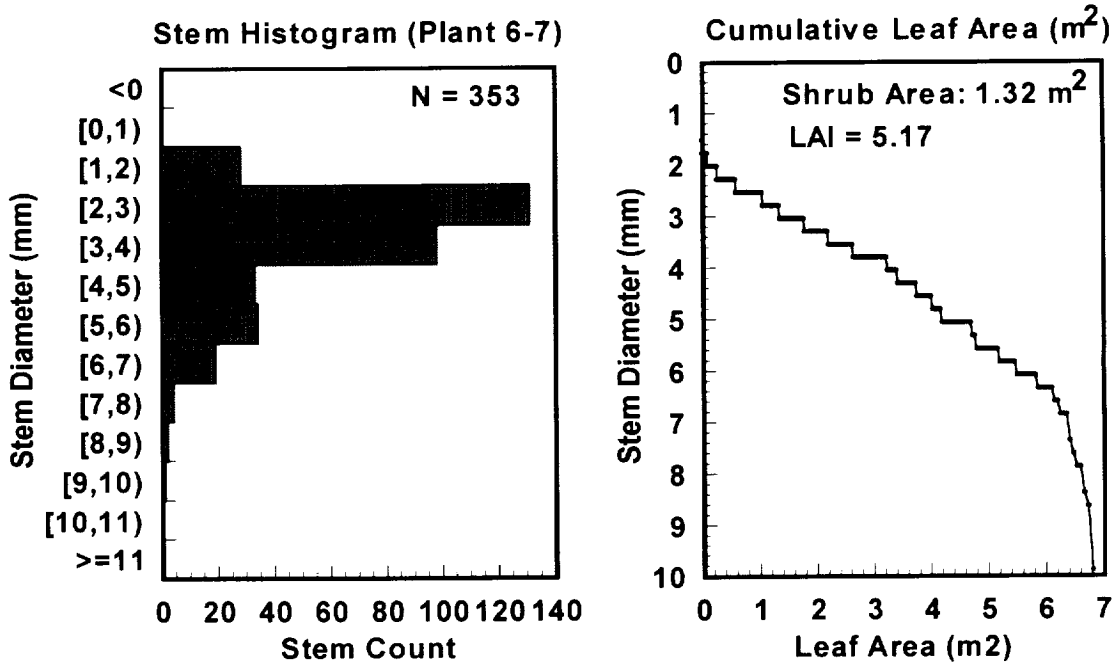

Figure 3. Stem diameter, leaf area relationship. An example calculation is shown for Plant 6-7.

3.3 AVIRIS Processing

An alternate approach, based on multitemporal AVIRIS data was used to determine whether changes in canopy liquid water matched expected patterns in leaf area development as stands aged. In order to test this hypothesis, five AVIRIS scenes were analyzed over the study site, acquired primarily within a seasonal window after full leaf area development in early June and prior to senescence in October. Data sets acquired during this window included September 22, 1994, June 12 and August 18, 1996 and July 23 1997. A late season data set, acquired on October 18, 1995, showed early signs of senescence in most of the clones.

Once acquired, reflectance was retrieved and liquid water and water vapor mapped for each scene using the modified Modtran-2 radiative-transfer approach described by Green et al. (1993) and Roberts et al. (1997). Field spectral data from two bare soil transects measured in 1997 were used to correct for radiometric and wavelength discrepancies between AVIRIS and Modtran. After correcting the 1997 data, a

temporally invariant target was located in the scene and used to improve reflectance retrieval for the remaining scenes from 1994, 1995 and 1996. Example spectra for Aug. 12, 1996 are shown in Figure 2.

4 Results

4.1 Field Study

LAI for the 25 study plants ranged between 1.8 for one of the smallest resprouts to 8.75 for one of the largest, with most of the resprouts ranging between 4 and 6.5 (Fig. 4). Liquid water fits ranged between 0.05 and 0.38 cm in the 1002-1068 nm region and 0.025 and 0.23 cm in the 1132-1200 nm region. Lower liquid water estimates at the longer wavelength are consistent with the fact that the 1132-1200 nm water band is a stronger absorption feature and thus scattered NIR light will penetrate to a shallower depth within the crown. When plotted against liquid water, estimated from the spectral data, LAI and liquid water proved to have a positive, linear relationship with r^2 values of 0.646 and 0.721 in the 1002-1068 and 1132-1200 nm liquid water absorptions (Fig. 4). Differences in the slopes of these linear relationships can also be attributed to the greater strength of the 1132-1200 nm water band.

The validity of the LAI-liquid water relationship is supported by analysis using more standard approaches such as the NDVI (NIR-red)/(NIR+red) and VI (NIR/red). For example, the plot of NDVI against LAI demonstrates that the NDVI becomes progressively more asymptotic with increasing LAI, matching most published observations. The VI, in contrast, shows a much more linear relationship, showing only slightly lower fits than liquid water. In both cases, liquid water provides the superior estimate and shows a linear relationship even to the highest value observed in the resprouts.

4.2 AVIRIS Multitemporal Study

Based on prior work with the clonal *Populus*, leaf area would be expected to reach peak development in June, sustain a high level throughout the summer, then begin to senesce in the Fall, during October. As a result, with the exception of the 1995 data, which was acquired while plants were senescing, differences in LAI observed from 1994 to 1997 should be a product of long term differences in stand age, not phenological changes. Between 1994 and 1997, stand age varied between less than one year to over six years. Over this period of time, LAI would be expected to show yearly increases for the first three years, followed by slight declines over the remaining three years (Heilman et al., 1996).

In order to test whether the expected patterns were observed in liquid water, four stands (plus replicates) were located in the study site, two stands that were originally planted in 1992 and two planted during April, 1994. In order to determine whether leaf angles had an impact on the liquid water retrievals, stands were selected both from the clone with more horizontally oriented leaves, TxD and the more vertically oriented DxN. Temporal patterns in liquid water were also compared to the NDVI, to determine whether similar patterns were observed in that measure.

Temporal analysis of the older stands (Fig. 5, top left) demonstrated few changes in liquid water from 1994 to 1997. The only major temporal change was observed in 1995, in which the TxD showed a marked decrease in liquid water and the DxN a slightly lower decrease, attributed to late season senescence and a loss of leaf area. In all cases, the TxD showed a slightly lower liquid water than the DxN, which can be attributed to either lower leaf area, or the effect of differences in leaf angles. In comparison, the NDVI showed little temporal variation (Fig. 5, row 2). Calculation of liquid water directly from AVIRIS reflectance, using the same program used for the field data, yielded similar results to those produced from the reflectance retrieval. Comparison of field data to AVIRIS spectra, demonstrated higher liquid water estimates for full stands relative to small resprouts, equal to close to 1 mm of water.

Analysis of changes in liquid water in the younger stands demonstrated a uniform increase in liquid water over the first three years, followed by a slight decline in the fourth year (Fig. 5, top right). Unlike observations in the older stands, NDVI showed marked changes, dramatically increasing in the first two years followed by little change in the third year. The VI was not calculated because it proved too sensitive to minor atmospheric correction problems in the red wavelengths.

Patterns in the liquid water matched expected patterns based on stand age and seasonality. In comparison, the NDVI shows little variation except in very young stands.

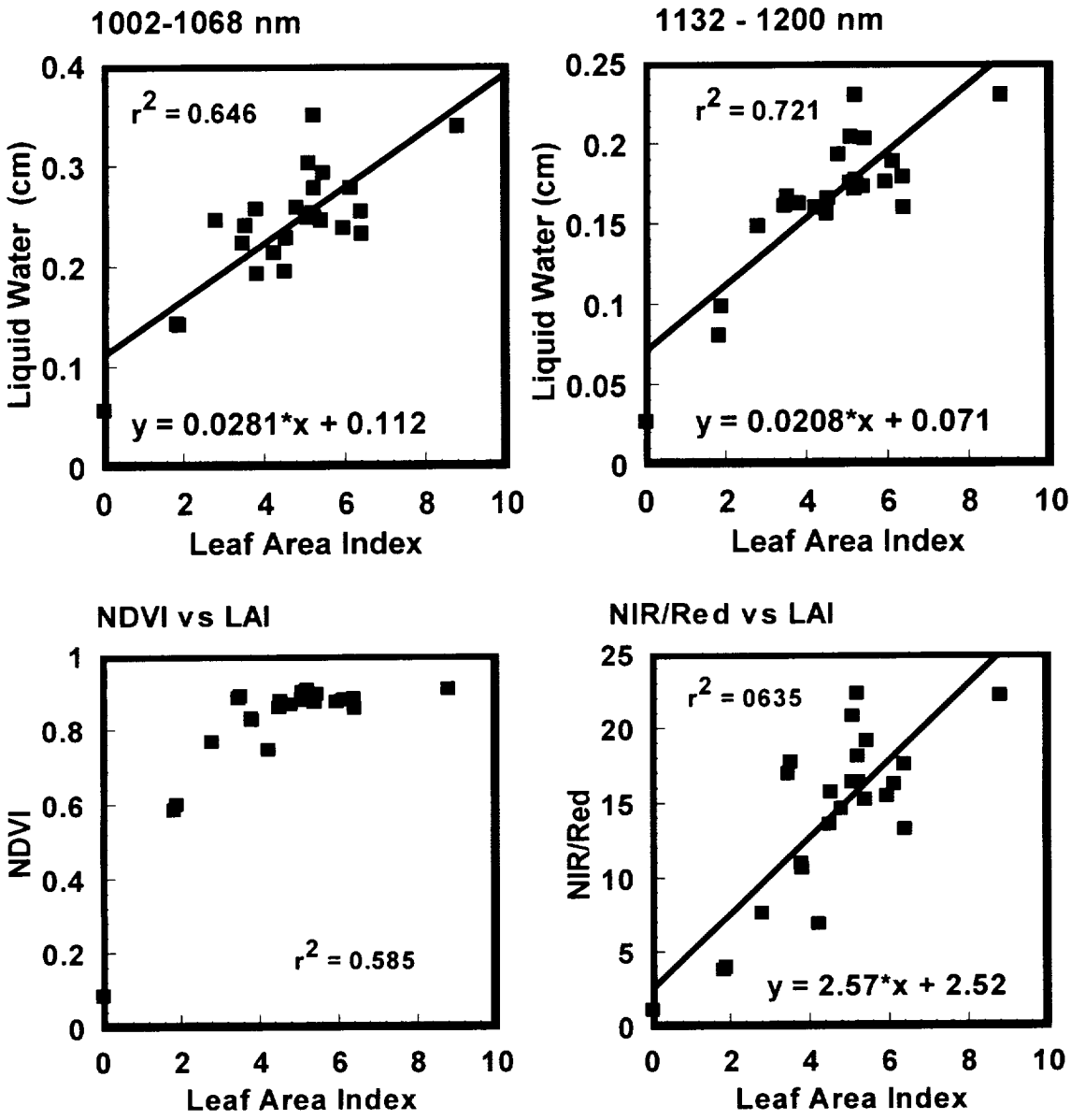

Figure 4. Comparison of LAI to liquid water thickness, NDVI and VI.

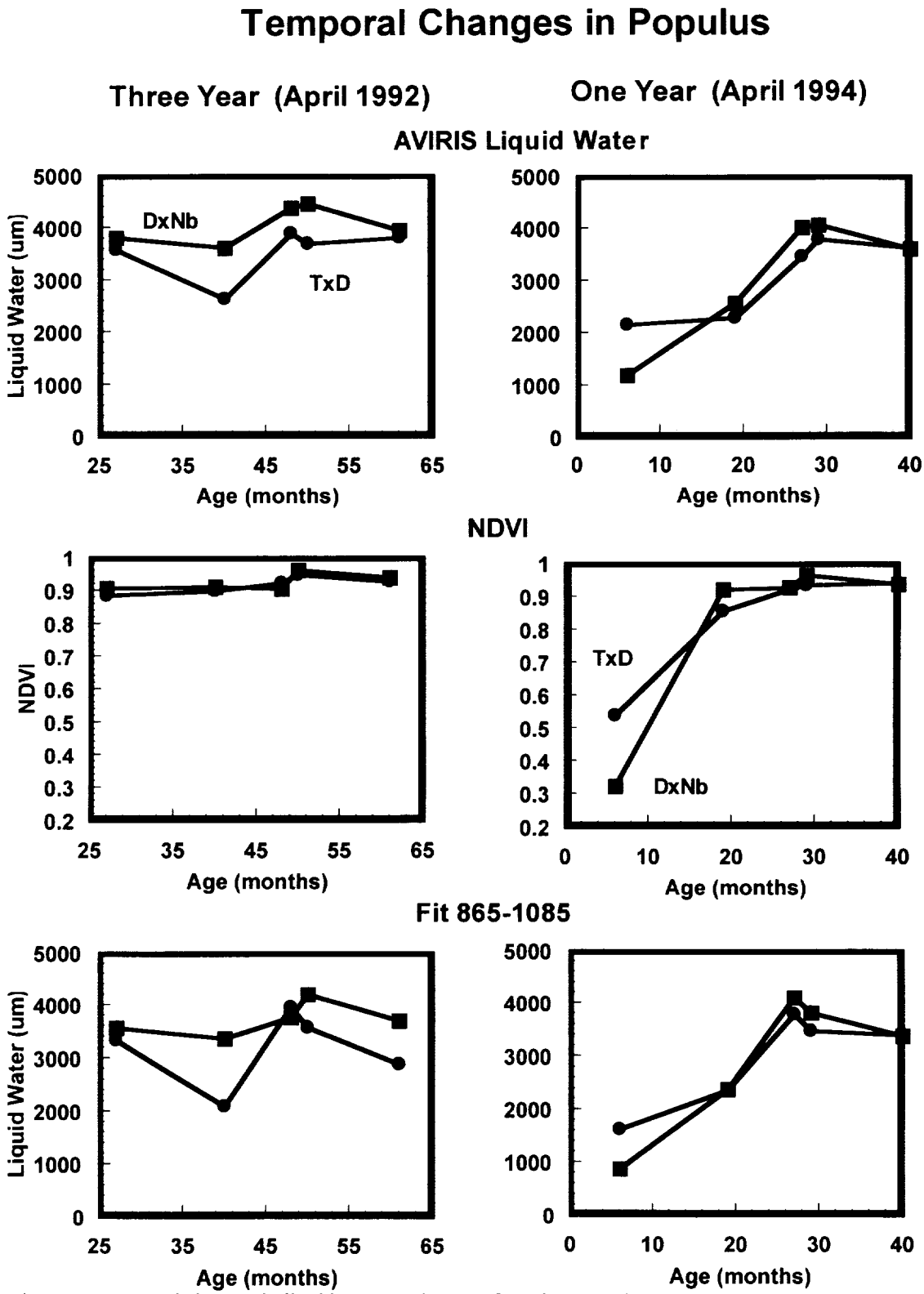

Figure 5. Temporal changes in liquid water and NDVI for select Populus stands from 1994 to 1997. Plots to the left show results for stands planted in 1992, plots on the right show stands planted in 1994.

5 Summary

In this study we tested the hypothesis that LAI is linearly related to liquid water. There were two components of the study, a field study using reflectance measurements of *Populus* resprouts which were harvested to determine LAI and a temporal study of AVIRIS data that tracked changes in liquid water as stands aged over a 4-year period. The field study demonstrated that LAI and liquid water are linearly correlated up to LAI 8.75. In comparison, the NDVI/LAI relationship showed the expected asymptotic relationship which saturated near an LAI of 3.0. The VI showed a surprisingly good linear relationship.

AVIRIS analysis showed temporal patterns in the liquid water which matched expected patterns based on stand age and seasonality. In this instance, the only significant pattern in the older stands was due to senescence in the October, 1995 data set. In the younger stands, liquid water increased for the first three years followed by a decline in the fourth year. In comparison, the NDVI showed little variation except in very young stands.

These results suggest that liquid water retrieved from AVIRIS may form a new, potentially powerful technique for mapping stand structure. However, there remain several important research directions that should be pursued. These include sensitivity analysis to determine how the relationship varies between very different types of vegetation (e.g. resprouts, conifers) and how it varies seasonally with water status (as in chaparral). Furthermore, methods should be explored that avoid the use of correlative relationships between field data and remotely sensed measures of liquid water.

6 Acknowledgements

Support for this research was provided by DOE grant W/GEC95-062A as part of the Westgec program. AVIRIS data used in this study were acquired by NASA. Computer equipment was supplied as part of a start-up package at U.C. Santa Barbara in the Department of Geography and through a UCDRD grant for collaborative research with Los Alamos National Laboratory (STB/UC:97-50). Field spectral measurements were collected using equipment on loan from the Jet Propulsion Laboratory. A portion of this research was carried out at the Jet Propulsion Laboratory, California Institute of Technology, under a contract with the National Aeronautics and Space Administration. In particular, we wish to thank Boise-Cascade for allowing access to the Wallula fiber farm and their readiness to supply supporting information and technical assistance since 1994.

7 References

Adams, JB, Smith, MO and Gillespie, AR, 1993, Imaging spectroscopy: interpretation based on spectral mixture analysis, In Pieters C.M., and Englert, P., eds. Remote Geochemical Analysis: Elemental and Mineralogical Composition 7: 145-166, Cambridge Univ. Press., NY.

Asrar, G, Myneni, RB, and Kanemasu, ET, 1989, Estimation of plant-canopy attributes from spectral reflectance measurements, in Theory and Applications of Optical Remote Sensing, (Asrar, G., ed), John Wiley and Sons, NY, 252-296.

Badhwar, GD, MacDonald, RB, and Mehta, NC, 1986, Satellite-derived leaf-area-index and vegetation maps as input to global carbon cycle models - a hierarchical approach, 7(2): 265-281. *Int. J. Remote Sens.*

Dorman, JL, and Sellers, PJ, 1989, A global climatology albedo, roughness length and stomatal resistance for atmospheric general circulation models as represented by the Simple Biosphere Model (SiB). *J. Applied Met.* 28:833-855

Gamon, JA, Field, CB, Roberts, DA, Ustin, SL, and Riccardo, V, 1993, Functional patterns in an annual grassland during an AVIRIS overflight, *Rem. Sens. Environ.*, 44: 2/3: 239-253.

Green, RO, Conel, JE, Margolis, JS, Bruegge, CJ, and Hoover, GL, 1991, An inversion algorithm for retrieval of atmospheric and leaf water absorption from AVIRIS radiance with compensation for atmospheric scattering, in *Proc. 3rd Airborne Visible/Infrared Imaging Spectrometer (AVIRIS) Workshop* (R.O. Green, Ed.), JPL Publication 91-28, Pasadena, CA, 20-21 May, pp. 51-61.

Green, RO, Conel, JE and Roberts, DA, 1993, Estimation of aerosol optical depth and additional atmospheric parameters for the calculation of apparent reflectance from radiance measured by the Airborne Visible/Infrared Imaging Spectrometer, *Summaries of the 4th Annual JPL Airborne*

Geoscience Workshop Vol. 1. AVIRIS Workshop, (R.O. Green, Ed.), JPL Publication 93-26, 25-29 Oct., Washington D.C., 73-76.

Hall, FG, Shimabukuro, Y, and Huemmrich, KF, 1995, Remote sensing of forest biophysical structure using mixture decomposition and geometric reflectance models, *Ecological Applications*, 5(4): 993-1013.

Heilman, PE, Hinckley, TM, Roberts, DA, and Ceulemans, R, 1996, Production physiology, Ch. 18, in Biology of Populus and its Implications for Management and Conservation (Stettler, R., Bradshaw, H., Heilman P., and Hinckley T., Eds)., NRC Research Press, Ottawa.

NOAA National Environmental Satellite, Data and Information Service, 1994, Climatological data: Washington: 98(1-12):

NOAA National Environmental Satellite, Data and Information Service, 1996, Climatological data: Washington: 100(1-12):

Potter, CS, Randerson, JT, Field, CB, Matson, PA, Vitousek, PM, Mooney, HA, and Klooster, SA, 1993, Terrestrial ecosystem production: a process model based on global satellite and surface data, *Global Biogeochem. Cycles*, 7:811-841.

Roberts, DA, Brown, KJ, Hinckley, TM, Green, RO, and Ustin, SL, 1995, Remote estimates of canopy coupling and architecture using an imaging spectrometer: conifer vs. hardwood, 1995 Ecological Society of America, Snow Bird, Utah, July 30-Aug 3, 1995.

Roberts, DA, Green, RO, and Adams, JB, 1997, Temporal and spatial patterns in vegetation and atmospheric properties from AVIRIS, *Remote Sens. Environ* 62: 223-240.

Running, SW, Nemani, R, Peterson, DL, Band, LE, Potts, DF, Pierce, LL, and Spanner, MA, 1989, Mapping regional forest evapotranspiration and photosynthesis by coupling satellite data with ecosystem simulation. *Ecology* 70(4):1090-1101.

Sellers, PJ 1985, Canopy reflectance, photosynthesis and transpiration. *Int J. Remote Sens.* 6(8): 1335-1372.

Sellers, PJ,1987,Canopy reflectance, photosynthesis and transpiration. II. The Role of Biophysics in the Linearity of Their Interdependence. *Remote Sens. Environ.* 21: 143-183

Spanner, MA, Pierce, LL, Running, SW, and Peterson, DL, 1990, The seasonality of AVHRR data of temperate coniferous forests: relationship with leaf area index, *Remote Sens. Environ.* 33:97-112.

Tucker, CJ, 1979, Red and photographic infrared linear combinations for monitoring vegetation, *Remote Sens. Environ.* 8:127-150.

Tucker, CJ, Vanpraet, C, Boerwinkel, E, and Gaston, A, 1983, Satellite remote sensing of total dry matter production in the Senegalese Sahel, *Remote Sens. Environ.* 13:461-474.

Ustin, SL, Roberts, DA, Scheer, G, Castaneda, CM, Jacquemoud, S, Pinzon, J, and Palacios, A, 1998, estimating canopy water content of chaparral shrubs using optical methods, *Remote. Sens. Environ.* in press.

MAPPING THE DISTRIBUTION OF WILDFIRE FUELS USING AVIRIS IN THE SANTA MONICA MOUNTAINS

Dar Roberts[1], M. Gardner[1], J. Regelbrugge[2], D. Pedreros[1] and S. Ustin[3]

1. Department of Geography, EH3611, University of California, Santa Barbara, CA 93106
2. USDA Forest Service, Forest Fire Laboratory, 4955 Canyon Crest Dr., Riverside, CA 92507
3. Department. of Land, Air, and Water Resources, University of California, Davis, CA, 95616,

1 Introduction

Catastrophic wildfires, such as the 1990 Painted Cave Fire in Santa Barbara or Oakland fire of 1991, attest to the destructive potential of fire in the wildland/urban interface. For example, during the Painted Cave Fire, 673 structures were consumed over a period of only six hours at an estimated cost of 250 million dollars (Gomes et al., 1993). One of the primary sources of fuels is chaparral, which consists of plant species that are adapted to frequent fires and may actually promote its ignition and spread of through volatile organic compounds in foliage (Philpot, 1977). As one of the most widely distributed plant communities in Southern California (Weislander and Gleason, 1954), and one of the most common vegetation types along the wildland urban interface, chaparral represents one of the greatest sources of wildfire hazard in the region.

An ongoing NASA funded research project was initiated in 1994 to study the potential of AVIRIS for mapping wildfire fuel properties in Southern California chaparral. The project was initiated in the Santa Monica Mountains, an east-west trending range in western Los Angeles County that has experienced extremely high fire frequencies over the past 70 years (Office of Emergency Services, 1995). The Santa Monica Mountains were selected because they exemplify many of the problems facing the southwest, forming a complex mosaic of land ownership intermixed with a diversity of chaparral age classes and fuel loads. Furthermore, the area has a wide diversity of chaparral community types and a rich background in supporting geographic information including fire history, soils and topography. Recent fires in the Santa Monica Mountains, including several in 1993 and the Calabasas fire of 1996 attest to the active fire regime present in the area. The long term objectives of this project are to improve existing maps of wildland fuel properties in the area, link AVIRIS derived products to fuel models under development for the region, then predict fire hazard through models that simulate fire spread. In this paper, we describe the AVIRIS derived products we are developing to map wildland fuels.

2 Background

A number of studies have focused on fire hazard assessment (Cosentino et al., 1981; Burgan and Shasby, 1984; Yool et al., 1985; Chuvieco and Congalton, 1989 and Stow et al., 1993; Clarke et al., 1994). In general, remote sensing has been used to classify vegetation into fuel classes then combined through a GIS with collateral information such as slope, aspect, elevation and fire history to assess hazard (Cosentino et al., 1981; Burgan and Shasby, 1984; Yool et al., 1985; Chuvieco and Congalton, 1989 and Stow et al., 1993). For example, Chuvieco and Congalton (1989) used Landsat Thematic Mapper data to classify vegetation by fuel class then used elevation, slope, aspect and proximity to roads to generate a fire hazards index. Burgan and Shasby (1984) merged Landsat MSS, aerial photography and digital elevation data to map seven fuel classes near Missoula Montana. Fuel classes were assigned to a National Fire Danger Rating (NFDR) fuel model to calculate the Energy Release Component (ERC) (heat energy/unit area) for each image element, which was then used as a measure of hazard. Changes in fuel moisture were modeled from digital topography (e.g. insolation) and weather data to predict changes in moisture content. Cohen (1991) used laboratory reflectance data of several chaparral dominants to monitor spectral changes in foliage through a growth season. He evaluated the tasseled cap as a means of monitoring seasonal drying in vegetation as changes in greenness, brightness and wetness. Stow et al., (1993) extended the use of the tasseled cap to analyze a pair of TM scenes from the beginning and end of the 1986-1987 growing season in Southern California. Differences were stratified by vegetation community type, stand age (fire history),

and slope and aspect. They found that end of season changes in greenness for mixed chaparral varied with stand age and matched field measures of total and live standing biomass, although seasonal changes in illumination were the most dominant differences.

Imaging spectrometry, through improved characterization of the chemistry and physical properties of natural surfaces and atmospheres has the potential of significantly improving our ability to map fuels and predict fire hazard. Important fuels properties and associated remotely sensed measures are summarized in Table 1. Important AVIRIS capabilities include: 1) the ability to retrieve apparent surface reflectance in a spatially variable atmosphere, providing temporally robust measures of surface properties; 2) canopy liquid water retrievals, providing direct estimates of moisture content and; 3) improved classification of vegetation. When combined with spectral mixture models to estimate the areal proportions of live and dead crown components, these tools provide a new, unique approach to fire hazard assessment. The importance of collateral information (e.g. fire history, digital topography) for fire hazard assessment is clear: canopy depth, stand age and surface winds are all parameters of critical importance to fire modeling, yet cannot be derived from remote sensing. For this reason, GIS is a significant component of our research effort. Important GIS layers are also described in Table 1.

Table 1. Important fuel properties

Fuel Property	**Remotely Sensed Measure**
Total Fuel Load (kg/ha)	
Live fuels (Green leaves, live stems)	NDVI, Green Vegetation Fraction* , Liquid Water
Dead fuels (litter, stems, twigs)	Non-Photosynthetic Vegetation (NPV)*
Vertical Structure of Fuels	Shade Fraction*
Percent Moisture Content	
Live	Equivalent Liquid Water Thickness**
Dead	na
Species Composition	Classification
Ignition Properties	
Indirect Measures of Above	
Collateral Information (GIS)	
Fire history (Stand age), soils (Site quality), DEM (Insolation, moisture, site quality)	

* From Spectral Mixture Analysis (SMA), Adams et al., (1993); Roberts et al., (1993)
** Green et al., (1993); Roberts et al., (1997a).

3 Methods

3.1 Data

In order to map fuels and monitor seasonal and interannual changes in vegetation, seasonal pairs of AVIRIS data were acquired in the spring and fall of 1994, 1995 and 1997. Due to poor atmospheric conditions during the spring of 1996, no AVIRIS scenes were acquired at that time. However, AVIRIS data were acquired on 17 and 23 October, 1996, before and after the Calabasas fire. In order to cover the entire range, at least two flight lines were flown with each date, one due east and one due west. A minimum of 17 scenes were required to cover the entire range for each date.

Supporting field data for image analysis and accuracy assessment were acquired during several field campaigns in 1995, 1996 and 1997. Field data included spectral reflectance measurements of a homogeneous ground target at Zuma beach during each AVIRIS overpass using an Analytical Spectral Devices (ASD) full range instrument on loan from JPL. Additional spectral data were acquired to develop a regionally specific spectral library for the area (Roberts et al., 1997b) consisting of soils and plant spectra of all chaparral and non-chaparral dominants during the spring and fall (see Gardner, 1997 and Ustin et al., 1998). Additional leaf and branch spectra were collected in the field for later measurement using a Cary-5 laboratory spectrometer at UC Davis. Data for accuracy assessment included close to 300 polygons covering all dominant natural cover types in the region. Data recorded for each polygon included percent cover and species composition. Initial accuracy assessment is summarized in Gardner (1997).

3.2 AVIRIS Processing

Scenes acquired in fall 1994, spring 1995, both dates in 1996 and spring 1997 were processed to retrieve surface reflectance, map column water vapor and equivalent liquid water thickness using the approach of Green et al., (1993). Once processed to apparent reflectance, spectral fractions for green vegetation , non-photosynthetic vegetation, soils and shade were mapped using simple spectral mixture analysis and reference endmembers (Adams et al., 1993; Roberts et al., 1993, 1997c; Ustin et al., 1998). Reference endmembers for the simple models were selected using the approach described by Smith et al. (1990) and Roberts et al., (1997c) from regionally specific spectral libraries developed for the Santa Monica Mountains. During this process, three sets of three endmember models (GV-NPV-shade, GV-Soil-Shade, NPV-Soil-Shade) were generated for each image, then compared to select the model that provided the minimum RMS error and generated physically reasonable fractions for each endmember. A similar approach, based on minimum RMS is described by Painter et al., (1998).

Species maps were generated for each image using Multiple Endmember Spectral Mixture Analysis (MESMA: Roberts et al., 1998), using the modified approach described by Gardner (1997) and Roberts et al., (1997b). MESMA differs from simple spectral mixture models in that it allows the number and types of endmembers to vary on a per-pixel basis. In this manner, it overcomes some of the errors inherent in simple mixture models (e.g., fraction errors, endmember ambiguity), while significantly increasing the number of materials that can be mapped as distinct from their spectra. To date, MESMA has been applied to map snow grain size and snow covered area (Painter et al., 1997), semi-arid vegetation (Okin et al., 1998) and chaparral (Gardner, 1997; Roberts et al., 1997b;1998) and is currently being applied to boreal forest and temperate rain forest. Vegetation maps developed using MESMA are currently limited to fall 1994 and fall 1996 because the spring library is still being organized. All AVIRIS products, including maps of column water vapor, liquid water, spectral fractions and vegetation dominants were coregistered to a georeferenced SPOT Image available from the U.C. Santa Barbara Map and Imagery Library, resampled to a 20 meter resolution.

3.3 GIS Layers

GIS layers developed for the study included a digital elevation model, fire history from 1925 to 1996 and 1930s vegetation (Weislander and Gleason, 1954; Office of Emergency Services, 1995). Fire history maps, developed by the Los Angeles County Fire Department, were processed to develop maps showing the age of the last fire and fire frequency since 1925.

4 Results

A summary of the data developed for this project is shown in Table 2. Fully georeferenced products are available for the entire range (17+ scenes) for fall 1994, spring 1995, fall 1996 (pre and post Calabasas fire) and spring 1997. Spectral fractions have been generated for all of the images described. MESMA-derived vegetation maps have only been generated for fall images. Fuels, destructively harvested by the USDA forest service in 1995, have been located in the GIS. These are currently being used to develop a model that relates AVIRIS fraction images, vegetation cover and liquid water to fuels sampled on the ground. A specific, near-term objective has been to develop fuels layers for the Calabasas area before and after the fire in 1996, and use these data as inputs into a fire-spread model to simulate the Calabasas fire. The fire spread simulation will be conducted by Dr. Jim Bossert, of Los Alamos National Laboratory.

Table 2. AVIRIS products. Products are labeled as none, incomplete (inc) or complete (com). Incomplete means some, but not all scenes have been processed. Complete processing covers the entire range.

Date	Reflectance Retrieval		Spectral Fractions				MESMA	Georeferencing
	Liquid Water	Water Vapor	GV	NPV	Soil	Shade		
940411	Inc	Inc	None	None	None	None	None	None
941019	Com	Com	Com	Com	Com	Com	Com	Com
950509	Com	Com	Com	Com	Com	Com	Com	Com
950526	Inc	Inc	None	None	None	None	None	None
951012	Inc	Inc	None	None	None	None	None	None
951020	Inc	Inc	None	None	None	None	None	None
951026	Inc	Inc	None	None	None	None	None	None
961017	Com	Com	Com	Com	Com	Com	Com	Com
961023	Com	Com	Com	Com	Com	Com	Com	Com
970407	Com	Com	Com	Com	Com	Com	Com	Com

Some of the potential of liquid water and spectral fractions as indicators of fire hazard are illustrated for the Calabasas fire (Figs. 1& 2). Liquid water was mapped for 17 October and 23 October , several days before and after the fire (Fig. 1). The fire began in the north-central portion of the region, in an area dominated by grasslands and coastal sagebrush, mapped as having low liquid water (Fig. 1). It spread rapidly southwards until it reach the vicinity of Malibu Canyon where it slowed significantly, then crossed through rugged terrain and moved rapidly to the coast. Once at the coast it burned west and northwest, burning chaparral to the northwest and coastal sagescrub and grasslands to the west. On the post-fire liquid water image (Fig.1, right frame), the fire scar is clearly indicated by a region of low liquid water due to the removal of most green vegetation. Spectral fractions of the same region (Fig. 2) provide more detailed information regarding surface cover before and after the fire. For example, the region where the fire started (northeast portion of image) was modeled as consisting of high fractions of NPV and low fractions of GV and soil (Fig 2., a to c). Once it progressed to the coast, the fire was restricted primarily to regions mapped as having low GV and higher NPV fractions, a noteworthy exception being the central portion of the area, which consisted of hard chaparral and had higher GV and lower NPV fractions. The post-fire image shows the fire-scar as consisting primarily of soil, which had replaced either GV or NPV depending on the vegetation type.

5 Summary

AVIRIS has the potential of significantly improving our capability to assess fire hazard through improved mapping of vegetation and fuels properties. Critical AVIRIS capabilities include robust retrieval of apparent surface reflectance, the capability of mapping canopy liquid water and improved classification of vegetation. Spectral mixture analysis, applied to reflectance data using reference endmembers adds additional relevant information including estimates of green (live) and non-photosynthetic fuels. In this paper, we describe the data layers we have been developing from AVIRIS which will be used to assess fire hazard and simulate fire spread in the Santa Monica Mountains. Near-term objectives of this project include integrating AVIRIS products with field measures of wildland fuels, then incorporation of spatially explicit maps of fuels in a fire spread model. One key objective will be to test the sensitivity of fire spread simulations to fuels using the pre and post Calabasas AVIRIS data sets.

6 Acknowledgements

Support for this research was provided by grants from the National Aeronautics and Space Administration, Terrestrial Ecosystems and Biogeochemical Dynamics Branch, and Solid Earth and Natural Hazards program (NAGW-4626-I and NAG2-1140). Computer equipment was supplied as part of a start-up package at U.C. Santa Barbara in the Department of Geography and through a UCDRD grant for collaborative research with Los Alamos National Laboratory (STB/UC:97-50). Coregistration software was kindly supplied by J. Steven Cothern of the University of Washington. Field spectral measurements were collected using equipment on loan from the Jet Propulsion Laboratory. A portion of this research was carried out at the Jet Propulsion Laboratory, California Institute of Technology, under a contract with the National Aeronautics and Space Administration.

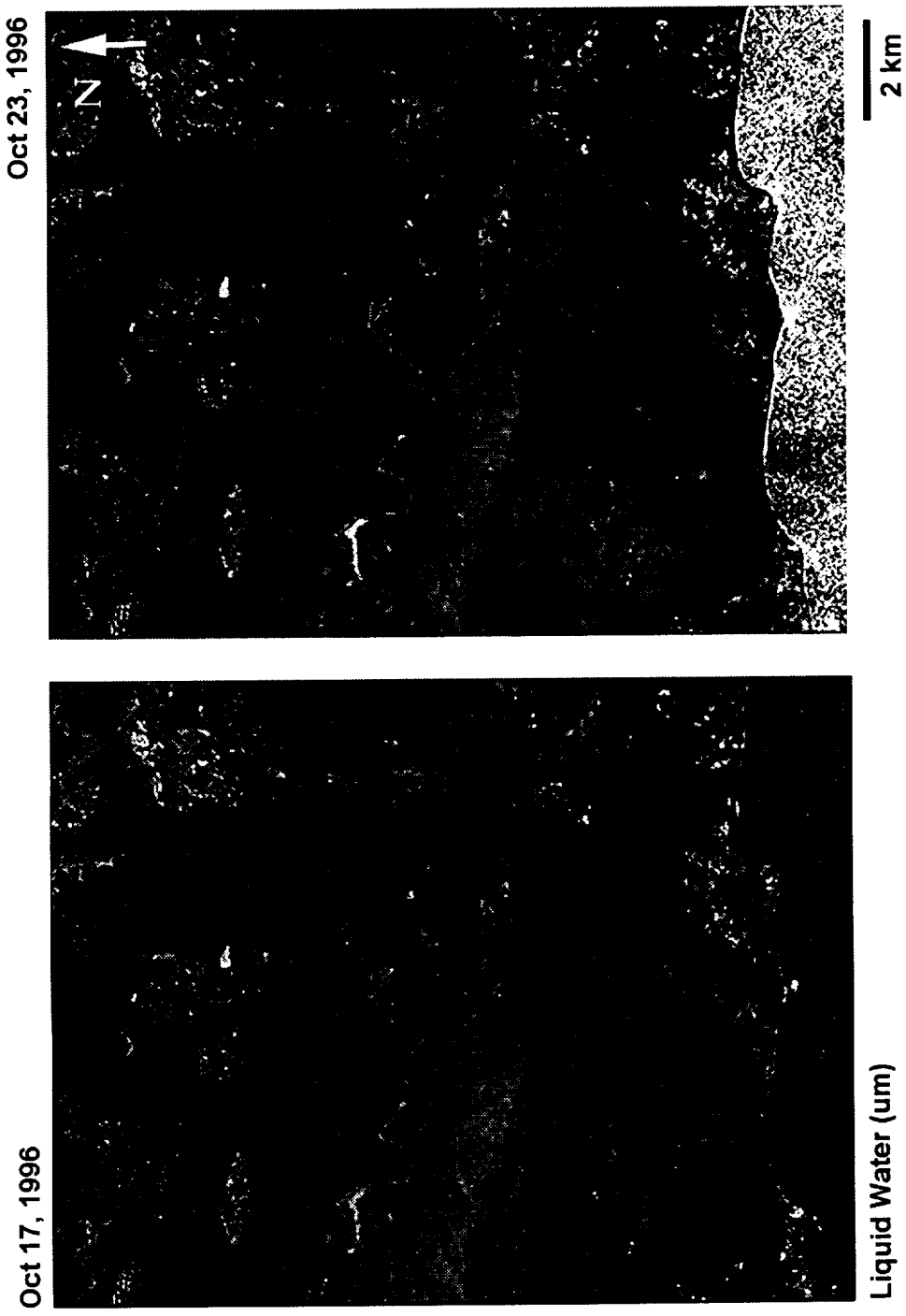

Figure 1. Equivalent liquid water images of the Calabasas area before and after the Calabasas fire.

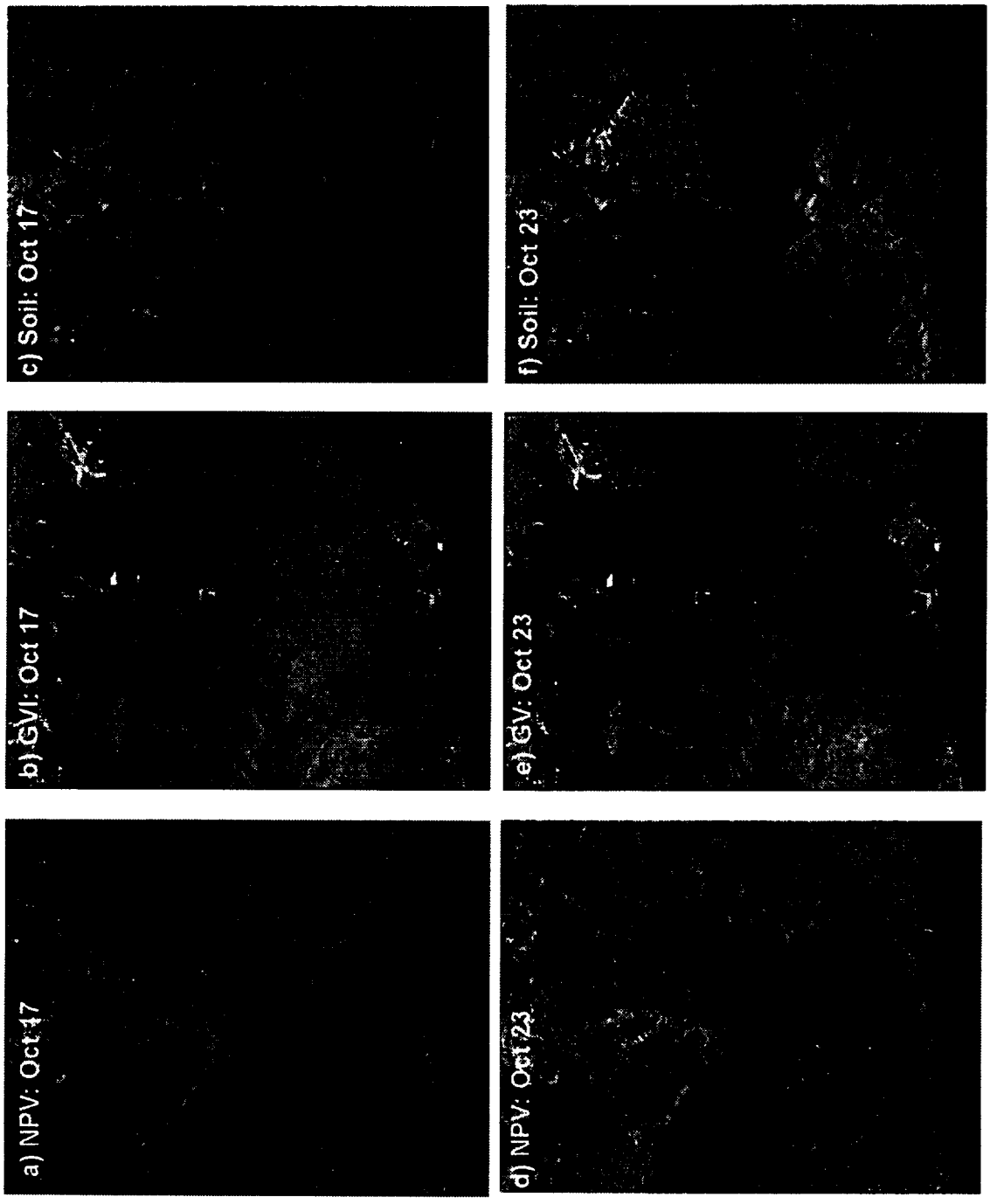

Figure 2. Fraction images for NPF, GV, and Soil for the Calabasas area before and after the fire.

7. References

Adams, JB, Smith, MO and Gillespie, AR, 1993, Imaging spectroscopy: Interpretation based on spectral mixture analysis, In Pieters C.M., and Englert, P., eds. Remote Geochemical Analysis: Elemental and Mineralogical Composition 7: 145-166, Cambridge Univ. Press., NY.

Burgan, RE, and Shasby, MB, 1984, Mapping broad-area fire potential from digital fuel, terrain and weather data, *J. For.*, 8: 228-231.

Clarke, KC, Brass, JA, and Riggan, PJ, 1994. A cellular automaton model of wildfire propagation and extinction. *Photogramm. Eng. Remote Sens* 60(11): 1355-1367.

Chuvieco, E, and Congalton, RG, 1989, Application of remote sensing and geographic information systems to forest fire hazard mapping, *Rem. Sens. Environ*, 29:147-159.

Cohen, WB, 1991, Chaparral vegetation reflectance and its potential utility for assessment of fire hazard, *Photogramm. Eng. Remote Sens* 572: 203-207

Cosentino, MJ, Woodcock, CE, and Franklin, JE, 1981, Scene analysis for wildland fire fuel characteristics in a mediterranean climate., Presented at the 15th Int. Symp. Rem. Sens. Environ., Ann Arbor, MI, 1981. 11 pp.

Gardner, M, 1997, Mapping chaparral with AVIRIS using advanced remote sensing techniques, University of California Masters Thesis, 58 pp.

Gomes, D, Graham, OL, Marshall, EH and Schmidt, AJ, 1993, Sifting through the ashes, lessons learned from the Painted Cave Fire, South Coast Historical Series, Graduate Program in Public Historical Studies, Univ. of California, Santa Barbara, 194 pp.

Green, RO, Conel, JE and Roberts, DA, 1993, Estimation of Aerosol Optical Depth and Additional Atmospheric Parameters for the Calculation of Apparent Surface Reflectance from Radiance Measured by the Airborne Visible-Infrared Imaging Spectrometer (AVIRIS), *Summaries of the 4th Annual JPL Airborne Geoscience Workshop, Oct 25-29,* Vol. 1. AVIRIS Workshop, Washington D.C., 73-76.

Office of Emergency Services (1995), Santa Monica fire history maps, 1935 to 1954, 1954 to 1974 and 1974 to 1994, Joint OES-FEMA Disaster Field Office, 245 S. Los Robles Ave., 4th floor, Pasadena, CA, 91101.

Okin, GS, WJ Okin, DA Roberts, and BC Murray, 1998. Multiple endmember spectral mixture analysis: application to an arid/semi-arid landscape, this volume.

Painter, TH, Roberts, DA, Green, RO, Dozier, J, 1997, Estimating Snow Cover and Grain Size from AVIRIS data with Spectral Mixture Analysis and Modeled Snow Spectra, in SPIE Conf. Vol 3118, Imaging Spectrometry III, 12 p., San Diego, CA July 27-Aug 1, 1997.

Painter, TH, Roberts, DA, Green, RO, and Dozier, J., 1998, Improving Mixture Analysis Estimates of Snow-Covered Area from AVIRIS Data, *Rem. Sens. Environ.* in press.

Philpot, CW, 1977, Vegetative features as determinants of fire frequency and intensity. Presented at the Symposium on Environmental Consequences of Fire and Fuel Management in Meditteranean Ecosystems, Palo Alto, CA, Aug 1-5, 1977, pp. 12-16.

Roberts, DA, Adams, JB, and Smith, MO, 1993, Discriminating Green Vegetation, Non-Photosynthetic Vegetation and Soils in AVIRIS Data, *Rem. Sens. Environ.*, 44: 2/3 255-270.

Roberts, D.A., Gardner, M., Church, R., Ustin, S., Scheer, G.,and Green, R.O., 1998, Mapping Chaparral in the Santa Monica Mountains using Multiple Endmember Spectral Mixture Models, *Rem. Sens. Environ.* in press.

Roberts, DA, Green, RO, and Adams, JB, 1997a,Temporal and Spatial Patterns in Vegetation and Atmospheric Properties from AVIRIS, *Remote Sens. Environ* 62: 223-240.

Roberts, DA, Gardner, M, Church, R, Ustin, SL, and Green, RO, 1997b, Optimum Strategies for Mapping Vegetation using Multiple Endmember Spectral Mixture Models, in SPIE Conf. Vol 3118, Imaging Spectrometry III, 12 p., San Diego, CA July 27-Aug 1, 1997.

Roberts, DA, Batista, G, Pereira, J, Waller, E, and Nelson, B, 1997c, Change Identification using Multitemporal Spectral Mixture Analysis: Applications in Eastern Amazonia, in Remote Sensing Change Detection: Environmental Monitoring Applications and Methods, (Elvidge, C. and Lunetta R., Eds.), Ann Arbor Press, Ann Arbor, MI, in press.

Smith, MO, Ustin, SL, Adams, JB, and Gillespie, AR, 1990, Vegetation in deserts: I A regional measure of abundance from multispectral images, *Remote Sens. Environ.*, 31: 1-26.

Stow, D. Hope, A., McKinsey, D., and Pray, H., 1993, Deriving dynamic information on fire fuel distribution in southern California chaparral from remotely sensed data., *Landscape and Urban Planning*, 24: 113-127.

Ustin, SL, Roberts, DA, Scheer, G., Castaneda, CM, Jacquemoud, S., Pinzon, J., and Palacios, A., 1997, Estimating Canopy Water Content of Chaparral Shrubs Using Optical Methods, *Rem. Sens. Environ.* in press.

Wieslander, AE, and Gleason, CH, (1954), Major brushland areas of the Coastal Ranges and Sierra Cascades Foothills in California, USDA Forest Service, California Forest and Range Experiment Station miscellaneous paper 15.

Yool, SR, Eckhardt, DW, and Cosentino, MJ, 1985, Describing the brushfire hazard in southern California. *Anal. Assoc. Am. Geograph.* 75: 431-442.

Mapping Chestnut Oak Forest Associated With Silicified Hydrothermally Altered Rocks in the Carolina Slate Belt Using Airborne Visible/Infrared Imaging Spectrometer (AVIRIS) Data

Lawrence C. Rowan
James K. Crowley
Robert G. Schmidt
John C. Mars
U. S. Geological Survey
National Center MS 954
Reston, VA 20192 USA

Cathy M. Ager
U. S. Geological Survey
Denver Federal Center MS 973
Denver, CO 80225 USA

ABSTRACT

The Carolina slate belt is a 10- to 50- kilometer-wide zone of 350- to 600- million-year-old volcanic and sedimentary rocks extending from Georgia to Virginia. An older group of heterogeneous volcanic rocks is unconformably overlain by an extensive unit of rhyodacitic to dacitic rocks. These units were intruded by granitic to dioritic complexes which resulted in hornfels and hydrothermally altered rocks ranging from quartz-sericite to nearly pure quartz. Gold and silver deposits and pyrophyllite deposits are associated with the hydrothermally altered rocks, particularly along northeast-trending shear zones.

Mineral resource studies in the slate belt are complicated by the complex geology, deep weathering of bedrock, and dense vegetation cover over much of the area. To augment conventional geologic mapping and mineral resource studies in the area the U. S. Geological Survey has been evaluating the use of Landsat images and, more recently, Airborne Visible-Infrared Imaging Spectrometer (AVIRIS) data for mapping spectral reflectance variations in the forest canopy that might be related to altered, potentially mineralized rocks. Previous analysis of a December 1, 1981, Landsat Multispectral Scanner (MSS) image showed good spatial correspondence between known areas of hydrothermally altered, commonly mineralized rocks and pixels derived by thresholding a principal component image. Field studies showed that most of these areas are topographically high and have a forest community of principally Quercus prinus (chestnut oak) and subordinate Pinus virginiana (Virginia pine) and Acer rubrum (red maple).

The understory is typically open with patches of Vaccinium sp. (blueberry). Analyses of Landsat Thematic Mapper images recorded on November 9, 1982, and also 1988, which is near the peak of autumn colors, essentially duplicated the earlier MSS results. However, in both of these studies, numerous areas underlain by unaltered silicic volcanics also showed as anomalies, reducing the

effectiveness of the Landsat-image maps for mineral resource studies.

Initial analysis of AVIRIS images recorded on June 26, 1996, indicates that chestnut oak growing on highly siliceous altered rocks can be distinguished from the chestnut-oak canopy on unaltered silicic volcanic rocks, as well as from the background canopy on other unaltered lithologic units. Calibration of 10 scenes of AVIRIS data was accomplished by using a modified version of the Atmosphere Removal Program (ATREM), and a laboratory spectrum representing a spectrally uniform plowed field. A matched-filter algorithm was used to map anomalous and background canopies in the 0.49 to 1.3 micrometer region. The resulting anomalous-class image was thresholded to retain only the highest digital numbers and, hence, the best matches to the AVIRIS canopy reference spectrum. The main difference between anomalous and background canopy spectra is weaker intensity of the 0.96 and 1.19 micrometer water absorption features in the anomalous canopy spectra. AVIRIS spectra of chestnut-oak canopy growing on unaltered silicic volcanic rocks are similar to those that characterize other background forest types. Soil analyses indicate that nutrients are anomalously low in residual samples representing the silicified altered areas. The spatial agreement with known hydrothermally silicified bedrock situated along the 10-scene strip of AVIRIS data is very high with no known omissions, except where forests have been cut or replanted. Two areas of silicified rocks were identified in this study that had not been previously documented. A few areas that were initially erroneously identified as being underlain by silicified rocks were eliminated subsequently by reprocessing these scenes using additional AVIRIS reference spectra.

EVALUATION OF LANDSCAPE STRUCTURE USING AVIRIS QUICKLOOKS AND ANCILLARY DATA

Eric W. Sanderson and Susan L. Ustin
Department of Land, Air and Water Resources, University of California, Davis, CA 95616

1. INTRODUCTION

Large scale earth system processes, like those likely to be affected by global climate change, result from a multitude of interactions between physical, chemical and biological systems operating over a variety of spatial and temporal scales (Hall et al., 1988; and many others). These processes taken together influence the configuration or structure of the landscape in which they are acting (Dunn, et al., 1991; Forman and Godron, 1988). Landscape structure is defined as the spatial relationships between distinctive ecosystem components and includes both the number of various patch types and their arrangement in space (Turner and Gardner, 1991; Turner, 1989). Because this configuration interacts with atmospheric conditions, both responding to and influencing climate as well as other ecological processes, we hypothesized that landscape structure might be used an integrated indicator of climate change at the landscape scale (Hunsaker et al, 1994; Norton and Slonecker, 1990). We use a number of commonly accepted landscape metrics to summarize the landscape structure (Turner et al., 1991; Riitters et al., 1995).

Currently the best tool for examining landscape structure is remote sensing, because remotely sensed data provide complete and repeatable coverage over landscapes in many climatic regimes. Many sensors, with a variety of spatial scales and temporal repeat cycles, are available. The Airborne Visible/Infrared Imaging Spectrometer (AVIRIS) has imaged over 4000 scenes from over 100 different sites throughout North America. For each of these scenes, one-band "quicklook" images have been produced for review by AVIRIS investigators. These quicklooks are free, publicly available over the Internet, and provide the most complete set of landscape structure data yet produced.

Quicklooks have several advantages for a survey of landscape structure. They are small (0.5 Mb) and easy to manipulate, yet retain a pixel size (40 m) which approximates the spatial resolution of current land observation satellite systems like Landsat -TM, -MSS and SPOT. Unlike panchromatic SPOT, they are free and easily available over the Internet; other free data (e.g. AVHRR) have much coarser spatial resolution. The single quicklook band is centered at approximately 700 nm (nominally 10 nm wide), which avoids major atmospheric absorbtions (Lillesand and Kiefer, 1994), yet is in a region where basic terrestrial materials, like water, soil/rock, vegetation, and snow/ice can generally be distinguished (Lillesand and Kiefer, 1994). Simple image processing techniques (contrast stretching, level slicing) allow the scenes to be classified into spectrally distinct landscape components for analysis. Though only a crude approximation of the landscape, these methods allow each scene to be analyzed in terms of the same component classes while retaining the spatial heterogeneity of the landscape.

A broad range of ecosystems representing a variety of climatic, geological and ecological conditions are represented in the quick look dataset. The dataset spans locations from 18° N to 56° N latitude and from 68° W to 126° W longitude, from boreal forest to tropical uplands, from coastal British Columbia to Key West, Florida. Eighteen of the twenty-seven North American vegetation types identified by Barbour and Billings (1988) and eleven of the fourteen North American physiographic regions identified by Vankat (1979) are represented in the dataset, including several examples each of montane conifer forest, boreal forest, temperate deciduous forest, desert scrub, Mediterranean scrub, prairie grasslands and tidal marshes. Though the dataset contains sites outside the United States, for this study we include only sites within the continental United States where ancillary data for comparison are available. Nevertheless, a short list of sites includes Mt. Rainier, WA, Biscayne Bay, FL, Los Angeles, CA, Rocky Mountain National Park, CO, Dismal Swamp, VA, Organ Pipe, AZ, Indian Pines, IN, and Suncook, NH. For most archive locations, several scenes are available, and for a few locations, multiple dates as well. Each scene is considered an independent sampling of that landscape type.

Climate interacts with landscape structure by influencing the amount of vegetation cover and the distribution of physiognomic types across the landscape (Prentice et al., 1993). Different plant communities have

distinct spatial arrangements which form particular structures. Climate may also influence landscape structure through landforming processes like erosion and fluvial geomorphology. For this study we represented climate using the climate water balance diagram which integrates the temperature and moisture requirements of plants (Stephenson, 1990). By examining the seasonal timing of water supply vs. evapotranspiratory demand, we calculate expressions for the average, annual water surplus and deficit.

Climate is not the only influence on landscape structure however, and in many cases not the dominant one. Human land use and topography often have dominant influences on landscape pattern. Human land use breaks up vegetation patterns, creates new ones (e.g. agriculture), and is relatively indifferent to climatic effects. Topographic variation interacts with regional climate to create local climatic zones which in turn influence vegetation distributions. Mountainous terrain dissects the landscape, creating more complicated and variable landscape structures. River basins and channels influence the kind and structure of nearby vegetation. Inter-correlations between climate, land use and topography are subtle and complicated, yet important for understanding the large scale causes of landscape structure.

Because of the important influence of land use and topography, these variables have also been included in our analysis. Fortunately, for the contiguous United States, free, publicly available datasets are available over the Internet. We downloaded the appropriate land use and topographic geographic information system (GIS) coverages and clipped out the portion of the coverage corresponding to the quicklook. For land use we summarized the percentage land use for several major categories: urban, agriculture, range, forest, wetland and barren. For topographic variation, we calculated mean and standard deviations of elevation, slope and aspect, as derived from 1:250,000 scale Digital Elevation Models (DEMs).

This paper describes the methodologies used to evaluate the landscape structure of quicklooks and generate corresponding datasets for climate, topography and land use. A brief discussion of preliminary results is included at the end. Since quicklooks correspond exactly to their parent AVIRIS scenes, the methods used to derive climate, topography and land use data should be applicable to any AVIRIS analysis.

2. METHODS

Analysis of landscape structure required integrating data from many sources over a common geographic location. This integration was accomplished using a combination of ARC/INFO (Environmental Systems Research Institute, Redlands, CA), perl (Larry Wall, Mountain View, CA) and shell programming. The data sources are summarized in Table 1 and described in the text below. An example for an AVIRIS scene acquired over Jasper Ridge, CA is illustrated in Figure 1. Figure 1a indicates the local area and approximate boundaries of this quicklook image.

2.1 AVIRIS Quicklooks

For the analysis, we wanted to obtain the greatest variation in landscape structure, climate, land use and topography possible within the constraints of the AVIRIS quicklook dataset. Although a large number of scenes were available, we were restricted to choosing scenes which were complete, entirely cloud free, and where position and time of acquisition data were available. Further, because most images are acquired in flightlines, to insure independent sampling, we restricted ourselves to only selecting one image per flightline and avoided using multiple flightlines over the same location. The final number of quicklooks used for analysis was 109. The center and corner coordinates of each quicklook were calculated from the beginning and ending flightline coordinates and reported number of lines in the flightline. Coordinates were projected to an Albers Conic Equal-Area projection, with central meridian at –95° longitude, and standard parallels at 29° 30' and 45° 30' latitude. This projection is commonly used for the continental United States and has a maximum scale distortion of 1.25% for the 48 states.

The selected quicklooks were downloaded either as raw data files or gif format from the AVIRIS Internet homepage, then uploaded into IDL (Research Systems Inc., Boulder, CO) for manipulation and analysis. Each quicklook was given a numeric code, 1-109, and a longer name composed of the date of acquisition, and flight, run and scene number (e.g. 940815B06.02). Flightline names provided by the AVIRIS staff were also retained (e.g. Jasper Ridge).

Table 1. Data Sources

Landscape Structure data – Remotely sensed AVIRIS quicklooks and selected full AVIRIS scenes (ftp://ophelia.jpl.nasa.gov/pub/docs/html/pub.htm)

Quicklooks are one band (typically band 35 about 700 nm), grayscale images (0.5 Mb) derived from AVIRIS images. They are not atmospherically calibrated and are stretched so that colors range 0 to 255. Quicklook scenes are available in gif format from 1992 through 1996. Scenes are indexed by flight, run and scene, with six scenes per quicklook strip. Approximately 4000 scenes are available between 1992-1996, of which 109 were analyzed. All scenes were from the continental United States, though scenes are also available from Alaska, Canada, Mexico and Brazil. Additional scenes were acquired prior to 1992 and after 1996, but were not used in this analysis.

Landscape Structure Metrics: Contagion, Perimeter to Area Ratio ("Compaction"), Perimeter to Area Ratio Normalized to a Square ("Shape"), Fractal Dimension, Angular Second Moment, Inverse Difference Moment, Spatial Autocorrelation ("Scale")

Climate data (http://www.ncdc.noaa.gov/homepg/online.html)

Soils data (ftp://ftp.ftw.nrcs.usda.gov/pub/statsgo/unix/data).

Historical climate data providing mean monthly average temperature and precipitation for a over 4000 sites worldwide, with concentration in North America and Europe. These data are used to calculate climatic water balance diagrams as described Stephenson (1990) and Eagleman (1976) for each site. Besides the temperature and precipitation data, this calculation requires having available soil water capacity, which is estimated from the STATSGO soils database (National Resource Conservation Service), with complete coverage for the contiguous USA.

Topographic data (http://edcwww.cr.usgs.gov/doc/edchome/ndcdb/ndcdb.html)

1:250,000 scale digital elevation models (DEM) are available for most of the contiguous United States from the US Geological Service. Minimum, maximum and average elevation, slope and aspect are derived from elevation data coinciding with the quicklook.

Land use/land cover (ftp://ftp.epa.gov/pub/EPAGIRAS – ARC/INFO export coverages)
(http:// edcwww.cr.usgs.gov/doc/edchome/ndcdb/ndcdb.html – GIRAS format)

Land use data mapped at the 1:250,000 scale by the USGS including descriptions of both human land use and vegetative cover. Data coincident with quicklook polygon are summarized by land use and vegetation type, on an area weighted basis.

Each scene was stored in both continuous and nominal representations. Remote sensing images are useful for landscape analysis because they provide, without modification, a continuous measure of the landscape structure, but can be easily classified into nominal measures as well. Landscape structure metrics typically apply either to continuous or nominal data, but not both. As presented, quicklooks have a continuous range of gray levels from 0 to 255. These represent non-atmospherically corrected, upwelling radiance from the ground surface. To classify the scenes, we used a simple density slice technique to roughly identify patches of soil and vegetation in the image. Typically vegetation is darker than soil in the quicklook band (~700 nm). We confirmed this pattern by taking five calibrated AVIRIS data cubes, for which quicklooks and field data were available. These five scenes (Jasper Ridge, CA; El Dorado National Forest, CA; Santa Monica Mountains, CA; Winters, CA; Petaluma Marsh, CA) were deliberately chosen from different climate types and vegetation communities in California. The data cubes were classified into vegetation, soil or water using the Spectral Angle Mapper algorithm implemented in ENVI (Research Systems Inc., Boulder, CO) and image derived endmembers for those classes. The AVIRIS scene classifications were qualitatively verified by field work conducted by the CSTARS Laboratory (Department of Land, Air and Water Resources, University of California, Davis) at these sites. These classified images were compared to their corresponding quicklooks to derive gray level thresholds which distinguished vegetation from soil, with a small intermediate class. Although initially we had also planned to classify open water, there was sufficient variability in the quicklook band to make the identification of water unreliable. Because the quicklook classifications have not

been rigorously confirmed by field reconnaissance, they are referred to as Class-V, Class-S and Class-I, so that it is clear they are based only on a simple remote sensing interpretation. An example of a quicklook and its classified product are shown in Figures 1c and 1d.

2.2 Landscape Structure Metrics

Landscape structure metrics fall into two broad classes: those which operate on nominal data (i.e. discrete classes) and those which operate over continuous data. We used landscape structure metrics recommended by Riitters et al. (1995) which represented in their analysis the main axes of landscape structure variation with a minimum of cross-correlation. These metrics all operate on nominal data and were applied to the classified quicklooks using algorithms programmed in IDL. These metrics are perimeter-area ratio, perimeter-area ratio normalized to a square ("shape"), fractal dimension, and contagion. We also recorded the number of patches, the number of patches less than four contiguous pixels (considered "small patches"), and the proportions of each class in each scene. Small patches were not used in calculating other landscape metrics (see discussion). We decided to supplement these measures with three which operate on the continuous image. These are scale based on an autocorrelation threshold, and two texture measurements (angular second moment, inverse difference moment) (Musick and Grover, 1991). We also examined histograms of gray levels where appropriate.

2.3 Climatic Water Balance

To estimate the climate, we decided to follow the practice of many ecologists in calculating the average, long term, climatic water balance for each site. Vegetation at the regional scale has been shown to be strongly influenced by the amount of water surplus, water deficit and their seasonal timing (Stephenson, 1990; Major, 1977). The climate water balance diagram is based on comparison of the potential evapotranspiration (based on temperature and latitude of the site) with actual evapotranspiration (based on potential evapotranspiration and available water from the soil and precipitation). Water surpluses occur when available water is greater than potential evapotranspiration; water deficits when there is insufficient water to meet potential evapotranspiratory demand (i.e. the difference between potential and actual evapotranspiration). Potential and actual evapotranspiration are calculated at monthly time steps based on long term averages of temperature and precipitation at each site.

We obtained mean monthly temperatures and total precipitation from the Global Historical Climatological Network (Petersen et al., 1997), available for free over the Internet. This database has over 6000 precipitation stations and over 4000 temperature stations, with a large concentration of stations in North America, each with a historical record of at least 10 years. For each weather station, we averaged their long term records, then found the five closest stations within 100 km of each site. These five stations were averaged to estimate monthly temperature and precipitation at the quicklook site. Stations were reviewed to remove potentially unrepresentative data from the means (e.g. a weather station on the other side of a mountain range from the quicklook site).

Potential evapotranspiration at each site was calculated using the method of Thornthwaite and Mather (1955), which requires knowledge of only the mean monthly temperature, latitude and available soil water capacity of the site. Though more sophisticated methods are available, it is unclear whether the results are significantly better for large extent studies like this one (Milly, 1994). Using this method and the average precipitation, we used mass balance to calculate actual evapotranspiration, annual water deficit and surplus, given an estimate of the available soil water capacity.

In the past scientists have often assumed a uniform level of available soil water capacity for all sites (Eagleman, 1976; Major, 1977), but today it is possible to get a geographically specific estimate using the Natural Resources and Conservation Service State Soil Geographic (STATSGO) database (USDA, 1994). The STATSGO database provides 1:250,000 scale maps of soils and soil properties for the continental United States with a minimum mapping unit of about 625 ha. By overlaying each quicklook polygon on the appropriate soil coverage (each available for an entire state), we calculated an area-weighted average available water capacity for each site. Soil water capacity has a strong influence on the annual water deficits and surpluses because it determines both the amount of water stored in the soil and the proportion of actual to potential evapotranspiration, making estimations of this parameter an important step in accurate water balance calculations. A representative water balance diagram is shown in Figure 1b.

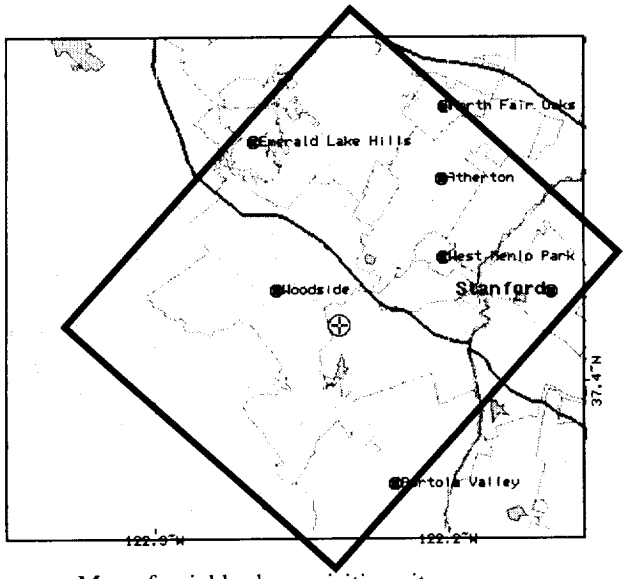

a. Map of quicklook acquisition site.

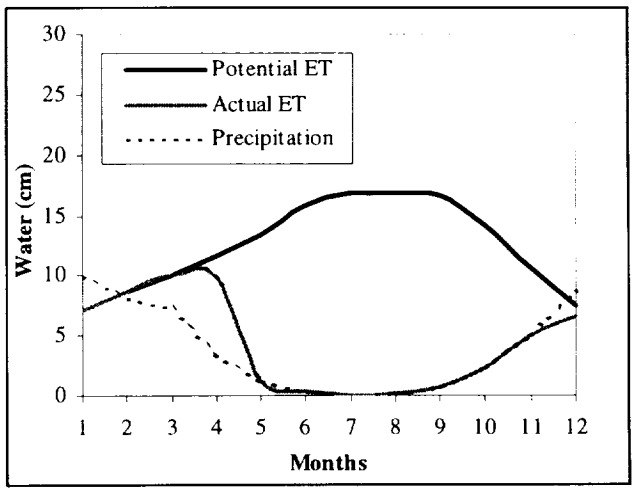

b. Climate water balance diagram.

c. AVIRIS quicklook.

d. Classified AVIRIS quicklook.

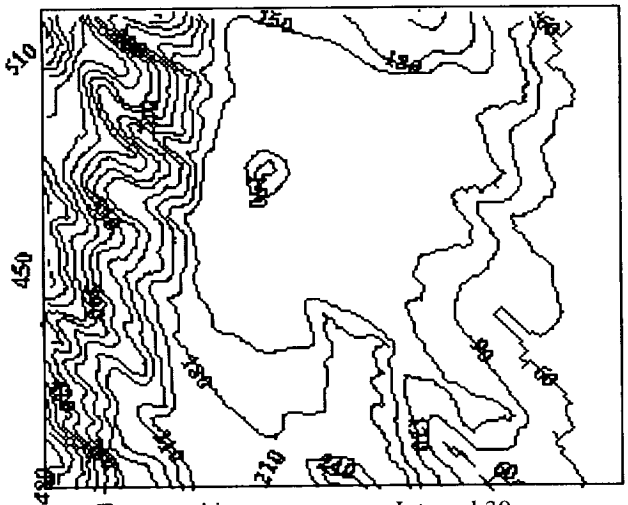

e. Topographic contour map. Interval 30 m.

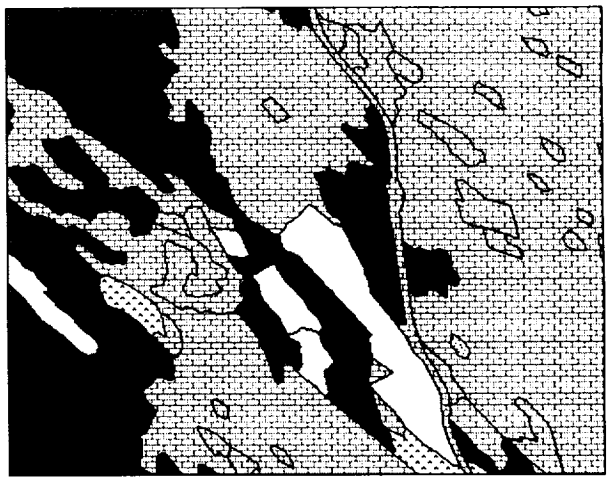

f. Land use / land cover map.

Figure 1. Quicklook and Ancillary Data for AVIRIS image acquired August 15, 1994 over Jasper Ridge, California.

2.4 Topographic Data

Topographic data were acquired in the form of 1° digital elevation models (1:250,000 scale DEMs) from the USGS EROS Data Center for free over the Internet (USDI, 1994). These DEMs were developed by the Defense Mapping Agency from digitized topographic maps and photographic data sources, then interpolated to provide a lattice of elevation measurements at 3 arc-second spacing (approximately every 75 x 90 m in the continental United States, depending on latitude). The absolute horizontal accuracy of the resulting DEM is 130 m; the vertical accuracy is 30 m. For each site, the appropriate DEM was identified using an on-line map by state and county, downloaded, uncompressed and delimited, then imported into ARC/INFO. The DEM lattice was converted to a grid, then projected to an Albers Equal Area projection where x, y, and z dimensions were all expressed in meters. The corresponding quicklook area was clipped from the grid. Slope and aspect grids were derived from the DEM and then summarized by determining the minimum, maximum, mean and standard deviation for elevation, slope and aspect at each site. An example of the topographic data available is shown in Figure 1e.

2.5 Land Use Data

Land use data were acquired from the Land Use and Land Cover (LULC) database, which describes the vegetation, water, natural surface and cultural features of the land surface for the United States at 1:250,000 scale (USDI, 1990). The LULC coverages are distributed by the USGS EROS Data Center in the Geographic Information Retrieval and Analysis System (GIRAS) format, though for this study, we used ARC/INFO export coverages prepared by the US Environmental Protection Agency (see Table 1). The LULC maps are polygon coverages which were manually interpreted from high altitude aerial photography from NASA and other sources with a minimum polygon size of 4 ha (though for some non-urban, non-manmade land use types, the minimum polygon size is 16 ha.) Each polygon is coded with a Level 1 land use/land cover type, for example urban or built-up land, agricultural land, rangeland, forest land, water, wetland, barren land, tundra, or perennial snow and ice. Each of these codes is further divided into more specific, Level 2 land cover/land use codes, for example, forest land is further described as either deciduous forest, evergreen forest or mixed forest. The LULC data are presented in an Albers Equal Area Conic projection.

Land use coverages are identified by using an on-line map to find the appropriate 1:250,000 quadrangle. Each quadrangle has a corresponding EPA code which identifies the appropriate coverage to download and then import into ARC/INFO. The quicklook area of interest is clipped from the LULC coverage and summarized by proportional area of the Level 1 land use/land cover type. The LULC data have been used for several past landscape structure studies (e.g. Riitters et al., 1995; Hunsaker et al., 1994), but provide a much different sense of the landscape than remotely sensed data because they have been interpreted into homogenous polygons. An example of the land use data is shown in Figure 1f.

2.6 Analysis of Landscape Structure and Ancillary Data

Preliminary analysis of the landscape structure and ancillary datasets has consisted of univariate statistical summaries and calculation of Pearson correlation coefficients. Latitude and longitude of the scene centers were included in the correlation analysis. Only correlation coefficients significant at the 0.05 level or better were considered. Summary statistics are presented in Table 2. The correlation matrix among the analysis variables is shown in Table 3. Statistical analyses were all performed using SAS (SAS Institute, Cary, NC).

3. RESULTS AND DISCUSSION

3.1 Synopsis of the Landscape Structure and Ancillary Datasets

Substantial variation in landscape structure, climate, land use and topography is represented in this continental scale dataset. Landscape structure metrics show a large amount of variation; all coefficients of variation are greater than 0.25 except for fractal dimension and the fraction of small patches. The number of patches is quite

Table 2. Summary Statistics for landscape structure, climate, topography and land use/land cover data.

	Mean	Coefficient of Variation	Minimum	Maximum	Count
Landscape Structure					
Number of Patches	3986	0.37	679	8552	109
Number of Small Patches	3031	0.37	594	6696	109
Percentage of Small Patches	76.23%	0.05	67.18%	87.48%	109
Percentage of Class -V	49.63%	0.50	4.10%	88.98%	109
Percentage of Class -M	20.61%	0.50	1.63%	64.45%	109
Percentage of Class -S	29.76%	0.69	6.28%	94.27%	109
Perimeter - Area Ratio	0.4516	0.18	0.0410	0.7526	109
"Shape"	0.1353	0.20	0.0736	0.2529	109
Fractal Dimension	1.3383	0.05	1.2168	1.5429	109
Contagion	0.3628	0.38	0.1384	0.8354	109
Scale, by autocorrelation (pixels)	5.05	1.01	1.45	45.96	109
Texture: Angular Second Moment	3.72E-04	0.94	5.33E-05	1.95E-03	109
Texture: Inverse Difference Moment	0.1128	0.41	0.0489	0.2435	109
Climate Water Balance					
Annual Actual Evapotranspiration (cm)	59.63	0.56	9.19	135.75	106
Annual Water Deficit (cm)	51.10	1.00	0.00	170.36	106
Annual Water Surplus (cm)	50.14	0.89	0.00	185.19	106
Soil Water Capacity (cm)	10.33	0.65	0.07	28.79	109
Topography					
Mean Elevation (m)	822.02	1.13	-0.50	3429.50	109
Standard Deviation of Elevation (m)	90.84	1.05	0.20	355.40	109
Mean Slope (degrees)	5.30	1.12	0.01	21.49	109
Standard Deviation of Slope (degrees)	3.72	0.87	0.04	11.28	109
Mean Aspect (degrees)	174.57	0.21	77.03	270.00	109
Standard Deviation of Aspect (degrees)	91.59	0.26	0.00	143.02	109
Land use / land cover					
Percentage of Urban	6.44%	2.37	0.00%	88.69%	107
Percentage of Agriculture	18.99%	1.46	0.00%	99.37%	107
Percentage of Range	26.42%	1.23	0.00%	96.39%	107
Percentage of Forest	39.58%	0.97	0.00%	100.00%	107
Percentage of Open Water	1.71%	2.65	0.00%	32.18%	107
Percentage of Wetland	2.65%	3.54	0.00%	64.69%	107
Percentage of Barren	1.08%	3.24	0.00%	21.85%	107

high in comparison to landscape analyses of interpreted data (like the LULC maps) because the remotely sensed images capture the heterogeneity of the landscape that interpreted data tends to smooth. The proportion of small patches (defined as less than four contiguous pixels) was unexpectedly high, varying between 67-87% of all patches. Because small patches have a relatively small range of landscape structures, these patches were not used for calculating the other landscape structure metrics. However removing them from the analysis means that the other metrics are calculated over only 15-33% of the total patches.

The proportions of classes V, M and S (representing vegetation, mixed and soil, approximately) varied dramatically across the quicklook datasets. The proportion of vegetated surface varied from 4-89% and the proportion of bare soil varied from 6-94%. The scale, as estimated from the autocorrelation function, varied from 1-

46 pixels (40-2020 m), indicating that the quicklooks have an appropriate grain (40 m) for capturing variation of these landscapes. Scale was positively correlated with the proportion of class S in a scene and negatively correlated to the number of patches.

Variation in texture measures (angular second moment and inverse difference moment) were strongly positively correlated with contagion, since these metrics measure the homogeneity of the landscape, though from the perspective of continuous and nominal data, respectively. These measures were positively correlated with the proportion of class V in a scene, and negatively correlated with classes M and S.

The climatic water balance annual totals show significant variation site to site. Annual water surpluses vary from 0 at many sites in the western United States to over 185 cm, and deficits from 0-170 cm. Interestingly, highest surpluses and deficits were both recorded in Washington. Estimates of annual actual evapotranspiration and deficit are in similar ranges to those calculated by Eagleman (1976) and range over values that Stephenson (1990) associated with vegetation types from deciduous forest to desert scrub. Substantial variation in the available soil water capacity (from 0.07 – 28.79 cm) indicates how important this parameter is to the climatic water balance. Many earlier authors assumed constant available soil water capacities of 10 cm (Major, 1977) or 15.24 cm (Eagleman, 1976), which although good approximations can lead to serious errors.

Quicklook sites varied in elevation from sea level to over 3400 m. Slopes also varied from near flat to over 20%. The variation in slope and elevation within a quicklook scene (measured by the standard deviation of those variables) tended to increase with elevation, since most high elevation sites were in mountainous terrain.

Land use also varied widely across the sites. Agricultural, rangeland and forest land use types were the most prominent in the dataset overall, though urban and wetland land use/land cover types were locally dominant in some scenes. Agricultural land use is strongly, positively correlated with available soil water capacity.

3.2 Correlative Hypotheses between Landscape Structure and Climate, Topography and Land Use

Analysis of the correlation matrix between the various landscape structure metrics and the presumptive landscape forming elements of climate, topography and land use shows an intricate pattern of inter-correlation (Table 3). Analysis of this correlation matrix is leading to hypotheses which will be tested using path analysis.

For example, there is a strong positive correlation between annual actual evapotranspiration and the proportion of forestland in the scene, as predicted by Stephenson (1990). The proportion of forestland is in turn positively correlated with the proportion of Class V (roughly vegetation), and the proportion of Class V is correlated with homogenous, contagious landscapes as measured by angular second moment, inverse difference moment and contagion. Simultaneously, however, mean elevation is negatively correlated with both actual evapotranspiration and the proportion of Class V. Does elevation drive the pattern of actual evapotranspiration which then drives the amount of vegetation and the homogeneity of the landscape, or do actual evapotranspiration and elevation both act independently on the amount of vegetation? A similar set of hypotheses can be formulated for the relationship between elevation, rangeland, proportion of class S, and heterogeneous landscapes. Forest and range land uses may express climate derived landscape structure more clearly than other land uses because they are based on potential vegetation types which are largely climate driven.

Another set of hypotheses involves factors governing the compactness of patch shape. The available soil water capacity is positively correlated with the proportion of agricultural land use in a scene. However agriculture is negatively correlated with mean elevation, variation in elevation and mean slope. Agriculture is also positively correlated with the more compact shapes (indicated by perimeter-area ratio and fractal dimension) and negatively correlated with the fraction of small patches in the landscape.

Table 3. Correlation Matrix between Landscape Structure Metrics, and Climate, Land Use and Topography Variables.

	1	2	3	4	5	6	7	8	9	10	11	12	13	14	15	16	17	18	19	20	21	22	23	24	25	26	27	28	29	30	31	32
1. No. of Patches	1.00																															
2. Perimeter-Area Ratio	0.27	1.00																														
3. Shape	-0.04	0.80	1.00																													
4. Fractal Dimension	-0.24	-0.18	0.18	1.00																												
5. No. of Small Patches	0.99	0.20	-0.11	-0.23	1.00																											
6. % Small Patches	-0.13	-0.09	-0.57	0.27	-0.03	1.00																										
7. Contagion	-0.66	-0.57	-0.24	0.59	-0.60	0.66	1.00																									
8. % Class - V	0.02	-0.15	-0.03	0.17	0.06	0.37	0.42	1.00																								
9. % Class - M	0.31	0.34	0.03	-0.47	0.25	-0.53	-0.75	-0.59	1.00																							
10. % Class - S	-0.18	0.01	0.02	0.03	-0.20	-0.18	-0.14	-0.91	0.21	1.00																						
11. Scale	-0.38	0.01	0.00	0.18	-0.39	-0.08	0.08	-0.29	-0.03	0.37	1.00																					
12. Angular Second Moment	-0.48	-0.35	-0.14	0.45	-0.45	0.36	0.67	0.53	-0.49	-0.40	-0.07	1.00																				
13. Inverse Difference Moment	-0.64	-0.30	-0.01	0.67	-0.61	0.32	0.68	0.47	-0.49	-0.32	0.04	0.90	1.00																			
14. Annual Actual ET	-0.03	-0.05	0.12	0.17	0.00	0.26	0.36	0.68	-0.44	-0.61	-0.25	0.38	0.37	1.00																		
15. Annual Deficit	-0.27	-0.14	-0.09	0.18	-0.27	0.06	0.21	-0.17	-0.17	0.29	0.33	0.08	0.08	-0.23	1.00																	
16. Annual Surplus	0.15	-0.09	-0.17	-0.14	0.16	0.04	-0.13	-0.01	0.16	-0.07	-0.19	-0.07	-0.09	-0.18	-0.73	1.00																
17. Soil Water Capacity	-0.14	-0.01	0.15	0.24	-0.16	-0.12	0.06	0.11	-0.07	-0.10	-0.07	0.22	0.28	0.16	-0.06	0.01	1.00															
18. % Urban	0.34	0.07	-0.04	-0.27	0.36	0.06	-0.18	0.06	0.05	-0.10	-0.02	-0.08	-0.11	0.14	0.02	-0.14	0.07	1.00														
19. % Agriculture	-0.14	0.29	0.47	0.35	-0.19	-0.42	-0.16	-0.08	0.08	0.05	-0.07	0.12	0.28	0.00	-0.16	0.12	0.49	-0.06	1.00													
20. % Rangeland	-0.07	0.03	-0.09	-0.17	-0.09	-0.13	-0.17	-0.62	0.42	0.54	0.28	-0.32	-0.31	-0.54	-0.01	0.12	-0.15	-0.15	-0.22	1.00												
21. % Forest	0.07	-0.27	-0.25	-0.04	0.11	0.40	0.34	0.60	-0.43	-0.51	-0.23	0.25	0.12	0.40	0.04	0.01	-0.18	-0.20	-0.44	-0.60	1.00											
22. % Water	-0.16	0.00	0.07	0.37	-0.16	0.11	0.17	0.06	-0.16	0.01	0.07	0.13	0.24	0.11	0.02	-0.13	0.02	0.10	0.01	0.04	-0.19	1.00										
23. % Wetland	-0.15	-0.01	0.08	0.12	-0.15	0.02	0.08	0.12	-0.13	-0.07	0.13	0.07	0.09	0.16	0.05	-0.18	0.02	-0.05	-0.08	-0.07	-0.09	0.04	1.00									
24. % Barren	0.01	0.17	0.11	-0.11	-0.01	-0.05	-0.02	-0.20	0.10	0.27	0.15	-0.15	-0.13	-0.04	-0.01	-0.08	-0.07	-0.02	-0.05	0.29	-0.26	-0.05	-0.02	1.00								
25. Mean Elevation	0.14	0.00	-0.17	-0.32	0.12	-0.13	-0.26	-0.33	0.34	0.23	0.08	-0.35	-0.42	-0.55	0.16	-0.04	-0.38	-0.25	-0.40	0.21	0.13	-0.18	-0.20	0.00	1.00							
26. Std. Dev. Elevation	0.14	-0.14	-0.30	-0.24	0.16	0.13	-0.04	0.06	-0.03	-0.06	0.06	-0.20	-0.29	-0.27	0.27	0.05	-0.42	-0.16	-0.49	-0.10	0.47	-0.13	-0.22	-0.12	0.62	1.00						
27. Mean Slope	0.10	-0.19	-0.33	-0.21	0.12	0.20	0.05	0.13	-0.10	-0.10	-0.03	-0.13	-0.23	-0.19	0.28	0.06	-0.43	-0.19	-0.50	-0.14	0.51	-0.13	-0.19	-0.13	0.55	0.91	1.00					
28. Std. Dev. Slope	0.18	-0.19	-0.38	-0.30	0.20	0.17	-0.03	0.01	-0.03	0.01	0.03	-0.21	-0.34	-0.29	0.28	0.10	-0.46	-0.16	-0.55	-0.05	0.45	-0.12	-0.21	-0.07	0.57	0.92	0.93	1.00				
29. Mean Aspect	-0.06	0.05	0.11	0.05	-0.06	-0.03	0.09	0.03	-0.10	0.02	-0.06	-0.04	-0.03	0.04	0.09	0.04	-0.08	-0.09	0.02	-0.07	0.13	-0.10	-0.11	-0.02	-0.02	0.01	0.08	0.04	1.00			
30. Std. Dev. Aspect	-0.04	-0.06	0.06	-0.04	-0.05	0.01	0.16	0.18	-0.27	-0.08	-0.07	0.13	0.07	0.13	0.06	-0.10	-0.17	-0.09	-0.15	-0.12	0.22	0.00	0.04	0.01	0.08	0.11	0.17	0.16	-0.03	1.00		
31. Latitude	-0.23	-0.15	-0.21	0.07	-0.23	-0.02	0.15	0.08	-0.04	-0.07	-0.01	0.17	0.14	-0.22	0.13	0.24	0.05	-0.19	-0.05	-0.16	0.33	-0.24	-0.04	-0.21	0.21	0.32	0.33	0.35	0.07	0.11	1.00	
32. Longitude	-0.09	-0.01	0.17	0.16	-0.08	0.16	0.34	0.43	-0.29	-0.38	-0.25	0.45	0.43	0.64	-0.27	-0.20	0.14	0.05	0.04	-0.23	0.13	0.02	0.19	0.01	-0.28	-0.43	-0.44	-0.51	-0.02	0.11	-0.21	1.00

Pearson Correlation Coefficient Matrix.

Colored by significance levels: P < 0.001; 0.001<P<0.01; 0.01<P<0.05

4. ACKNOWLEDGEMENTS

The authors gratefully acknowledge the support to E.W. Sanderson from an Earth System Science Research Fellowship granted by NASA, 1995-GlobalCh00404, to support this research.

5. REFERENCES

Barbour, M.G. and Billings, W.D. 1988. *North American Terrestrial Vegetation.* Cambridge University Press: New York.

Dunn, C.P., Sharpe, D.M., Guntenspergen, G.R., Stearns, F. and Yang, Z. 1991. Methods for analyzing temporal changes in landscape pattern, in eds. Turner, M.G. and Gardner, R.H. *Quantitative Methods in Landscape Ecology: The Analysis and Interpretation of Landscape Heterogeneity.* Springer-Verlag: New York.

Eagleman, J.R. 1976. *The Visualization of Climate.* Lexington Books: Lexington, MA.

Forman, R.T.T. and Godron, M. 1986. *Landscape Ecology.* Wiley: New York.

Hall, F.G., Strebel, D.E., and Sellers, P.J. 1988. Linking knowledge among spatial and temporal scales: vegetation, atmosphere, climate and remote sensing. *Landscape Ecology* 2:3-22.

Hunsaker, C.T., O'Neill, R.V., Jackson, B.L., Timmins, S.P., Levine, D.A. and Norton, D.J. (1994) Sampling to characterize landscape pattern. *Landscape Ecology* 9(3): 207-226.

Lillesand, T.M. and Kiefer, R.W. 1994. *Remote Sensing and Image Interpretation, Third Edition.* Wiley: New York.

Major, J. 1977. California climate in relation to vegetation, in eds. Barbour, M.G. and Major, J. *Terrestrial Vegetation of California.* California Native Plant Society.

Milly, P.C.D. 1994. Climate, interseasonal storage of soil water, and the annual water balance. *Advances in Water Resources.* 17: 19-24.

Musick, H.B. and Grover, H.D. 1991. Image textural measures as indices of landscape pattern, in eds. Turner, M.G. and Gardner, R.H. *Quantitative Methods in Landscape Ecology: The Analysis and Interpretation of Landscape Heterogeneity.* Springer-Verlag: New York.

Norton, D.J. and Slonecker, E.T. 1990. The ecological geography of EMAP. *Geo Info Systems* 1:33-43.

Peterson, T.C. and Vose, R.S. 1997. An overview of the Global Historical Climatology Network temperature data base, *Bulletin of the American Meteorological Society*, submitted.

Prentice, I.C., Monserud, R.A., Smith, T.M., and Emanuel, W.R. 1993. Modeling large-scale vegetation dynamics, in eds. Solomon, A.M. and Shugart, H.H. *Vegetation Dynamics & Global Change.* Chapman & Hall: New York.

Riitters, K.H., O'Neill, R.V., Hunsaker, C.T., Wickham, J.D., Yankee, D.H., Timmins, S.P., Jones, K.B., and Jackson, B.L. 1995. A factor analysis of landscape pattern and structure metrics. *Landscape Ecology* 10(1): 23-59.

Stephenson, N.L. 1990. Climatic control of vegetation distributions: the role of the water balance. *The American Naturalist* 135(5): 649-670.

Thornthwaite, C.W. and Mather, J.R. 1955. The water balance. *Publications in Climatology*, 10(3): 195-311.

Turner, M.G. 1989. Landscape ecology: the effect of pattern on process. *Annual Review of Ecology and Systematics* 20: 171-197.

Turner, M.G. and Gardner, R.H. 1991. Quantitative methods in landscape ecology: an introduction. in eds. Turner, M.G. and Gardner, R.H. *Quantitative Methods in Landscape Ecology: The Analysis and Interpretation of Landscape Heterogeneity.* Springer-Verlag: New York.

Turner, S.J., O'Neill, R.V., Conley, W., Conley, M.R., and Humphries, H.C. 1991. Pattern and scale: statistics for landscape ecology, in eds. Turner, M.G. and Gardner, R.H. *Quantitative Methods in Landscape Ecology: The Analysis and Interpretation of Landscape Heterogeneity.* Springer-Verlag: New York.

U.S. Department of Agriculture. 1994. *State Soil Geographic (STATSGO) Database: Data Use Information.* National Resources Conservation Service, National Soil Survey Center, Misc. Publication 1492. Washington, D.C.

U.S. Department of Interior. 1990. *Land Use and Land Cover Digital Data from 1:250,000- and 1:100,000-scale Maps: Data Users Guide 4.* U.S. Geological Survey. Reston, VA.

U.S. Department of Interior. 1994. *Digital Elevation Models: Data Users Guide 5.* U.S. Geological Survey. Reston, VA.

Vane, G., Green, R.O., Chrien, T.G., Enmark, H.T., Hansen, E.G., and Porter, W.M. 1993. The Airborne Visible/Infrared Imaging Spectrometer (AVIRIS). *Remote Sensing of the Environment* 44:127-143.

Vankat, J.L. 1979. *The Natural Vegetation of North America.* Wiley: New York.

The AVIRIS Low Altitude Option - An Approach to Increase Geometric Resolution and Improve Operational Flexibility Simultaneously

Charles M. Sarture, Christopher J. Chovit, Thomas G. Chrien, Michael L.Eastwood, Robert O. Green, Charles G. Kurzweil

Jet Propulsion Laboratory
California Institute of Technology
Pasadena, CA

From 1987 through 1997 the Airborne Visible-InfraRed Imaging Spectrometer has matured into a remote sensing instrument capable of producing prodigious amounts of high quality data. Using the NASA/Ames ER-2 high altitude aircraft platform, flight operations have become very reliable as well. Being exclusively dependent on the ER-2, however, has limitations: the ER-2 has a narrow cruise envelope which fixes the AVIRIS ground pixel at 20 meters; it requires a significant support infrastructure; and it has a very limited number of bases it can operate from. In the coming years, the ER-2 will also become less available for AVIRIS flights as NASA Earth Observing System satellite underflights increase.

Adapting AVIRIS to lower altitude, less specialized aircraft will create a much broader envelope for data acquisition, i.e., higher ground geometric resolution while maintaining nearly the ideal spatial sampling. This approach will also greatly enhance flexibility while decreasing the overall cost of flight operations and field support. Successful adaptation is expected to culminate with a one-month period of demonstration flights.

PARAMETRIC GEOCODING OF AVIRIS DATA USING A GROUND CONTROL POINT DERIVED FLIGHTPATH

Daniel Schläpfer, Peter Meyer, and Klaus I. Itten

Remote Sensing Laboratories (RSL),
Department of Geography, University of Zurich, CH-8057 Zurich, Switzerland
Phone: +41 1 635 51 45, Fax: +41 1 635 68 46, E-mail: dschlapf@geo.unizh.ch

1. INTRODUCTION

The position of scanning airborne systems (e.g. of the AVIRIS instrument [Vane et al. 1988]) never is as stable as the behaviour of sensors on spaceborne platforms. Thus, geometric distortions occur due to variations of the flightpath as well as of the attitude (given by roll, pitch and heading angles) of the plane. These distortions can not be corrected by ground control point based traditional georeferencing procedures easily, since the movements can not be approximated satisfyingly by polynomial transformations of the image. A linewise calculation has to be performed instead, to consider the behaviour of the plane.

Various projects have been carried out at the RSL, which require an exact localization of ground truth measurement or need the information from a digital elevation model (DEM) fitting to the scanner data (e.g. in-flight calibration of the DAIS sensor [Schaepman et al., 1997], limnological investigations on Swiss lakes (in progress), or water vapor retrieval over complex terrain, using the digital elevation model [Schläpfer et al., 1997]). The geocoding issue therefore had to be addressed, resulting in the presented algorithm and application. The described georeferencing procedure is based on a parametric approach and theoretically allows sub-pixel accuracy even in steep terrain. A predecessor of the algorithm was developed by Meyer [Meyer et al., 1993 and Meyer, 1994].

To achieve accurate results, all auxiliary data have to be provided at highest accuracy possible. Since these requirements seem to be very hard to fulfill, a ground control point based procedure has been developed to recalibrate the offsets of the attitude angles as well as to reconstruct the flightpath. It was possible to geolocate AVIRIS data in mountainous terrain at accuracies of 1-2 pixels, using this GCP based PARGE algorithm (PARametric GEocoding).

2. THE PARGE ALGORITHM

2.1 Features

The described package supports the following features:

- consideration of the exact navigation data by line or by pixel
- exact correction of roll, pitch and true heading (no small angle approximations)
- consistent data structure for various airborne imaging instruments
- ground control point based algorithms for auxiliary data offsets estimation and flightpath reconstruction
- output to desired DEM geometry
- two implemented geocoding algorithms for different accuracy requirements:

1st: sub-pixel accuracy achieved by a DEM-oversampling algorithm (considering the cornerpoints of each pixel)
2nd: pixel accuracy using a pixel centre based triangulation algorithm

- nearest neighbor techniques after triangulation prevent data modifications
- fully IDL (Interactive Data Language, RSI Inc.) based and therefore portable application with window based user interface and on-line help system

2.2 Input Data

For an exact geometric rectification a variety of input data is required. Often some parts of this data are not known exactly and must be estimated or interpolated from external sources. This can occur even in generally well documented test sites, which were flown with high performance sensors. The three categories of input data are:

a) Navigation data, consisting of location (longitude, latitude, height) and engineering data (roll, pitch and true heading). This data should be resampled exactly per line or per pixel of the scanner image.

b) The Digital Elevation Model has to be in the same coordinate system as the airplane data. The resolution has to be based on the image nominal pixel size. The DEM initiates the final geometry of the geocoded image.

c) Image general information consists of exact information on FOV (field of view) and IFOV (instantaneous field of view), scanning frequency, starting time, coordinates of first nadir point, missing lines, and dimensions of the image.

2.3 Geometric Algorithm

The parametric processor starts with an estimate of the 'theoretic look angle vector' (L), oriented from a horizontal plane faced to direction north. This vector has to be turned in three dimensions to get the 'effective look angle vector' (L_t):

$$L_t = [R] \cdot [P] \cdot [H] \cdot L, \qquad (1)$$

where $[R]$, $[P]$ and $[H]$ are the coordinate transformation matrices for roll, pitch and true heading respectively. The calculation order is of interest, since matrix multiplications are not commutative. The order of equation (1) is based on the measurement order of the gyros. The sensor is virtually turned from a north looking flight to the actual position (see Denker [1996]).

The following steps are performed during the main processing algorithm:

- *Calculate the current observation geometry (see Figure 1):* The theoretic look angle vector (L) is calculated between the airplane position and a supposed 'flat' DEM, using the instruments FOV and the pixel position information. This vector is transformed to the effective look angle vector (L_t) afterwards using equation (1).

- *Find the intersection point on the surface:* There are various possibilities to intersect a vector with an irregular plane (as the DEM is). Meyer [1994] used a minimizing procedure of the angle between L_t and a number of surrounding test vectors. The intersection procedure used in the PARGE algorithm calculates a height profile along the footprint of L_t and searches for a point of equal height on L_t.

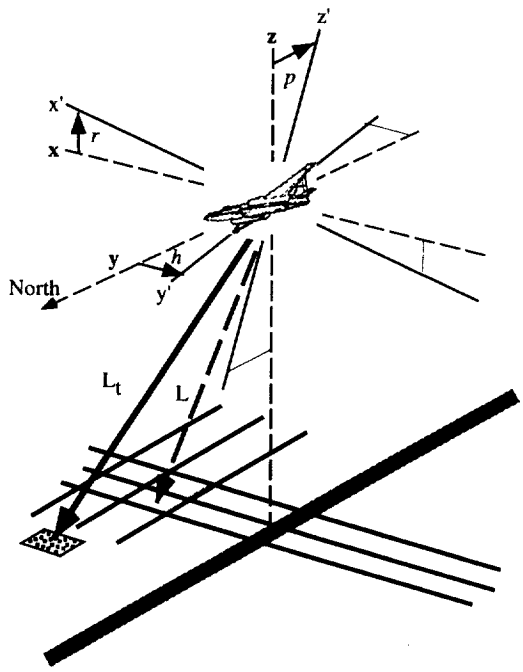

Figure 1: Transformation of the theoretical look angle vector L to the effective look angle vector L_t. *r, p* and *h* denote roll, pitch and true heading angles respectively [modified after Meyer, 1994].

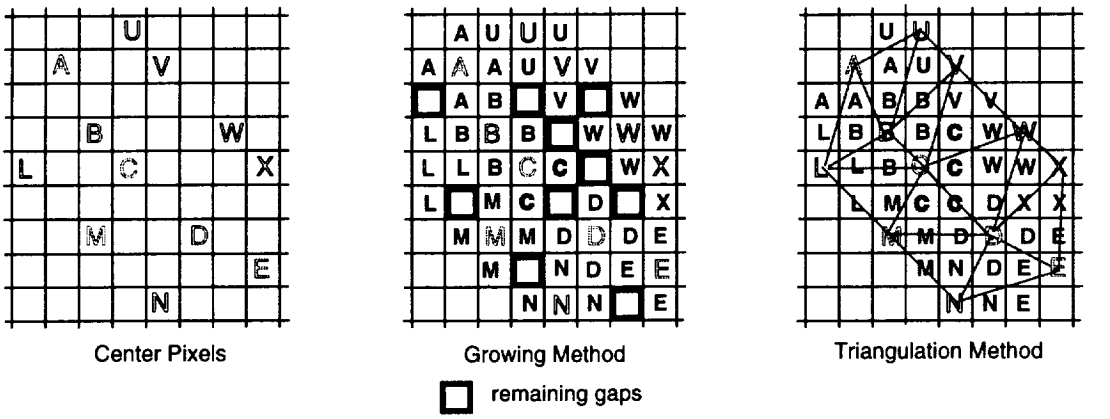

Figure 2: Gap filling methods for slightly oversampled output images. Residual gaps may occur with the fast growing method, whereas the triangulation method covers the area completely.

- *Map the image coordinates:* The image pixel and line coordinates are written to the intersection point position in the DEM geometry. The result of this procedure is a 'remapping array', consisting of the indices of the raw image coordinates, mapped on the DEM.

- *Gap filling:* In order not to lose too much information of the raw image, the resolution of the final DEM (and image) has to be taken slightly higher than of the original image data. It is not possible to avoid, that some of the image data will be repeatedly mapped, while that some other parts will be lost because of the aircraft motion. If the instabilities are relatively high, there will be a high number of pixels of the final image with no information from the scanner. These gaps have to be filled by image processing techniques in order to get an area dependent representation of the image data. Three methods to resolve this problem were tested:

i) The Oversampling Method was proposed by Meyer [1994] and uses a temporary DEM, with up to 16 times the original pixel number. At this high resolution, it is possible to calculate the position of all four corners of each pixel and to fill this area with the correct pixel position. Afterwards the DEM is resampled to final geometry using a modus filter procedure.

ii) The Growing Method (see Figure 2) is a simple technique, which expands each final pixel by a surrounding cross. If an adjacent pixel is already occupied, no replacing will occur. This technique is fast, and yields satisfying results, if no high accuracy is required and the DEM-pixels are about the size of the original image.

iii) Our favored procedure is the Triangulation Method. The center pixel locations are triangulated to remap the missing pixels, based on a gridding procedure (see Figure 2). It guarantees a true nearest neighbor technique while filling all occurring gaps between the center pixels. Another advantage of this method is its independence of final product resolution. The produced TIN (Triangular Irregular Network) can be used to achieve whatever image final resolution is required.

- *Final processing:* The result of the main processor is an array with the indices of the original image pixels on each mapped DEM pixel. This array can be applied as an index directly to the original image data to perform the final geocoding. This step is applied band by band, which makes the processing of a band sequential raw data cube very fast.

3. IMPLEMENTATION OF THE ALGORITHM

The algorithm was implemented based on the requirements for 'real world' hyperspectral sensors as AVIRIS or DAIS [Oertel, 1994]. It was a main goal, to create an interactively usable application with all main features between raw input data and image output. A consistent data format was created, containing image and DEM description as well as all sets of the auxiliary data. The format helps to reconstruct the processing steps and to store intermediate

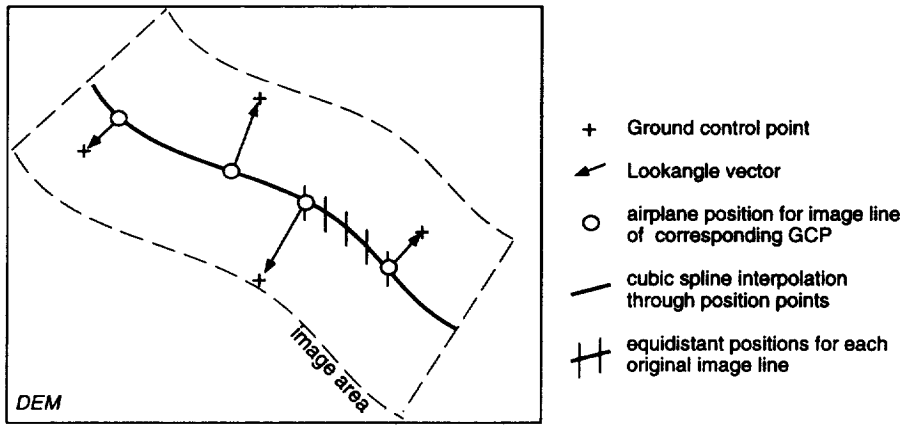

Figure 3: The ground control points based flightpath reconstruction procedure

status reports. Some minor viewing and analysis capabilities for the DEM and the image data were introduced too, but are not a key part of the package.

3.1 Ground Control Points Module

A ground control point (GCP) based offsets estimation tool was developed for the PARGE application. The inversion of the geocoding algorithm allows one to calculate the position of the airplane for each GCP. The differences of this estimated position to the real navigation data are analyzed to obtain the offsets statistically. The auxiliary data offsets can be calculated for roll, pitch, heading, x-navigation, y-navigation, height and/or FOV. Each of these offsets potentially depend on each other. Thus, iterations may be done between them; e.g. the heading offset is iterated together with the pitch offset over sloped terrain.

The flightpath normally is provided with a data set. If none is available, a flightpath reconstruction procedure is applied based on a number of GCPs: The x-y position of the plane is determined for each GCP and an average flight height is derived from the statistics of additional GCPs. The position (and height) then is calculated using a cubic spline interpolation between the aircraft position points (see Figure 3). Errors may be introduced into this procedure if the height is not constant during the overflight and if the GCP accuracy is lower than the resolution of the resulting image. The procedure needs approximately one or two GCP for 100 image lines for flightpath calculation and another GCP for the offsets determination within the same area.

3.2 Processing Timeframe

The whole processing (work and computing) can take from a few hours up to a week per scene, depending on the quality of the auxiliary data available. A typical schedule for an image of 512 x 614 pixels may look as follows:

1. Get all data, including image, DEM, navigation data and airplane attitude data. Convert them to physical units (radian/meters) test all data by a quick preview (1h - 6h of work).
2. Check the flightpath and introduce a number (5-20) of ground control points. Eventually reconstruct the flightpath (1h - 8h of work).
3. Calculate or test the attitude values offsets, using your ground control points, exclude bad GCPs (2h - 4h of work).
4. Run the center pixel geocoding on a subset of the image and check the position on the DEM (15 - 30 min.).
5. Run the main geocoding processor on the whole image (30 min. - 2h runtime, depending on the computing speed).
6. Remap single bands and afterwards the whole cube (10 - 50 min. runtime).

Based on the above numbers, a fast processing would be possible within about 5 hours of work and 1-2 hours of runtime. This time increases proportionally with the required quality of the geocoding and the number of lines to be processed.

4. RESULTS.

4.1 Geocoding of AVIRIS '95 Data

The new algorithm was applied to AVIRIS 1995 data over complex terrain in Camarillo, California. (The results for a 1991 AVIRIS dataset, which were obtained with a predecessor of the algorithm were already described by Meyer et al. [1993].)

The internal navigation system of the airplane provided poor resolution at low absolute accuracy, since there was no differential GPS system mounted during the 1995 AVIRIS campaign. Therefore it was necessary to reconstruct the flightpath from the image data, using the described procedure. The roll angle was set to zero because AVIRIS roll compensation was switched on. These two restrictions lead to a lower accuracy of the geocoding than potentially possible.

The fast pixel centre based algorithm could be used for the required final USGS DEM resolution of 30m. The processing of the standard AVIRIS image (614x512 pixels) was performed within half an hour on a Sun SPARC 20 workstation. This time would increase by about a factor 4 if e.g. 15m end resolution would be chosen. The geocoded image is shown in Figure 4 in comparison with a DEM shadow view image.

Figure 4: The geocoded AVIRIS image of Camarillo (CA) in comparison with the USGS DEM shadow view image.

4.2 Quality Assessment

The quality of geocoding results is difficult to quantify. Possible methods are:

- calculate the location residuals of ground control points, which were not used for the prior offsets or flight line calculation
- compare with the DEM along terrain lines or in specific mountainous areas (see Figure 4)
- overlay digital linegraphs (see Figure 5)
- correlation analysis with digital maps (if such are available)

For the described scene location residuals of 10-20m were found for independent GCPs. This difference is within the accuracy of GCP determination. Ridge lines of the mountains fit within one pixel shift (Figure 4) and the roads are located on the image within the same 1-2 pixel accuracy.

The quality of the procedure was found to be within the validity of the input data. The accuracy of the GCPs remains the main limitation as long as the flightpath has to be reconstructed, but also insufficient gyro calibration can cause problems for this kind of processing.

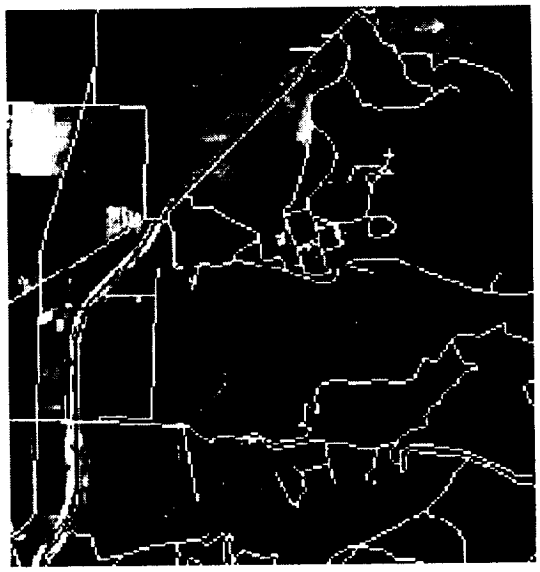

Figure 5: Comparison of a subset of the geocoded AVIRIS image with USGS digital linegraphs of roads (white) and water (black)

5. CONCLUSIONS

A new geocoding processor was implemented using a parametric approach. It allows to correct for attitude and flightpath dependent distortion even for unstable sensor platforms such as for low level airplanes. The algorithm is now in a test status for hyperspectral sensors. The final tests are to be performed in the winter 1997/1998, and the package is planned to be operational by spring 1998. Currently, the sensors DAIS and AVIRIS are supported, further airborne systems might be introduced later.

AVIRIS geocoding leads to satisfying results using USGS DEMs. Higher resolved DEMs could increase the accuracy of the geocoding at high spatial resolution. Further work could be done on accurate residual roll determination on roll compensated AVIRIS images. The accuracy of AVIRIS pitch and true heading calibration was not examined by the authors neither. Another main issue is the introduction of DGPS based flightpath determination for airborne scanners in general. The presented GCP flightpath determination only is a rough aid for missing or insufficient navigation data; the accuracy is significantly decreased compared to a geocoding with known exact flightpath. Nevertheless, the results are still better than those achieved with traditional georeferencing methods applied to images of unstable platforms, flown over rugged terrain.

The IDL based package will be made available to selected users for well defined purposes and to testing customers in a first release. It is not suited for fully operational use yet, since it still requires some expertise for accurate data preparation and processing decisions. After testing of the application our focus will be on a higher automatization level and faster processing time to obtain a real operational system. The latter might be achieved with upcoming faster computers. Another effort has to be done on quality assessment, to allow a calculation of the accuracy values for each geocoded image.

6. ACKNOWLEDGMENTS

We want to acknowledge the following institutions and persons: The Swiss National Science Foundation and the Paul Scherrer Institute (PSI, Villigen CH) for the financial support of this work; the JPL, Pasadena for the free AVIRIS imagery; and Johannes Keller (PSI) and Peter Keller (RSL) for their conceptional hints.

REFERENCES

Denker J.S., 1996: *See How It Flies.* Available from World Wide Web: <http://www.monmouth.com/~jsd/how/htm/>, ISBN 7016405, chapter 19

Meyer P., Larson S.A., Hansen E.G., and Itten K.I., 1993: *Preprocessing: Geocoding of AVIRIS Data using Navigation, Engineering, DEM, and Tracking System Data.* Proc. of the Fourth Annual JPL Airborne Geoscience Workshop, JPL, Pasadena, pp. 127-132

Meyer P., 1994: *A parametric approach for the Geocoding of Airborne visible/infrared Imaging Spectrometer (AVIRIS) Data in rugged terrain,* Remote Sensing of Environment, Vol. 49, Nr. 2, pp. 118-130

Oertel D., 1994: The First Stage of the Digital Airborne Imaging Spectrometer DAIS-7915 Laboratory Calibration at DLR Oberpfaffenhofen. Proceedings of the First International Airborne Remote Sensing Conference and Exhibition; Application, Technology and Science, Vol. II, Strasbourg (F), pp II-214 - II-224

Strobl P., Mueller A., Schläpfer D., and Schaepman M., 1997: *Laboratory Calibration and In-flight Validation of the Digital Airborne Imaging Spectrometer DAIS 7915 for the 1996 Flight Season.*Proceedings of SPIE AeroSense'97, Orlando, FL, pp. 8

Schaepman M., Schläpfer D., Strobl P., and Mueller A., 1997: *Ground Spectroradiometric Measurements in Support of the Validation of the Calibration of DIGITAL Airborne Imaging Spectrometer (DAIS 7915) Data.* Airborne Remote Sensing Conference Copenhagen, pp. 217-223

Schläpfer D., Keller J., and Itten K.I., 1997: *Retrieval of the Horizontal and the Vertical Water Vapor Distribution from AVIRIS Data.* 7th int. ISPRS Symposium on Spectral Signatures, Courchevel (in press).

Vane G., Goetz A.F.H., 1988: *Terrestrial Imaging Spectroscopy.* Remote Sensing of Environment, Nr. 24, Elsevier Science Publishing Co., Inc., New York, pp. 1-29

A Method for Material Classification in AVIRIS Data with Unknown Atmospheric and Geometric Parameters

David Slater and Glenn Healey
Computer Vision Laboratory
Electrical and Computer Engineering
University of California
Irvine, CA 92697
dslater,healey@ece.uci.edu

Abstract

The measured spectral radiance signature for a material can vary significantly due to atmospheric conditions and scene geometry. We show using a statistical analysis of a comprehensive physical model that the variation in a material's spectral signature lies in a low-dimensional space. The spectral radiance model includes reflected solar and scattered radiation as well as the effects of atmospheric gases and aerosols. The MODTRAN 3.5 code was employed for computing radiative transfer aspects of the model. Using the new model, we develop a maximum likelihood algorithm for material classification which is invariant to atmospheric conditions and scene geometry. The algorithm is demonstrated for material classification in AVIRIS data.

1 Introduction

The development of airborne hyperspectral imaging spectrometers has provided an important tool for studying the distribution of materials on the surface of the earth. Two such sensors, the Hyperspectral Digital Imagery Collection Experiment (HYDICE) [1] and the Airborne Visible/Infrared Imaging Spectrometer (AVIRIS) [7], obtain over two hundred spectral measurements per spatial location over the spectral range 0.4μm-2.5μm. One goal of these sensors is to provide a spectrum at each spatial location which can be used to recognize the imaged materials. Unfortunately, the sensor radiance measurements are affected by the atmospheric and geometric conditions under which they were obtained. In order to extract intrinsic surface properties, atmospheric and geometric effects must be accounted for. Some methods for atmospheric correction are based on knowledge about the spectral reflectance of surfaces on the ground [3] [6]. Another approach [8] is to measure downwelling irradiance on the ground to factor out atmospheric effects. Neither of these approaches is feasible for fully automated material classification.

In this paper, we analyze the effects of atmospheric and geometric factors on the 0.4μm-2.5μm radiance spectra measured by an airborne imaging spectrometer. We begin by presenting

a model for image spectral irradiance. Using this model and the MODTRAN 3.5 atmospheric modeling program [2] we generate a set of spectra which span the range of atmospheric and geometric conditions. We show that these spectra are accurately represented by a low-dimensional linear model. We use this model to derive a maximum likelihood approach to material classification which is invariant to atmospheric and geometric conditions.

2 Modeling Radiance Spectra

Consider a surface with normal $\overline{n}$ on the ground at elevation z_g with an associated coordinate system defined by polar angle θ and azimuthal angle ϕ. The surface is viewed by a sensor at elevation z from direction (θ_v, ϕ_v) and the solar direction is (θ_o, ϕ_o) as shown in figure 1. The spectral radiance incident upon sensor location (x, y) is given by

$$\begin{aligned}\rho(x,y,\lambda) &= T_u(z_g,z,\theta_v,\phi_v,\lambda)R(x,y,\lambda)[KT_d(z_g,\theta_o,\phi_o,\lambda)E_o(\lambda)cos(\theta_o) \\ &\quad + \int_{\phi=0}^{2\pi}\int_{\theta=0}^{\frac{\pi}{2}} E_s(\theta,\phi,\lambda)cos(\theta)sin(\theta)d\theta d\phi] + P(z_g,z,\theta_v,\phi_v,\lambda) \qquad (1)\end{aligned}$$

where $T_u(z_g, z, \theta_v, \phi_v, \lambda)$ is the upward atmospheric transmittance, $R(x, y, \lambda)$ is the spectral reflectance of the matte surface projecting to sensor location (x, y), K is a binary constant which accounts for occluding bodies in the solar to surface path, $T_d(z_g, \theta_o, \phi_o, \lambda)$ is the downward atmospheric transmittance, $E_o(\lambda)$ is the extraterrestrial solar radiance, $E_s(\theta, \phi, \lambda)$ is the scattered sky radiance (i.e. excluding direct solar radiance) per unit solid angle incident on the surface from direction (θ, ϕ), $P(z_g, z, \theta_v, \phi_v, \lambda)$ is the path scattered radiance, and λ denotes wavelength. Thus, the three primary contributors to the observed spectral radiance $\rho(x, y, \lambda)$ for a surface are due to reflected solar illumination, reflected sky illumination, and path radiance. To illustrate the wide variability of radiance spectra, figure 2 is a plot of two calculated radiance spectra for a white matte surface under two different atmospheric and geometric configurations.

3 Signature Dimensionality Analysis

3.1 Physical Background

The atmosphere is a heterogeneous mixture of many gases and aerosols, several of which interact with electromagnetic energy in the visible and near infrared through scattering and absorption as modeled in equation (1) by $T_u(z_g, z, \theta_v, \phi_v, \lambda)$ and $T_d(z_g, \theta_o, \phi_o, \lambda)$. In order to interpret accurately measured spectra, it is necessary to account for the effects of these attenuating constituents. Moreover, spatial and temporal variation in the concentration of atmospheric components makes it impossible to derive a single atmospheric correction function which will work in all circumstances.

Scene geometry also plays an important role in the observed radiance spectrum. From (1), path scattered radiance and atmospheric transmittance depend on sensor and surface altitude.

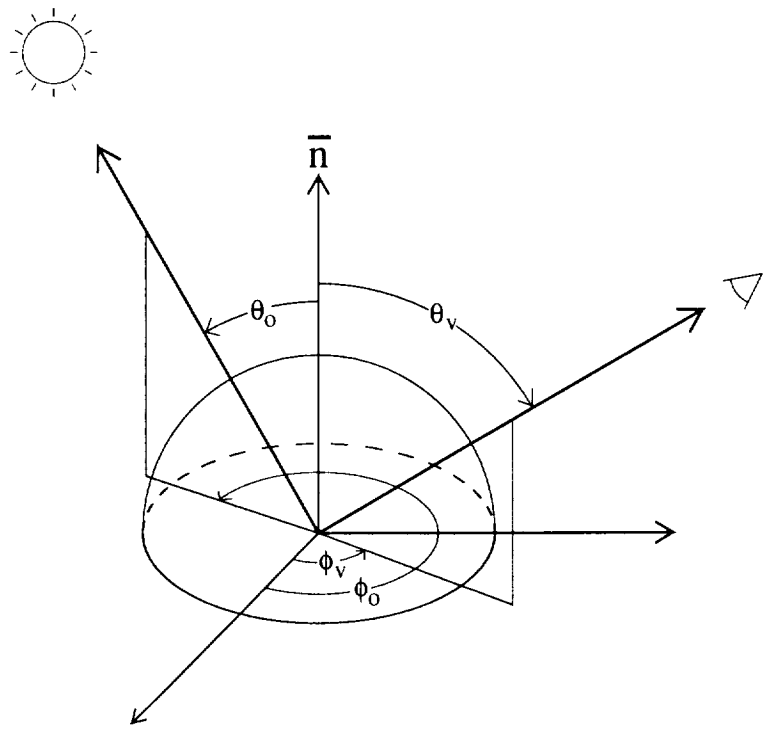

Figure 1: Surface, sensor, solar geometry

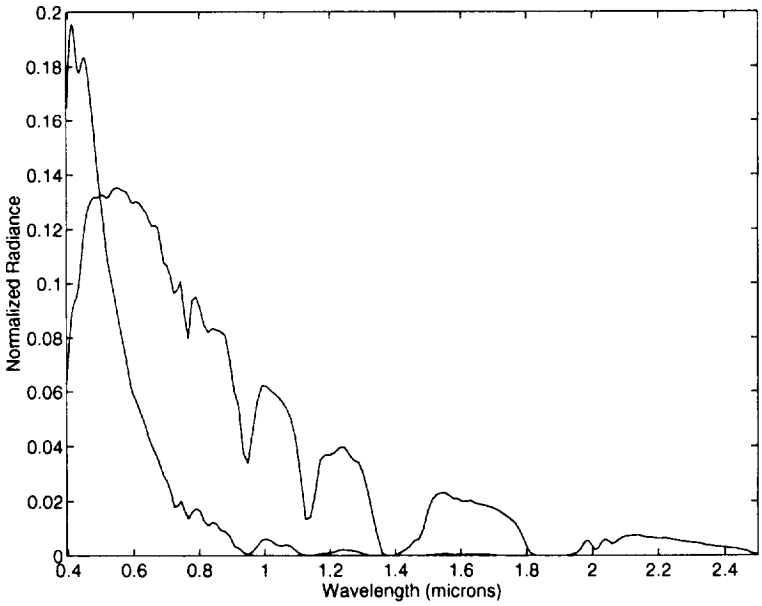

Figure 2: Radiance spectra of a uniform reflecting surface under two different conditions

Solar zenith angle also has a strong influence on the downward atmospheric transmittance because atmospheric path length increases with increasing zenith angle. In addition, nonuniformly distributed occluding bodies such as clouds can block direct solar radiation.

3.2 Linear Models for $L_i(\lambda)$

In this section, we analyze the dimensionality of spectral signatures induced by atmospheric and geometric effects. We rewrite equation (1) as

$$\rho_i(\lambda) = L_i(\lambda)R(\lambda) + P_i(\lambda) \tag{2}$$

where the spatial coordinates have been dropped and the subscript i denotes a particular set of atmospheric and geometric conditions. Note that $L_i(\lambda)$ and $P_i(\lambda)$ depend on atmospheric and geometric properties, but not on surface properties. In addition, for relatively clear conditions, $P_i(\lambda)$ accounts for less than 10% of the total radiance measured by a sensor [3] motivating us to focus on $L_i(\lambda)$ in the following analysis.

Judd *et al.* [5] showed empirically that the spectral distribution of daylight over the visible wavelengths can be well approximated by a linear combination of a small number of basis functions. We apply a similar approach using the physical model in (1) to approximating $L_i(\lambda)$ over 0.4μm - 2.5μm using

$$L_i(\lambda) \approx \sum_{j=1}^{N} \sigma_{ij} l_j(\lambda) \tag{3}$$

where the functions $l_j(\lambda)$ define a fixed basis and the constants σ_{ij} are weighting coefficients.

For a discrete function $L_i(\lambda)$ which is sampled at W wavelengths, define the quality of the approximation in (3) by the squared error

$$E_i = \sum_{k=1}^{W} \left(L_i(\lambda_k) - \sum_{j=1}^{N} \sigma_{ij} l_j(\lambda_k) \right)^2 \tag{4}$$

For a set $L_1(\lambda), L_2(\lambda), \ldots, L_M(\lambda)$ of discrete functions corresponding to different atmospheric and geometric conditions, the total squared error associated with a set of basis functions is

$$E_T = \sum_{i=1}^{M} E_i \tag{5}$$

Consider a $W \times M$ matrix X with each column containing a discrete function $L_i(\lambda)$. We can compute an orthonormal basis for the column space of X using the singular value decomposition [4]

$$X = U\Sigma V^T \tag{6}$$

For any N, the first N columns of U provide an orthonormal basis set $l_1(\lambda), l_2(\lambda), \ldots, l_N(\lambda)$ which minimizes E_T.

Scene Parameter	Values
H_2O (cm)	0.39, 0.88, 1.44, 2.14, 3.11, 4.33
O_3 (atm cm)	0.07, 0.11, 0.12, 0.14, 0.15
O_2 (atm m)	8407.9, 8604.0, 9179.4, 9453.2, 10536.8, 11713.4
CH_4 (atm cm)	0.83, 0.84, 0.85, 0.86, 0.87
NO (atm cm)	0.0001, 0.0002
N_2O (atm cm)	0.189, 0.199, 0.202, 0.209, 0.214, 0.221
CO (atm cm)	0.064, 0.065, 0.066, 0.067, 0.070, 0.072
CO_2 (atm m)	15.24, 16.61, 17.63, 17.82, 18.92, 19.36
Solar-zenith angle	5°, 15°, 25°, 35°, 45°, 55°, 65°, 75°
Aerosol type	rural, urban, maritime, desert
Visibility (km)	5, 23, 50, 70, 85, 100
Sensor Altitude (km)	0, 1, 2, 3, 4, 5, 6

Table 1: Range of atmospheric and geometric parameters for linear model computation

An important question is how many $l_j(\lambda)$ basis functions are required to approximate accurately a large set of $L_i(\lambda)$ functions corresponding to different atmospheric and geometric conditions. The first step is to construct a representative set of $L_i(\lambda)$ functions. We generated such a set using (1) and MODTRAN 3.5. The set consisted of 4032 functions spanning the range of atmospheric and geometric parameters listed in Table 1. These functions were then used to compute $l_j(\lambda)$ using (6). Figure 3 is a plot of $\frac{E_T}{M}$ as a function of N for the 4032 spectra database. Note that $\frac{E_T}{M}$ is small when $N = 5$.

4 Invariant Recognition

In this section, we describe an approach to recognizing materials having a known spectral reflectance function $R(\lambda)$ under unknown outdoor conditions. Using a discrete form of (2), a multispectral sensor obtains a vector of W measurements at each spatial location given by

$$\rho(\lambda_i) = L(\lambda_i)R(\lambda_i) + \eta(\lambda_i) \qquad 1 \leq i \leq W \tag{7}$$

where $\eta(\lambda_i)$ is zero mean gaussian noise for the ith band and we neglect path radiance. If the elements $L(\lambda_i)$ are represented by

$$L(\lambda_i) = \sum_{j=1}^{N} \sigma_j l_j(\lambda_i) \qquad 1 \leq i \leq W \tag{8}$$

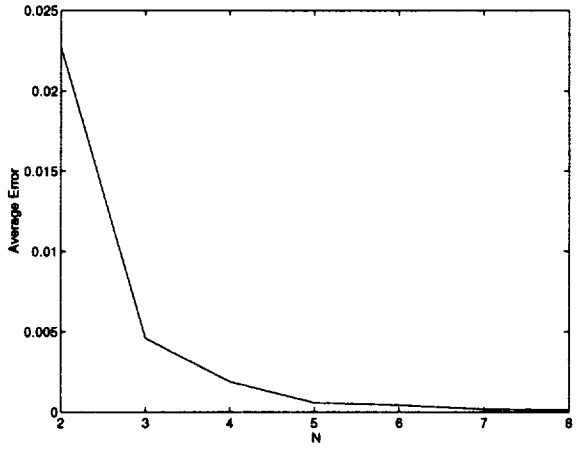

Figure 3: Error for linear model

as in (3), then (7) can be written

$$\rho(\lambda_i) = \sum_{j=1}^{N} \sigma_j v_j(\lambda_i) + \eta(\lambda_i) \qquad 1 \leq i \leq W \tag{9}$$

where $v_j(\lambda_i) = R(\lambda_i) l_j(\lambda_i)$. Let ρ, v_j, R, and η be W-dimensional column vectors composed of elements from $\rho(\lambda_i)$, $v_j(\lambda_i)$, $R(\lambda_i)$, and $\eta(\lambda_i)$ for $1 \leq i \leq W$. The conditional probability of measuring sensor vector ρ for a material with spectral reflectance vector R is

$$P(\rho|R) = \frac{1}{(2\pi)^{0.5W}|\Sigma|^{0.5}} \exp\left(-0.5 D^T \Sigma^{-1} D\right) \tag{10}$$

where Σ is the covariance matrix of the noise vector η and

$$D = \rho - \sum_{j=1}^{N} \sigma_j v_j \tag{11}$$

From (10), maximum likelihood estimates for the parameters $\sigma_1, \sigma_2, \ldots, \sigma_N$ can be obtained by differentiating $D^T \Sigma^{-1} D$ with respect to $\sigma_1, \sigma_2, \ldots, \sigma_N$ and setting each of the N equations to 0. The estimated parameters can be substituted into (10) to obtain the likelihood of the measurement vector ρ for a material with reflectance vector R. This likelihood can be computed at each spatial location in the image and thresholded for illumination-invariant material classification.

5 Experimental Verification

To verify the applicability of the linear model to real data, we examined several measured spectra. The spectra were obtained under relatively clear conditions so that the path scattered

radiance $P_i(\lambda)$ is small. Thus, we determine $L_i(\lambda)$ by

$$L_i(\lambda) = \frac{\rho_i(\lambda)}{R(\lambda)} \tag{12}$$

using available spectral reflectance data $R(\lambda)$. We fit several of these measured $L_i(\lambda)$ functions using the linear model computed in section 3. Each side of figure 4 is a plot of $L_i(\lambda)$ and the corresponding fit using 5 basis functions. We see that although the spectra were obtained under different conditions, the five dimensional model is quite accurate for each case. As an additional test of the model, we classified surface materials in the Cuprite, Nevada AVIRIS [7] images shown in figures 5(a) and 6(a) using the method in section 4 in conjunction with spectral reflectance data obtained from the USGS Spectroscopy Laboratory. The complex three dimensional geometry of the Cuprite scene requires an illumination-invariant classification approach because ground orientation, as well as the presence of shadowing surfaces such as mountains, affects the spectral distribution of illumination falling on surface materials. Both sides of Figure 4, in fact, are $L_i(\lambda)$ functions incident on the same material at different locations in these scenes. Figures 5(b) and 6(b) show the results of classification. The white areas in figures 5(b) and 6(b) are Alunite, the light gray areas are Kaolinite, and the dark gray areas are a mixture of Alunite and Silica. Figure 7(a) is a plot of a measured radiance spectrum of Alunite with its corresponding fit, figure 7(b) is a plot of a measured radiance spectrum of an Alunite/Silica mixture with its corresponding fit, and figure 8 is a plot of a measured radiance spectrum of Kaolinite with its corresponding fit. The classification results are in strong agreement with the mineral distribution in the region.

6 Summary

In this paper, we examined the effects of variations in the atmospheric conditions and scene geometry on outdoor illumination functions. Using a physical model, we generated spectra which enumerate a large range of conditions. The calculated spectra were used to compute a linear model for the space of atmospheric and geometric variation. We showed that a five parameter linear model is adequate to represent the gamut of atmospheric and geometric effects. This model can be used for automated material classification invariant to atmospheric conditions and scene geometry. We verified the accuracy of the linear model using several measured spectra corresponding to ground regions with known spectral reflectance.

References

[1] R. W. Basedow, D. C. Armer, and M. E. Anderson. HYDICE system: Implementation and performance. In *SPIE Proceedings*, volume 2480, pages 258–267, 1995.

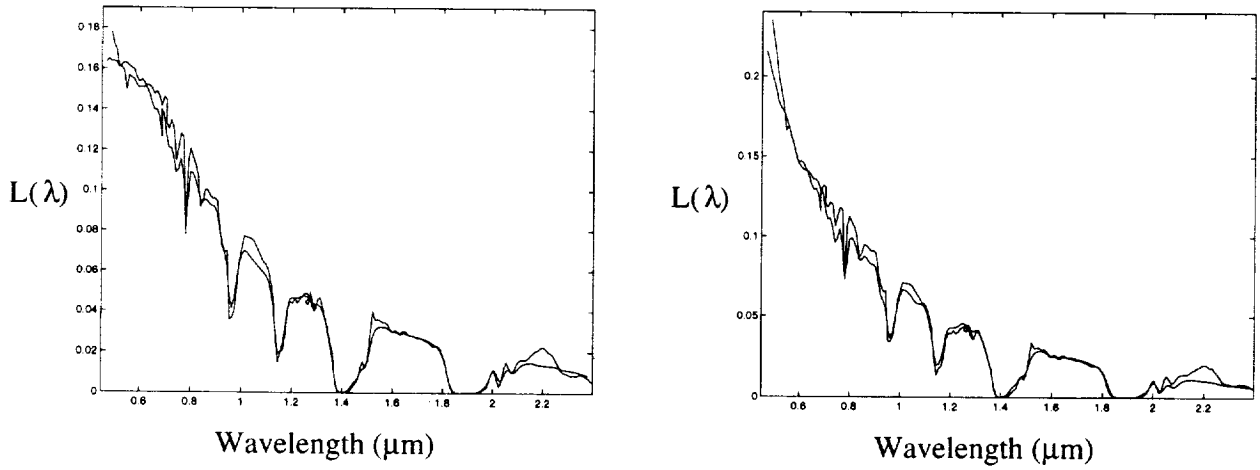

Figure 4: Measured spectra and fits

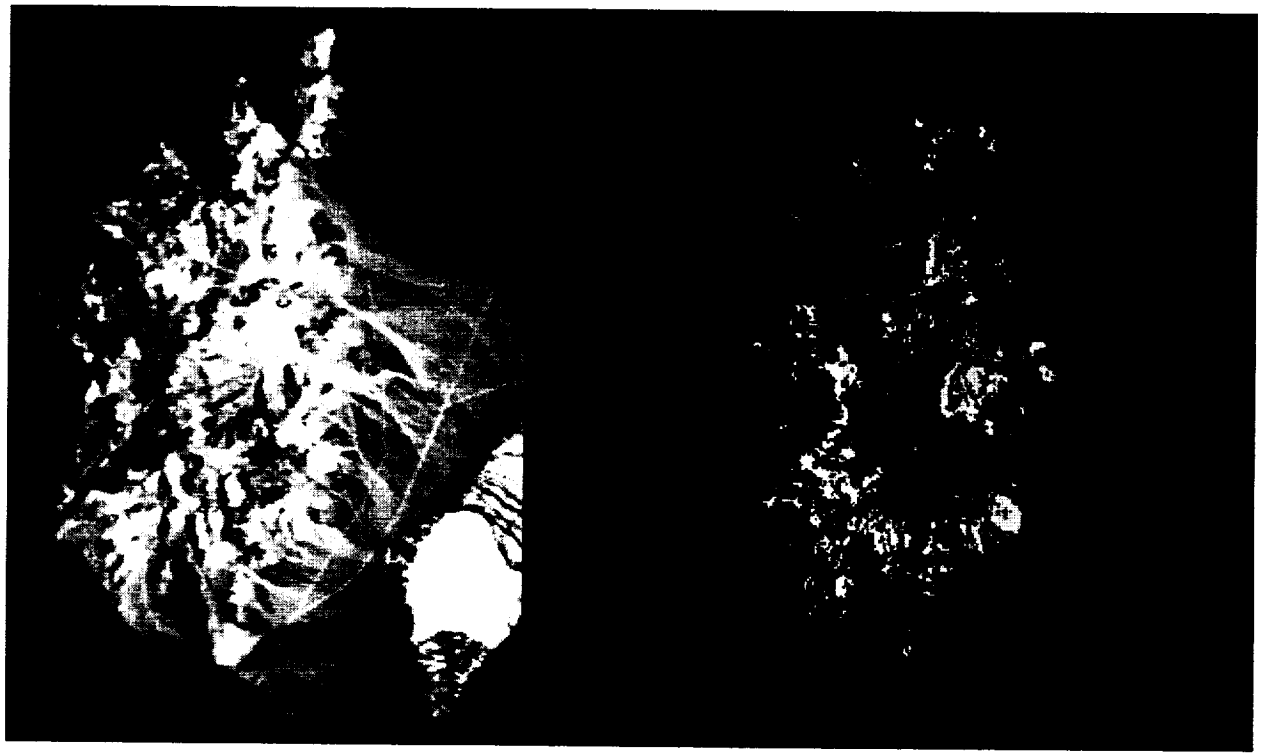

Figure 5: (a) AVIRIS image 1 of Cuprite, Nevada. (b) Classification results for AVIRIS image 1.

Figure 6: (a) AVIRIS image 2 of Cuprite, Nevada. (b) Classification results for AVIRIS image 2.

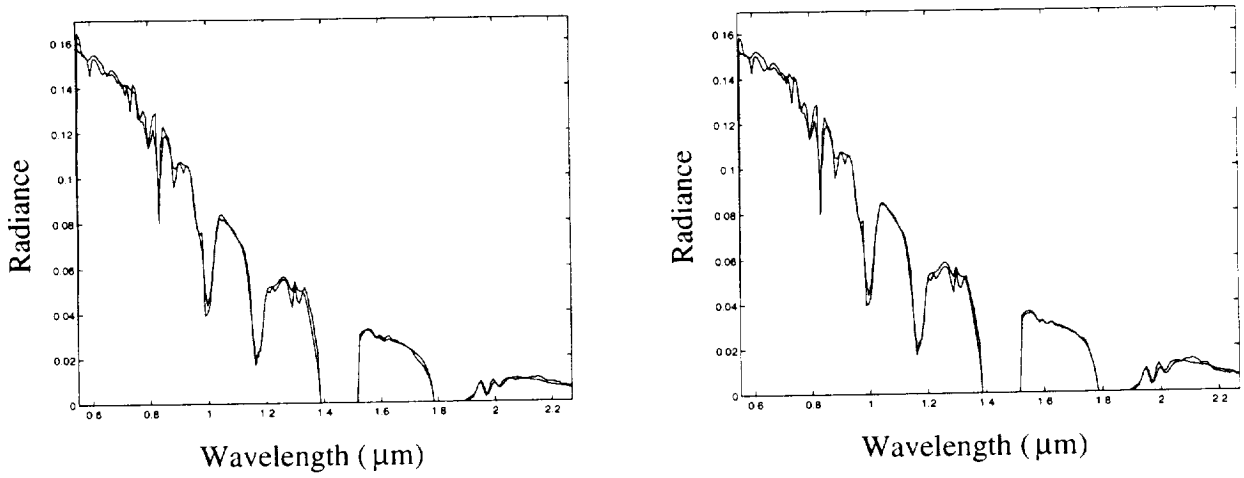

Figure 7: (a)Measured Alunite radiance and fit. (b) Measured Alunite/Silica mixture radiance and fit.

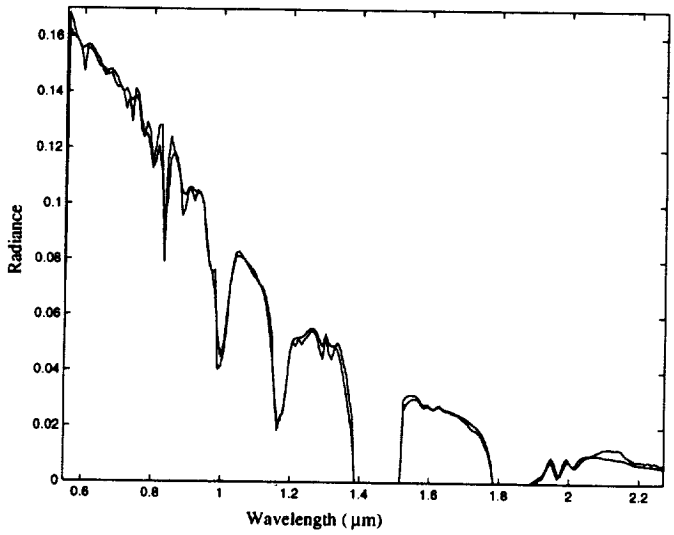

Figure 8: Measured Kaolinite radiance and fit

[2] A. Berk, L. S. Bernstein, and D. C. Robertson. MODTRAN: a moderate resolution model for LOWTRAN 7. Technical Report GL-TR-89-0122, Geophysics Laboratory, Bedford, Massachusetts, 1989.

[3] B. C. Gao and A. F. H. Goetz. Column atmospheric water vapor and vegetation liquid water retrievals from airborne imaging spectrometer data. *Journal of Geophysical Research*, 95(D4):3549–3564, 1990.

[4] G.H. Golub and C.F. van Loan. *Matrix Computations*. Johns Hopkins University Press, Baltimore, MD, 1983.

[5] D. B. Judd, D. L. MacAdam, and G. Wyszecki. Spectral distribution of typical daylight as a function of correlated color temperature. *Journal of the Optical Society of America*, 54(8):1031–1040, 1964.

[6] R. Richter. Correction of atmospheric and topographic effects for high spatial resolution satellite imagery. In *Proceedings of the SPIE, Algorithms for Multispectral and Hyperspectral Imagery III*, pages 216–224, Orlando, Florida, 1997.

[7] G. Vane, R. O. Green, T. G. Chrien, H. T. Enmark, E. G. Hansen, and W. M. Porter. The airborne visible/infrared imaging spectrometer (AVIRIS). *Remote Sensing of the Environment*, 44:127–143, 1993.

[8] D. J. Williams, A. Royer, N. T. O'Neill, S. Achal, and G. Weale. Reflectance extraction from CASI spectra using radiative transfer simulations and a rooftop irradiance collector. *Remote Sensing of the Environment*, 44:165–178, 1993.

Using Imaging Spectroscopy to Better Understand the Hydrothermal and Tectonic History of the Cuprite Mining District, Nevada

Gregg A. Swayze, Roger N. Clark, Alex F.H. Goetz[1], K. Eric Livo, and Steven S. Sutley

U.S. Geological Survey, Box 25046 MS964 DFC Denver, Colorado 80225
[1]Center for the Study of Earth from Space/CIRES, University of Colorado, Boulder, Colorado

1.0 Introduction

The Cuprite area consists of two acid-sulfate hydrothermal alteration centers straddling U.S. Highway 95 in southwestern Nevada. Alteration in the hydrothermal centers involves Tertiary volcanic rocks in the eastern center and Cambrian metasedimentary rocks in the western center (Abrams et al., 1977). The purpose of this study was to determine if these late-Miocene hydrothermal centers developed independently or whether they were created by lystric-faulting of a single conduit along an east-dipping detachment that moved the cooler upper portion of the system to the east relative to the hotter lower portion. The answer has implications for mineral exploration. Geology of the area was studied using imaging spectroscopy, isotopic dates, geologic maps, drill hole data, and D-C resistivity soundings.

2.0 Method and Results

Alteration zones were studied with imaging spectroscopy using radiance data collected in 1995 by the Airborne Visible/Infrared Imaging Spectrometer (AVIRIS) flown aboard a NASA ER-2 at 20 km altitude. Spectral changes in alunite and muscovite absorptions were used to map paleotemperatures in both centers. Spectral maps of Fe-bearing minerals, clays, sulfates, carbonates, micas, and siliceous sinter were produced using the U.S. Geological Survey Tricorder algorithm (Clark, et al., 1990). These maps reveal that the western center lacks a siliceous cap, has a core of low-grade kaolinite-muscovite and propylitic rock surrounded by a high temperature alunite zone, and that this center was eroded to a deep level, exposing the high temperature kaolinite polymorph dickite and a pyrite-rich zone. AVIRIS spectra also reveal that muscovites become progressively more Al-rich near intrusive dikes of quartz latite in the southern portion of the western center. This muscovite compositional variation probably correlates with increased paleotemperatures near these intrusive bodies. In contrast, spectral maps indicate that the eastern center has an extensive siliceous cap surrounded by a high to intermediate temperature alunite zone, lacks a propylitic core (at least at the present level of exposure), has extensive kaolinite zones lacking dickite, and has volumetrically insignificant jarosite, all consistent with present exposure near the top of the hydrothermal system (Swayze, 1997).

Tabular clasts of Cambrian phyllite, altered to alunite, eroded from the western center, and deposited in a conglomerate below the Spearhead member of the Stonewall Flat Tuff in the eastern center, are evidence that the western center had formed, was uplifted, and eroded prior to 7.6 Ma. Continuous exposures of the Stonewall Flat Tuff and underlying conglomerate can be traced from the argillic zone into the alunite and siliceous zones of the eastern center, implying that this center formed after 7.6 Ma. New ^{40}Ar-^{39}Ar isotopic dates indicate that the alunite-zone rocks cooled below alunite closure temperatures in both centers by 6.9 - 6.5 Ma with late stage vein alunites forming at 6.2 Ma in the western center (Swayze, 1997). A K-Ar isotopic date from unaltered olivine basalt that erupted onto altered conglomerate, between the centers, implies that all hydrothermal activity ceased by 6.2 Ma. Altogether, hydrothermal activity spanned at least 1.4 m.y. in the western center and had a shorter duration in the eastern center.

Quartz latite intrusives were intersected in 6 of 9 drill holes in the pediment between the hydrothermal centers (Swayze, 1997). Variations in the depth to basement, revealed in drill holes, indicate complex block faulting under the pediment. Total throw on the north-south trending steeply east-dipping normal fault bounding the eastern margin of the western center is about 400 m. A geoelectric profile revealed that a thick (possibly up to 170 m) post 6.5 Ma conglomerate overlies a fault-tilted gently west-dipping Tertiary volcanic section under the pediment (Swayze, 1997). A large zone of low resistivity dipping beneath the eastern center is probably the northward extension of a quartz latite dike which may have been the source of hydrothermal fluids that formed the centers.

3.0 Conclusions

The geologic and geophysical evidence collected during this study is most consistent with the separate development, both temporally and spatially, of two hydrothermal centers at Cuprite. These centers formed during and subsequent to activity in the nearby Stonewall Mountain volcanic center. Abundant jarosite in the western center marks the location of oxidized pyrite from an initial stage of mineralization. The lack of a later stage of Cu-sulfide mineralization may explain the absence of gold in the western center. Because the eastern center developed independently, it is a likely target for future exploration, especially in the west-dipping hydrothermal conduit below its siliceous cap.

Imaging spectroscopy at Cuprite revealed that the western center is exposed at a deep, once hotter level and that the eastern center is exposed at a shallow, cooler level very near the original paleosurface. These conculsions are based on spectral identification of mineral assemblages and their compositions characteristic of different paleotemperature regimes within the hydrothermal centers. These spectroscopic tools can be use to remotely understand the structure of other hydrothermal systems on the Earth as well as other planets.

4.0 References

Abrams, M.J, R.P. Ashley, L.C. Rowan, A.F.H. Goetz, and A.B. Kahle, 1977, "Mapping of hydrothermal alteration in the Cuprite mining district, Nevada using aircraft scanner images for the spectral region 0.46-2.36 μm," *Geology*, **5**, p. 713-718.

Clark, R.N., A.J. Gallagher, and G.A. Swayze, 1990, "Material absorption band depth mapping of imaging spectrometer data using a complete band shape least-squares fit with library reference spectra," Proceedings of the Second Airborne Visible/Infrared Imaging Spectrometer (AVIRIS) Workshop, Jet Propulsion Laboratory Publication 90-54, p. 176-186.

Swayze, G.A., 1997, **The hydrothermal and structural history of the Cuprite Mining District, Southwestern Nevada: An integrated geological and geophysical approach**, Ph. D. Dissertation, University of Colorado, Boulder, Colorado, p. 399.

Using Imaging Spectroscopy to Cost-Effectively Locate Acid-Generating Minerals at Mine Sites: An Example from the California Gulch Superfund Site in Leadville, Colorado

Gregg A. Swayze, Roger N. Clark, Kathleen S. Smith, Philip L. Hageman, Stephen J. Sutley, Ronald M. Pearson[1], Gary S. Rust[2], Paul H. Briggs, Allen L. Meier, Michael J. Singleton[3] and Shelly Roth

U.S. Geological Survey, Box 25046 DFC, Denver, Colorado 80225
[1]U.S. Bureau of Reclamation, P.O. Box 25007 D-8321, DFC, Denver, CO 80225
[2]ISSI Inc., 999 18th St. Suite 1180 South Tower, Denver, CO 80202
[3]Earth and Planetary Sciences, Campus Box 1169, Washington University
St. Louis, MO 63130

1. Introduction

The Leadville mining district, located at an elevation of 3000 m in the Central Colorado Rockies, has been mined for gold, silver, lead and zinc for more than 100 years. This activity has resulted in the dispersal of waste rock and tailings, rich in pyrite and other sulfides, over a 30 km^2 area including the city of Leadville. Oxidation of these sulfides releases lead, arsenic, cadmium, silver, and zinc into snowmelt and thunderstorm runoff, which drains into the Arkansas River, a main source of water for Front Range urban centers and agricultural communities. The U.S. Environmental Protection Agency (EPA), U.S. Bureau of Reclamation (USBR), contractors, and responsible parties are remediating the mined areas to curtail further releases of heavy metals into various drainage tributaries of the Arkansas River. Mineral maps made by the U.S. Geological Survey (USGS) from AVIRIS data collected over this mining district were used to focus remediation efforts by locating the point sources of acid drainage.

2. Method

The sulfide oxidation process is biologically driven along complex chemical pathways with feedback reactions that enhance the speed and magnitude of oxidation (Nordstrom, 1982). Release of heavy metals is facilitated by sulfide oxidation, since many of the sulfides contain the heavy metals (e.g. Pb, As, Cd, Ag, and Zn). The oxidation-weathering process of many sulfide minerals produces low pH water in which the heavy metals dissolve as aqueous phases that are then transported as runoff into nearby streams creating acid mine drainage. Secondary minerals such as copiapite, jarosite, schwertmannite, goethite, ferrihydrite, and hematite are formed by sulfide oxidation and subsequent precipitation from metal-rich water. These secondary minerals are Fe-rich and usually hydroxyl-bearing, making it possible to identify them on the basis of their characteristic spectral signatures. As the pH of a mining impacted stream increases by mixing with higher pH water from tributaries, these secondary minerals precipitate out as stream bed coatings or suspended sediments. Because some of the heavy metals can substitute for Fe, they may also precipitate from solution as constituents of secondary minerals or as contaminants sorbed onto the surfaces of the secondary minerals (Smith and Macalady, 1991; Alpers et al., 1994). Subsequent pulse of low pH water may dissolve the secondary minerals or desorb metals thus remobilizing the heavy metals and transferring them downstream.

The sulfide mineral pyrite is the primary source of acid drainage. Because direct spectral detection of pyrite is hampered by its low reflectance level, its broad Fe-absorption, and rapidly formed coating of secondary minerals, pyrite can only be detected when it is coarse grained or compositionally impure (G. Plumlee, pers. comm., 1996). However, our observations indicate that pyrite weathers first to jarosite, and then to goethite (Table 1), forming a sequence where the degree of oxidation is indicated by the type of secondary mineral exposed at the surface. Therefore, an indirect way to find oxidizing pyrite is to look for areas where the secondary minerals grade through the established oxidation sequence (e.g. those areas with jarosite surrounded by goethite). Quite fortuitously, the presence of heavy metals and low pH often associated with the mine waste prevent the growth of vegetation over most waste piles leaving them exposed and suitable for detection with remote sensing.

Table 1. Pyrite and Secondary Minerals

Pyrite	FeS_2 *
Jarosite	$(H_3O, 0.5Pb, Na, K)Fe^{3+}_3(SO_4)_2(OH)_6$
Goethite	α-FeO(OH)
Hematite	α-Fe_2O_3

* Formulas from Fleischer (1980)

The large size of the Leadville mining district and presence of spectrally detectable secondary minerals associated with pyrite oxidation makes imaging spectroscopy effective for locating those minerals related to the acid mine drainage sources. AVIRIS data was collected over Leadville on July 27, 1995 (see Swayze et al., 1996). Data were calibrated from radiance to reflectance using ATREM (Gao et al, 1993) and a ground calibration site as described in Clark et al. (1995b).

Calibrated AVIRIS reflectance data were spectroscopically mapped using the Tricorder algorithm (Clark et al., 1995a and references therein; Clark et al., in prep.,).[1] Tricorder, an expert system, is capable of simultaneously analyzing spectra of solids, liquids, and gases. Tricorder's primary subroutine is a modified least-square shape-matching algorithm which compares spectra of unknown materials to hundreds of reference library spectra and identifies the best match. This subroutine uses thresholds on band depth, fit, and continuum slope to help constrain the spectral matching. The spectral library used to map AVIRIS Leadville data contains 160 reference spectra of individual secondary minerals and mineral mixtures. Because the 0.4 - 1.35 μm spectral region is dominated by electronic absorptions due to transition metals (such as Fe) and the 2.0 to 2.5-μm region is dominated by molecular vibrational absorptions, maps of the spectrally dominant materials in each wavelength region were produced for the Leadville AVIRIS scene.

3.0 Mapping Results

Mineral maps created by Tricorder reveal characteristic mineral assemblages centered over the mine dumps and tailings which are rich in pyrite. Field checks demonstrate that highly acidic water formed in the pyrite-rich piles is gradually neutralized as it spreads away from the dumps. This process deposits progressively less acidic secondary minerals in rough concentric zones centered on the dumps, creating diagnostic patterns easily recognized on the electronic absorption mineral map. The centers of the zones are jarosite-rich and have a high acid-generating capacity that produces acidic water containing heavy metals. This zone is surrounded by a jarosite + goethite zone which is itself surrounded by an outer most goethite zone. To facilitate comparison with features on the ground, the mineral map was geometrically registered and overlaid on orthophoto information for the Leadville area. It shows concentric secondary mineral zones around many of the waste piles helping to pinpoint the sources of acid drainage. Such an engineering product allows rapid prioritization of remediation sites.

3.1 Ground Truth

To test the hypothesis that the secondary mineral zones can be used to indirectly measure pH and metal mobility, a ground verification leach study was conducted at the pile with the clearest pattern of concentric mineral zones. Rock samples were collected and spectral reflectance measurements were made every 10 m along a 250 m traverse across the mineral zones at the Venir waste rock pile located 4 km southeast of Leadville at an elevation of 3600 m. Distances along the traverse were measured using a tape starting from the western end of the traverse line. The traverse starts in the forest west and down slope from the Venir pile and proceeding up the

[1]Clark, R.N., G.A. Swayze, and T. V.V. King, in prep., "Imaging spectroscopy: a new tool for identifying and mapping materials: minerals, amorphous materials, environmental and man-made materials, vegetation species, health and water content, water, ice, snow, and atmospheric gases: the USGS Tricorder algorithm," to be submitted to *Science*.

steep west side onto the flat top of the pile. The traverse then continues past abandoned buildings on the eastern margin of the pile and extends into forest east and slightly up slope of the pile.

The locations of rock samples relative to the mineral zones were determined by two methods. The first method involved registering the mineral maps made from AVIRIS data to a registered aerial photo of the Venir pile then plotting the sample points on the composite image. This presentation gives the correlation of each sample to mineralogy determined spectrally from AVIRIS. The second method used mineralogy determined from the field spectra. A minimum of 10 spectra were measured at each sample collection station with an ASD FR spectrometer. Spectra were averaged, corrected to true reflectance with a NIST spectralon correction, and then mapped for mineralogy with the Tricorder algorithm. This gives the correlation of each sample to mineralogy determined on the ground.

The AVIRIS mineral maps show the pile as a jarosite zone surrounded by a broad skirt of goethite slightly wider on the down slope side of the pile. A thin jarosite + goethite zone maps along the steep west-facing slope of the pile forming a transition zone between the jarosite zone and outer goethite skirt. This jarosite + goethite zone continues around the southern and eastern margin of the pile pinching out along the north margin where the jarosite zone is in direct contact with the goethite skirt. Correlation between AVIRIS and ground spectra is nearly one-to-one except near buildings with rusted metal roofs. In these areas the roofs contribute a goethite spectral component in addition to that from jarosite on the ground resulting in a combined jarosite + goethite spectral signature at the 17 x 17 meter spatial scale of AVIRIS pixels at this elevation. The ground spectra indicate that the actual jarosite + goethite zone is much narrower along the eastern margin of the pile. Because of this spectral interference the geochemical measurements described below were keyed to mineral zones derived from the ground traverse.

3.2 pH and Metal Mobility Tests

The rock samples were analyzed for leachate pH and metal mobility using wet chemistry. Samples were sieved and the < 4 mm fraction was split for grinding and bulk chemical analysis for elements with inductively coupled plasma - atomic emission spectroscopy (ICP-AES). The remaining unground sample split was subjected to the EPA 1312 Synthetic Precipitation Leach Procedure (SPLP) which involved adding 2 liters of slightly acidified deionized water to 100 g of sample and agitating the mixture for 18 hours. Leachate pH was measured before filtering and trace metals were measured with inductively coupled plasma - mass spectroscopy (ICP-MS) on the filtered leachate.

Results of the chemical analyses show that the mineral zones can be used to map pH and metal mobility. For instance, pH of the leachate is 4.5 - 6 in the goethite zones, 2.5 - 3.5 in the jarosite + goethite zone, and 2.3 - 2.5 in the jarosite zone (Figure 1). Bulk trace metal concentrations show only a weak correlation to mineral zones with the ranges of metal concentrations in each zone overlapping the others (Figure 2). However, leachable trace metal concentrations show a good correlation to the mineral zones with metals 20 - 100 times more mobile in the jarosite and jarosite + goethite zone compared to the goethite zone. Leachable metal concentrations vary over nearly three orders of magnitude compared to only one order of magnitude for the bulk metal concentrations. This relationship indicates that bulk metal concentration, usually measured with field x-ray florescence (XRF), does not accurately predict the leachability of trace metals. The jarosite and jarosite + goethite zones pose a serious contamination threat if they boarder streams capable of transporting metal-rich water and suspended sediment. Because jarosite quickly decomposes outside of its pH range, it is rapidly coated with goethite. Areas where the goethite zone intersects streams may mark the deposits of storm events during which acid drainage traveled beyond the jarosite and jarosite + goethite zones.

4. Conclusions

Spectral mineral maps made with AVIRIS data using the USGS Tricorder algorithm have assisted remediation efforts at the California Gulch Superfund Site at Leadville, Colorado. The maps identified concentric zones of secondary minerals in bull's-eye patterns that pinpoint the sources of acid drainage. Field tests verify that spectral mineral maps can be used to indirectly measure pH and metal mobility of surface runoff emanating from these waste rock and tailings piles. Use of XRF bulk metal concentrations to screen wastes may overestimate the amount of material that needs to be remediated. A GIS system that integrates mineral maps with

topography and drainage information could be used to screen drainage basins for those areas contributing the most acid and metals to nearby streams.

Mineral maps made from AVIRIS data provided a rapid method to screen entire mining districts for sources of acid and metals. What it took 52 days to do on the ground and in the lab for the Venir pile (i.e. sample collection, preparation, and leaching) was done using AVIRIS and Tricorder in a little over two days. Use of mineral maps created from AVIRIS data has saved taxpayers $2 million and accelerated remediation by 2.5 years at the California Gulch Superfund Site (S. Vance, EPA, pers. comm, 1997). This technology can be used to save time and money at other mine sites where carbonate in the waste rock is unable to neutralize the acidity created by pyrite oxidation. Additional studies are underway at the Ray Mine in Arizona, and in the Mother Load Gold Belt in California. Widespread use of this screening technique depends on the willingness of the EPA to approve its use for cleanup on a production basis.

5. References

Alpers, C.N., D.W. Blowes, D.K. Nordstrom, and J.L. Jambor, 1994, "Secondary minerals and acid mine-water chemistry," in *The Environmental Geochemistry of Sulfide Mine-Wastes, Short Course Handbook,* (eds.) D.W. Blowes and J.L. Jambor, vol. 2, Waterloo, Ontario, Canada, Mineralogical Association of Canada, May 1994, p. 247-270.

Clark, R.N., and G.A. Swayze, 1995a, "Mapping minerals, amorphous materials, environmental materials, vegetation, water, ice, and snow, and other materials: The USGS Tricorder Algorithm," *Summaries of the Fifth Annual JPL Airborne Earth Science Workshop*, January 23-26, (ed.) R.O. Green, Jet Propulsion Laboratory Publication 95-1, p. 39-40.

Clark, R.N., G.A. Swayze, K. Heidebrecht, R.O. Green, and A.F.H Goetz, 1995b, "Calibration to surface reflectance of terrestrial imaging spectrometry data: comparison of methods," *Summaries of the Fifth Annual JPL Airborne Earth Science Workshop*, January 23-26, (ed.) R.O. Green, Jet Propulsion Laboratory Publication 95-1, p. 41-42.

Fleischer, M., 1980, *Glossary of Mineral Species,* Mineralogic Record, Tucson, Arizona, 192 p.

Gao, B.C., K.B. Heidebrecht, and A.F.H. Goetz, 1993, "Derivation of scaled surface reflectances from AVIRIS data," *Remote Sensing of Environment*, v. 44, p. 165-178.

Nordstrom, D.K., 1982, "Aqueous pyrite oxidation and the consequent formation of secondary iron minerals," in *Acid Sulfate Weathering*, eds. J.S. Kittrick et al., Soil Society of America, p. 37-56.

Smith, K.S., and D.L. Macalady, 1991, "Water/sediment partitioning of trace elements in a stream receiving acid-mine drainage," Second International Conference on the Abatement of Acidic Drainage, NEDEM, Montreal, Canada, Sept. 16-18., p. 435-450.

Swayze, G.A., R.N. Clark, R.M. Pearson, and K.E. Livo, 1996, "Mapping acid-generating minerals at the California Gulch Superfund Site in Leadville, Colorado using imaging spectroscopy," Summaries of the Sixth Annual JPL Airborne Earth Science Workshop, JPL Publication 96-4, vol. 1, March 4-8, p. 231-234.

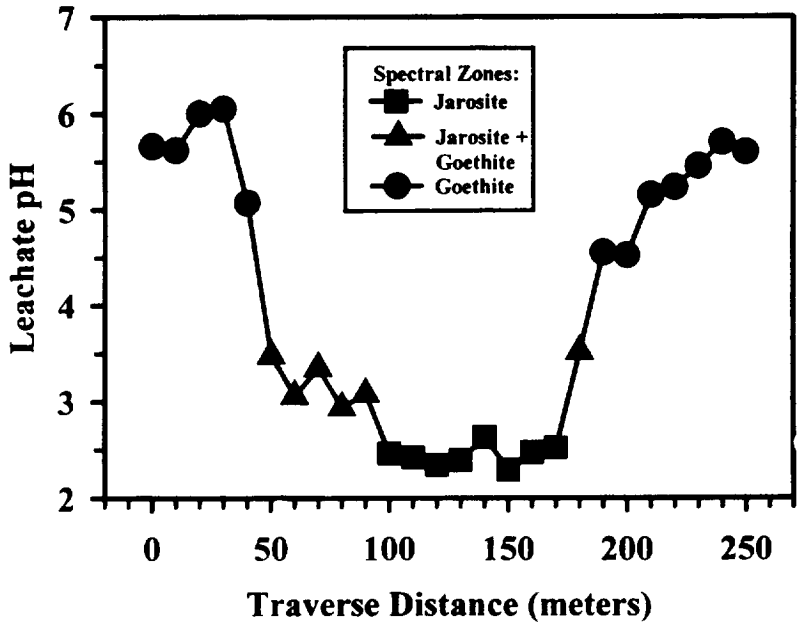

Figure 1. Leachate pH as a function of distance along the traverse across the Venir waste rock pile.

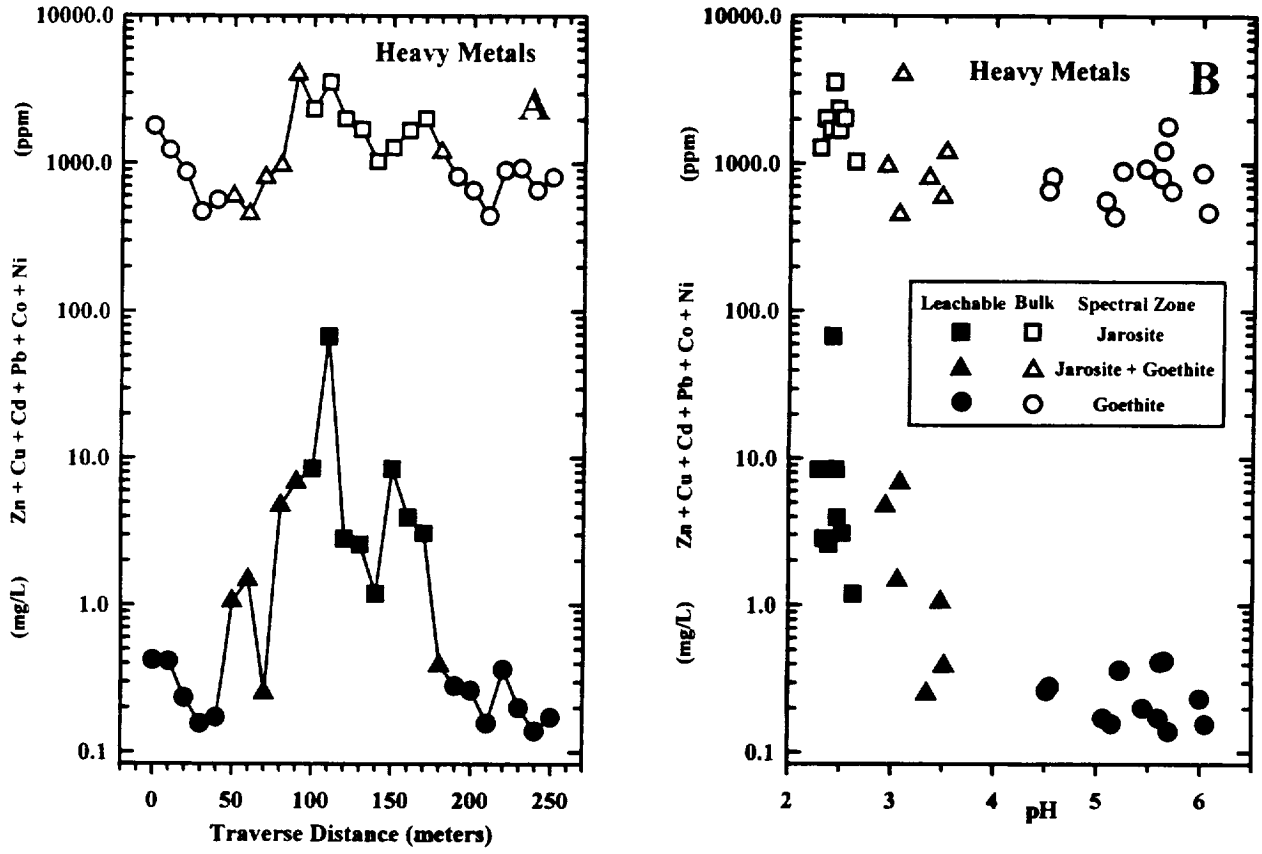

Figure 2. A) Concentration of bulk and leachable heavy metals across the Venir waste rock pile. B) Ficklin diagram of heavy metals versus leachate pH. Leachable heavy metals vary over nearly three orders of magnitude with metals in the jarosite and jarosite + goethite zones 20-100 time as mobile as in the goethite zone.

EVALUATION OF THE USE OF DARK AND BRIGHT TARGETS FOR THE IN-FLIGHT CALIBRATION OF AVIRIS

K. Thome[1], R. Parada[1], S. Schiller[2], J. Conel[3], J. LaMarr[1]

[1]Optical Sciences Center, University of Arizona
PO Box 210094, Tucson AZ 85721

[2]Physics Department, South Dakota State University,
Box 2219, Brookings SD 57007

[3]Jet Propulsion Laboratory, M/S 169-237,
California Institute of Technology
4800 Oak Grove Dr., Pasadena CA 91109-8099

1. INTRODUCTION

One of the goals of NASA's Mission to Planet Earth (MTPE) is to create a set of long-term observations for the study of global change using multiple sensors on multiple platforms (Asrar and Dozier, 1994; Slater et al., 1996; Barnes and Holmes, 1993). These sensors will monitor environmental changes on a global scale for both terrestrial and aquatic targets (Hooker et al., 1992). For instance, the Earth Observing System's AM-1 platform has five sensors with each sensor having its own calibration team. Critical to the success of MTPE is ensuring the accuracy of the radiometric measurements over the lifetime of each platform and traceability between platforms. This can only be accomplished for the 18-year MTPE program through vicarious calibration (Slater and Biggar, 1996).

Vicarious calibration refers to methods of in-flight calibration that do not rely on onboard calibrators. Hovis et al. (1985) made one of the earliest vicarious calibrations by measuring the radiance above a ground target from a high-altitude aircraft to verify the degradation of the Coastal Zone Color Scanner's shorter wavelength bands. Since then, many types of vicarious calibration have been developed. For example, Kaufman and Holben (1993) propose using large-view angles and molecular scatter to characterize the short-wave, visible channels of the Advanced Very High Resolution Radiometer. Vermote et al. (1992) propose a similar approach for Systeme Pour l'Observation de la Terre-1 (SPOT), Haute Resolution Visible (HRV) cameras but used data at longer wavelengths to determine contributions from aerosols and sea-surface reflection.

The two methods used in this work rely on in-situ measurements to improve accuracy and are referred to as the reflectance- and radiance-based techniques (Slater et al., 1987). The reflectance-based method relies on ground-based measurements of the surface reflectance and atmospheric extinction at a selected site to predict top-of-the-atmosphere radiance at the time of satellite overpass. The radiance-based approach refers to methods such as that of Hovis et al. (1985) where the radiance from the target is measured by a well-characterized and well-calibrated radiometer at the same time the sensor to be calibrated views the target. The advantage of this technique is that the radiometer can be carried in an aircraft above most of the influence of the atmosphere, greatly reducing uncertainties from the atmospheric characterization. These two techniques have been used successfully for the SPOT HRV (Gellman et al., 1993), Landsat-5 Thematic Mapper (TM) (Slater et al., 1987, Thome et al., 1993), a Daedalus scanner (Balick et al., 1991), and the Airborne Visible and Infrared Spectrometer (AVIRIS) (Vane et al., 1993). The test sites for this past work have all been high-reflectance, land targets.

Included in MTPE are sensors designed for ocean-color studies. These sensors have high sensitivity and will saturate over the high-reflectance sites typically used for vicarious calibration. Thus, the vicarious calibration of these sensors requires low reflectance targets. The use of water sites is a natural choice since the operational conditions of the sensor is more closely reproduced. Using low-reflectance targets adds complexities to vicarious calibration due to the fact that the atmosphere contributes a much higher portion of the radiance at the sensor. In order to achieve the same calibration uncertainty levels, the atmospheric characterization must be better than is

necessary when using high-reflectance targets. The use of water targets also requires developing more sophisticated radiative transfer codes to account for the specular reflection of the air-water interface as well as factors such as the surface's wave-slope distribution, the diffuse water and foam reflectances, and the coupling of radiance between water and atmosphere.

The AVIRIS sensor is a natural choice to evaluate the use of both bright and dark targets for vicarious calibration of satellite sensors. The hyperspectral nature of the sensor allows the bands of the MTPE sensors to be synthesized, allowing uncertainties of the vicarious calibration to be determined for the specific sensor bands. AVIRIS is also capable of flying at high altitude, thus closely simulating the atmospheric path seen by satellite sensors. In addition, the preflight calibration and characterization of AVIRIS, coupled with the reliability of AVIRIS, makes it a good choice for testing vicarious calibration.

In this work we present the reflectance-based and radiance-based results from two campaigns. The first was to Lake Tahoe in June 1995 and marked the first attempt by the Remote Sensing Group (RSG) at the University of Arizona (UA) to use a dark water surface for vicarious calibration. Radiance data from a low-altitude aircraft, surface measurements of water reflectance, and atmospheric characterization were used to predict the radiance at the altitude of the AVIRIS sensor. The vicariously-derived calibration coefficients are compared to those obtained from a preflight calibration of AVIRIS. The reflectance-based method agrees at the 0.3-7.7% level with the preflight coefficients, while the radiance-based method differs from the preflight results by 1.0-17.5%. The second campaign was a joint vicarious campaign held in June 1997 to evaluate the accuracy of reflectance-based, vicarious calibrations. Six groups participated in this campaign and made independent measurements of surface reflectance and atmospheric transmittance on five different days. The results of this campaign, using a high-reflectance playa, were compared to those of the AVIRIS sensor to look for biases in the reflectance-based approach. Results from this campaign showed that the radiance at AVIRIS could be predicted to better than 5% for most bands not affected by atmospheric absorption.

2. METHODS

2.1 Reflectance-based Method

The reflectance-based method relies on characterizing the surface of, and the atmosphere over, a test site at the time of a sensor overpass. The results of the measurements are used as input to a radiative transfer code to predict a normalized radiance at the sensor that is converted to absolute radiances via an assumed solar irradiance curve. The atmospheric characterization typically relies on solar extinction measurements and these data are converted to spectral optical depths that are used to describe aerosol parameters and columnar amounts of gaseous absorbers (Gellman et al., 1991; Biggar et al., 1990; King et al., 1978; Flittner et al., 1993; Thome et al., 1992). Surface characterization typically consists of measuring the upwelling signal from the test site and ratioing to data collected while viewing a panel of known reflectance to obtain the surface reflectance of the site (Biggar et al., 1988). Past work shows that the uncertainties expected from the reflectance-based approach are better than 5% for spectral regions in the VNIR that not affected strong absorption (Biggar et al., 1994). The same study shows that the primary source of uncertainty is due to uncertainties in the aerosol parameters such as refractive index and size distribution. Uncertainties in the surface reflectance are also a significant error source. Biggar et al. (1994) shows that reasonable improvements in equipment and data collection methods should bring these uncertainties to less than 3.5%.

For low reflectance targets, uncertainties in the predicted radiance due to atmospheric uncertainties are higher due to the relative importance of atmospheric signal contributions. The successive orders of scattering (SOS) radiative transfer code has been used for the Lake Tahoe data (Deuzé. et al., 1989). The primary advantage of using the SOS transfer code is its ability to handle a rough ocean surface and polarization of the radiance field. Gaseous absorption is computed separately using the Second Simulation of the Satellite Signal in the Solar Spectrum (6S) transfer code (Vermote et al., 1995). Band integrated transmittance values for ozone and water vapor are computed using columnar measurements while absorption from oxygen and other molecular gases is computed using standard

atmospheric models. The Lunar Lake data set is processed using a hyperspectral version of a Gauss-Seidel iteration radiative transfer code and MODTRAN3 to determine the exo-atmospheric solar irradiance and gaseous transmittance (Thome et al., 1996).

2.2 Radiance-based Method

The radiance-based method uses aircraft-based measurements of the spectral radiances over a calibration site at sensor overpass. An atmospheric correction is made for the effects between the aircraft and sensor being calibrated using the atmospheric and surface reflectance data collected for the reflectance-based approach. As with the reflectance-based method, the RSG uses the SOS code for radiance-based calibrations over water targets and the 6S code to compute gaseous absorption. Over bright land targets, the hyperspectral Gauss-Seidel iteration code is used. These codes are used to transfer the aircraft-level radiances to sensor level. Past work shows the uncertainties expected from the radiance-based approach are less than 3% for regions in the VNIR not affected strong absorption and that the primary source of uncertainty is the calibration of the radiometer in the aircraft (Biggar et al., 1994). Reasonable improvements in equipment and data collection methods should bring these uncertainties to less than 2.0%.

3. CALIBRATION AT LAKE TAHOE

3.1 Test Site Description

Data were collected for a vicarious calibration of AVIRIS on June 22, 1995. This field campaign was a joint effort between the RSG, the Marine Research Group of the University of South Florida, the Naval Research Laboratory, and the Jet Propulsion Laboratory (JPL). Lake Tahoe is a deep graben-fault lake located on the California-Nevada border (39.1° N, 120.0° W) at an elevation of about 1.9 km above mean sea level (MSL). At this elevation, the aerosol loading is low. Since aerosol signal contributions constitute one of the largest sources of uncertainty in the vicarious calibration process, low aerosol loading is a desirable feature for any prospective site. Other benefits from the use of this lake include its large size (approximately 19 km by 32 km), the high probability of cloud-free conditions, the presence of a high contrast shore line to facilitate image registration, and the relatively clear water. Disadvantages of this location include the low upwelled signal levels (due to the smaller optical depths between the site and sensor), and the need to make assessments of adjacency effects from the vegetation surrounding the lake.

During the calibration period, the aerosol loading was low (aerosol optical thickness of 0.051 at 560 nm) and only a few scattered cumulus clouds were present. Winds were light, averaging around 0.75 m/s throughout the morning. Image data were acquired by AVIRIS at approximately 18:19 Universal Coordinated Time (UTC). The viewing geometry for the portion of the lake where reflectance data were collected was at a nadir angle of 1.7 degrees and azimuth of 186.1 degrees. An average of 48 pixels was used to compute the mean, dark-corrected band readings corresponding to the portion of the lake where surface reflectance measurements were made.

3.2 Radiance-based Vicarious Calibration

The radiometer used in the radiance-based approach was a seven-band system that essentially simulates the solar-reflective bands of TM with an additional band in the shortwave IR. For this work, only the first four bands were used corresponding to center wavelengths of 0.49, 0.56, 0.66, and 0.83 μm. The radiometer was mounted in a Cessna-180 airplane and flown at an altitude of 3.9 km above sea level. Simultaneous video was collected to aid in the registration of the low-altitude data to the AVIRIS data. Three passes of the test site were made around the time of the AVIRIS overflights. The atmospheric and lake reflectance data collected in conjunction with the reflectance-based method were also used for the radiance-based calibration process. Calibration coefficients for the seven-band radiometer were obtained using a solar-radiation-based technique (Biggar et al., 1993). The resulting calibration coefficients determined for AVIRIS from the radiance-based approach are given in Table 1.

The differences at the two shorter bands are quite small, 1-4%, and get much larger at the two longer-wavelength bands. This is somewhat expected, since the radiance decreases at these longer wavelengths due to reduced scattering leads to lower signal to noise. Uncertainties in the calibration of the MMR are relatively constant with wavelength at a value of 3.0% for band 1 and 2.5% for band 4. The largest source of uncertainty in the measured radiance by the MMR is the pointing error of the radiometer. For the case shown in this work, a 2° pointing uncertainty gives changes in radiance of 5.2% for band 1 to near 50% for band 4. This is primarily due to the larger relative importance of specularly reflected sunlight at the longer wavelengths.

Table 1
Results of June 22, 1995 AVIRIS calibrations. Calibration coefficients are quoted in units of ($W\ m^{-2} sr^{-1} \mu m^{-1}$) / DN for Barnes MMR band centers.

Method	Band 1	Band 2	Band 3	Band 4
Preflight	0.2344	0.1785	0.1603	0.1113
Reflectance-based	0.2525	0.1791	0.1627	0.1121
Radiance-based	0.2440	0.1768	0.1388	0.0918

3.3 Reflectance-based results

Surface measurements of the water properties at the time of the AVIRIS overflight were made from a research vessel on the lake. An anemometer was used to measure wind speed around the time of sensor overpass. Diffuse water reflectance was measured using a hand-held spectroradiometer designed and built by the group from the University of South Florida. Due to the relatively calm state of the water, foam contributions are assumed to be negligible. The resulting calibration coefficients determined from the reflectance-based method for the four MMR bands are presented in Table 1. The differences between the AVIRIS results and the reflectance-based values range from 0.3% for band 2 to 7.7% for band 1.

This is remarkably good agreement for a first attempt at this type of calibration. The larger differences at the shorter wavelengths are expected because of the larger signal due to scattering. Thus, any uncertainties in characterizing the atmosphere will lead to larger uncertainties in the predicted radiance at shorter wavelengths. Modeling of the reflectance uncertainty shows that the largest uncertainties in predicted radiance will occur at longer wavelengths. This is true both for effects due to wave-slope uncertainties as well as measuring the diffuse reflectance. Thus, the differences seen here are most likely dominated by atmospheric uncertainties.

4. CALIBRATION AT LUNAR LAKE

4.1 Test Site Description

The purpose of the Lunar Lake campaign was to have several groups collect data for reflectance-based calibrations for comparison. Lunar Lake was selected because its high reflectance and the low aerosol in the region reduce uncertainties due to atmospheric effects. The area is spatially uniform with portions of the playa varying by less than 0.5% of the reflectance over 10^4 m^2 areas and this reduces uncertainties in determining the surface reflectance. The playa is slightly smaller than an ideal site, being approximately 3 km by 5 km in size, but this should not be a factor in any comparisons between groups. The surface of the playa is also very hard and resistant to change from people walking on it. This makes the site suitable for an experiment where several groups would be walking on the site for several days with multiple collections each day. The primary area used for the work described here was a 360-m by 120-m representative area of the playa assumed to approximate 48, 30-m pixels. This area was located at approximately 38 degrees 23 minutes North and 115 degrees 59 minutes West and was laid out in an east-west orientation.

While several groups participated in the campaign, including groups from Japan and Canada, results from only three of the groups are discussed here. These three groups are from the UA, JPL, and South Dakota State University (SDSU). The field work consisted of several data collections per day for several days. The times were

selected to correspond approximately to the time of the EOS-AM1 platform overpass. All groups essentially used the same approach for collecting surface reflectance data using ASD FieldSpec FRs for the measurements and referencing playa data to measurements of Spectralon® panels to convert to reflectance. Atmospheric measurements were primarily made using solar radiometers constructed in the UA's Electrical and Computing Engineering Department. The JPL and SDSU groups used automated versions of these solar radiometers while the UA group operated a manual version. The JPL and SDSU groups also collected measurements of downwelling global and diffuse irradiance using multi-filter, shadow-band radiometers and the UA group made similar measurements with an occulting disk system.

4.2 Reflectance-based results

The primary purpose of the campaign was to compare the results of vicarious calibrations that will be similar to those used for the vicarious calibration of EOS AM-1 sensors. From a previous campaign, it was known that a primary cause of differences between vicarious results is in the retrieval of surface reflectance (Thome et al., 1998). For this campaign, efforts were made to more closely examine retrieved surface reflectance. Table 2 gives an example of some of the results obtained for measurements of the playa surface for several bands from the ASTER, ETM+, and MISR sensors. As can be seen, the retrieved reflectances agree very well. Similarly good results were obtained for predicted radiances for the several data sets that were collected for looking at predicted radiances at the top of the atmosphere with differences less than 5% for most bands and less than 12% for all bands. Further evaluation of the entire set of results is currently underway in an attempt to understand the causes of differences.

Two overflights of the AVIRIS sensor were scheduled during the campaign. The overpass on June 27 occurred during cloudy skies, and no ground data were collected coincident with the overflight. The other overflight took place on June 23. In this work, we present the results from the UA group only, since the focus of this paper is to look at differences in using bright and dark targets for vicarious calibration. Future work will include more detailed discussions of the AVIRIS results in reference to the results from all of the groups at the Lunar Lake campaign. The output from the UA radiative transfer code for atmospheric scattering and ozone absorption is at one-nm intervals. The results are based upon inputs derived from inversion of solar radiometer data. Atmospheric transmittance was determined using MODTRAN3 based on input columnar water vapor from solar radiometer data. The data were then band-averaged over 10-nm intervals to derive radiances that could be directly compared to those from AVIRIS. Figure 1a shows the radiances derived from AVIRIS and those based on the field data for the VNIR portion of the spectrum and Figure 1b shows results for the SWIR. Figure 2 shows the percent difference between the reflectance-based radiances and those from AVIRIS.

There are several notable features to note in Figures 1 and 2. First is that the percent difference is large in regions of strong water vapor absorption. This is due to poor surface reflectance retrievals in these bands due to low signal. To avoid this problem, it is possible to curve fit the spectral reflectance in regions of strong atmospheric absorption. This is currently underway and should improve the comparisons in these spectral regions. Also noticeable is the larger discrepancies at shorter wavelengths. There are several possible causes for this. The first is that the spectral reflectance of the Lunar Lake Playa is rapidly changing with wavelength at the short end of the

Table 2
Retrieved surface reflectances of Lunar Lake Playa from June 24, 1998 for sensor bands given

	MISR 1	MISR 2	MISR 3	MISR 4	ASTER 2	ASTER 4	ASTER 5	ETM+ 1	ETM+ 5	ETM + 7
UA	0.268	0.411	0.488	0.521	0.483	0.523	0.482	0.303	0.523	0.467
JPL	0.292	0.411	0.480	0.516	0.480	0.531	0.482	0.324	0.523	0.472
SDSU	0.267	0.410	0.492	0.526	0.488	0.532	0.491	0.303	0.532	0.475

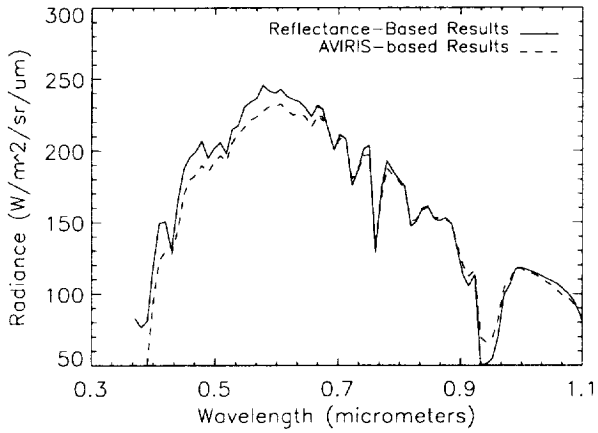

Figure 1a At-sensor radiances in the VNIR at AVIRIS from measurements and reflectance-based predictions.

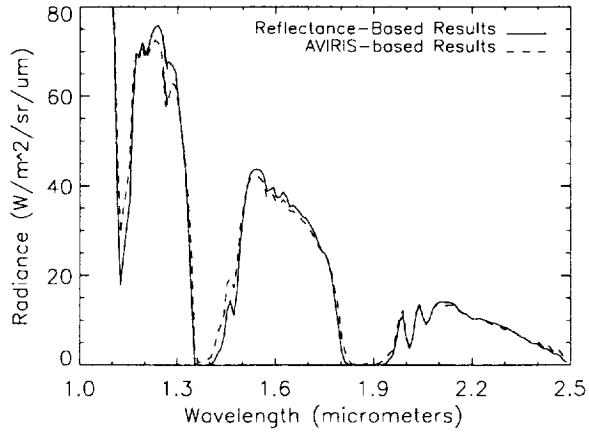

Figure 1b At-sensor radiances in the SWIR at AVIRIS from measurements and reflectance-based predictions.

spectrum. Shifting the input surface reflectances by 4 nm gave much better agreement at these wavelengths. Studies of the surface reflectance data are currently underway to determine if this shift is feasible. Another explanation is that laboratory calibrations of radiometers are typically less accurate at shorter wavelengths due to the low output of laboratory sources. However, it is doubtful that the large differences at these wavelengths could be entirely due to this effect. Finally, the effects of the atmosphere are more important at short wavelengths due to greater scattering. If the aerosols are improperly characterized, then this would be more noticeable at shorter wavelengths. Even with these large differences, the agreement between the reflectance-based results and those from AVIRIS is quite good.

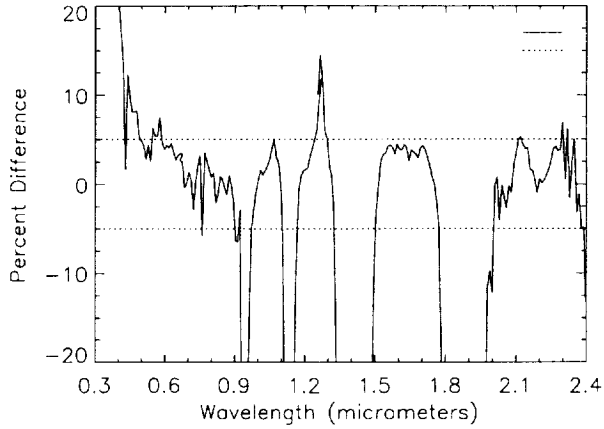

Figure 2 Percent difference between reflectance-based predictions of at-sensor radiance and the measured AVIRIS radiances

5. CONCLUSIONS

During a field campaign at Lake Tahoe on June 22, 1995, calibrations of AVIRIS were attempted using both the reflectance-based and radiance-based methods. This experiment shows that the use of dark water targets to calibrate radiometric sensors can result in meaningful sensor characterization. In particular, the reflectance-based method shows promise towards meeting the desired 2-3% uncertainty levels for ocean color sensors since experimental agreement of better than 1.5% is found for the Lake Tahoe AVIRIS experiment. Similarly promising results were found from reflectance-based calibrations at Lunar Lake with large portions of the spectrum having less than a 5% difference between the reflectance-based predictions and the measured AVIRIS radiances. These results are still in the preliminary stage and it is likely that further study of this data set will lead to even better agreement. The results of the radiance-based calibration at Lake Tahoe are quite good at the shorter wavelengths where atmospheric scattering leads to larger signals and smaller effects of specularly reflected solar energy. The results also showed the sensitivity to radiometer pointing when using water targets for vicarious calibration.

6. ACKNOWLEDGEMENTS

This work was funded by NASA grants NGT-30239 and NAGW-3543 and NASA contract NAS3-5171. The authors wish to thank JPL for supplying the needed AVIRIS imagery and M. Chami for the initial processing of the Lake Tahoe image. A portion of the research described in this paper was performed by the Jet Propulsion Laboratory, California Institute of Technology under a contract with the National Aeronautics and Space Administration. We also acknowledge C. Curtis from the Department of Physics at the University of Arizona, B. Richards from the Tahoe Research Group of the University of California at Davis, B. Steward from the USF, and the staff of the Truckee-Tahoe airport for their assistance with the Lake Tahoe campaign. The Lunar Lake campaign could not have been successful without the participation and assistance of people to numerous to list here. We thank them for their help with a very successful experiment.

7. REFERENCES

Asrar, G. and J. Dozier, 1994, *EOS, Science Strategy for the Earth Observing System*, AIP Press, New York.

Balick, L. K., C. J. Golanics, J. E. Shines, S. F. Biggar, and P. N. Slater, 1991, "The in-flight calibration of a helicopter-mounted Daedalus multispectral scanner," Proc. Spie #1493, pp 215-223.

Barnes, R.A. and A.W. Holmes, 1993, "Overview of the SeaWiFS ocean sensor," Proc. SPIE #1939, pp. 224-232.

Biggar, S.F., D.I. Gellman, and P.N. Slater, 1990, "Improved evaluation of optical depth components from Langley plot data," *Remote Sens. Environ.*, Vol. 32, pp. 91-101.

Biggar, S. F., J. Labed, R. P. Santer, P. N. Slater, R. D. Jackson, and M. S. Moran. 1988. "Laboratory calibration of field reflectance panels," Proceedings of SPIE #924, pp. 232-240.

Biggar, S. F., P. N. Slater, and D. I. Gellman. 1994. "Uncertainties in the in-flight calibration of sensors with reference to measured ground sites in the 0.4 to 1.1 μm range," *Rem. Sens. Env.*, Vol. 48, pp. 242-252.

Biggar, S. F., P. N. Slater, K. J. Thome, A. W. Holmes, and R. A. Barnes, 1993, "Preflight solar-based calibration of SeaWiFS," Proc. SPIE Conf. #1939, Orlando, Florida, pp. 233-242.

Deuzé, J.L., M. Herman, and R. Santer, 1989, "Fourier series expansion of the transfer equation in the atmosphere-ocean system," *J. Quant. Spectrosc. Radiat. Transfer*, Vol. 41, pp. 483-494.

Flittner, D. E., Herman, B. M., Thome, K. J., Simpson, J. M., Reagan, J. A., 1993, "Total ozone and aerosol optical depths inferred from radiometric measurements in the Chappuis absorption band," *J. of Atmos. Sci.*, Vol. 50, 1113-1121.

Gellman, D.I., S.F. Biggar, M.C. Dinguirard, P.J. Henry, M.S. Moran, K.J. Thome, and P.N. Slater, 1993, "Review of SPOT-1 and -2 calibrations at White Sands from launch to present," Proc. SPIE #1938, pp. 118-125.

Gellman, D.I., S.F. Biggar, P.N. Slater, and C.J. Bruegge, 1991, "Calibrated intercepts for solar radiometers used in remote sensor calibration," Proc. SPIE #1493, pp. 175-180.

Hooker, S.B., W.E. Esaias, G.C. Feldman, W.W. Gregg, and C.R. McClain, 1992, *SeaWiFS Technical Support Series: Volume 1, An Overview of SeaWiFS and Ocean Color*, NASA Technical Memorandum 104566 (NASA Goddard Space Flight Center, Greenbelt, MD).

Hovis, W.A., J.S. Knoll, and G.R. Smith, 1985, "Aircraft measurements for calibration of an orbiting spacecraft sensor," *Appl. Opt.*, Vol. 24, pp. 407-410.

Kaufman, Y.J. and B.N. Holben, 1993, "Calibration of the AVHRR visible and near-IR bands by atmospheric scattering, ocean glint and desert reflection," *Int. J. Remote Sensing*, Vol. 14, pp. 21-52.

King, M. D., Byrne, D. M., Herman, B. M., Reagan, J. A., 1978, "Aerosol size distributions obtained by inversion of spectral optical depth measurements," *J. Atmos. Sci.*, Vol. 35, 2153-2167.

Slater, P. N., Biggar, S. F., 1996, "Suggestions for radiometric calibration coefficient generation," *J. of Atmos. and Oceanic Tech.*, Vol. 13, pp. 376-382.

Slater, P.N., S.F. Biggar, K.J. Thome, D.I. Gellman, and P.R. Spyak, 1996, "Vicarious radiometric calibrations of EOS sensors," *J. Atmos. Oceanic Technol.* Vol. 13, pp. 349-359.

Slater, P.N., S.F. Biggar, R.G. Holm, R.D. Jackson, Y. Mao, M.S. Moran, J.M. Palmer, and B. Yuan, 1987, "Reflectance- and radiance-based methods for the in-flight absolute calibration of multispectral sensors," *Remote Sens. Environ.* Vol. 22, pp. 11-37.

Thome, K.J., B.M. Herman, and J.A. Reagan, 1992, "Determination of precipitable water from solar transmission," *J. Appl. Meteor.*, Vol. 31, pp. 157-165.

Thome, K. J., C. L. Gustafson-Bold, P. N. Slater, and W. H. Farrand, 1996, "In-flight radiometric calibration of HYDICE using a reflectance-based approach," Proc. SPIE Conf. #2821, pp. 311-319.

Thome, K.J., D.I. Gellman, R.J. Parada, S.F. Biggar, P.N. Slater, and M.S. Moran, 1993, "In-flight radiometric calibration of Landsat-5 Thematic Mapper from 1984 to present," Proc. SPIE #1938, pp. 126-130.

Thome, K.J., S. Schiller, J. Conel, K. Arai, S. Tsuchida, 1998, "Results of the 1996 joint, EOS vicarious calibration campaign to Lunar Lake, Nevada," *Metrologia,* in Press.

Vane, G., R.O. Green, T.G. Chrien, H.T. Enmark, E.G. Hansen, and W.M. Porter, 1993, "The Airborne Visible/Infrared Imaging Spectrometer (AVIRIS)," Remote Sens. Environ., Vol. 44, pp. 127-143.

Vermote, E., D. Tnaré, J. L. Deuzé, M. Herman, and J. J. Morcrette, 1995, *Second Simulation of the Satellite Signal in the Solar Spectrum (6S)*, Laboratoire d'Optique Atmosphérique, Université des Sciences et Technique de Lille.

Vermote, E., R.P. Santer, P.Y. Deschamps, and M. Herman, 1992, "In-flight calibration of large field of view sensors at short wavelengths using Rayleigh scattering," *Int. J. Remote Sensing*, Vol. 13, pp. 3409-3429.

DIURNAL REFLECTANCE CHANGES IN VEGETATION OBSERVED WITH AVIRIS

V.C. Vanderbilt[1], V.G. Ambrosia[1] and S.L. Ustin[2]
[1]Ames Research Center, Moffett Field, CA 94035
[2]University of California, Davis, CA 95616

1. INTRODUCTION

Among the most important short-term dynamic biological processes are diurnal changes in canopy water relations. Plant regulation of water transport through stomatal openings affects other gaseous transport processes, often dramatically decreasing photosynthetic fixation of carbon dioxide during periods of water stress. Water stress reduces stomatal conductance of water vapor through the leaf surface and alters the diurnal timing of stomatal opening. Under non-water stressed conditions, stomates typically open soon after dawn and transpire water vapor throughout the daylight period. During stress periods, stomates may close for part of the day, generally near mid-day. Under prolonged stress conditions, stomatal closure shifts to earlier times during the day; stomates may close by mid-morning and remain closed until the following morning — or remain closed entirely.

Under these conditions the relationship between canopy greenness (e.g., measured with a vegetation index or by spectral mixture analysis) and photosynthetic fixation of carbon is lost and the remotely sensed vegetation metric is a poor predictor of gas exchange. Prediction of stomatal regulation and exchange of water and trace gases is critical for ecosystem and climate models to correctly estimate budgets of these gases and understand or predict other processes like gross and net ecosystem primary production (Kittel et al., 1995).

Plant gas exchange has been extensively studied by physiologists at the leaf and whole plant level and by biometeorologists at somewhat larger scales (Gates, 1980), (Nobel, 1983). While these energy driven processes follow a predictable if somewhat asymmetric diurnal cycle dependent on soil water availability and the constraints imposed by the solar energy budget, they are nonetheless difficult to measure at the tree and stand levels using conventional methods.

Ecologists have long been interested in the potential of remote sensing for monitoring physiological changes using multi-temporal images. Much of this research has focused on day-to-day changes in water use, especially for agricultural applications (Moran et al., 1997). Ustin et al. (1998) showed seasonal changes in canopy water content in chaparral shrub could be estimated using optical methods. Vanderbilt et al. (1991) followed asymmetric diurnal changes in the reflectance of a walnut orchard, but could not attribute specific reflectance changes to specific changes in canopy architecture or physiology.

Forests and shrub lands in California experience prolonged periods of drought, sometimes extending six months without precipitation. The conifer and evergreen chaparral communities common to the foothill region around the central valley of California retain their foliage throughout the summer and have low transpiration rates despite high net radiation and temperature conditions. In contrast, grasslands and drought resistant deciduous species in the same habitat are seasonally dormant in summer. Because of differences in the mechanisms of drought tolerance, rooting depth and physiology between different plant communities in the region, it is likely that they display differences in diurnal water relations. The presence of diverse plant communities provides an opportunity to investigate possible diurnal landscape patterns in water relations that could be observed by an airborne hyperspectral scanner. This investigation of AVIRIS data collected over forest and shrub land represents the continuation of a prior investigation (Ustin et al., 1992) involving spectral mixture analysis of diurnal effects in the same AVIRIS data set.

2. METHODS

Eleven AVIRIS hyper spectral data scenes, Table 1, were collected over a common test site during a 3 hr 20 mn interval bracketing solar noon on 22 September 1989 from the NASA-Ames ER-2 aircraft (Flight 89-167) flying at an average altitude of 19.7 km (65,000 feet) above ground level (AGL).

Table 1. AVIRIS data collection times (Pacific daylight time) and solar directions (degrees).

Scene number	1058	1061	1064	1067	1070	1073	1076	1079	1082	1085	1090
Collection time	11:50	12:10	12:30	12:51	13:09	13:30	13:49	14:10	14:30	14:50	15:10
Solar elevation	45.53	47.20	48.18	48.48	48.48	48.19	47.22	45.52	44.05	41.52	39.29
Solar azimuth	151.2	161.4	168.6	176.5	183.5	191.2	198.3	205.7	212.2	218.5	223.9

2.1. Site description

The test site, located at (41°21'00"N, 121°57'30"W), approximately 10 km southeast of volcanic Mt. Shasta in the Cascade Range of north-central California, is volcanic in origin with a cinder cone, Black Fox Mountain, bordering its eastern edge. The site averages 1,200 m above sea level and slopes 1.5% to the southeast, displaying minimal topographic relief. The sandy, highly reflective soils appear either light gray or light red, contain little clay and little organic matter and appear to have little water holding capacity. The area is dominated by extensive stands of mature Ponderosa pine (Pinus Ponderosa) and extensive mixed stands of 'shrub' containing primarily manzanita (Arctostaphylos manzanita) and ceanothus (Ceanothus thyrsiflorus) and smaller amounts of Christmas berry (Heteromeles arbutifolia). Other species observed at locations northeast of and immediately outside of the test site — and which may also grow in small stands of minor importance within the test site — include white fir (Abies concolor), California black oak (Quercus kelloggii) and tanbark oak (Lithocarpus densiflora).

We observed that within the test site, Ponderosa pine appears to grow preferentially on light red soils while the light gray soils tend to support (a) shrubs or (b) very sparsely distributed grasses making these areas appear essentially as 'bare soil.' Clear cut areas display light red soils. The shrub and bare soil areas display no evidence of having previously been clear cut — all of which suggests a link between cover type and soil parent material. During AVIRIS data collection, all soils appeared dry; meteorological data suggested that no rain had fallen during the three days prior to AVIRIS data collection.

2.2. AVIRIS data analysis.

All scenes were co-registered to the first scene (1058) using a second order polynomial and more than 20 randomly selected control points. The root mean square (RMS) image rectification error of each scene was less than 1.0 pixel in both the X and Y dimensions. The data were not corrected for atmospheric effects. The solar elevation and solar azimuth corresponding to each scene were determined from the data collection time and geographic location of the scene center point. The dimensions (470 x 399 pixels) of the almost flat, almost horizontal test site were selected in order to exclude from the analysis process adjacent sloping terrain and its corresponding radiance data values which vary asymmetrically as a function of solar azimuth direction relative to solar noon (Vanderbilt et al., 1991).

Sixteen spectral classes were derived from an unsupervised cluster classification analysis involving five AVIRIS wavelength bands — band numbers 13 (512.9 nm), 18 (562.1 nm), 30 (680.3 nm), 50 (838.8 nm), and 139 (1653 nm) — of the first scene (1058). These wavelength bands, for these data collected in 1989, represent the approximate center wavelength positions of the Landsat Thematic Mapper bands 1, 2, 3, 4 and 5. A sixth band, also included in the cluster analysis, provided information of the spatial texture of the scene as represented by a 3x3 variance filter of AVIRIS band 30. The result obtained from the cluster analysis of each pixel of the first scene (1058) was assumed to apply to the corresponding pixel in each of the 10 other overlaid and registered AVIRIS images.

Analysis of color infrared photography, collected with the AVIRIS data, helped establish the correspondence between the 16 spectral classes and eight information classes: bare soil, shrub, and six Ponderosa pine classes — each class distinguished by its apparent crown closure: 100-90%, 89-80%, 79-70%, 69-50%, 49-30% and low density pine. The number of pixels within each of the eight information classes is shown in Table 2.

The mean spectrum of each information class was determined as the average within each wavelength band of all AVIRIS spectra in that class. Thus, for example, the mean spectrum of bare soil was obtained by averaging

27329 individual bare soil spectra, Table 2. The mean spectra do not include effects due to per pixel slope and aspect; these effects were assumed to be inconsequential for the comparatively flat test site.

Table 2. Number of pixels in each information class.

Information class	Ponderosa pine crown closure						shrub	bare soil
	percent							
	100-90	89-80	79-70	60-50	49-30	<30		
Number of pixels	10198	8215	39623	19723	11668	60982	9792	27329

2.3. Ancillary data.

Sun photometer data were collected continuously in eight wavelength bands between 400 nm and 1100 nm on September 22, 1989 between approximately 6 hr 30 mn and 17 hr Pacific daylight time using an instrument constructed at the University of Arizona. The data were analyzed by Dr. Carol Bruegge of JPL who estimated the atmospheric optical depth and aerosol optical depth for each wavelength band as a function of time during the day.

The water potential of needles on branches harvested from several Ponderosa pine trees was estimated with the aid of pressure bomb measurements collected continuously between approximately 6 hr and 17 hr on September 22, 1989. Each of the sampled trees was mature, located apart from a nearby extended stand of Ponderosa pine and was either an isolated tree or a member of a small group of trees. Both sunlit and shaded branches were measured between 6 hr and approximately 10 hr; after 10 hr only shaded needles were measured.

3. RESULTS

Fig. 1 shows both the first scene (1058) of AVIRIS data as well as the results from its classification represented with the aid of a gray scale for which the darkest gray level corresponds to the Ponderosa pine 100-90% crown closure class and the lightest gray level, the bare soil class. The bottom-to-top direction in each image represents a northeast compass direction. The homogeneous area approximately 80 columns x 150 rows represented by an intermediate gray level and located in the extreme upper right corner of the image is a Ponderosa pine plantation. Recent clear cut areas appear as sharply defined bright areas usually amid dark areas such as near the bottom right of Fig. 1b.

A comparison, Fig. 2a-b, of the mean spectra, when normalized by the mean soil spectra (a 'flat field' correction), derived from scenes 1058 and 1079 collected before and after solar noon at similar 45.5° solar elevations shows that the reflectance of shrub decreased at all wavelengths while that of Ponderosa pine 100-90% crown closure increased at all wavelengths. Two mean spectra for bare soil measured at similar solar elevations near noon, Fig. 2c, appear almost coincident, providing an indication that the temporal stability of the AVIRIS sensor is excellent. Use of the bare soil spectra to normalize the shrub and Ponderosa pine spectra was assumed to reduce the magnitude of the small variations in the data attributable to noise in the AVIRIS sensor. In addition use of such a flat field correction allows comparisons against a surface, the dry bare soil, that may reasonably be assumed to exhibit spectrally unchanging, Lambertian reflectance properties over the relatively short 3 hr 20 mn time period and limited range of solar elevations, 39° to 48°.

Fig. 3 shows the mean of each information class measured at two wavelengths at each of 11 data collection times. In the red wavelength region, the largest response at each data collection time is due to bare soil; the smallest, 90-81% cc Ponderosa pine. In the near infrared wavelength region, the largest response at each data collection time is due to shrub; the smallest, 100-91% cc Ponderosa pine. With few exceptions the maximum value of each curve occurs near solar noon, approximately 13 hr (1 PM) local time.

Figure 4 shows that during a 3 hr 20 mn time period bracketing solar noon, the normalized light reflected by Ponderosa pine having 90-100% crown closure increased approximately five percent while that of shrub decreased monotonically by approximately 25%. Fig. 4, similar to Fig. 2 but representing multiple data collection times, shows that for 100-91% cc Ponderosa pine at all measured times the response, normalized using the bare soil 'flat field,' is greater than the normalized response at 11 hr 50 mn; that of shrub monotonically decreases with increasing time from 11 hr 50 mn. Thus, starting from collection of the first scene, the normalized spectra of pine increase while those of shrub decrease. Fig. 4c shows that the response of bare soil, the data used to perform the 'flat field' normalization on the shrub and pine spectra, is greatest near solar noon, decreasing approximately in a symmetric fashion with time measured from noon. For each chart in Fig. 4, the response does not change with wavelength like

that of a green leaf; each curve is comparatively smooth, revealing, for example, no abrupt changes near the location of the red edge at 700 nm.

A Langley plot analysis of the sun photometer data, Fig. 5a, shows that morning and afternoon data for each wavelength band appear to lie on the same line, suggesting atmospheric properties changed little during the period of AVIRIS data collection. This is supported by the results, Fig. 5b, showing the atmospheric optical depth at each wavelength changed little during the day. Dividing the optical depth into its Rayleigh and aerosol component parts, Fig. 5c, shows that the aerosol optical depth, particularly in the red and near infrared wavelength region, Fig. 5d, was extremely low, less than 0.02 throughout the period of AVIRIS data collection. These results show that the atmosphere was exceptionally clear — almost transparent throughout the day at these wavelengths. Its light transmitting properties in the red and near infrared wavelength region changed at most by 1% during the period of AVIRIS data collection. The data reveal no evidence of clouds.

The water potential of sunlit and shaded Ponderosa pine needles, Fig. 6, varied with time during the day, showing a large decrease from approximately -10 bars to -17 bars near 9 hr. The water potential of the shaded needles appears to trend upward from approximately -16 bars to -14 bars during the time period when AVIRIS data were collected.

4. DISCUSSION

These results, Fig. 4, reveal that during a 3 hr 20 mn time period bracketing solar noon the light reflecting properties of the two most important cover types within this test site changed substantially and differently: the normalized spectra of Ponderosa pine increased while those of shrub decreased monotonically with time. By normalizing these spectra using AVIRIS bare soil spectra from each of the 11 scenes, we have minimized effects in the results due both to sensor variation with time and to changing solar elevation. Because of this normalization procedure, we believe these results are real and not due to artifacts in the data.

If the canopy were unchanging and azimuthally symmetric, theory (Vanderbilt et al., 1991) shows that morning and afternoon canopy reflecting properties should exhibit mirror symmetry about solar noon. Assuming that canopy architecture is azimuthally symmetric (a reasonable assumption) and given that the atmospheric changes, Fig. 5, were insignificantly, data collected at identical morning and afternoon solar elevations should be identical — provided the canopy did not change. Yet comparing morning and afternoon results, Fig. 2, corresponding to a 45° solar elevation shows that during this 2 hr 20 mn time period the normalized spectra of Ponderosa pine increased by approximately 4% and shrub decreased by approximately 20%.

Thus, the AVIRIS images, when properly normalized and properly analyzed, show that the reflectance properties of the two canopies changed substantially and differently — and therefore that the two canopies changed. The canopy changes appear not to be due to asymmetric changes in the soil reflecting properties, as Figs. 3 and 4c show that these properties changed approximately symmetrically about solar noon. For a given set of illumination and observation directions, two canopy properties — architecture and the spectral scattering and absorbing properties of canopy components (leaves, stems, soil, etc.) — determine the canopy reflectance.

Pigments determine in part the spectral scattering and absorbing properties of canopy components. However, if the canopy reflectance changes were attributable entirely to changes in canopy pigments — pigment configuration changes with increasing water stress, for example, then the results, Fig. 4, should exhibit increasing evidence of pigment absorption as the canopy reflectance changed. The canopy reflectance properties, Fig. 4a-b, show only limited evidence of pigment absorption, decreasing, Fig. 4b, to 0.75 as a set of almost parallel lines. However, the evidence, albeit small, of differential pigment absorption can not be ignored. For example, near the red edge at a wavelength of 687 nm, the curve representing data collected at 3:10 PM trends downward approximately 5% over a wavelength interval of approximately 75 nm, a wavelength dependent change suggesting pigment involvement; yet this 5% change should be interpreted in light of the overall 25% decrease from data collected at 11:50 AM, which suggests that most of the 25% decrease is not wavelength dependent and therefore not pigment dependent. Thus, the results suggest that the changes in the reflecting properties of these two canopies are attributable less to pigment changes and more to changes in architecture at one or more of three scales — canopy, leaf and cell.

These results, Figs. 1-6, do not provide indication of the specific architectural changes which manifest the changes in the canopy reflectance. The measurements of pine needles, Fig. 6, suggest that shaded needle water

potential decreased during the day, although not during the AVIRIS data collection time period. Changes in architecture at the canopy, leaf and cell scales attributable to the effects of decreasing leaf water potential are well documented for agricultural plant canopies. Other factors which could potentially affect the canopy asymmetrically about solar noon include the effects of wind. Wind speed which increases during the day presumably could potentially modify the architecture at the canopy and leaf scales, resulting in canopy asymmetric reflectance changes. Wind velocities at the test site during collection of AVIRIS data were not recorded. But memory indicates winds at ground level were light and variable in the high pressure weather system at the test site; we do not believe winds were a factor changing the architecture of the canopy or leaves in a diurnally consistent manner. Thus, in the absence of other identified sources of canopy change, we believe the asymmetric changes in the reflecting properties of the two canopies, changes evident in the results, Figs. 2-4, manifest the species specific response of these two canopies to their diurnally changing water status.

5. CONCLUSIONS

The results of this research show that during more than a two hour time period canopy reflectance properties changed substantially and asymmetrically about solar noon. The results show that the reflectance properties changed because the architecture of the plants changed at one or more scales — cell, leaf and canopy. There is no substantial evidence indicating the canopy changes may be attributed to changes in plant pigment properties. In the absence of other causes, we attribute the asymmetric changes in canopy reflectance properties to changes in canopy water relations.

6. Acknowledgement

We thank Dr. Carol Bruegge of NASA's Jet Propulsion Laboratory for her analysis of the sun photometer data.

REFERENCES

Gates, D.M., 1980, *Biophysical ecology*, Springer-Verlag, New York, 611 pp.

Kittel, T.G.F., N.A. Rosenbloom, T.H. Painter, and D.S. Schimel, 1995, "The VEMAP integrated database for modelling United States ecosystem/vegetation sensitivity to climate change." Journal of Biogeography, vol. 22, nos. 4/5, pp. 857-862.

Moran, M.S., Y. Inoue, and E.M. Barnes, 1997, "Opportunities and Limitations for Image-Based Remote Sensing in Precision Crop Management." Remote Sensing of Environment, vol. 61, no. 3, pp. 319-346.

Nobel, P.S., 1983, *Biophysical plant physiology and ecology*, W.H. Freeman, San Francisco, 608 pp.

Ustin, S.L., G.J. Scheer, C.M. Castaneda, A. Palacios, S. Jacquemoud, D.A. Roberts, and R.O. Green, 1998, "Estimating canopy water content of chaparral shrubs using optical methods." Remote Sensing of Environment (in press).

Ustin, S.L., M.O. Smith, and J.B. Adams, 1992, "Multi-temporal diurnal AVIRIS images of a forested ecosystem." In Summaries of the Third Annual JPL Airborne Geoscience Workshop, Robert O. Green (ed.). NASA, Jet Propulsion Laboratory 92-14, vol. 1, pp. 141-143.

Vanderbilt, V.C., S.L. Ustin, K.M. Berger, W.F. Caldwell, J.A. Clark, B.D. Ganapol, E.S. Kasischke, S.N. Martens, R.E. Pettigrew, and R.A. Rousseau, 1991, "Biophysical information in asymmetric and symmetric diurnal bidirectional canopy reflectance." IEEE Transactions of Geoscience and Remote Sensing, vol. 29, pp. 875-889.

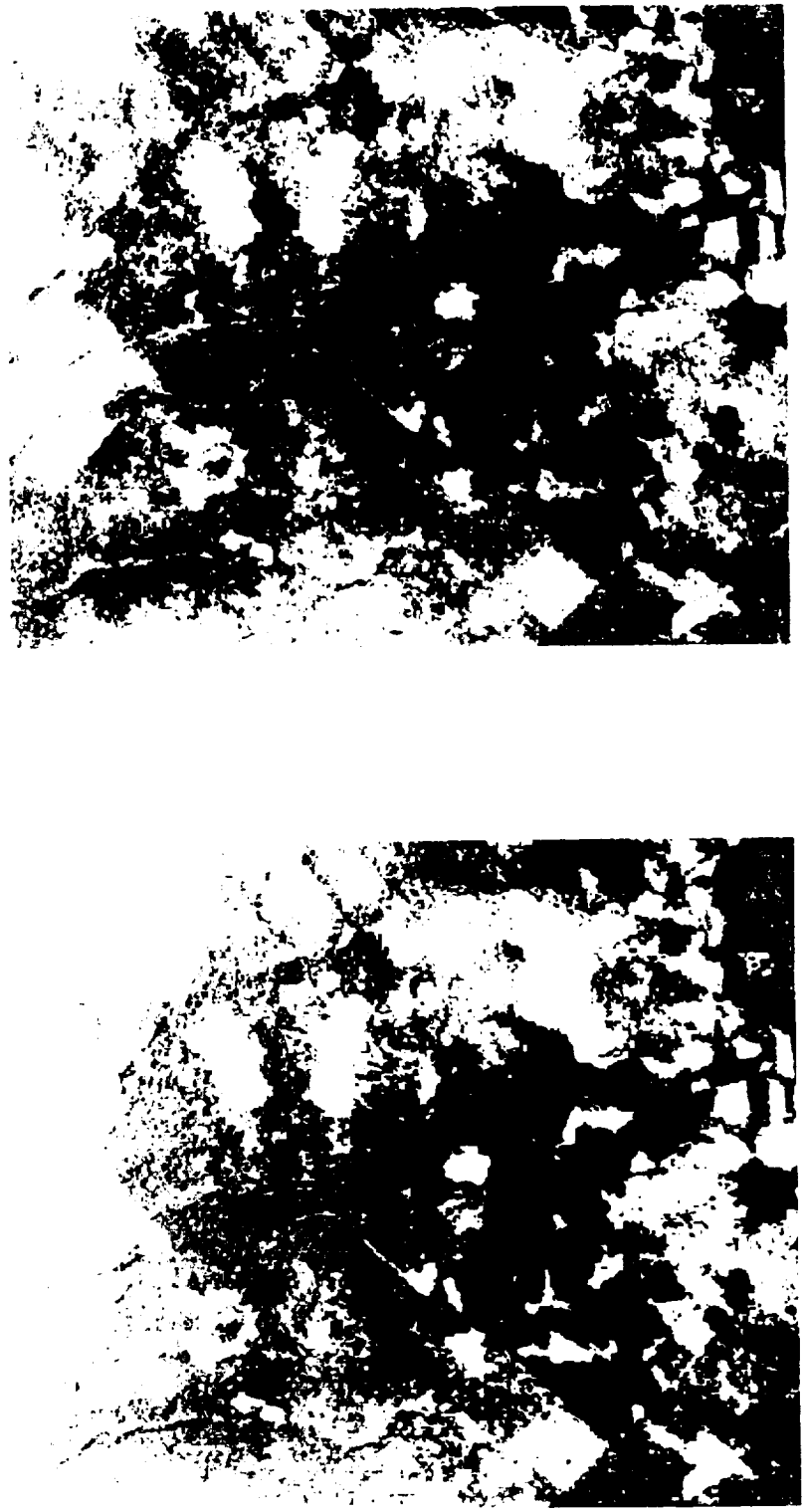

Fig. 1. The AVIRIS data (top) collected September 22, 1989 near Mt. Shasta, California were clustered to display (bottom) eight information classes: bare soil, shrub land and six classes of Ponderosa pine.

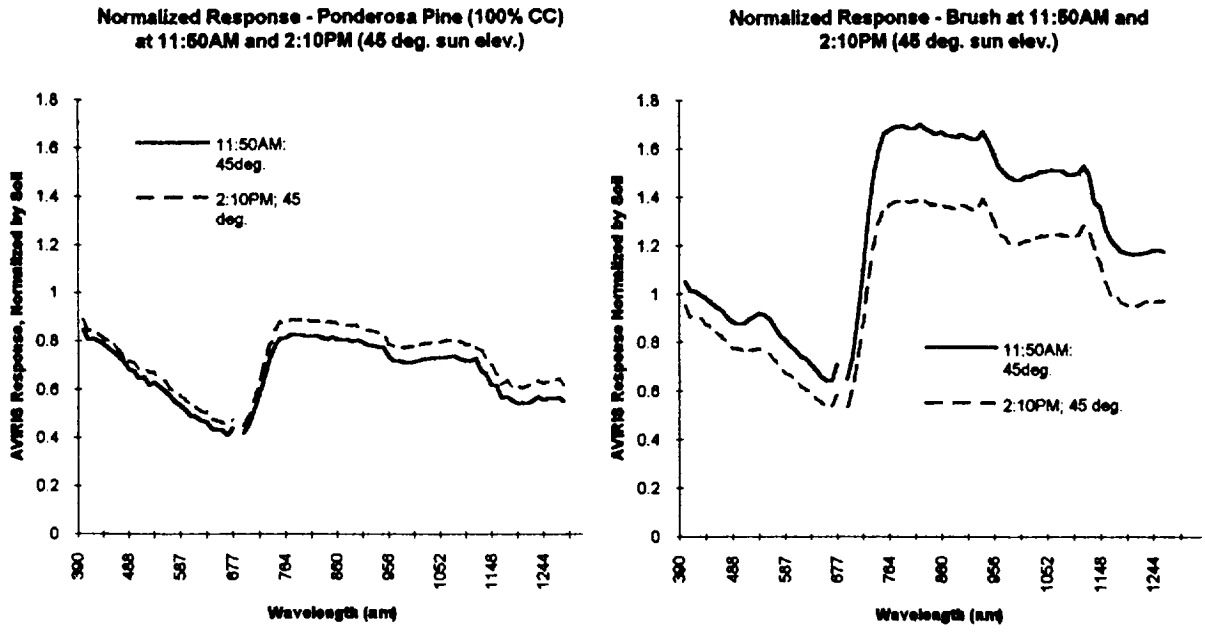

Fig. 2a-b. Mean spectra, normalized by the mean soil spectra collected before and after solar noon at similar 45.5° solar elevations, shows that the reflectance of shrub decreased at all wavelengths while that of Ponderosa pine 100-90% crown closure increased at all wavelengths.

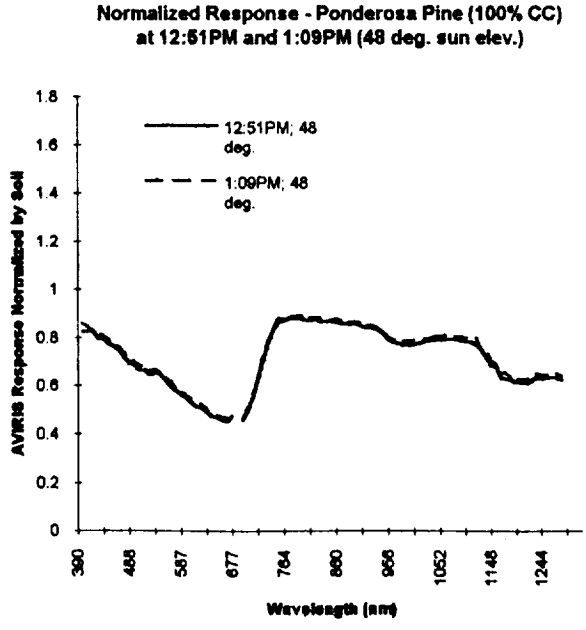

Fig. 2c. Two mean spectra for bare soil measured at similar solar elevations near noon, Fig. 2c, appear almost coincident, providing evidence that the temporal stability of the AVIRIS sensor is excellent.

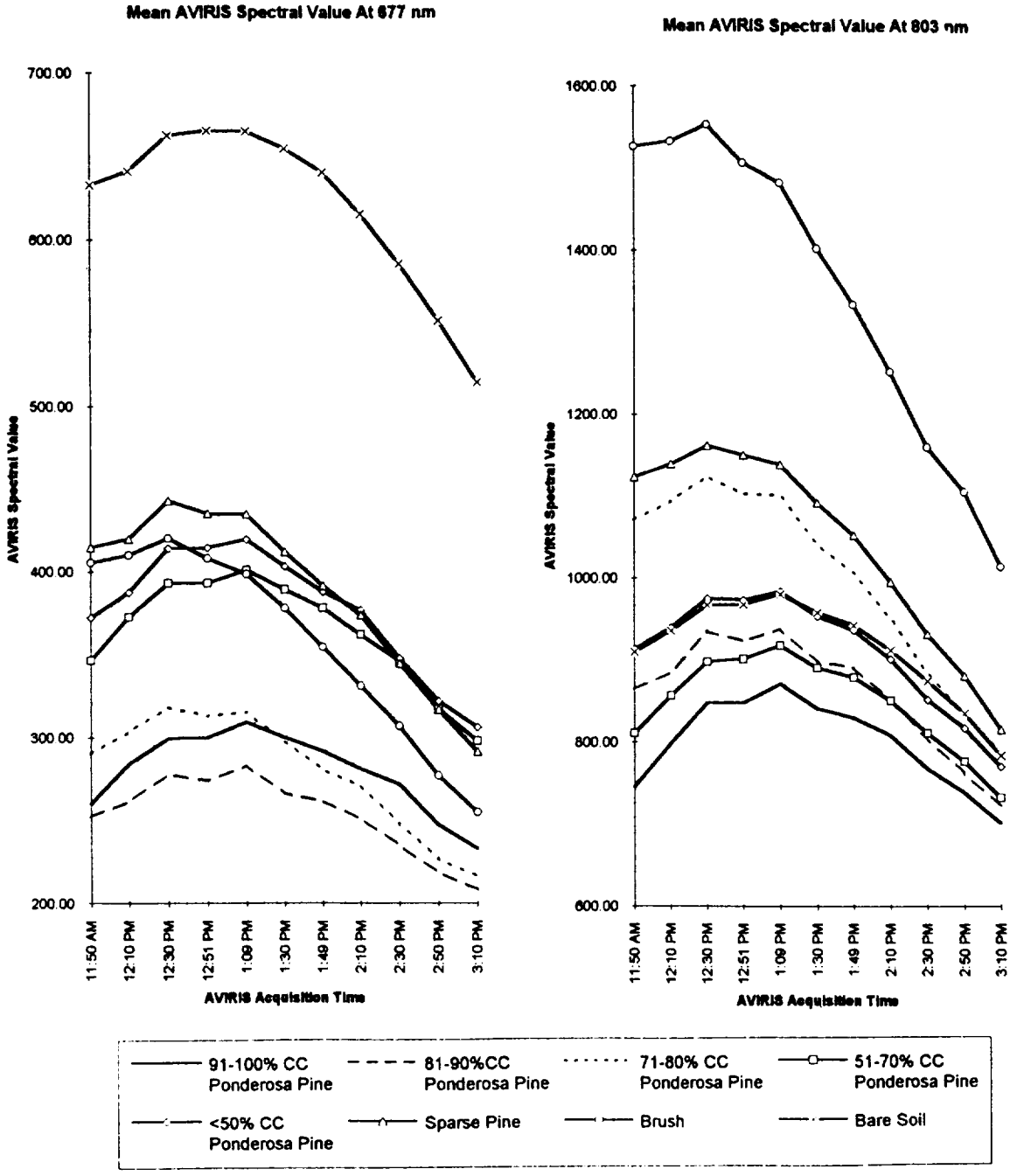

Fig. 3. AVIRIS data for eight information classes were collected within the test site approximately every 20 mn during a 3 hr 20 mn period. Solar noon occurred at approximately 13 hr.

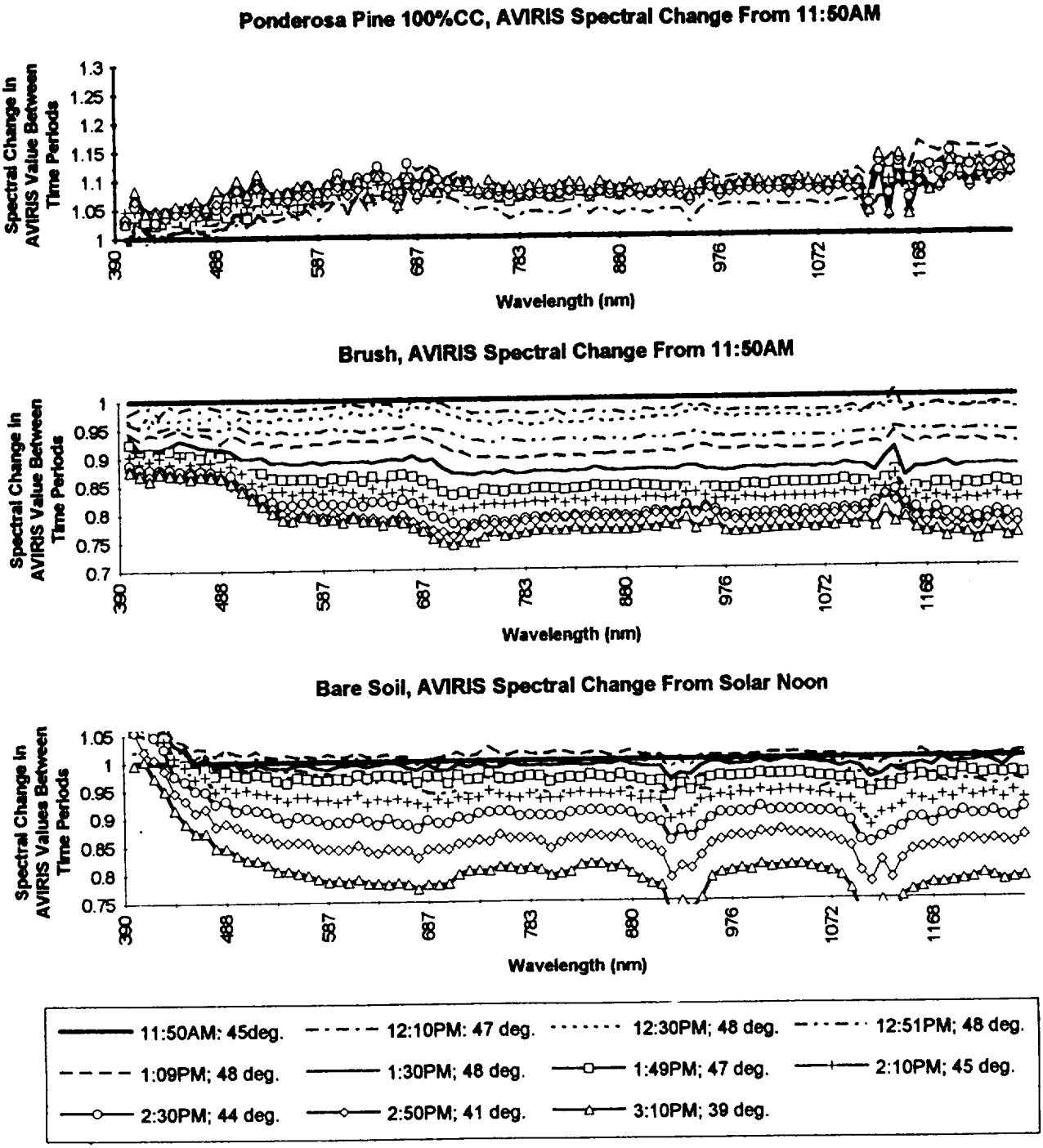

Fig. 4. The mean spectra of two information classes, shrub land and Ponderosa pine 100% crown closure, were normalized by dividing by the mean spectra of bare soil, thereby reducing effects in the results due to sensor variation.

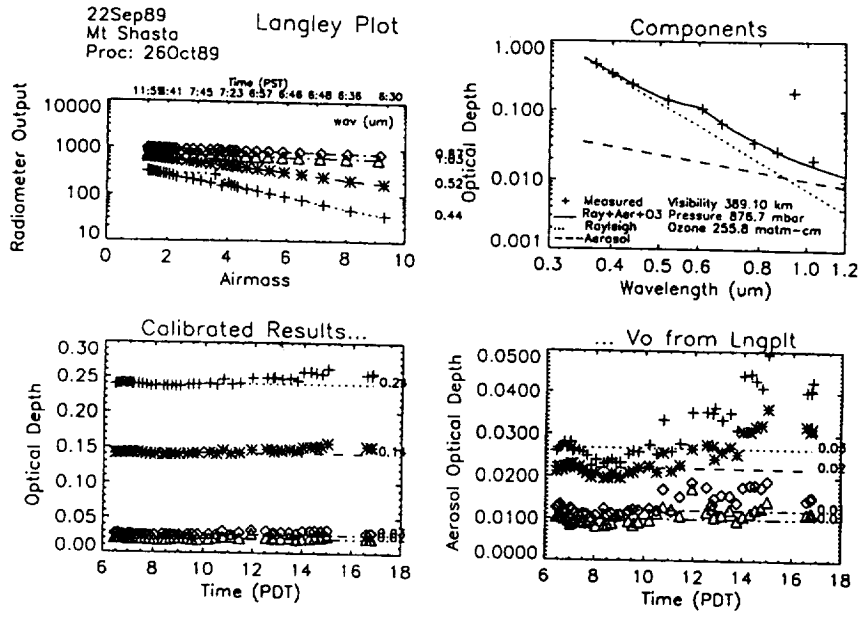

Fig. 5. Atmospheric optical depth and aerosol optical depth were estimated as a function of time from analysis of the sun photometer data.

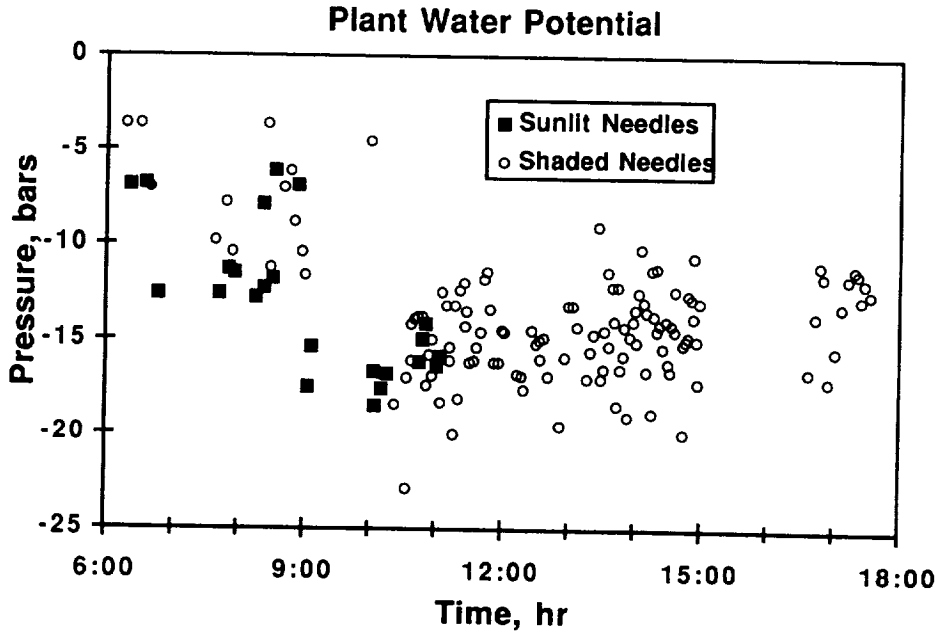

Fig. 6. The water potential of shaded and sunlit branches harvested from Ponderosa pine was measured during AVIRIS data collection.

A METHOD TO ACCESS ABSOLUTE FIPAR OF VEGETATION IN SPATIALLY COMPLEX ECOSYSTEMS

Carol A. Wessman [1,2], Elizabeth M. Nel [1], C. Ann Bateson [1] and Gregory P. Asner [1]

[1] Cooperative Institute for Research in Environmental Sciences
[2] Environmental, Population and Organismic Biology
University of Colorado, Boulder, CO 80309-0216

1. INTRODUCTION

Arid and semi-arid lands compose a large fraction of the earth's terrestrial vegetation, and thereby contribute significantly to global atmospheric-biospheric interactions. The thorny shrubs and small trees in these semi-arid shrub lands have counterparts throughout much of the world's tropical and subtropical zones (Brown 1982) and have captured substantial areas of the world's former grasslands (Johnston 1963, Brown 1982, Schofield and Bucher 1986, Archer 1990). The objective of our field and remotely sensed measurements in the semi-arid shrublands of Texas is to monitor interannual variability and directional change in landscape structure, ecosystem processes and atmosphere-biosphere exchanges. To understand the role ecosystems play in controlling the composition of the atmosphere, it is necessary to quantify processes such as photosynthesis and primary production, decomposition and soil carbon storage, and trace gas exchanges. Photosynthesis is the link whereby surface-atmosphere exchanges such as the radiation balance and exchange of heat, moisture, and gas can be inferred. It also describes the efficiency of carbon dioxide exchange and is directly related to the primary production of vegetation. Our efforts in this paper focus on the indirect quantification of photosynthesis, and thereby carbon flux and net primary production, via remote sensing and direct measurements of intercepted photosynthetically active radiation (IPAR).

While it is well known that NDVI is strongly correlated to certain biophysical parameters, in the past such correlations have typically been used at the scale of remotely sensed imagery to illustrate *relative* variance of the fraction of photosynthetically active radiation intercepted (fIPAR) by the canopy. We use spectral mixture analysis in combination with ground data to predict *absolute* values of fIPAR at the image level. We reproduce previously established relationships between fIPAR, leaf area index (LAI), and traditional spectral vegetation indices (SVIs), and utilize a spectral mixing algorithm to quantify the relative contribution of sub-pixel green vegetation components to full pixel fIPAR and LAI values. Spectral mixture analysis (SMA) can be used to remove non-green contributions from pixel-scale reflectance and thus permit the calculation of fIPAR based on the fractions of only green photosynthesizing vegetation in a highly mixed landscape. Correction of fIPAR measurements for the fraction of green biomass has been shown to improve relationships with ground-based NDVI measurements (Gamon et al. 1993). Moreover, SMA separates functionally different woody and herbaceous vegetation forms. We compare the abilities of traditional SVIs and our SMA model in predicting both *relative* and *absolute* ground values of fIPAR at both a transect and a landscape scale.

2. METHODS

2.1 Study Site

The Texas Agricultural Experiment Station La Copita Research Area is located in Jim Wells County, 15 km south west of Alice, Texas (27°40'N; 98°12'W) in the eastern portion of the Central Rio Grande Plain. The vegetation is described as subtropical thorn woodland (McMahan et

al. 1984), or semi-arid savanna parkland (Archer et al. 1990), and is characterized by intermittent low-lying closed-canopy wooded drainages surrounded by a matrix of herbaceous uplands. The greater proportion of La Copita is characterized by large honey mesquite trees (*Prosopis glandulosa*) subtended by a variety of woody shrubs. Scattered thoughout the herbaceous zones are clusters of woody shrubs surrounding individual mesquite trees (mottes) as well as more extensive groves consisting of a contiguous wooded canopy of multiple mesquite trees and shrub understories. Occasional playa (lakebed) sites, lowlands dominated by open grassland with varying degrees of woody overstory, are scattered across the ranch.

Anthropogenic disturbances are largely related to brush control and include the application of herbicides in strips at various dates ranging back to 1983, clearing of brush by chaining in 1979, selective burning, and rotational grazing by cattle. The soils within the uplands generally consist of a fine sandy loam whereas the drainages consist of a non-directional clay loam (Scifres and Koerth 1987). The climate is subtropical with hot summers and mild winters. Mean annual rainfall (680 mm) is bimodaly distributed, with maxima in May/June and September (Scifres and Koerth, 1987).

2.2 Field Measurements

Our study at the La Copita Research Area involved two distinct stages. First, a high resolution ground sampling of fIPAR was made along transects in 2 of our 8 landscapes (L1 and L6) for the purpose of intensive ground truthing in the evaluation of the relationships between fIPAR and the SVI/SMA-derived values (Kennedy and Wessman *in review*). Second, measurements of selected landscape units were made across the entire ranch to define the natural range in variation of fIPAR and LAI for SMA extrapolation. The landscape units were selected to characterize different vegetation structural forms as described above. Within each of 8 landscapes distributed throughout La Copita, the following sites were established: 1 grove site, 1 drainage site, 3 mottes without *Prosopis* overstory, 3 mottes with *Prosopis* overstory, and 3 herbaceous sites. An additional 6 sites were established in recently burned herbaceous zones. Within the 6 playas sampled, 3 woody sites and 3 herbaceous sites were established.

PAR was measured using a line quantum sensor held in each of the 4 cardinal directions while the incident radiation was simultaneously being measured with a point quantum sensor mounted on a rangepole. The two sensors were calibrated to each other by logging 6 entries of incident PAR simultaneously several times during the course of a day, and then adjusting the line quantum data during the data processing phase. We calculated fIPAR according to $fIPAR = (PAR_i - PAR_t) / PAR_i$ where PAR_i is the incident PAR and PAR_t is the PAR transmitted through the canopy.

A LICOR Plant Canopy Analyzer was used to collect leaf area index (LAI) data for all the landscape sites within the same week as the AVIRIS overflight. LAI was not measured along the transects. Measurements were made at ground level to include both over- and understudy for total LAI. These data are included in this paper, although fIPAR was of primary interest.

Transect measurements

Approximately 1200 fIPAR measurements were made to best quantify fIPAR variation along transects spanning the upland regions of Landscapes 1 and 6 (Kennedy and Wessman *in review*). Landscape 1 was sampled with two N-S transects 7 meters apart and approximately 320 m in length. Landscape 6 was sampled with two E-W transects 7 meters apart and approximately 270 m in length. PAR measurements were made at 4-meter intervals along each transect. All the fIPAR measurements that fell into one AVIRIS pixel (post-georegistration) were averaged to create a single fIPAR value to be compared directly with the single image value for that pixel.

Landscape measurements

Total fIPAR measurements (below understory) were made for each of the 181 sites from all 8 landscapes. Four to six replicates of measured fIPAR were averaged to yield a single fIPAR value per site. Since the PAR measurements were made during two separate time periods (July 7-10 and August 9-10) and were to be compared with AVIRIS imagery acquired on August 8, the data were organized into both the mean of the two months as well as the separate month of August. In the following analysis, the average of the July-August fIPAR data was used.

2.3 Image processing

AVIRIS imagery was acquired on 8 August 1993. Atmospheric effects within the image were removed with a solar and atmospheric model (ATREM, Gao et al. 1993). Noise within the image was reduced by applying a maximum noise fraction (MNF) transformation (Green et al. 1988). Georegistration was focused on the pixels running the length of the transects. Aerial photography was incorporated into the registration procedure for highly accurate registration and location of ground fIPAR measurements (Kennedy and Wessman *in review*). The RMS error of prediction for procedure was less than 0.8 meters.

ENVI (Environment for Visualizing Images, Research Systems Inc.) was used to calculate values of NDVI and SAVI. NDVI was calculated according to NDVI = (NIR - R) / (NIR + R) where NIR refers to the reflectance at 0.83 μm and R refers to the reflectance at 0.68 μm. SAVI was calculated according to SAVI = ((NIR - R) / (NIR + R + L)) (1 + L) where L (the soil-adjustment factor) = 0.5.

A spectral mixture model (Bateson and Curtiss 1996) was used to produce 5 endmembers characteristic of the La Copita ranch. Each pixel was assumed to consist of combinations of a short-stature "grass" endmember, a taller stature "shrub" endmember, soil, shade, and litter. It was assumed that the grass endmember described the herbaceous component and that the "shrub" endmember described the taller stature woody vegetation dominating the drainages and groves. We used the landscape-unit fIPAR/LAI data from Landscapes 1 through 8 to determine median values for the herbaceous zone (0.389/1.135) and the grove/drainage class (0.928/3.415). Assuming fIPAR values of the litter, shade and soil endmembers to be zero, SMA-weighted values of fIPAR and LAI were then calculated according to:

weighted fIPAR = (grass fraction * herb median fIPAR) + (shrub fraction * grove/drainage median fIPAR)

weighted LAI = (grass fraction * herb median LAI) + (shrub fraction * grove/drainage median LAI).

Pixel-scale fIPAR, calculated from geo-registered and aggregated field measurements, were then regressed against (1) the NDVI and SAVI values and (2) SMA-weighted median values for those same pixels.

3. RESULTS AND DISCUSSION

Figure 1 shows the distribution of the ground measurements of fIPAR and LAI split by vegetation type. As expected, the greatest fraction of light is intercepted by the woody landscape components such as the drainages, groves, mottes, and woody playa sites. The least amount of light is intercepted in the herbaceous zone, with slightly more interception in the burned herbaceous zone where grasses are regenerating rapidly due to disturbance, and yet more interception in the herbaceous playa which is characterized by a tall thick grass cover. This trend is mimicked in the LAI data with the exception of a greater data spread in the playa sites.

Five endmembers were derived from the SMA (Figure 2). The grass endmember was characterized by a higher NIR plateau than the woody vegetation. Litter was distinguished from soil largely based on lignin-cellulose features near 1.7 and 2.3 μm.

All regressions of the transect fIPAR data with the remote sensing data were significant (Table 1). In fact, the correlation coefficients were all very similar. However, the intercept and slope values were significantly different. Of all the relationships, only that of the SMA produced a slope not significantly different from 1.0; with a y-intercept of -0.02 , the SMA:fIPAR regression line was essentially the 1:1 line. This suggests that the SMA model approximates the true field values well and that field data must be incorporated into any model if the absolute field values are to be adequately predicted.

Table 1. Regression coefficients of field data and remotely sensed values.

	y-intercept	slope	R2	p
NDVI	-0.54	2.29	0.77	<0.0001
SAVI	-0.82	5.08	0.74	<0.0001
SMA-weighted landcape units	-0.02	1.02	0.74	<0.0001

Given the goal of predicting absolute values of ground fIPAR rather than merely describing relative variance across the landscape, the predictor equations developed using the ground transect data set were used to predict fIPAR values for the entire La Copita Ranch:

(a) Field fIPAR = -0.54 + 2.29 * NDVI
(b) Field fIPAR = -0.02 + 1.02 * SMA-weighted scaled fIPAR

The ranges of the fIPAR values derived from (a) and (b) models for the ranch were compared to the ranges established using the SMA model on the transects (Figure 3). Note that the relative distribution of mean fIPAR values derived from the NDVI model for the different landscape units appears somewhat similar to the SMA, but the range of absolute values differ substantially within and across groups.

4. CONCLUSIONS

It has been shown that field measures of fIPAR discriminate well between different vegetation functional groups at the La Copita Research Area in South Texas. Woody, herbaceous and mixed sites intercept significantly different amounts of PAR. This suggests that variation in photosynthetic rates will be significant in highly mixed landscapes and a lack of sensitivity to the green vegetation in mixed conditions may impair large-scale fIPAR estimates.

Comparison of our SMA model with traditional remote sensing indices such as NDVI showed that both measures perform equally well in predicting relative variance in field fIPAR data at the transect scale. In other words, there is no significant difference between the results of simple linear regression between field fIPAR values and NDVI values/SMA model values. We have shown that, while NDVI is strongly correlated to field fIPAR values, in its unscaled form it cannot shed light on the absolute values of field fIPAR. Moreover, NDVI values across the entire heterogeneous region show a wider variation than those derived from the SMA model. Given the close approximation of the SMA model to the actual fIPAR values and the fact that the scaling of the SMA was accomplished using the measured range in fIPAR values for several landscapes, it is possible that the NDVI values are influenced by the varying (sub-pixel) structure of the landscape across the ranch.

The SMA model allows for sub-pixel identification of relative fractions of photosynthesizing endmembers, which can then be weighted and scaled using spot field measurements obtained thoughout the study area. In fact, identification and measurement of landscape units may be the best sampling strategy in heterogeneous environments. In combination with spectral mixture analysis, which gives the abundance of those units at sub-pixel scales, appropriate scaling of the actual values of functional properties can be made without confounding influences from litter and soil.

5. ACKNOWLEDGMENTS

This work was supported by NASA Earth Observing System (EOS) Interdisciplinary Science Grant NAGW-2662.

6. REFERENCES

Archer, S. 1990. Development and stability of grass/woody mosaics in a subtropical savanna parkland, Texas, U.S.A. *Journal of Biogeography* 17: 453-462.

Bateson, C.A. and B. Curtiss. 1996. A method for manual endmember selection and spectral unmixing. *Remote Sensing of Environment*. 55:229-243.

Brown, D. E. (ed.). 1982. Biotic communities of the American southwest-United States and Mexico. *Desert Plants* 4: 101-106.

Gamon, J. A., C. B. Field, D. A. Roberts, S. L. Ustin and R. Valentini, 1993. Functional patterns in an annual grassland during an AVIRIS overflight. *Remote Sensing of Environment*, 44: 239-253.

Gao, B.-C., K.B. Heidebrecht and A.F.H. Goetz. 1993. Derivation of scaled surface reflectance from AVIRIS data. *Remote Sensing of Environment* 44(2):165-178.

Green, A.A., M. Berman, P. Switzer, and M.D. Craig. 1988. A transformation for ordering multispectral data in terms of image quality with implications for noise removal. *IEEE Transactions on Geoscience and Remote Sensing* **26**(1):65-74.

Johnston, M. C., 1963. Past and present grasslands of southern Texas and northeastern Mexico. *Ecology* 44:456-466.

Kennedy, R.E. and C.A. Wessman. Vegetation indices and fIPAR in a structurally complex landscape. *Landscape Ecology* In review

McMahan, C. A., R. G. Frye, and K. L. Brown, 1984. The vegetation types of Texas. Texas Parks and Wildlife Dept., Austin, Tx.

Schofield, C. J. and E. H. Bucher, 1986. Industrial contributions to desertification in South America. *TREE* 1: 78-80.

Scifres, C. J. and B. H. Koerth, 1987. Climate, soils and vegetation of the La Copita Research Area. MP-1626, July 1987. The Texas Agricultural Experiment Station, The Texas A&M University System, College Station, Texas.

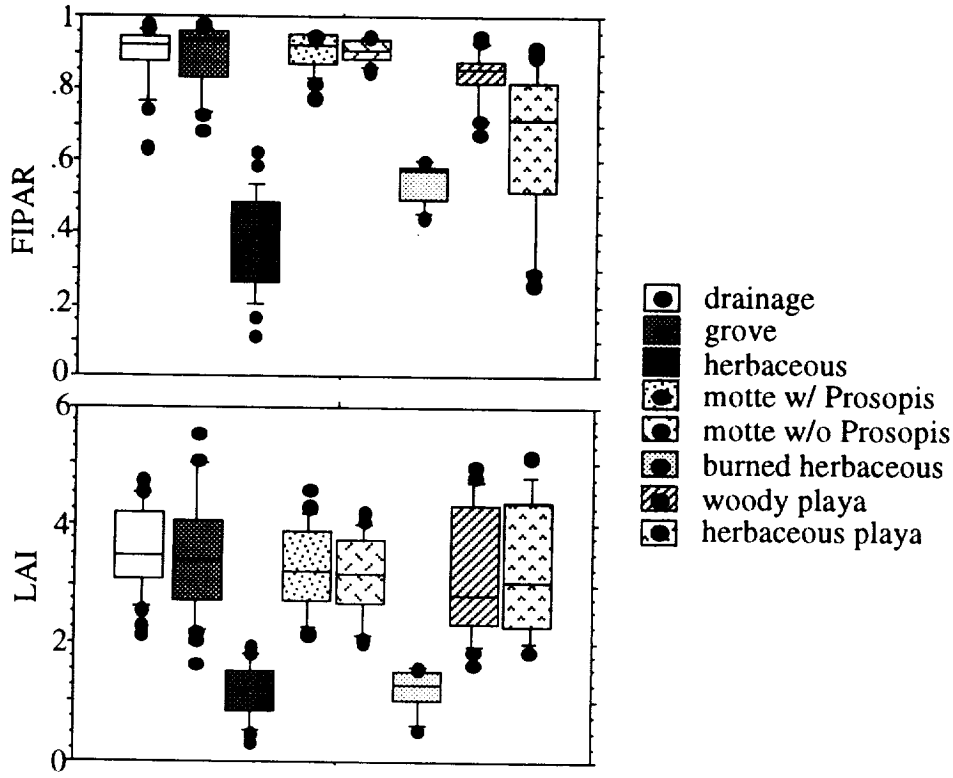

Figure 1. Distribution of ground-measured FIPAR and LAI showing the 10th, 25th, 50th, 75th, and 90th percentiles.

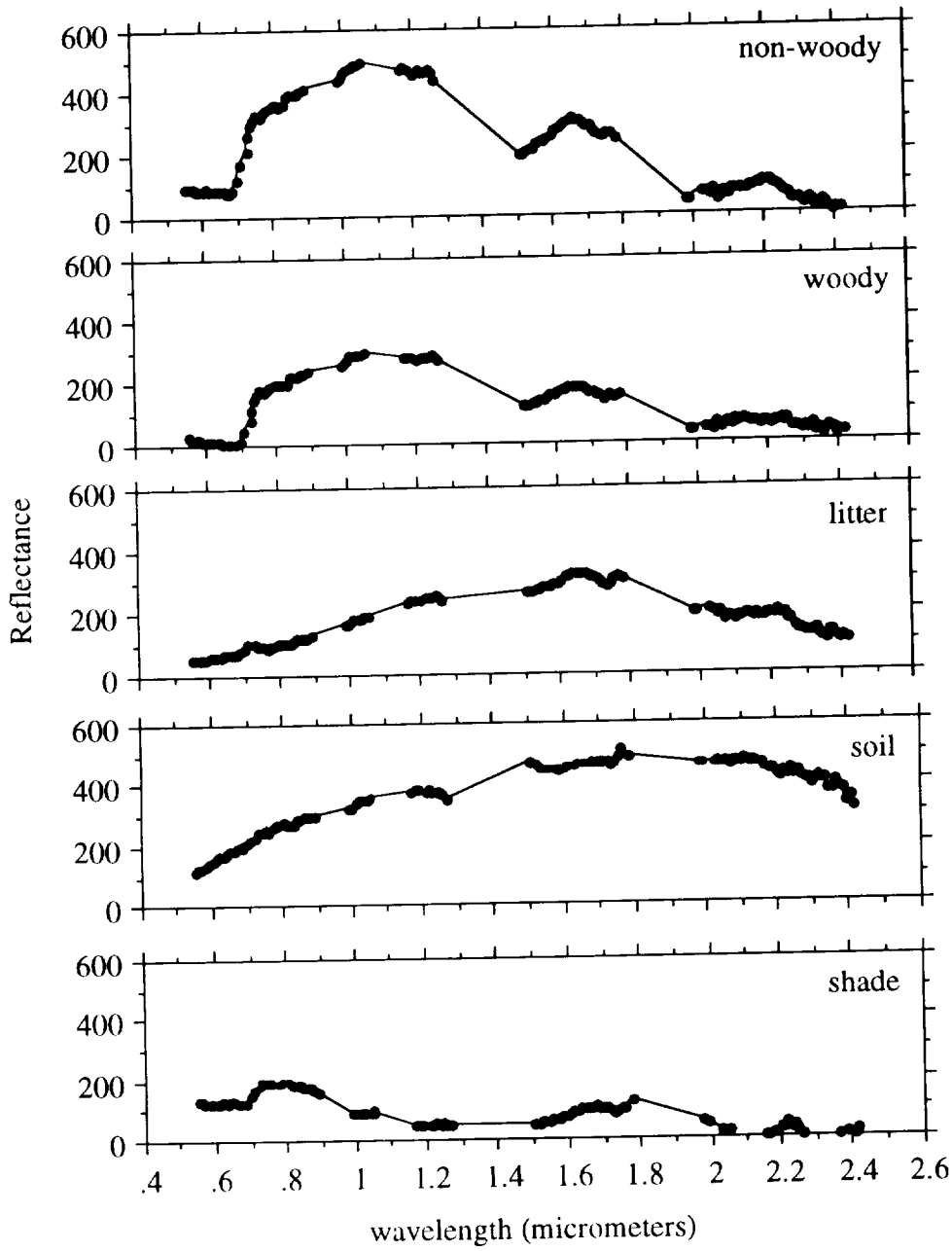

Figure 2. Five endmembers resulting from spectral unmixing. The breaks in the data are indicative of bad bands in the AVIRIS imagery.

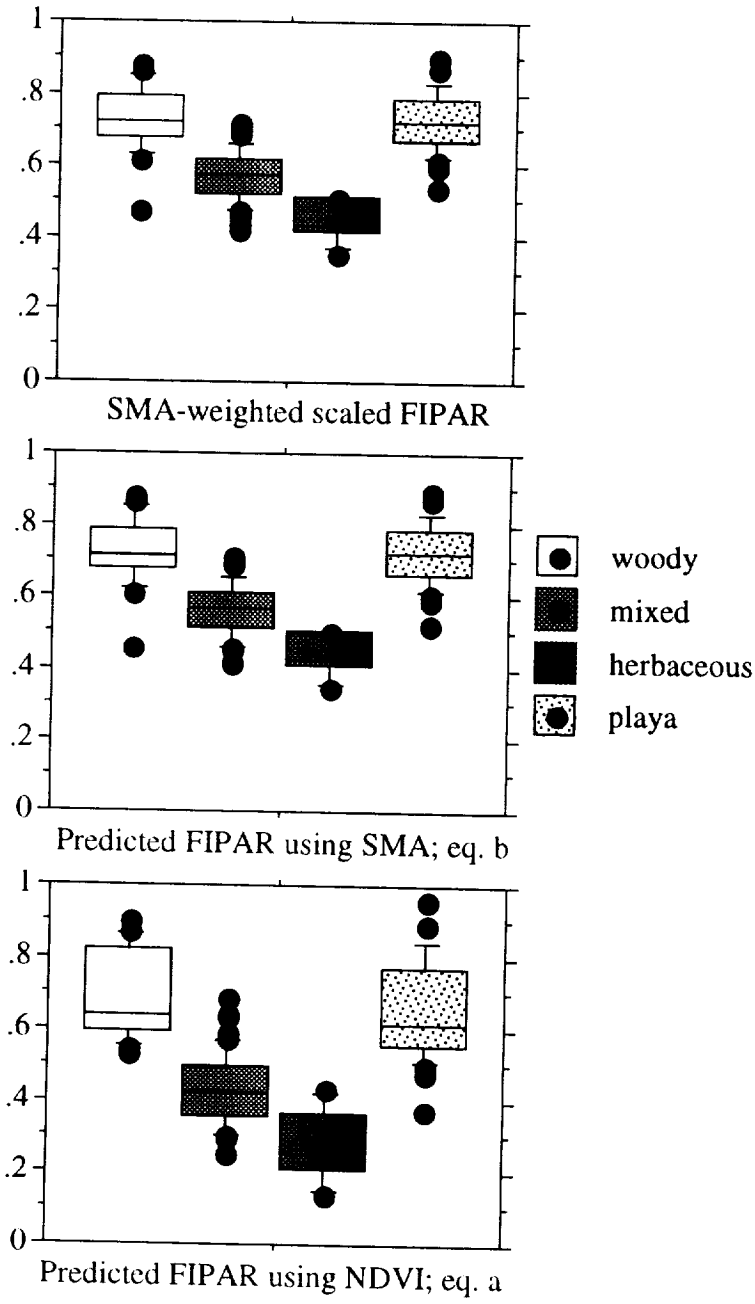

Figure 3. Distribution of fIPAR values for: (a) the SMA-weighted scaled fIPAR for 4 transects in 2 landscapes, and for the entire La Copita ranch derived from the (b) SMA and (c)NDVI models.

REPORT DOCUMENTATION PAGE

Form Approved
OMB No. 0704-0188

1. AGENCY USE ONLY *(Leave blank)*	2. REPORT DATE	3. REPORT TYPE AND DATES COVERED
	12/19/98	Final -- Jan. 12-16, 1998

4. TITLE AND SUBTITLE
Summaries of the Seventh JPL Airborne Earth Science Workshop January 12-16, 1998, Volume 1. AVIRIS Workshop

5. FUNDING NUMBERS
C - NAS7-1407

060132-A.1.74061

6. AUTHOR(S)
Robert O. Green, Editor

7. PERFORMING ORGANIZATION NAME(S) AND ADDRESS(ES)
Jet Propulsion Laboratory
California Institute of Technology
4800 Oak Grove Drive
Pasadena, CA 91109-8099

8. PERFORMING ORGANIZATION REPORT NUMBER
JPL Publication 97-21, Vol. 1

9. SPONSORING / MONITORING AGENCY NAME(S) AND ADDRESS(ES)
National Aeronautics and Space Administration
Washington, DC 20546-0001

10. SPONSORING / MONITORING AGENCY REPORT NUMBER
RF295-BP62181014000

11. SUPPLEMENTARY NOTES

12a. DISTRIBUTION / AVAILABILITY STATEMENT

12b. DISTRIBUTION CODE

13. ABSTRACT *(Maximum 200 words)*

This publication contains the summaries for the Seventh JPL Airborne Earth Science Workshop, held in Pasadena, California, on January 12-16, 1998. The main workshop is divided into three smaller workshops, and each workshop has a volume as follows:

1. Airborne Visible/Infrared Imaging Spectrometer (AVIRIS) Workshop
2. Airborne Synthetic Aperture Radar (AIRSAR) Workshop
3. Thermal Infrared Multispectral Scanner (TIMS) Workshop

14. SUBJECT TERMS
earth sciences, imaging spectrometers, infrared imagery, infrared spectrometers, multispectral scanners

15. NUMBER OF PAGES
435

16. PRICE CODE

17. SECURITY CLASSIFICATION OF REPORT	18. SECURITY CLASSIFICATION OF THIS PAGE	19. SECURITY CLASSIFICATION OF ABSTRACT	20. LIMITATION OF ABSTRACT
Unclassified	Unclassified	Unclassified	Unlimited